Les grands lacs périalpins : archives du fonctionnement de la zone critique

William Rapuc

UNIVERSITÉ SAVOIE MONT BLANC

THÈSE

Pour obtenir le grade de

DOCTEUR DE L'UNIVERSITÉ SAVOIE MONT BLANC

Spécialité : **Sciences de la Terre, de l'Univers, et de l'Environnement**

Arrêté ministériel : 25 Mai 2016

Présentée par

William RAPUC

Thèse dirigée par **Fabien ARNAUD (EDYTEM)**
codirigée par **Pierre SABATIER (EDYTEM)** et
co-encadrée par **Jérôme GAILLARDET (IPGP)**

préparée au sein du **Laboratoire Environnements, Dynamiques et Territoires de la Montagne (EDYTEM) – UMR 5204**
dans **l'École Doctorale Sciences et Ingénierie des Systèmes de l'Environnement et des Organisations (SISEO)**

Les grands lacs périalpins : archives du fonctionnement de la zone critique

Thèse soutenue publiquement le **11 Juin 2021**,
devant le jury composé de :

Mme. Marie REVEL
Maîtresse de conférences, Université Côte d'Azur, GEOAZUR, Rapportrice
M. Christophe COLIN
Professeur des Universités, Université Paris Saclay, GEOPS, Rapporteur
Mme. Stéphanie GIRARDCLOS
Maîtresse d'enseignement et de recherche, Université de Genève, Earth & Environmental Sciences, Examinatrice
M. Sébastien BERTRAND
Assistant Professor, Universiteit Gent, Department of Geology, Examinateur
M. Matthias HINDERER
Professor, Technische Universität Darmstad, Institut für Angewandte Geowissenschaften, Examinateur
M. Julien BOUCHEZ
Chargé de recherche, Institut de Physique du Globe de Paris, Invité

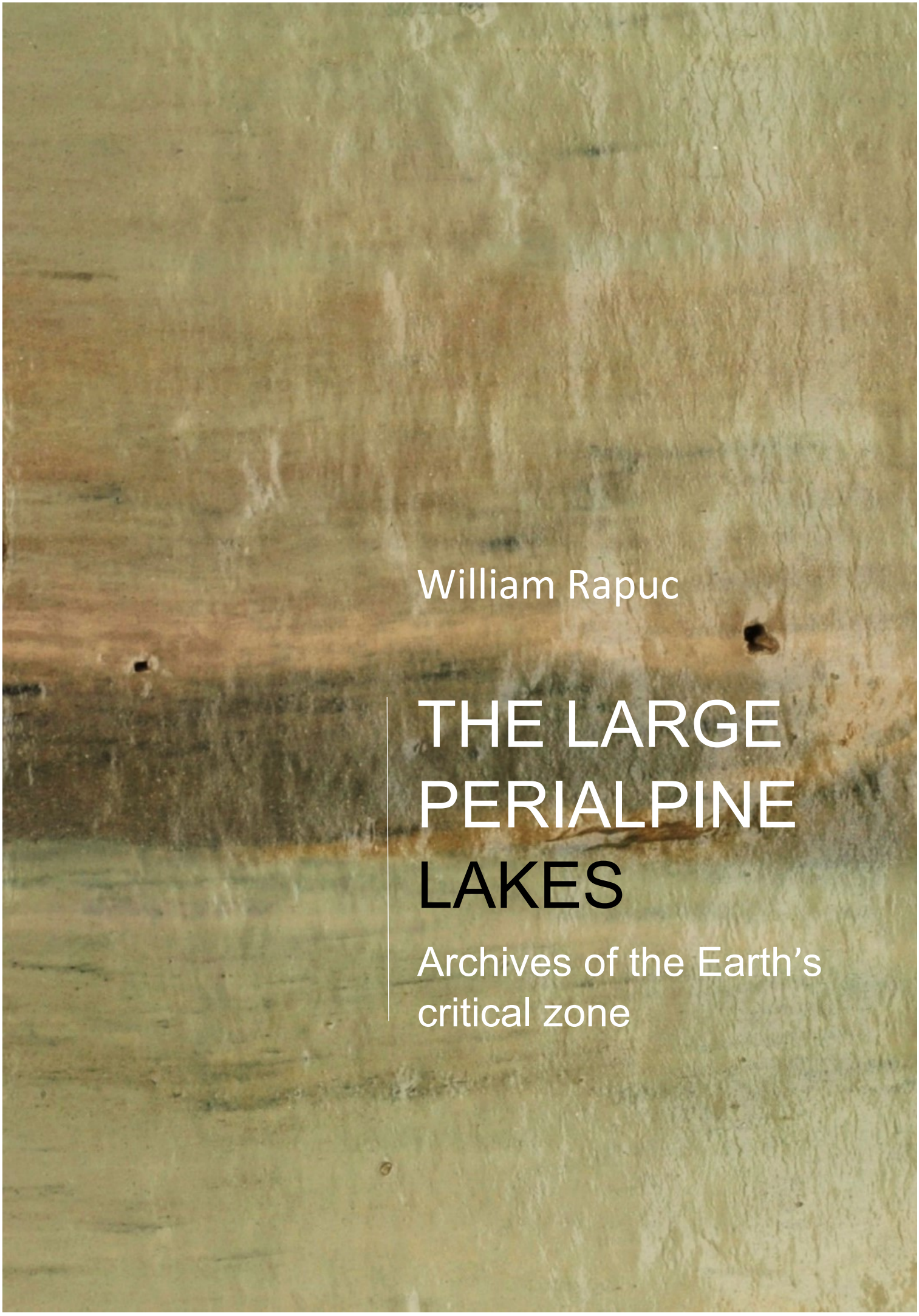

William Rapuc

THE LARGE PERIALPINE LAKES

Archives of the Earth's critical zone

A mon père,

La Terre est un livre sublime que nous ne devons pas nous lasser de lire

Camille Flammarion

Remerciements

Quelle belle tribune que voilà, une page vierge qui sera lue, sans doute même la plus lue de ce manuscrit… une page à remplir d'un texte qui peut pour une fois être lyrique si son auteur le souhaite. Je ne vous cache pas qu'il peut s'agir d'un soulagement certain pour qui n'a eu de cesse de respecter les codes des publications scientifiques jusqu'alors. Je m'excuse par avance auprès des lectrices et lecteurs qui s'attendraient ici à des remerciements synthétiques, il n'en sera rien…

Si je devais résumer les trois ans et demi qui viennent de s'écouler, et trouver un nouveau titre à cette thèse, je pense que « La vie rêvée de William Rapuc » conviendrait plutôt. Bien qu'il y ait déjà un résumé scientifique à ce manuscrit, j'espère que ce chapitre fera office de résumé plus personnel. Toutefois, il serait trop facile de réduire cette thèse, et le doctorat en général, à une période de bonheur sans fin. Une thèse, c'est aussi beaucoup d'incertitudes. Encore en ce moment, à l'heure avancée où j'écris ces quelques lignes, qui pourtant seront « presque » les dernières de ce manuscrit, je doute d'arriver à le finir à temps… Une thèse c'est aussi beaucoup de questionnements, une remise en question régulière de la valeur du travail réalisé, la peur de l'après, qui, tenace, ne m'a finalement jamais abandonné. Comment ne pas avoir peur du lendemain quand on sait ce que l'on quitte et ce que l'on perd. Et puis une thèse, comme tout travail de recherche j'en ai peur, peut aussi être sans fin. Heureusement, le doctorant n'est que rarement seul, et certains êtres chers l'aident volontiers à y mettre un point final.

En effet, si la thèse finit un jour, c'est bien grâce aux soutiens, toujours nombreux, qui jalonnent le long sentier doctoral. Il me faut donc commencer par un mot de Jérôme Poulenard qui, dès le début de ma thèse m'a rappelé « qu'une thèse ne se fait pas seul ». Par conséquent, j'aimerais ici, comme il est de coutume, remercier l'ensemble des personnes qui ont fait de ce travail ce qu'il est mais aussi et surtout, qui m'ont permis de vivre un rêve éveillé depuis septembre 2017. Je ferai mon possible pour n'oublier personne, mais par avance pardon à celles et ceux qui ne feraient pas partie de cette liste, il est des moments de la nuit où ma mémoire n'est plus ce qu'elle a été et bien que ces lignes demeurent importantes, j'ai toujours trouvé que les instants partagés avec vous ont bien plus de valeurs que les mots…

Merci tout d'abord aux membres du jury qui ont accepté de lire, de rapporter et d'examiner ce travail. Merci à Marie Revel, Christophe Colin, Stéphanie Girardclos, Sébastien Bertrand, et Matthias Hinderer. Merci pour le temps accordé à la lecture et à l'intérêt porté à ce travail.

S'il en est un parmi les autres que je me dois de remercier, et par qui je dois commencer, c'est bien toi Pierre. Sans toi, il est évident que je n'en serais pas là. Je pense que je me souviendrai toute ma vie de ce cours de géochimie de licence où, arrivé en retard d'une heure, j'ai eu le « courage » de venir te demander un stage. Je me souviendrai aussi de ce trajet vers les Corbières il y a 8 ans, où pour la première fois nous avons évoqué ensemble l'idée d'une thèse. Depuis ce moment je crois que je te dois, à peu de choses près, l'ensemble de mon parcours scientifique, de mes choix d'orientation, de ma culture scientifique, de ma capacité de rédaction et j'en passe. Merci de m'avoir initié à la sédimentologie et à la géochimie, d'avoir, à toute heure, répondu à mes questions, souvent nombreuses au début, et calmé mes doutes, et merci de m'avoir toujours fourni une quantité invraisemblable d'opportunités. Je ne pense pas me tromper en écrivant ici que tu as fait de moi le chercheur que j'espérais devenir.

Fabien, si tu arrives en second c'est bien qu'il fallait un premier. Je crois que si je dois à Pierre des qualités scientifique, à toi je dois ma passion pour le terrain, l'envie quasi-irrépressible d'aller carotter un lac de plus, une carotte de plus, un mètre de plus, au point parfois de prélever plus que de raison (mais ce n'est pas le sujet ici n'est-ce pas ?!) ! Merci d'avoir pensé à moi pour ce magnifique projet de recherche, dans la continuité des tiens. Merci d'avoir su être présent, malgré tes responsabilités, dans les moments où j'en ai eu besoin. Merci d'avoir pris le temps pour ces longues, peut-être trop longues, heures de discussions scientifiques. Si j'hérite de Pierre une certaine productivité, de toi j'espère garder les réflexions et l'envie de toujours aller plus loin dans la compréhension des processus, de lever le doute sur chaque détail, de m'interroger sur chaque point. Merci aussi pour ces moments de partage qui, je le sais, sont rares entre un doctorant et son directeur. Je mesure donc ma chance. Je pense ici à nos sorties skis, aux bières bues sur le terrain, au bar, ou chez toi. Reste en forme pour l'hiver prochain et que ta passion de la glisse ne t'abandonne jamais !

Enfin, merci à vous deux de m'avoir considéré comme un jeune collègue, d'avoir su me motiver tout au long de ces années, de m'avoir souvent laissé libre tout en entretenant une relation toujours constructive et bienveillante.

Jérôme, merci pour ton accueil à l'IPGP. Sans toi et mes nombreux séjours à Paris, cette thèse n'aurait pas pu aboutir et serait restée à l'état de joli projet. Merci de m'avoir intégré à cette équipe qui s'est avérée formidable. J'aurai bien sûr aimé échanger plus avec toi, il aurait sans doute fallu pour cela que je sois davantage présent. Mais je sais que nous aurons l'occasion de discuter plus amplement dans un futur proche. Merci d'avoir accepté de m'encadrer, merci pour tes relectures et tes conseils, pour être venu me voir à Chambéry et avoir écopé la barque, et merci pour tes cours de cartographie !

J'ai eu la chance de ne pas être encadré par trois, mais bien par quatre chercheurs pendant cette thèse. Julien, merci de m'avoir consacré autant de temps lors de mes séjours à l'IPG. Je tiens à te remercier pour tout le temps que tu as passé à me former en salle blanche, à m'encadrer et à mesurer ces échantillons au spectromètre, à m'écouter et à m'aider dans mes réflexions et les traitements de données à toute heure. J'espère avoir l'opportunité de continuer à travailler avec toi dans le futur et je te souhaite beaucoup de réussite dans tes nombreux projets !

Si pendant cette thèse j'ai eu l'impression de faire partie d'une famille, c'est essentiellement grâce à l'ensemble des personnes que j'ai pu côtoyer.

Je pense en premier lieu aux membres du laboratoire EDYTEM, des stagiaires aux retraités (eh oui Gilles, même à toi !), en passant par tous les doctorants et permanents de ce laboratoire extraordinaire. Maintenant je peux bien vous l'avouer, je n'aurai fait de thèse ailleurs qu'ici pour rien au monde. Au sein de cette grande famille, une équipe se détache, celle des archives. Merci à Fayçal Soufi, Jérôme Poulenard, Erwan Messager, Charline Giguet-Covex, Anne-Lise Develle-Vincent, Cécile Pignol et à toutes les autres personnes toujours disponibles. Grâce à vous je n'ai jamais eu peur de poser une question, ou d'exposer mon travail, bien que souvent très préliminaire.

Fayçal, c'est avec toi je pense que j'ai passé le plus de temps au laboratoire. Impossible de te résumer ici, tu as égayé toutes mes heures passées au labo de sédimento. Merci pour ton humour, ton écoute, nos blagues dont celles de l'aquarium. J'ai bien essayé de retarder au maximum ma fin de thèse mais il faut bien finir un jour. Je te souhaite une bonne fin de carrière et une excellente retraite !

Anne-Lise, ou maman, j'hésite, merci de m'avoir pris sous ton aile, de m'avoir formé depuis tout petit aux joies des mesures XRF. Je ne compte plus le temps que l'on a pu passer à parler de Simone ou de

Manganèse ! J'ai adoré nos discussions, sans doute parce que tu me connais mieux que moi-même, et le temps que l'on a pu partager au labo !

Charline, j'ai vraiment apprécié notre séjour à Stockholm et nos sorties sur le terrain que ce soit en Maurienne, ou dans la vallée du Rhône. Oui je dois avouer que tu avais raison, on allait planter la voiture en s'avançant sur ce chemin… C'était plus fort que moi.

Erwan, Jérôme, merci pour votre gentillesse et votre temps, pour ces discussions scientifiques mais pas que. J'espère pouvoir passer encore beaucoup de temps avec vous sur le terrain. Et merci d'être passé me voir en Ubaye !

Bien que tu ne sois plus vraiment ici, merci à toi Bruno. Tu as un peu été mon premier encadrant. Merci de m'avoir emmené pour la première fois sur le terrain faire ce joli carottage dans le Queyras. Merci à toi de m'avoir impliqué dans tous ces projets. J'espère pouvoir continuer à travailler avec toi et surtout à monter toujours plus haut notre VTT.

Parmi les gens avec qui j'ai travaillé, une place spéciale est réservée à mon cher Christian Crouzet. Notre relation n'avait sans doute pas pris le meilleur départ possible quand j'étais étudiant, sans doute que la structurale n'était pas faite pour moi. Mais je dois dire que ça a été un plaisir de travailler avec toi sur ces nombreux projets ! A bientôt, les skis aux pieds !

Merci aussi à tous les doctorants et stagiaires qui ont fait partie de cette équipe. Ce fut un plaisir de travailler et d'échanger avec vous.

Une pensée émue pour toute l'équipe de sportifs qui a animé mes midis, soirées, weekend et autre : Ludo, Fabien (quand tu t'es joint à nous), Jacques, Florence, Manu, Camille et tous les autres. Qu'est-ce qu'on a ri !

Mais EDYTEM, c'est aussi et surtout un laboratoire pluridisciplinaire ou mutlidisciplinaire ? Bref, un laboratoire où l'on peut parler aussi bien de pollution de l'air, que de sédiments de lac ou bien même de droits d'accès aux rives de ces mêmes lacs… Merci à tous pour le temps passé avec vous, à parler de sciences, à boire des bières, à organiser ou faire des sorties ski. Merci pour votre écoute et pour votre accueil chaleureux ! Merci aussi à Carole et Christine, pour avoir toujours trouvé le temps de m'aider dans toutes mes démarches administratives. Je souhaite profondément que l'esprit si particulier qui anime ce laboratoire ne le quitte jamais !

Vous êtes tellement nombreux que je ne sais par où, par qui ni même comment commencer… J'adresse à tous les doctorants du laboratoire un immense merci pour les moments partagés. Merci aux anciens qui étaient déjà partis ou allaient le faire quand je suis arrivé : je pense à Manon, Laurent et Géraldine. Merci à ceux qui étaient là quand je suis arrivé, ça a été un grand plaisir de partager tout ce temps avec vous. Anne, merci pour ton immense gentillesse, pour ton amitié et ton écoute, pour nos belles sorties en montagne, à bientôt en Ubaye ou dans le Beaufortain. Merci à toi Claire, encore désolé pour la sortie vélo qui t'a été fatale, et merci de m'avoir proposé ton aide pour la mise en page. Merci Céline pour toutes ces balades, en ski de fond ou autre. Je suis heureux que tu aies trouvé ton bonheur dans le Champsaur. Merci à vous, Madame Nikolli, quelle chance que j'ai d'être compté parmi vos amis, merci pour tous ces repas, ces sorties, ces discussions qui en appellent d'autres à chaque fois. Je n'ai pas de doute sur le fait que tu seras vite recrutée ni sur le fait que tes autres projets seront couverts de succès. Jacques, merci pour ces belles sorties ski et vélo, merci de m'avoir proposé toutes ces missions de terrain et d'avoir partagé toutes ces bières aussi. Enfin, merci à toi PA, je suis fier de te compter parmi mes amis, j'ai hâte de pouvoir à nouveau skier avec toi, désolé d'avoir dû rédiger cet hiver, ça ne sera pas tout

le temps comme ça. Merci pour ton écoute et ton soutien. Merci aussi à Chiara, Xavi, Grégoire, Thérèse et à celles et ceux que j'oublie sans doute…

Un merci particulier à celles et ceux qui sont arrivés en même temps que moi, nous avons connu trois ans particuliers que nous avons traversés ensemble. Même s'il y a eu des moments délicats pour chacun d'entre nous je suis heureux de vous avoir rencontrés. Un grand merci donc à Ana, Léna, Claire B., Sophie-Anne, Guilhem et Tim. Léna, merci de m'avoir toujours accueilli chez toi quand j'en ai eu besoin, pour tous ces repas, ces discussions, ces sorties. Je te souhaite beaucoup de courage pour la fin de ta rédaction mais je sais que tu t'en sors et t'en sortiras à merveille.

Merci aussi à Matthieu, Norine, Maude, Manu et Hege qui sont maintenant, pour la plupart d'entre eux sur le point de finir. J'ai été heureux de partager ces soirées et sorties avec vous et je vous souhaite une excellente continuation dans votre thèse et en dehors. Merci aussi aux plus « jeunes », qui ont apporté un nouvel élan et une belle dynamique à ce grand groupe de doctorants, merci à Tanguy, Stéphane, Agathe, Julia D., Floriane, Louis, Mathilde, Jules, Julien, Aurélie, Yoann, Maëva, Ella, Anne-Sophie, Léo, Lise, Charlotte. J'espère n'oublier personne. Merci aussi à tous les stagiaires, assistants et invités qui sont venus grossir les rangs du laboratoire pendant mon séjour, merci à Maëva, Antoine, Alexandre, Alexandre, et à tous les autres.

Cette thèse m'aura permis de vivre mille vies, entre différents laboratoires, villes ou pays. Mais s'il est un lieu parmi les autres où j'ai passé du temps, c'est bien l'IPGP et Paris. J'ai d'abord eu du mal à m'intégrer, c'est vrai. Sans doute à cause de mon manque d'attirance bien visible pour notre chère capitale. J'espère que vous ne m'en avez pas trop tenu rigueur, vous avez été formidables dans votre accueil, et ça a été un réel honneur de travailler et d'échanger avec vous tous. Merci à tous les membres de l'équipe de G2E et autres personnes que j'ai rencontré : Laëticia, Pascale, Delphine, Barth, Bibi, Catherine, Eric, Jean-Séb, Sylvain, Pamela, Nicole, Quentin, Laetitia, Paco, Alida, et tous les autres pour votre accueil. Je me dois aussi de remercier plus particulièrement deux autres personnes.

Damien, je ne te remercierai jamais assez pour le temps que tu as passé avec moi et sans moi derrière le spectro, à essayer de faire en sorte que l'on arrive enfin à avoir des données de lithium correctes. Merci pour ces discussions aussi, pour ton accueil, les blagues, les bières, les (ou plutôt la) sortie(s) de course à pied. Je te souhaite de tout cœur de t'en remettre et je t'envoie tout mon courage !

Matthieu, merci pour ton accueil, ta gentillesse, les nombreux repas et bières partagées. Heureusement que tu étais là pendant les nombreuses soirées passées à travailler tard, voire trop tard souvent. C'était un plaisir de travailler avec toi !

Durant cette thèse, j'ai eu le plaisir de passer énormément de temps sur le terrain, pour aider les autres en montagne, ou pour carotter une fois de plus. Mais j'ai aussi eu la chance d'y aller régulièrement dans le cadre de ma thèse. J'aimerais donc remercier toutes les personnes qui m'ont proposé une sortie terrain en montagne ou ailleurs, mais aussi et surtout celles et ceux qui ont pris de leur temps pour m'aider au cours de mes missions, souvent longues et physiques. Un grand merci tout d'abord à l'ensemble de l'équipe du C2FN, Laurent, Alain et Fred. Votre aide sur les différentes missions a été la clé de la réussite de celles-ci. Merci pour ce temps passé en Italie notamment, il restera pour longtemps dans ma mémoire ! Merci aussi à toi Uli. Depuis ce séjour en Slovénie, jusqu'à la mission d'Iseo. Merci pour ces longues discussions et ses réflexions enrichissantes. Merci Edouard pour ton temps et ta patience, pour tes repas gastronomiques après de longues journées de travail, j'espère te revoir bientôt. Merci Andrea de m'avoir accueilli à Milan, m'avoir guidé dans les nombreuses démarches administratives et m'avoir fait découvrir tous ces « agri-turismo » !

Je me dois aussi de remercier Flavio Anselmetti d'être venu réaliser les profils sismiques à Iseo. Merci aussi de m'avoir accueilli plusieurs fois à Berne, pour ces sorties de vélo ou ces baignades dans l'Aare ! J'espère pouvoir revenir rouler ou skier bientôt avec toi !

Merci à Qi de m'avoir accompagné en Italie à peine sorti de l'aéroport en provenance de Chine. Ton efficacité sur le terrain, ta gentillesse et ta bonne humeur sont légendaires ! I hope to see you soon!

Merci à tous les membres de l'Association des Carabinieri du lac Iseo qui ont pris le temps de nous aider sur le terrain et qui nous ont gentiment prêté leur navette pour réaliser la sismique sur le lac. Merci pour votre temps. Repose en paix Cesare !

Merci Ana ! Tout n'a pas été rose c'est sûr, mais c'est ça aussi la vie. Je garderai toujours à l'esprit notre balade en Italie, entre Iseo et la plaine du Pô, entre les spots de campings et les hôtels découverts au dernier moment, entre l'escalade et les baignades, les arrestations et les rigolades, mais aussi les entretiens et l'échantillonnage, parce qu'on y allait quand même pour bosser. J'ai été heureux de passer tout ce temps avec toi, je n'oublierai jamais nos soirées et discussions interminables. Je te souhaite le meilleur en Slovénie ou ailleurs, et aussi mais surtout, énormément de bonheur !

Merci à tous les doctorants et personnels venus partager un moment sur les différentes missions de carottage, à toi Manu de m'avoir formé et accompagné sur la première mission « BTP » mais aussi pour avoir mis les skis de fond dans le coffre quand j'en avais besoin ! Merci à Bernard pour le pilotage de la plateforme, à Raphaël pour le coup de main avec les ancres, à Manon, Claire, Kévin, Maude, Matthieu, Kim, Alexandre, Mathilde, Erwan, Charline, Anne-Lise, Xiaqing et tous les autres que j'oublie, et bien sûr merci à toi Camille pour la baignade !

Une thèse, c'est aussi des échanges, des idées et de la rédaction. Sur ces points, je dois reconnaitre que j'ai eu la chance de tomber sur des collègues réceptifs et qui ont bien voulu travailler avec moi sur des projets qui pouvaient avoir l'air farfelu.

Speedy, Lil'Kév, Kévin, tu as tellement de surnoms que je ne sais plus lequel je dois utiliser. Je n'en reviens toujours pas qu'on ait pu travailler ensemble et finir ce joli projet. Merci pour ta patience, je ne sais plus combien de réunions j'ai raté car je m'amusais en montagne ou ailleurs, et le nombre de fois où tu as dû me relancer… J'espère que tu ne m'en veux pas trop, puis on a quand même fini par y arriver ! Je te souhaite de rapidement obtenir le travail de tes rêves, et aussi et surtout beaucoup de bonheur dans la vie qui t'attend.

Kim, avec toi aussi ça l'aura fait ! Je ne sais combien de soirées Jaja on a passées à travailler ensemble à une époque où le laboratoire ne fermait pas à double tour à 19h. Merci beaucoup pour ton aide en SIG, pour nos nombreuses discussions scientifiques et les bières qui vont avec, j'espère qu'il ne s'agissait que du début de notre collaboration, je suis sûr qu'un jour viendra où l'on travaillera ensemble dans le même laboratoire, le tien sans doute !

Je souhaite aussi remercier M. Petrucci, sans qui la géologie n'aurait été qu'une discipline parmi tant d'autres. Merci d'avoir su la rendre passionnante et de m'avoir montré la voie de l'Université. Je regrette seulement ne pas pouvoir vous faire lire ce manuscrit.

Me voilà arrivé au moment délicat où il me faut remercier des personnes, devenues des amis, avec qui j'ai partagé des moments incroyables et qui ont su être là pour moi tout au long de ce voyage.

Tout d'abord merci Florence pour toutes ces sorties à skis, ces nombreux couloirs, ces vols en parapente où l'espace d'un instant il ne reste plus que le silence et la beauté des lieux, merci pour ces moments simples mais toujours agréables.

Merci à toi Yves, pour ces sorties à vélo toujours plus ambitieuses, sans doute parfois trop. Pour ce Paris-Roubaix mémorable, et les soirées non moins mémorables qui ont émaillé ce séjour. Merci aussi d'avoir pris de ton temps, souvent, pour parler avec moi et pour me permettre d'avancer personnellement.

Dans cette aventure, je n'ai jamais été vraiment tout seul, notamment parce que j'ai rencontré Manu. Tu auras été là du début à la fin, un soutien infaillible dans les moments difficiles, que ce soit dès le début de ma thèse ou après, peu importe le sujet, il y avait toujours une oreille pour m'écouter. Merci aussi de m'avoir relancé sportivement, et de m'avoir laissé croire que j'avance plus vite que toi. Je te souhaite beaucoup de bonheur dans ta vie, avec ton fils et Claudia et j'espère avoir la chance de partager encore de belles aventures avec toi !

Camille, enfin, que dire, je crains que le silence de nos multiples sorties en montagne, toujours plus incroyables, résume bien mieux notre amitié que les mots que je pourrais employer. Je me contenterai donc de dire que si je devais donner une définition à l'amitié, c'est de toi dont je parlerais en premier.

Merci aussi à tous mes amis, lointains, de Savoie et d'Ubaye. Je ne vous remercierai jamais assez pour votre patience, mais ça y est, c'est fini, nous allons à nouveau pouvoir partager des moments ensemble sans que je parle de cette thèse à finir. Merci à vous Sylvain, Jessy, Eléa, Lucie, Alex, Emile, Babou, Julien. Pardon à tous les autres, qui n'auraient pas été cités, et avec qui j'ai hâte de passer du temps à nouveau.

Un immense merci à ma famille, mes oncles, ma tante, mes cousins que j'ai hâte de retrouver pour fêter ce diplôme que j'espère obtenir. Merci à ma sœur Macha qui a toujours su m'écouter et accepter mon caractère particulier. Je te souhaite de t'épanouir dans ta nouvelle vie. Ça y est, c'est fini, on va pouvoir s'amuser ! Je vous souhaite à toutes et tous le meilleur, vous avez été des soutiens incroyables, des sources d'inspirations inépuisables !

Merci à ma mère, eh oui on y vient ! D'abord merci pour ta relecture, ensuite pour ton écoute, je pense que tu maîtrises ce sujet de thèse au moins aussi bien que moi. Merci aussi pour ton soutien sans faille quand j'en ai eu besoin, pour tous nos échanges et pour tous les moments qu'il nous reste à partager. En bref, merci de m'avoir supporté…

Cette fois-ci c'est bon, c'est fini, je te le promets. Ce n'était sans doute pas le moment le plus évident à vivre, mais tu auras été parfaite, du début à la fin. Il faut parfois reconnaitre lorsque l'on est chanceux ! Je n'ose imaginer ce qu'aurait été la fin de cette rédaction sans toi et il en va de même pour le futur qui s'ouvre devant moi. Un immense merci à toi Julia !

Nous voilà arrivés à la fin de ce chapitre qu'a été ma thèse, merci à celles et ceux qui ont eu le courage de le lire et le partager en entier, vous ne devez finalement pas être si nombreux que ça,

« Le coq a chanté, nous avons bien ri, le temps a passé, le conte est fini »

Wiwi

Résumé de la thèse

Par ses effets sur la zone critique et sur les sociétés humaines avec notamment la détérioration des sols, des stocks de carbone dans les sols, et de la production alimentaire, l'érosion est devenue un sujet scientifique de première importance à l'échelle globale, et en particulier dans les zones de montagne où ses effets sont amplifiés. Les préoccupations croissantes concernant les effets délétères de l'érosion ont conduit l'Europe et les Nations Unies à classer l'érosion des sols comme l'une des principales menaces pour l'humanité et à appeler à une évaluation quantitative de la perte de sol sur de grandes échelles spatiales et temporelles. Ces évaluations permettront de mieux apprécier les effets relatifs des principaux facteurs de contrôle de l'érosion à court ou moyen terme que sont le climat (i.e., à travers les régimes de précipitations et les avancées et retraits des glaciers) et les activités humaines (à travers l'utilisation des terres et la gestion du couvert végétal).

Cette thèse propose de fournir des éléments quant à l'évaluation des taux d'érosion sur des périodes pluri-centennales à millénaires dans les Alpes Européennes à partir d'archives sédimentaires lacustres et d'interroger les effets des différents facteurs forçant l'érosion au cours du temps. Une analyse multi-indicateurs des séquences sédimentaires a été conduite sur deux grands lacs périalpins, ceux du Bourget (France) et d'Iseo (Italie), utilisées comme archives de l'érosion de la zone critique sur de grand bassin versants. Cette méthode est combinée à une approche « source-puits » offrant la possibilité de suivre les sources des apports de sédiments (sous-bassins versants et/ou types de roches) vers un puits (le lac) à travers le temps. Cette approche permet de démêler les impacts relatifs du climat et des activités humaines sur les taux d'érosion, à condition que chaque source de sédiments soit sensible à un type donné de forçage. La comparaison des taux d'érosion obtenu avec des modèles d'érosion actuelle ainsi qu'avec des données déjà disponibles permet la validation de nos résultats. Enfin, l'utilisation de modèles de mélanges issus de données de la composition isotopique des sédiments, permet l'obtention d'information quantitative quant à l'impact de ces différents facteurs forçant.

Cette thèse s'est tout d'abord intéressée à l'identification et la description des processus sédimentaires à l'œuvre dans les grands lacs périalpins, peu étudiés dans le passé du fait de la complexité que représentaient les prélèvements sédimentaires à ces profondeurs. Ces processus ont un impact direct sur la qualité du signal d'érosion enregistrés dans les lacs et leur interprétation correspond au premier verrou scientifique levé par ce travail. Une méthodologie d'identification semi-automatisée a ainsi été mise en place. Ici nous avons démontré que la disponibilité en sédiment dans le lac et son bassin versant avait un impact direct sur l'enregistrement des événements extrêmes comme les crues ou l'activité sismique.

Une fois les événements extrêmes identifiés et décrits, l'érosion continue des bassins versants a pu être étudiée. Au cours de l'Holocène, les taux d'érosion dans les Alpes augmentent progressivement à partir de 4.2 ka BP avant d'augmenter drastiquement aux alentours de la période Romaine et du Moyen-Age. Bien que l'évolution climatique régionale, avec une humidification progressive à partir de 4.2 ka BP, favorise l'augmentation des taux d'érosion, elle ne peut expliquer seule les taux mesurés. L'Homme, par la transformation des paysages et l'utilisation des sols, dû à l'agriculture, le pastoralisme et l'extraction de minerai notamment, a impacté la zone critique et induit une augmentation de l'érosion sans précédent au cours de l'Holocène.

Abstract

Erosion has become a scientific subject of prime importance worldwide due to its impacts on the Critical Zone and on human societies. Among other impacts, by destroying soils, erosion alters ecosystems services, the soils carbon stocks, and the food production. More than elsewhere the impacts of erosion are amplified in mountainous environment. Increasing concern about these deleterious effects have led Europe and the United Nations to rank soil erosion as one of the main threats to mankind, and to call for quantitative evaluation of soil loss over large spatial and long temporal scales. These evaluations imply notably to better assess the relative effects of the main factors controlling erosion. In particular, climate (e.g., through the precipitation regimes and glaciers advances and retreats) and human activities (through land-use and vegetation cover management) have been identified as major controls on long-term changes in erosion rates.

This work offers to provide (i) a quantitative evaluation of erosion rates over centennial to multi-millennial time scales in European Alps from lake sediments and (ii) to disentangle the impact of the different factors forcing the erosion. A multi-proxy analysis of the lake sediments was led on Lake Bourget (France) and Lake Iseo (Italia), two large peri-Alpine lakes, used as archives of the critical zone erosion over large catchments. The combination with a “source-to-sink” approach offers the possibility to track the sources of sediment inputs (sub-catchments and/or rock types) to a sink (e.g., a lake) through time, making it in turn possible to disentangle the relative impacts of climate and human activities upon erosion rates, provided that each sediment source is sensitive to a given type of forcing. The comparison between erosion rates measured with the results of current modelled rates and with data from the literature allows for the validation of our results. Then, quantitative information on the impact of each forcing factors on erosion are obtained from the use of mixing models from sediments isotopic composition.

First, this work focussed on the identification and the description of the sedimentary processes occurring in the deep and large peri-Alpine lakes, sparsely studied before, due to the high complexity of the coring at such depths. These processes have a direct impact on the quality of the erosion signal recorded in lake sediments. Interpretating these sedimentary processes was the first scientific problem resolved by this work. By doing so, a new semi-automatised methodology of identification of the event layers was also developed during this PhD. The sediment availability in lakes and catchments was identified as the first driver of extreme event (i.e., flood and earthquakes) recording in lake sediments.

Once the extreme events identified and described, the continuous erosion of the catchments could have been studied. During the Holocene, erosion rates in the Alpes progressively increase from 4.2 ka BP before rising drastically around the Roman Period and the Middle Ages. Regional climate evolution has favoured the increase of the erosion rates from 4.2 ka BP due to a progressive increase of the precipitation amounts but cannot explain alone the erosion rates measured. Human activities, by the transformation of the landscapes and the land use, due to agriculture, pastoralism and ore mining for instance, impacted the Critical Zone and led to an unprecedented increase of the erosion over the Holocene.

Table des matières

Table des illustrations

Partie I | Présentation Générale

CHAPITRE I | Introduction et contexte général

La Zone Critique (ZC) est définie comme la mince pellicule superficielle de la Terre à l'interface lithosphère – atmosphère – hydrosphère – biosphère (Fig. I-1; Anderson et al., 2007; Brantley et al., 2007; Chorover et al., 2007). Cette zone est critique car elle est le support de l'essentiel des formes de vie terrestres et car elle est le lieu de développement et des principaux enjeux des sociétés humaines (National Research Council, 2000). Le fonctionnement et les flux de matières qui circulent au sein de la ZC sont modifiés par trois forçages principaux : le climat, la géodynamique et les activités humaines (Fig. I-1). Ces forçages influencent la ZC en terme quantitatif (augmentation des flux particulaires minéral ou organique) mais également en terme qualitatif (modifications de cycles biogéochimiques et du paysage). L'émergence des sociétés humaines en tant que facteur géologique a modifié les équilibres subtils de la ZC, aboutissant à des perturbations majeures telles qu'une libération rapide et sans précédent du carbone de la lithosphère vers l'atmosphère (Crutzen, 2006) mais aussi à des perturbations des cycles de nutriments (Steffen et al., 2015), des modifications des cycles de l'érosion (Borrelli et al., 2020; Syvitski et al., 2005) et de l'altération (Amundson et al., 2007). Tous ces facteurs associés à l'augmentation actuelle de la pression anthropique sur la ZC représentent des menaces potentielles pour l'avenir de l'humanité. De nombreuses études visant à suivre dans le temps l'évolution de la ZC à partir d'instrument de mesures ont permis de mieux comprendre le fonctionnement et les interactions entre les différents compartiments et de mieux prévoir les impacts futurs résultant du climat, de la tectonique ou des activités humaines (Brantley et al., 2017; Gaillardet et al., 2018; Richter and Mobley, 2009). Cependant, étant donné qu'elle relie des processus à différentes échelles temporelles, et afin de mieux prévoir les impacts futurs des différents forçages, l'évolution de la ZC doit être documentée sur des périodes qui ne peuvent être évaluées par des observations directes actuelles, nécessitant ainsi le recours aux paléo-sciences (Dearing et al., 2015).

L'érosion est un processus géologique entrainant le transfert de matériaux sédimentaires minérals ou organiques solides et dissouts depuis les zones de haute montagne vers les bassins sédimentaires (Fig. I-1). Les sédiments constituent la fraction solide de ce flux de matière. Du fait de l'érosion, ces sédiments sont créés au niveau de points hauts, ou « sources », et transportés jusqu'à des bassins sédimentaires continentaux ou marins, considérés comme réceptacle ultime du cycle de l'érosion et appelés ci-après « puits ». Les cours d'eau sont de loin le premier vecteur de transport des sédiments à l'échelle globale et le premier agent de distribution des produits de l'érosion continentale vers les océans (e.g., Milliman and Meade, 1983). De nombreux facteurs, tels que la lithologie, le relief, le climat, l'utilisation des sols ou la saisonnalité des précipitations déterminent le taux d'érosion (i.e., la vitesse à laquelle un paysage s'érode au cours du temps) en un lieu et pour une période donnés (Fig. I-2; Ahnert, 1970; Gayer et al., 2019; Hilton and West, 2020). Au cours du temps, trois facteurs dominent les fluctuations de l'érosion : les fluctuations climatiques, l'activité tectonique et l'activité humaine. Sur de longues périodes de temps, l'érosion a en retour un impact direct sur la topographie, la tectonique et le climat (e.g., Gayer et al., 2019; Hilton and West, 2020).

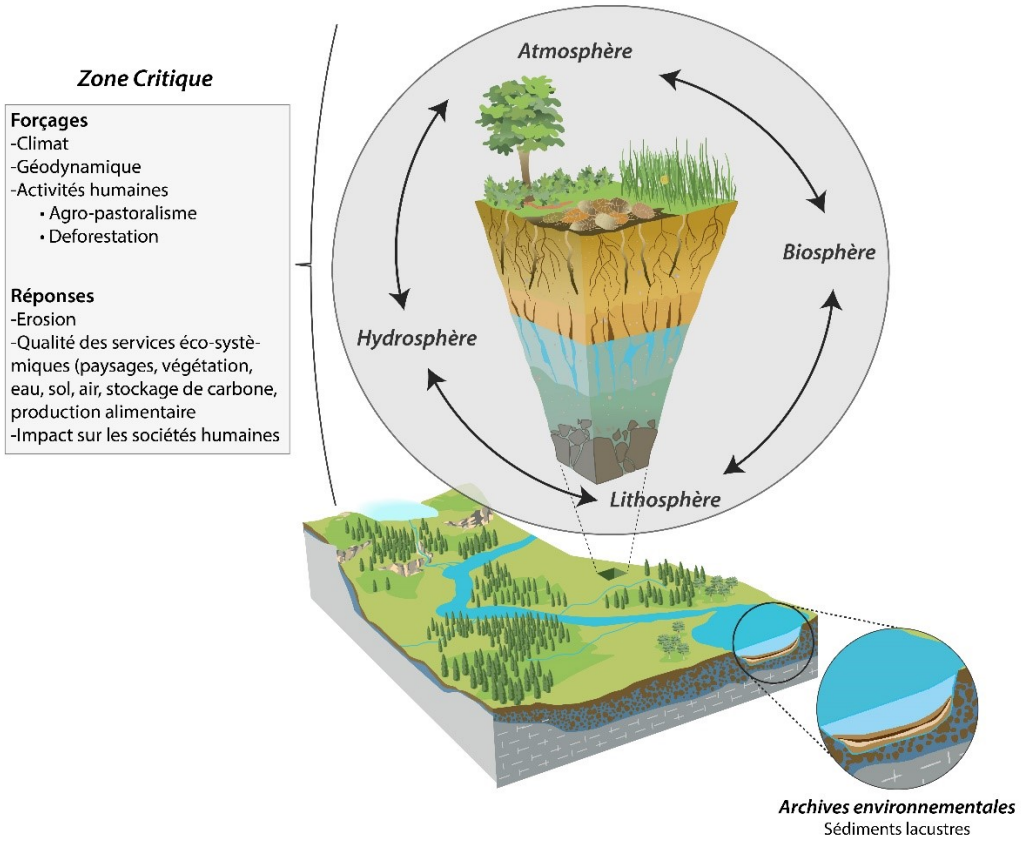

Fig. I-1- Le sol au sein de la zone critique et du paysage, modifié d'après Chorover et al. (2007). Ici sont représentés (i) le fonctionnement de la Zone Critique entre les différentes enveloppes et (ii) sa réponse en lien avec des forçages œuvrant à différentes échelles de temps. Les réponses de l'évolution de ce fonctionnement intégré à l'échelle du paysage sont enregistrées dans les archives environnementales

Actuellement, l'érosion est aussi le principal processus conduisant à la dégradation de la Zone Critique. Avec la détérioration des sols, l'érosion impacte notamment les stocks de carbone dans les sols et la biomasse (Fig. I-1,Fig. I-2), la production alimentaire, les services écosystémiques, la biodiversité et la qualité de l'eau potable (e.g., Bosco et al., 2008; Panagos et al., 2015; Rusco et al., 2008). Ainsi, l'érosion affecte directement les sociétés humaines (Montgomery, 2012) et est devenue un sujet scientifique de première importance à l'échelle globale (Borrelli et al., 2020; FAO, 2015; Panagos et al., 2015b; Rusco et al., 2008). Du fait du relief et de la faible couverture végétale, l'érosion impacte particulièrement les zones de montagne comme les Alpes (Fig. I-3; Bosco et al., 2008). Les préoccupations croissantes concernant les effets délétères de l'érosion ont conduit l'Europe et les Nations Unies à classer l'érosion des sols comme l'une des principales menaces pour l'humanité et à appeler à une évaluation quantitative de la perte de sol sur de grandes échelles spatiales et temporelles (e.g., Panagos et al., 2015). Ces évaluations sont nécessaires afin de mieux quantifier les effets relatifs des principaux facteurs de contrôle de l'érosion de la ZC à court ou moyen terme que sont le climat (i.e., à travers les régimes de précipitations et les avancées et retraits des glaciers) et les activités humaines (à travers l'utilisation des terres et la gestion du couvert végétal). Dans le cadre de ce travail de recherche, l'activité tectonique dans les Alpes est, elle, considérée comme stable aux échelles de temps de l'Holocène.

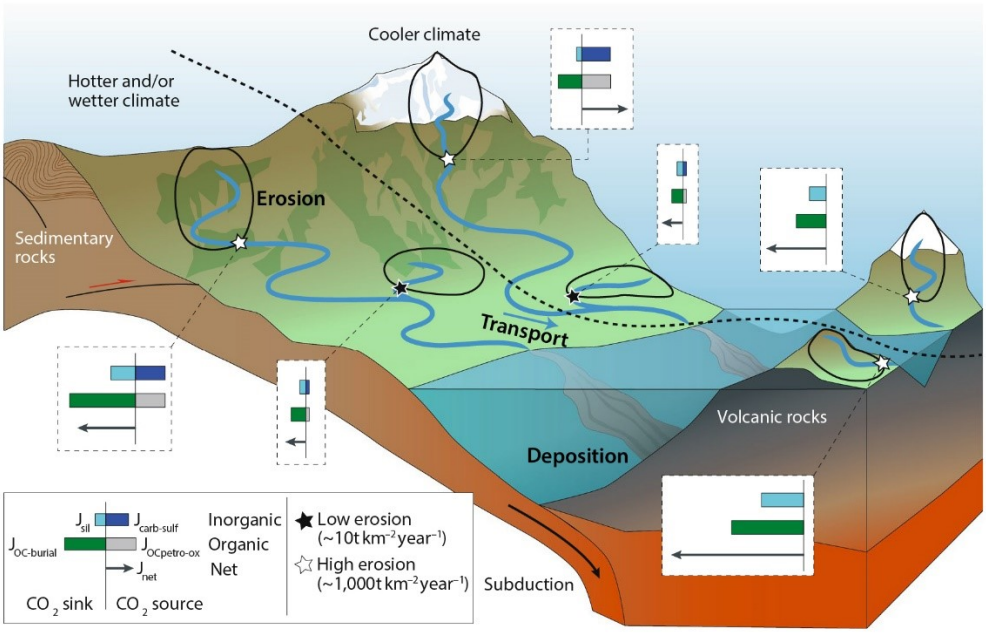

Fig. I-2-Une nouvelle vision des montagnes, de l'érosion et du cycle du carbone. Tiré et modifié de Hilton and West, (2020). Ici sont représentés les flux de carbone inorganique (avec Jsil pour l'altération des silicates, et Jcarb-sulf pour l'oxydation du sulfure), et organique ($J_{OCburial}$ pour l'enfouissement du carbone organique, et $J_{OCpetro-ox}$ pour l'oxydation du carbone organique des roches).

Toutefois, évaluer les taux d'érosion à grande échelle est complexe car ces taux sont très dépendants de la méthode utilisée pour les déterminer (e.g., Hinderer et al., 2013). Actuellement, plusieurs types de méthodes permettent d'obtenir des taux d'érosion sur de grandes étendues : les mesures par nucléides cosmogéniques (Granger and Riebe, 2014) les mesures plus conventionnelles d'évaluation de l'apport sédimentaire des cours d'eau (Hinderer et al., 2013; Holeman, 1968; Walling, 1994), les modèles numériques (Borrelli et al., 2020; Panagos et al., 2015b). Toutefois, ces méthodes sont complexes à mettre en œuvre en raison du nombre important de paramètres ou de données préalables nécessaires à la mesure. De plus, aucune de ces méthodes ne permet d'évaluer, de façon quantitative l'impact des différents facteurs forçant l'érosion de la ZC au cours du temps.

Il semble donc nécessaire de combler cette lacune de connaissance en fournissant des contraintes empiriques, en particulier dans le but d'évaluer les taux d'érosion sur des échelles de temps allant de la centaine à quelques milliers d'années, échelles au cours desquelles les forçages climatique et humain sont les moteurs les plus probables de l'érosion dans les Alpes (Arnaud et al., 2016). Pour cela, les archives naturelles telles que les sédiments lacustres semblent être idéales car elles permettent d'enregistrer l'évolution de l'érosion d'un bassin versant entier, de façon continu et sur de longues périodes de temps (Arnaud et al., 2016; Bajard et al., 2016; Dearing, 1991; Edwards and Whittington, 2001; Gathorne-Hardy et al., 2009; Giguet-Covex et al., 2011; Page and Trustrum, 1997). La combinaison des sédiments lacustres avec une approche «source-puits» (Collins and Walling, 2002) offre la possibilité de suivre les sources des apports de sédiments vers le lac à travers le temps, ce qui permet de démêler les impacts relatifs du climat et des activités humaines sur les taux d'érosion, à condition que chaque source de sédiments soit sensible à un type donné de forçage.

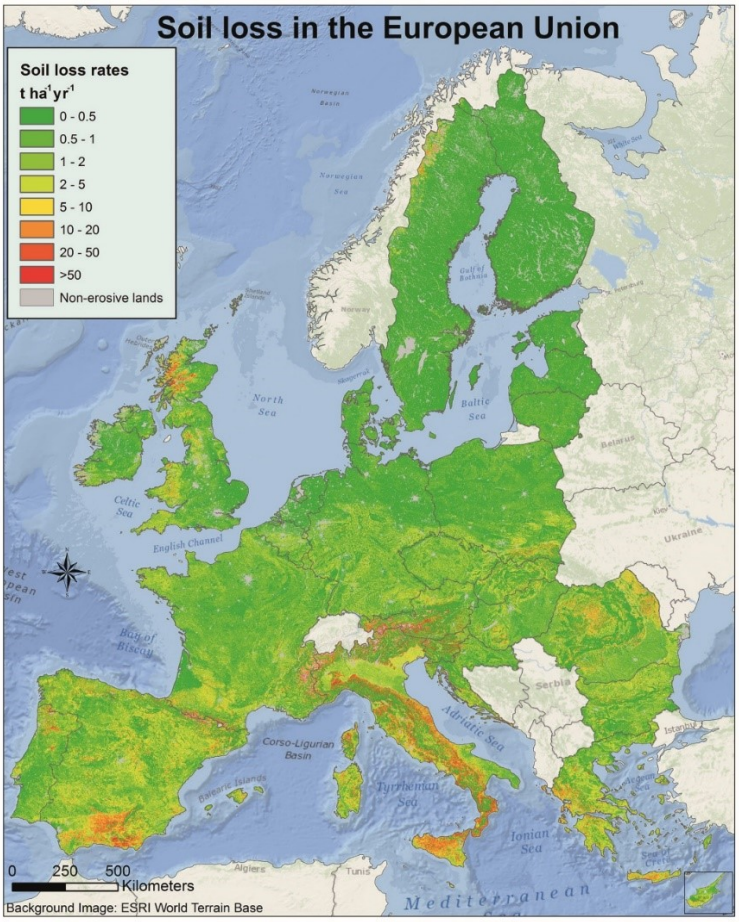

Fig. I-3- Carte des taux d'érosion des sols dans l'Union Européenne (année de référence : 2010) basée sur le modèle R.U.S.L.E2015 (tirée de Panagos et al., 2015).

La problématique de ce travail de thèse est, pour une zone donnée que sont les Alpes Européennes et à partir d'une approche rétrospective de type source-puit basée sur des archives sédimentaires lacustres, de démêler et quantifier les effets des forçages climatiques et humains sur l'érosion de la ZC au cours de l'Holocène.

Pour répondre à cette problématique, une analyse multi-indicateurs des séquences sédimentaires a été conduite sur deux grands lacs périalpins, ceux du Bourget (France) et d'Iseo (Italie), utilisés comme archives de l'érosion de la ZC sur de grand bassin versants. Cette méthode a été combinée à une approche « source-puits ». Dans un premier temps, il a été nécessaire de décrire et de distinguer la sédimentation continue, enregistrant les produits de l'érosion au cours du temps, et la sédimentation évènementielle, correspondant à l'occurrence des événements extrêmes climatiques et tectoniques. En effet, les Alpes constituent une région particulièrement active en termes de transport sédimentaire. A l'instar du régime hydrologique, fortement impacté par la torrentialité, le régime de l'érosion y est particulièrement variable et la sédimentation évènementielle se doit d'être comprise avant d'interpréter les fluctuations sédimentologiques en termes de variations des phénomènes d'érosion. Ensuite, la comparaison des taux d'érosion obtenus avec des modèles d'érosion actuelle ainsi qu'avec des données déjà disponibles a permis la validation de nos résultats. Pour finir, l'utilisation de modèles de mélanges issus de données de la composition isotopique des sédiments, a permis d'obtenir des informations quantitatives quant à l'impact des différents facteurs forçant.

Après ce premier chapitre introductif, ce manuscrit présentera en chapitre II un état de l'art des différentes méthodes couramment employées pour évaluer les taux d'érosion à grande échelle. La méthode sélectionnée pour répondre à la problématique de la thèse sera ensuite détaillée. Les sites d'études sélectionnés seront présentés en détails dans le chapitre III. Les chapitres IV, V et VI permettront de décrire et d'interpréter les processus sédimentaires à l'œuvre dans les différents bassins sédimentaire du Lac Iseo et du Lac du Bourget. Une attention particulière sera portée à l'identification et la caractérisation des dépôts sédimentaires causés par des événements extrêmes dans les différents bassins de ces lacs. Le chapitre VII détaillera une nouvelle méthode développée au cours de cette thèse permettant de faciliter la détection et l'interprétation de la sédimentation instantanée. Une synthèse des apports sur la connaissance des processus sédimentaires dans les grands lacs périalpins sera présentée dans le chapitre VIII. Les chapitres IX et X constituent quant à eux le cœur de la réponse apportée à la problématique de ce travail de thèse. Dans le chapitre IX, nous proposons une quantification de l'impact des forçages climatique et anthropique sur l'érosion au cours des 2000 dernières années dans les Alpes Italiennes. Pour finir, dans le chapitre X, les effets du climat et de l'activité humaine au cours de l'Holocène seront discutés dans le lac du Bourget et une comparaison entre les deux sites d'études sera réalisée. Le chapitre XI présentera une synthèse des apports de connaissances sur l'évolution de l'érosion au cours de l'holocène dans les alpes. Enfin, cette thèse se conclura par un chapitre XII présentant les principales conclusions de ce travail de recherche ainsi que les perspectives majeures s'ouvrant à l'issu de ce travail.

CHAPITRE II | Approches méthodologiques

Afin de déterminer quels processus contrôlent l'érosion de la ZC dans les Alpes au cours de l'Holocène il est nécessaire de sélectionner une approche permettant d'arriver à cette fin avec un minimum de contraintes et de biais. Avant toutes choses, il apparaît nécessaire de définir le terme d'« érosion » et exposer le sens qui lui sera attribué tout au long de ce travail de thèse. L'emploi du terme « érosion » fait référence dans ce travail à l'érosion physique ou mécanique affectant les roches mères ainsi que l'ensemble du régolithe, c'est-à-dire l'ensemble des sols recouvrant la roche mère. Ce travail de thèse s'intéressera principalement aux produits de l'érosion transportés par l'eau et déposés au fond des lacs périalpins, l'eau étant le principal facteur de perte de sol en Europe (Panagos et al., 2015b).

1. État de l'art des méthodes actuellement utilisées pour estimer l'érosion

Parmi la multitude de méthode utilisées pour évaluer les taux d'érosion on retrouve quatre méthodes principales : la mesure de l'apport sédimentaire dans les cours d'eau d'un bassin versant, l'utilisation de nucléides cosmogéniques ainsi que celle de modèles numériques et enfin l'utilisation des archives naturelles, comme les sédiments marins et lacustres. Ces méthodes sont utilisées dans de nombreuses études et présentent toutes des avantages et des inconvénients divers.

1.1. Mesure de l'apport sédimentaire des cours d'eau

Les mesures basées sur l'estimation de l'apport sédimentaire (« sediment yield » en anglais) dans les cours d'eau permettent d'obtenir une mesure approximative du taux d'érosion de l'intégralité du bassin versant situé directement en amont du point de mesure (Holeman, 1968; Walling, 1994). Cette méthode consiste à mesurer la concentration en matière en suspension ($g.m^{-3}$) ainsi que le débit ($m^3.s^{-1}$) d'un cours d'eau à un point choisi pour être représentatif du bassin versant étudié. Le produit des deux variables, divisé ensuite par la superficie (km^2) du bassin versant considéré, permet d'obtenir une valeur de l'apport sédimentaire ($g.s^{-1}.km^{-2}$, exprimé en général en $t.km^{-2}.a^{-1}$). Cet apport sédimentaire est défini comme la masse de sédiments qui, sur un laps de temps donné est délivré par unité de surface érodée. L'apport sédimentaire est donc exprimé en unité de masse par unité de surface et de temps (Hinderer et al., 2013). Cette méthode présente l'avantage d'obtenir une intégration spatiale de l'érosion sur de grandes superficies en fonction du point de prélèvement choisi. Toutefois, seule une fraction du matériel récemment érodé dans le bassin versant atteint réellement l'exutoire du bassin et donc le point de mesure. Le sédiment accumulé au pied des zones d'érosion, dans les zones de dépôts intermédiaires, ainsi que dans les plaines d'inondations situées en amont du point de mesure n'est pas pris en compte. La mesure de l'apport sédimentaire correspond donc à une évaluation minimale de l'érosion réelle du bassin considéré. De plus, lorsqu'elle est mesurée ponctuellement dans un cours d'eau, comme c'est le cas dans la majorité des études actuelles (Hinderer et al., 2013), l'apport sédimentaire intègre une période de temps très courte (journalière à décennale) et ne peut permettre d'étudier l'évolution des taux d'érosion sur le long terme. Ces courtes périodes peuvent être impactées par des fluctuations à court terme,

dépendantes d'un facteur en particulier, comme l'utilisation des sols. Ces mesures ne permettent donc pas d'interroger l'évolution de l'influence de chaque facteur forçant au cours du temps.

1.2. Nucléides cosmogéniques

Les nucléides cosmogéniques sont produits dans les minéraux par les rayons cosmiques secondaires qui pénètrent dans les premiers mètres de sols et de roches (Granger and Riebe, 2014). Parce que les rayonnements cosmiques sont rapidement atténués avec la profondeur, la concentration de nucléides cosmogéniques dans un minéral indique combien de temps ce minéral a passé près de la surface ou à quelle vitesse le matériel situé directement au-dessus du minéral a été retiré (Lal, 1991). Plusieurs nucléides peuvent être utilisés en fonction des cas considérés, comme le béryllium-10 (^{10}Be) ou le chlore-36, pour ne citer que les isotopes les plus utilisés. Un paysage subissant l'érosion fournit des sédiments qui peuvent être analysés pour déterminer son taux d'érosion (Fig. II-1). Les concentrations en nucléides cosmogéniques étant inversement proportionnelles au taux d'érosion, la concentration en ^{10}Be par exemple, pondérée par le flux sédimentaire, reflète le taux d'érosion moyen à l'échelle du bassin versant (Granger and Schaller, 2014).

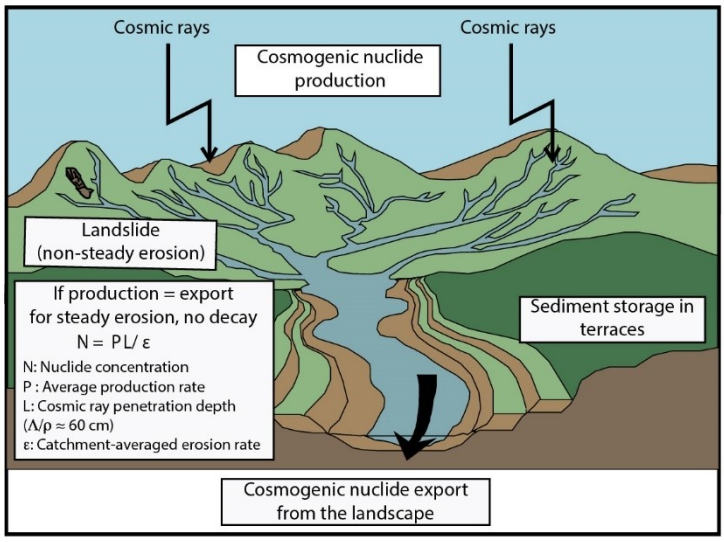

Fig. II-1- Figure de synthèse de l'intérêt de l'utilisation des nucléides cosmogéniques pour évaluer les taux d'érosion d'un paysage subissant l'érosion, tiré de Granger and Schaller, (2014).

A l'inverse des mesures conventionnelles de l'apport sédimentaire dans les cours d'eau, l'utilisation des nucléides cosmogéniques nécessite seulement l'échantillonnage de quartz, voire de feldspath (ou de calcite suivant le cas). Les mesures peuvent être réalisées à la fois sur des échantillons de roches provenant de la surface dont on cherche à évaluer le taux d'érosion, ou bien à partir d'échantillons de sols ou de sédiments. En considérant les mesures réalisées à partir de sédiments de rivières, l'utilisation des nucléides cosmogéniques permet d'obtenir une valeur du taux d'érosion (ou de dénudation) à l'échelle du bassin versant situé en amont du point couvrant de longues périodes (de la centaine au million d'années). Toutefois, pour utiliser ces méthodes, les taux de production des nucléides cosmogéniques ainsi que de nombreux autres paramètres, tels que le masquage topographique (« topographic shielding ») doivent être pris en compte (Granger and Riebe, 2014). L'histoire des sédiments analysés doit ainsi être évaluée avant tout calcul de taux d'érosion. De plus, seules des périodes de temps relativement longues sont couvertes par une telle méthode, ce qui ne permet pas d'évaluer l'impact des fluctuations

climatiques de courtes périodes, ou les changements d'utilisation des sols et donc l'impact des activités humaines sur les taux d'érosion d'un bassin versant qui peuvent être appréhendés par certains radioéléments de plus courtes périodes (Evrard et al., 2020; Le Gall et al., 2017). De plus, cette technique ne permet d'obtenir qu'une valeur moyenne du taux d'érosion sur une période donnée, ne permettant pas d'examiner les fluctuations du taux d'érosion au cours du temps (Granger and Riebe, 2014, et les références y figurant).

1.3. Modèles d'érosion

De nombreux types de modèles d'érosion (Borrelli et al., 2021), tels que les modèle U.S.L.E, R.U.S.L.E, ANSWERS, WEPP, SEDEM, permettent de réaliser des estimations de taux d'érosion à grande échelle. Du fait de leur grand nombre, une synthèse concise ne sera pas proposée ici. Seul quelque exemple seront présentés, comme une étude récente réalisée à l'échelle de l'Union Européenne qui a permis d'évaluer de façon quantitative et avec une précision spatiale sans précédent, la perte de sol liée à l'érosion par le ruissellement et/ou le creusement des cours d'eau (Panagos et al., 2015b). L'utilisation du modèle R.U.S.L.E, correspondant actuellement au modèle le plus répandu (Bezak et al., 2021; Borrelli et al., 2021), nécessite l'obtention de paramètres précis, comme la pente de la zone considérée, un facteur d'érodibilité des sols ou encore l'état actuel de l'utilisation des sols. En fonction de la superficie des zones étudiés, l'estimation des valeurs de chacun de ces paramètres peut être réalisée à partir de mesures empiriques sur le terrain ou à partir de données spatiales dérivée d'image satellites notamment. Toutefois, à cause de la complexité des terrains étudiés, l'estimation des valeurs de chaque paramètre est généralement obtenu par une combinaison d'équations dépendante des caractéristiques de la zone étudiée (e.g., Ghosal and Das Bhattacharya, 2020; Panagos et al., 2015a), ce qui rend l'utilisation des modèles complexe (Fig. II-2). De plus, deux synthèses récentes sur l'utilisation des modèles d'érosion à travers le monde concluent à un manque de tentatives de validations des données obtenues (Bezak et al., 2021; Borrelli et al., 2021). Parmi les nombreux modèles d'érosion des sols développés au cours du temps (Angima et al., 2003; Borrelli et al., 2020; Millward and Mersey, 1999; Panagos et al., 2015b; Renard et al., 1991), seuls des évaluations de l'érosion actuelle ou des projections de l'érosion future en sont obtenues. Très peu de modèles permettent d'évaluer l'évolution de l'érosion au cours du temps et leur utilisation dans le but de mesurer l'impact de chaque forçage sur l'érosion n'est pour le moment pas répandue.

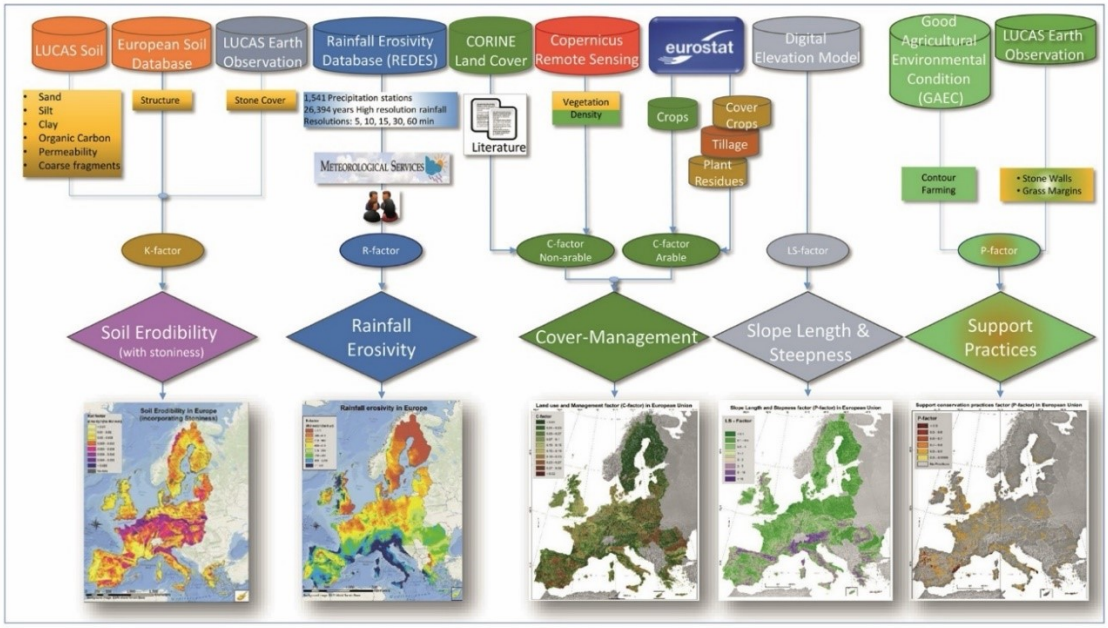

Fig. II-2- Données d'entrée utilisées pour l'estimation des facteurs de perte de sol du modèle RUSLE2015. Figure directement tirée de Panagos et al., (2015).

1.4. Mesure de l'apport sédimentaire dans les archives sédimentaires

Les bassins sédimentaires situés à l'aval d'un bassin versant sont des réceptacles naturels pour les sédiments provenant de l'érosion de ce dernier. Dans ce sens, de nombreuses études ont été réalisées à partir de séquences sédimentaires lacustres ou marines pour reconstituer les taux d'érosion des bassins versants considérés au cours du temps (e.g., Bajard et al., 2017; Clift, 2006; Foucher et al., 2014; Molnar, 2004; Willenbring and von Blanckenburg, 2010). La méthode consiste généralement à calculer le volume, la masse totale ou le taux d'accumulation de sédiment pour tout ou partie de la zone de dépôt, pour une période donnée. La superficie de la zone fournissant le sédiment est ensuite estimée. Le rapport entre la masse totale déposée par unité de temps et la superficie de la zone subissant l'érosion permet d'obtenir la charge sédimentaire accumulée dans le bassin sédimentaire étudié. Dans le cas des bassins lacustres, cette estimation est basée sur une séquence sédimentaire, prélevée dans la partie distale du bassin sédimentaire (i.e., loin de l'embouchure des affluents) et datée par diverses méthodes (^{14}C, comptages de varves, radionucléides de courtes périodes, paléo-magnétisme, etc.). De plus, lorsqu'ils ne sont pas perturbés par des événements climatiques ou géodynamiques extrêmes, les bassins sédimentaires enregistrent l'érosion de façon continue et sur de grandes périodes. Certains bassins sont localisés à l'aval de zone de drainage vastes, ce qui permet d'interroger l'évolution de l'érosion sur de grande échelles spatiales. Toutefois, sur le continent, cette méthode a souvent été appliquée à des petits bassins sédimentaires lacustres, à l'aval de petit bassins versants de montagnes (Bajard et al., 2016; Brisset et al., 2017; Edwards and Whittington, 2001; Giguet-Covex et al., 2011; Page and Trustrum, 1997; Rothacker et al., 2018; Sabatier et al., 2014, 2021), mais très rarement à de grands bassins (e.g., Arnaud et al., 2016). En effet, les bassins sédimentaires à l'aval de grands bassins versants correspondent généralement à des lacs larges et profonds, où le prélèvement de sédiment n'est pas aisé. Ces lacs sont souvent caractérisés par de nombreuses sources d'apports sédimentaire potentiels et de multiples processus de sédimentation complexifiant l'étude de l'enregistrement des produits de l'érosion.

2. Sélection des méthodes adéquates pour répondre à la problématique

A partir des informations disponibles dans la littérature, il semble que peu de méthodes aient été développées dans le but de démêler et de quantifier l'impact des forçages humains et climatiques sur l'évolution de l'érosion au cours du temps. Il semble donc que l'évaluation sur une longue période de l'évolution de l'apport sédimentaire enregistrée dans un bassin sédimentaire situé à l'exutoire d'un grand bassin versant, soit la méthode la plus probante pour répondre à la problématique initiale. En effet, l'apport sédimentaire correspond à une quantification de l'érosion minimale à l'échelle d'un bassin versant. Pour ce travail de thèse nous avons choisi de nous intéresser à l'évolution de l'érosion au cours de l'Holocène, enregistré dans des sédiments de lacs situés à l'exutoire de grands bassins versants alpins. Les raisons de ces choix sont exposées et justifiées ci-après, avant de présenter dans le détail de la méthode appliquée.

La période de temps choisie pour l'étude doit être suffisamment longue pour : (i) couvrir des périodes où l'Homme n'est pas encore présent dans la zone d'étude, ou qu'il n'y pratique aucune activité favorisant l'érosion et (ii) couvrir divers états du climat. Ainsi, l'effet des fluctuations climatiques et des activités humaines sur l'érosion pourra être évaluée. Il est aussi nécessaire que la période de temps choisie soit suffisamment courte pour que le signal d'érosion ne soit pas impacté par les effets de la tectonique, par exemple par la création de relief (surrection). Toutefois, les séismes et la tectonique active, par les glissements de terrains qu'ils provoquent, peuvent avoir un effet sur les taux d'érosion à court terme dans un bassin versant (e.g., Howarth et al., 2012; Wang et al., 2020). Le travail présenté dans ce manuscrit s'intéresse à évaluer l'évolution de l'érosion au cours de l'Holocène, c'est-à-dire des derniers 11700 ans. Cette période semble idéale pour répondre à la problématique initiale. En effet les activités humaines et agricoles ne se sont développées que depuis le Néolithique et les fluctuations climatiques ne sont pas majeures comme entre les période glaciaire et interglaciaire mais restent significatives, avec des variation de température qui ont eu lieu au cours des derniers millénaires avant l'actuel (Bader et al., 2020; Mann et al., 2009). Une attention particulière sera portée à l'évolution de l'activité sismique de la région d'étude afin d'évaluer l'impact potentiel de la tectonique active sur le signal d'érosion obtenu.

2.1. Archives sédimentaires lacustres

Afin d'obtenir un signal d'érosion continu et couvrant une telle période, il est nécessaire d'avoir recours à des archives naturelles. Les archives sédimentaires lacustres sont connues pour permettre l'évaluation de l'évolution de l'érosion (Fig. II-3) en continu et sur de longues périodes de temps sur le bassin versant considéré (e.g., Bajard et al., 2017). L'une des premières étapes de l'études des séquences sédimentaires lacustres comme archives de l'érosion est la datation. Ici nous avons choisi de combiner des datations au carbone 14 (^{14}C) à partir de macro-restes végétaux pour le temps long (MacDonald et al., 1991), et un comptage de varve associé à des données de radionucléides de courte période pour les premiers centimètres de sédiment (Appleby, 2001; Arnaud et al., 2002; Bruel and Sabatier, 2020). Comme exposé ci-dessus, l'utilisation des sédiments lacustres comme archives de l'évolution de l'érosion présente diverses contraintes. Nous nous proposons donc de détailler ces contraintes ci-après et d'expliquer dans le même temps comment nous avons tenté d'en repousser certaines.

2.1.1. *Traçage des sources de sédiments*

Les lacs présents à l'embouchure de grands bassins versant sont généralement vastes, profonds et influencés par des sources d'apports de sédiments diverses dont il est parfois difficile d'identifier la source. Pour étudier les processus impactant l'érosion au cours du temps il est nécessaire de lever le doute sur l'origine des sédiments (Dearing, 1991). À cette fin, une approche source-puit sera utilisée (Collins and Walling, 2002). Lorsque les produits d'érosion particulaires, ou sédiments détritiques, se déposent au fond d'un bassin sédimentaire, ils s'y mélangent avec les sédiments produits dans le lac, appelés sédiment authigènes (Fig. II-3). Il est donc aussi nécessaire de distinguer la part de sédimentation liée à l'érosion de celle liée à la production sédimentaire lacustre. Pour cela, des analyses sédimentologiques et géochimiques, combinant divers traceurs tels que la composition élémentaire des sédiments, la taille des grains, ainsi que des analyses des caractéristiques magnétiques des sédiments doivent être réalisées (Dearing, 1991). D'autres processus complexes devront être considérés, comme les variations des conditions d'oxydo-réduction qui peuvent impacter l'eau et le sédiment dans la zone de dépôts et influencer l'enregistrement sédimentaire (Davison, 1993).

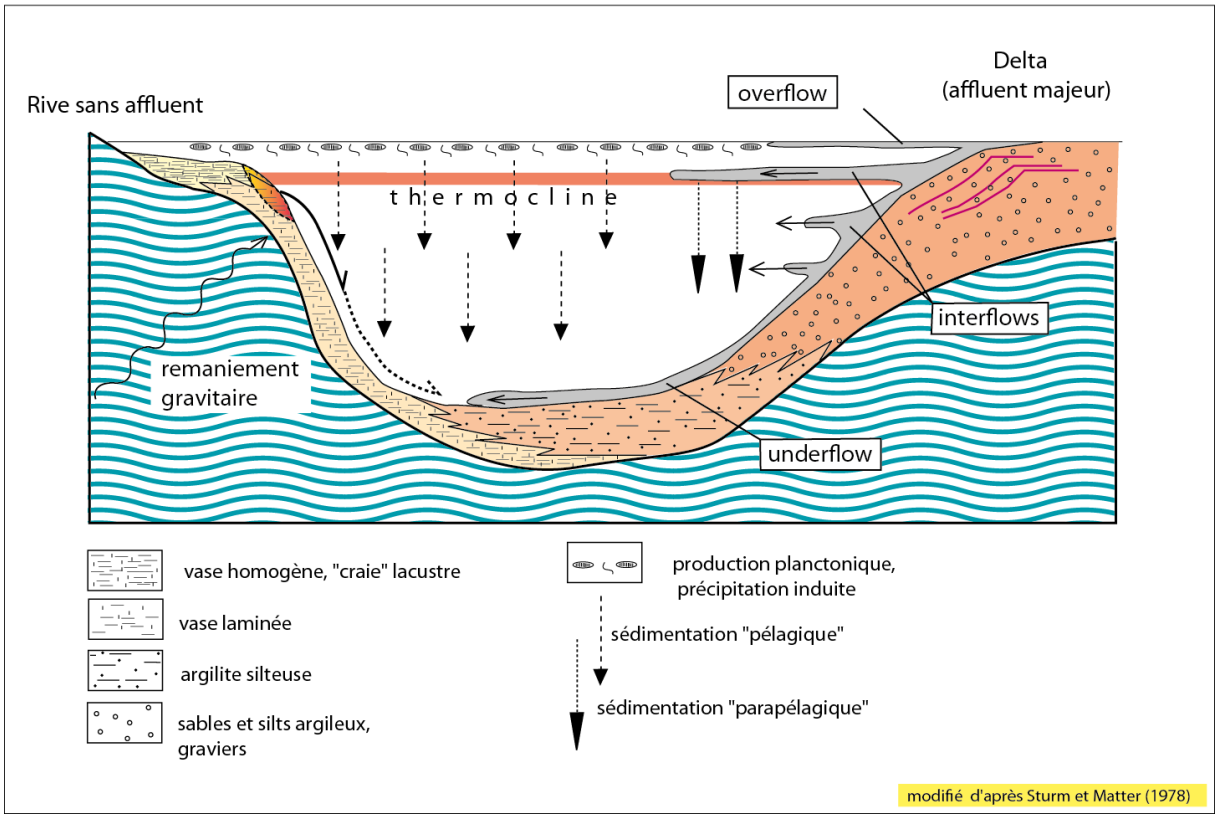

Fig. II-3- Schéma synthétique des différents mécanismes et types de sédiments associés, dans le cas d'une sédimentation clastique, dans un lac oligotrophe, c'est-à-dire un milieu pauvre en nutriment et avec une production biogénique faible, avec une stratification thermique annuelle. Schéma tiré de Sturm and Matter, (1978) et modifié par Christian Beck.

2.1.2. Démêler sédimentation instantanée et continue

La sédimentation continue décrite ci-dessus peut être impactée par des phénomènes extrêmes comme des événements de précipitations intenses entrainant des crues dans le bassin versant et des dépôts associés dans le lac (Glur et al., 2013; Sturm and Matter, 1978; Vannière et al., 2013; Wilhelm et al., 2012; Wirth et al., 2013b), ou par des événements géodynamiques comme des séismes qui peuvent entrainer des déstabilisations de pente, tant en dehors que dans le lac et se caractériser également par le dépôts de couches sédimentaires spécifiques (Fig. II-3,Fig. II-4; Beck, 2009; Moernaut et al., 2014; Wilhelm et al., 2016). Les dépôts de sédiments dans les bassins lacustres provoqués par de telles événements sont dits « instantanés » par rapport à la sédimentation continue au sein de laquelle ils s'insèrent en raison de leur cinétique de dépôt de plusieurs ordres de grandeur supérieure (quelques millimètres, voire centimètre par heure, par rapport à quelques millimètres par an, en général) (e.g., Fouinat et al., 2017; Gilli et al., 2013; Moernaut et al., 2014; Wilhelm et al., 2017, 2012; Wirth et al., 2013b). Ces dépôts peuvent parfois être érosifs à leur base et remobiliser une partie de la sédimentation continue précédemment déposées, perturbant ainsi l'enregistrement de l'érosion du bassin versant au cours du temps. Plusieurs études ont montré que lorsque l'érosion dans un bassin versant augmente, la disponibilité en sédiment augmente, induisant aussi une augmentation de la sensibilité des lacs à enregistrer des événements extrêmes (Rapuc et al., 2018; Wilhelm et al., 2016a). En Nouvelle-Zélande, des études récentes ont aussi montré que des séismes de magnitude importante (M_w > 7,6) pouvaient avoir un impact sur les signaux d'érosion enregistrés dans les sédiments lacustres régionaux (Howarth et al., 2012; Wang et al., 2020). Avant de produire un signal d'érosion à partir des sédiments lacustres, il est donc nécessaire d'étudier les processus sédimentaires à l'œuvre dans le lac et de procéder à une identification systématique des dépôts liés à la sédimentation évènementielle. Une fois identifiés et datés, une chronique de ces dépôts doit être réalisée et comparée au signal d'érosion afin d'évaluer l'effet de l'érosion sur la fréquence de ces dépôts (Fig. II-4), ou a contrario l'effet des événements extrêmes sur l'érosion dans le bassin versant.

Les dépôts liés à la sédimentation évènementielle sont généralement identifiés et décrits à l'œil nu (e.g., Vannière et al., 2013; Wilhelm et al., 2012), ou grâce à des logs à haute résolution : géochimique avec des données d'XRF core scanner (e.g., Wilhelm et al., 2013) ou magnétique à partir de donnée de susceptibilité magnétique (e.g., Lauterbach et al., 2012), en général. Après comptage, l'interprétation des processus à leur origine est réalisée à partir de données de composition élémentaire, de la variation de la taille des grains et parfois, de la fabrique magnétique des sédiments constituant les dépôts. Étudier les dépôts évènementiels présents dans une séquence sédimentaire est donc coûteux en temps. Pour faciliter l'identification de ces dépôts, il nous a paru intéressant de développer une méthode automatisée de détection. Certaines études ont tenté de développer ce type d'approches récemment (e.g., Støren et al., 2010; Vannière et al., 2013) en étudiant l'évolution d'un marqueur comme la couleur du sédiment en fonction de la profondeur, mais aucune n'a pu être appliquée avec succès sur différents sites d'études. Une partie du travail de recherche développé durant cette thèse a permis de mettre en place une nouvelle méthode, basée sur des techniques d'imagerie hyperspectrales, permettant de détecter et d'interpréter l'origine des dépôts liés à la sédimentation évènementielle dans les séquences sédimentaires lacustres. Cette avancée méthodologique est détaillée dans le **chapitre VII** ainsi qu'en **annexe II**.

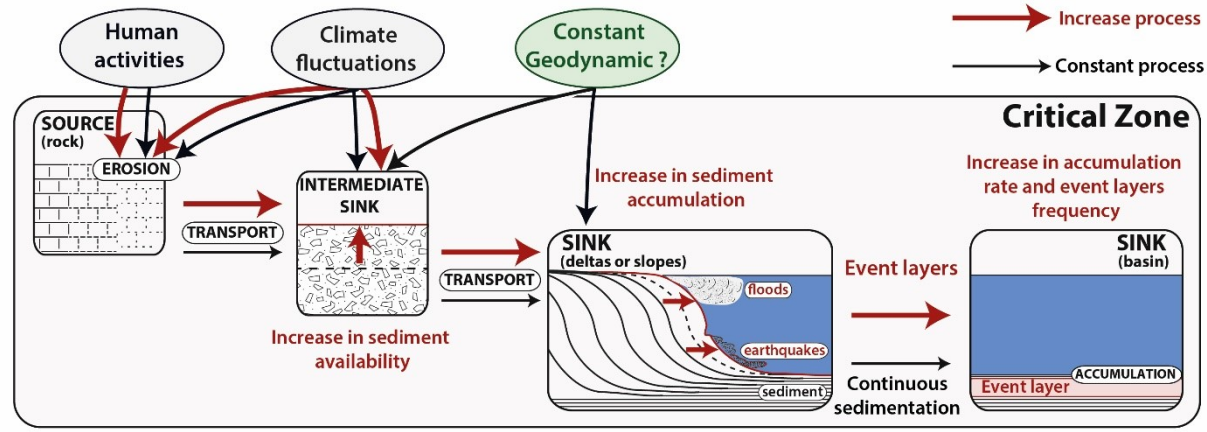

Fig. II-4- Modèle conceptuel du cycle d'érosion de la zone critique dans un grand bassin versant et des effets des trois principaux facteurs de forçage : climat, géodynamique et activités humaines. Ici la géodynamique est considérée comme constante, si l'un des facteurs vient à augmenter son influence, la réaction induite se traduit par l'augmentation de l'érosion, de l'accumulation de sédiment dans le bassin lacustre ainsi que par l'augmentation de la fréquence des dépôts liés à des événements extrêmes.

2.1.3. Carottage de bassins profonds

Le fait d'utiliser des lacs profonds entraine d'autres défis, tels que le carottage à de grande profondeur. En effet très peu de lacs profonds ont été carottés et peu de séquences suffisamment longues permettant de couvrir de longues périodes y ont été prélevées. Les techniques disponibles jusqu'à présent ont un coût économique élevé et demandent un temps important. L'acquisition d'une nouvelle barge de carottage UWITEC par le C2FN de la division technique de l'Institut National des Sciences de l'Univers (INSU), en lien avec le projet EQUIPEX CLIMCOR, nous a permis de réaliser des carottages à plus faible coût et permettant de prélever de longues séquences sédimentaires (plusieurs dizaines de mètres) par plusieurs centaines de mètres de fond (plus de 250 m). Ce matériel a été utilisé à grande profondeur pour la première fois dans le cadre de cette thèse.

Fig. II-5- Photo de la plateforme de carottage du C2FN sur le lac d'Iseo. Source : Andrea Piccin

2.2. Sélection des zones d'études

Comme exposé en Introduction, l'érosion est maximale dans les zones de montagnes du fait des pentes importantes et de la sensibilité de l'environnement aux fluctuations climatiques et aux impacts de l'activité humaine. Les Alpes Européennes représentent donc un terrain d'étude idéal pour évaluer les effets de l'homme et du climat sur l'érosion au cours de l'Holocène. En effet, l'activité humaine s'y est fortement développée depuis le Néolithique (e.g., Pini et al., 2016) et les fluctuations climatiques y ont été importantes, surtout depuis 4200 ans et la transition vers un climat plus humide et froid à l'échelle régionale entrainant des ré-avancées glaciaires (e.g., Arnaud et al., 2016; Büntgen et al., 2011; Joerin et al., 2008; Wirth et al., 2013b). Toutefois, à l'échelle des Alpes et de l'Europe occidentale, l'évolution du climat Holocène et les activités humaines depuis le Néolithique restent peu documentées et contraintes.

Pour répondre à la problématique énoncée, et produire des informations représentatives de l'impact des différents forçages de l'érosion à l'échelle des Alpes, il est nécessaire de sélectionner des bassins versants présentant (Fig. II-6) :

(i) Une surface importante, avec un lac situé à l'exutoire et enregistrant les produits sédimentaires issus de l'érosion du bassin ;

(ii) Une ou des zones dans lesquelles l'impact de l'homme est demeuré nul ou presque pendant tout ou partie de la période considérée. Par l'effet des précipitations et des avancées et reculs glaciaire, il est très fortement probable que les fluctuations climatiques aient impacté à la fois l'érosion des parties hautes et basses altitudes des bassins versants. Afin de démêler les effets des différents forçages, il faut donc sélectionner des bassins versants présentant des zones de haute altitude présentant des glaciers, le signal d'érosion de cette zone étant impacté uniquement par les fluctuations climatiques ;

(iii) Au moins une zone influencée par les activités humaines dans la période considérée, afin d'évaluer l'impact de l'homme sur l'érosion.

(iv) Des caractéristiques facilement identifiables permettant de distinguer les proportions des apports sédimentaires de chaque zone. Des différences de lithologie entre les zones de hautes montagnes et les zones de plaines où l'activité humaine est concentrée devraient permettre de tracer les contributions de chaque zone, et donc de chaque forçage.

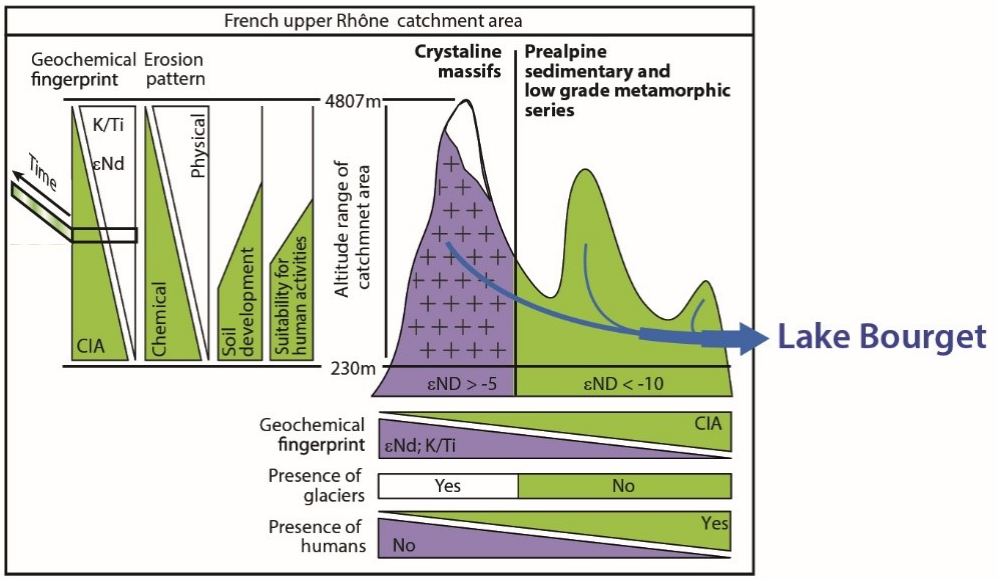

Fig. II-6- Exemple de caractéristiques de bassin versant intéressant pour notre approche. Il s'agit ici du bassin versant du lac du Bourget (Alpes françaises). Modifiée d'après Arnaud et al., (2016).

Pour ce travail nous avons sélectionné deux grands lacs périalpins, le lac du Bourget (Fig. II-6) et le lac Iseo. Ces deux lacs et leur bassin versant répondent à l'ensemble des critères énoncés ci-dessus. Ces lacs sont localisés sur deux faces des Alpes différentes, impactés par des climats différents au cours de l'Holocène, ainsi qu'une histoire de l'activité humaine différente liée à des courants de Néolithisation différents. Le détail des caractéristiques des deux sites d'études est donné dans le chapitre III.

2.3. Méthode source/puits

Afin de démêler les effets du climat et des activités humaines sur l'évolution de l'érosion au cours du temps, il apparaît nécessaire d'utiliser une méthode source/puits (« source to sink » en anglais). En effet, dans le cas où chaque forçage impacte une zone du bassin versant en particulier, l'identification de caractéristiques permettant de tracer la contribution de ces zones au cours du temps aidera à distinguer les effets de chaque forçage. Les méthodes de traçage des sources de sédiments sont régulièrement utilisées pour interroger l'origine des résidus d'érosion d'un bassin versant (e.g., Colin et al., 1999; Collins et al., 2017; Collins and Walling, 2002; Evrard et al., 2020; Haddadchi et al., 2013; Laceby et al., 2017, 2015; Revel-Rolland et al., 2005; Sabatier et al., 2010). La méthode consiste à prélever des échantillons de « source » qui sont analysés pour caractériser chaque source potentielle d'apport sédimentaire (Fig. II-7). Une fois leur signature identifiée à partir de paramètres sélectionnés, la contribution des sources est évaluée en mesurant les mêmes paramètres dans les échantillons du « puits », les sédiments de lac dans notre cas. La difficulté réside ici dans les choix de méthodes adéquates, permettant de distinguer les signatures des différentes sources. Un arbre de décision méthodologique détaillé a été réalisé par Collins et al. (2017).

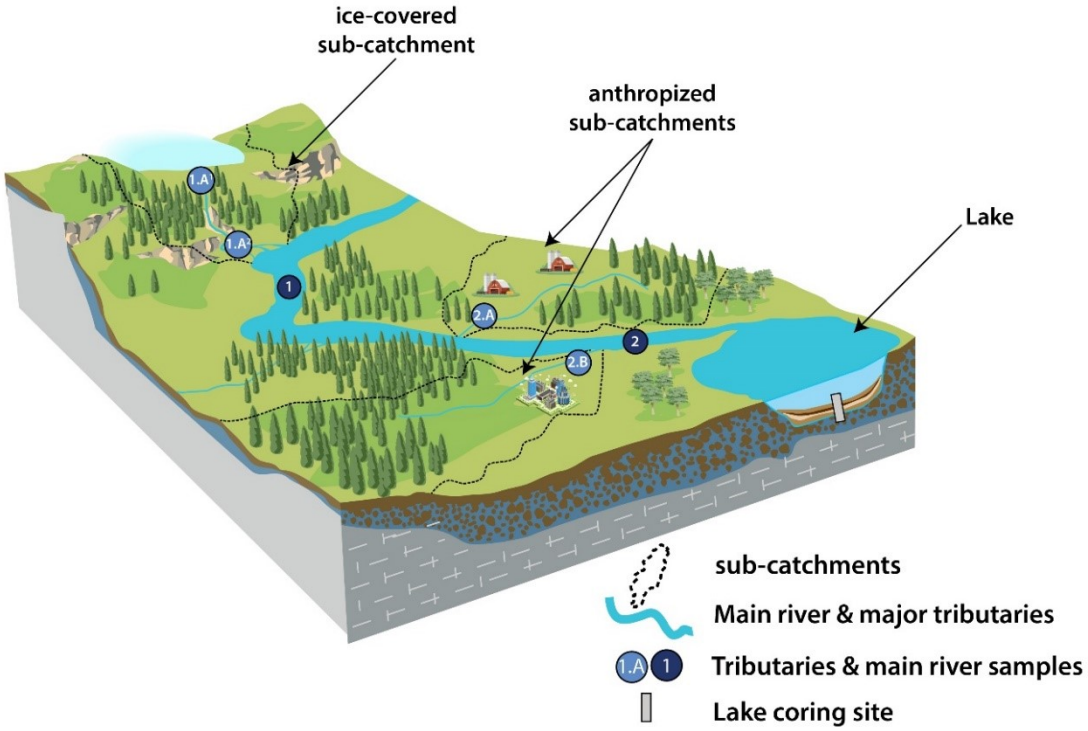

Fig. II-7- Schéma simplifié de la méthode « source – puits ». Les échantillons d'affluents sont censés être représentatifs de l'ensemble de leur sous bassin-versant. Figure modifiée de Chorover et al. (2007).

Dans notre étude, pour obtenir des échantillons représentatifs de chaque source nous avons choisi :

(i) De ne pas échantillonner directement les roches mères ou les sols mais d'obtenir une signature de l'ensemble d'un sous-bassin versant via les sédiments de rivière.

(ii) De privilégier un échantillonnage dans des laisses de crues sur le bord des affluents principaux à proximité de leur confluence avec le cours d'eau principal. Ainsi chaque sous-bassin versant peut être échantillonné et caractérisé (Fig. II-7). Nous faisons l'hypothèse que l'échantillon prélevé à l'exutoire d'un sous-bassin est représentatif des produits d'érosion de l'intégralité de la zone situé en amont du point de prélèvement. Nous sommes conscients du fait que nos échantillons n'ont pas de représentativité temporelle et que, lors d'événements de précipitations extrêmes localisées, une zone peut être soumise à une érosion plus intense qu'une autre et être ainsi sur-représenté dans nos échantillons ;

(iii) Pour corriger ce biais, nous avons choisi de diviser les sous-bassins versants en fonction des différentes lithologies présentent en prélevant des échantillons en amont de l'exutoire principal, afin de couvrir toutes les signatures possibles ;

(iv) De réaliser des échantillonnages de laisse de crues dans le cours d'eau principal après chaque confluence majeure afin de vérifier l'influence de chaque sous bassin versant dans le mélange (Fig. II-7).

Afin de déterminer les signatures de chaque source nous avons choisi d'utiliser la composition isotopique en strontium et néodyme. Ces isotopes radiogénique sont des traceurs régulièrement utilisés notamment en paléocéanographie pour tracer les sources des masses d'eau océaniques (e.g., Pena and Goldstein, 2014; Tachikawa et al., 2021, 2020) et en paléoclimatologie pour

tracer les sources des apports de produits d'érosion (e.g., Arnaud et al., 2012; Cogez et al., 2015; Colin et al., 1999; Mologni et al., 2020). La composition en isotopes radiogéniques varie à la surface de la Terre du fait de la différenciation chimique de la Terre, des différents comportements des éléments pères et fils pendant la formation du magma, et de l'âge de la croûte continentale. Deux types de roches différentes ou d'âges différents auront ainsi une signature isotopique différente (Goldstein and Hemming, 2003). Nous avons donc choisi d'utiliser la composition isotopique en Néodyme (Nd) et en Strontium (Sr), car de nombreuses études ont montré que ces isotopes peuvent être utiles lorsqu'ils sont associés ensemble pour tracer les caractéristiques des terrains sources (e.g., Cogez et al., 2015; Colin et al., 1999; Frank, 2002; Goldstein and Hemming, 2003; Jewell et al., 2021; Nakano et al., 2004; Revel-Rolland et al., 2005). La composition isotopique des sédiments de lac et des échantillons de rivières a donc été analysée pour chaque site d'étude, la méthode utilisée pour ces analyses est détaillée dans les chapitre IX et X.

Enfin nous avons dû choisir une taille de grains sur laquelle réaliser les analyses (Collins et al., 2017). Ici, les sédiments accumulés dans les puits (i.e., les lacs) présentent une taille médiane comprises entre 10 et 30 µm en fonction des sites (Arnaud, 2005). Toutefois pour se conformer aux études précédemment réalisées sur le lac du Bourget (Revel-Rolland et al., 2005) nous avons choisi d'utiliser la fraction inférieure à 63 µm. Cette fraction a été utilisée avec succès dans la majorité des études publiées sur le traçage de source et est également représentative de la granulométrie des sédiments transportés par la plupart des rivières dans les climats tempérés (Collins et al., 2017). L'utilisation d'une fraction de particules plus fine que celle-ci réduirait le potentiel d'incertitudes liées à la taille des grains. Une fraction plus fine serait aussi moins représentative des sédiments transportés dans une rivière (Collins et al., 2017). Toutefois, nous sommes conscients que la sédimentation continue dans les bassins profonds des grands lacs est généralement constituée de grains de taille inférieure à 63 µm. Les résultats obtenus en utilisant la fraction inférieure à 63 µm peuvent être faussés si l'outil utilisé dans le traçage de source est sensible à la taille des grains analysés, c'est-à-dire, si la probabilité d'un fractionnement isotopique lié au tri mécanique des grains lors du dépôt dans le bassin sédimentaire est non nulle. La composition isotopique en Nd n'est généralement pas impactée par la taille des grains, toutefois, il n'en va pas de même pour la composition isotopique en Sr (Dasch, 1969; Feng et al., 2009). Une attention particulière sera portée à ce biais potentiel lors de l'interprétation des données dans la suite du manuscrit.

Pour aller plus loin

Afin de démêler et quantifier les effets des forçages humains et climatiques, un modèle de mélange a été réalisé pour chaque site (Haddadchi et al., 2013). Le signal d'érosion de la zone du bassin versant où l'activité humaine est nulle a été interprété comme un traceur de l'effet du climat sur l'érosion au cours du temps. Une fois cet effet quantifié, et en faisant l'hypothèse que l'impact du climat en haute altitude est proche de celui des zones de basses altitude, l'impact de l'activité humaine a pu être quantifié.

Afin de valider les données de flux d'érosion produit à partir des archives de sédiments lacustres, une comparaison avec les données d'érosion actuelle issue de modèle numérique ou d'autres études locales et régionales a été réalisée. Cette étape de validation est nécessaire afin de pouvoir discuter des fluctuations des signaux d'érosion dans le passé.

CHAPITRE III | Sites d'études

Les deux sites choisis pour réaliser cette thèse sont le lac Iseo en Italie et le lac du Bourget en France. Il s'agit de deux grands lacs périalpins, situés à l'exutoire de vastes bassins versants ce qui permet d'investiguer l'évolution de l'érosion sur de grandes superficies. Ces deux lacs ont aussi été choisis pour être représentatifs de secteurs influencés par différents processus climatiques ainsi que différentes histoires humaines, c'est-à-dire les Alpes méridionales et nord-occidentales, respectivement. Enfin, chacun de ces lacs se situe dans un bassin versant où de nombreuses études, que ce soit à partir d'archives naturelles, de sites archéologiques ou de données historiques ont apporté des informations sur l'évolution de la présence des activités humaines, notamment agro-pastorales.

1. Lac Iseo

1.1. Lac, limnologie et bathymétrie

Le lac Iseo (45°44.205′N ; 10°4.340′E) se situe dans les Alpes italiennes, en Lombardie, au Nord de la plaine du Pô, à l'extrémité Sud du Val Camonica, à une altitude de 185 m au-dessus du niveau de la mer (abrévié ci-après par « a.s.l » pour « above see level »). Le Lac Iseo (nom latin « Sebino ») est long de 25 km et présente une superficie d'environ 60,9 km². Il s'agit du plus petit des quatre grands lacs du Nord de l'Italie. La dépression où le lac est situé est un ancien canyon d'origine miocène qui a été érodé à nouveau lors des différentes périodes d'avancée glaciaire du Pléistocène (Bini et al., 1978). Le remplissage sédimentaire actuel est supposé avoir été initié depuis le retrait des glaciers postérieurement au dernier maximum glaciaire (Bini et al., 1978). De nombreuses études ont déjà été réalisées sur le lac Iseo, celles-ci discutent (i) la chimie des eaux du lacs (e.g., Lau et al., 2020), (ii) l'hydrodynamique (e.g., Pilotti et al., 2018, 2013), (iii) la morphologie du lac (Bini et al., 2007) ainsi que (iv) la sédimentation instantanée enregistrée dans l'un des bassins sédimentaires (Lauterbach et al., 2012).

Le lac Iseo est actuellement méromictique (Ambrosetti and Barbanti, 2005; Salmaso et al., 2003), c'est-à-dire que les eaux de surface et du fond du lac se mélangent moins d'une fois par an (Wetzel, 2001). Depuis les années 1980, et le dernier mélange observé (Salmaso et al., 2003), les concentrations en oxygène des eaux profondes n'ont eu de cesse de diminuer, entraînant le développement de conditions d'anoxie permanente depuis les années 1990. La profondeur de thermocline, limite sous laquelle se situe l'hypolimnion (i.e., la couche thermique la plus profonde du lac, présentant une température stable) est d'environ 50 à 80 m d'après les données de l'agence régionale de protection de l'environnement de Lombardie (http://arpalombardia.it/). A partir de ces profondeurs, la saturation en oxygène et les valeurs de pH diminuent fortement, tandis que la concentration en calcium dissous augmente.

La carte bathymétrique du lac Iseo met en évidence la présence de deux bassins séparés par l'île de Monte Isola (Fig. III-1), plus grande île lacustre d'Europe. Le bassin principal s'étend à l'Ouest de l'île et présente une profondeur maximale de 256 m en dessous de la surface du lac (abrévié ci-après par « b.l.s » pour « below lake surface »). Le plateau de Monte Isola se situe à l'Est de

l'île et est isolé du bassin profond par un escarpement d'environ 180 m de haut. Au sud de ce plateau, un second escarpement, d'une trentaine de mètre, sépare le plateau du second bassin du lac Iseo, le bassin de Sale Marasino, profond d'environ 100 m b.l.s (Fig. III-1).

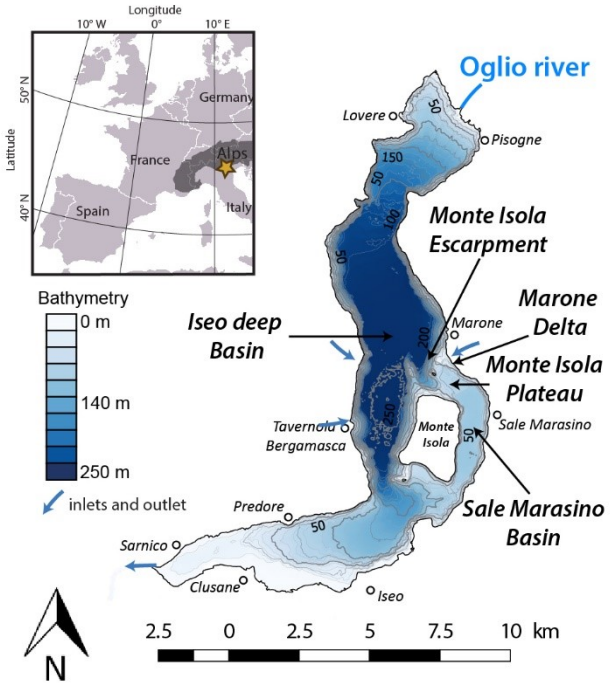

Fig. III-1- Carte bathymétrique du lac Iseo, tirée et modifiée de Rapuc et al., (2019). La bathymétrie du lac Iseo est modifiée à partir des données de Pilotti et al., (2013), les données sont disponibles à l'adresse suivante : https://hydraulics.unibs.it/hydraulics/attivita-scientifica/laghi_pvbs/lake-iseo-data-set/.

1.2. Bassins versants et apports sédimentaires

Le lac Iseo est situé sur le cours de la rivière Oglio, qui est donc à la fois son principal affluent et son exutoire (Fig. III-1). Toutefois, en termes d'apports sédimentaire, les deux bassins du lac ne sont pas alimentés par les mêmes bassins versants : l'Oglio alimente en effet le bassin profond, mais pas la zone située à l'est de l'île de Monte Isola. En effet, l'escarpement situé au nord du plateau de Monte Isola empêche les sédiments transportés par des courants s'écoulant sur le fond du lac (underflows) d'atteindre le plateau de Monte Isola et le bassin de Sale Marasino. De plus, dans des conditions de courant ordinaire, les entrées d'eau les moins chargées en sédiment de l'Oglio qui se disperse dans le lac au niveau de la thermocline (on parle de courant d'interflow) sont détournées vers le flanc ouest du lac du fait de la force de Coriolis (Pilotti et al., 2013, 2018). Par conséquent, en termes d'apports sédimentaires, le bassin de Sale Marasino et le plateau de Monte Isola ont un bassin versant réduit aux seules pentes situées à l'est du lac, drainées par l'Opolo et le Bagnadore, deux petits cours d'eau de versant dont les embouchures dans le lac sont situées au niveau du village de Marone. Cette zone est principalement recouverte de colluvions quaternaires (Presbitero et al., 2011). La partie haute de ce bassin versant ainsi que l'île de Monte Isola présentent une épaisse couverture de marnes, de calcaires et de dolomies datant du Trias supérieur et du Jurassique inférieur. Quelques affleurements d'andésite et de rhyolite sont présents dans la partie haute de ce sous-bassin versant (Presbitero et al., 2011).

Les apports sédimentaires dans le bassin profond sont restreints à l'Oglio et aux quelques cours d'eau de versants situés sur les pentes à l'ouest du lac. En effet, le bassin profond est protégé

des apports sédimentaires de l'Opolo et du Bagnadore par la présence d'une ride située au nord-ouest de Monte Isola.

L'Oglio prend sa source dans le Massif de l'Adamello, au nord-est, et draine un bassin versant qui s'étend sur plus de 1777 km² (Fig. III-2). Ce bassin versant présente une altitude maximale de 3539 m a.s.l au niveau du massif de l'Adamello et une altitude moyenne d'environ 1400 m a.s.l (Letizia Garibaldi et al., 1999). En termes de lithologie, le bassin versant du lac Iseo peut se diviser en trois grandes catégories : (i) la couverture sédimentaire Mésozoïque, le socle varisque métamorphique ainsi que le batholithe de l'Adamello (https://www.cartografia.servizirl.it/cargviewer/). La couverture sédimentaire des Alpes du Sud est localisée dans la partie sud du bassin versant (Fig. III-2) et est composée principalement de marnes, de calcaires et de dolomies datant du Trias au Crétacé (Bini et al., 2012). Quelques affleurements de grès du Permien sont localisés dans la partie sud-est du bassin. Le socle varisque est quant à lui localisé au nord et à l'ouest du bassin versant. Il est constitué de pélites, de schistes, de gneiss et d'amphibolites : roches de faible à haut grade métamorphique (Chiesa et al., 2011; Gosso et al., 2012). Dans la partie nord-est du bassin versant, au niveau du massif de l'Adamello affleure une série calco-alcaline plutonique (Fig. III-2) constituant le batholithe de l'Adamello (Brack et al., 2008; Mittempergher et al., 2021). Cette série s'est intrudée dans le socle varisque au cours du Cénozoïque, il y a 30 à 40 Ma. Le batholithe est composé principalement de roches plutoniques felsiques : tonalites, granites, granodiorites et quartzodiorites, associées à quelques affleurements de roches mafiques à ultramafiques (Brack et al., 2008).

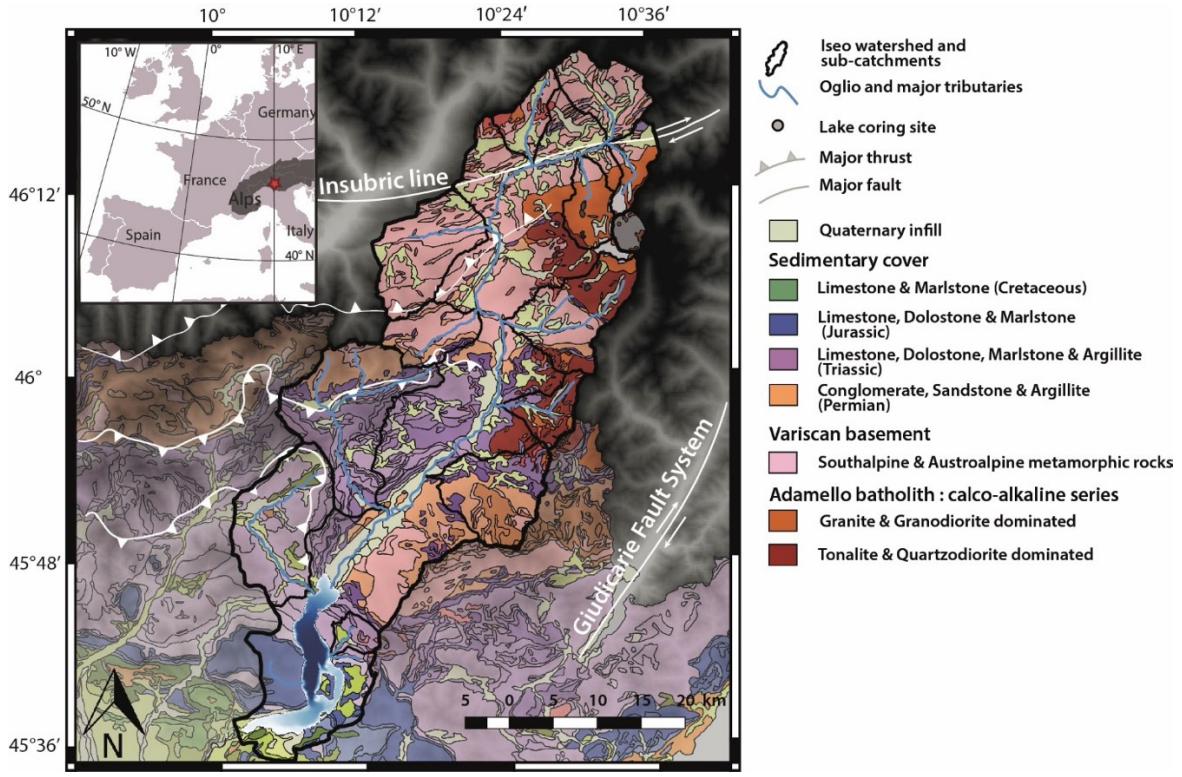

Fig. III-2- Carte géologique du bassin versant du lac Iseo, superposée à une carte de relief. Les informations géologiques sont modifiées à partir de la carte géologique de la région Lombardie (CARG project ; https://www.cartografia.servizirl.it/cargviewer/). Les principales failles, les principaux affluents, ainsi que les sous-bassins versants de l'Oglio sont aussi représentés.

1.3. Contexte climatique

La zone d'étude est influencée par un climat subméditerranéen, où la distribution des précipitations saisonnière est caractérisée par des taux précipitations les plus élevés durant l'été et l'automne (Wirth et al., 2013a). Les événements de précipitations extrêmes dans le bassin versant sont liés soit à des phénomènes convectifs locaux (c'est-à-dire des orages d'été) soit à des systèmes frontaux atlantiques combinés à des systèmes convectifs orographiques à méso-échelle, se développant sur la partie Nord de la mer Méditerranée. Ces derniers se produisent principalement de la fin du printemps à l'automne (Trigo et al., 2002; Winschall et al., 2012). Le bassin versant de l'Oglio comprend un nombre important de glaciers et de glaciers rocheux (Fig. III-3), dont le glacier de l'Adamello, l'un des plus vastes glaciers de Lombardie (Scotti et al., 2013). La majeure partie de ces glaciers est située dans le massif de l'Adamello et secondairement dans les zones d'altitudes situées directement au sud du massif (Fig. III-3). Bien qu'ils aient fortement régressé par rapport au début du 20ème siècle, le climat plutôt humide de la région, avec des cumuls de précipitations annuels supérieurs à 1200 mm.yr-1, contribue à limiter le retrait de ces glaciers dans le contexte actuel de réchauffement climatique actuel (Scotti et al., 2013).

1.4. Activités humaines

Le terme Val Camonica désigne le bassin versant de l'Oglio en amont du lac Iseo. Cette zone est connue pour avoir hébergé parmi les plus anciennes sociétés agro-pastorales d'Europe. La présence de gravures rupestres néolithiques, évoquant notamment des parcellaires agricoles a généré un grand nombre d'études archéologiques (e.g. Anati and Cittadini, 1994; Arcà and Fossati, 2006; Nash, 2011; Nash and Chippindale, 2002) et justifié le classement du site par l'UNESCO au titre du patrimoine mondial de l'humanité.

Si les premières traces d'occupation humaine dans la vallée datent du Mésolithique (Anati and Cittadini, 1994), le développement des pratiques agricoles est attesté dès 4500 av. J.-C., (Gehrig, 1997; Pini et al., 2016). Des études archéologiques et palynologiques ont montré que la grande majorité des occupations humaines était localisée dans la partie sud du bassin versant, à proximité du lac Iseo, depuis le Néolithique (e.g., Marziani and Citterio, 1999; Pini, 2002; Pini et al., 2016). De nombreuses informations sur l'occupation des rives du lac sont aussi disponibles (Benedetti and Predali, 2013; Condina, 1986; Gregorini et al., 2012; Predali, 2013, 2010, 2008). Actuellement, la majeure partie des zones urbaines et agricoles est encore localisée dans la partie sud du bassin versant (Fig. III-3).

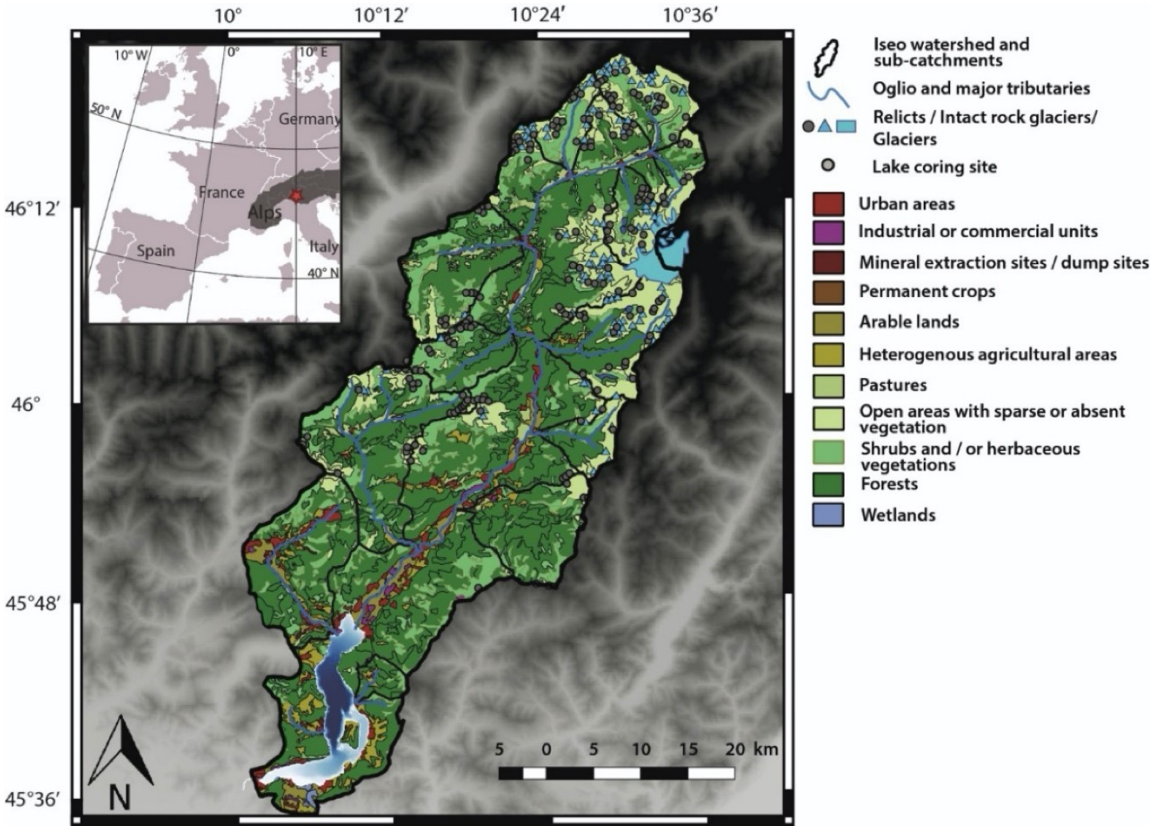

Fig. III-3- Carte de l'utilisation des sols dans le bassin versant du lac Iseo, superposée à une carte de relief. Les données d'utilisation des sols dérivent de la carte de CORINE land cover pour la région Lomabrdie, disponible à l'adresse suivante : http://www.geoportale.regione.lombardia.it/. La localisation des différents types de glaciers ont été obtenu à partir des données de Scotti et al. (2013).

2. Lac du Bourget

2.1. Lac, limnologie et bathymétrie

Le Lac du Bourget est le plus grand lac naturel entièrement situé en France (44,5 km²). Il s'agit d'un lac périalpin situé au nord-ouest des Alpes françaises (45°45.3'N ; 5°51.3'E), à 235 m a.s.l. Long de 18 km et large de 2,8 km, il s'est formé à la faveur du retrait glaciaire postérieur au dernier maximum glaciaire (Nicoud et al., 1987). D'après la carte bathymétrique, le lac du Bourget présente deux bassins, un premier profond de 145 m, situé dans sa partie nord et un second, moins profond (100 m b.l.s environ), situé dans sa partie sud (Fig. III-4). Il est alimenté de manière permanente par 3 cours d'eau : la Leysse, le Tillet et le Sierroz qui alimentent en sédiment le bassin sud du lac (Chapron, 1999).

Le lac du Bourget est un lac monomictique, c'est-à-dire un lac dont les eaux superficielles et les eaux profondes subissent un mélange une fois par an. Cependant, la réoxygénation de son hypolimnion, lors du mélange hivernal de l'eau, n'est en général que partielle, les zones les plus profondes restant, de ce fait, désoxygénées toute l'année. Le reste du lac subit également une hypoxie qui augmente progressivement avec la mise en place de la stratification thermique estivale (Jacquet et al., 2005; Jenny et al., 2013). Pendant la majeure partie de l'année, l'eau du fond du lac présente donc une concentration en oxygène, voire nulle par rapport à la surface et aux apports d'eau des affluents. Le lac du Bourget a connu plusieurs périodes d'hypoxie de ces eaux profondes au cours du dernier siècle, entre 1933 et 1975, puis de 1997 à l'actuel, durant

lesquelles un volume important des eaux profondes est resté anoxique toute l'année. Les sédiments du lac du Bourget ont déjà été étudiés pour comprendre par exemple (i) l'histoire de l'eutrophisation du lac (Giguet-Covex et al., 2010; Jenny et al., 2013), (ii) l'évolution de la fréquence des crues régionales (Arnaud et al., 2005; Chapron et al., 2002, 2005; Debret et al., 2010; Evin et al., 2019; Jenny et al., 2014b), (ii) l'évolution de l'érosion dans le bassin versant (Arnaud et al., 2012; Revel-Rolland et al., 2005) ou (iv) les dépôts induits par des séismes (Chapron et al., 1999).

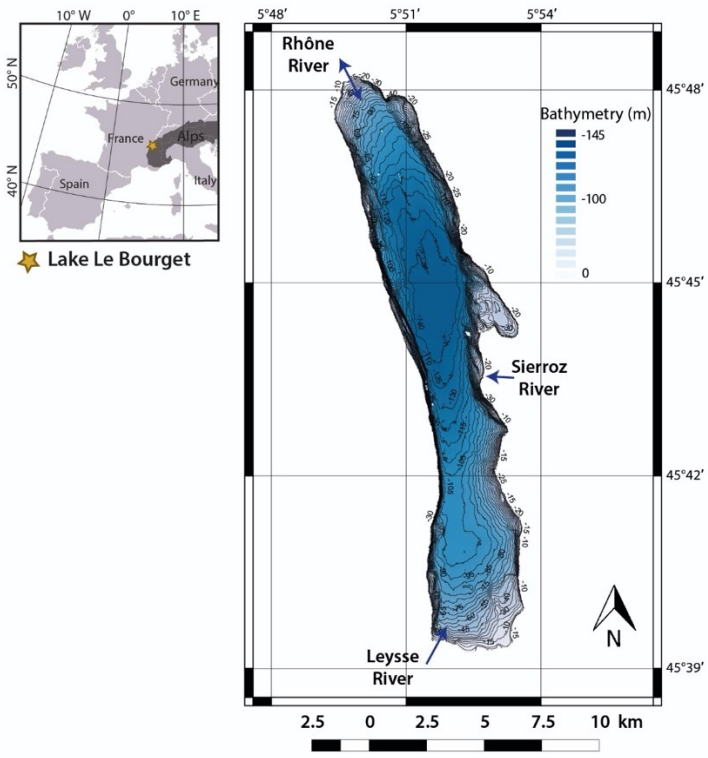

Fig. III-4- Carte bathymétrique du lac du Bourget, les principaux affluents ainsi que l'exutoire du lac sont représentés. Les données de bathymétrie sont issues et modifiées à partir du travail de Ledoux et al., (2010).

2.2. Bassins versants et apports sédimentaires

La Leysse, le Sierroz et le Tillet, petites rivières dont les embouchures se situent au sud et à l'est du lac, respectivement (Fig. III-4), alimentent en eau du lac du Bourget, qui s'écoule ensuite vers le Rhône par le canal naturel de Savière (Jenny et al., 2014b). Dans ces conditions, le lac du Bourget présente un bassin versant réduit de 588 km² (Giguet-Covex et al., 2010). Cependant, lorsque le Rhône est en crue, le courant s'inverse et les eaux rhodaniennes riches en sédiments pénètrent dans le lac via le canal de Savière et lors des épisodes les plus intenses débordent les levées du Rhône et submergent le marais de Chautagne avant de finir dans le lac. Lors de ce type d'événement, le bassin versant du lac du Bourget correspond à la totalité de la partie française drainée par le Rhône en amont du lac. En effet, le lac Léman agit comme un piège à sédiment parfait, ainsi les sédiments provenant de la partie suisse du bassin versant du Rhône sont totalement piégés dans le lac et ne contribuent pas aux apports sédimentaires du lac du Bourget (Arnaud et al., 2012). En considérant la partie française de l'aire drainée par le Rhône, le bassin versant du lac du Bourget avoisine les 4600 km² (Giguet-Covex et al., 2010). Dans ce cas, les principaux affluents du lac sont (i) l'Arve, avec un bassin versant d'environ 1980 km² et drainant

notamment le massif du Mont-Blanc, et (ii) le Fier, avec un bassin versant d'environ 1330 km² (Fig. III-5).

La situation dans laquelle le Rhône entre de manière intermittente dans le lac Bourget n'a pas toujours prévalu. Au cours du Tardiglaciaire (entre 18 000 et 11 700 ans avant l'actuel), la zone actuellement occupée par le marais de Chautagne, au nord du lac était entièrement occupée par la plaine d'inondation du Rhône (Chapron, 1999; Nicoud et al., 1987). Le Rhône s'écoulait alors directement dans le lac du Bourget. Suite à une période d'accumulation de sédiments au niveau de l'embouchure du Rhône, ce dernier a abandonné le lac du Bourget par son flanc gauche (Arnaud et al., 2012). Cela a permis le développement de la zone marécageuse de Chautagne. La datation de la base de l'accumulation tourbeuse de Chautagne vers 10 000 cal. BP (Disnar et al., 2008) donne un âge minimum pour l'abandon du lac par le Rhône en régime d'étiage. Les nombreuses études portant sur la sédimentation dans le lac ont mis en évidence que, dans la partie nord du bassin du lac, l'influence des crues du Rhône contribue de 10 à 40% à la sédimentation totale (Arnaud et al., 2012; Giguet-Covex et al., 2010). Le reste de l'accumulation sédimentaire du bassin profond du lac correspond à des dépôts de carbonates authigènes ainsi qu'à des dépôts organiques, la Leysse et le Sierroz ne contribuant que de façon minoritaire aux flux sédimentaires (Arnaud et al., 2012; Revel-Rolland et al., 2005).

En termes d'apports sédimentaires, le bassin versant du lac du Bourget couvre donc une large zone d'environ 4600 km² s'étendant du massif du Mont-Blanc (4809 m a.s.l) aux massifs subalpins des Aravis et des Bauges (Arnaud et al., 2012). L'Arve, puis le Rhône et leurs affluents drainent des terrains géologiques divers, allant des massifs cristallins externes de la zone du Mont-Blanc à la molasse miocène (Fig. III-5). La partie haute de la vallée de l'Arve, dans la vallée de Chamonix, présente à l'affleurement des roches plutoniques felsiques, essentiellement des granites, associées à des roches métamorphiques de type gneiss et micaschistes. Le fond de vallée est majoritairement caractérisé par la présence d'une couverture de marne. En dehors de cette zone, l'ensemble du bassin versant du Rhône et de l'Arve est composé en majorité de roches sédimentaires : schistes, flysch à helminthoïdes, marnes, calcaires, grès, datant de la fin du Paléozoïque et du Mésozoïque principalement (Gidon, 1977). Le Sierroz, la Leysse, la partie basse de la vallée de l'Arve ainsi que la vallée du Rhône en aval de sa confluence avec l'Arve drainent des terrains de type molassique et les zones à calcaire et marnes de la chaîne du Jura (Fig. III-5).

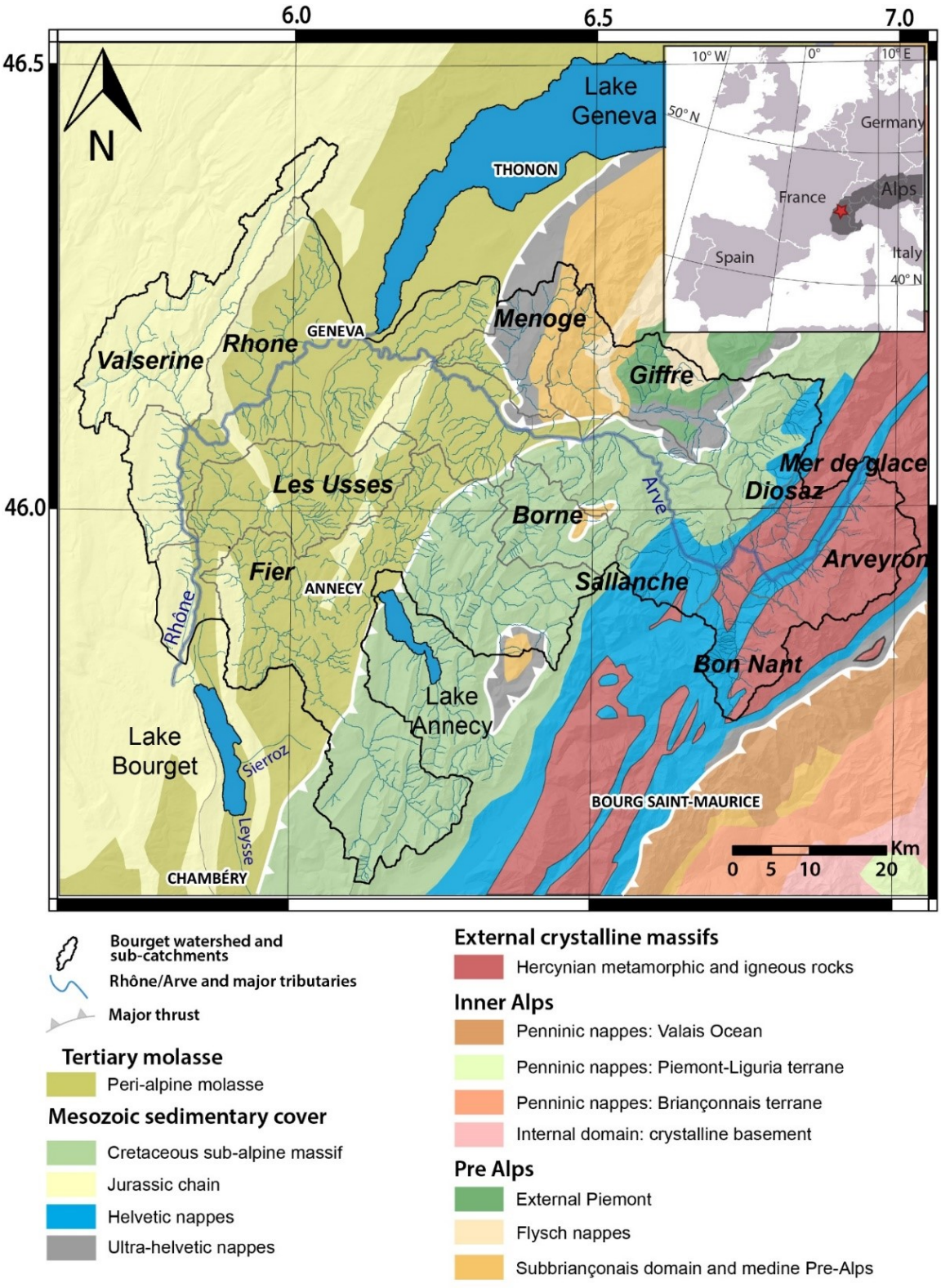

Fig. III-5- Carte géologique du bassin versant du lac du Bourget tirée et modifiée de Gidon, (1977). Les chevauchements majeurs ainsi que les cours d'eau principaux sont représentés.

2.3. Contexte climatique

La région du bassin versant du lac du Bourget est influencée par un climat de type montagnard. Les reliefs exposés à l'ouest arrêtent la plupart des perturbations océaniques et reçoivent donc des quantités de précipitations importantes. La présence des courants méditerranéens au sud et des reliefs des Alpes à l'est et du Massif central à l'ouest attenue l'influence océanique dans la zone et favorise le développement de tendances anticyclonique. La distribution des précipitations saisonnière est caractérisée par des cumuls de précipitations plus élevés durant l'hiver et le printemps (https://meteofrance.com). Les zones de relief et d'altitude sont caractérisées par des précipitations plus importantes (> 1700 mm.an-1), tandis que les zones de plaines sont plus sèches (entre 1000 et 1400 mm.an-1). Les massifs à proximité du lac sont soumis à des précipitations d'ouest ainsi qu'aux orages. Dans la vallée du Chambéry, l'essentiel du déplacement des masses d'air s'effectue en suivant un axe nord-sud (Blanchet, 1990). La partie haute du bassin versant, au niveau de la vallée de Chamonix, présente un nombre important de glaciers de grande tailles (Gardent, 2014), dont notamment la Mer de Glace, qui, avec une superficie d'environ 40 km², est le plus grand glacier français.

2.4. Activités humaines

Du fait de la superficie importante du bassin versant du lac du Bourget, de multiples sources d'informations sont disponibles quant à l'évolution des activités humaines au cours de l'Holocène (e.g., Bajard, 2017; Bajard et al., 2020; Frayn, 1984; Gauthier, 2002; Gauthier and Richard, 2008; Racimo et al., 2020; Rey, 2016; Segard, 2009). Dès le Néolithique, les activités pastorales se développent à basses altitudes dans l'ensemble des Alpes occidentales avant d'augmenter sensiblement leurs intensités aux alentours de 3600 ans avant l'actuel (Bajard et al., 2020). Suite à une ouverture du milieu par l'homme via la déforestation, les activités pastorales dans les zones d'altitude des Alpes françaises du Nord ont continuées à se développer après l'âge du Bronze (Bajard et al., 2020; David, 2010) et ce jusqu'au Moyen Age tardif, où ces dernières étaient réparties à toutes les altitudes. Une diversification des cultures a aussi été observées dans les zones de basses à moyenne altitude depuis l'âge du Bronze (Giguet-Covex et al., 2021).

Pour la période actuelle, l'essentiel des activités humaines : agricoles, pastorales ainsi que les centres urbains sont localisés en fond de vallée et proche des zones humides (https://www.data.gouv.fr/fr/datasets/corine-land-cover-occupation-des-sols-en-france/).

Partie II | Processus sédimentaires à l'œuvre dans les grands lacs périalpins

CHAPITRE IV | Holocene-long record of flood frequency in the Southern Alps (Lake Iseo, Italy) under human and climate forcing

Article 1 | Publié dans Global and Planetary Change

https://doi.org/10.1016/j.gloplacha.2019.02.010

Received 20 August 2018; Received in revised form 29 January 2019; Accepted 15 February 2019

William Rapuc[1], Pierre Sabatier[1], Fabien Arnaud[1], Antoine Palumbo[1], Anne-Lise Develle[1], Jean-Louis Reyss[1], Laurent Augustin[2], Edouard Régnier[3], Andrea Piccin[4], Emmanuel Chapron[5], Jean-Pascal Dumoulin[3] and Ulrich von Grafenstein[3]

[1] Univ. Grenoble Alpes, Univ. Savoie Mont Blanc, CNRS, EDYTEM, 73000 Chambéry, France
[2] Division technique de l'INSU, Centre de Carottage et de Forage National, CNRS, France
[3] LSCE, Université de Versailles Saint-Quentin, Commissariat à l'Energie Atomique–CNRS, 91198 Gif-sur-Yvette, France
[4] Regione Lombardia, D.G. Territorio e Urbanistica, Struttura Sistema Informativo Territoriale, 20124 Milano, Italy
[5] Laboratoire GEODE, UMR 5602 CNRS-Université Toulouse Jean Jaurès, Maison de la Recherche, 31058 Toulouse, France

Abstract

A high-resolution sedimentological and geochemical analysis of a 21 m sediment sequence of Lake Iseo (Southern Alps, Italy) allowed for the reconstruction of the long-term flood frequency by visual identification of the event layers over the last 12 kyr cal BP. In a previous study that was undertaken on another sediment core from Lake Iseo, these layers were attributed to extreme surface runoff events. However, in this former core, large mass-wasting deposits that induce significant hiatuses did not permit a continuous record of flood events to be established. Such disturbances were absent in the core studied in the present paper. This permitted to establish a high-resolution continuous Holocene record. Based on the flood chronicle and sedimentological and XRF geochemical analyses, we found evidence of a major palaeohydrological transition at approximately 3.8 kyr cal BP, which was previously described as occurring in the western Mediterranean region. The oldest part of the record indeed presents a very low frequency of flood events (< 1 flood/century), while after 4 kyr cal BP, the flood frequency increased. This pattern appears to be in agreement with other Southern Alpine paleo flood records. The transition is interpreted as a nonlinear climate response to the orbital-driven gradual decrease in summer insolation at 60°N, which together with the influence of the Mediterranean mesoscale precipitation events, is typical for the Mediterranean climate. However, the comparison of the flood record with the archaeological and historical data from the watershed suggests that human activity during the Roman period in the vicinity of the main tributaries also influenced the flood frequency. Even in a large Alpine lake and more than 2000 years ago, extreme precipitation events that were recorded

through the sedimentation process can hence be impacted by the anthropization of the catchment area pointing the requirement of deeper studies of Earth surface critical zone pluri-millennial dynamics.

KEYWORDS:

Lake sediment; Holocene; Flood chronicle; Human impact; Southern Alps

1. Introduction

In mountainous areas, floods are among the most damaging climatic events in terms of economic and societal losses (Gaume et al., 2009; Glur et al., 2013). In the context of global climate changes, the intensification of catastrophic events, such as floods, is expected in European regions (Hirabayashi et al., 2013). Indeed, even if a decrease in summer precipitation is expected in the Alps by the year 2100, extreme precipitation events that are associated with convective rainfall are assumed to increase (Giorgi et al., 2016). However, tendencies at the regional and local scales are still uncertain, and the study of these extreme events represents a major issue for natural hazards assessment (Stocker et al., 2013). The use of geological paleoclimate records is necessary to understand the past variations of these events in contrasting climatic contexts (Beniston et al., 2007). Lake sediments are widely used to reconstruct paleo-flood activity, as flood events are recorded in a long-term and continuous way (Bøe et al., 2016; Giguet-Covex et al., 2012; Gilli et al., 2013; Glur et al., 2013; Moreno et al., 2008; Noren et al., 2002; Wilhelm et al., 2012; Wirth et al., 2013b).

In ideal conditions, paleo-flood records that are obtained from lake sediment can be used as a proxy of local or regional extreme paleo-hydrological patterns (Sabatier et al., 2017; Wilhelm et al., 2013; Wirth et al., 2013b). In the context of an environment that is stressed by human activities, soil is more easily mobilized by precipitation events. Indeed, land-use and forest clearance generally increase soil erodibility and runoff efficiency (Brisset et al., 2017; Cosandey et al., 2005). Recently, several studies have shown that human activities in the small-size watershed could influence the frequency of floods that are recorded in mountain lake sediments (Brisset et al., 2017; Giguet-Covex et al., 2012). However, in a recent review, Arnaud et al., (2016) proposed that the influence of human activity upon geological record of erosive events should be minimal in a large lake fed by a large, diversified catchment area. To go a step further in discriminating climate and human impact on lake sediment-based flood chronicles, we propose here the study of a lowland lake fed by a medium-sized catchment area and located in a region where the long-term regional climate trend and human activity are well-documented.

We studied a sediment sequence from Lake Iseo at the downstream end of the Val Camonica valley in Northern Italy. Various paleoclimate records from this region already exist, which will be used to discuss the regional representativeness of our new flood chronicle (Magny et al., 2009, 2012; Vannière et al., 2013; Wirth et al., 2013b). Human activities were also well-documented in the Val Camonica from the first settlements and in the first trace of agricultural practices that are dated to the Mesolithic (Anati and Cittadini, 1994) and the Neolithic periods (Gehrig, 1997), respectively. A high number of rock carvings and archaeological sites were discovered and studied in the Val Camonica valley (Anati and Cittadini, 1994; Arcà and Fossati, 2006; Nash, 2011; Nash and Chippindale, 2002). Information about human activities along the shores of Lake Iseo are also accessible, including periods of human presence on the delta, the date of the creation

of main Marone infrastructure as well as the age and location of archeological sites (Benedetti and Predali, 2013; Condina, 1986; Gregorini et al., 2012; Predali, 2013, 2010, 2008).

Here, we used a multi-proxy approach to combine the sedimentology and geochemistry to identify millimetric flood layers of a well-dated lake Iseo sediment sequence and, thus, to understand the long-term influence of human activities on the flood activity recorded in low elevation lake catchments in the alpine area.

2. Study Site and Geological Settings

Lake Iseo (45°44.205'N; 10°4.340'E) is a large lowland lake in Northern Italy, with a length of 25 km and a surface area of 60.9 km². This perialpine lake is located in Lombardy, north of the Po plain (Fig. IV-1-A), at the southern-end of the Val Camonica valley at an altitude of 185 m above sea level (a.s.l). The depression that hosts the lake corresponds to a Miocene canyon that was reshaped and re-eroded by several glacier advances during the Pleistocene epoch (Bini et al., 1978). The main tributary and the unique outlet of Lake Iseo are part of the Oglio River, which has its headwaters in the Adamello massif in the Northern part of Val Camonica (Fig. IV-1-B). This valley is known for a high number of rock carvings that are registered on the UNESCO World Heritage List, as they provide indications of human presence in the Iseo region since the Mesolithic (9000 – 6000 BC) period (Anati and Cittadini, 1994). Numerous archeological sites that are dated from the Camuni and Roman periods are also present around the Lake and in the southern-end of Val Camonica, north of Lake Iseo (Condina, 1986). In this region, the first trace of sparse agricultural activities was found in pollen records that date to approximately 7 kyr cal BP (Gehrig, 1997).

The bathymetric map highlights the presence of two basins in Lake Iseo separated by Monte Isola, which is the largest lake island in Italy (Fig. IV-1-B). The main basin spreads West of Monte Isola and presents a maximum water depth of 256 m below lake surface (b.l.s). East of Monte Isola, the lake morphology presents a shallower sub-basin (approximately 100 m deep) named Sale Marasino Basin. Northward, this basin is separated from Monte Isola Plateau (70 m b.l.s) by a 30-m-high escarpment. Monte Isola Plateau is isolated from the deeper basin by the 180-m-high Monte Isola Escarpment.

In terms of water supply, the Monte Isola Plateau (MIP) and the Sale Marasino Basin (SMB) are mainly fed by the Oglio River and small tributaries coming from the slopes, east of the Sale Marasino and Marone towns. MIP and SMB are located 11.4 km away from the Oglio inlet and are separated from the main basin by a 180-m-high escarpment (Fig. IV-1-B&C). This difference in elevation appears to be important enough to prevent underflows or interflows from the Oglio River from reaching the Monte Isola Plateau. Moreover, under ordinary flow conditions and under higher a discharge rate, the Oglio river is deflected toward the western shore of the lake due to the Coriolis influence (Pilotti et al., 2018, 2013). The overflow plume is, thus, generally brought to the western shore of Lake Iseo (Pilotti et al., 2018) and is unlikely to influence the Monte Isola Plateau and the Sale Marasino Basin on the eastern shore.

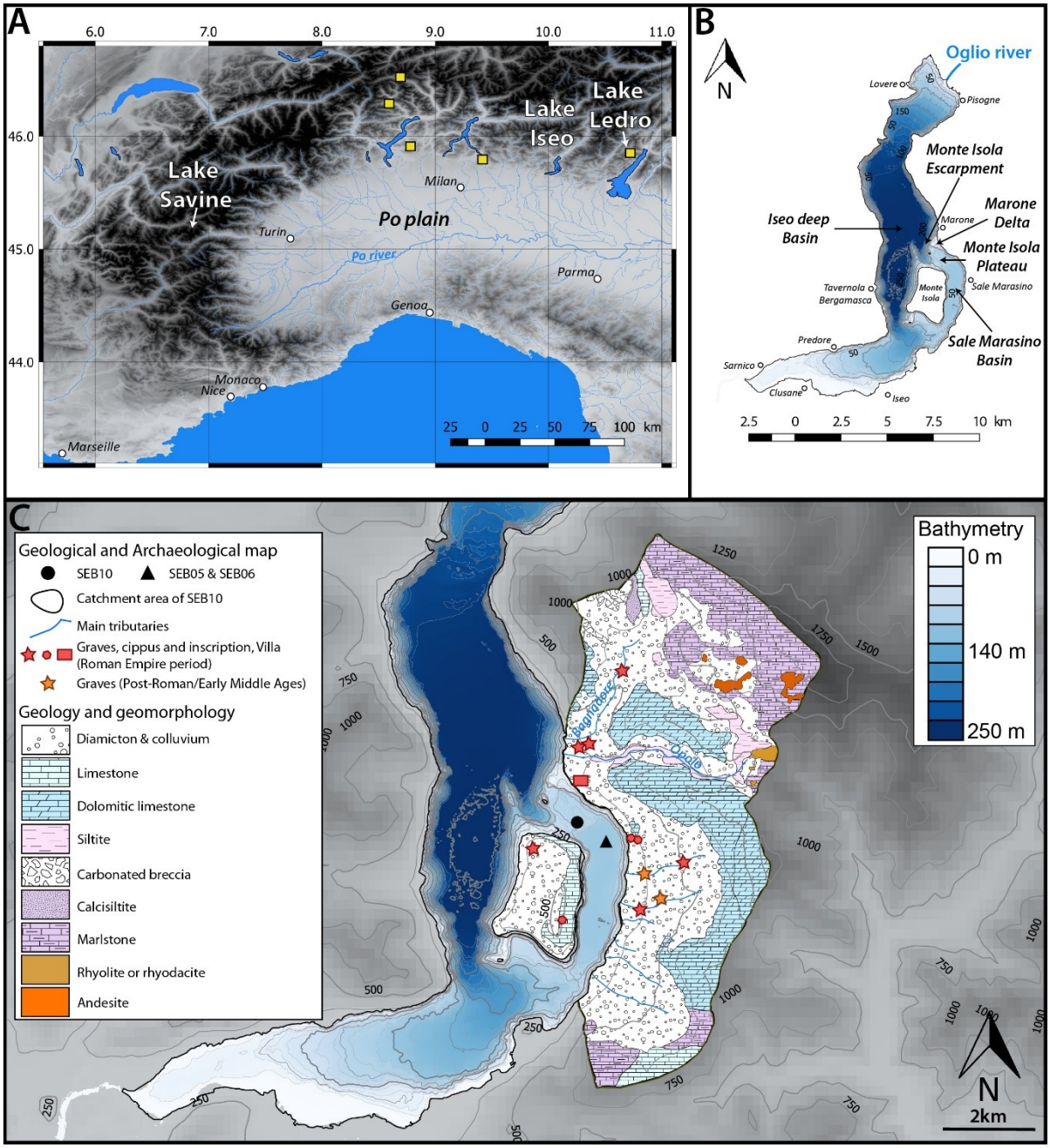

Fig. IV-1- Lake Iseo location and settings. (A) Locations of Lake Iseo (Italy) and the different lakes used hereafter for comparison: Lake Savine (France), Lake Ledro (Italy). The yellow squares correspond to the location of the different lakes that were used by Wirth et al., (2013) to construct a flood chronicle for the southern Alps. (B) Lake Iseo Bathymetric map associated with the description of the different morphological features and the main cities. (C) Geological map and archaeological sites of the watershed draining the Marone and Sale Marasino towns.

Therefore, in terms of the sediment supply, the catchment area of MIP and SMB is limited to the slopes East of the shores. This catchment is mainly drained by two tributaries: the Opolo and the Bagnadore torrents (Fig. IV-1-C). The inlet of these two rivers is located in the Marone village, which is in the northern part of the MIP. Other small gullies are present on the mountain slopes East of Sale Marasino and on Monte Isola, however, as a first approximation, we will consider the Opolo and Bagnadore as the main terrigenous sediment sources on our study site.

The watershed of MIP and SMB is mainly composed of Quaternary colluvium, which cover the valley bottoms and the lower part of the slopes around Sale Marasino and Marone. The Upper

part of the catchment and the main summits are composed of a thick pile of Upper Triassic/Lower Jurassic dolomitic limestone (Fig. IV-1-C). Triassic marlstones outcrops are present in the upper part of Opolo and Bagnadore river catchments and the southern end of the catchment area. Jurassic limestones were also reported on Monte Isola and in the southeast part of the watershed. Few Andesite and Rhyolite outcrops are present in the upper part of the Opolo and Bagnadore catchment areas. These magmatic features that originated from the Upper Triassic tectonic collapse in the region were associated with normal faults (Buffoli, 2014; Presbitero et al., 2011).

3. Materials and Methods

3.1. Seismic Survey, Coring and Lithological Description

A high-resolution seismic reflection survey using a broad-band (300–2400 Hz) single-channel boomer device (Bini et al., 2007) was conducted on Lake Iseo in 2002. This survey was previously used to select a coring site in the Eastern sub-basin, which provided the first Holocene flood record (Lauterbach et al., 2012). However, a large mass-wasting deposit that induced an important hiatus prevented a continuous record from being established on those sequences. Therefore, a new seismic survey using a 3.5 kHz system and covering the MIP and SMB with a seismic network of shoreline-parallel and perpendicular transects with approximately 200 m distance was conducted in 2007 (data already included in Lauterbach et al., 2012). This helped to select a new coring site on Monte Isola plateau between Monte Isola and Marone (45° 43.312'N; 10° 5.771'E) at an approximately 70-m-water depth, in which earthquake-induced mass-wasting deposits were absent. In 2010, 23.2-m-long sediment sections from three holes in close vicinity were retrieved from the lake by using a 90-mm diameter piston corer on a Uwitec coring platform (EDYTEM/LSCE/C2FN). All sections were split, photographed at high resolution (20 pixels.mm^{-1}), described and logged in detail using the Munsell color chart. The identification of specific layers on the overlapping sections allowed us to construct a 21.4-m-long composite sediment sequence (hereafter called SEB10).

3.2. Grain-size Analysis

We performed grain-size analyses on 425 samples throughout the uppermost 10 meters on the SEB10 sediment core. Samples were chosen from continuous sedimentation and interbedded deposits. The analyses were conducted under sonicate but without any chemical pretreatment at the EDYTEM laboratory using a Malvern MasterSizer S™ (Malvern Instruments Ltd) with a grainsize range between 0.06 µm and 800 µm. Hereafter, we will use, the median (Q50) and the coarsest fraction (Q90), among other factors, to characterize all of the sedimentary layers. In order to characterize the deposit energy of instantaneous deposits thicker than 5mm, we will use the Q90max, i.e. the highest Q90 of the whole sequence (Wilhelm et al., 2013).

3.3. Loss on Ignition (LOI)

A 10-cm evenly spaced discrete sampling step was applied on the uppermost 10 meters of the SEB10 sequence to perform Loss on Ignition following the protocol that was defined by Heiri et al., (2001). The detrital layers were not included in the collected samples. This analysis was conducted to quantify the organic matter and carbonate content throughout the sediment sequence. Before the LOI analysis, the dry bulk density (DBD) was calculated from the same sediment samples by performing a constant volume sampling and weighing the sediment after 72

h of drying at 60°C. Then, the sediment samples were first dried and crushed before being heated in an oven at 550°C for 4 h and at 950°C for 2 h. The relative weight loss during the first (hereafter, LOI550°C) and second heating phases (hereafter, LOI950°C) corresponds to the fractions of organic matter and of carbonate, respectively.

3.4. Geochemical Properties

To characterize the variations of major elements throughout SEB10 sediment sequence, we performed X-ray fluorescence (XRF) geochemical analyses on the EDYTEM laboratory's AVAATECH Core Scanner (Avaatech XRF Technology). A continuous 5-mm step measurement was applied with a run at 10 kV and 0.3 mA for 30 s to detect lightweight elements, such as Al, Si, K, Ca, Ti, Mn, and Fe, and a second run was performed at 30 kV and 0.4 mA for 40 s to detect Br, Rb, Sr and Zr. The XRF core scanning results are expressed hereafter as peak intensities counting (cps). Then, a principle component analysis (PCA) was conducted on the XRF data to identify principal sediment end-members and correlations between the detected elements (Sabatier et al., 2010).

3.5. Dating

On the SEB10 sediment sequence, we combined short-lived radionuclides (^{210}Pb, ^{137}Cs, ^{241}Am), varve counting and ^{14}C to build a precise age-depth model of the uppermost 12.65 meters. The first 40 cm of the sequence was sampled with a 1-cm sampling step to measure short-lived radionuclide contents at the Laboratoire Souterrain de Modane using the well-type germanium detectors (Reyss et al., 1995). Thirty-two samples of vegetal macro-organic remains were used to perform 14C measurements at the LMC14 laboratory (CNRS). Dates were calibrated at 2 sigma using the Intcal13 calibration curve (Reimer et al., 2013), and the age-depth model was performed using the R code package "clam" in R software (Blaauw, 2010).

4. Results

4.1. Sedimentology

4.1.1. Sedimentary units

Along the 21.4 m of the SEB10 sedimentary sequence, six different units from the top to the bottom of the core were observed and described (Fig. IV-2). As this study focuses on the Holocene time scale, only the first 12 m of the sequence will be described here, as the deepest 10 m correspond to Late glacial deposits, which is confirmed hereafter by age-depth modeling (see section 4.2.2).

Unit 1 (0-19 cm) is composed of dark-greenish-gray clay (5GY 4/4) that presents a thin alternation of dark green, light gray and gray laminae on the first 19 cm of the core. This unit matches with the one that was described first by Lauterbach et al., (2012) and was identified as an organic gyttja that corresponds to the recent eutrophication period of lake Iseo. The values of LOI550°C vary between 9 to 11 % with a mean value of 10.7 %, while LOI950°C values range between 17.3 and 15.5 % with a mean value of 16.3 %. Across this unit, we count 53 laminae successions. From 19 cm to 1057.5 cm, the SEB10 core is mainly composed of gray clay frequently interbedded by thin dark-brown clay-to-silty layers. This section was subdivided into four different units according to the color variations from the top to the bottom of the record (Fig. IV-2). Unit IIa (19-276.6 cm) presents olive-gray clay (5Y/5/2) that becomes slightly lighter. The

LOI550°C results range between 6.4 to 9.3 %, with a mean value of 7.3 %, and the LOI 950°C results in this unit range between 3.5 to 14.2 % with a mean value of 8.2 %. Unit IIb (276.6-596.8 cm) is light-olive-gray and presents more frequent intercalation of dark-brown clay-to-silty layers. This unit presents a lower LOI550°C mean value of 6.3 %, with values ranging from 4.9 to 7.5 % and a higher 10.6 % LOI950°C mean value, with values ranging from 4.6 to 14.4 %. Unit IIc (596.8-925 cm) is light-gray and slightly bluish (5 GY 7/1) and is composed of an alternation of beige and dark clayey laminae. This unit presents values of LOI550°C ranging between 5.2 to 8.2 % with a mean value of 6.3 %, and the values of LOI950°C range between 3.7 and 15.6 % with a mean value of 8.2 %. Unit IId (925-1057.5 cm) is composed of gray (2.5Y/6/1) clay showing pale-yellow, reddish-yellow and olive-gray color alternations with very few silty layers and laminae. In this unit, the LOI550°C results range between 5.7 and 7.4 % with a mean value of 6.2 %, and the LOI950°C results range between 3 to 10.5 % with a mean value of 8.1 %. Unit III (1057.5-1187.5 cm) is defined as a gray clay unit (5Y/5/1) wherein the sediment becomes lighter without silty layers with very few organic debris, and it presents beige-orange laminated sections (Fig. IV-2).

4.1.2. *Geochemistry analyses*

From the XRF analyses, Unit I shows low values of Ti [>10,000 counts per second (cps)] and K (>45,000 cps) and high values of Ca (> 250,000 cps). From the top of the sediment section to Unit III, the Ti and K signals increase. The Br signal is constant over the first 12 m of the SEB10 sediment core, except for several peaks that correspond to specific deposits. The Ca signal is highly variable but does not allow a distinction between the different units.

The Br and Ca contents that were obtained from the XRF analyses were combined to the LOI results in linear regression tests. The relationship between the LOI950°C and the Ca content is positive, with an R^2 of 0.54 (p-value < 3.1×10^{-18}), which suggests that the Ca content could be used as a high-resolution proxy of carbonate. In the literature, the Br content is usually a proxy of organic matter (Bajard et al., 2016); nevertheless, here, the relationship with LOI550°C is poorly constrained with a positive R^2 of 0.14 (p-value > 0.56).

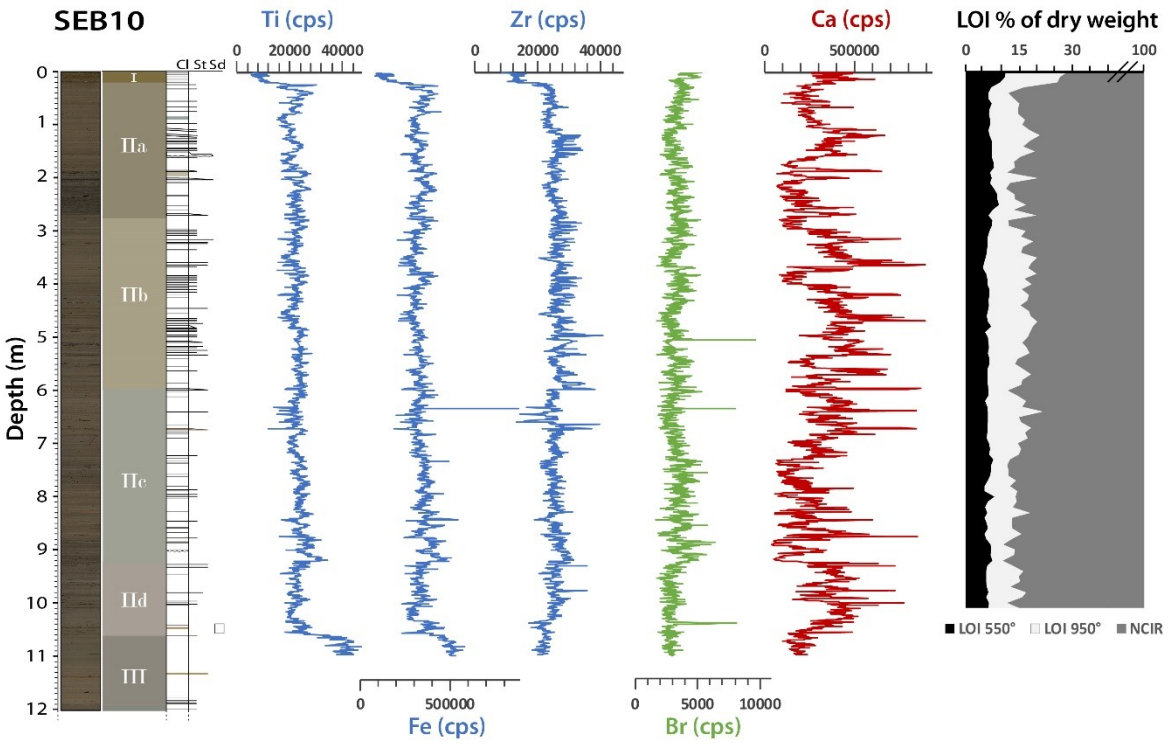

Fig. IV-2- Main sedimentological and geochemical results. A picture of the first 12 m of the SEB10 sediment sequence is associated with the lithological description (with corresponding units named I, IIa, IIb, IIc, IId and III), geochemical results (Ti, Fe, Zr, Br, and Ca contents) and Loss on Ignition (LOI).

A principal component analysis was conducted on the XRF data and provides variables and individual factor maps (Fig. IV-3), which highlight the relationships between the different elements and the geochemical distribution within sediment units. Dimensions 1 and 2 (denoted as Dim1 and Dim2) represent 62.3 % of the total variability. From the variables factor map, three end-members were identified. The first one, which is denoted as terrigenous, is positively correlated with Dim1 and yields high positive loadings for the major terrigenous elements (Al, Si, K, Ti, Rb, Fe). The second one, which is denoted as "organic matter" yields positive values for Br and is negatively correlated with Dim2. However, as the Br signal is poorly correlated with LOI550°C, this end-member will not be used hereafter. The third one is negatively correlated with Dim1 and is positively correlated with Dim2. This pole yields high positive values for Ca and Sr and is, thus, interpreted as representative of the carbonates input from the watershed, as Sr is usually present in marine limestone, which constitutes a major part of the watershed outcrops. The Individuals factor map (Fig. IV-3) highlights the specificity of each unit: (i) Unit I is negatively correlated with terrigenous end-members, which is due to its high organic matter (LOI550° > 11 %, Lauterbach et al., 2012) and carbonate (LOI950°C > 17 %) contents. (ii) Unit III is positively correlated with Dim1 and, thus, to the detrital end-member, and it is also characterized by low Ca and Sr contents. (iii) Unit IIa, IIb, IIc and IId are not well distinguishable from this map, but there is a decreasing trend of the contents of terrigenous elements, which is clearly visible from Unit III to Unit II.

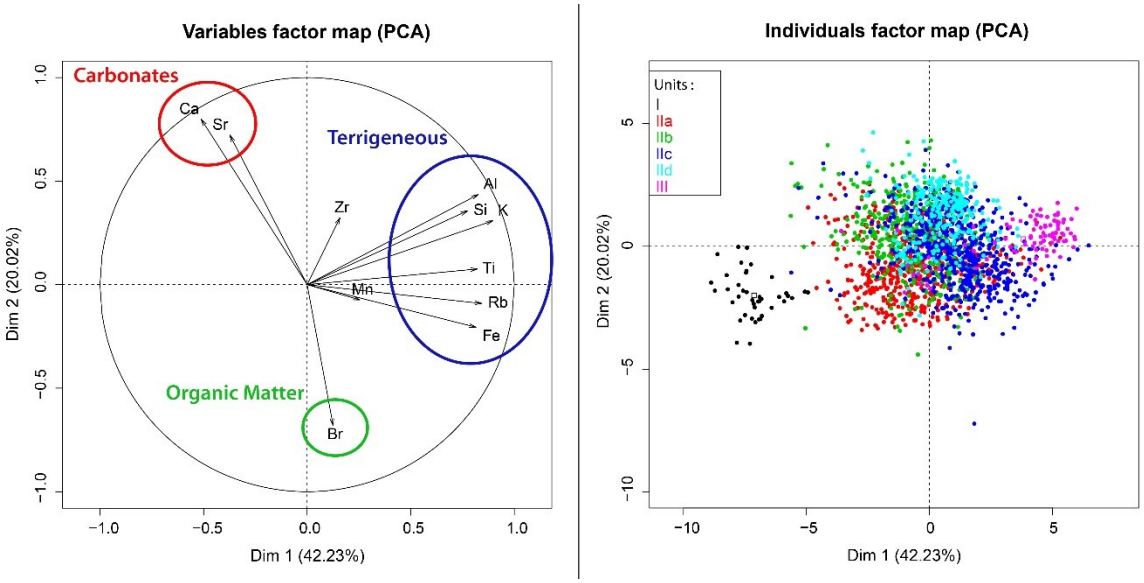

Fig. IV-3- Variable and Individual factor maps from the PCA. (A) Variable factor map with three endmembers (terrigenous, organic matter and carbonates). (B) Individual factor map with sedimentological units added as an illustrative variable.

4.1.3. Graded beds

Several layers that are clearly distinguishable from the normal sedimentation by their colors and textures were observed along the sedimentary sequence. The first type of deposits, which are denoted hereafter as Type 1 (T1), correspond to thin millimetric to centimetric dark-brown deposits with a silty base. These deposits are very similar to the detrital layers that were observed on the Sale Marasino plateau sediment sequence by Lauterbach et al., (2012).

When T1 layers were thicker than the 5mm sampling step (49 over 148), it was possible to individually characterize both their grainsize and geochemical fingerprint. In those deposits $Q90_{max}$ values are between 20 and 80 µm and vary from 60 at the base to 20 µm at the top of a random graded bed, and median values ($Q50_{max}$) are between 3 to 10 µm (Fig. IV-4) and Zr/Fe ratio and Mn present a peak at the base of each sequence. In order to verify the attribution of thinner-than-5mm visually-determined layers to the T1 deposit type, we lowered the sampling step down to 1mm on a 50cm-long core section (Fig. IV-4). This confirmed the presence of a peak in Mn in each of the layers in agreement with the observation made on thicker ones. The Zr/Fe peak was not systematically observed, however a relative enrichment in Zr or Fe was evidenced for each layer, as marked by Zr/Ti and Fe/Ti ratio, respectively. Based on those observations, we decided to classify all of the 148 brown deposits identified from the background sedimentation by a visual lithological description as T1 deposits. The majority (91 on 148 deposits) of these T1 deposits were observed in Unit IIb (276.6-596.8 cm), whereas very few were counted in Units IIc, IId and III. The T1 deposits range between 1 and 41 mm with a mean size of 5.8 mm.

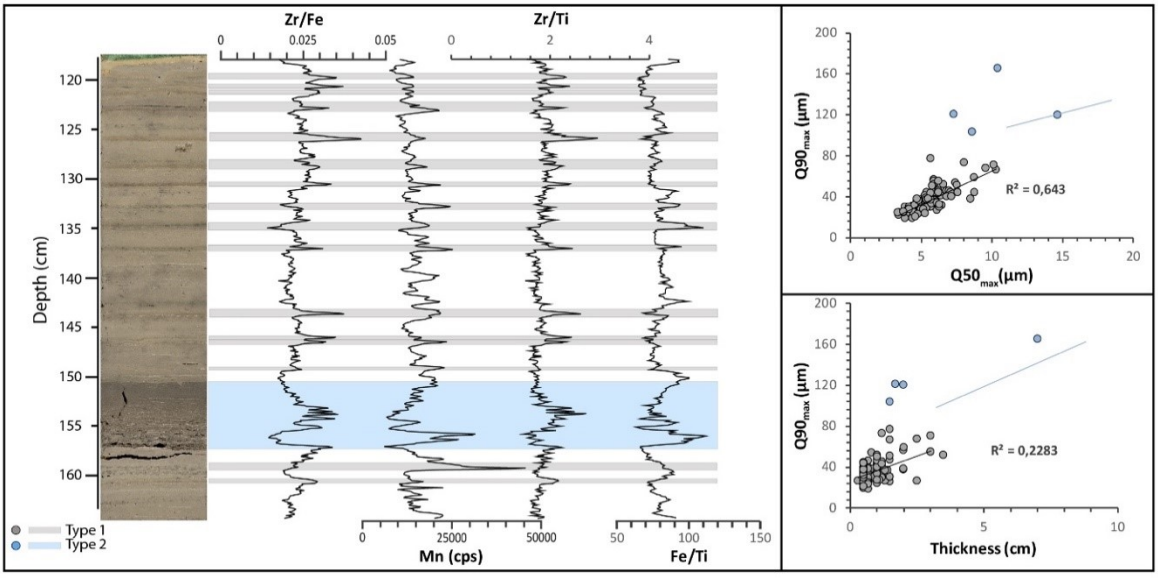

Fig. IV-4- Detailed results for the two types of graded layers that were observed in the SEB10 sequence. The left panel presents the SEB10-02A picture according to the master core depth in cm associated with the Zr/Fe, Mn, Zr/Ti and Fe/Ti signals that were derived from the XRF-CS analysis at 1 mm resolution. The Type 1 layers (T1) are highlighted in gray, while T2 are highlighted in blue. The upper-right panel presents the relation between Q90max (the highest Q90 value of each graded-bed) and the median (Q50max) expressed in µm. The lower-right panel presents the relation between Q90max and the thickness of each deposit. The coefficients of determination were calculated for the T1 deposits.

Four other deposits were also identified in the SEB10 sediment sequence and will be denoted as Type 2 deposits (T2) hereafter. T2 deposits present a mean thickness of 47 mm and are, thus, comparatively thicker than T1 deposits (mean thickness of 5.8 mm). Based on a grain-size analysis and the relationship between $Q90_{max}$ and $Q50_{max}$, they are coarser than T1 with relatively higher $Q90_{max}$ (>100 µm) (Fig. IV-4). The base of these deposits is made of coarse silt and fine sand. They are also less well sorted than T1 (mean sorting of 3.9 for T2 compared to 2.9 for T1). The proportion of silt and sand progressively decreases from the bottom to the top. The T2 deposits are, thus, normally graded beds. The Zr/Fe and Mn signals also present peaks in the T2 layers, but the signals are more complex within the base of these deposits (Fig. IV-4). The T2 layer that is presented in Fig. IV-4 shows low values of Zr/Fe, followed by peaks in the middle of the deposit. Several peaks of the Mn signal are also observable. These four T2 layers could be interpreted as thicker and coarser expressions of the T1 layers. However, the differences in the grain size and in the XRF signals could be important enough to be related to a difference in the triggering mechanisms and lead us to distinguish between these two types of deposits which we however attribute to instantaneous deposits.

4.2. Chronology

4.2.1. Short-lived radionuclides

The ^{210}Pb excess profile ($^{210}Pb_{ex}$) shows a regular decrease (Fig. IV-5-A) from 400 mBq.g^{-1} to low activities (<50 mBq.g^{-1}). Here, we use a logarithmic scale to plot these data and to underscore a well-constrained single-point alignment that shows a constant sedimentation rate of 3.12±0.06 mm yr^{-1} (R^2=0.97) for the uppermost 30 cm, for which the most superficial sample showed very low $^{210}Pb_{ex}$ and was not considered. The ^{137}Cs profile shows a clear peak between 4.8 and 7.3 cm with a maximum activity (>1300 mBq.g^{-1}) at 7.3 cm; this peak is associated with a peak of

^{241}Am (>3 mBq.g-^{1}) and is widely attributed in the literature to nuclear fallout from the 1986 Chernobyl accident (e.g., Appleby et al., 1991). The ^{241}Am profile presents a peak (>3 mBq.g^{-1}) between 13 and 15 cm with moderate ^{137}Cs activity and a first increase at 17 cm. These two depths correspond to the maximum nuclear weapon tests at AD 1963 at 13.5 cm and with the first appearance of ^{137}Cs dated to AD 1955 (Appleby et al., 1991). These two peaks are in good agreement with the sedimentation rate that was derived from the $^{210}Pb_{ex}$ profile.

Fifty varves were identified and counted from the top of the sediment section to 15 cm, which provides a 3 mm yr^{-1} sedimentation rate that is highly comparable with the rate that was derived from the CFCS model and ^{137}Cs and ^{241}Am profiles (Fig. IV-5-A). The first varve was dated at 1960 AD and could correspond to the beginning of the lake eutrophication (Jenny et al., 2013), which is quite identical to the timing that was observed in Lake Varese in Northern Italy (Bruel et al., 2018), where both climatic and anthropogenic impacts played a role into lake anoxia.

Thus, we added these chronological data into the age-depth model to constrain it for the upper portion of the sedimentary record (Fig. IV-5-B).

Table IV-1- Radiocarbon ages for the SEB10 sediment sequence. Composite depth was calculated by excluding the thicknesses of each graded beds that were considered as instantaneous deposits. Samples in bold correspond to dates excluded from the age-depth model.

Sample Name	Core	MCD (cm)	Composite Depth(cm)	Radiocarbon age	Age cal yr BP 2 σ range	Sample type
SacA 25929	SEB10-P1	21.5	21.5	165 ± 30	-3-288	wood
SacA41380	SEB10-1A	170.5	149.3	1090 ± 30	938-1057	wood
SacA41381	SEB10-1B	239.5	206.1	1700 ± 30	1545-1696	wood
SacA 25937	SEB10-1B	323.6	281.9	2340 ± 30	2316-2455	wood
SacA41382	SEB10-1B	411.5	350.2	2900 ± 40	2926-3163	wood
SacA 25926	SEB10-1C	439.6	374.3	2890 ± 35	2899-3155	wood
SacA 25927	SEB10-1C	453.5	384.2	2945 ± 30	2999-3206	wood
SacA 25928	SEB10-1C	453.5	384.2	2975 ± 30	3009-3315	wood
SacA41387	SEB10-2B	486.4	409.0	3180 ± 30	3359-3454	charcoal
SacA 25936	SEB10-1C	512.3	432.1	3330 ± 30	3479-3636	wood
SacA 25934	SEB10-1C	548.6	463.5	3515 ± 35	3697-3881	wood
SacA 25935	SEB10-1C	612.5	523.3	3805 ± 35	4086-4380	wood
SacA41383	SEB10-1D	718.8	624.1	5090 ± 30	5749-5912	wood
SacA41389	SEB10-2D	745.8	648.9	5280 ± 30	5946-6180	wood
SacA41390	SEB10-2D	779.3	682.4	5805 ± 30	6504-6672	wood
SacA41384	SEB10-1D	785.8	688.9	6120 ± 40	6905-7157	vivianite
SacA 25932	SEB10-3A	786.6	689.4	5715 ± 40	6411-6630	wood
SacA 25930	SEB10-3B	854.4	755.3	6670 ± 40	7474-7606	wood
SacA41388	SEB10-2D	865.3	765.9	7090 ± 50	7829-8008	charcoal
SacA41391	SEB10-2D	887.5	786.1	7630 ± 45	8374-8537	wood
SacA 25939	SEB10-3B	897.7	796.3	7400 ± 45	8060-8347	wood
SacA41392	SEB10-2D	915.3	813.9	8090 ± 40	8787-9132	wood
SacA 25941	SEB10-2E	1060.0	955.5	10305 ± 50	11842-12386	wood
SacA 25933	SEB10-3C	1165.0	1060.5	11970 ± 60	13618-14023	wood
Ouverture 1	SEB10-3C	1165.5	1061.0	12040 ± 60	13752-14056	twig
SacA 25942	SEB10-2F	1188.7	1084.2	12520 ± 60	14354-15101	wood
SacA 25938	SEB10-2F	1266.5	1162.0	13440 ± 70	15932-16408	wood

4.2.2. *^{14}C & Age-depth model*

Twenty-seven samples of terrestrial macroremains were analyzed to provide a radiocarbon age. After calibration, 3 of these 27 samples (Table IV-1) presented ages that were too old to fit the SEB10 age-depth model, which was probably linked to the reworking of old material (Fig. IV-5-B). The first outlier was sampled at 21.5 cm and was too old compared to the $^{210}Pb_{excess}$ profile that was obtained at that depth (Fig. IV-5-B). Both the second and third outliers are present within a group of other radiocarbon dates and emerge slightly from the trend of their respective groups due to old age. Thus, they were rejected from the model to avoid reversals and inconsistencies (Fig. IV-5-B). The two kinds of graded layers that were previously described have been interpreted as instantaneous deposits, and the sum of their depths represent 104.5 cm for the first 12 m of the sediment sequence. To provide the best age-depth model, an event-free depth was created by subtracting all of the thicknesses of the instantaneous deposits from the SEB10 sequence sediment depth (Arnaud et al., 2002). The age-depth model was generated with the remaining 24 calibrated ages and the short-lived radionuclide ages. The best fit was obtained with the R code package "clam" (Blaauw, 2010) by applying a smooth spline model with 0.42 for the smooth parameter. The sedimentation rate presented hereafter was calculated without event layers. Finally, we reintegrated all instantaneous events to the age-depth model (Fig. IV-5-B) to provide a date for all instantaneous deposits.

The first 10.5 m of SEB10 sequence covers the last ≈12, 000 years (Fig. IV-5-B) with a mean sedimentation rate of 1 mm yr^{-1}. The sedimentation rate over this sequence varies from 3.23 to 0.39 mm yr^{-1}, with several peaks (Fig. IV-6-A). From 12 to 8.7 kyr cal BP, the sedimentation rate is quite constant and varies between 0.6 to 0.4 mm yr^{-1}. A first increase is observed (Fig. IV-5-B) from 8.7 kyr cal BP until a maximum rate of 0.81 mm yr^{-1} at 6.5 kyr cal BP is reached. The sedimentation rate then decreases until 5 kyr cal BP, with a minimum of 0.63 mm yr^{-1}. From 5 to 1 kyr cal BP, the sedimentation rate is highly variable and presents two maxima: one at 3.8 kyr cal BP with 1.48 mm yr^{-1} and one at 3 kyr cal BP with 1.58 mm yr^{-1}. This second increase follows directly after a period of decrease between 3.8 to 3.3 kyr cal BP, with a minimum rate of 1.17 mm yr^{-1}. From 3 kyr cal BP, the sedimentation rate decreases slightly until 1 kyr cal BP (0.94 mm yr^{-1}). Finally, the sedimentation rate increases to the top of the SEB10 sequence with a maximum rate of 3.21 mm yr^{-1} in 1960 AD.

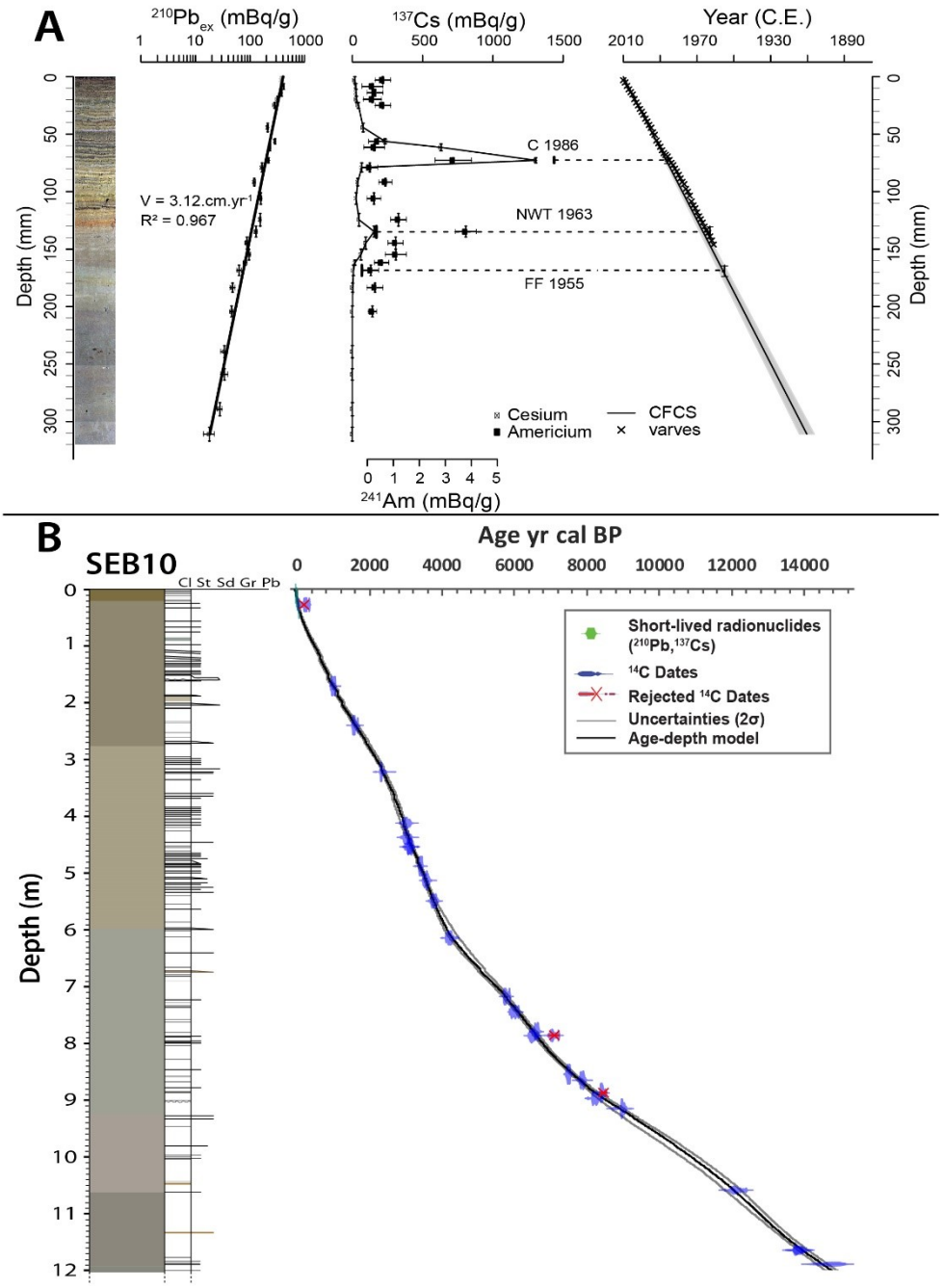

Fig. IV-5- Age-depth models. (A) Short-lived radionuclide data: $^{210}Pb_{ex}$ in logarithmic scale associated with the ^{241}Am and ^{137}Cs profiles with the picture of the top 35 cm of SEB10 sequence. (B) Age-depth model associating radiocarbon and short-lived radionuclide dates.

5. Discussion

5.1. Instantaneous deposits

The two kinds of detrital layers that were identified visually are graded beds, which are rich in angular allochthonous carbonates and silicates and present a silty to sandy base. Those are characteristic features of flood-triggered deposits (Sturm and Matter, 1978). To better understand those deposits and their origins, we used the 1 mm XRF resolution between 120 and 165 cm of the SEB10 Mastercore (Fig. IV-4). As described previously, several T1 deposits present a peak of Zr/Fe and Mn at their base. The Zr/Fe ratio is linked to grain-size variations within the deposits: Zr is generally yielded by heavy minerals, while Fe is linked to aluminum silicates or oxides. A peak of the Zr/Fe ratio is, thus, expected to correspond to a coarser grain-size, which is generally attributed to a flood origin for underflow deposits (Wilhelm et al., 2013). A high Mn content in lake sediment could be linked to an oxygenation of the lake-sediment interface, by which Mn-Ca carbonates and Mn oxides can precipitate at the oxic/anoxic transition (Elbaz-Poulichet et al., 2014). When a flood occurs, the oxygen-rich water that is brought by the underflow reaches the lake water's-sediment interface and is conducted to the Mn precipitation. Thus, a peak of Mn can be interpreted as flood-induced lake bottom oxygenation and is linked to a detrital input (Sabatier et al., 2017). From Fig. IV-4, it appears that the T1 deposits did not always present a Zr/Fe peak but rather sometimes present a depletion of Zr/Fe. This could be due to the lateral variability of the geochemical composition of a turbidite (Bertrand et al., 2012). Indeed, if the analyzed layer corresponds to the distal or the proximal part of a turbidite, the composition will vary according to the principle that heavy or large minerals, such as zircons, will be deposited closer to the delta than will lightweight minerals, such as clay or oxides that are rich in Fe. Depending on the intensity of the underflow, the Zr/Fe ratio signal will then vary at the coring site. However, this can be solved by using a proxy of terrigenous input, which is supposed to be constant and not segregated laterally during flood deposits; one such proxy is Ti because it is yielded by Ti-oxides as well as by most of the silicates by substitution of Al. Then, plotting Zr/Ti and Fe/Ti was used to identify all the underflows (Fig. IV-4): a distal part of a turbidite will be enriched in Fe compared to Ti, whereas a proximal part of a turbidite will be enriched in Zr compared to Ti. Moreover, all of the T1 deposits present a peak of Mn signal at their base (Fig. IV-4), which reflects the fact that they are all linked to sediment input from underflows, which oxygenated the lake floor (Sabatier et al., 2017). The combination of Zr/Fe, Zr/Ti, Fe/Ti and Mn peaks at the base of the T1 deposits led us to interpret these underflow layers as flood-triggered deposits. This interpretation is reinforced by the location of the coring site: the SEB10 sediment sequence is located on Monte Isola Plateau, where it avoids any slides from the escarpments. This interpretation is also in line with the previous work of Lauterbach et al., (2012) which observed and interpreted similar type of deposit as flood-triggered deposits on Sale Marasino plateau based on sediment microfacies, sediment lightness and magnetic susceptibility. The floods recorded here are linked to the sediment inputs from Opolo and Bagnadore streams and from few gullies from the watershed.

T2 deposits present coarser grain size values and are thicker compared to T1. They are also generally thinner for the same $Q90_{max}$ values and present higher sorting values. Zr/Fe and Mn signals show multiple peaks within the base of those layers. The Zr/Fe peaks imply a weaker sorting in the base of those layers. The presence of Mn peaks allows for the possibility that a delta

collapse or a slide from the slopes are less probable, as the Mn peaks imply an oxygen-rich water input during the deposition. Thus, T2 deposits could be interpreted as a more proximal record of an underflow. However, the T2 deposit that is identified at 153 cm is dated at 865 ± 46 yr cal BP and could correspond to a slide that was induced by the same seismic event as that which produced the E1 large scale mass-wasting deposit that was identified by Lauterbach et al. (2012) in the SEB06 core and was dated at 759 ± 62 yr cal BP. Then, it is still unclear if those layers correspond to a single flood-input or a slide from previously deposited sediment on the Marone delta. Thus, we decided to remove them from the flood-chronicle that is presented hereafter. As there are only four T2 deposits, their absence does not have a significant impact on this chronicle.

From the last 12,000 years of the sedimentary record of the SEB10 sequence, 148 floods were identified visually and were dated through the T1 deposits to build a flood chronicle.

5.2. Flood chronicle

A flood chronicle was built and presents the variation of the number of floods that were recorded in the SEB10 sedimentary sequence per 100 years. In addition, the siliciclastic terrigenous flux (SCTF; g cm^{-2} yr^{-1}) was calculated in order to link the flood chronicle and the evolution of erosion processes in the catchment area. SCTF was computed as the product of the % of non-carbonate ignition residue (NCIR), derived from the LOI analyses, and the sedimentation rate and the sediment density. The NCIR represents more than 80 % of the total sedimentation; thus, the SCTF could be interpreted as the total terrigenous flux. This flux depends on the sedimentation rate that is calculated without instantaneous deposits and thus represents the long-term detrital inputs from the watershed that will be used here as a proxy of erosion (Fig. IV-6-A). Several different periods of can be distinguished from the flood chronicle and the SCTF (Fig. IV-6-B):

(i) The sedimentation on the MIP before 12 kyr cal BP (Unit III) corresponds to Lateglacial deposits (LGD) according to the high values of detrital elements (Fig. IV-2);

(ii) The transition between LGD and the Holocene is marked by a decrease in detrital input from 12. Between 12 and 4.2 kyr cal BP (Unit IId & IIc), the sedimentation rate was low; very few floods were recorded on the SEB10 sediment sequence. At that time, the erosion in the watershed is low which can be due to the early development of Holocene soils just after the glaciers retreat (Bajard et al., 2016). Between 8.2 and 5.5 kyr cal BP (Unit IIc) the SCTF shows a slight increase, possibly due to a rise in erosion in the watershed;

(iii) From 4.2 to 2.1 kyr cal BP (Unit IIb), the erosion in the watershed increases sharply, according to the SCTF that reaches its highest value at 3.8 kyr cal BP. This peak is simultaneous with the outset of an increase in flood frequency (3.8 kyr cal BP). Between 3.8 and 2.9 kyr cal BP, the flood frequency signal varied intensely with peaks at 3.6, 3.3 and 2.9 kyr cal BP (Fig. IV-6-B);

(iv) According to SCTF and the flood chronicle, the intensity of the erosion in the watershed decreases between 2.1 and 0.4 kyr cal BP (Unit IIa). Only one peak of high flood frequency is observable between 0.73 and 0.63 kyr cal BP (1220–1320 AD). From 0.4 kyr cal BP, the SCTF and the sedimentation rate defer from the flood chronicle and attested an increase of the erosion in the watershed;

(v) During the last 50 years (Unit I), the sedimentation processes change and varves appear probably due to the beginning of the Lake Eutrophication.

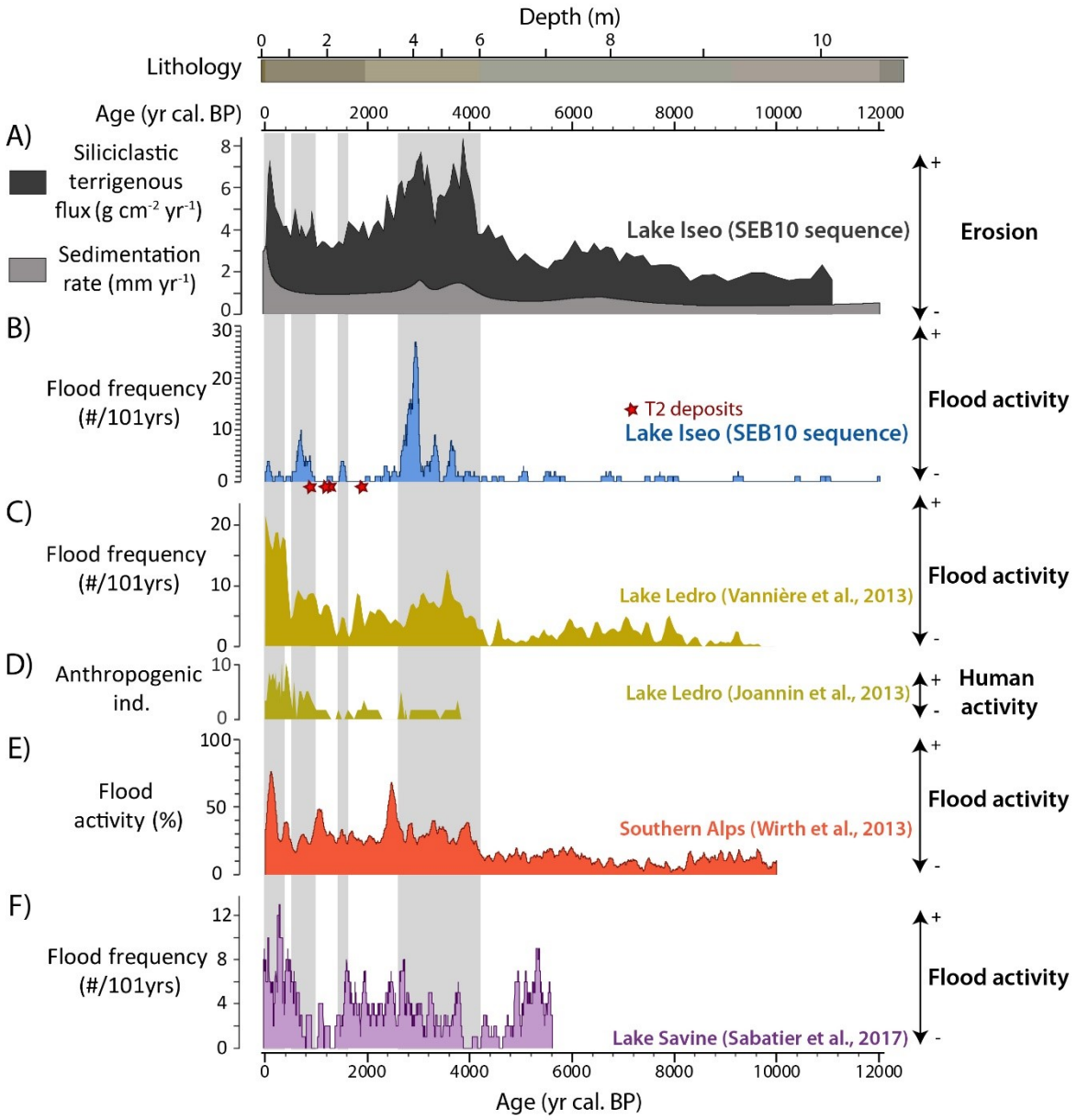

Fig. IV-6- Comparison between (A) SEB10 sedimentation rate and terrigenous flux with (B) SEB10 flood frequency and T2 deposits ages (red stars), (C) Lake Ledro flood activity and (D) Anthropogenic indicator (Joannin et al., 2013; Vannière et al., 2013), (E) the Southern Alps flood chronicle (Wirth et al., 2013b) and (F) Lake Savine flood activity (Sabatier et al., 2017). Gray shadings highlights the periods of high erosion recorded in Lake Iseo.

In addition, peaks of high detrital flux on the SEB06 sediment core are also documented during high flood frequency periods of the SEB10 flood chronicle between 4.2 and 3.5 kyr cal BP and between 3 and 2.8 kyr cal BP (Lauterbach et al., 2012).

In the Alps, regardless of human influences, the flood frequency is generally higher during periods of cold and wetter climate, and vice versa (Czymzik et al., 2013; Giguet-Covex et al., 2012; Swierczynski et al., 2013; Wilhelm et al., 2012; Wirth et al., 2013b). Moreover, lowland lakes, such as Lake Iseo, are less influenced by flash flood events and are generally more sensitive to long rain-triggered floods with a large spatial extent (Arnaud et al., 2016; Czymzik et al., 2013; Swierczynski et al., 2013). The floods that are chronicled from the SEB10 sequence are, thus, supposed to be first influenced by regional climate variation.

The period between 12 kyr and 4.2 kyr cal BP of the SEB10 flood chronicle is identical to other records from the Italian Alps, with low flood activity and low erosion (Vannière et al., 2013; Wirth et al., 2013; Fig. IV-6-B, C & E). This time range is known as a stable warm and dry climate period in the Alps, in particular during the Holocene Climatic Optimum (9 to 5 kyr cal BP). Even if the human activity started in Italy and in the Val Camonica with the first settlements during the Mesolithic and the development of land use from the Early Neolithic (Rottoli and Castiglioni, 2009), no archaeological sites from these periods were discovered around Marone and Sale Marasino. Moreover, the Lake Ledro (653 m a.s.l) pollen record (Joannin et al., 2013; Fig. IV-6-D) presents no anthropogenic indicators of that time.

From 4.2 kyr cal BP, the SCTF starts to increase until a peak at 3.8 kyr cal BP. The SCTF serves as a proxy of the erosion in the watershed. SCTF could be dominated by both long-term weak-to-medium intensity regional precipitation trends and changes in the vegetal cover, land use and multiple other factors linked to human activity (Bajard et al., 2017a, 2017b). Between 4.2 and 3.8 kyr cal BP, the anthropogenic indicator index of Lake Ledro, which is the closest anthropogenic record in the region, shows no human impact (Joannin et al., 2013). The long-term increase of the SCTF at that period is, thus, supposed to be linked to a transition toward regionally wetter climate conditions (Isola et al., 2019). Here, the increase of the SCTF is synchronous with the increases that were observed on other Alpine Lakes flood chronicles (Fig. IV-6-C, E & F). This trend is also broadly observable in Northern Atlantic regions and is generally considered to be a nonlinear response to the progressive decrease of summer insolation at 60°N (Magny et al., 2013). This change in the insolation pattern induced a switch toward a wetter and colder climate in Southern Europe and was linked to a more negative NAO and a southward migration of the Westerlies, thus producing an increase in the precipitation in the Southern Alps (Wirth et al., 2013b). This trend was also observed for the Lake Savine flood chronicle in the French Alps (Fig. IV-6-F), which presents the same shift toward higher flood frequency with a delay of 300 years (Sabatier et al., 2017). This small gap could be linked to both age-depth model uncertainties and to the more northern position of this lake.

From 3.8 kyr cal BP and the peak of SCTF, the flood frequency that was recorded for the SEB10 sequence starts to increase. This lag between the SCTF and the increase in the SEB10 flood frequency is possibly due to passing a critical threshold of precipitation intensity and/or erosion in the watershed, thus leading to the deposition of detrital layers onto the lake floor. The peaks of flood frequency on the SEB10 sediment sequence at 3.3 kyr and 2.9 kyr cal BP are synchronous with periods of high lake levels at Lake Ledro (Magny et al., 2009). However, the period from 3.6 kyr cal BP to 2.7 kyr cal BP is also known as a period of intense human activities in the Southern Alps with: (i) attested forest opening in the Swiss Alps (Dapples et al., 2002) and (ii) forest opening and an increase of the land use in the Lake Ledro watershed (Joannin et al., 2014; Vannière et al., 2013). Nevertheless, no archaeological sites from this period were discovered in the Marone watershed. By being part of a regional trend, the increase of the erosion in the watershed at 4.2 kyr cal BP seems to be driven by regional climatic conditions and is linked to a transition toward a wetter climate, with an increase in the influence of Mediterranean mesoscale precipitation events (Sabatier et al., 2017). However, if the extreme values that were observed in the flood chronicle at 3.3 and 2.9 kyr cal BP can be explained by a regionally more humid climate (Magny et al., 2009), it is doubtless that human activities by forest opening and land-use has favored soil erosion

and, thus, influenced the record of flood activity at that time (Brisset et al., 2017; Giguet-Covex et al., 2012).

From 2.5 kyr cal BP, the flood chronicle seems disconnected from other flood chronicles and regional trends (Fig. IV-6 & Fig. IV-7-A). Between 2.1 and 1.6 kyr cal BP (150 BC – 350 AD), no flood events were recorded in the SEB10 sediment sequence, although this period coincides with the Roman Empire period, which is characterized both by intense land-use and high flood frequency in geological records of lakes Ledro and Savine (Fig. IV-6-C, F) and relatively high SCTF values in the SEB10 sequence (3.9 g cm^{-2} yr^{-1} on average between 2 and 1.5 kyr cal BP). The lack of recorded floods could be explained by a modification of the courses of Opolo and Bagnadore streams. This could be due to natural avulsion after an important flood event or by artificial embankment on the eastern shores of Lake Iseo (Fig. IV-7-B&C). Indeed, a Roman Villa was occupied until almost 311 AD, and several graves were discovered close to the current location of the Marone village center (Fig. IV-7-B, Condina, 1986). The location of those archeological sites (Fig. IV-7-B) suggests that the Marone Delta was occupied during Roman times, which led to a possible modification of the Opolo and Bagnadore torrents courses to prevent avulsions (Fig. IV-7-B). Thus, the Opolo and Bagnadore streams were probably flowing into Lake Iseo in the northern part of the Marone delta at that time. When the stream confluences are located North of the Marone delta, there was no possible sediment input on Monte Isola Plateau, as the sediment is directly thrown into the Lake Iseo deeper basin (Fig. IV-7-B). To justify this statement, it should be pointed out that two historical flood events almost entirely damaged Marone village in 1953 and 1963, bringing huge amounts of sediment from Opolo and Bagnadore watersheds (Benedetti and Predali, 2013) but did not lead to detrital deposits in our Monte Isola Plateau sediment core. From the 16th century, Opolo and Bagnadore streams were dammed in the center of Marone, and their flows were connected to the northern part of the Marone delta (Predali, 2013, 2008). According to the bathymetric map, only the Marone delta developed on the MIP, which means that the natural courses of Opolo and Bagnadore streams were located on the southern part of the delta.

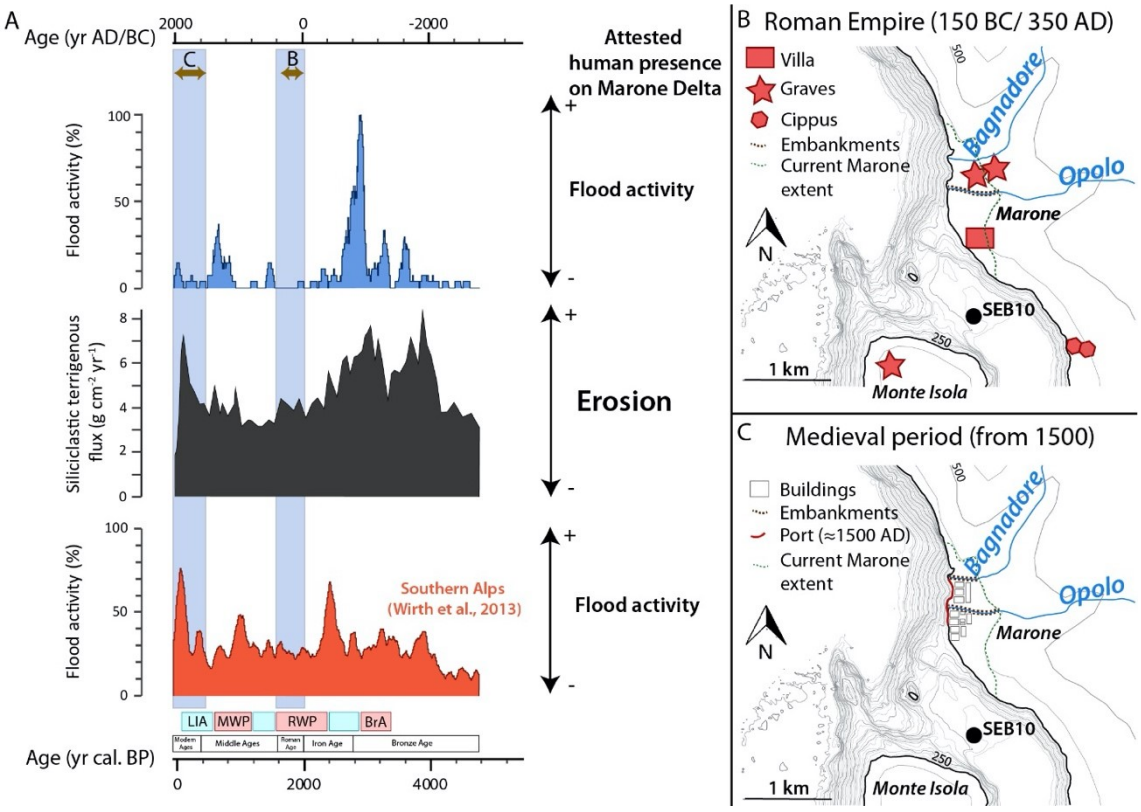

Fig. IV-7- (A) Comparison between SEB10 flood activity (calculated with the assumption that the highest frequency recorded correspond to 100 % of flood activity), the Southern Alps flood chronicle (Wirth et al., 2013) and the total solar irradiance (W.m²) curve (Steinhilber et al., 2012) from 4.8 kyr cal BP to the present. Light blue shading highlights periods of attested human presence on the Marone Delta. Blue and red boxes represent a period of attested cold/wet and warm/dry climate respectively. LIA: Little Ice Age; MWP: Medieval Warm Period; RWP: Roman Warm Period; BrA: Bronze Age Optimum (B) Sketch of the location of Roman archeological sites on the Marone delta (Condina, 1986) and supposed flow direction of the Opolo and Bagnadore streams during the Roman Empire Period (150 BC/ 350 AD). (C) Sketch of the Marone village during the Little Ice Age (from 1500 AD) and the location of attested embankments of the Bagnadore and Opolo streams (Gregorini et al., 2012).

Between 1.6 and 1.4 kyr cal BP (350–550 AD), the increase of flood activity recorded in the SEB10 sequence could be linked to the abandonment of Roman sites on the lake shores during the fall of the Roman Empire (Fig. IV-7-A). If the stream banks are not maintained, avulsions could occur, and the streams could flow again in the southern part of the Marone delta, thus bringing sediment to the Monte Isola Plateau.

Another example of the human influence on the SEB10 flood chronicle is apparent when considering the flood activity during the Little Ice Age (LIA) and the Medieval Warm Period (MWP) (Fig. IV-7-A&C). Indeed, the LIA is a colder and wetter period presenting high flood activity while the MWP is a drier and warmer period with low flood activity (Fig. IV-7; Sabatier et al., 2017; Vannière et al., 2013; Wirth et al., 2013). However, the SEB10 flood chronicle shows the exact opposite, with high and low flood activity occurring during the MWP and the LIA, respectively. Therefore, the SCTF signal increases between 0.5 and 0.1 kyr cal BP, which confirms significant erosion in the watershed, probably due to a wetter climate or an increase of land use. This apparent paradox can be solved when considering human occupation dynamics. Indeed, during the MWP, the site of the current Marone village was abandoned, and local people settled on the surrounding hills (Predali, 2010), thus leaving the streams free to avulse. Inversely, during the LIA, the Marone village was created (Fig. IV-7-C), the population increased and the necessity to dam

the streams in the northern part of the Marone delta appeared around at least 377 yr cal BP (1573 AD) to favor the development of the manufacturing companies and to protect the city (Gregorini et al., 2012). Thus, from 400 yr cal BP, the possible sediment input is limited to the small gullies of Monte Isola and Sale Marasino, which explains the low activity that was recorded.

6. Conclusions

This study presents one of the first detailed and continuous flood chronicles spanning the last 12 kyr cal BP in Northern Italy. The flood frequency is low from 12 to 4.2 kyr cal BP, which is consistent with the warmer and drier climate condition of the Early and Mid-Holocene and with other regional flood records that were reconstructed from lake sediments. From 4.2 kyr cal BP, the terrigenous flux in Lake Iseo, which is followed from 3.8 kyr cal BP by the flood frequency, increased until 2.9 kyr cal BP, as previously described for the western Mediterranean region. This transition is interpreted as a nonlinear climate response to the orbital-driven gradual decrease in summer insolation at 60°N, which induced the development of extreme meso-scale precipitation events in the Mediterranean region (Magny et al., 2013). Three peaks of high flood activities were observed at 3.6, 3.3 and 2.9 kyr cal BP and probably correspond to short-term regional wetter conditions. However, if the chronicle is in phase with the regional climate conditions until 2 kyr cal BP, human impact should be considered to have been a flood-triggering mechanism since at least 3.6 kyr cal BP. Indeed, forest opening and land use are documented in southern Alps from at least 4 kyr cal BP, and human presence on the watershed is expected to have influenced the flood frequency toward higher values during wetter periods until 2 kyr cal BP. From 2 kyr cal BP to the present, human activity in the watershed is proposed to be the main driver of the flood frequency that was recorded in Lake Iseo sediments. The two streams at the origin of the sediment inputs at the coring location were dammed on several occasions during the Roman Period (2 kyr cal BP), which directly prevented sediment input during flooding and, thus, explains the disappearance of flood deposits. From 2 kyr cal BP, the chronicle is, thus, highly dependent on the anthropization of the river banks. In this instance, this chronicle cannot be used as a proxy of the regional paleohydrology due to the human influences in the watershed that were observed from at least 2 kyr cal BP. The lack of an in-depth study of the evolution of human activities on the shores of Lake Iseo could have led to a misinterpretation of the flood activity. Thus, the use of a flood chronicle that is based on lake sediments to reconstruct past hydrological conditions should always be linked to a thorough study of the human activity in the watershed, even in a large lake and low elevation system.

Acknowledgments

We thank the Laboratoire Souterrain de Modane (France) for the gamma spectrometry measurements, the CNRS-INSU ARTEMIS national radiocarbon AMS measurement program at Laboratoire de Mesure du ^{14}C (LMC14) in the CEA Institute at Saclay (French Atomic Energy Commission) for ^{14}C measurements and EDYTEM (Environnement, Dynamique et Territoires de Montagne, France) for the X-ray fluorescence analyses. We are grateful to the Autorita' di bacino lacuale dei laghi d'Iseo, Endine e Moro for permission to core Lake Iseo. Daniel Arnaud (INSU, C2FN) helped with coring. Coring was funded by INSU (Institut National des sciences de l'Univers, CNRS, France) and CEA (Commissariat à l'Energie Atomique et aux Energies Alternatives) through ISOMEX/PALEOMEX. We thank Adrian Gilli for his participation in the 2007 seismic survey. We are also grateful to Ana Brancelj for her valuable help during the bibliographical work.

CHAPITRE V | Instant sedimentation in a deep Alpine lake (Iseo, Italy) controlled by climate, human and geodynamic forcing

Article 2 | En review dans Sedimentology

William Rapuc[1], Fabien Arnaud[1], Pierre Sabatier[1], Flavio S. Anselmetti[2], Andrea Piccin[3], Laura Peruzza[4], Antoine Bastien[1], Laurent Augustin[5], Edouard Régnier[6], Jérôme Gaillardet[7] & Ulrich Von Grafenstein[6]

[1]Univ. Savoie Mont Blanc, CNRS, EDYTEM, 73000 Chambéry, France
[2]Institute of Geological Sciences and Oeschger Centre for Climate Change Research, University of Bern, Baltzerstrasse 1+3, 3012 Bern, Switzerland
[3]Regione Lombardia, D.G. Territorio e Urbanistica, Struttura Sistema Informativo Territoriale, 20124 Milano, Italy
[4]Istituto Nazionale di Oceanografia e di Geofisica Sperimentale—OGS, Sgonico, TS, Italy
[5]Division technique de l'INSU, Centre de Carottage et de Forage National, CNRS, France
[6]LSCE, Université de Versailles Saint-Quentin, Commissariat à l'Energie Atomique–CNRS, 91198 Gif-sur-Yvette, France
[7]Université de Paris, Institut de physique du globe de Paris, CNRS, Paris F-75005, France

Abstract

The sedimentary processes in the deep basin of large peri-Alpine lakes have not been studied much on long timescales due to high coring complexity of such lake systems. In 2018, a 15.5 m-long sediment section was retrieved from the deep basin of Lake Iseo (Italy) at 251 m water depth. A seismic survey associated to a multi-proxy approach with sedimentological and geochemical analyses, reveals that event deposits correspond to 61.4 % of the total sedimentation during the last 2000 years. The great heterogeneity of textures, colours, and grain-size distribution between the different types of event layers can be explained by the high number of potential sources of sediment in this large lake system. By combining a proxy of sediment sources with proxies of transport processes, flood events were distinguished from destabilisations of the slopes and the main delta. The three thickest mass wasting deposits correspond to major regional earthquakes events of 1222 CE, 1117 CE and around 700 CE. From a thorough comparison with regional climatic fluctuations and human activities in the watershed, it appears that periods of high sediment remobilization can be linked to a preceding increase in erosion in the watershed mainly under human forcing. Hence, even in large catchments, human activities play a key role on erosion processes and on sediment availability, disrupting the recording of the extreme events in lacustrine archive.

KEYWORDS

Lake sediment, Flood frequency, Earthquake records, Human activity, Erosion

1. Introduction

Several studies based on natural archives have recently shown how much human activities played a key role upon erosion and sediment transport processes throughout the Holocene and more particularly over the last two millennia (Arnaud et al., 2016; Brisset et al., 2017; Dotterweich et al., 2013; Doyen et al., 2013; Edwards and Whittington, 2001; Francke et al., 2019; Fuchs, 2007; Giguet-Covex et al., 2012; Giosan et al., 2017; Rapuc et al., 2019; Silva-Sánchez et al., 2014; Simonneau et al., 2013; Walsh et al., 2019; Zádorová et al., 2013). Indeed, the expanse of grazing, agriculture as well as the deforestation that often accompanied them may trigger a general destabilization of slopes and an increase in sediment flux towards depositional sinks (Edwards and Whittington, 2001). In European Alps, human activities have increased erosion from the end of the Neolithic (~4 kyrs BP) and even more significantly at the beginning of the Iron Age and during the Roman Period (e.g. Giguet-Covex et al., 2011; Simonneau et al., 2013; Vannière et al., 2013; Joannin et al., 2014; Bajard et al., 2016; Rapuc et al., 2018; Regattieri et al., 2019; Andrič et al., 2020). Even if lake sediments provide a continuous and well-preserved natural archive of such variations, strong and sudden inputs of sediment can disturb this record. Indeed, sediment availability in small lake basins and watersheds plays a key role in the sensitivity of the lake to record extreme events such as floods, avalanches or earthquakes (Brisset et al., 2017; Fouinat et al., 2018; Rapuc et al., 2018; Wilhelm et al., 2016a). It has been shown that human-triggered soil destabilisation may lead to an apparent increase in flood frequency by increasing the amount of sediment available for erosion (Brisset et al., 2017; Fouinat et al., 2017; Giguet-Covex et al., 2012). Whether it is climate- or human-triggered, a rise in erosion results in increasing sediment fluxes which makes steep lake flanks, in particular in its delta area, much less stable. It has been shown that the hence-acquired meta-stability increases the sensitivity of lake sediment to record the occurrence of earthquakes (Wilhelm et al., 2016a). By modifying the cycles of erosion and sediment transport processes, human activities hence impact the sedimentation in the different sinks.

However, previous studies were led in small-scale lakes and catchment areas. Very few investigations were conducted in large peri-Alpine lowland lake basins fed by large catchment area, although such lakes are particularly promising targets to reconstruct past hydroclimate changes at a regional scale (Arnaud et al., 2016; Wagner et al., 2008; Wessels, 1998). Compared to smaller water bodies, large lakes are challenging to study due to the (i) multiple sediment sources linked to multiple inflows, (ii) an inhomogeneity of the in-lake biogenic sedimentation at different water depth and location, (iii) several processes that can impact the continuous sedimentation such as floods or earthquakes (Sauerbrey et al., 2013; Sturm and Matter, 1978); making more difficult the interpretation of the erosion signal. It is also very challenging to recover pluri-millennial sediment sequence in those lake that are very often deeper than 100m and where the total Holocene sediment accumulation often overcomes 20m and sometimes 50m.

Here, thanks to a new coring system, we present a novel study with a long sediment core from a large peri-Alpine lake sampled in the deep basin of Lake Iseo at the downstream end of the Val Camonica valley in northern Italy. In this region, human activities are well-documented in the Val Camonica (e.g. Anati and Cittadini, 1994; Gehrig, 1997; Marziani and Citterio, 1999; Pini, 2002; Pini et al., 2016) and various regional paleoclimate records already exist (e.g. Büntgen et al., 2016, 2011; Joannin et al., 2014; Vannière et al., 2013; Wirth et al., 2013b). The main objective

of this study was to identify the main sedimentary processes in such deep Alpine lakes under Geodynamic, Human and Climate forcing. A multi-proxy approach, combining a seismic survey with sedimentological and geochemical analyses, allow to document that the fluctuations in numbers and intensities of these events (floods, earthquakes) are related to sediment availability in the deep basin and in the lake catchment.

2. Study Site

Lake Iseo (45°44.205′N; 10°4.340′E) is located in Lombardy, North of the Po plain (Fig. V-1-A), at the southern end of the Val Camonica valley at an altitude of 185 m a.s.l (above sea level). Lake Iseo (Latin name "Sebino") is, with a length of 25 km and a surface area of 60.9 km^2, the smallest of the four majors Italian perialpine lakes. The depression that hosts the lake is a former Miocene canyon that was reshaped and re-eroded by several glacier advances and retreats during the Pleistocene epoch. It current infilling is assumed to have been set since the last post-Late Glacial Maximum retreat (Bini et al., 1978). Lake Iseo is currently meromictic (Ambrosetti and Barbanti, 2005; Salmaso et al., 2003). The last observed complete mixing of the deep water occurred in the 1980s (Salmaso et al., 2003). From then, oxygen concentrations have continuously decreased within the deep water and conditions of permanent anoxia developed during the 1990s. Instrumental data provided by A.R.P.A (Regional Agency for the Protection of the Environment, http://arpalombardia.it/) indicates that the limit of the depth of the hypolimnion varies between 80 and 100 m. At these depths, the oxygen saturation and pH values decrease sharply, while dissolved calcium concentrations increase.

Lake Iseo bathymetry shows two sub-basins separated by Monte Isola (Fig. V-1-B). The smaller basin, Sale Marasino Basin, is 100 m deep and disconnected from the main basin and from the sediment input of the Oglio river by the Monte Isola plateau in its northern part. The Holocene sedimentation of this area was already studied (Lauterbach et al., 2012; Rapuc et al., 2019). The main basin is however much deeper (251m) and had never been cored. It is located North-West of Monte Isola (Fig. V-1-B) and is protected from underflows coming from all the inlets located in the Marone delta or feeding Monte Isola Plateau and the Sale Marasino Basin by the presence of a ridge North-West of Monte Isola (Fig. V-1-B).

The Oglio river, originates from the Adamello Massif. It is the main tributary and the outlet of Lake Iseo (Fig. V-1-B). This river drains a relatively large watershed (1,842 km^2) with a maximum elevation of 3539 m a.s.l in the Adamello Massif, in the northern part of Val Camonica and a mean altitude of 1400 m a.s.l (Garibaldi et al., 1999). The watershed of Lake Iseo extends up to 60 kilometres Northwards into the Val Camonica valley and only several kilometres to the East and West of the lake. It is mainly composed of Triassic, Jurassic and Cretaceous limestones and marlstones in the southern part, with some outcrops of Permian sandstones. In the northern part of the Val Camonica, metamorphic rocks linked to the Alpine orogeny with Tertiary tonalites, granodiorites and quartzodiorites are outcropping. Glaciers and rock glaciers are present in the north-eastern part of the watershed (Scotti et al., 2013). The Val Camonica is well-known for its abundance of rock carvings that are registered on the UNESCO World Heritage List (Ruggiero and Poggiani Keller, 2014). These archaeological evidences provide indications of human presence in the Iseo region since the Mesolithic period (9 – 6 kyrs BC) and agro-pastoral practices as early as 6.5 kyr BP.

The Val Camonica valley and more broadly the north-eastern part of the Italian Alps are affected by a moderate to high seismic hazards (Giardini et al., 2013; Pagani et al., 2018; Stucchi et al., 2004; Wiemer et al., 2015). The tectonic setting is the result of complex collisional and post-collisional phases of the Alpine orogeny (Dal Piaz et al., 2003). The current crustal shortening in the area is estimated to ~1 mm.yr^{-1} (Serpelloni et al., 2005), and several devastating earthquakes have been recorded in the last millennium (Fig. V-1-A; for the most updated Italian earthquake catalogue see Rovida et al., 2020, 2019). The local seismic activity (magnitude M<6) is ascribed to fold-and-thrust systems, mainly West-East oriented, blind faults toward the Po Plain, and North-South oriented in the Garda Lake area (DISS Working Group, 2018; Livio et al., 2009).

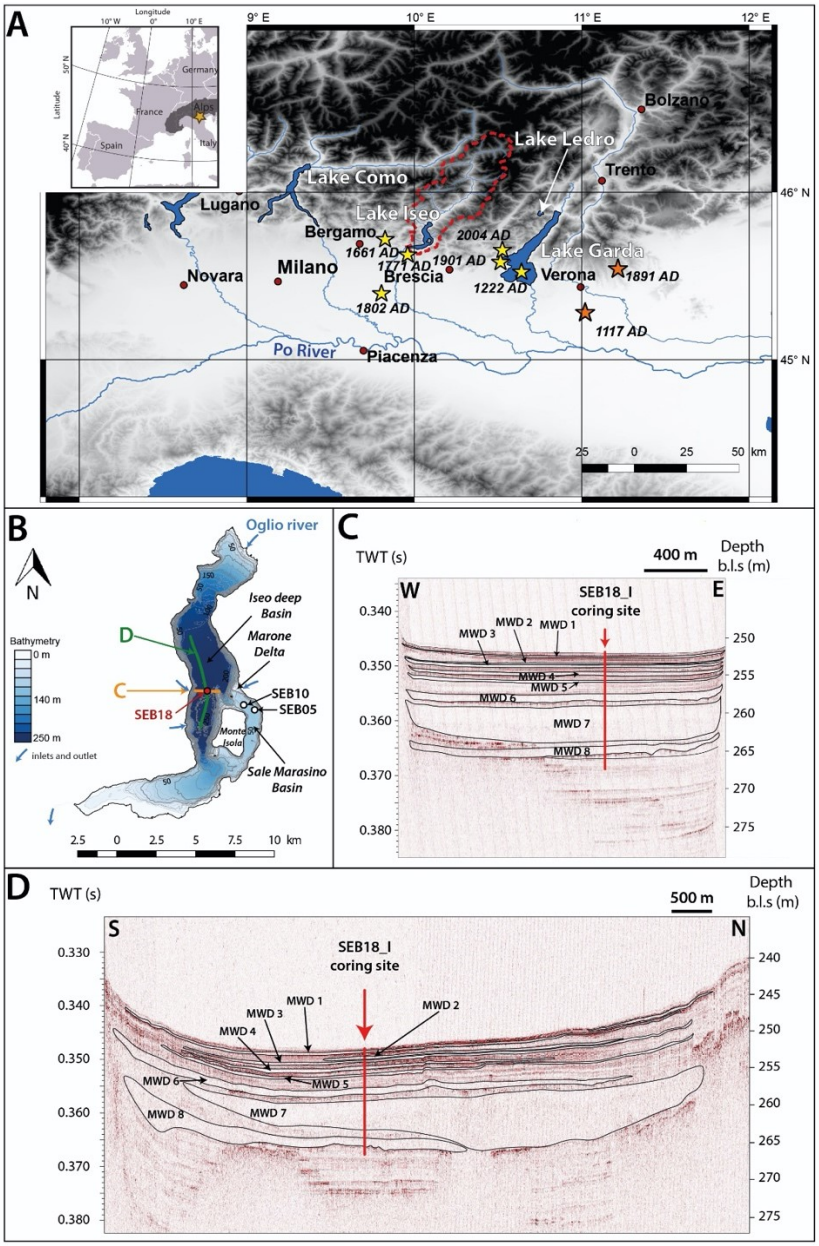

Fig. V-1- Lake Iseo location and settings. (A) Location of Lake Iseo (Italy), its watershed (red dashed line) and different lakes of the Italian southern Alps: Lake Como, Lake Garda, and Lake Ledro. The orange and yellow stars correspond to the location of historic earthquakes with a Magnitude ⩾ 6 and < 6, respectively. (B) Lake Iseo Bathymetric map associated with the description of the different morphological features and the different coring sites. Seismic profiles W-E (C) and S-N (D) oriented across the deep basin showing the coring site location (vertical red line) and the principal generations of mass wasting deposits (MWD, coloured lines). The depth of the seismic profile is expressed in metres below lake surface (m b.l.s.), assuming a mean P-wave velocity of 1450 m.s-1 in water and sediments.

3. Materials and Methods

3.1. Seismic survey

Two previous studies were made on sediment cores from Lake Iseo (Fig. V-1-B), retrieved from the Sale Marasino isolated basin (SEB05&06) and the Monte Isola Plateau (SEB10), which separates the Sale Marasino basin from the main Iseo basin that is fed by the Oglio river. Hence, none of those sites receives any sediment input from the Oglio river (Lauterbach et al., 2012; Rapuc et al., 2019). A seismic reflection survey was conducted in the deepest basin in July 2018 to select a suitable coring site, minimizing the amount of reworked sediment and presenting the thinnest mass wasting deposits (MWD). For this survey, ≈ 51 km of 3.5 kHz pinger (Geoacoustics Limited, Yarmouth, United Kingdom) single-channel data were acquired with a shooting interval of 500 ms and recorded the SEG-Y data with a sample frequency of 24 kHz. A bandpass filter (1500 – 6500 Hz) was applied. The coring location, SEB18_I (45° 43.536'N ; 10° 3.888'E), was selected in the centre of the deep basin at the intersection of two perpendicular seismic lines, North-West of Monte Isola by 251 m water-depth (Fig. V-1-B). This area is protected from the Marone delta sediment input by the ridge North-West of Monte Isola and is supposed to be only influenced by the sediment input from the Oglio river and from small gullies and tributaries coming from the hills, West of the coring site.

3.2. Coring, and lithological description

In October 2018, 39.2 m of sediment was retrieved (Fig. V- Sup Fig. 1) from six different holes in close vicinity (less than 20 m). For this survey, two UWITEC 90-mm diameter piston corers (Uwitec, Mondsee, Austria) were used, the pushing power was provided using a semi-manual UWITEC downhole hammer, operated from an UWITEC platform (EDYTEM/LSCE/C2FN). Two meters-long sections from the different holes were taken with a 1 m offset to ensure a sufficient overlap to provide a continuous record (Fig. V- Sup Fig. 1). Most of the sections were split, photographed at high-resolution (20 pixels.mm^{-1}), described and logged in detail using the Munsell colour chart. The identification of specific layers on the overlapping sections combined with correlations of XRF-core scanner signals allowed the creation of a 15.5-m-long composite sediment sequence (hereafter called SEB18, Supplementary Data 1). One gap occurs in the sequence from 1342.4 to 1362.4 cm: between two sections where an overlapping section is missing. While describing the core sections, specific attention was given to the identification of layers interbedded within the continuous sedimentation. These event layers were visually documented, described, measured, and logged.

3.3. Loss on ignition

Loss on ignition (LOI) analysis was conducted to estimate the organic matter and carbonate content throughout the sediment sequence. As many layers interrupt the sediment section, we applied a 10 cm evenly spaced discrete sampling step on the continuous sedimentation to perform LOI following the protocol that was defined by Heiri et al. 2001. Several discrete samples were also collected in the main event layers. Before the LOI analysis, the dry bulk density (DBD) was calculated from the samples by performing a constant volume sampling and by weighting the sediment after 72 h of drying at 60 °C. Then, the sediment samples were crushed before being heated in a muffle furnace at 550 °C for 4 h and at 950 °C for 2 h. The relative weight loss during

the first (hereafter, LOI550) and second heating phases (hereafter, LOI950) corresponds to the fractions of organic matter and of carbonate, respectively. Finally, the non-carbonate ignition residue (NCIR) was obtained by removing LOI550 and LOI950 from the initial dry weight.

3.4. Geochemical analyses

To characterize variations of major elements, we performed X-ray fluorescence (XRF) geochemical analyses on the EDYTEM laboratory's AVAATECH Core Scanner (Avaatech XRF Technology, Alkmaar, The Netherlands) throughout the SEB18 sediment sequence. We applied a continuous 5 mm step measurement with two runs: one at 10 kV and 0.3 mA for 30 s, to detect lightweight elements, such as Al, Si, K, Ca and Ti and a second run performed at 30 kV and 0.4 mA for 40 s, to detect Mn, Fe, Br, Rb, Sr and Zr. The XRF core-scanning results are expressed hereafter as count per second (cps) within each element-attributed X-ray fluorescence energy range. To identify principal sediment end-members and correlations between the detected elements, a principle component analysis (PCA) was conducted on the whole XRF dataset (Sabatier et al., 2010).

3.5. Chronology

On SEB18 sediments, we combined varve counting, short-lived radionuclides (^{210}Pb, ^{137}Cs, ^{241}Am), and ^{14}C to build a reliable age-depth model along the 15.5 m of the composite section. Varves were counted on the first 37 cm of SEB18_I_Pil02 section. Then, 38 samples were collected over the first 48.1 cm of the sequence to measure short-lived radionuclide activities at the Laboratoire Souterrain de Modane using the well-type germanium detectors (Reyss et al., 1995). Shortlived radionuclide chronology was carried out using R code package "serac" (Bruel and Sabatier, 2020). Thirteen samples of vegetal macro-organic remains were used to perform 14C measurements at the LMC14 laboratory (CNRS). Dates were calibrated at 2-sigma using the Intcal20 calibration curve (Reimer et al., 2020). We used the R code package "clam" (Blaauw, 2010) to compute the age-depth model of the non-event sections.

4. Results

4.1. Seismic imagery

Assuming a P-wave velocity (Vp) of 1450 m.s^{-1}, the seismic signal penetrated 25 to 30 m of sediment below the lake floor. In areas where free gas occurs, particularly near deltas where high amount of organic matter is buried, penetration is less, and characteristic high-amplitude anomalies occur that mark the gas front (Fig. V-1-B, C & D). The seismic facies comprise sections where seismic reflectivity is high and subparallel reflections with high lateral continuity occur; these are interpreted as regularly stacked continuous sedimentation. The associated reflections all onlap the steep lateral sides of the lake basin. Intercalated within these reflective sections, several transparent to chaotic deposits typical of mass-wasting deposits (MWD) (e.g. Chapron et al., 2016; Strasser et al., 2013) interrupt the continuous sedimentation. They often show high amplitude reflections at their bases. The upper part of these MWDs is usually transparent, indicating a megaturbidite/homogenite unit representing the latest stage of event sedimentation when the fine particles eventually settle. The lower parts of MWDs may show some internal architecture with reflections indicating various basal flow units. Some of the MWDs show a mound-like geometry with larger thickness in the centre of the basin (Fig. V-1-D). At least, eight

MWDs are identifiable across the deep basin of Lake Iseo, with three deposits presenting a metric thickness (Fig. V-1-C & D). Most of these deposits seem to cover the entire basin, and, considering their geometry, to originate from its southern or northern part.

The three thickest MWDs are labelled MWD6, 7 and 8 (Fig. V-1-C, D & Fig. V-2). Interpolation of their thicknesses over the whole basin result in volume estimates of $11 \cdot 10^6$ m^3 for MWD6 and a combined $89 \cdot 10^6$ m^3 volume calculated for both MWD7 and MWD8 as they are stacked and partly hard to be subdivided on the seismic data.

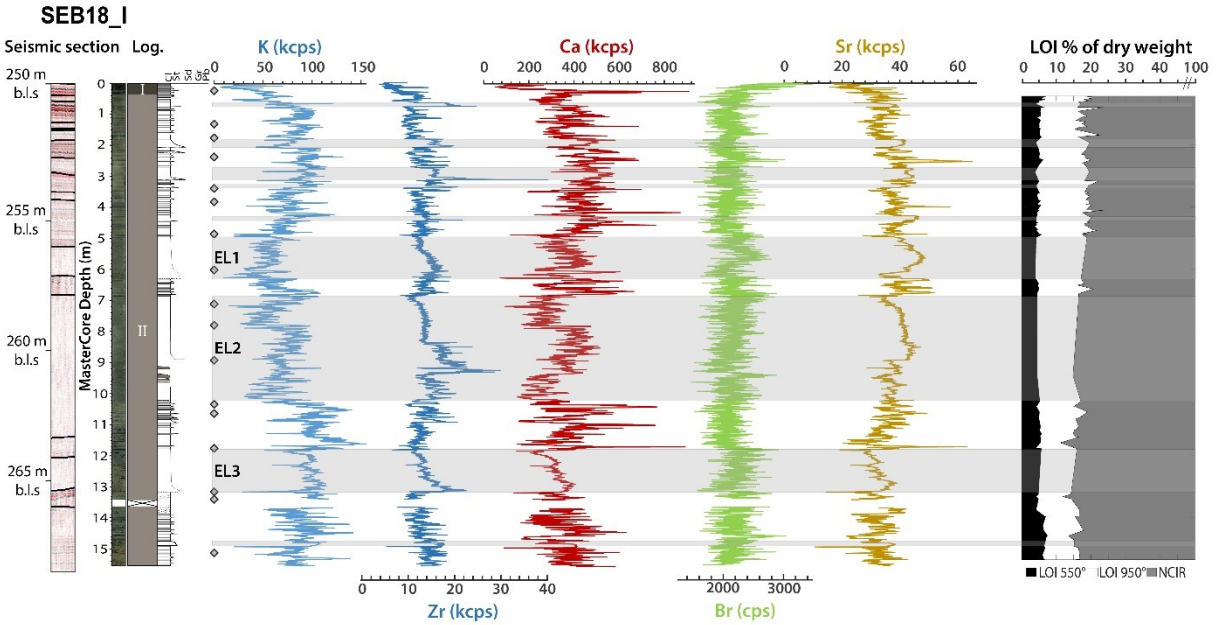

Fig. V-2-Sedimentological and geochemical data. A close-up view of the seismic profile (Fig. 1C) section is compared with lithological and geochemical data. A core image of the 15.5 m of the SEB18 sediment sequence and stratigraphic units are associated with the grain-size sensitive lithological column, selected geochemical results (K, Zr, Ca, Br, and Sr contents) and LOI. The depth of the seismic section is expressed in metres below lake surface using a Vp of 1450 m.s-1 and is scaled approximately to fit the length of the sediment core. Grey shadings represent the thickest graded layers. Grey diamonds represent junction between the different sections of SEB18 sediment sequence.

4.2. Sedimentology

4.2.1. Lithologies and stratigraphic units

Continuous sedimentation occurs in 39 % of the SEB18 sediment section. They are visually distinguishable from homogeneous or graded layers interpreted as event layers and accounting for 61 % of the total accumulation. Within the continuous sedimentation, two stratigraphic units can be distinguished (Fig. V-2): Unit I (0 – 32.3 cm) is composed of dark grey clay becoming greenish at the base of the unit. It is composed of thin alternations of light greyish olive clayey (10Y 6/2), grey (5y 5/1), pale yellow (5Y 7/3) and/or dark laminae (5Y 2.5/1). Fifty-eight laminae successions were counted in this unit that also includes several graded layers. This unit coincides with the varved organic gyttja which has already been described in cores retrieved in Lake Iseo (Lauterbach et al., 2012; Rapuc et al., 2019) and related to the recent eutrophication period of Lake Iseo. LOI was not measured in this unit.

In Unit II, from 32.3 cm to the bottom of the core (1550.9 cm), the continuous sedimentation of the SEB18 sedimentary section is composed of grey clay (10YR 5/1) featuring dark spots that disappear after oxidation. The LOI550 ranges between 3.8 and 7.5 %, with a mean value of 5.3

%. The LOI950 ranges between 5.7 and 18.2 % with a mean value of 12.2 %. The continuous sedimentation of Unit II is interrupted by numerous graded layers that are described below. The grain-size of the continuous sedimentation is largely dominated by fine silts and clays (Q90 < 20 µm).

4.2.2. Event layers

Event layers were macroscopically identified and counted. Their colours vary from dark grey to light brown (2.5Y 5/2), very dark greyish brown (10YR 3/2), dark grey (10YR 4/1) and black (10YR 2/1). These layers either have a normally graded upward-fining grain-size pattern like turbidite type deposits or they display homogeneous lithologies termed "homogenites" (Hieke, 1984; Kastens and Cita, 1981). As they interrupt the continuous sedimentation, they are considered as instantaneous event layers. Thickest layers present fine to medium sand at their bases (Q90 > 200 µm). Most of the layers are thin (i.e., below 1 cm), but three of them are complex sequences that are more than 1m-thick: (i) Event layer 1 (EL1) is comprised between 493.5 and 626.1 cm, i.e., 1.32 m-thick, (ii) Event layer 2 (EL2) is 3.37 m-thick and located between 682.3 and 1020 cm and, (iii) Event layer 3 (EL3) is comprised between 1178.5 and 1320.7 cm, I.e., 1.42 m-thick (Fig. V-2). EL1 and EL3 present a fine graded sandy base followed by a thick homogeneous layer, composed of very fine sand to silt and a thin dark clayey top. EL2 is the thickest sequence interbedded within SEB18 sediment pile. It presents a lower part made of medium to fine sand associated with mud-clasts. This is followed by homogeneous silts from 891. 5 cm to 683.7 cm and a thin clayey top. EL1, 2 and 3, such as most of layers thicker than 5 cm, present an erosive base. The three thickest layers are also identifiable on the seismic profiles (Fig. V-1-C, D & Fig. V-2) as they are correlated to MWD6, 7 and 8, respectively, and seem to originate from the Oglio delta in the northern part of the deep basin. A total of 146 ⩾ 1 mm-layers have been identified measured for thickness (average thickness: 6.5 cm; median thickness: 1.2 cm).

4.2.3. Geochemical analyses

Unit I shows low values of K (< 70 kcps), of Zr (< 10 kcps with only one peak at 15 kcps) and an upward increase of the Br values to the top of the unit (from 2000 to 3000 cps). In the continuous sedimentation, the Zr and K signals increase downcore (Fig. V-2) towards the base of the sediment sequence (Unit II). No clear trend is visible for other elements, as Ca, Br and Sr display relatively constant values. Several event layers present a peak of Zr at the base and an increase of K value towards the top (Fig. V-2). Br and Ca are very variable and fluctuate within the event layers, while Sr shows low variability. The samples that were collected in these thickest event layers for LOI550 and LOI950 measurements did not present significant changes compared to others. values. Individual and variables factor maps were obtained from a PCA conducted on the XRF data (Fig. V-3). These biplots highlight the geochemical distribution within the two different sedimentary units and the relationships between the different elements. Dimensions 1 and 2 (denoted as Dim1 and Dim2) represent 52.7 % of the total variability. Three chemical end-members were identified from the variables factor map. The first one is positively correlated with Dim1, yields high positive loadings for the major terrigenous elements (Al, Si, K, Ti, Rb, Fe), and is thus denoted as "terrigenous". The second end-member, shows negative loadings on Dim2 and allows the discrimination of Br, Mn and Pb. Br was previously correlated in other cores of the same lake to organic matter content and Mn to oxygenation processes in the lake (Rapuc et al., 2019), Pb is probably complexed with organic matter. This pole is then denoted as "organic matter-related elements". The third end-member, shows positive correlation with Dim2 and yields

high positive values for Zr, Ca and Sr. Sr is usually present in marine limestone, which constitutes a major part of the watershed's outcrops. Zr is generally associated with coarse grain-size explaining the peak at the base of each thick coarse graded layers. Thus, this end-member is interpreted as representative of the carbonates and coarsest terrigenous inputs from the watershed, characterised by the presence of reworked marine carbonates (Ca, Sr) and heavy minerals (Zr). It is thus denoted as "coarse terrigenous fraction".

To understand the specificity of the two stratigraphic units and the different event layers, an individual factor map was drawn (Fig. V-3-B). From this map, Unit I is negatively correlated with terrigenous end-member and positively with the organic matter end-member. This confirms its important organic content already observed in other cores from Lake Iseo (Lauterbach et al., 2012; Rapuc et al., 2019). Unit II presents a large variability but is positively correlated with the terrigenous end-member and is also characterized by low Ca, Zr and Sr. The event layers present a wide distribution on the individual factor map but are characterised by relatively low organic matter content. PCA analyses and XRF data did not allow to directly classify event layers in different types.

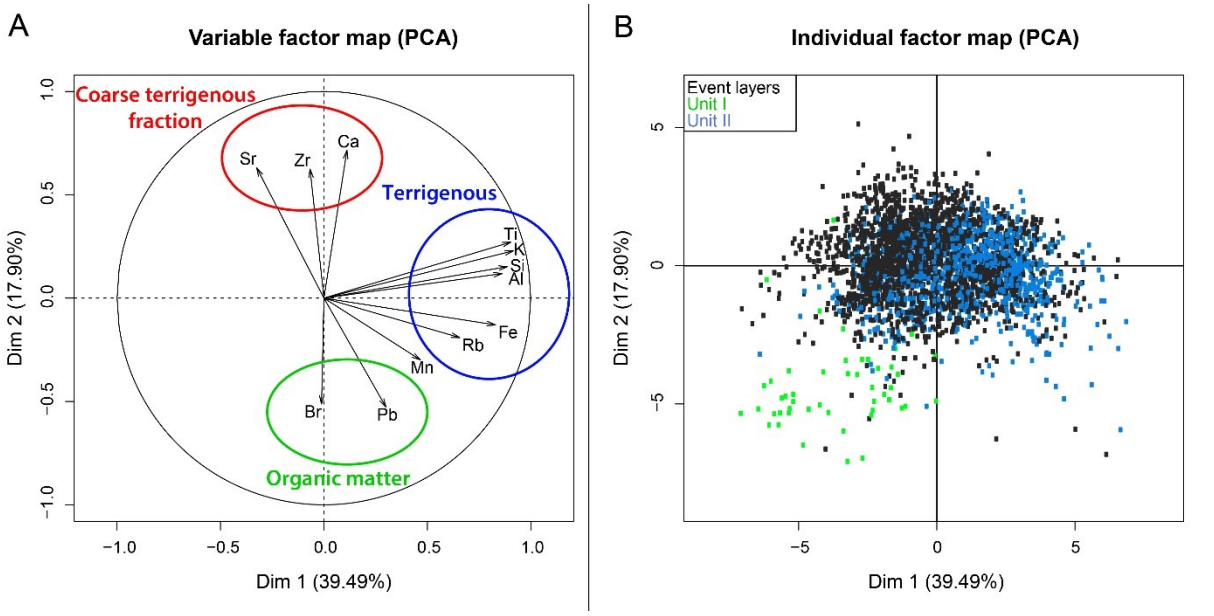

Fig. V-3- Variable and individual factor maps from the PCA. (A) Variable factor map with three end-members (terrigenous, organic matter and coarse terrigenous fraction linked to carbonates). (B) Individual factor map with the two sedimentological units added as an illustrative variable and compared with the event layers.

4.3. Chronology

4.3.1. Short-lived radionuclides and varve counting

From the first 37 cm, 58 varve couplets were identified and counted, yielding a mean sedimentation rate of ~ 5.3 mm.yr^{-1} including event deposits (Fig. V-4-A). This counting allows to assign the earliest varve to 1960 CE corresponding to the beginning of the eutrophication of the Monte Isola Plateau, already established by varve counting from the SEB10 sediment sequence (Rapuc et al., 2019). This timing is quite identical to the one observed in Lake Varese, in northern Italy (Bruel et al., 2018). The age of the uppermost turbidite matches with a well-documented flood event that occurred in 1994 CE (Guzzetti and Tonelli, 2004; Luino et al., 2002).

The ^{210}Pb excess profile (^{210}Pb$_{ex}$) profile shows a regular decrease (Fig. V-4-A) from 470 mBq.g^{-1} to low activities (<30 mBq.g^{-1}) punctuated by distinct drops. Following Arnaud *et al.* (2002), these low values of ^{210}Pbex corresponding to event deposits were excluded from the construction of an event-free sedimentary record as they were considered as instantaneous. We use here a logarithmic scale to plot ^{210}Pb$_{ex}$ event free data and to underscore a single-point alignment that indicates a constant sedimentation rate of 4.41 ± 0.06 mm yr^{-1} (R^2=0.88) for the uppermost 48 cm thanks to the Constant Flux Constant sedimentation model (Bruel and Sabatier 2020).

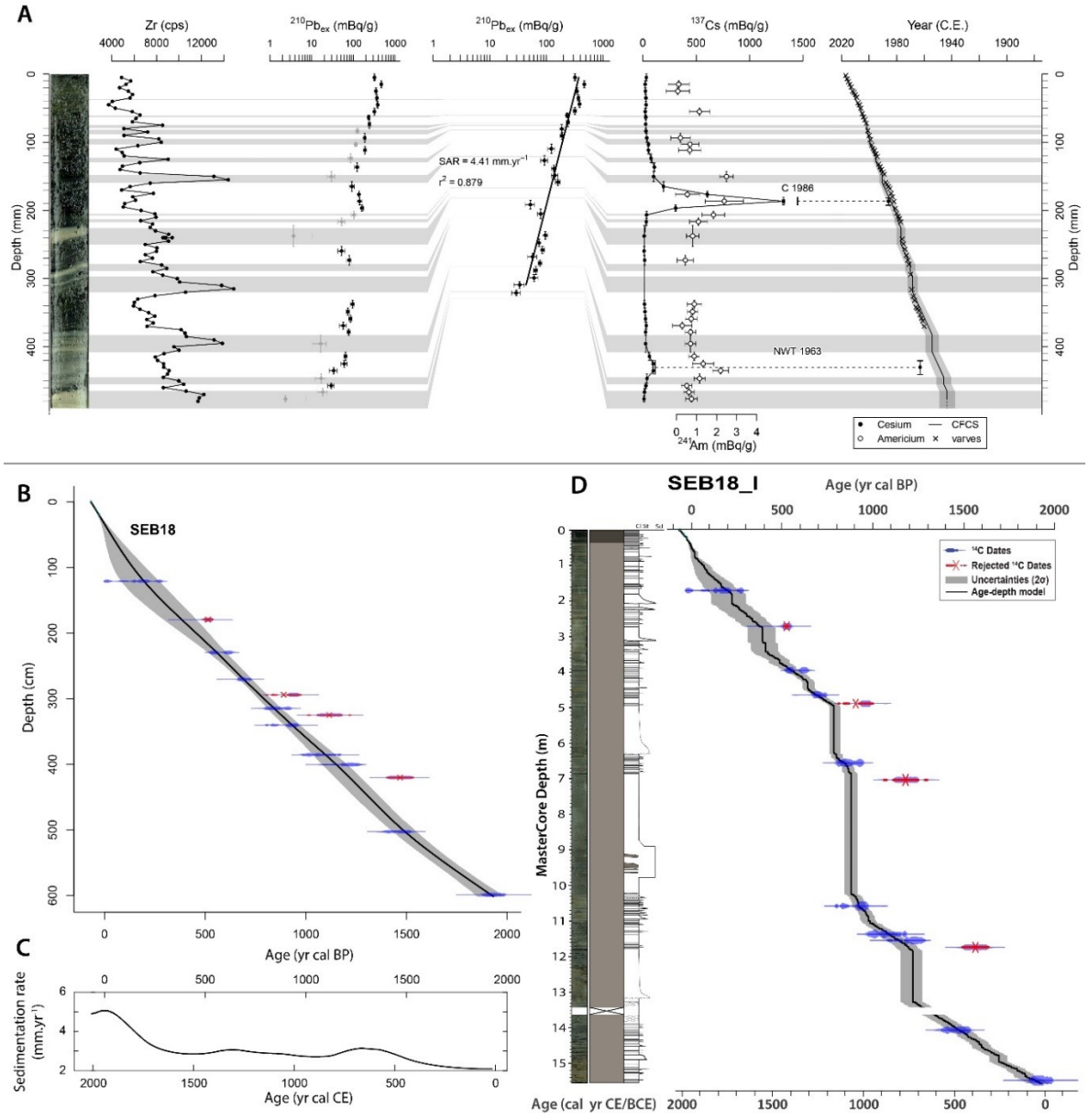

Fig. V-4- Age-depth models. (A) Short-lived radionuclide data: 210Pbex in logarithmic scale associated with the 241Am and 137Cs profiles with the picture of the top 48 cm of SEB18 sequence. (B) Age–depth model in event-free depth. (C) Sedimentation rate (without event layers) obtained from the age-depth model, (D) Complete age-depth model associating radiocarbon and varve counting.

The ^{137}Cs profile shows a clear peak between 16.7 and 19.7 cm with a maximum activity (>1300 mBq.g^{-1}) at 18.7 cm; this peak is associated with a peak of ^{241}Am (>2.3 mBq.g-^{1}) and is widely attributed in the literature to nuclear fallout from the 1986 CE Chernobyl accident (e.g., Appleby

et al., 1991). The ^{241}Am profile presents a peak (> 2.2 mBq.g^{-1}) at 43.5 cm with a peak in the ^{137}Cs (>97 mBq.g^{-1}) profile between 42.5 and 43.5 cm. These peaks correspond to the maximum nuclear weapon tests at 1963 CE (Appleby et al., 1991). The 1986 CE peak is in good agreement with the sedimentation rate that was derived from the ^{210}Pb$_{ex}$ profile and the varve counting. The ^{210}Pb$_{ex}$ profile presents and offset from the 1963 CE peak, probably due to a change in the sedimentation rate around 40 cm. These chronological markers were added into the age-depth model to constrain it for the upper portion of the sediment section.

4.3.2. ^{14}C & Age-depth model

Thirteen samples of terrestrial macro-remains were analysed to provide radiocarbon ages. Once calibrated, 4 of these 13 dates (Table V-1) were not used because they presented ages older than the best-fit age-depth curve of the SEB18 sequence. These four ages were consistently sampled from the top of detrital event layers: these macro-remains are interpreted as originating from reworked from previously deposited sediment in the lake.

The thickness of each layer was subtracted from the SEB18 sediment sequence depth to create an event-free depth (Fig. V-4-B) and to obtain the best age-depth model. We use the combination of varve counting and the nine remaining calibrated ages to generate the age depth-model with a smooth spline model with 0.4 for the smooth parameter. The sedimentation rate presented hereafter (Fig. V-4-C) was calculated from the event-free depth and is not influenced by the variation of the event layer occurrence. To provide a date for all event layers, we reintegrated all event layers to the age-depth model (Fig. V-4-D).

The SEB18 sequence covers the last 2000 yrs (21 – 2018 CE) with a continuous sedimentation rate that varies between 5.1 and 2.1 mm.yr^{-1} with a mean of 3.1 mm.yr^{-1}. Three periods of gradual increase of sedimentation rate are identified (Fig. V-4-C) in the sequence. The first one occurs between 500 and 800 CE with a maximal sedimentation rate of 3.2 mm.yr^{-1}. After a small decrease until approximately 900 CE (2.7 mm.yr^{-1}), the sedimentation rate increases gradually and presents high values (3.06 mm.yr^{-1}) between 1000 and 1400 CE. From 1500 CE towards the top, the sedimentation rate increases sharply and reaches its highest value of 5 mm.yr^{-1}.

Table V-1 - Radiocarbon ages for the SEB18 sediment sequence. Event-free depth was calculated by excluding the thicknesses of each graded beds considered as event layers. Samples in bold correspond to dates excluded from the age-depth model (Fig. V-4-B&C).

Sample name	Core	MCD (cm)	Event-free depth (cm)	Radiocarbon age	Age cal yr BP 2 σ range	Type
SAC-A 57155	SEB18_I_C_01A	169.8	120.8	170±30	-3-289	stem
SAC-A 57512	**SEB18_I_B_02A**	**271.8**	**179.3**	**465±30**	**490-538**	**plant debris**
SAC-A 57513	SEB18_I_C_02A	395	229.3	555±30	520-639	plant debris
SAC-A 57156	SEB18_I_B_03A	463.7	270.4	745±30	662-726	plant debris
SAC-A 57514	**SEB18_I_C_03A**	**488.2**	**294**	**1015±30**	**802-978**	**plant debris**
SAC-A 57157	SEB18_I_B_04A	653.2	314.7	950±30	796-925	plant debris
SAC-A 57515	**SEB18_I_C_04A**	**702.9**	**324.9**	**1190±30**	**1007-1226**	**wooden debris**
SAC-A 57516	SEB18_I_B_06A	1058.7	340.2	1000±30	799-966	plant debris
SAC-A 57158	SEB18_I_C_06A	1136.4	385.4	1150±30	980-1173	plant debris
SAC-A 57517	SEB18_I_C_06A	1153.4	400.5	1255±30	1085-1277	plant debris
SAC-A 57518	**SEB18_I_B_07A**	**1183.4**	**420.2**	**1575±30**	**1401-1535**	**twig**
SAC-A 57519	SEB18_I_B_08A	1406.9	502.8	1550±30	1379-1526	plant debris
SAC-A 57520	SEB18_I_B_08B	1548.9	598.7	1980±30	1876-1992	plant debris

5. Interpretation and Discussion

5.1. Provenance of continuous sedimentation

On average, LOI analyses indicate that organic matter accounts for 5.3 % of the continuous sedimentation, whereas carbonates represent 12.2 %. Hence, most of this sedimentation is made of siliciclastic material (Fig. V-2). As Lake Iseo is a temperate hardwater meromictic lake, where the deep water does not mix every year (Garibaldi et al., 2003), we assume that calcite precipitate in the lake as it is the case worldwide for this lake's type (Küchler-Krischun and Kleiner, 1990). The ARPA instrumental data indicate that pH values decrease sharply between 80 and 100 m b.l.s at the upper limit of the hypolimnion (Fig. V-5-A). This is accompanied by dissolved calcium concentration increase (Fig. V-5-B). Depending on the particle sizes and the settling times, some carbonate dissolution can occur at great depth in hard water lakes (Ramisch et al., 1999). In Lake Lugano, another peri-Alpine lake, it has been shown that only calcite with a diameter larger than 40 µm reach the lake bottom at 288 m (Ramisch et al., 1999). As authigenic carbonates in lakes have a low sinking velocity and usually present a diameter lower than 20 µm, as demonstrated in Lake Bourget (Arnaud, 2005), they are not likely to be preserved during their settling in the deep basin of Lake Iseo and are not supposed to contribute significantly to its continuous sedimentation. Then, fine-grained authigenic biogenic carbonates can only be preserved above a certain depth, where re-dissolution processes do not impact small size particles: above the hypolimnion on slopes and plateau (Fig. V-5-C&D) presenting an inclination lower than the theoretical angle of repose of wet clayey material (>30°, Glover, 1997). In the Iseo deep basin, as settling times plays an important role, most of the carbonates recorded in the continuous sedimentation are supposed to be linked to detrital inputs from the watershed through erosion of the limestone and marlstone bedrock, which is strongly suggested by the correlation between Ca, Sr and Zr (Fig. V-2 & Fig. V-3-A).

Oglio river waters and thus the sediment inflow by the Oglio plume are deflected towards the western shore of Lake Iseo due to the Coriolis influence (Pilotti et al., 2018, 2013). In normal flow conditions (~ 50 $m^3.s^{-1}$; Groppelli *et al.*, 2011; Hogg *et al.*, 2013), the water underflow coming from the Oglio inlet only influences the first 100 m of depth of the lake basin, while the horizontal length of overflow intrusion is limited to 3 km (Hogg et al., 2013). Thus, most of sediment input from the Oglio river during normal flow conditions is accumulated close to the delta or on the north-western shores of Lake Iseo. Therefore, the input of detrital sediment in the deep basin is mainly related to flood events: when the current is strong enough, underflows can flow beyond the delta and lead to the settling of thin particles after the decrease of the turbiditic current in the deep basin. It is thus very likely that the continuous detrital sedimentation of the deep basin of Lake Iseo corresponds to the decantation of the end of underflows linked to minor flood events. A minority of this sedimentation can also be linked to gullies and small rivers from the hillslopes West and East of the deep basin.

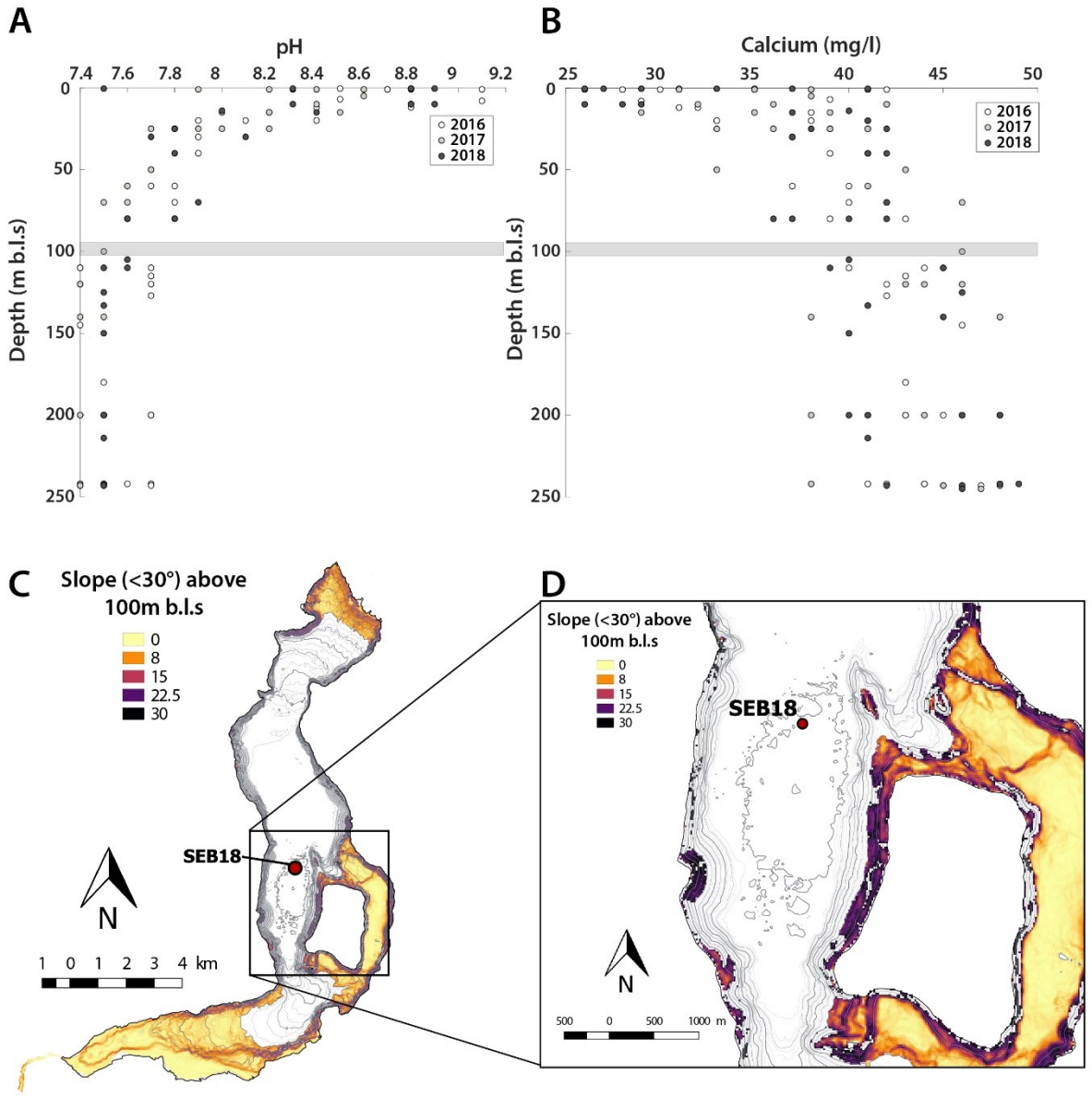

Fig. V-5- pH (A) and dissolved calcium (B) profiles, recorded in the deep basin of Lake Iseo, close to the coring site, in 2016, 2017 and 2018 by ARPA (http://arpalombardia.it/). (C) Map presenting slopes of Lake Iseo with an inclination lower than 30° above 100 m b.l.s. where authigenic carbonates could accumulate (D) Zoom on map C in the deep basin around the coring site.

5.2. Origin and trigger of the event layers

In large lowland lake systems, several mechanisms can trigger event layers, such as : (i) considerable lake-level fluctuations, (ii) destabilisation of slopes and deltas due to sediment overloading or (iii) to seismic shaking and, (iv) flood events (e.g. Rapuc et al., 2018; Sauerbrey et al., 2013). Here, we found no historical evidence of significant fluctuations of the outflow level, thus, lake level triggering mechanism cannot be invoked to explain thick layers recorded in the deep basin. Due to the high sedimentation rate recorded (Fig. V-4-C), sediment overloading on the lake slopes, on the delta of the Oglio, or on those of small tributaries are likely to induce MWD leading to the deposition of graded layers in the deep basin of Lake Iseo. Equally, this high sedimentation rate implies a high sensitivity of the lake to seismic shaking (Rapuc et al., 2018; Wilhelm et al., 2016a). With a mean sedimentation rate of 3.06 mm.yr^{-1}, the probability for an

earthquake to induce a MWD and related event layers in Lake Iseo is higher than in most of previously studied Alpine lakes (Wilhelm et al., 2016a). Moreover, such lake basins with sharp shelves and a flat lake floor provide typical settings for mass movements (Sauerbrey et al., 2013). In terms of flooding, as previously mentioned, most of floods contribute to the continuous sedimentation in the deep basin of Lake Iseo with the distal low-velocity underflows reaching the coring site with the finest suspended particles. In contrast to these signatures in the continuous sedimentation, floods can also be recorded in the deep basin as event layers either when (i) strong underflows linked to extreme flood events produce a current important enough to reach the deep basin and produce a turbidite layer distinguishable from the continuous sedimentation as for the 1994 CE event, or when (ii) flood events come from nearby tributary rivers. In summary, only two main mechanisms can be at the origin of the event layers recorded in the SEB18 sequence: (i) extreme flood events from the Oglio river or flood events from gullies and small tributaries coming from the western hillsides of the lake, and (ii) destabilisations of slopes and delta triggered by seismic shaking after sediment overloading.

In SEB18 sequence, 146 graded layers were identified and interpreted as event layers. Colours and textures from macroscopic observations, PCA and XRF alone were insufficient to distinguish and classify these layers and to link them to a specific triggering mechanism. This is probably due to the multiple provenances of sediment particles in the deep basin of Lake Iseo. Only a thorough knowledge of the functioning of the sedimentation in the lake, associated with a multiproxy approach, can help to disentangle the different origins of the sediment in event layers and allows the interpretation of their triggering mechanisms. To do so, we had to identify the potential source areas and transport mechanisms of each event layer.

5.2.1. Locating potential source areas

We assumed there could be only two potential sources of sediment making the event layers: (i) detrital sediment from the Oglio river and/or delta and (ii) sediment from lake slopes overhanging SEB18 coring site (lateral sources). To distinguish those source areas, we had to consider together the chemical composition and the thickness of event layers.

Indeed, whereas deltas are obvious sources of event layers, through stream flood and delta collapse, any sediment accumulation overhanging SEB18 coring site could potentially slide down to the lake bottom, if it is thick enough. A thick accumulation may not occur on slopes > 30° in the absence of progradation process. Moreover, in the absence of major terrigenous input such accumulation should be made of in-lake produced biogenic compounds. If such a source exists it hence requires to present slope < 30° and be favourable for biogenic matter accumulation, which in hard-water lakes is mainly made of calcite (e.g. Giguet-Covex et al., 2011; Groleau et al., 2000; Küchler-Krischun and Kleiner, 1990). However, it has been shown that the preservation of biogenic calcite in lakes drastically decreases with depth, depending on carbonate particle size (Ramisch et al., 1999). In the case of Lake Iseo, water chemistry indicates the reach of a steady state in $[Ca^{2+}]$ around 100 m (Fig. V-5), suggesting that below this depth, most of the biogenic calcites settling from the surface has been dissolved. One may thus assume that, if lateral sources of event layers exist, they should be located on < 30° and < 100 m deep slopes overhanging SEB18. Fig. V-5-C&D show the distribution of such areas.

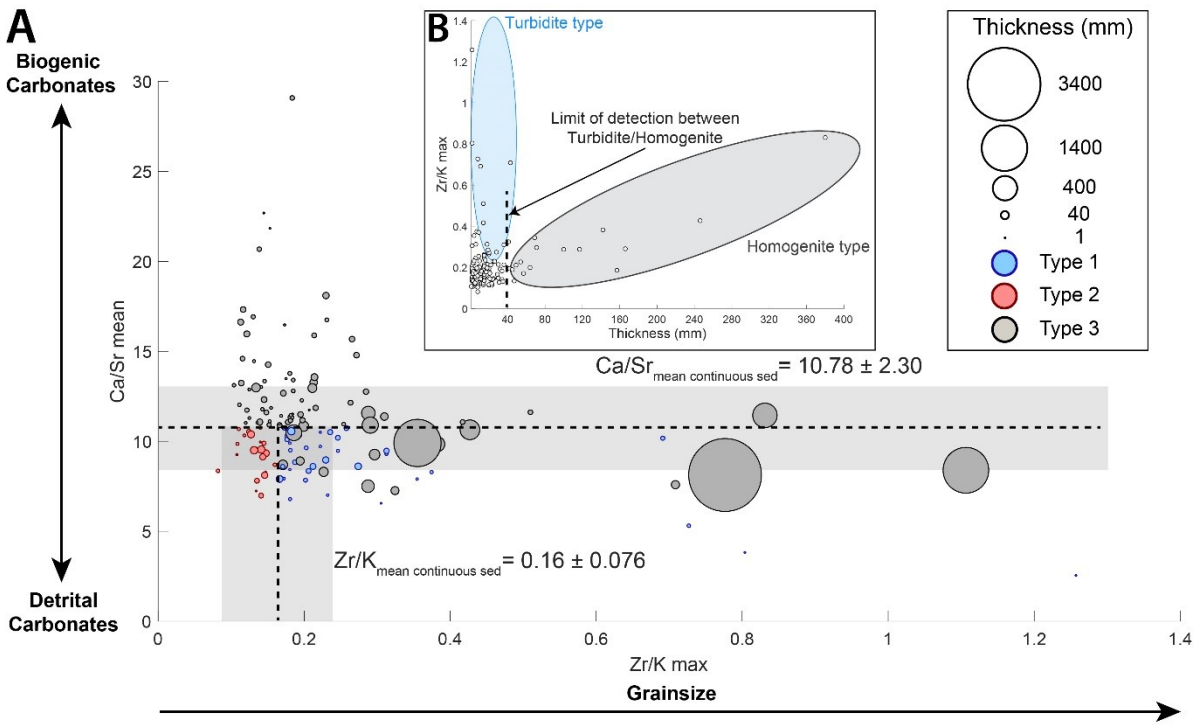

Fig. V-6- (A) Scatter plot of Ca/Srmean versus Zr/Kmax with the thickness indicate by dot sizes of each event layers. (B) Scatter plot of Zr/Kmax values versus the thickness of each event layers.

5.2.2. *Chemical distinction between sediments coming from the delta and from lateral sources*

Distinguishing those sources basically consists in distinguishing biogenic vs. detrital dominant source of carbonate. Given that lacustrine waters are depleted in strontium relatively to seawaters (e.g. Brown and Severin, 2009 and references therein; Faure et al., 1967), lacustrine biogenic carbonates generally present a Ca/Sr ratio higher than marine carbonates that partly constitute the lake watershed geologic basement (Faure et al., 1967). Hence, the Ca/Sr ratio can be used to distinguish sediment with dominant detrital inputs (lower Ca/Sr value) from sediment more influenced by in-lake biogenic carbonate precipitation (higher Ca/Sr value). As the continuous sedimentation is composed by no or very few biogenic carbonates, due to carbonate dissolution in the water column (Fig. V-5), the mean Ca/Sr value of an event layer (Ca/Sr_{mean}) with a detrital origin is supposed to be equal or lower than the mean Ca/Sr value of the continuous sedimentation (Ca/Sr_{consed}). On the contrary, event layers with a $Ca/Sr_{mean} > Ca/Sr_{consed}$ are interpreted as relatively enriched in lacustrine biogenic carbonate and thus deriving from lateral sources (Fig. V-6-A).

5.2.3. *Distinguishing flood- and mass wasting- deposits originating from the delta*

If we can distinguish lateral from detrital (Oglio delta origin) sediment sources, it remains uncertain whether a detrital event layer was triggered by a flood or by a collapse of the Oglio delta. Due to the distal position of SEB18 relative to the Oglio delta, only massive delta collapse-triggered deposits or extreme flood-triggered underflows which may run over long distance on the bottom of the lake may reach the coring site. The relationship between the maximum grain-size and the thickness of event layers may here be useful to discriminate the transport processes leading to the deposition of these layers (Fig. V-6-B, Wilhelm et al., 2013). MWD are generally more

sediment-loaded than flood-triggered underflows (Fanetti et al., 2008; Wilhelm et al., 2013). Consequently, the grain-size in MWD is lower than those of underflow deposits due to a more important dilution of coarse particles by the clayey matrix that supports the sediment transport. Hence, we may assume that, for a given grain-size, a MWD will be much thicker than a flood-triggered deposit (Wilhelm et al., 2013).

To represent potential variations in grain-size within the 146 event layers, we used the maximum value of Zr/K ratio, a chemical proxy of grain-size (e.g. Cuven et al., 2011; Rapuc et al., 2019; Sabatier et al., 2017; Wilhelm et al., 2013). Indeed, in lake sediments, Zr is interpreted as a proxy of heavy minerals, while K is linked to fine-grained particles such as clay (Cuven et al., 2010; Kylander et al., 2011). Layers presenting Zr/Kmax values lower than the mean continuous sedimentation value were separated from the other detrital layers and their transport processes were not interpreted. A hierarchical clustering on principal components (HCPC) was conducted and allows to distinguish two groups of event layers depending on their thickness and Zr/K_{max} values (Supplementary Data 2; Fig. V-6-B). The first cluster presents layers with the highest Zr/K_{max} values (Fig. V-6-B). These layers are interpreted as composed of coarse grains with a low volume of transported sediment, which requires strong water currents such as turbiditic currents during floods and resulting underflows (Sturm and Matter, 1978). Event layers linked to a MWD are not linked to water flow and thus are supposed to present on average, a lower grain-size for a similar thickness (Fig. V-6-B; Wilhelm et al., 2013). We hence interpret layers from the second cluster as homogenite-type deposits linked to MWD from slopes or deltas.

5.2.4. Attributing triggering mechanism to event layers

The combination of Ca/Sr_{mean} as a proxy of the sediments source, with Zr/K_{max} and the thickness of each event layer as proxies of transport processes, allows to distinguish and interpret the origin among the three different types of layers (Fig. V-6). Type 1 regroups thin layers (< 40 mm) presenting a high Zr/K_{max} and a low Ca/Sr_{mean} values (Fig. V-6). These layers are interpreted as composed of detrital sediment transported by an underflow. Underflows that reach the deep basin of Lake Iseo can only be linked to extreme flood events from the Oglio river or from the small hillslopes' tributaries. Forty flood layers were hence counted and represent a total thickness of 42 cm. Twenty-one layers, accounting for a thickness of 28 cm present low Zr/K_{max} and low Ca/Sr values, reflecting thin detrital layers or inputs depleted in biogenic carbonates. These layers, labelled as Type 2 layers, are not interpreted because they can be linked either to floods from small tributaries associated with a weak current that does not transport coarse grains or to MWDs from slopes depleted in biogenic carbonates, namely, located in the hypolimnion (below 100 m b.l.s.) where biogenic production is poorly preserved due to low oxygen concentration and pH (Fig. V-5). Type 3 regroups (i) layers presenting high Ca/Sr_{mean} and low Zr/K_{max} values that are composed of sediment enriched in biogenic carbonates coming from smooth slopes above 100 m b.l.s around the core site (Fig. V-5-D) and (ii) thick layers (> 40 mm) composed of detrital materials (low Ca/Sr) that originates from the Oglio delta or smaller tributaries deltas. The relationship between the thickness and the Zr/K_{max} of this last group corresponds to a slide or slump-like transport (Fig. V-6-B). Type 3 layers regroup the three thickest deposits and all layers composed of sediment previously deposited in the lake and remobilized after seismic shaking or sediment overloading. Eighty-five layers linked to such process were counted and represent 8.81 m of sediment in the SEB18 sequence. Fifteen layers originate from the Oglio delta, and the other 69 layers, enriched in biogenic carbonate, probably originate from lateral slopes. This result

suggests that Lake Iseo sediment accumulation is a good candidate to have recorded seismic activity.

To strengthen the interpretation of event layer triggering mechanisms, we compare the ages of several events with the Italian historical seismic catalogue (CPTI15, Rovida et al., 2020, 2019) and local documented flood events (Guzzetti and Tonelli, 2004; Luino et al., 2002). The three thickest Type 3 layers (EL1, EL2 and EL3) originate from the Oglio delta which is several kilometres long and is the principal source that can produce 1.3 to 3.4 m thick detrital layers. Altogether, those 3 events moved a total of ~ 100 km^3 to the lake basin. EL1 (11 km^3), is dated between 1120 and 1220 CE; considering ^{14}C dating uncertainties, it can be correlated to the 1222 CE earthquake that caused heavy damage in the Brescia area (less than 30 km distance from the lake). Despite the fact that the earthquake source cannot be precisely identified from both geological surveys (e.g. Livio et al., 2009) and macroseismic data (Guidoboni et al., 2005); the earthquake parameters are largely imprecise (see a comparison of epicentral location, and derived magnitude at https://emidius.mi.ingv.it/ASMI/event/12221225_1230_000), the historical chronicle refer to repeated events, and damages that are compatible with low frequency, long duration shakings. This seismic event had moreover been identified yet in another Lake Iseo sub-basin (SEB05 & 06 sequences; Lauterbach et al., 2012) and in Lake Como (Fig. V-1, Fanetti et al., 2008) where it has been associated to a ~ 3 km3 megaturbidite deposit. The thickest Type 3 layer, EL2, is dated between 1020 and 1125 CE and can be attributed to the 1117 CE earthquake: this event is one of the strongest and most damaging historical earthquakes documented in northern Italy (Galadini et al., 2001; Gasperini et al., 2004). It occurred probably South of Verona (about 80 km distance, south-eastward of Lake Iseo) with damage of intensity VII MCS both in Brescia and Milan; the expected shakings in the lake area should have been therefore similar to the one caused by the 1222 earthquake. Alternatively, this layer could be attributed to the 1065 CE Brescia earthquake, for which only two macroseismic observations (Brescia, VIII; Milan, Felt) are available, and the level of ground motion at Lake Iseo is highly speculative. The continuous sedimentation intercalated between these two thick event layers represents around 93 years, which, considering that the base of EL2 is erosive, almost corresponds to the time gap between the two historical seismic events. The oldest thick Type 3 layer, EL3, is dated between 640 and 830 CE. For this event there is no earthquake in the Italian historical macroseismic archive (https://emidius.mi.ingv.it/ASMI/) that could reasonably be associated to the layer, but it is known that in Middle Ages the database is incomplete, also for major events. The nearest earthquake in time and space is the one referred to Treviso in 778 CE, but the expected ground motion at Lake Iseo due to this earthquake, cannot be responsible for massive slope instabilities. Another megaturbidite that led to a ~ 10.5 km^3 sediment deposit resulting from large MWD from steep slopes was recorded in Lake Como (Fanetti et al., 2008) and might coincide with another megaturbidite deposit in Lake Sils dated at ~ 700 CE (Blass et al., 2005).

Concerning Type 1 layers, some of the most recent layers present the same ages as local and regional historical flood events such as the 1991, 1960, 1952 floods that impacted the city of Darfo Boario Terme (Luino et al., 2002) or the 1994 regional flood event that impacted the Po Plain (Guzzetti and Tonelli, 2004).

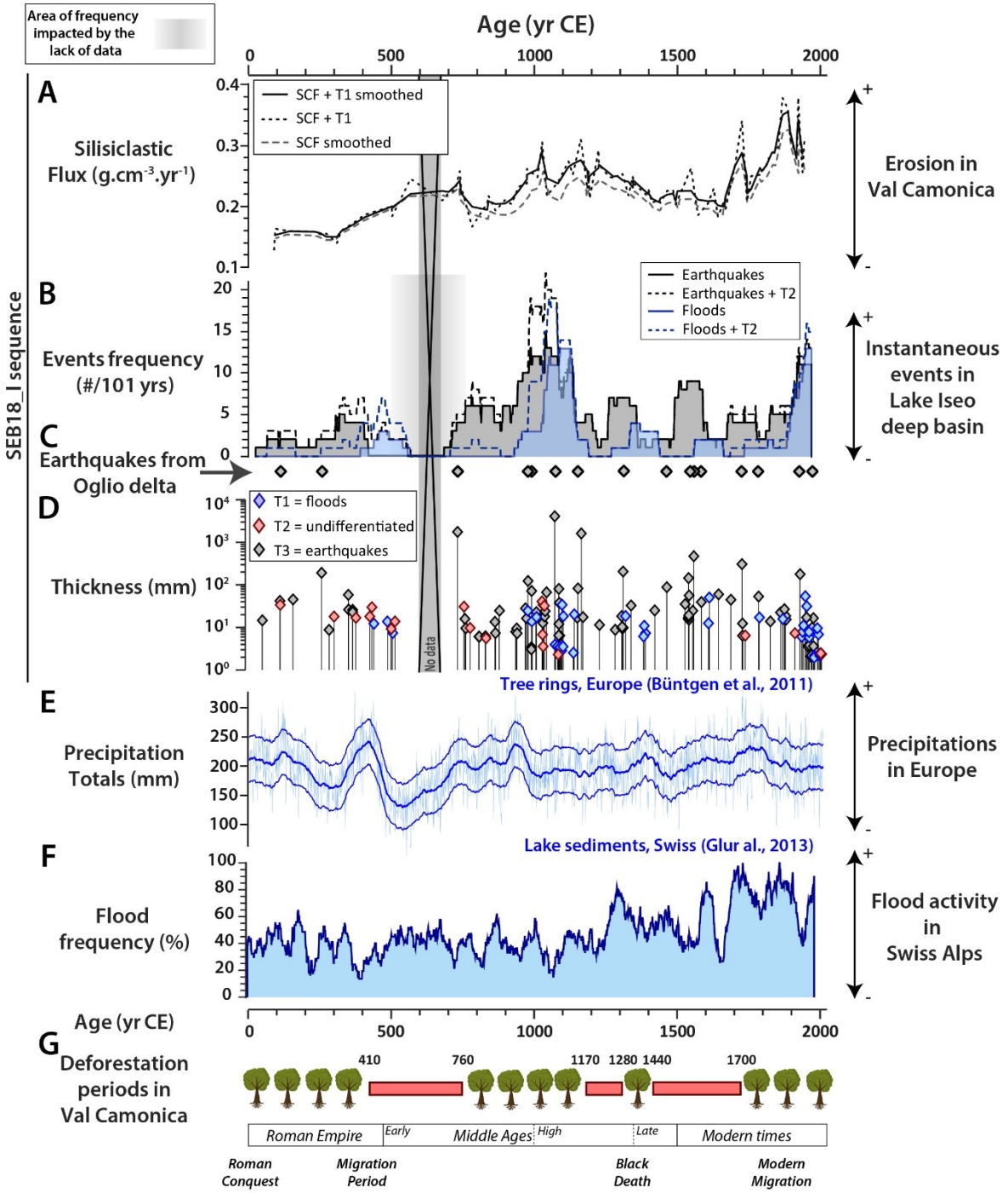

Fig. V-7- Comparison of the main results obtained from SEB18 sediment sequence and regional climatic and human information plotted against the age. (A) SEB18 SCF. (B) SEB18 flood and earthquake frequency obtained from Type 1 and Type 3 layer's ages, respectively, Type 1 and 2, and Type 3 and 2 sums are plotted in dotted lines. (C) Type 3 layers with a detrital composition. (D) Thickness of each kind of layers. The area of frequency impacted by the lack of data is represented in grey shadings. (E) reconstructed AMJ precipitation totals modified from Büntgen et al. (2011). (F) 50-year moving average of flood events from Swiss lakes, modified from Glur et al. (2013). (G) Periods of deforestation in the Val Camonica deduced from Marziani and Citterio, (1999), Pini, (2002) and Pini et al. (2016).

5.3. Link between sediment inputs and the frequency of sediment remobilization

The siliciclastic flux (SCF; g.cm−2.yr−1) was calculated to characterize the evolution of erosion processes in Lake Iseo catchment (Fig. V-7-A). SCF was computed as the product of the % of NCIR by the sedimentation rate and by the sediment DBD (Rapuc et al., 2019). To avoid spikes the density was smoothed using a weighted arithmetic mean corresponding to: $x = DBDx_{n-1} \times 0.25 + xDBD_n \times 0.5 + DBDx_{n+1} \times 0.25$ with x standing for density values at depth n. The SCF could be interpreted as the evolution of total terrigenous flux in the deep basin of Lake Iseo and used as a proxy of erosion (Bajard et al., 2017). However, Type 1 layers were interpreted as flood events and correspond to detrital input from the watershed. We computed another SCF, SCF*, using the sedimentation rate calculated by adding flood layers thicknesses as suggested by Bajard et al. (2020). SCF* presents a general increase of about 50% between the early Common Era and 750 CE. Two other periods of enhanced erosion in the watershed are registered between 950 and 1350 CE and from 1650 CE to the present. The frequency of Type 1 & 3 layers, interpreted as linked to flood and earthquakes events, respectively, are presented as variation of the number of events per 101 years (Fig. V-7-C&D). Interpretation of fluctuations of these frequencies between 580 and 670 CE should be taken with caution due to a gap in the sediment section.

5.3.1. Flood and sediment availability

The flood frequency recorded during the Roman Period differs from the local and regional trends: several studies attested evidence of increase flood occurrences at that time (e.g. Glur et al., 2013; Rossato et al., 2015; Vannière et al., 2013; Wirth et al., 2013b) but no increase is detected in the Lake Iseo deep basin until approximately 950 CE. This increase led to high frequency between 950 and 1150 CE which are in good agreement with periods of high flood frequencies recorded in river sediments of north-eastern Italy (Rossato et al., 2015) and in Lake Ledro (Vannière et al., 2013; Wirth et al., 2013a). Yet, these high frequencies are disconnected from the trend observed in the Swiss Alps (Fig. V-7; Glur et al., 2013). There is also no increase recorded in the Iseo deep basin during the Little Ice Age (LIA) when all the local and regional studies record an important flood activity due to a colder and wetter climate (Glur et al., 2013; Vannière et al., 2013; Wirth et al., 2013a, 2013b). During the last century, a sharp increase is recorded, starting at ~1890 CE (Fig. V-7), which seems to be in agreement with the observed frequency in the Swiss Alps (Fig. V-7; Glur et al., 2013) but differ from the regional trend (Wirth et al., 2013a, 2013b).

The flood frequency recorded in the deep basin of Lake Iseo does not directly follow regional climate fluctuations. Periods of high flood frequency occur during time of high SCF values, that are representative of erosion in the Val Camonica and then, of the sediment available to be remobilized by a precipitation event in the watershed. The highest flood frequency recorded occurred together with the occurrence of the two biggest historical earthquakes that impacted the Val Camonica (i.e., 1117 CE and 1222 CE). Those earthquakes might have favoured sediment availability in the watershed, leading to an increase of sediment remobilization by precipitation and thus turbidites recorded in lake sediments. Such a phenomenon has already been reported elsewhere, for instance in the New-Zealand Southern Alps (Howarth et al., 2012; Wang et al., 2020).

5.3.2. *Earthquakes and sediment availability*

The earthquake frequency recorded in Lake Iseo deep basin starts to increase at 750 CE to reach high values (12 per 101 years) between 950 and 1150 CE. High frequencies are also recorded during 1250 – 1350, 1500 – 1600 CE periods and from 1850 CE to the present. Here we observed that the frequency of recorded earthquakes is high during or just after a long period of sediment accumulation in the lake (Fig. V-7-A) and decreases sharply after the remobilization of a large volume of sediment from slopes or the delta (Fig. V-7-C). Indeed, after the occurrence of the three thickest layers, linked to ~778, 1117 and 1222 CE earthquake events, no deposits from the Oglio delta are recorded for a long period, leading to an apparent decrease in the earthquake frequency.

Moreover, from the seismic profiles (Fig. V-1-C & D) and previous seismic survey conducted on Lake Iseo deep basin (Bini et al., 2007), no important MWDs seems to occur underneath the bottom of the SEB18 sediment sequence (21 CE). In the sediment succession of Sale Marasino Basin, the only thick deposits linked to seismic activity occurred within the last 2500 years (Lauterbach et al., 2012). A possible explanation could be the progressive increase of erosion in the watershed from the Neolithic, reaching high levels during the Roman Period, as attested by previous works in Lake Iseo (Lauterbach et al., 2012; Rapuc et al., 2019) and regionally (e.g. Andrič et al., 2020; Giguet-Covex et al., 2011; Joannin et al., 2014; Vannière et al., 2013). Indeed, when long term erosion increases, the accumulation of sediment on lake slopes and delta increases, leading to high sediment availability to earthquake induced remobilization and thus the sensitivity of the lake to record earthquake change (Gastineau et al., 2021; Rapuc et al., 2018; Wilhelm et al., 2016a).

It has been established on faults in Central Italy, especially in the Apennine, that periods of high seismic activities last several hundred years and are spaced by long quiescence periods (e.g. Benedetti et al., 2013; Verdecchia et al., 2018). The link between high earthquake frequency periods registered in Lake Iseo and sediment availability is then reinforced by the absence of short-term seismic variability evidence in the Italian regions that could have been at the origin of the here recorded frequency evolution.

5.4. Linking human-influence and sediment supply

At the beginning of the Roman Period the SCF* in the deep basin of Lake Iseo is high (0.15 $g.cm^{-3}.yr^{-1}$) compared to what have been measured in other peri-Alpine lakes (Arnaud and Révillon, 2015), suggesting that erosion in the Val Camonica is already important and increases until 750 CE (Fig. V-7). From the Iron Age, a high number of rock carvings and several Camuni cities are identified in the southern part of the watershed, indicating that the Camuni society was well developed (Anati, 2009; Anati and Cittadini, 1994; Casini and De Marinis, 2009). Several palynological records indicate that agricultural activities first start around 4 kyrs BP in the Val Camonica, associated with human-induced deforestation and fire activity in the southern-Alps (Comiti, 2012; Gobet et al., 2000; Iglesias et al., 2019) and mid-altitude pastoralism from 3 kyrs BP (Pini, 2002; Pini et al., 2016). All of these evidences, associated with previous studies on lake sediment in the southern and Julian Alps (Andrič et al., 2020; Joannin et al., 2014; Rapuc et al., 2019, 2018), suggest that human activities already impact the erosion and sediment transport processes in the main watersheds of the southern Alps before the Roman Period.

The first period of erosion increase recorded on the SEB18 sequence (Fig. V-7-A) starts during the Roman Period. This period is characterized by an increase in agricultural activities in the Val Camonica (Pini, 2002), a population rise in the southern Alps and northern Italy (Cascio and Malanima, 2005; Comiti, 2012) and intense pastoralism practices (Carrer, 2015). From the fall of the Western Roman Empire to the middle of the Early Middle Age (400 – 750 CE) the abandonment of forest management plans in northern Italy (Comiti, 2012), the ore-extraction increase (Marziani and Citterio, 1999; Pini et al., 2016) and pastoral activities increase in the Val Camonica (Allevato et al., 2013; Gehrig, 1997; Pini, 2002; Pini et al., 2016) conducted to an increase of both deforestation and land-use in high-Alpine valleys, directly enhancing the erosion (Fig. V-7-A). The climate is first warm and dry during the Roman Period, then precipitation rise and temperatures decrease in the Alps during the Migration Period (300 – 500 CE), before to more warm and dry conditions during the Early Middle Ages (Büntgen et al., 2016, 2011). Even if the SCF* start to rise during the setting of wetter and colder climate (Fig. V-7), climatic fluctuations and erosion in the Val Camonica are decorrelated over the rest of this period. As erosion is supposed to rise during wetter periods (Nearing et al., 2005), climate fluctuation only cannot explain the erosion trend recorded in Lake Iseo until the Early Middle Ages.

The second period of intense erosion is spanned from the High to the Late Middle Ages (950 – 1350 CE). This period presents strong societies developments in Europe, associated with economic and agricultural growths (Büntgen et al., 2011). From 900 CE, the population in Italy starts to increase until the great Plague (Cascio and Malanima, 2005). In the southern Alps, several studies reported an increase of land use between 800 and 1300 CE (Joannin et al., 2014; Paladin et al., 2020; Ravazzi et al., 2013) associated with agricultural activities development in the Val Camonica (Pini, 2002) and the replacement of pre-existing structures from 900 CE in the whole Europe (Büntgen et al., 2011). Altogether, these societal developments are at the origin of a period of intense deforestation between 800 and 1400 CE visible in Europe (Büntgen et al., 2011), South to Lake Garda (Ravazzi et al., 2013) and also in the watershed of Lake Iseo between 1170 and 1280 CE (Fig. V-7; Gehrig, 1997; Marziani & Citterio, 1999; Pini, 2002; Pini et al., 2016). In Europe, precipitation amount increases until 950 CE accompanied by a warmer climate from 800 to 1250 CE (Büntgen et al., 2011), known as the Medieval Warm Period. The climatic influence on the erosion processes in Lake Iseo watershed cannot be excluded, however, few floods are recorded in southern Alps at that time (Fig. V-8; Glur et al., 2013; Wirth et al., 2013b, 2013a) making climatic impact on sediment transport during the Early and High Middle Ages less predominant.

Between 1347 and 1351 CE, the Great Plague impacted all of Europe, causing the death of almost half of the population (Büntgen et al., 2011). This event led to a sharp decrease of the population in Italy (Cascio and Malanima, 2005). An important abandonment of agricultural practices appears at that time and led to partial reforestations (Joannin et al., 2014). This increased the stability of the hillslopes in the southern Alps, reducing the sediment mobilization by the rivers. There is no evidence of a decrease of the precipitation amount (Büntgen et al., 2011) that might explain the reduction of erosion at that time (Fig. V-7).

The third period of intense erosion starts at 1650 CE with a first SCF peak at around 1730 CE and last until the present days. This increase appears during the Little Ice Age, when conditions are colder and wetter throughout the Alps (Büntgen et al., 2016, 2011). After 1440 CE, a new period

of intense deforestation for ore extraction is recorded in Val Camonica (Marziani and Citterio, 1999) that lasted until ~1700 CE. This deforestation is also visible across Europe and linked more generally to a recovery of human activities and land use after the Great Plague (Büntgen et al., 2011). After 1500 CE and until the end of the LIA, the precipitation amount across Europe and in the Alps increases simultaneously with a decrease of the temperature. This led to a natural reforestation in uninhabited areas (e.g. Joannin et al., 2014). However, in the southern Alps, the hillslopes instability increases due to climate-induced glaciers advances during the LIA (Le Roy et al., 2015) associated with human exploitation of the forest (Fouinat et al., 2018), leading to an increase of erosion in Alpine watersheds and channel aggradation in the Po plain between 1600 and 1800 CE (Comiti, 2012). Until 1688 CE, there was no plan of forest management in the Italian Alps that could have prevent erosion (Comiti, 2012). The recovery of human activities in the southern Alps associated with higher precipitation rates during the LIA are probably at the origin of the increase of detrital input in Lake Iseo from 1650 CE (Fig. V-7).

The highest erosion recorded in the deep basin of Lake Iseo is reached at 1880 CE and corresponds to the end of the LIA. The remobilization of the sediment derived from glaciers advances and post-LIA hillslopes destabilisation associated to low forest covers with the most intense period of land-use can explain the recent erosion in Val Camonica (Comiti, 2012).

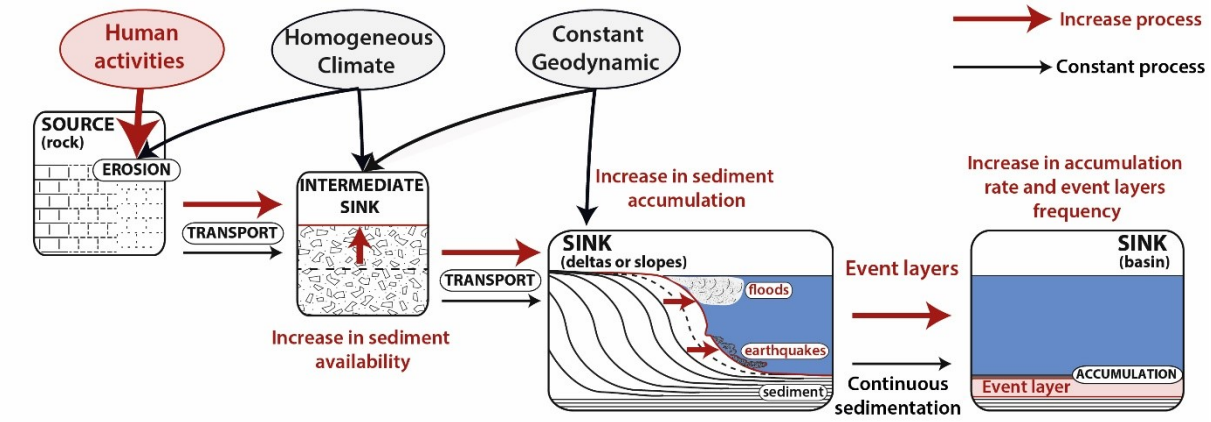

Fig. V-8- Conceptual model of the erosion cycle in a large catchment and the effects of the three main forcing factors (human activities, climate and geodynamic).

5.5. Human influence on erosion and transport processes

The comparison between the sedimentary processes that occurred in Lake Iseo deep basin and the knowledge of geodynamic, climate and human activities throughout the last 2000 years in the Italian southern Alps helped to understand the drivers of the local erosion. It appears that from the Roman Period, human activities by increasing agricultural activities, grazing and deforestations have induced a general increase in sediment input towards depositional sinks (Fig. V-8). After a delay due to transport processes and sediment storage in the watershed, the increased amount of sediment brought to intermediate sinks is stocked on lake deltas and slopes. This abnormal sediment accumulation led to an increase of the sedimentation rate in the deep basin and, after periods of high sediment input, cause an increase of destabilisation of slopes or delta due to seismic shaking or sediment overloading (Gastineau et al., 2021; Rapuc et al., 2018; Wilhelm et al., 2016a). Equally, due to increase sediment availability in lake catchment, the sediment load during a flood event increase, leading to an increase of flood frequency recorded in lake

sediments independent of climate fluctuations (Fig. V-8) as previously observed in other lake systems (e.g. Brisset et al., 2017; Giguet-Covex et al., 2012; Howarth et al., 2012). Then, even in large lake catchments, human activities through deforestation, pastoralism, and agriculture, affect the erosion processes and the resulting sediment transport and remobilization. The increase of sediment availability by human activity causes a disconnection between the recorded instantaneous event frequency from the occurrence of their geodynamic or climatic triggers, and thus impacts the sensitivity of a lake as a natural archive to record the earth-surface processes.

6. Conclusion

In a large and deep lake, like Iseo, the sediment may originate from several different sources which makes difficult to disentangle the processes that triggered the deposit of event layers. The use of XRF ratios, namely Ca/Sr ratio as a proxy of in-lake sediment sources, and Zr/K ratio associated with the thickness of each layer as proxies of transport processes allowed us to attribute most of them to flood or mass wasting events. Considering the evolution of the terrigenous input, we showed that the apparent frequency of earthquakes recorded in Lake Iseo deep basin is influenced by the sediment available to be remobilized, which in turn depends on the erosion rate within the catchment area. Human practices and, to a lesser extent, climate fluctuations have impacted the available sediment within both the lake slopes and the catchment areas and thus the recording of extreme geodynamic and climatic events. Even in large catchment areas, human activities can play a key role on erosion processes and sediment availability which may affect the recording of the earth-surface processes. Hence, discussing instant events frequency recorded in sediments from deep lakes should only be done after a thorough study of the human activity in the watershed.

Acknowledgements

This work was conducted in the framework of the CRITLAKE project funded by the AAP Université Savoie Mont Blanc in 2018 and thanks to the support of the entire staff of the C2FN-DT-INSU associated to the CLIMCORE project. Thanks to Qi Lin for his support and great help on the coring survey. Thanks to the Associazione Nazionale dei Carabinieri (Cesare Miniaci, Michele Liso, and colleagues) for the assistance on the lake, the use of their boat for the seismic survey and the anchoring of the platform. 14C analyses were acquired thanks to the CNRS-INSU ARTEMIS national radiocarbon AMS measurement programme at Laboratoire de Mesure 14C (LMC14) in the CEA Institute at Saclay (French Atomic Energy Commission). The authors would also like to thank the Laboratoire Souterrain de Modane facilities for the gamma spectrometry measurements. Thanks to Kim Genuite for the valuable help with GIS processing and the creation of the maps. Thanks to Lucilla Benedetti, Roberta Pini, Giulia Valerio and Marco Pilotti for their helpful advices. Thanks to Christian Crouzet for his help in the understanding of transport processes at the origin of the main layers.

The data that support the findings of this study are available from the corresponding author upon reasonable request.

Supplementary Data 1

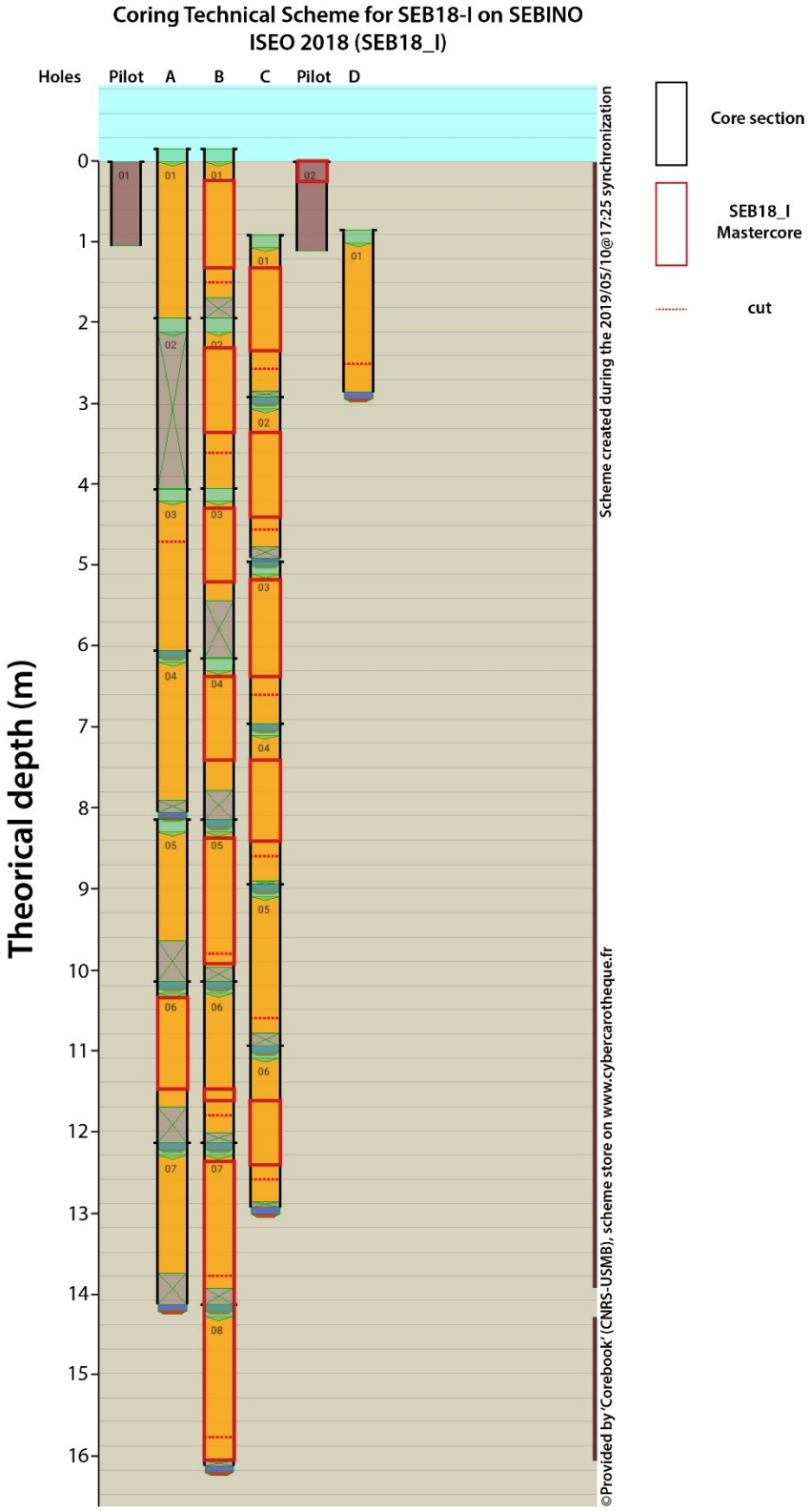

Supplementary Figure 1 – Coring technical scheme for SEB18_I sediment section. All cores retrieved from the deep basin during the SEB18_I coring survey are represented against a theorical depth (m). SEB18_I theorical sediment section is represented in red

Supplementary Data 2

To distinguish layers presenting Ca/Sr_{mean} values lower than the value of the continuous sedimentation and Zr/K_{max} values higher than the value of the continuous sedimentation in Lake Iseo we used a hierarchical clustering on principal components obtained from a PCA. Six clusters were chosen to best divide layers. Clusters 2, 4 and 6 vary following the thicknesses variations and Cluster 1, 3 and 5 fluctuate depending on Zr/K_{max} signal. As stated by Wilhelm et al. (2013), turbidite-type deposits, generally linked to flood events, present higher grain-size values (here represented by Zr/Kmax) for a same thickness compare to homogenite-type deposits. Then we decided to regroup the clusters following Zr/K_{max} signal variation together and to interpret them as turbidite-type deposits. Similarly, clusters following thickness signal variation were regrouped and interpreted as homogenite-type deposits.

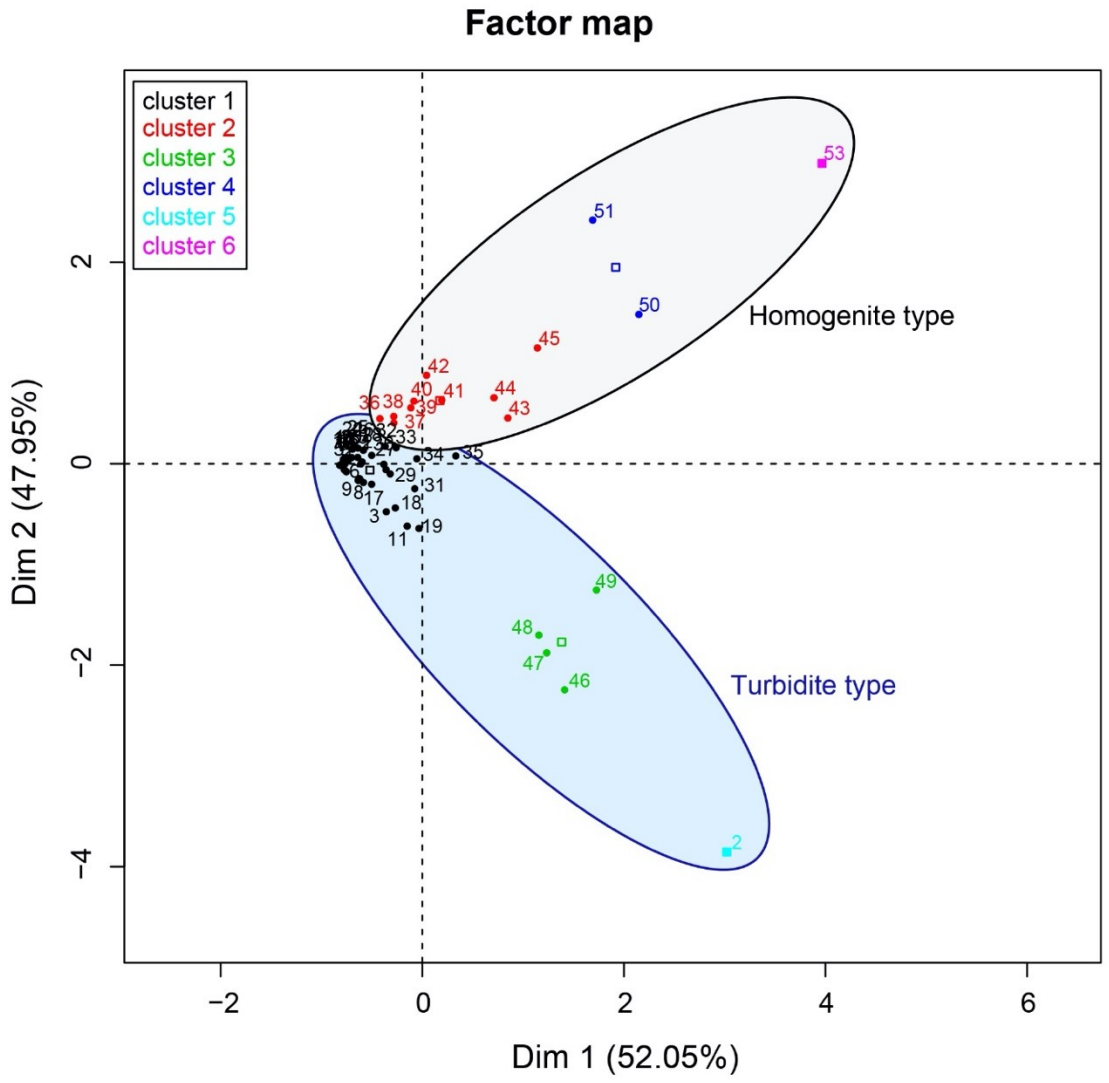

Supplementary Figure 2 – Factor map from a hierarchical clustering on principal component analysis (HCPC) realized on the layers presenting a detrital composition (low Ca/Sr_{mean} values) and Zr/K_{max} values higher than the values of the continuous sedimentation.

Supplementary Table 2 – Age, depth, thickness, Zr/K_{max}, Ca/Sr_{mean} values and associated cluster from the HCPC for layers

Age (yr CE)	Depth (cm)	Thickness (mm)	Zr/K max	Ca/Sr mean	Cluster	Types
2001	8,7	2	0,80	3,82	3	1
1999	9,8	2	1,26	2,54	5	1
1994	12,6	6	0,18	6,79	1	1
1991	15,2	8	0,73	5,30	3	1
1981	20,6	2	0,18	10,29	1	1
1979	21,4	2	0,19	10,27	1	1
1962	35,2	6	0,25	9,47	1	1
1962	34,4	8	0,18	9,50	1	1
1953	42,75	25	0,23	8,96	1	1
1948	51,65	11	0,69	10,17	3	1
1948	48,95	43	0,71	7,59	3	1
1940	56,25	7	0,37	8,29	1	1
1936	59,15	5	0,17	7,93	1	1
1930	69,5	142	0,38	9,84	4	3
1869	113,35	15	0,25	10,20	1	1
1788	152,4	14	0,19	8,84	1	1
1785	156,4	42	0,19	8,91	2	3
1727	193,8	246	0,43	10,64	6	3
1613	252,15	41	0,32	7,26	1	1
1610	255,6	10	0,19	10,72	1	1
1585	265	32	0,19	10,37	2	3
1542	321,05	45	0,19	10,34	2	3
1528	345,55	29	0,17	7,91	2	3
1464	368,75	71	0,30	9,26	2	3
1389	396,7	6	0,31	9,30	1	1
1385	398,55	9	0,20	9,63	1	1
1383	399,75	5	0,18	10,27	1	1
1320	422,45	15	0,21	8,35	1	1
1153	633,25	69	0,34	10,24	2	3
1140	642,6	18	0,31	9,47	1	1
1137	644,6	2	0,31	6,56	1	1
1102	655,55	15	0,26	10,73	1	1
1097	659	28	0,27	8,61	1	1
1095	661,2	4	0,35	7,90	1	1
1094	662,25	3	0,22	10,50	1	1
1094	661,8	4	0,22	9,71	1	1
1084	677,3	2	0,18	10,64	1	1
1084	677,1	2	0,19	10,44	1	1
1083	678,4	4	0,18	9,90	1	1
1083	677,7	4	0,18	10,30	1	1
1082	678,75	3	0,18	8,43	1	1
1074	681,5	4	0,23	7,01	1	1
1043	1030,8	54	0,23	8,30	2	3
1006	1064,5	16	0,24	10,51	1	1
993	1069,55	13	0,18	10,10	1	1
991	1073,75	57	0,17	8,69	2	3
979	1081,3	22	0,21	8,60	1	1
978	1087,8	100	0,29	7,51	2	3
504	1391,7	6	0,17	10,72	1	1
487	1398,25	11	0,17	8,59	1	1
439	1412	10	0,20	7,84	1	1
256	1481,85	157	0,19	10,47	4	3
111	1526,1	34	0,18	10,56	2	3

CHAPITRE VI | Sédimentation instantanée dans le lac du Bourget et chronique des paléo-crues du Rhône

1. Objectif et synthèse du travail réalisé

Le lac du Bourget est le second lac périalpin étudié dans ce projet de thèse. De nombreuses études se sont déjà intéressées aux processus sédimentaires à l'œuvre dans le lac (Arnaud, 2005; Arnaud et al., 2005; Chapron et al., 2005; Debret et al., 2010; Evin et al., 2019; Giguet-Covex et al., 2010; Jenny et al., 2014b; Ledoux et al., 2010). Comme exposé dans le chapitre II, la sédimentation dans le lac du Bourget n'est pas classique : le Rhône est le principal affluent du lac en terme d'apports sédimentaires, mais il ne pénètre dans le lac que lorsqu'il est en crue (Arnaud et al., 2012).

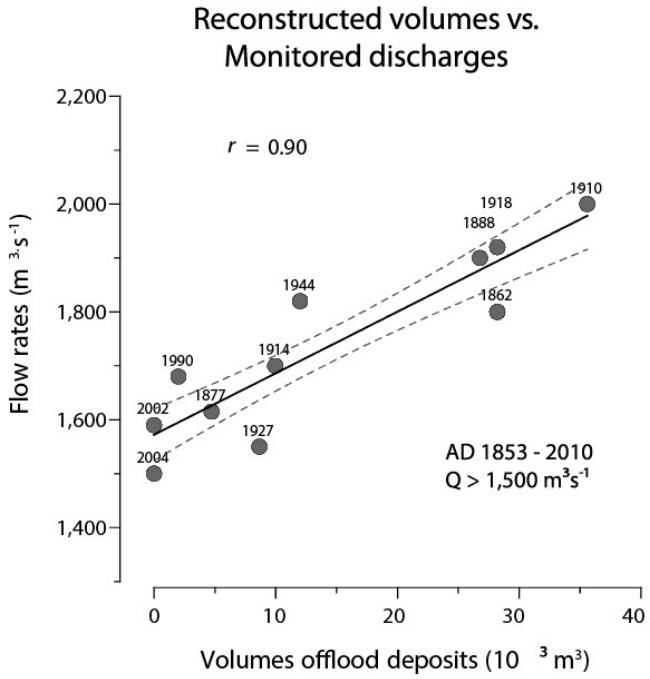

Fig. VI-1- Graphique de corrélation entre les volumes des événements de crues reconstituées dans les sédiments du lac du Bourget et les débits obtenus à partir de données instrumentales. Une relation positive et linéaire est observable (r = 0,90 ; p = 0,000). Figure tirée de Jenny et al. (2014b).

Parmi les études précédentes, Jenny et al. (2014b) ont développé avec succès une méthodologie permettant de documenter les occurrences et les magnitudes des paléo-crues du Rhône à partir des sédiments du lac du Bourget. La méthode repose sur une approche basée sur des transects de séquences sédimentaires prenant en compte la variabilité dans le temps et dans l'espace de la dispersion et du dépôt des sédiments lors des crues. Cela a permis de reconstituer une chronique continue des occurrences de crue du Rhône supérieures à 1500 $m^3.s^{-1}$ au cours des 350 dernières années, ainsi que d'estimer l'ampleur des crues à partir des volumes de sédiments déposés lors de ces événements (Fig. VI-1; Evin et al., 2019; Jenny et al., 2014b).

Toutefois, la période couverte par ces données ne permet pas d'interroger les effets des forçages climatiques et humains sur la fréquence et la magnitude des événements de crues du Rhône. Pour obtenir un enregistrement de paléo-crues du Rhône s'étendant jusqu'au dernier millénaire, dix carottes de 3 mètres de long ont été prélevées au printemps 2017 sur des sites que Jenny et al. (2014b) avaient identifiés comme les plus pertinentes pour documenter les crues passées (Fig. VI-2).

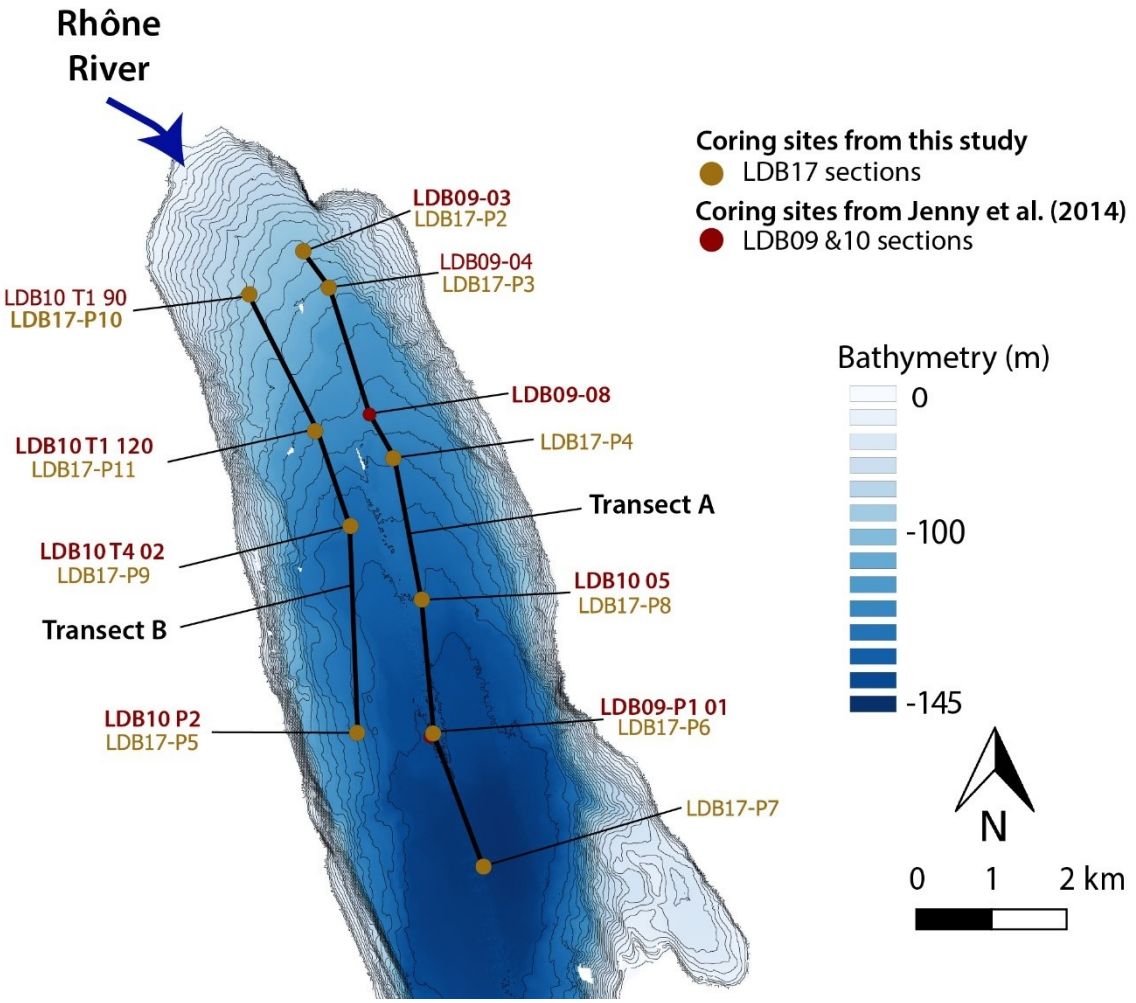

Fig. VI-2- Bathymétrie du lac du Bourget et sites de carottage des campagnes de prélèvements de Jenny et al. (2014b) et de la campagne de 2017.

Au cours de cette thèse, une corrélation stratigraphique entre les deux ensembles de carottes, celles de Jenny et al. (2014b) et celles des nouveaux transects a été entreprise (Fig. VI-3 et Fig. VI-4). Ces nouvelles données ont permis de dater les dépôts de crues du nouveau transect de séquences par rapport à l'ensemble des données de Jenny et al. (2014b), qui était basée sur 2 marqueurs de ^{137}Cs et 16 crues historiques au cours des 450 dernières années. Afin de mieux contraindre la chronologie de la partie la plus ancienne des nouvelles séquences sédimentaires, trois échantillons de macro-restes végétaux ont été envoyés pour datation au radiocarbone au laboratoire de radiocarbone de Poznań (Fig. VI-5 et Table VI-1).

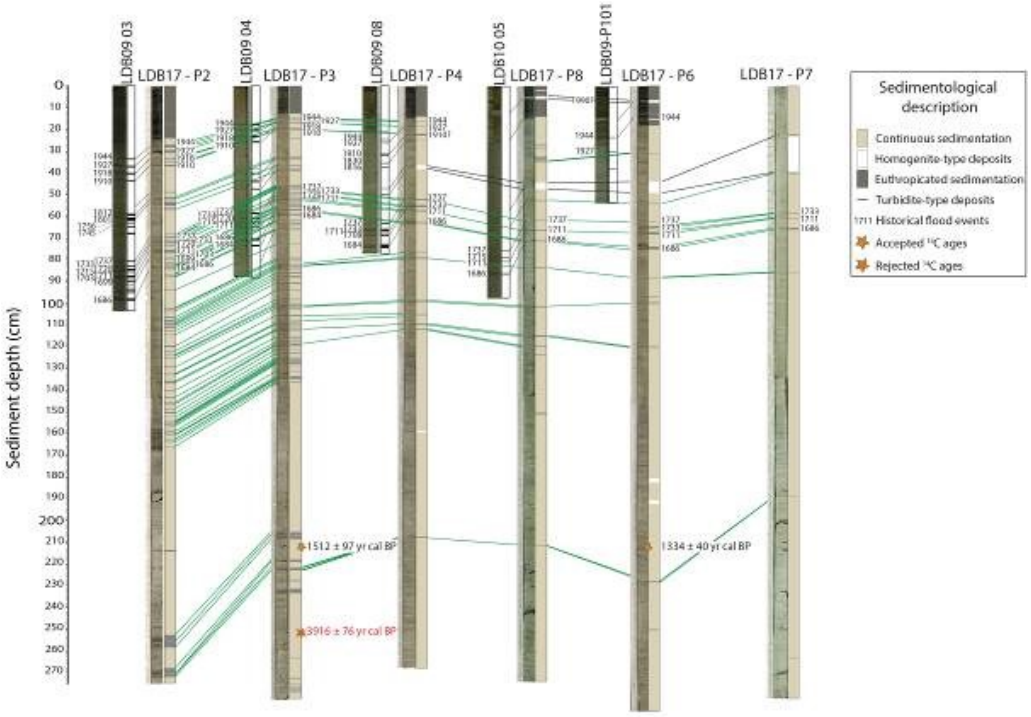

Fig. VI-3- Corrélation stratigraphique des carottes de Jenny et al. (2014b) et de cette étude (ensemble de données 2017) le long du transect A. Les dates des crues historiques de Jenny et al. (2014b) sont utilisés pour contraindre la chronologie des séquences sédimentaires de 2017 au cours des derniers siècles. Deux échantillons de radiocarbone aident à contraindre la chronologie au cours du dernier millénaire. Les dates de crues historiques sont données en années CE et les âges radiocarbone en années calibrées BP.

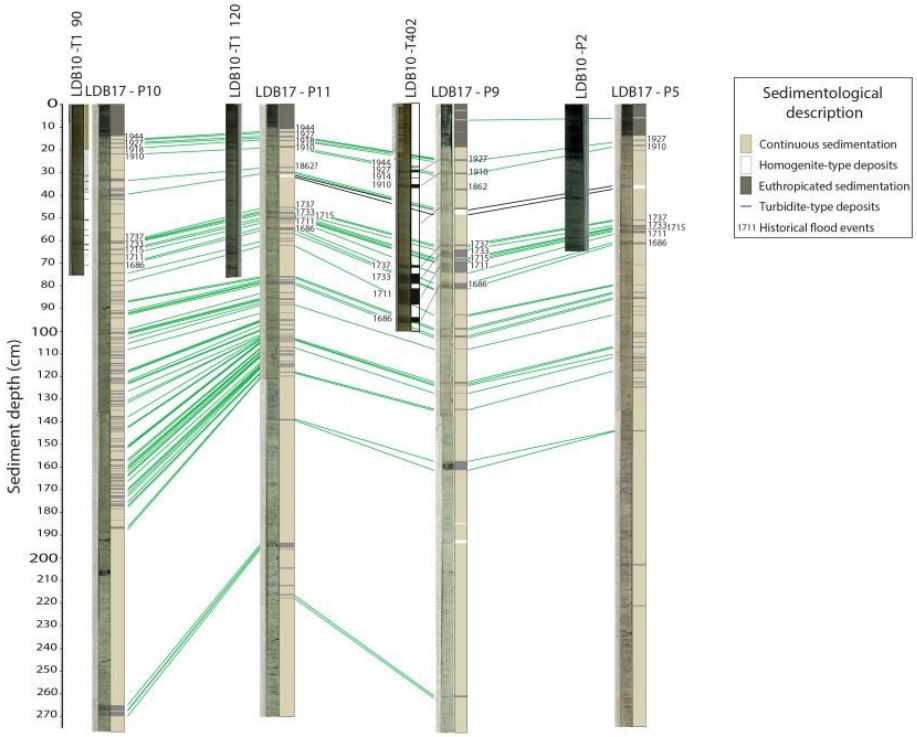

Fig. VI-4- Corrélation stratigraphique des carottes de Jenny et al. (2014b) et de cette étude (ensemble de données 2017) le long du transect B. Les dates des crues historiques de Jenny et al. (2014b) sont utilisés pour contraindre la chronologie des séquences sédimentaires de 2017 au cours des derniers siècles. Deux échantillons de radiocarbone aident à contraindre la chronologie au cours du dernier millénaire. Les dates de crues historiques sont données en années CE et les âges radiocarbone en années calibrées BP.

Toutefois, en raison du nombre plus faible de séquences sédimentaires des transects prélevés en 2017, par rapport aux nombres de séquences de Jenny et al. (2014b) et d'Evin et al. (2019), la reconstitution des volumes sédimentaires apportés par chaque crue n'était pas une approche possible pour estimer les débits de crue.

Table VI-1 – Ages radiocarbone pour les séquences sédimentaires LDB17-P6B et LDB17-P3B. La calibration des âges a été réalisée à partir de la courbe de calibration IntCal20 (Reimer et al., 2020). L'âge radiocarbone en gras a été rejetée étant donné son âge trop élevé par rapport au modèle (produit en combinant les données des événements historiques et les âges radiocarbones).

Sample Name	Core	MCD (cm)	Radiocarbon age	Age cal. yr BP 2σ range	Age cal yr AD-BC 2σ range	Sample type
LDB17-1	LDB17-P6B	212.4	1430 ± 30	1334 ± 40	575-657 AD	wood
LDB17-2	LDB17-P3B	212.8	1635 ± 30	1512 ± 97	340-535 AD	wood
LDB17-3	**LDB17-P3B**	**252.8**	**3620 ± 35**	**3916 ± 76**	**2125-1890 BC**	**wood**

En outre, Jenny et al. (2014b) ont montré que plus les dépôts de crues sont distaux, c-à-d éloignées du delta, et étendus dans le bassin sédimentaire, plus intense était l'événement de crue à l'origine de ces dépôts. Par conséquent, nous avons utilisé (i) les séquences sédimentaires les plus éloignés de l'embouchure du Rhône (LDB17-P5, P6 et P7) atteinte par chaque dépôt de crue et (ii) le nombre total de carottes où chaque dépôt de crue a été trouvé comme indicateur de l'intensité de la crue. Cela a permis de distinguer les crues extrêmes des grandes crues (Fig. VI-6).

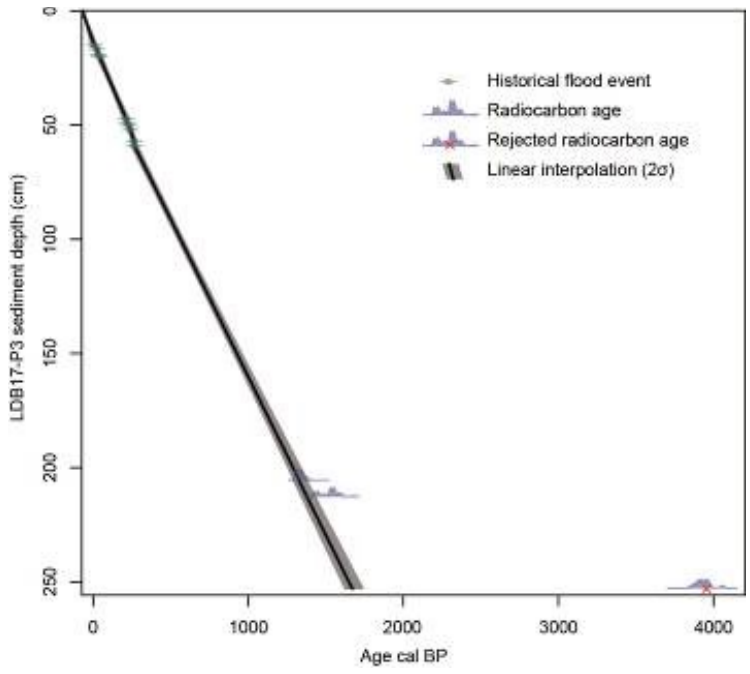

Fig. VI-5- Modèle âge-profondeur de la séquence sédimentaire LDB17-P3 du lac Bourget. Ce modèle est basé sur les événements d'inondations historiques de Jenny et al. (2014b) et trois âges radiocarbone AMS calibrés à partir de la courbe de calibration IntCal20 (Reimer et al., 2020). Dans le logiciel « R » le package « clam » a été utilisé (version 3.0.2 R Development Core Team, 2011) pour générer un modèle âge-profondeur (Blaauw, 2010).

Nous avons finalement comparé l'enregistrement des paléo-crues du Rhône nouvellement reconstruit avec les précédentes données publiées afin d'évaluer sa robustesse. Cette comparaison a d'abord été réalisée avec l'ensemble de données de Jenny et al. (2014b), mis à jour par Evin et al. (2019), qui ont reconstitué l'occurrence de 32 crues jaugées et / ou historiquement connues ainsi que leur intensité respective au cours des 350 dernières années (Fig. VI-6). Notre nouvel enregistrement comprend 27 sur les 32 crues précédemment identifiées et les cinq crues caractérisées comme extrêmes correspondent bien aux plus grands événements des études précédentes. Les crues manquantes dans notre jeu de données peuvent être liée au plus petit nombre de séquences sédimentaire prélevées par rapport à Jenny et al. (2014b) et Evin et al. (2019). La comparaison a ensuite été étendue aux 2000 dernières années avec le jeu de données de Arnaud et al. (2016), qui correspond aux apports détritiques apportés par les crues du Rhône dans la zone proximale et sur le flanc Ouest du lac (Fig. VI-6). Ces apports détritiques sont très faibles dans la partie la plus ancienne de l'enregistrement et ont largement augmenté pendant le petit âge glaciaire (1200 - 1860 CE). Cette période d'augmentation des apports détritiques correspond bien à une fréquence plus élevée des crues enregistrés dans les séquences de 2017. Par conséquent, ces comparaisons appuient la robustesse de notre enregistrement étendu de paléo-crues du Rhône.

Ce travail, mené en collaboration avec Bruno Wilhelm (IGE) a permis de créer la première chronique de crue présentant la fréquence et l'intensité des événements sur les 2000 dernières années dans le lac du Bourget. Ce projet s'inscrit dans un projet de recherche plus large, ayant pour but de reconstituer l'évolution des fréquences et des intensités des événements de crues au cours de l'Holocène à travers les Alpes Européennes (voir résumé ci-après). Dans le cadre de ce projet, un premier article scientifique est en cours de révision à *Nature Geoscience*. Les données présentées ci-dessus correspondent au seul jeu de donnée original présent dans cet article.

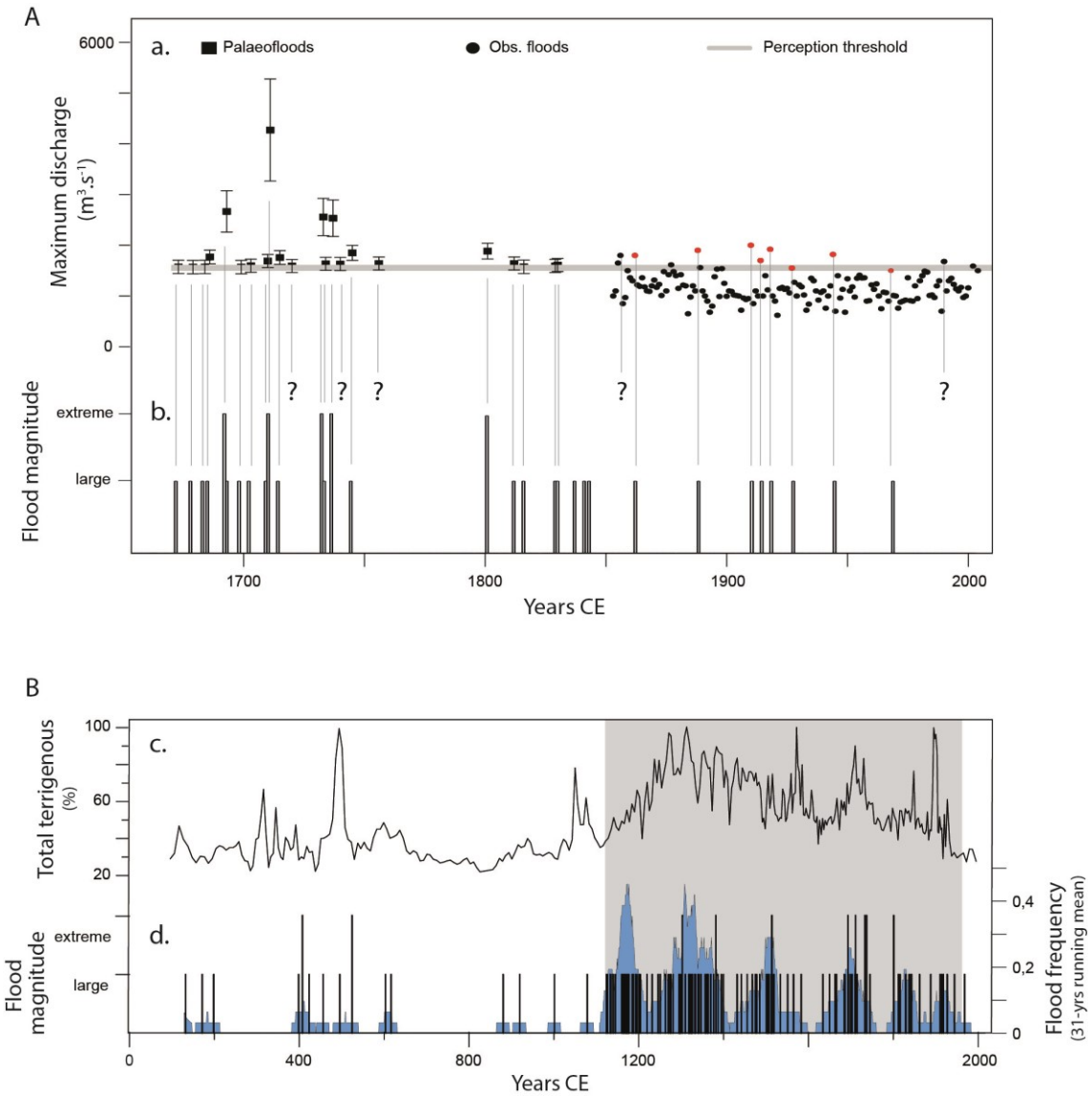

Fig. VI-6- Reconstitution de la fréquence et de l'intensité des paléo-crues du lac du Bourget au cours des 350 dernières années (A) et des deux derniers millénaires (B). Au cours des 350 dernières années, le nouvel enregistrement (b.) est comparé à la chronique d'Evin et al. (2019) (a.), qui est une mise à jour de l'ensemble des données de Jenny et al. (2014b) qui combinaient les débits de paléo-crues reconstruits de 1650 à 1852 (carrés noirs) et les débits annuels de crue de 2010 à 1852 (points noirs et rouges). Les points rouges indiquent les crues enregistrées dans la séquence sédimentaire parmi les crues annuelles jaugées (points noirs). Au cours des 2000 dernières années, le nouvel enregistrement (d) est comparé aux données d'Arnaud et al. (2016), présentant l'évolution des apports détritiques des crues du Rhône dans la zone proximale et sur les flancs Ouest du lac du Bourget. Figure réalisée par Bruno Wilhelm.

2. Application of the acquired dataset

Flood hazard under natural and anthropogenic climate changes in the European Alps

Article | En révision dans Nature Geoscience

Wilhelm B.[1], Rapuc W.[2], Amann B.[3], Anselmetti F.S.[4], Arnaud F.[2], Blanchet J.[1], Brauer A.[5], Czymzik M.[6], Giguet-Covex C.[2], Gilli A.[7], Glur L.[8], Grosjean M.[9], Irmler R.[10], Nicolle M.[11], Sabatier P.[2], Swierczynski T.[5], Wirth S.B.[12]

[1]UGA, CNRS, IRD, Institute for Geosciences and Environmental research (IGE), Saint-Martin d'Hères, France;
[2]UGA, Université Savoie Mont Blanc, CNRS UMR 5204, EDYTEM, F-73000 Chambéry CEDEX, France;
[3]Renard Centre of Marine Geology, Ghent University, 9000 Ghent, Belgium;
[4]Institute of Geological Sciences and Oeschger Centre for Climate Change Research, Univ. of Bern, 3012 Bern, Switzerland;
[5]GFZ German Research Centre for Geosciences, 14473 Potsdam, Germany;
[6]Leibniz Institute for Baltic Sea Research Warnemünde (IOW), Germany;
[7]Geological Institute, ETH Zurich, Zurich, Switzerland;
[8]Helvetia Insurance, Rosenbergstrasse 20, 9001 St. Gallen, Switzerland;
[9]Oeschger Centre for Climate Change Research and Institute of Geography, University of Bern, 3012 Bern, Switzerland;
[10]formerly Institut für Geographie, Friedrich-Schiller Universität Jena, Germany;
[11]Normandie Univ, Unirouen, Unicaen, CNRS, M2C, 76000 Rouen, France;
[12]Centre for Hydrogeology and Geothermics, University of Neuchâtel, Neuchâtel, Switzerland

Abstract

Flooding is already one of the costliest natural hazards, which climate change is expected to globally exacerbate, resulting in further increasing human and economic losses. This concern is reinforced in mountainous areas such as the densely populated European Alps. This region experiences warming at a rate that is twice as high as that in the Northern Hemisphere, which will likely result in increasing flood-causing heavy rainfall. However, no consistent climate change signal has been identified in flood observations in the European Alps. Based on an extensive collection of paleoflood records from the Alps, we demonstrate here that large (⩾10 years) floods were 25-50% less frequent under +0.5-1.2°C climate warming, whether naturally or anthropogenically forced. This decreasing trend is not conclusive in records shorter than 200 years but persistent in records ranging from 200 to 9000 years. Our data also suggest that trends in extreme (⩾100 years) floods may differ, with a possible increase in such flood occurrence with warming in certain small, unattended Alpine catchments in relation to strong local intensification of extreme rainfall. Our study — arising from the largest database of continuous, geology-based flood series — demonstrates how paleoflood records contribute to capturing complex climate-flood relationships and assist in improving flood hazard assessment and projections, still encompassing too large uncertainties for appropriate risk management at the regional scale

CHAPITRE VII | XRF and hyperspectral analyses as an automatic way to detect flood events in sediment cores

Article 3 | Publié dans Sedimentary Geology

https://doi.org/10.1016/j.sedgeo.2020.105776

Received 22 July 2020, Received in revised form 21 September 2020, Accepted 22 September 2020

William Rapuc[1], Kévin Jacq[1,2] Anne-Lise Develle-Vincent[1], Pierre Sabatier[1], Bernard Fanget[1], Yves Perrette[1], Didier Coquin[2], Maxime Debret[3], Bruno Wilhelm[4] and Fabien Arnaud[1]

[1] Université Grenoble Alpes, Université Savoie Mont Blanc, CNRS, EDYTEM, LE Bourget du lac, France

[2] Université Savoie Mont Blanc, LISTIC, 74944 Annecy Le Vieux, France

[3] Université De Caen, CNRS, LM2C, 76821 Mont-Saint-Aignan, France

[4] Institute for Geosciences and Environmental research (IGE), UGA, CNRS, IRD,Grenoble, France

Abstract

Long-term changes in flood activity have often been reconstructed to understand their relationships to climate changes. This requires identification of flood layers according to certain characteristics (e.g., texture, geochemical composition, grain-size) and then to count them using naked-eye observation. This method is, however, time-consuming, and intrinsically characterized by a low resolution that may lead to bias and misidentification. To overcome this limitation, high-resolution analytical approaches can be used, such as X-ray fluorescence spectroscopy (XRF), X-ray computed tomography, or hyperspectral imaging (HSI). When coupled with discriminant algorithms, HSI allows for automatic identification of event layers. Here, we propose a new method of flood layers identification and counting based on the combination of both HSI and XRF core scanner analyses, applied to a Lake Bourget (French Alps) sediment sequence. We use a hyperspectral sensor from the short wave-infrared spectral range to create a discrimination model between event layers and continuous sedimentation. This first step allows the estimation of a classification map, with a prediction accuracy of 0.96, and then the automatic reconstruction of a reliable chronicle of event layers (including their occurrence and deposit thicknesses). XRF signals are then used to discriminate flood layers among all identified event layers based on site-specific geochemical elements (in the case of Lake Bourget: Mn and Ti). This results in an automatically generated flood chronicle. Changes in flood occurrence and event thickness through time reconstructed from the automatically generated floods chronicle are in good agreement with the naked-eye-generated chronicle. In detail, differences rely on a larger number of detected flood events (i.e., increase of 9% of the number of layers detected) and a more precise layer thickness estimation, thanks to a higher resolution. Therefore, the developed methodology opens a promising avenue to increase both the efficiency (timesaving) and robustness (higher accuracy) of paleoflood reconstructions from lake sediments. Also, this

methodology can be applied to identify any specific layers (e.g., varve, tephra, mass-movement turbidite, tsunami) and, thereby, it has a direct implication in paleolimnology, paleoflood hydrology and paleoseismology from sediment archives.

KEYWORDS

Lake sediment, hyperspectral analyses, XRF geochemical analysis, Automatic flood chronicle

1. Introduction

Changes in flood occurrence and magnitude are expected due to climate change in many regions, affecting an increasing number of people (Hirabayashi et al., 2013; Blöschl et al., 2019). Large uncertainties still exist on such changes and long-term flood records are of high value to fully understand climate-flood relationships (Merz et al., 2014; Wilhelm et al., 2019). To this end, numerous studies are undertaken on geological records such as lake sediments to reconstruct centennial to millennial flood records (Noren et al., 2002; Moreno et al., 2008; Giguet-Covex et al., 2012; Wilhelm et al., 2012, 2017; Glur et al., 2013; Wirth et al., 2013; Sabatier et al., 2017; Corella et al., 2019; Rapuc et al., 2019). Flood events produce turbidity currents in the lake basin that will usually lead to a normally graded detrital layer that differs from the surrounding continuous sedimentation (Sturm and Matter, 1978; Gilli et al., 2013). However, other processes such as earthquakes, spontaneous delta front collapses, and lake-level changes, can also produce turbidity currents in lakes (Sauerbrey et al., 2013; Wilhelm et al., 2017; Rapuc et al., 2018). In most of these studies, to count and differentiate the event layers, the sediment facies are first described visually, then several sedimentological and geochemical analyses are undertaken. From those results, the event layers are identified, allowing the interpretation of a potential trigger. Then, layers with the same characteristics are usually identified and counted all along the core by naked-eye observation to ultimately produce a flood chronicle. Those methods are, however, time-consuming, have a low spatial resolution potential, and they can be destructive (e.g., through grain-size measurements, total organic carbon analyses). More importantly, naked-eye identification and counting can lead to inaccuracy and misidentification due to human bias and intrinsic low resolution. To overcome this limitation, an automatic layer detection method coupled to a high-resolution analysis is required and would also allow results to be fully reproducible.

As several parameters such as color, texture, grain-size and chemical composition vary between flood events and the continuous sedimentation in a lake, we propose to go further than Vannière et al., (2013) who first proposed an automatic way to detect events layers based on RGB images. In this study, we explore the use of short-wave infrared hyperspectral imaging (HSI) applied on the Lake Bourget (France) sediment sequence. HSI has shown potential to highlight organic matter (Butz et al., 2017; Schneider et al., 2018; Speta et al., 2018; Van Exem et al., 2018; Jacq et al., 2019), mineral compounds (Lampinen et al., 2019; Tusa et al., 2019) and particle size (Jacq et al., 2019) in lake sediments. The partial least squares discriminant analysis (PLS-DA) was used to discriminate event layers from continuous sedimentation, as presented in a previous study (Jacq et al., 2020). This results in an event layer chronicle including depth and thickness for each event layer with a 200 µm resolution. In a second step, XRF element geochemistry performed with an Avaatech core-scanner analyses with a high resolution of 500 µm are used to interpret the trigger of the event layers and create a flood chronicle. To test the accuracy of this new method, we compare our results to a naked-eye flood chronicle for the same core.

2. Study Site

Lake Bourget (18 km long, 2.8 km wide, 231.5 m.a.s.l) is one of the largest natural lake in France (44.5 km²). This lake is a peri-alpine hard water lake located in the northwestern part of the French Alps (Fig. VII-1) and was formed by the retreat of Würmian glaciers (Nicoud et al., 1987). Three tributaries enter Lake Bourget: Leysse, Sierroz and the Rhône rivers (Fig. VII-1). The Rhône river is usually the outflow of Lake Bourget, but current reversal takes place during flood events and inflows in the lake. Including the Rhône River catchment, the catchment of Lake Bourget covers a large area (approx. 4600 km²) and diverse lithologies including granitic rocks of the Mont Blanc massif as well as Cretaceous limestones. Lake Bourget is a monomictic lake that presents a partial reoxygenation of its hypolimnion during winter water mixing followed by hypoxia that increases progressively during thermal stratification (Jenny et al., 2013). For most of the year, the bottom water of the lake thus presents low oxygen concentration compared to surface water and river water input. The sediments of Lake Bourget have already been studied to understand the history of the lake eutrophication (Giguet-Covex et al., 2010; Jenny et al., 2013), and regional flood activity (Chapron et al., 2002, 2005; Arnaud et al., 2005; Debret et al., 2010; Jenny et al., 2014b; Evin et al., 2019), to characterize the evolution of erosion in the watershed (Revel-Rolland et al., 2005; Arnaud et al., 2012) or to study seismically induced deposits (Chapron et al., 1999). From all those studies, it appears that the northern part of the lake basin is influenced by flood events from the Rhône River, contributing from 10 to 40% to the total sedimentation, and can generate event layers due to underflows during high-energy flood events (Arnaud et al., 2012; Giguet-Covex et al., 2010).

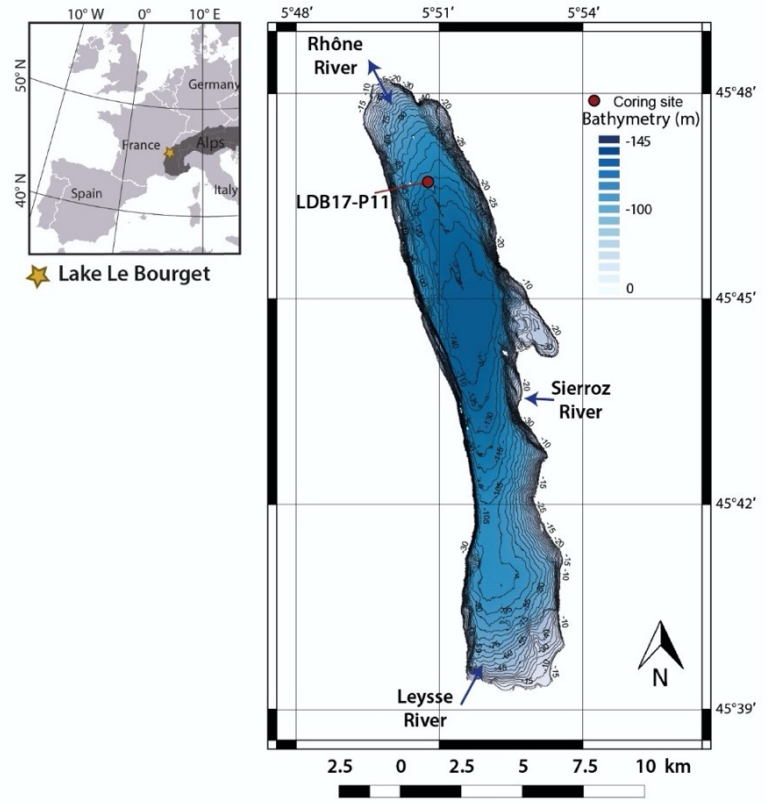

Fig. VII-1- Location of Lake Bourget in the European Alps, its bathymetry, and location of the coring site (LDB17-P11).

The continuous background sedimentation in the Northern part of Lake Bourget is mainly composed of an alternation of very dark grey and very light grey clayey laminae over the first centimeters with a predominance of diatoms, authigenic calcite crystals and organic matter (Giguet-Covex et al., 2010). This upper part presents the highest TOC values, i.e., 2.5% (Millet et al., 2010) and results from the eutrophication of the lake initiated in the middle of the 20th century (Debret et al., 2010; Giguet-Covex et al., 2010; Jenny et al., 2013). The sediment composition evolves downwards, authigenic carbonates remain the major component but the concentration in detrital particles increase associated to a progressive decrease of TOC values (Debret et al., 2010; Millet et al., 2010).

The deposits linked to flood events in the proximal part of the Lake Bourget basin are characterized by a dark to very dark grey color (10 YR 4/1, Munsell soil color chart) and are easily distinguishable from the light grey continuous background sedimentation (Giguet-Covex et al., 2010). The thickness of these deposits varies from millimeter to centimeter scale. These fine-silty to clayey deposits are mainly composed of allochthonous silicates and enriched in detrital elements (Giguet-Covex et al., 2010; Jenny et al., 2014b). Some homogenite-type deposits were also observed in the sediment of Lake Bourget and correspond to light grey deposits rich in autochthonous carbonates (Chapron et al., 1999). Arnaud et al. (2012) showed that the Ti signal, from XRF data, is the best proxy to represent detrital input in Lake Bourget. Jenny et al. (2014b) and Evin et al. (2019) evidenced that the flood-sediment pathways are always changing in Lake Bourget, which explains why grain-size is not used as a proxy of flood deposits.

3. Materials and Methods

3.1. Coring and lithological description

In 2017, a sediment core (LDB17-P11, length 271 cm) was retrieved from the northern basin of Lake Bourget (45° 46.778'N, 5° 50.552'E, 113 m water depth, Fig. VII-1) using a UWITEC gravity corer with a hammer. This site was selected because it is highly influenced by the detrital sediment input from the Rhône River (Jenny et al., 2014b). The section was cut in two parts (A & B), split in half, photographed at high resolution (20 pixels mm^{-1}), and described and logged in detail using the Munsell color chart. Therein, the study focuses on the upper section (LDB17-P11A, 121.5 cm) that presents the highest number of event layers. The sediment retrieved in the LDB17-P11A sediment core can be subdivided into two different units (Fig. VII-2). The upper part (0 - 10.4 cm depth) of the core composed of dark-greenish-grey clay (5GY 4/4) presents a thin alternation of dark grey, light grey and brown laminae and is equivalent to the one observed and described previously in Lake Bourget by Giguet-Covex et al. (2010) and Jenny et al. (2013). This unit corresponds to a laminated organic gyttja linked to recent eutrophication of the bottom water of Lake Bourget (Giguet-Covex et al., 2010; Jenny et al., 2013). The second unit (10.4 – 121.5 cm depth) is characterized by a homogeneous clayey to silty light grey sediment that is predominantly composed of carbonate particles and a few diatoms. This unit is often interrupted by darker deposits, rich in detrital compounds (silicate and carbonate) that were previously interpreted as turbidite-type deposits induced by underflow linked to flood events incoming from the Rhône river (Giguet-Covex et al., 2010; Jenny et al., 2014b).

3.2. Spectroscopic analysis

Two non-destructive high-resolution spectroscopic methods were applied to the sediment core. The Short Wave Infrared (SWIR) and XRF were used to estimate the molecular and elementary properties of event layers.

3.2.1. Hyperspectral analysis

The SWIR sensor covers the spectral range from 1000 nm to 2500 nm with 12 nm bandwidth, so that the spectra is composed of 144 spectral bands, and the spatial resolution at sampling is 200 µm. Hyperspectral acquisition protocols proposed by Butz et al. (2015) and Jacq et al. (2020) were followed and they are composed of three main steps : (1) The sample needs to be prepared to be as flat as possible and reveal sedimentary structures ; (2) both camera and scanner must be adjusted to obtain squared pixels and an optimal signal to noise ratio ; and (3) the data must be calibrated with the white (spectralon) and dark (shutter closed) normalizations to obtain the reflectance spectra of the sample.

Several pre-processing steps can be used to remove noise or highlight discriminant spectral information. Spectral detrending (Barnes et al., 1989) was used to correct the spectra from the baseline as chosen in a previous study (Jacq et al., 2020).

3.2.2. Geochemical properties

XRF geochemical analysis was performed on the EDYTEM laboratory's Core Scanner (Avaatech XRF Technology) to characterize the variations of major elements throughout LDB17-P11A sediment sequence. A continuous 0.5 mm step measurement was applied with a run at 10 kV and 0.25 mA for 20 s to detect lightweight elements, such as Al, Si, K, Ca, Ti, and a second run was performed at 30 kV and 0.4 mA for 20 s to detect Mn, Fe, Br, Rb, Sr, and Zr. The XRF core scanner results are expressed hereafter as peak intensities by counts per second (cps). Then, a principal component analysis (PCA) was conducted on the XRF data to identify principal sediment end-members and correlations between the detected elements (Sabatier et al., 2010). Due to the 500 µm resolution, only the layers thicker than 0.5 mm can be detected with XRF data, and only layers thicker or equal to 1 mm will be described to increase the reliability of the study.

3.3. The methodology of detection and interpretation of event layers

To detect and interpret the event layers present in a sediment core we used a combination of HSI and XRF that can be summarized as follows (Fig. VII-2): (i) Opening and visual description of the core to identify and count the different types of event layers; (ii) Hyperspectral analysis associated with data treatment and the selection by the user of some event layers as reference layers to produce a chronicle; (iii) Perform XRF analysis at high-resolution; (iv) From knowledge of the in-lake sedimentary processes, using previous researches and/or sedimentological and geochemical analyses (XRD, energy dispersive X-ray spectroscopy, XRF, grain-size, anisotropy of magnetic susceptibility), selection of one proxy of detrital input, one proxy of grain-size or transport processes, and if needed one proxy of oxygenation of the lake bottom water from XRF data; and (v) Combination of hyperspectral chronicle and XRF data to create (vi) an interpreted flood chronicle and calculate the thicknesses of each flood layer. The main step of this method will be developed hereafter. All these steps were processed in Matlab software (R2020a), using the following method: https://github.com/JacqKevin/HSI_SupervisedClassification.

3.3.1. *Hyperspectral classification and event layer chronicle estimation*

First, data need to be manually labelled to create a training dataset. This requires that a user manually select rectangles on a pseudo-RGB image that correspond to reference event layers or continuous sedimentation layers. The selected pixels are then extracted to create a calibration set to estimate the classification model parameters and produce a validation set to test its performances. A PLS-DA is used for classification modelling (Wold et al., 1984; Barker and Rayens, 2003). This method is based on the PLS approach that reduces the spectral data in latent variables maximizing the spectral variability and the co-variability between the spectra and variables of interest. The model performances are estimated with the calibration and prediction accuracies that estimate the ratio of pixels that are successfully classified into their corresponding classes. A qualitative assessment is also realized to check the accuracy of the prediction map. The optimal classification model allows discriminating the event layers from the continuous sedimentation with a classification map (Fig. VII-3).

Based on a previous study of Jacq et al. (2020), hyperspectral classification can discriminate event layers from continuous sedimentation with the SWIR image. A discrimination model was estimated (Fig. VII-3) and presents a calibration accuracy of 0.97, validation accuracy of 0.96, and qualitative relevance of 5/5.

Then, a summed profile of the classification map is calculated, normalized by the number of width pixels, it can be seen as the occurrence probability of an event (Fig. VII-3). This profile was smoothed to remove artifacts and mis-classifications with a Savitzky-Golay filter (Savitzky and Golay, 1964). A double threshold was fixed to find the event layer boundaries and to create the chronicle. The first threshold was set at 50% of the width. It allowed us to find thin and thick deposits without selecting artifacts or mis-classification, but thicker deposits (greater than 5 mm) can result from the amalgamation of several close layers. The second threshold at 15% of the width was used to divide the deposits. Finally, each deposit can be separated, and their depth and thickness estimated to create an event layer chronicle without information about event triggers. In some lake environments, the thickness of flood layers may be informative about flood intensity (Wilhelm et al., 2013, 2019; Sabatier et al., 2017) but it is not the case in Lake Bourget. Here, thickness estimation is thus only considered for further applications on other lakes. Hence, a cumulative sum was also calculated to test the accuracy of an automatic model on the detection of the number and thickness of event layers. Therein, only layers with thickness greater than 1 mm are used because this represents the resolution limit used to build the naked-eye chronicle, and the XRF analysis resolution did not allow for characterization of thinner deposits. Once the method is validated, the event layer chronicle can be exploited at the limit of XRF data resolution.

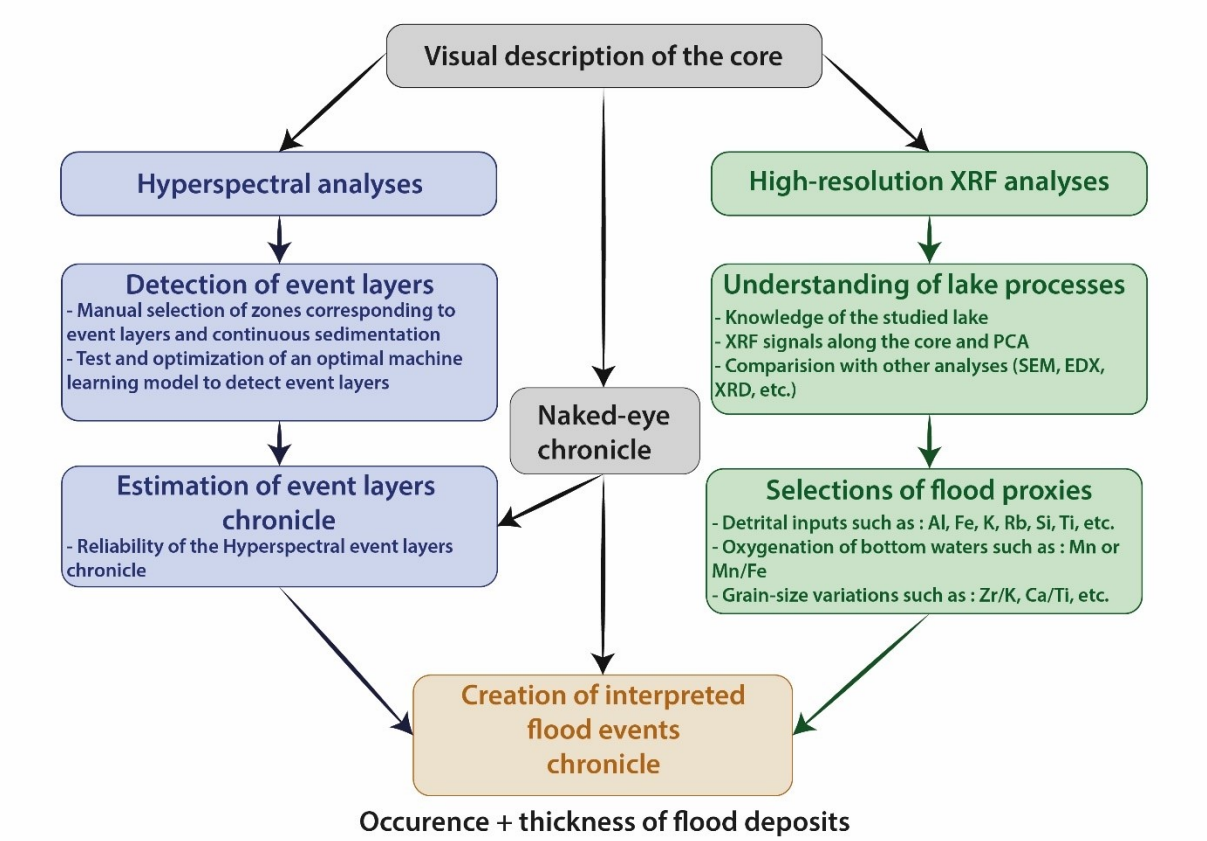

Fig. VII-2-Summary of the methodology developed for the semi-automatic detection and interpretation of flood event layers in lake sediments based on the combination of hyperspectral and XRF data and the comparison with a naked eye study.

3.3.2. *Flood proxies derived from XRF*

In a lake system, several mechanisms can trigger an event layer : (i) lake level fluctuations, (ii) snow avalanches, (iii) eruptions, (iv) sediment overloading on slopes or deltas, (v) destabilization of slopes and deltas by seismic shaking, and (vi) flood events (e.g., Sauerbrey et al., 2013; Rapuc et al., 2018). Regardless of the lake system considered, to discriminate the triggering mechanisms of each deposit it is necessary to select a combination of proxies allowing for interpretation of (1) the sources and (2) the grain-size of the sediment composing the event layers and (3) the transport processes leading to deposition of the sediment. Here we focused only on a way to discriminate flood layers from surrounding sedimentation using XRF signals, but this method can apply to any other triggers. Floods induce an input of sediment rich in detrital material coming from the watershed, and they generally produce a turbiditic underflow in the lake, leading to sediment sorting and deposition of a graded layer (Sturm and Matter, 1978). When the oxygen-rich water, coming from the watershed during a flood, reaches the water-sediment interface due to an underflow, the Mn and Fe present in dissolved form precipitate as Mn and Fe oxy-hydroxides at the base of the induced turbiditic layer. Thus, a peak of Mn or Fe can be interpreted as flood-induced lake bottom oxygenation and is linked to detrital input (Wilhelm et al., 2016; Sabatier et al., 2017; Rapuc et al., 2019). However, changes in the oxic/anoxic state of the bottom water of the lake will also lead to similar changes in Fe and Mn (Davison, 1993; Elbaz-Poulichet et al., 2014). Because it can be affected by oxic and reduction processes, Fe does not seem to be a good proxy to trace detrital input from flood events and will not be used in this study. Thus, ratios

such as Zr/Fe, used to represent grain-size variations in lake sediment and interpreted as a proxy of grain size (Wilhelm et al., 2013) should not be used with much confidence when studying a flood deposit in lakes influenced by changes in the oxygenation of lake bottom water. Depending on lake mechanics and the available knowledge, the user can select one or several proxies to interpret event layers.

3.3.3. *XRF flood proxies and HSI chronicle combination*

The selected XRF profiles were smoothed to reduced noise with a Savitzky-Golay filter (Savitzky and Golay, 1964). Then, all the peaks were detected with local maxima. Some constraints can be used with the peak height, prominence, width, and distance between two consecutive peaks, but no such constraint was used in this study. Finally, a depth matching of the HSI event layers and the XRF profiles was made. For each event layer detected by HSI, the presence or absence of XRF peaks in this area will characterize the type of event. Thus, the instantaneous chronicle made by HSI was interpreted thanks to the XRF to obtain a chronicle by type of each event.

3.3.4. *Comparison with the naked eye chronicle*

The comparison of the two (HSI+XRF and naked-eye) chronicles relied on results of event frequency and cumulative thickness calculated as the sum of the number of deposits counted every 10 cm and the cumulative thickness of the deposits, respectively. Then correlation and standard error were calculated to measure similarity and distance between the naked-eye and estimated chronicles. A quantile-quantile plot was also used to compare the respective distributions in depth and thickness.

4. Results

4.1. Visual description of the core and naked-eye chronicle

Event layers, characterized by a dark to very dark grey color (10 YR 4/1), were counted visually along the LDB17-P11A sediment core (Fig. VII-2). As these layers are easily distinguishable from continuous sedimentation, we counted all the deposits with a thicknesses $\geqslant$ 1 mm. To improve the accuracy of our results, the counting of these deposits was repeated by another observer. Fifty-six event layers were counted, with a maximum thickness of 11.0 mm and a mean thickness of 3.4 mm. One other deposit, interrupting the continuous sedimentation, was identified between 31.5 and 32.1 cm deep (Fig. VII-3; Fig. VII-4). This deposit is composed of light grey silty to clayey sediment rich in carbonates and corresponds to a homogenite-type deposit linked to a seismic event that occurs close to the lake in 1822 (Chapron et al., 1999). To build a flood chronicle, the homogenite-type deposit was removed, and the sum of the number of deposits counted every 10 cm and the cumulative thickness of the deposits was plotted against the depth of the core.

4.2. Hyperspectral analyses

On the LDB17-P11 section, 21 rectangles were selected in approximately 5 minutes, covering 1.20 % of the total section area. From this selection, an HSI discrimination model was built on the entire sequence, allowing the estimation of a chronicle (Fig. VII-4), with the depth and thickness of each layer. However, the model cannot distinguish between turbidite-type and homogenite-type deposits (Fig. VII-3). Thus, the hyperspectral model cannot be used directly to classify the different kinds of events layers and discuss their origin. One hundred and ten deposits were

counted using the SWIR camera, 86 have a thickness greater than 1 mm, and are used hereafter. These present a mean thickness of 4.5 mm and a maximum thickness of 15.5 mm.

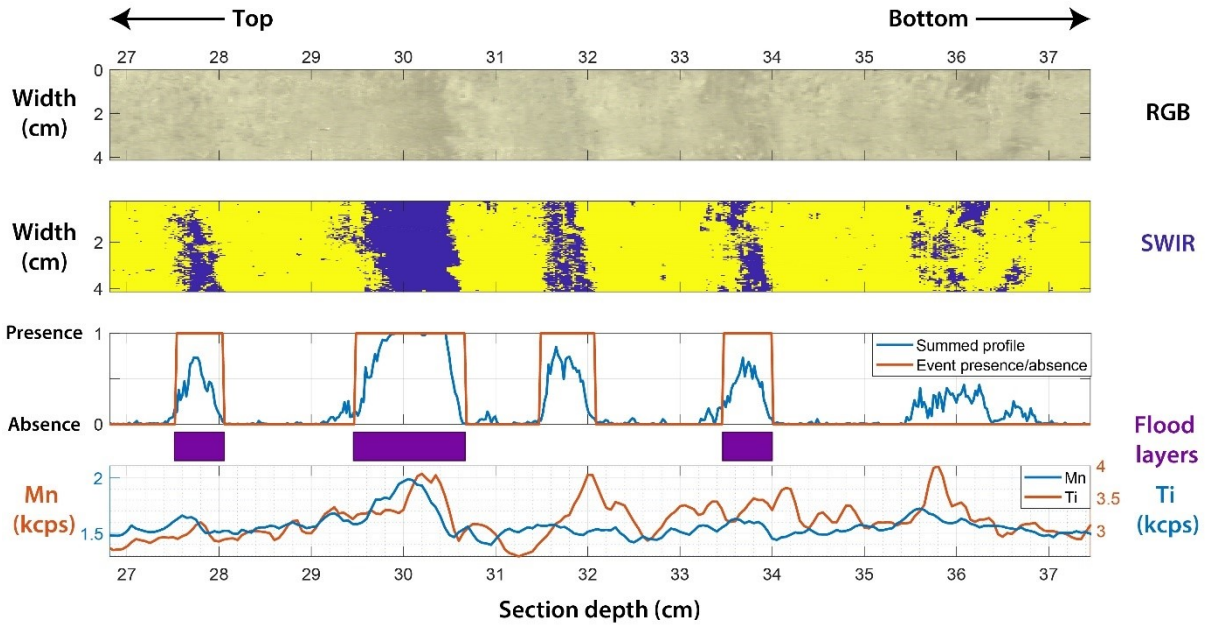

Fig. VII-3 - Details of RGB images and SWIR classification map, associated with summed profile derived from hyperspectral imaging model. The orange line shows the detected event layers from HSI model. In the Lake Bourget example, Mn and Ti signals were chosen to interpret flood layers. Location and thickness of flood layers detected by the combination of HSI and XRF data are represented by purple rectangles.

4.3. High-resolution XRF analyses

From the XRF analyses, Unit I shows low values of Ti [> 3 kilo counts per second (kcps)], Fe (> 100 kcps), and K (> 9 kcps) and high values of Ca (> 145 kcps). From the top of the sediment section to the base of Unit II, the Ti, K, Fe, and Mn signals increase (Fig. VII-4). The Ca signal is quite constant over the first 121 cm of the LDB17-P11A sediment core. The event layers present peaks of Ti, Fe, Mn, and K and low values of Ca (Fig. VII-4). The Zr/K ratio presents important peaks at the base of each event layer and low values at the top (Fig. VII-4). The only homogenite-type deposit identified in the core section presents relatively low values of Ti, Fe, and K and show a relatively high value of Ca and Mn signal. A peak of Zr/K is present at the base of this deposit. The variability of the Mn and Fe signal increases downward (Fig. VII-4).

From the XRF data, a PCA was conducted and provides variables and individual factor maps (Fig. VII-5), which highlight the relationships between the different elements and geochemical distributions within sediment units. Dimensions 1 and 2 (denoted as Dim1 and Dim2) represent 73.9% of the total variability of the signal. From the variables factor map, three end-members were identified. The first, which is denoted as terrigenous, is positively correlated with Dim1 and yields high positive loadings for the major terrigenous elements (Zr, Fe, Ti, Rb, Mn, Al, Si, and K). This pole can be subdivided into two-parts, (i) the upper part including Zr, Fe, Rb, Ti, and Mn, that are particles usually linked to coarse grains or reduction–oxidation processes in lake sediment (Davies et al., 2015 and references therein), and (ii) the lower part including Al, Si and K. The second end-member, which is denoted as "organic matter" yields positive values for Br and is negatively correlated with Dim1 and positively with Dim2. The third end-member is negatively

correlated with Dim1 and with Dim2 (Fig. VII-5-A). This pole yields high positive values for Ca and is interpreted as representing carbonates produced by biologic activity in the lake, as Sr is usually present in marine limestone that constitutes a significant part of the outcrops in the watershed of Lake Bourget, and is here anticorrelated with Ca. The individual factor map (Fig. VII-5-B) identifies specific features in each unit. (i) Unit I is negatively correlated with terrigenous end-members, which is due to its high organic matter content. (ii) Unit II can be separated into two parts, one positively correlated with Dim1 and, thus, to the detrital end-member, and one part that is characterized by a high Ca content. Values for the event layers identified as turbidites by Giguet-Covex et al. (2010) are almost exclusively positively correlated with the terrigenous end-member and especially with the upper part of this pole, while values obtained for the homogenite-type deposit are closer to the carbonate pole. From previous knowledge of sedimentary processes in Lake Bourget (Giguet-Covex et al., 2010; Arnaud et al., 2012; Jenny et al., 2013), and XRF and PCA results, we selected Ti as a proxy of detrital input from the river and Mn as a proxy of oxygenation of the water at the sediment interface. Indeed, when it is present at the base of an event layer and combined with a peak of a proxy of detrital input, a peak of Mn can be used as a proxy of oxygenation of the bottom water, and thus be used to detect and interpret flood layers.

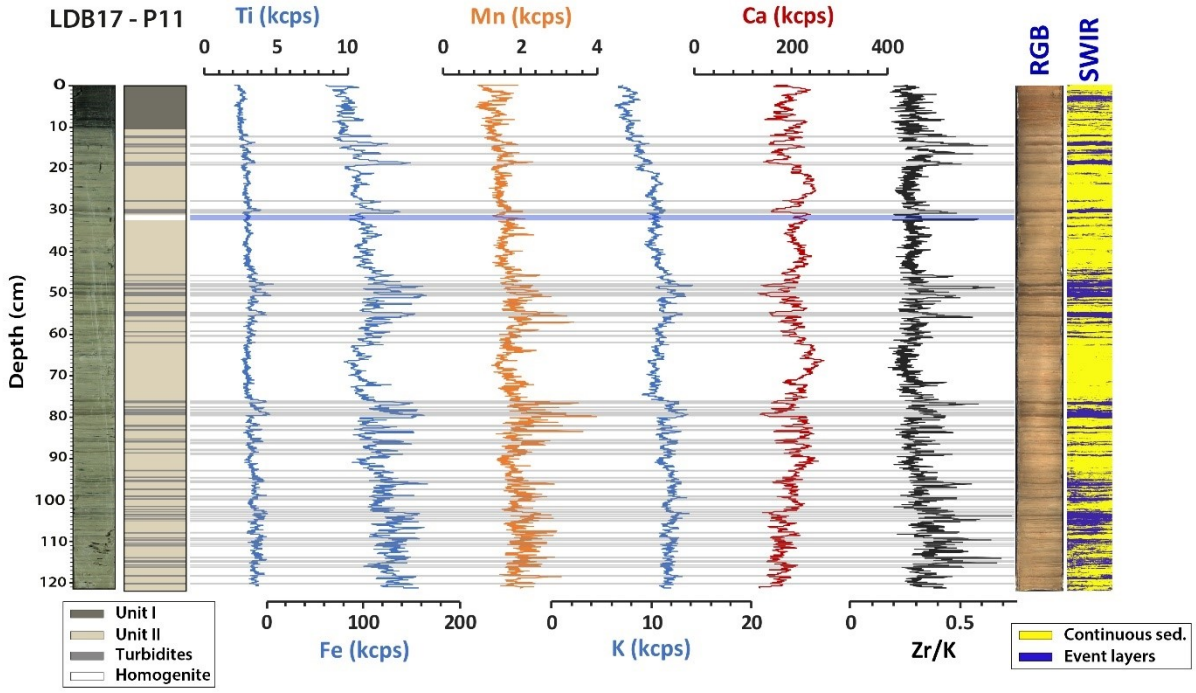

Fig. VII-4 - Main results obtained on LDB17-P11A sediment section : the picture of the core, the stratigraphic log with the turbidite-type deposits identified by a visual description of the core represented in grey and the homogenite-type deposit in white, the main XRF data used hereafter (Ti, Fe, Mn, K, Ca and Zr/K ratio), the picture of the core in RGB colors, the discrimination model showing event layers identified using hyperspectral camera SWIR.

4.4. Creation of interpreted flood event chronicle

The combination of Ti and Mn signals allowed to automatically provide a paleoflood record from the HSI event layer chronicle. Sixty-one layers present both Ti and Mn peaks and are identified as flood events with a maximum thickness of 15.5 mm and a mean thickness of 5.6 mm. Twenty-one layers have only a peak of Mn, three layers only present a peak of Ti, and one layer does not present any peak of Ti and Mn. The homogenite-type deposit between 31.50 and 32.10 cm depth, linked to a seismic event that occurs close to the lake in 1822 AD (Chapron et al., 1999) is

correctly discarded by the model (Fig. VII-3). Then, a flood chronicle was estimated with the 61 identified flood layers.

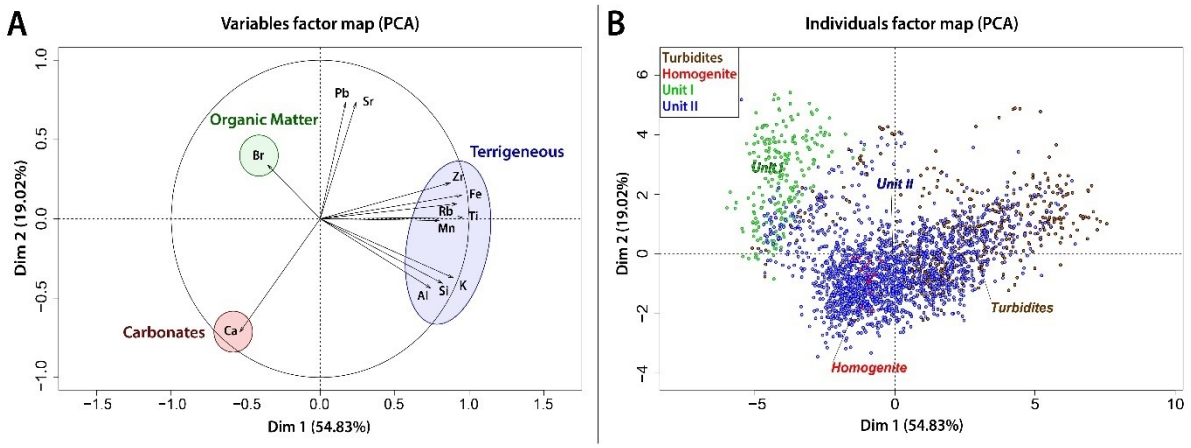

Fig. VII-5 - Variable and individual factor maps from the PCA. (A) Variable factor map with three end-members (terrigenous, organic matter, and carbonates). (B) Individual factor map with sedimentological units added as an illustrative variable.

5. Discussion

5.1. Naked-eye versus HSI chronicles

Naked-eye observation could not be used to interpret the triggering mechanisms of event layers because different processes can lead to a turbiditic current into a lake. Then, from naked-eye observation, these deposits can only be considered as event layers interrupting continuous sedimentation. The HSI chronicle of event layers is compared to the naked-eye one to test the robustness of the developed methodology (Fig. VII-6-A, B). The comparison is made on event frequency and cumulative thickness, both calculated as a sum of 10 cm. The HSI frequency is in great agreement with the naked-eye chronicle ($r = 0.86$ and $SE = 3.04$). The cumulative thickness derived from the SWIR camera is also very close to the one obtained from naked-eye observation ($r = 0.85$ and $SE = 1.94$). Thus, HSI differentiates event layers from continuous sedimentation. However, differences can be seen at the base and the top of the sediment section between the HSI and naked-eye chronicles. From 5.0 to 10.4 cm depth, the HSI chronicle presents a higher event frequency. This can be explained by the presence of varves (Fig. VII-4). Indeed, Unit I in Lake Bourget presents laminated sediment with a thin alternation of dark grey, light grey, and brown laminae that are hardly distinguishable visually. From 90 cm downwards, the HSI chronicle presents values of event frequency higher than expected compared to the naked-eye chronicle. This can be explained by the presence of an increasing number of very thin laminae that are non-distinguishable visually (< 1 mm). The higher number of thin layers detected by the HSI model (Fig. VII-4) explains higher values for the calculated cumulative thickness at the top and base of the core. Differences between HSI and naked-eye frequencies are thus mainly linked to human identification bias and the intrinsic low resolution of naked-eye observation. However, if HSI identification presents some bias, the combination with XRF signals can correct this effect by discarding layers that do not present peaks of selected geochemical proxies. From HSI analysis, the detected layers can only be considered as event layers interrupting the continuous sedimentation, and the origin of those deposits cannot be discussed further as the geochemical properties used for their differentiation are not available from HSI data.

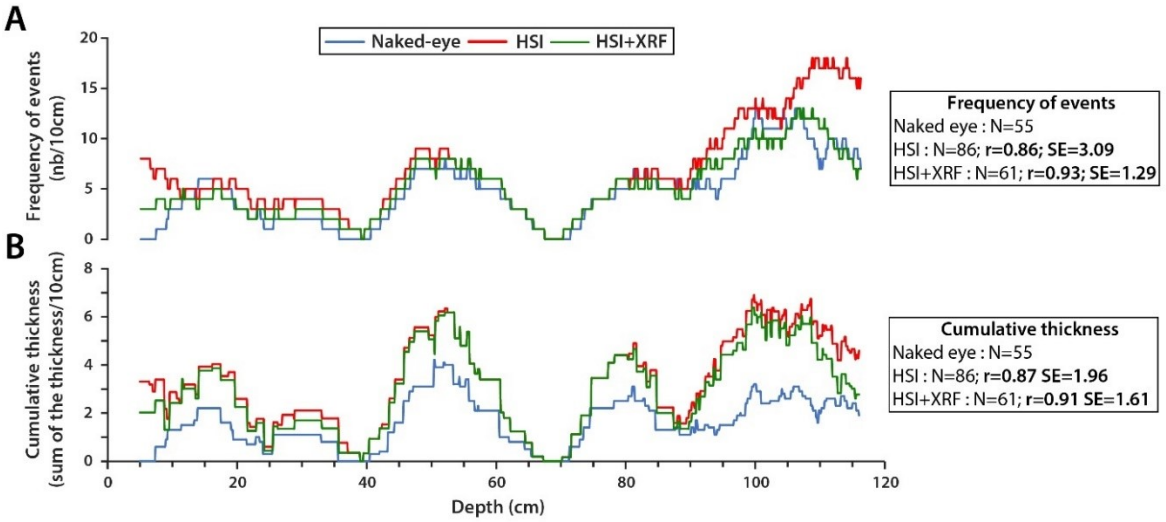

Fig. VII-6 - Comparison between the different models of the event layers and flood chronicles obtained, the naked-eye models are represented in blue, the HSI chronicle in red and the combination HSI+XRF in green. (A) Frequency of events calculated as the sum of events layers per 10 cm. (B) Cumulative thickness derived from the above chronicles. N = number of event layers detected, r = correlation coefficient, SE = standard error.

5.2. Automatic detection of flood layers

The (HSI+XRF) flood record is compared to the naked-eye one to test the robustness of the flood chronicle obtained (Fig. VII-6; Fig. VII-8). The frequency of this flood chronicle is highly comparable with the naked-eye chronicle, with r = 0.92 and SE = 1.27, as well as the cumulative thickness with r = 0.88 and SE = 1.61, respectively (Fig. VII-6). The (HSI+XRF) flood chronicle presents a better correlation with the naked-eye chronicle than the HSI chronicle alone. This can be explained by a potential over-detection of event layers by the HSI model that has been corrected by the addition of XRF signals. Indeed, a total of twenty-five deposits were discarded from the HSI model after incorporation of the XRF data interpretation. Compared to the HSI chronicle, the correlation between (HSI+XRF) and naked-eye frequencies is also higher at the top and the base of the core (Fig. VII-6; Fig. VII-8). Even if a higher number of floods are detected compare to the naked-eye chronicle, these events are confirmed by the XRF signals.

Twenty-one layers detected by the HSI model present a single Mn peak (Fig. VII-8), generally located at their base (Fig. VII-3). The homogenite-type deposit located between 31.50 and 32.10 cm depth and corresponding to the 1822 seismic event is one of them. A majority of these layers is probably linked to destabilization of slope sediments due to earthquake shaking or sediment overloading (Chapron et al., 1999). The slopes of Lake Bourget are enriched in authigenic carbonate and present a lower concentration in detrital elements (Arnaud et al., 2005). During sediment flows, water from shallower parts of the lake basin will be brought to the water-sediment interface where the concentration in oxygen is lower and will then lead to precipitation of Fe and Mn oxy-hydroxides without increasing the input of detrital elements to the lake floor. Five of these layers are located in Unit I, corresponding to a varved organic gyttja linked to recent eutrophication of the lake. The presence of a Mn peak in these laminae can be the result of changes in the oxic/anoxic regime of the bottom water at the period of sediment deposition. All these statements confirm that the Mn signal alone cannot be used to distinguish the different triggering mechanisms of event layers in a lake presenting rapid changes in oxygenation state of bottom waters, by mixing processes, and it needs to be associated with a proxy of detrital or

carbonate inputs. This also indicates that the combination of HSI model and XRF signals allows us to distinguish different triggering mechanisms for the detected event layers. Three event layers present a peak of Ti signal only (Fig. VII-8), which can be the result of the presence of a higher content of detrital elements without re-oxygenation of the deep water. This can be due to (i) a slide of previously deposited sediment from the delta, or (ii) a weak flood event, or more probably to (iii) a flood event occurring during the winter period, when water mixing in the lake occurs. At that period, underflows cannot cause re-oxygenation of deep water which explains the lack of a peak of Mn. However, these layers present a respective thickness of 1.7, 1.9 and 2.9 mm, and are distributed all along the sediment section (Fig. VII-8), then their removal from the chronicle will not have a significant impact. One other deposit does not present any peak of Mn or Ti and is located at 121 cm depth. This event layer is interpreted as an artifact linked to a change in sediment color and surface geometry at the end of the sediment section.

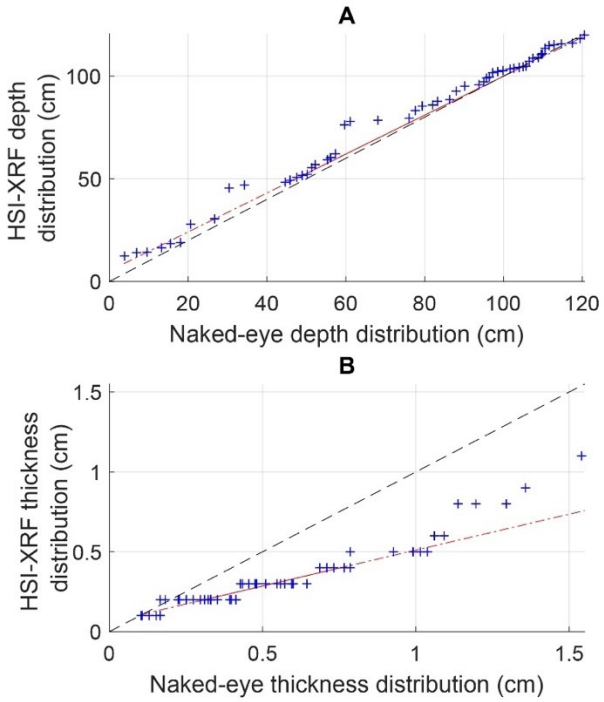

Fig. VII-7 - Quantile-Quantile plot to compare the naked-eye and the HSI-XRF distributions of the (A) depth and the (B) thickness.

The quantile-quantile plots in Fig. VII-7 allow comparison of the event layer distributions identified by naked-eye logging with the (HSI+XRF) combination. The depth QQ-plot (Fig. VII-7-A), similar to the event frequency (Fig. VII-6), shows a good agreement between chronicles. The thickness QQ-plot (Fig. VII-7-B) highlights differences with thicker deposits estimated by (HSI+XRF). This can be accounted for by (i) the curvature of the deposits and (ii) the eye resolution to see precisely the layer limits with colour variations, and this can also be seen with the millimetre steps of the naked eye chronicle.

Combining hyperspectral analysis and XRF data allows for a reliable semi-automatized flood chronicle (Fig. VII-8). This method can easily be used on other lake sediment sections to automatically detect flood layers as well as other types of event layers in a sediment sequence. The methodology could also be developed by combining other types of sensors, e.g. Visible and

near-infrared, XRD, SEM, EDS. For an (HSI+XRF) combination, the only input parameters that will vary are the XRF signals chosen by the user for the interpretation of deposit triggers, requiring a comprehensive understanding of in-lake sedimentary processes. This method allows us to detect thinner deposits compare to a naked-eye observation, with 24 deposits thinner than 1 mm on a 121 cm-long sequence and a more robust thickness estimation (Fig. VII-8) used as flood intensity proxy in some lake systems. However, the trigger of these thin deposits cannot be characterized due to the XRF resolution of this study. This methodology presents a strong advantage in that it is fast and non-destructive. Its limitations may be the large amount (here 450 Mega octets for 1 meter of core analyzed) of data generated by hyperspectral analysis and by the requirements of a comprehensive understanding of the sedimentary processes in the studied lake. The over-detection of the event layers by the HSI can be corrected using XRF data. However, an interesting perspective for future work would be its development to automatically detect event layers related to other triggers (e.g., lake level fluctuations, snow avalanches, eruptions, sediment overloading on slopes or deltas, destabilization of slopes and deltas by seismic shaking) and their classification by types of trigger. We think that the proposed methodology is useful to more precisely documented sedimentary events and related natural hazards but, will also improve the workflow by reducing analysis time on long sediment sections, allowing the rapid study of a number of sequences.

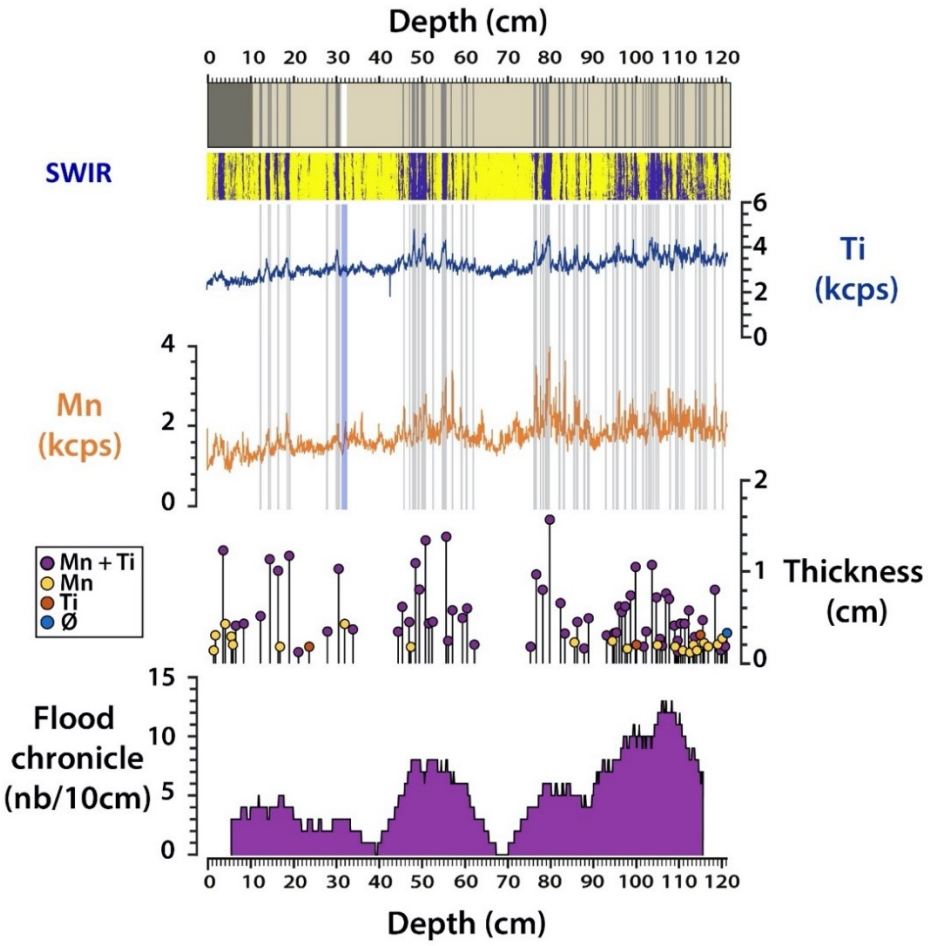

Fig. VII-8 - Synthesis of data used to produce the flood chronicle (naked-eye description, the event layers identified using hyperspectral camera SWIR and XRF data) and the main results obtained from the combination of XRF and HSI data (thickness of the event layers deposits, flood layers chronicle). Grey and blue shadings correspond to event layers identified visually.

6. Conclusion

This study presents the first semi-automatic method using multiproxy analyses to detect event layers in lake sediment in a fast and non-destructive way and allowing the direct interpretation of triggers of these deposits to create an event chronicle. One proximal sediment section of Lake Bourget was described visually, analyzed with a SWIR hyperspectral camera and XRF core-scanner. A naked-eye chronicle was made to test the accuracy of the method. From HSI analysis, event layers that differ from continuous background sedimentation were detected and counted to build an event layer chronicle that is in good agreement with the naked-eye chronicle. From XRF analysis and previous knowledge, Ti and Mn signals were selected to disentangle flood layers from other event layers. Indeed, the Ti signal is directly linked to detrital inputs into the lake coming from the main tributaries, and Mn variations are linked to water-sediment interface oxygenation during a flood event. If the event layer detected by the HSI analysis presents a peak of Mn and Ti, then they were interpreted as flood-induced deposits and added to the flood chronicle. The accuracy of this flood chronicle was then tested by comparison with the naked-eye chronicle previously made on this sediment section. The very good agreement between these two chronicles allows validation of this new method that can be applied to other sediment sections to detect event layers and to produce interpreted chronicles, and more widely used for event layer identification in other lake systems.

Acknowledgments

Hyperspectral imaging was processed at the University of Normandie-Rouen and was funded by the Region Normandie, which supports the scientific consortium SCALE UMR CNRS 3730.

CHAPITRE VIII | Synthèse des apports de connaissances sur les processus sédimentaires à l'œuvre dans les grands lacs périalpins

1. La sédimentation continue dans les lacs du Bourget et Iseo

Le lac Iseo et le lac du Bourget présentent tous deux des bassins profonds de plus d'une centaine de mètres ce qui les classent parmi les lacs les plus profonds d'Europe occidentale. Pourtant, si l'on s'intéresse à ce qui constitue la sédimentation continue de leurs bassins profonds, des différences apparaissent. Les mesures de pertes au feu réalisées indiquent des concentrations en carbonates faibles, avec une valeur moyenne aux alentours de 12% à 250 m de fond dans le bassin profond et de 10% à 100 m de fond au niveau du plateau de Monte Isola dans le lac Iseo (Chapitres III & IV). A l'inverse, ces concentrations dépassent les 70% de moyenne dans le lac du Bourget au cours de l'Holocène (Arnaud, 2005; Giguet-Covex et al., 2010). La part entre les sédiments silicatés et les sédiments carbonatées est donc totalement différentes entre ces deux lacs. Malheureusement, la part entre les carbonates détritiques, provenant de l'érosion de la partie carbonatée des bassins versants et les carbonates biogéniques, c'est-à-dire, précipité dans le lac à partir de l'activité biologique, n'a pu être évaluée dans aucun des lacs. Dans le lac du Bourget, la concentration en silice biogène est inférieure à 4% pour les sédiments de ces 200 dernières années (Giguet-Covex et al., 2010) et la gamme de variations de ces valeurs est de moins de 2%. Des données équivalentes ont été obtenus pour les sédiments des Grands Lacs d'Amérique du Nord (Conley, 1988). Il est donc possible de faire l'hypothèse que dans les grands lacs périalpins, la silice biogène n'est pas l'éléments principal composant la sédimentation continue.

La différence entre la concentration en carbonate et en éléments détritiques dans les deux lacs peut donc s'expliquer par (i) des apports détritiques de natures différentes et (ii) une préservation différente des carbonates biogéniques entre chaque lacs. En effet, soit les apports détritiques sont plus importants dans le lac Iseo, soit les apports détritiques dans le lac du Bourget sont en grande partie composés de carbonates détritiques, soit la préservation des carbonates authigènes dans le lac Iseo est moins importante que dans le lac du Bourget.

Dans le chapitre IV, nous avons montré que dans le lac Iseo, les concentrations en carbonates dissous dans la tranche d'eau augmentent fortement en deçà de 80 à 100 m de fond en relation avec une diminution des valeurs de pH de l'eau. Ces données indiquent qu'une dissolution des carbonates se produit à partir de 80m de fond dans le lac Iseo. Ceci est cohérent avec ce qui a été montré par le passé dans le lac Lugano (Ramisch et al., 1999) : à grande profondeur, dans des eaux dures, seule la calcite d'un diamètre supérieur à 40 µm atteint le fond du lac à 288 m. Les carbonates authigènes des lacs ont une faible vitesse de sédimentation et présentent généralement un diamètre inférieur à 20 µm, comme le montre les données de granulométrie des différentes fractions de carbonates mesurées dans le lac du Bourget (Arnaud, 2005). Dans

les lacs profonds, où les eaux se mélangent peu, comme dans le lac Iseo, les carbonates authigènes ne sont pas susceptibles d'être préservés lors de leur sédimentation dans le bassin profond et ne contribuent donc pas de façon significative à la sédimentation continue. La différence de profondeur et d'hydrodynamique entre les deux lacs, avec une absence de mélange des eaux de fond dans le lac Iseo depuis plusieurs décennies quand les eaux du lac du Bourget connaissent un brassage annuel, semble être à l'origine de la concentration en carbonates dans la sédimentation continue.

En effet, il est peu probable que le lac du Bourget soit influencé par des apports détritiques plus riches en carbonates que ceux du lac Iseo, les bassins versants de ces deux lacs présentant de vastes zones de couverture sédimentaire carbonatée. Toutefois, le fait que le Rhône entre dans le lac du Bourget seulement lors d'événements de crues peu avoir un impact sur la quantité de matériel détritique entrant dans le lac. Dans le cas du lac Iseo, l'Oglio, le cours d'eau drainant le bassin versant du lac, entre directement dans le lac, dans sa partie Nord. Le delta, à l'embouchure de l'Oglio, est très développé que ce soit dans sa partie aérienne ou dans sa partie sous-marine (Bini et al., 2007), ce qui signifie qu'il prograde au cours du temps sous l'effet de la charge sédimentaire apportée par l'Oglio. Ce n'est pas le cas du lac du Bourget où le delta du Rhône est peu construit relativement à celui de l'Oglio (Chapron et al., 2005).

Il n'est pas possible de distinguer les effets de la différence de dissolution des carbonates et de géomorphologie des deux lacs sur la composition de leur sédimentation continue, mais il est clair que cette dernière est appauvrie en particules détritiques dans le lac du Bourget relativement aux sédiments du lac Iseo. Lorsque l'érosion des deux bassins versant sera évaluée, il sera nécessaire de prendre en compte cette différence, qui pourra sans doute avoir un impact sur les taux d'érosion enregistrés.

2. La sédimentation instantanée dans les lacs du Bourget et Iseo

2.1. Synthèse des apports de ce travail de recherche

L'effet de la disponibilité en sédiments sur l'enregistrement des événements extrêmes dans les lacs a été exploré au cours de cette thèse. Il s'avère que dans les grands lacs périalpins, comme cela avait été démontré dans certains lacs d'altitude (e.g., Brisset et al., 2017; Wilhelm et al., 2016b) et dans une précédente étude réalisée sur un lac de plaine en Slovénie (Rapuc et al., 2018; papier disponible en Annexe I), la disponibilité en sédiment est l'un des paramètres principaux du contrôle de l'enregistrement des événements extrêmes dans les lacs. Un article de communication scientifique faisant la synthèse de cet état de fait est présenté ci-après. Par conséquent, l'homme et le climat, du fait de leur influence sur l'érosion et donc sur l'augmentation de la disponibilité de sédiments dans le lac et le bassin versant, ont un impact direct sur l'enregistrement des événements extrêmes dans les archives lacustres. Ce phénomène complexifie l'utilisation des archives lacustres dans le but de retracer les fluctuations paléo-hydrologique et /ou l'activité sismiques. Ces événements extrêmes entrainent généralement des courants de haute énergie ou des glissements de sédiments dans les lacs, perturbant ou érodant la sédimentation continue qui enregistre l'évolution et l'érosion de la Zone Critique au cours du temps. Avant d'interroger le fonctionnement de la zone critique à partir d'archive lacustres il est donc primordial d'étudier les processus sédimentaires à l'œuvre, en particulier dans les grands

lacs rendus sensibles à l'enregistrement des événements extrêmes par leur taux d'accumulation de sédiment important.

Pour ce faire et faciliter ce type d'études, le développement d'une méthode de détection des dépôts de sédiments liés aux événements extrêmes comme les crues et les séismes dans les lacs apparaissait nécessaire. Une méthode, permettant de détecter et d'interpréter de façon semi-automatique les dépôts instantanés dans les sédiments de lac a donc été développée à partir d'une séquence sédimentaire du lac du Bourget pendant cette thèse (chapitre VII). Cette méthode peut être appliquée à différents types de lacs et de sédiments. Le détail de la méthode présentée dans le chapitre VII, a fait l'objet d'une publication en cours de révision qui est présenté en annexe II. Il s'agit ici d'une avancée majeure dans le domaine de la sédimentologie, et malgré le volume conséquent de donnée lié à la technique choisi (utilisation d'images hyperspectrales), cette méthode permettra de gagner un temps précieux dans la détection et l'interprétation des dépôts instantanés dans les sédiments.

2.2. Les activités humaines perturbent l'enregistrement de la fréquence des crues dans les sédiments lacustres

Human activities disturb lake sediment records of past flood frequencies

Communication 1 | En cours de parution dans PAGES Magazine

William Rapuc, P. Sabatier and F. Arnaud

Université Grenoble Alpes, Université Savoie Mont Blanc, CNRS, EDYTEM, LE Bourget du lac, France

Human activities impact erosion and transport processes in catchments, hence disturbing paleoclimate recording. A thorough study of erosion patterns is therefore necessary to disentangle climate and human forcing when interpreting lake sediment-based flood chronicles.

Flood frequencies as a proxy of past extreme precipitation events

In the current context of global climate change, predicting the evolution of precipitation is particularly challenging: an increase of extreme events is expected globally due to the capacity of a warmer atmosphere to hold more water, although regional trends may differ (IPCC, 2012). Assessing this requires the acquisition of long-term hydrological datasets (Wilhelm et al., 2019). As flood occurrence and magnitude are linked to precipitation-regime fluctuation through time, the establishment of regional flood chronicles from natural archives could be a key to evaluate the evolution of precipitation regimes on emerged land (Wilhelm et al., 2017a).

Of all the natural archives that lend themselves to such reconstructions, lakes are a prime candidate, as they are widely spread across all continents and act as natural sinks, continuously trapping erosion products from an entire catchment over a long period (Wilhelm et al., 2018). Indeed, during flood events, water-transported detrital particles are deposited on the lake bottom in the form of graded layers that differ from the in-lake continuous sedimentation. The

identification of these events, by naked-eye observation or using new methodologies (Rapuc et al., 2020b), allows scientists to establish flood-occurrence chronicles. In some cases, the thickness and/or the maximum grain size of deposits can be used to assess the intensity of flood events and even decipher past current-flow velocities (Arnaud et al., 2016; Evin et al., 2019). Numerous studies have thus used flood frequency and intensities based on lake sediments to reconstruct hydrological variations through time (Czymzik et al., 2013; Glur et al., 2013; Wilhelm et al., 2018). However, within a given lake system, the amount and physical characteristics of river-borne sediment not only depend on precipitation patterns, but also on the sediment availability, which is a function of soil erodibility and transport processes.

Impact of human activities on erosion and transport processes

Sediment availability and transport processes are forced by both climatic fluctuations and human activities. Consequently, provided that the climatic conditions and methodologies of reconstruction are the same, discrepancies between flood chronicles in the same region should provide evidence of the influence of human activities. The Italian Southern Alps offer an ideal playground for such an experiment. Several lakes in this region have been studied and many flood chronicles have been produced; for example, Wirth et al., (2013) computed a Holocene synthesis of flood frequencies from five lake sediment sequences from the Southern Alps.

Recently, we produced two flood chronicles from two sediment sequences taken from Lake Iseo, a large perialpine lake. The SEB18 sequence was sampled in the deep basin of the lake, fed by a large catchment (1842 km²). The SEB10 sequence (Rapuc et al., 2019) was retrieved in a shallower basin fed by sediment from a small catchment area (46.5 km²). The SEB10 flood chronicle is consistent with the regional extreme precipitation trend until the Roman Period (approx. 2 kyr cal BP), with an important increase in recorded flood frequency around 4.2 kyr cal BP, reflecting a shift towards wetter climate in Europe (Fig. VIII-1; Wirth et al., 2013). However, the SEB10 sequence differs from the Southern Alps synthesis for periods when human activity is important in the Lake Iseo catchment (Fig. VIII-1). For instance, during the Little Ice Age (LIA, 1300–1860 CE), flood activity in the Southern Alps was high due to a regionally colder and wetter climate, resulting in more frequent precipitation events. However, very few flood layers were deposited in the shallower basin of Lake Iseo at that time. We interpreted that discrepancy as resulting from the anthropization of the main tributaries (streams or rivers flowing into a larger stream or a main stem) through damming, thereby reducing sediment flux to the lake (Rapuc et al., 2019). At that study site, the creation of dams and channels in catchments generally deflected the river flow and trapped sediment upstream, hence reducing the sediment flux to the lake basin and the apparent flood frequency in the lake sediment record.

A different scenario was documented in SEB18. In this sequence, high flood frequencies are recorded during the Medieval Warm Period (950–1250 CE), and frequencies are lower than expected during the LIA (Fig. VIII-1), in contrast to the regional trend (Sabatier et al., 2017; Wirth et al., 2013b). Here, human activity is suspected to have impacted the erosion cycle in the catchment through grazing, agricultural activities, and deforestation, all of which leading to soil destabilization (Fig. VIII-2). When soil erodibility increases and more sediment becomes available, the precipitation intensity necessary to entrain particles from the soil surface decreases (Renard et al., 1991). Hence, even a moderate precipitation event may be recorded as a graded layer in the lake basin, which artificially increases the flood frequency in the sediment record.

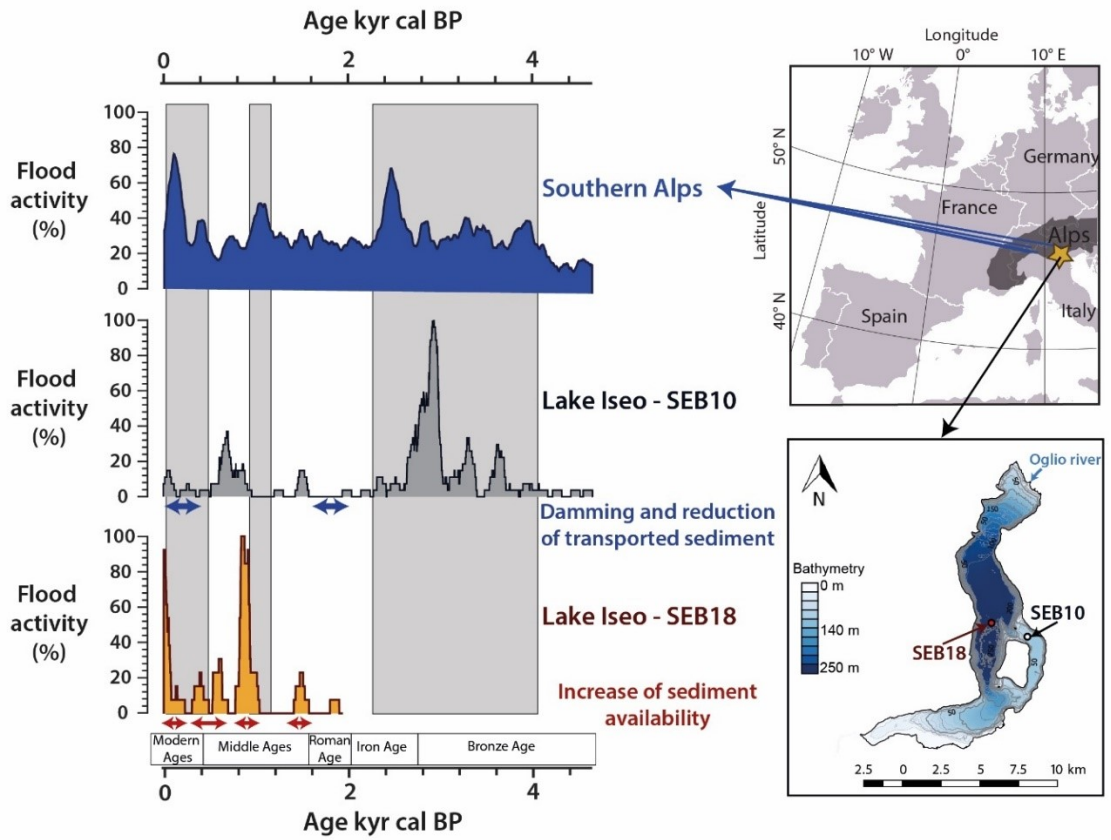

Fig. VIII-1- Flood activities modified from the Southern Alps synthesis of Wirth et al., (2013), the SEB10 (Rapuc et al., 2019) and SEB18 (unpublished yet) sediment sequences from lake Iseo. Activity is calculated as a ratio of the instantaneous frequency and the maximum frequency measured in the sequence.

The comparison of the SEB10 and SEB18 sequences, taken from different sedimentary basins in the same lake, revealed different lake sediment responses to the same climate forcing factors (Fig. VIII-1). Moreover, the rise in flood frequency recorded in SEB10 during the High Middle Ages (1000–1250 CE) is delayed by 200 years compared to the SEB18 record. As all other factors are similar at these two core locations, only human-triggered changes in sediment availability or transport processes at the scale of catchment areas can explain these differences.

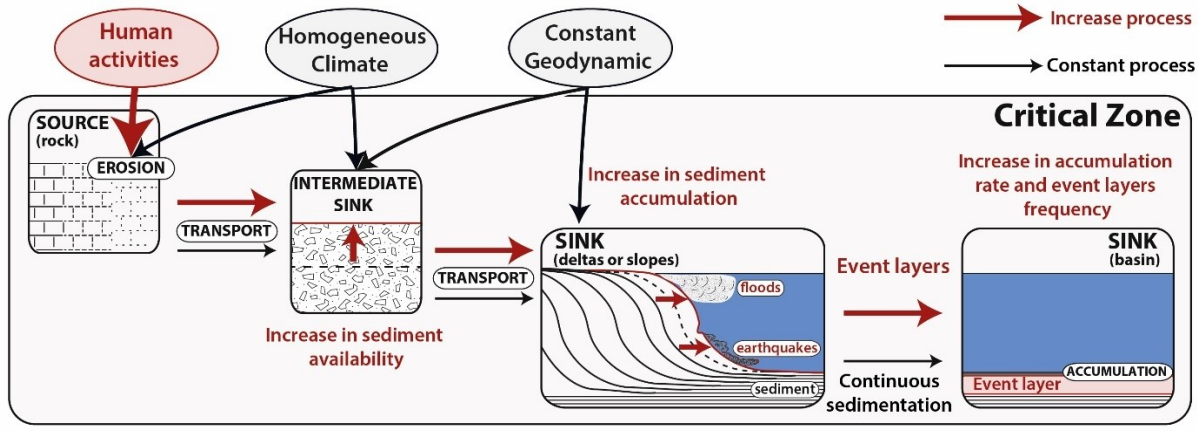

Fig. VIII-2 - Conceptual model of the Critical Zone erosion cycle in a large catchment and the effects of the three main forcing factors: climate, geodynamics and human activities.

Summary and future work

Flood chronicles (frequencies and magnitudes) from lake sediments are robust paleoclimatic proxies in the absence of human activity modifying sediment availability in the catchment. However, when human activity affects the Critical Zone (CZ), defined as the reactive skin of our planet at the interface of lithosphere-atmosphere-hydrosphere-biosphere, by increasing erosion, resulting in increased sediment transport and remobilization, the sensitivity of a lake as a natural archive of the CZ dynamic is disturbed. A human-triggered increase in soil erodibility and sediment availability may therefore result in a decoupling of the recorded flood frequency and the regional climatic conditions. Inversely, stream management can result in drastic decrease of river-borne sediment input. A similar phenomenon may result from other geodynamical processes, such as earthquakes (Rapuc et al., 2018): the sensitivity of a lake to record seismic shaking increases when sediment accumulation in the delta and on lake slopes increases (Fig. VIII-2). To study paleohydrologic or geodynamic fluctuations, the safest way is then to investigate sediments retrieved from high altitude zones (Sabatier et al., 2017). However, large lakes draining large catchment areas offer us the opportunity to observe large-scale precipitation patterns. They are thus valuable resources for reconstructions of past flood frequency, if we consider together the three main forcing factors driving erosion patterns and CZ dynamics throughout the Holocene: climate, geodynamics, and human activities (Fig. VIII-2).

Partie III | Évaluation quantitative des effets des forçages humains et climatiques sur l'érosion dans les Alpes au cours de l'Holocène

CHAPITRE IX | Quantitative evaluation of human and climate forcing on erosion in the Alpine Critical Zone over the last 2,000 years

Article 4 | En review dans Quaternary Science Letters

William Rapuc[1], Julien Bouchez[2], Pierre Sabatier[1], Kim Genuite[1,3], Jérôme Poulenard[1], Jérôme Gaillardet[2,4] and Fabien Arnaud[1]

[1] Univ. Grenoble Alpes, Univ. Savoie Mont Blanc, CNRS, EDYTEM, 73000 Chambéry, France
[2] Université de Paris, Institut de physique du globe de Paris, CNRS, F-75005 Paris, France
[3] UMR 6266 IDEES, University of Rouen Normandy, CNRS, 76130 Mont St-Aignan CEDEX, France
[4] Institut Universitaire de France

Abstract

Soil erosion is one of the main environmental threats affecting the Critical Zone (CZ) and thus ecosystem services and human societies. Through time, the physical erosion is linked to both, climate variations, and the landscape evolution under long-term human pressures. In mountainous areas where erosion is highest a combination of large spatial and temporal approaches allows to assess the effect of these forcing factors on erosion rates. Here, we apply a retrospective approach based on lake sediments to reconstruct the long-term evolution of erosion in alpine landscapes. Lake Iseo in Italian Alps acts as a natural sink for all the erosion products from a large catchment (1777 km²). This catchment is representative of the southern Italian Alps, where Holocene human activity and climate fluctuations are well known. The approach combines a source-to-sink method, using isotopic geochemistry (εNd, $^{87}Sr/^{86}Sr$) associated to a multiproxy study of a lacustrine sediment section covering the last 2000 years. The applied methodology allows us to disentangle the role of climate and land use as erosion forcing factors through their differential impact on the various rock types present in the catchment. Indeed, the high-altitudinal part of the Iseo catchment, where glacier advances and retreats drive the erosion, presents isotopic signature different from those of the sedimentary rocks located in the lower part of the catchment, where both human activities and precipitations impacted erosion through time. A chronicle of glacial erosion over the last 2000 years was produced. Once the climatic trend was highlighted, the signal of erosion of sedimentary rocks was investigated to understand the influence of humans. From the Roman Period to the Industrial Age several periods of deforestation and increased human pressure were documented. The past sediment yield inferred for sedimentary rocks exhibits the highest values (> 80 $t.km^{-2}.yr^{-1}$) at periods of intense human practices. Hence, since the late Roman Period, human activities seem to be the dominant forcing factor of the physical erosion in mountainous environment of northern Italy. This study presents the first reconstruction through time of sediment yield derived from lake sediments

associated with sediment sources identification and quantitative evaluation of the CZ erosion drivers.

KEYWORDS

Erosion, Human impact, Lake sediments, Source to sink method, isotopic mixing model

1. Introduction

Erosion is a geological process that, on long timescales, impacts the Earth's topography, tectonics and climate (e.g. Gayer et al., 2019 and references therein). Currently, erosion is also the main process leading to the deterioration of the Critical Zone (CZ), defined as the thin active layer at the Earth's terrestrial surface, which is hosting life forms. Among other impacts, by destroying soils, erosion alters food production, drinking water quality, ecosystems services, biodiversity, and soil carbon stocks (e.g. Bosco et al., 2008; Panagos et al., 2015). Erosion also affects directly human societies (Montgomery, 2012), especially in mountainous environments (Bosco et al., 2008) and has thus become a scientific subject of prime importance worldwide (Borrelli et al., 2020; FAO, 2015; Panagos et al., 2015b; Rusco et al., 2008). Increasing concern about these deleterious effects have led Europe and the United Nations to rank soil erosion as one of the main threats to mankind, and to call for quantitative evaluation of soil loss over large spatial and long temporal scales (e.g. Panagos et al., 2015 and references therein). These evaluations imply notably to better assess the relative effects of the main factors controlling erosion. In particular, climate (for example through the precipitation regimes and glaciers advances and retreats) and human activities (through land-use and vegetation cover management) have been identified as major controls on long-term changes in erosion rates (e.g. Panagos et al., 2015).

Besides the use of modelling approaches (e.g. Angima et al., 2003; Borrelli et al., 2020; Millward and Mersey, 1999; Panagos et al., 2015; Renard et al., 1991), this knowledge gap can be filled through the acquisition of empirical constraints provided by the study of lake sediment archives, in particular with the aim of evaluating erosion rates over the centennial to millennial time scales over which climatic and human forcing are the most likely drivers of erosion (e.g., Arnaud et al., 2016). Although regional syntheses of erosion rates over these time scales exist, in particular for the European Alps (e.g. Hinderer et al., 2013 and references therein), only a few studies have produced a quantitative assessment of erosion rates through time (e.g. Bajard et al., 2020), but none on the quantitative impact of the various factors. The "source-to-sink" approach (e.g. Collins and Walling, 2002) offers the possibility to track the sources of sediment inputs (sub-catchments and/or rock types) to a sink (e.g., a lake) through time, making it in turn possible to disentangle the relative impacts of climate and human activities upon erosion rates, provided that each sediment source is sensitive to a given type of forcing.

For this study, we selected Lake Iseo, located in the Italian Alps, at the downstream end of the Val Camonica valley, an area where human activities since the beginning of the Neolithic period are well documented (e.g. Pini et al., 2016 and references therein). Lake Iseo drains a large catchment that can be split into three main sediment source areas, distinguishable through the means of geochemical tools, and coinciding with different relative roles of climatic and human forcings on erosion over the centennial to millennial scales:

(i) The northernmost, high-altitude part of the catchment underlain by calco-alkaline series and where numerous glaciers have shaped the landscape (Scotti et al., 2013);

(ii) The mid- to high-altitude part of the catchment underlain by metamorphic Variscan basement rocks where both glaciers and human activities have impacted erosion (Pini et al., 2016; Scotti et al., 2013)

(iii) The southernmost, low- to mid-altitude part of the catchment underlain by Permian to Cretaceous sedimentary cover, and the locus of most human activities in the Val Camonica since the beginning of the late Holocene (Pini et al., 2016 and references therein).

To quantify the evolution of erosion in the catchment of Lake Iseo over the late Holocene, we selected a sediment sequence retrieved in the deep depositional basin of the lake, where most of the fine-grained sediment inputs from the catchment have been captured. This sediment sequence hosts the erosion products for the last 2,000 years (Rapuc et al., 2020). River samples were also collected from all the sub-catchments directly contributing to Lake Iseo. Neodymium (Nd) and Strontium (Sr) isotopic compositions and concentrations of river and lake sediments were used to constrain the results of a mixing model. Results from the model yielded quantitative contributions of each sediment source, allowing us to disentangle the effects of climate fluctuations and human activities on erosion in the Iseo catchment from the Roman Period to the present day.

2. Study sites

Lake Iseo (45°44.205′N; 10°4.340′E) lies in the Italian Alps, at the southern end of the Val Camonica valley at an altitude of 185 m a.s.l (above sea level). The lake is 25-km long and has a surface area of 60.9 km^2. The sedimentation in the deep basin was recently investigated through the study of the "SEB18" sediment sequence (Rapuc et al., 2020a), used in the present contribution.

Lake Iseo is fed in water and sediment by the Oglio River, which originates in the Adamello Massif, and is the main lake tributary and unique outlet (Fig. IX-1). Upstream from Lake Iseo, the Oglio River drains a large catchment of 1,777 km^2 with a maximum elevation of 3,539 m a.s.l in the Adamello Massif and a mean altitude of 1,400 m a.s.l (Garibaldi et al., 1999). The Oglio catchment is limited to the North and East by the Insubric line, one of the main lineaments of the European Alpine (Mittempergher et al., 2021), separating the Austroalpine domain (N) from the southern Alps (S). Rocks of high alpine metamorphic grade from the Austroalpine unit exist at the extreme northern limit of the catchment but constitute very small areas (Chiesa et al., 2011; Gosso et al., 2012).

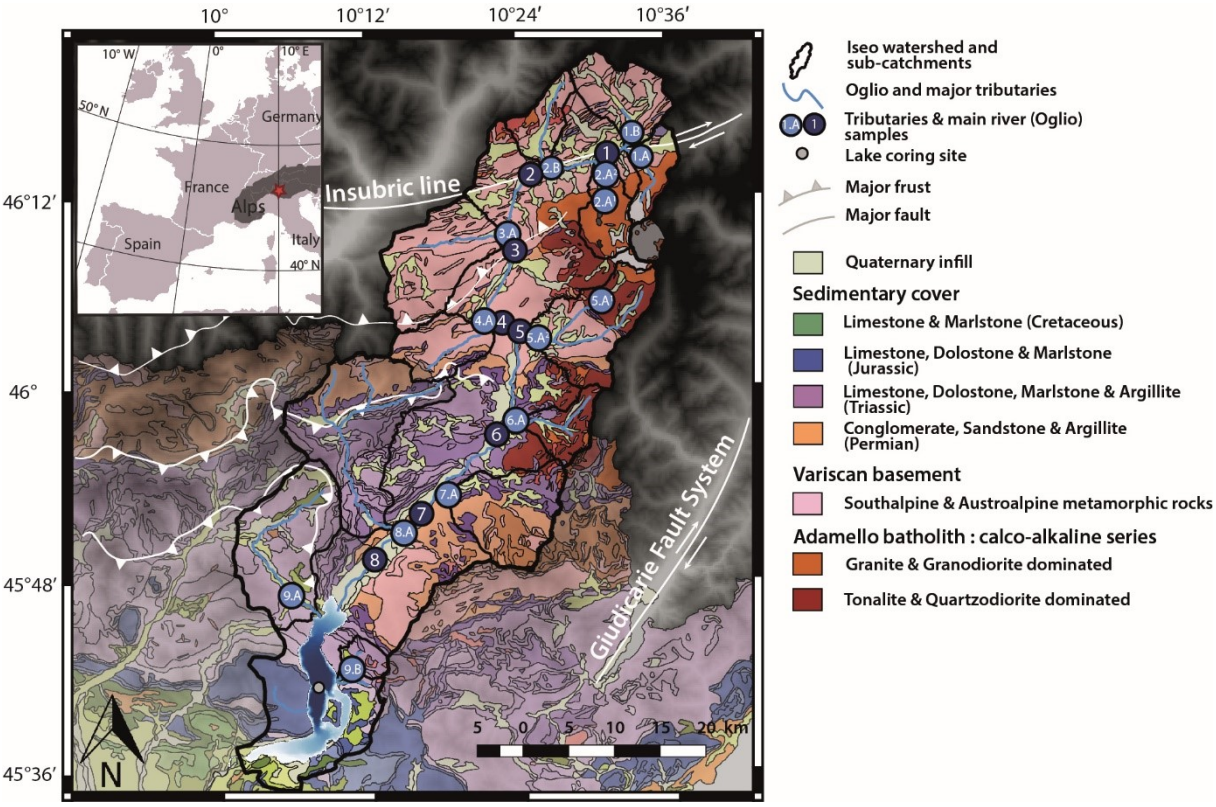

Fig. IX-1 - Geological map of the study area, superimposed on a shaded relief map, and location of sampling sites. The geological information is modified from the geological map of Lombardy (CARG project; https://www.cartografia.servizirl.it/cargviewer/). The tributaries (blue) and sub-catchments (boundaries in black) of the Oglio River and the SEB18 lake sediment coring site are also shown (grey circle). Lake Iseo bathymetry is modified from Pilotti et al. (2013) and is available at https://hydraulics.unibs.it/hydraulics/attivita-scientifica/laghi_pvbs/lake-iseo-data-set/.

The faulted Variscan basement of the southern Alps is made of Low- to high-metamorphic grade rocks (pelites, schists, amphibolites, gneiss) visible in the North and West part of the Upper Oglio catchment. To the South, the catchment is underlain by the sedimentary cover of the southern Alps, mainly composed of Triassic, Jurassic, and Cretaceous marlstones, limestones, and dolostones, associated with outcrops of Permian sandstones (Bini et al., 2012).

The NE part of the catchment area is underlain by the famous Adamello batholite which is a plutonic series of calco-alkalines of Cenozoic age (30 to 40 Ma) that intruded the old southern Alps Variscan basement (Mittempergher et al., 2021). The Adamello massif is mainly composed of felsic plutonic rocks such as tonalites, granites, granodiorites, and quartzodiorites, with some minor outcrops of mafic to ultramafic rocks (Brack et al., 2008). The Glaciers and rock glaciers are particularly numerous in this part of the catchment (Scotti et al., 2013) and are suspected to have strongly impacted erosion in the area.

In terms of human occupation, the southernmost area, closest to the lake, is located at low to mid altitude, and is where human activities are currently concentrated (Fig. IX-2). Archaeological and palynological studies also locate the main human settlements and agrarian activities within this area since the Neolithic (e.g. Marziani and Citterio, 1999; Pini, 2002; Pini et al., 2016). Human activities in rest of the catchment area is sparse, restricted to herd grazing and only minor urban areas, both for modern times (Fig. IX-2) and in the recent past (Pini et al., 2016).

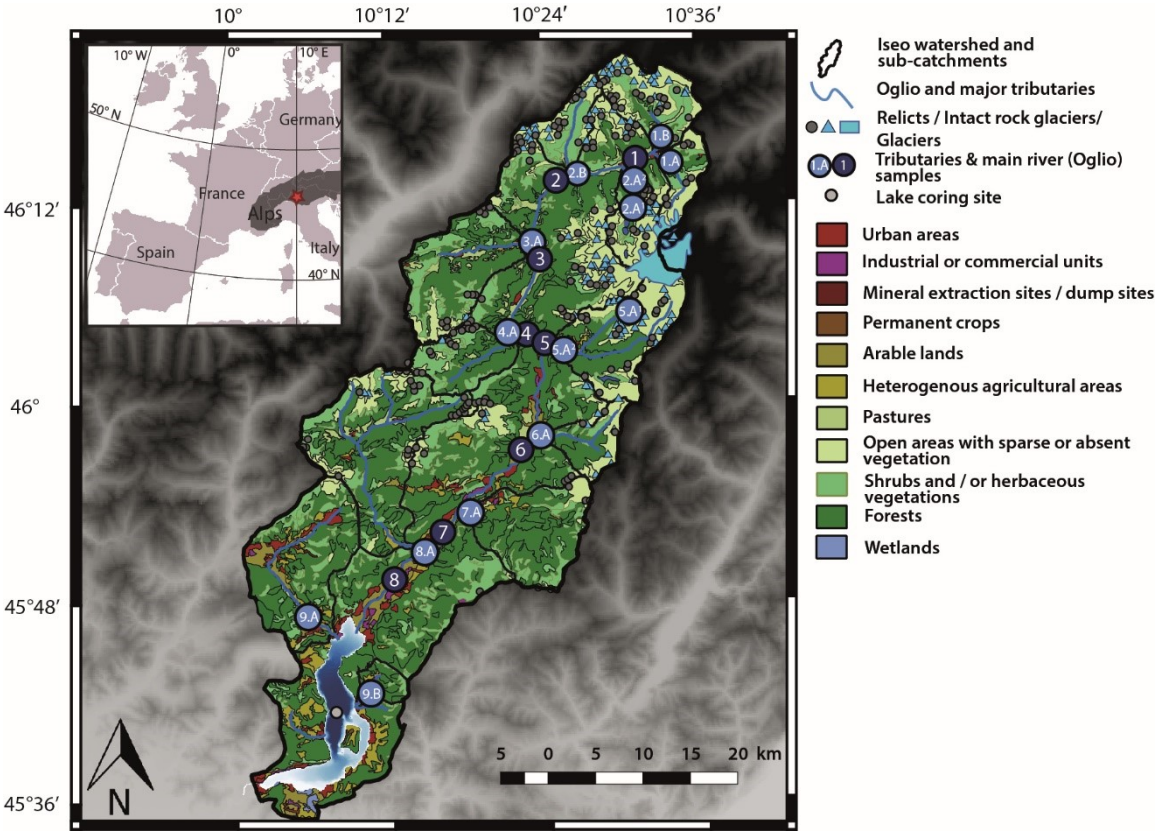

Fig. IX-2 - Land-use map of the study area, superimposed on a shaded relief map, and location of sampling sites. Land use information is derived from the CORINE land cover map for Lombardia, available here: http://www.geoportale.regione.lombardia.it/. Locations of glaciers, relicts, and intact rock glaciers are derived from Scotti et al. (2013).

3. Materials and Methods

3.1. Lake and river sediment samples

In October 2018, a 15.5-m-long sediment sequence called "SEB18" (45°43.536'N; 10°3.888'E) was retrieved from the deep basin of Lake Iseo, at 251 m below the lake surface (b.l.s). This sequence covers the last 2,000 years (Rapuc et al., 2020a). In the deep basin, continuous sedimentation accounts for only 39 %, with the rest of the accumulation being made of numerous interbedded thick to very thick (> 1 m) layers deposited during instantaneous events. The grain size of the material deposited during the continuous sedimentation is largely dominated by fine silts and clays (median < 10 µm; Rapuc et al., 2020). Thirty 1 cm-long sediment samples were collected using graduate syringes for geochemical analyses (sections 3.2 and 3.3). Due to the presence of event-specific sediment layers, a continuous sampling step was impossible to apply (supplementary Table S1). Sediment density was measured using sediment samples of an invariant 5 mL volume.

To characterize the source of sediments accumulated in Lake Iseo deep basin, 14 river sediments samples were collected in May 2018 from flood deposits in all sub-catchments directly contributing to the Oglio River, close to the confluence with the main river (Fig. IX-1; Table S2). Eight samples were also collected from flood deposits in the Oglio main valley at several hundred meters downstream of each confluence to test for the mixing between sub-catchment and main

river sediments (Fig. IX-1; Table S2). Sub-catchments covered by this sampling set represent 52 % of the Iseo catchment total area. Samples were collected manually, an aliquot of each sample was sieved, and only the fraction finer than 63 µm was saved for later analysis, to account for the fact that the sedimentation in the studied lake sediment core is mostly of silty to clayey nature.

Even in carbonate-dominated terrains, soil physical erosion occurs mostly through the removal of silicate phases, as carbonate minerals tend to be removed from soils through chemical dissolution. For this reason, our analysis focuses on siliciclastic material, and we removed the carbonate component of the lake and river sediments before geochemical analyses. Although the authigenic carbonate production is poorly preserved in the deep basin of Lake Iseo (Rapuc et al., 2020), this procedure also ensures that authigenic lake carbonates do not affect our interpretation. To that effect, after crushing in an agate mortar and drying at 60°C for 72 h in a laboratory oven, river and lake sediment samples were decarbonated by two successive 5 mL HCl 0.5N leaching steps to remove authigenic and detrital carbonate (supplementary S3). Major and trace elements of supernatants from each leaching step were measured by Q-ICP-MS (section 3.2) to evaluate the amount of calcium (Ca) and Sr lost. As discussed below, this leaching procedure did not lead to complete removal of the carbonate component from the river sediment samples, which might be due to the presence of dolomite in the sediment.

A series of river sediment samples was kept unleached and measured as bulk powder for isotope and major and trace element concentration measurements. All samples (bulk or residue from the leaching steps), then underwent a digestion using concentrated acid mixtures of HF, HNO_3, and HCl.

3.2. Major and trace elements

Major and trace element concentrations were measured using an Agilent 7900 quadrupole ICP-MS (Q-ICP-MS) at the High-Resolution Analytical Platform (PARI) of the Institut de physique du globe de Paris (IPGP), detailed information on the method is provided in S5. The detection limit was between 0.2 and 0.5 ppt depending on the element, and the internal errors were 5% on average. The weight loss during carbonate leaching of lake (and river in some cases) sediments was considered in the estimate of major and trace element concentrations of the residue, such that the reported concentrations relate to the mass of residue (that is, carbonate-free, and referred to as “silicate” in the following) component of the sediment (supplementary S4).

3.3. Isotopic composition

Isotope measurements were all performed at the PARI analytical platform of IPGP. After powder digestion, Sr and Nd were separated from the sample matrix by extraction chromatography. We used an Sr-SPEC resin (Eichrom) for Sr (Hajj et al., 2017) and a combination of TRU-spec and Ln-spec resins for Nd (Cogez et al., 2015). Sr and Nd isotope ratios were measured by multi-collector inductively coupled plasma mass spectrometry (MC-ICPMS; Neptune, Thermo-Fisher Scientific). Details of the methods are present in supplementary S5.

Sr measurement accuracy was checked through repeated measurements of the NIST pure-Sr, isotope reference material SRM 987 (2 S.D of 2.9 x 10^{-5}), and the NIST soil reference material SRM 2709a ($^{87}Sr/^{86}Sr$ = 0.70823 ± 0.00002; comparing well with the value provided by Brazier et al., 2020 of 0.70814 ± 0.00002). Each sample was measured up to three times during a session. For samples measured three times, the 95% confidence interval was obtained from

Student's *t*-distribution and ranged from 3 x 10^{-6} to 8 x 10^{-3}. For other samples measured less than 3 times, the 2 S.D of 4.9 x 10^{-5} estimated from the repeated measurements of the reference material NIST SRM 2709a (processed through powder digestion and separation as for samples) was used as an estimate of the 95% confidence interval.

Nd accuracy was checked through repeated measurements of a NIST pure-Nd, isotope reference material (143Nd/144Nd = 0.511418; Caro et al., 2006), with a measured 2 S.D of 2.7 x 10^{-6}, and the NIST soil reference material SRM2709a (0.512381 ± 0.000028). For convenience we report Nd isotope ratios as εNd values:

$$\varepsilon\mathrm{Nd} = \left(\frac{\left(^{143}\mathrm{Nd}/^{144}\mathrm{Nd}\right)_{samples}}{\left(^{143}\mathrm{Nd}/^{144}\mathrm{Nd}\right)_{CHUR}} - 1 \right) \times 10\,000$$

with $\left(^{143}\mathrm{Nd}/^{144}\mathrm{Nd}\right)_{CHUR}$ (CHUR standing for "chondritic uniform reservoir") equal to 0.512638 (Jacobsen and Wasserburg, 1980). Each sample was measured once twice during a session, and the 95% confidence interval of the measurement was estimated from the 2 S.D. was estimated at 0.4 εNd unit from repeated measurements of the NIST reference material SRM2709a at mass spectrometric signal levels similar to those of samples.

4. Results and interpretations

All the results of lake (sink) and river (source) sediment geochemistry are presented in Fig. IX-3 and Fig. IX-4 and in supplementary Table S1 & S2.

4.1. Lake samples

A detailed description of SEB18 is provided in Rapuc et al. (2020). The age depth-model of the SEB18 sequence was constrained by a combination of short-lived radionuclides, varve counting, and ^{14}C ages. The resulting mean sedimentation rate (SR) is 3.1 mm.yr^{-1} over the last 2,000 years. The material making the continuous sedimentation of the lake Iseo deep basin mainly consists of detrital silicates. Indeed, most of the lake authigenic carbonate is dissolved within the water column whereas the organic matter content is under 8 %, and detrital carbonates account for less than 18 % (Rapuc et al., 2020a).

In the siliciclastic fraction of Iseo Lake sediments, the ^{87}Sr/^{86}Sr ratio ranges between 0.730 and 0.722 with a significant increase from 97 to 1033 CE followed by a decrease until 1265 CE, and then relatively high values with successive high and lows until the present day (Fig. IX-3). Values of εNd are relatively invariant and range between -11.8 and -10.4 (Fig. IX-3), with only two notable excursions towards higher values from 907 to 1185 CE and from 1551 to 1872 CE.

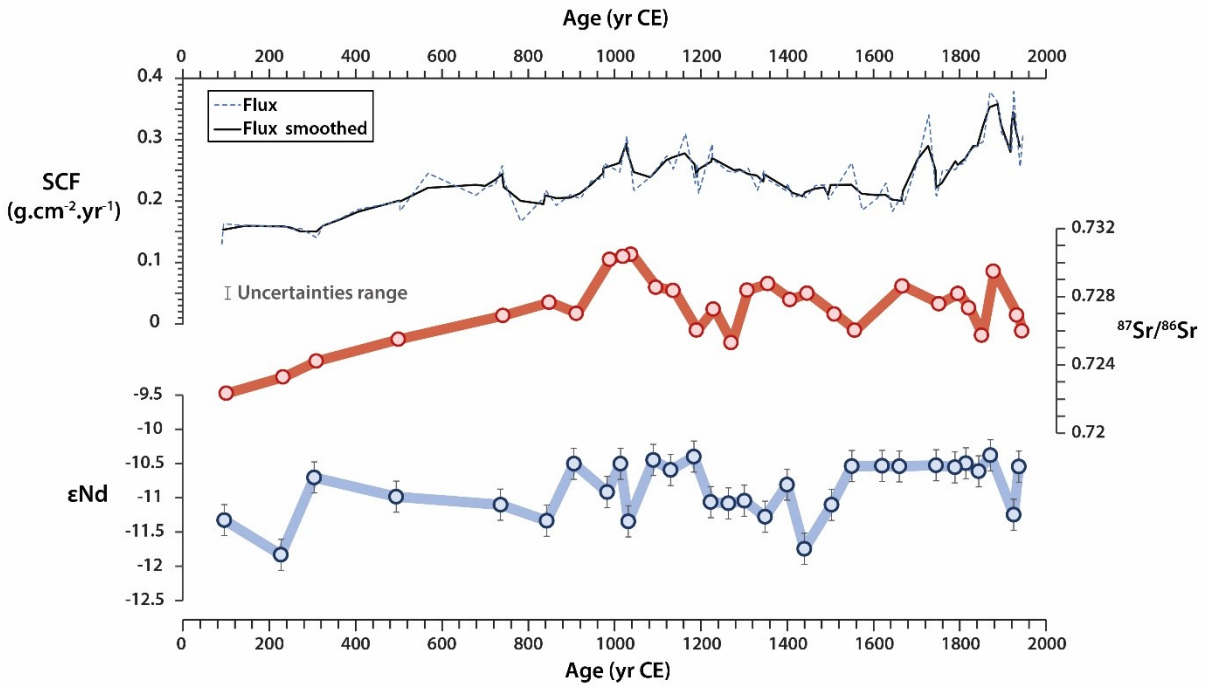

Fig. IX-3 - Silicate detrital sedimentation rate (SCF, for siliciclastic flux) and Sr and Nd isotope ratios of Lake Iseo over the last 2,000 years obtained from lake sediment SEB18 sediment sequence. The siliciclastic flux was obtained from loss on ignition analyses, age-depth modelling and density measurements (Rapuc et al., 2020a). Error bars on the 87Sr/86Sr and εNd curves represent the 95% confidence intervals corresponding to analytical uncertainty.

4.2. River samples

River sediments taken in Oglio sub-catchments are characterized by εNd values ranging from -5.5 to -13.4 (Fig. IX-4). Sediment samples from the northern, high-altitude basins, thus reflective of the calco-alkaline-type rock sources present the most radiogenic values: -5.5 to -6.3 for sub-catchments essentially underlain of tonalites (6.A and 5.A1) and -8.4 to -9.7 for granite dominated sub-catchments. Southern sub-catchments draining sedimentary rocks display εNd values ranging from -8.3 to -10.5, while sub-catchments dominated by Variscan metamorphic rocks present the highest variability in εNd values, from -10.1 to -13.4.

$^{87}Sr/^{86}Sr$ ratios for leached river sediment samples range from 0.708 to 0.726. Northern Oglio sub-catchments dominated by calco-alkaline series display low $^{87}Sr/^{86}Sr$ values, from 0.708 for tonalite-dominated catchments to 0.712 for granite-dominated catchments. Sub-catchments underlain mostly by Variscan metamorphic rocks are characterized by $^{87}Sr/^{86}Sr$ ratios ranging from 0.718 to 0.723. Southern sub-catchments draining sedimentary rocks present $^{87}Sr/^{86}Sr$ ratios from 0.725 to 0.726. At face value, none of the $^{87}Sr/^{86}Sr$ ratios from the sampled sub-catchments can explain the most radiogenic ratios observed in lake sediments (Fig. IX-4). Bulk values are presented in Table S2 and Fig. S2 and display systematically lower $^{87}Sr/^{86}Sr$ values for sub-catchments where limestones and dolostones crop out. Oglio River samples εNd values range between -7.5 and -11.8, whereas their 87Sr/86Sr ratios range from 0.716 to 0.721 (Fig. IX-4).

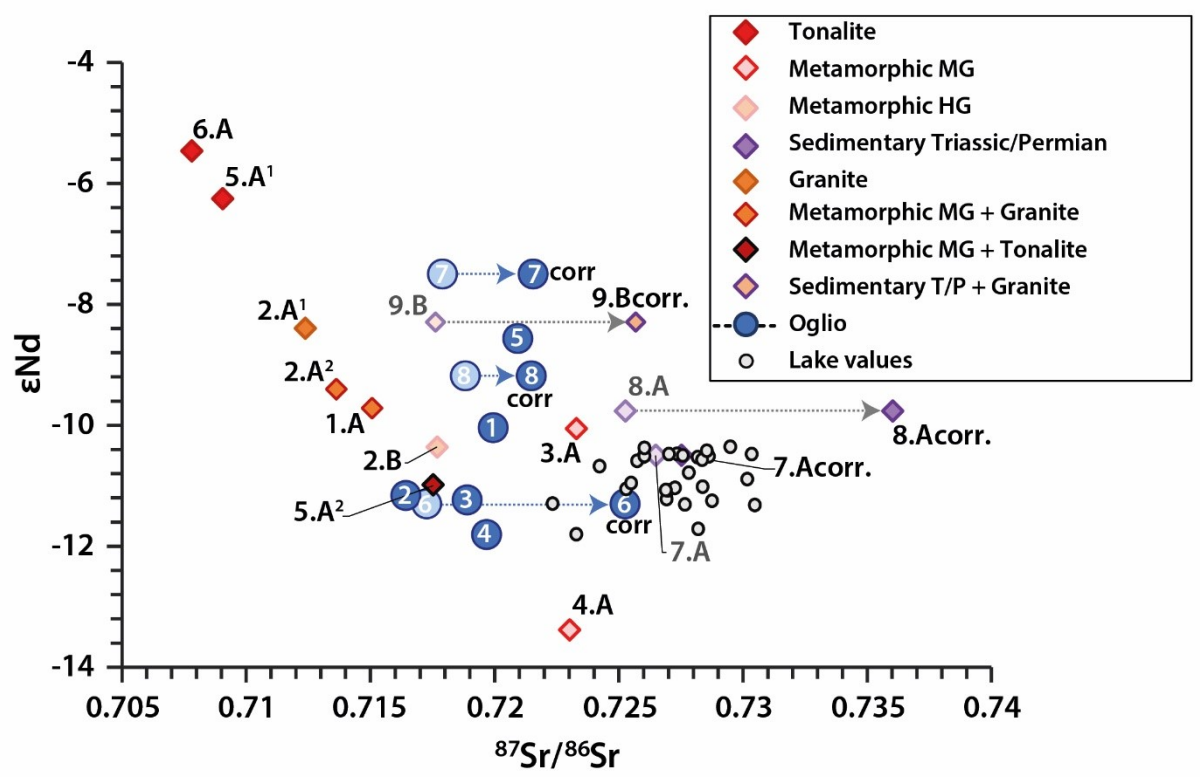

Fig. IX-4 - Nd and Sr isotope composition of Lake Iseo siliciclastic sediment samples (small grey circles), and of river sediment samples from the Oglio sub-catchments upstream from Lake Iseo (diamonds) and from the Oglio main valley (large blue circles). Oglio sub-catchments symbols (diamonds) are coloured as a function of the dominant rock types underlying the catchment. Oglio main valley sediment samples (blue circles) are numbered as in Fig. IX-1 & Fig. IX-2. Dotted arrows represent the correction from carbonate contribution performed for river samples originating from sub-catchments underlain by limestone, as constrained by mild acid leaching steps (section 3.1; supplementary S3).

4.3. Interpreting Sr and Nd isotope ratios in term of sediment source fingerprinting

Two main assumptions are made here for the interpretation of the Sr and Nd isotope data from Lake Iseo and Oglio River in terms of the contribution of each rock source to the detrital sediment input to the lake:

- All the major sediment sources contributing to detrital inputs to the lake were sampled.
- The isotopic signatures of the various potential rock sources have remained constant over the period considered.

Because we removed the carbonate component of the lake and river sediments, the Sr-Nd isotope signatures of lake samples can be interpreted as a mixture of the identified silicate sources. In order to quantitatively deconvolve the contributions of the dominant rock sources through time, end members need to be identified, and their signatures need to be constrained. To that effect, we selected sediment samples from sub-catchments presenting a homogeneous lithology (Fig. IX-5-A). Indeed, samples from the Oglio River and sub-catchments with heterogeneous lithology (Fig. IX-1) result from a mixture of several rock sources on their own, such that considering them would not provide independent constraints on the composition of the end members. River sediment samples for which only one out of the two isotope signatures was available were not considered either.

Out of the remaining 8 samples, three main sources can be identified and summarized into: i) calco-alkaline rocks ("A"), ii) metamorphic ("B") and iii) sedimentary ("C") rock sources.

Sub-catchments draining mainly rocks from the calco-alkaline series (6.A, $5.A^1$, $2.A^1$) were gathered into a single "calco-alkaline" source. Minor marlstone and limestone outcrops are also present in these areas, especially in $2.A^1$ sub-catchment (Fig. IX-1) which may explain the lower εNd values measured for some sub-catchment samples compared to the values reported for the rocks themselves (+3.8 to -4.9; Kagami et al., 1991). This end member is sourced from the high-altitude Adamello massif (Fig. IX-1). Several glaciers and rock glaciers are currently present in this area (Scotti et al., 2013). Sr-Nd isotope signatures of the sample 6.A (Fig. IX-4) were selected as a fingerprint of the contribution of the calco-alkaline source, as this sample is the closest to the Adamello massif outcrops signature (Kagami et al., 1991).

Sub-catchments draining mostly metamorphic rocks were combined into the "metamorphic" source. We note that these catchments are also partially underlain by sedimentary rock outcrops and Quaternary deposits. Samples from this source (2.B, 3.A and 4.A) present contrasted Sr-Nd isotope signatures, linked to their heterogeneous composition (Fig. IX-4). The sub-catchment of sample 4.A presents the highest proportion of metamorphic rocks (Fig. IX-1; https://www.cartografia.servizirl.it/cargviewer/), which constitutes the only rock source that can explain the lowest εNd values observed in lake sediment samples (Fig. IX-4). As a consequence, the isotope signatures of sample 4.A are used as a fingerprint for the contribution of metamorphic rocks in the Lake Iseo catchment. Due to the significant heterogeneity of the metamorphic source, the fractional input from this end member to Lake Iseo sediments over time are discussed with great caution hereafter.

The remaining samples 7.A and 8.A originate from sub-catchments dominated by sedimentary rocks and were thus gathered into the "sedimentary rock" source. This source shows εNd values between -10.5 and -9.7, associated to the highest $^{87}Sr/^{86}Sr$ ratios (> 0.725). However, these $^{87}Sr/^{86}Sr$ values are not high enough to explain the highest $^{87}Sr/^{86}Sr$ ratios observed in lake sediment samples. This is because the sub-catchments dominated by sedimentary rocks are actually underlain by marlstones and limestones/dolostones. Although our decarbonation protocol has likely removed a large fraction of the carbonate component present in the river sediment, we expect that relatively refractory carbonate minerals such as dolomite remain in the "silicate" residue of the leaching procedure. As a consequence, this residue hosts a non-silicate component, most likely characterized by relatively low $^{87}Sr/^{86}Sr$ ratios (Faure et al., 1978), and the contribution of which needs to be corrected for. Details about this correction are provided in supplementary S6. After correction, the Sr signature of river sediments from sub-catchments draining sedimentary rocks is sufficiently ^{87}Sr-enriched to explain the highest $^{87}Sr/^{86}Sr$ ratios observed in Lake Iseo sediments (Fig. IX-4). Areas corresponding to the "sedimentary rock" source are located at low to mid altitude, in the southern part of the Iseo catchment, and correspond to places of current intense human activities (Fig. IX-2). The Nd-Sr isotope signatures of sample 8.A were selected as a fingerprint of the "sedimentary rock" source as this sub-catchment presents the highest proportion of marlstone (Fig. IX-1; https://www.cartografia.servizirl.it/cargviewer/) and is the only one explaining the most radiogenic $^{87}Sr/^{86}Sr$ signature observed in lake samples.

The fractional contribution of each rock source can be estimated using a mixing model. The lake sediment Sr and Nd isotope compositions depend on (i) the Sr-Nd concentration and isotope signatures of each rock source, and (ii) the proportion of each contributing source in the mixture. This can be summarized by a system of 5 linear equations, expressed as follows:

$$[Sr]^M = [Sr]^A \times f_A + [Sr]^B \times f_B + [Sr]^C \times f_C \quad (1)$$

$$[Nd]^M = [Nd]^A \times f_A + [Nd]^B \times f_B + [Nd]^C \times f_C \quad (2)$$

$$f_A + f_B + f_C = 1 \quad (3)$$

$$\frac{^{87}Sr}{^{86}Sr}^M \times [Sr]^M = \frac{^{87}Sr}{^{86}Sr}^A \times [Sr]^A \times f_A + \frac{^{87}Sr}{^{86}Sr}^B \times [Sr]^B \times f_B + \frac{^{87}Sr}{^{86}Sr}^C \times [Sr]^C \times f_C \quad (4)$$

$$\varepsilon Nd^M \times [Nd]^M = \varepsilon Nd^A \times [Nd]^A \times f_A + \varepsilon Nd^B \times [Nd]^B \times f_B + \varepsilon Nd^C \times [Nd]^C \times f_C \quad (5)$$

with the superscript M standing for lake sediment ("mixture") values, and the superscripts A, B and C stand for the three rock sources values (calco-alkaline, metamorphic, and sedimentary rocks, respectively); f_x represents the fractional contribution of each rock source.

Solving this equation system leads to estimates of the relative contributions of sources A, B and C. Analytical solutions for f_A, f_B and f_C were obtained from Maple software (see supplementary S7). A Monte Carlo method was used to compute uncertainties on the fractional contributions. Random sampling within the analytical uncertainties of each parameter was executed using a Box–Muller transform (Box and Muller, 1958) for each of the 5,000 iterations of the Monte Carlo procedure. From the simulated parameter distributions, D84, D16, median and standard deviation were obtained for each proportion f_x (Table S4). The "sedimentary rocks" source contributes on average to $79.6^{+4.8}_{-5.7}$ % of the total siliciclastic sedimentation in Lake Iseo deep basin, whereas the calco-alkaline source is the smallest contributor with a mean contribution of $3.5^{+1.8}_{-1.5}$ % and the metamorphic source contribute to $16.7^{+6.1}_{-5.0}$ % on average (Fig. IX-5-B). Through the last 2,000 years, the "sedimentary rock" inputs to Lake Iseo remain predominant and increase progressively towards the Middle Ages and the Industrial Age.

Beyond accounting for analytical uncertainties, an additional sensitivity test was run to evaluate the impact of the Sr-Nd isotope signatures selected for each rock end member. "Geological" uncertainties of 0.005 on the $^{87}Sr/^{86}Sr$ ratio and of 0.8 epsilon-units on εNd, together with a 50 % relative uncertainty on Nd and Sr concentrations were attributed to each end member, and a Monte Carlo procedure was performed in the same manner as that laid out above (Table S5 and Fig. IX-5-B). Regardless of the exact composition of the three end members within the ranges given above, the "sedimentary rocks" source remains the predominant contributor to the continuous accumulation of siliciclastic material over time in Lake Iseo deep basin. Therefore, results from our mixing model can be reliably used to discuss the evolution of the contribution of each source in terms of temporal variations in erosion processes in the catchment.

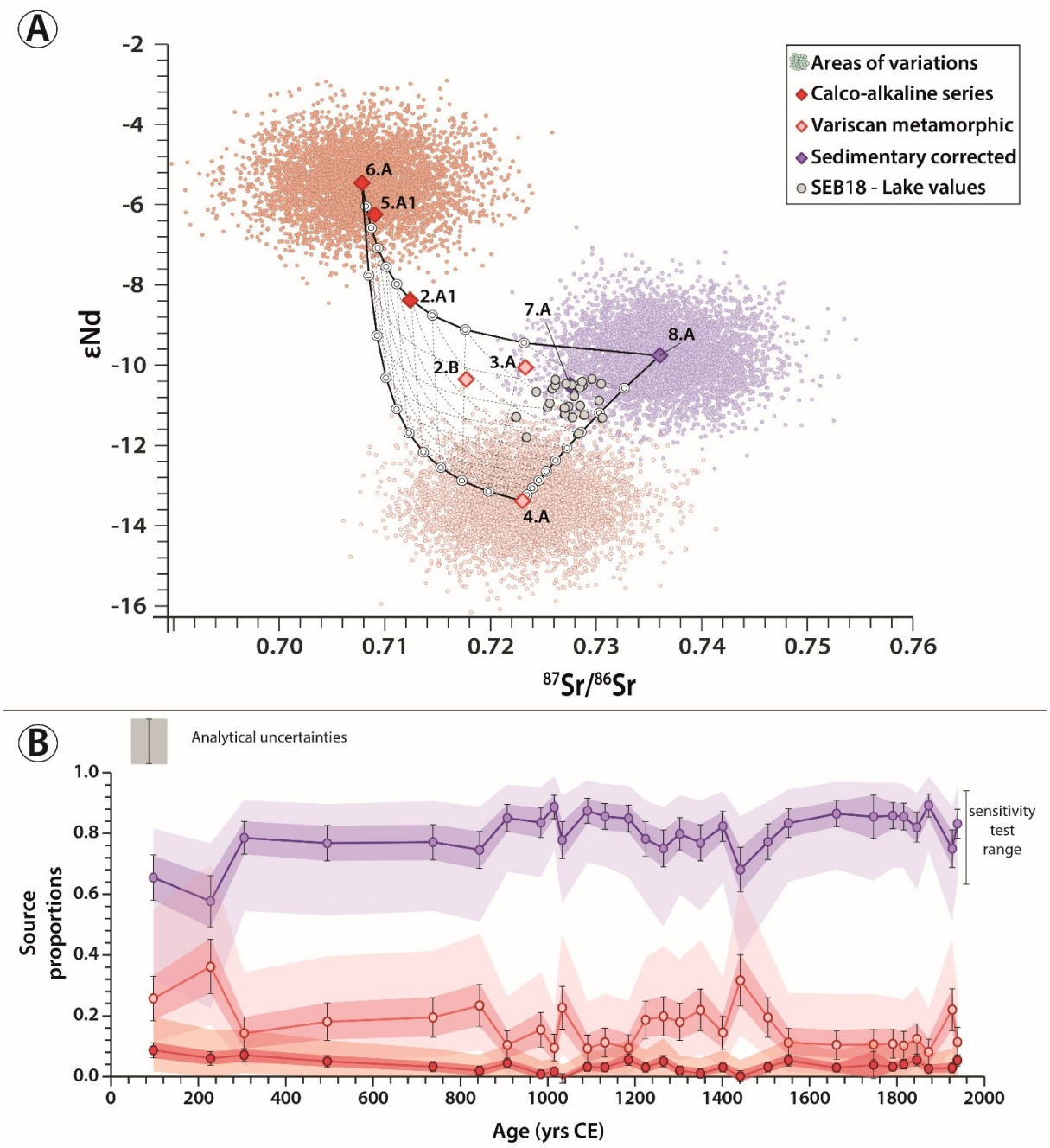

Fig. IX-5 - Results from the mixing model. (A) Nd-Sr isotope signatures of the three identified rock sources, used as end members for explaining the composition of lake sediments. Samples 6.A, 8.A and 4.A are used to constrain the composition of the rock end members. Lake sediments are shown as grey circles within an array described by mixing hyperbolae. The pink, red, and purple symbols correspond to the composition of each Monte Carlo iteration used for the sensitivity test. (B) Fractional contributions of each rock source to Lake Iseo sediment against time (yr CE). The propagation of analytical uncertainties is represented as error bars and by dark shaded areas, corresponding to the D84 and D16 of the distribution of the parameters obtained from Monte Carlo simulations. The light shaded areas represent the propagation of the uncertainty associated to the composition of the three rock sources, again with the D84 and D16 of the distribution of the parameters obtained from Monte Carlo simulations.

4.4. Evaluation of the sediment yield

Once the proportion of each sediment source to lake sediments has been calculated, river loads, and corresponding sediment yields can be estimated to obtain a quantitative assessment of catchment-scale erosion rates, for each area in the catchment. Sediment accumulated in a sinking basin, such as natural lakes, is partly composed of river silt-sized material and of authigenic deposits; sand-sized material such as river bedload being in general deposited along the sides of the river channel or in the delta (Hinderer et al., 2013). Few or none of the authigenic carbonates produced in Lake Iseo are preserved in the deep basin of the lake (Rapuc et al., 2020a), making this lake the ideal candidate to reconstruct the evolution of river suspended load through time, and thus of erosion rates in the contributing catchment. The time-dependent erosion flux from the catchment was determined by using the calculation of a siliciclastic flux (SCF; $g.cm^{-2}.yr^{-1}$) from the lake sediment samples (Rapuc et al., 2020a), calculation details are provided in supplementary S10.

The sediment yield is defined as the mass of sediment that, over a given time span, leaves a boundary, such as the outlet of a catchment. SY is expressed in units of mass per unit of area and time (Hinderer et al., 2013 and reference therein). This parameter is used here to enable comparison with previous studies on erosion in the Alps. To calculate SY for the Iseo catchment, the total amount of sediment stored in Lake Iseo per amount of time ($Stock_{sed}$) needs to be estimated:

$$Stock_{sed} = SCF \times Lake\ area \quad (7)$$

SR may vary spatially over the surface of a lake. To calculate a consistent $Stock_{sed}$ for the entire lake we consider only the fraction of the total lake area where SR should be commensurate with that measured at the coring site. We assume here that this area corresponds to the flat part of the deep basin as suggested by the seismic survey (Rapuc et al., 2020a), which lies below the slope discontinuity. Based on the lake bathymetry, we consider that the lake area with water depth below 210 m b.l.s should be taken into account in the calculation of $Stock_{sed}$, corresponding to a total of 18 km² (S11). The sediment stock is then multiplied by the contribution of each source to the lake sediment, in order to calculate changes in the source-specific sediment loads (SL, in $t.yr^{-1}$) through time:

$$SL = Stock_{sed} \times source\ proportion \quad (8)$$

To obtain an area-normalized sediment yield value for each source (SY_i), SL is normalized to the drainage area of each rock type. A value for total sediment yield (SY_{Total}) was also computed from the total SL:

$$SY_i = \frac{SL}{Source\ area} \quad (9)$$

$$SY_{Total} = \frac{SL}{Watershed\ area} \quad (10)$$

with SY_i and SY_{Total} expressed in $t.km^{-2}.yr^{-1}$. For the computation of SY_i and SY_{Total}, only the parts of the catchment area likely to be subjected to physical erosion are considered. For more detail on these calculations, see S12.

During the Industrial Age, $SY_{Sedimentary\ rocks}$ and $SY_{Calco\text{-}alkaline}$, representing area-specific erosion rates of the sedimentary and the calco-alkaline rocks areas in the Iseo catchment, show values around 100 and 10 $t.km^{-2}.yr^{-1}$, respectively (Fig. IX-6). $SY_{Sedimentary\ rocks}$ values for the recent times are coherent with estimates derived from the RUSLE model for similar contexts (Panagos et al., 2015; S13). Calculated $SY_{Sedimentary\ rocks}$ values for the twentieth century are also close to present-day sediment yield measurements on Alpine rivers (30 – 671 $t.km^{-2}.yr^{-1}$; Hinderer et al., 2013). Deviations between our calculations and previously reported values can be explained by storage of sediment in the lake delta (Hinderer et al., 2013) and by the absence of consideration of the bed load in our calculation. However, Hinderer et al. (2013) showed that in the southern crystalline Alps, where Lake Iseo is located, suspended load generally dominates over bed load. Altogether the present-day sediment yield estimated here for the Lake Iseo catchment is consistent with previously reported figures, lending support to our estimates of erosion rates through time.

5. Discussion

The calculated SY_{Total} is about 20 $t.km^{-2}.yr^{-1}$ during the Roman Period (Fig. IX-6-A). From then on, SY_{Total} values increase nearly two-fold until the Medieval Period, when it reaches values between 30 and 40 $t.km^{-2}.yr^{-1}$. Then, SY_{Total} values decrease slightly until 1661 CE, prior to a sharp increase again during the Industrial Age and until the present.

Over centennial to millennial time scales, erosion is mainly a result of climate, vegetation, and land use changes (e.g. Bosco et al., 2008; Panagos et al., 2015), the last two parameters being associated with human activities. To disentangle the impact of climate and human practices on erosion in the Lake Iseo catchment, we investigate separately the reconstructed sediment yields of the “sedimentary rock” and calco-alkaline areas. Indeed, no or very few human activities are reported in the high-altitude part of the catchment (e.g. Biagi and Starnini, 2015). Conversely, a great number of glaciers and rock glaciers are present in this area (Scotti et al., 2013), making erosion there highly sensitive to climate induced glacial fluctuations. In contrast, human activities are widely developed at low- to mid-altitude levels in the Val Camonica, meaning that human and climate have an unquestioned influence on erosion rates in the “sedimentary rock” area. No further investigation was conducted here on the sediment yields of the metamorphic area because of the lack of information about land use over time in this area, which was in addition certainly affected by a combination of glacier fluctuations and human activities such as grazing and deforestation (Fig. IX-6-B).

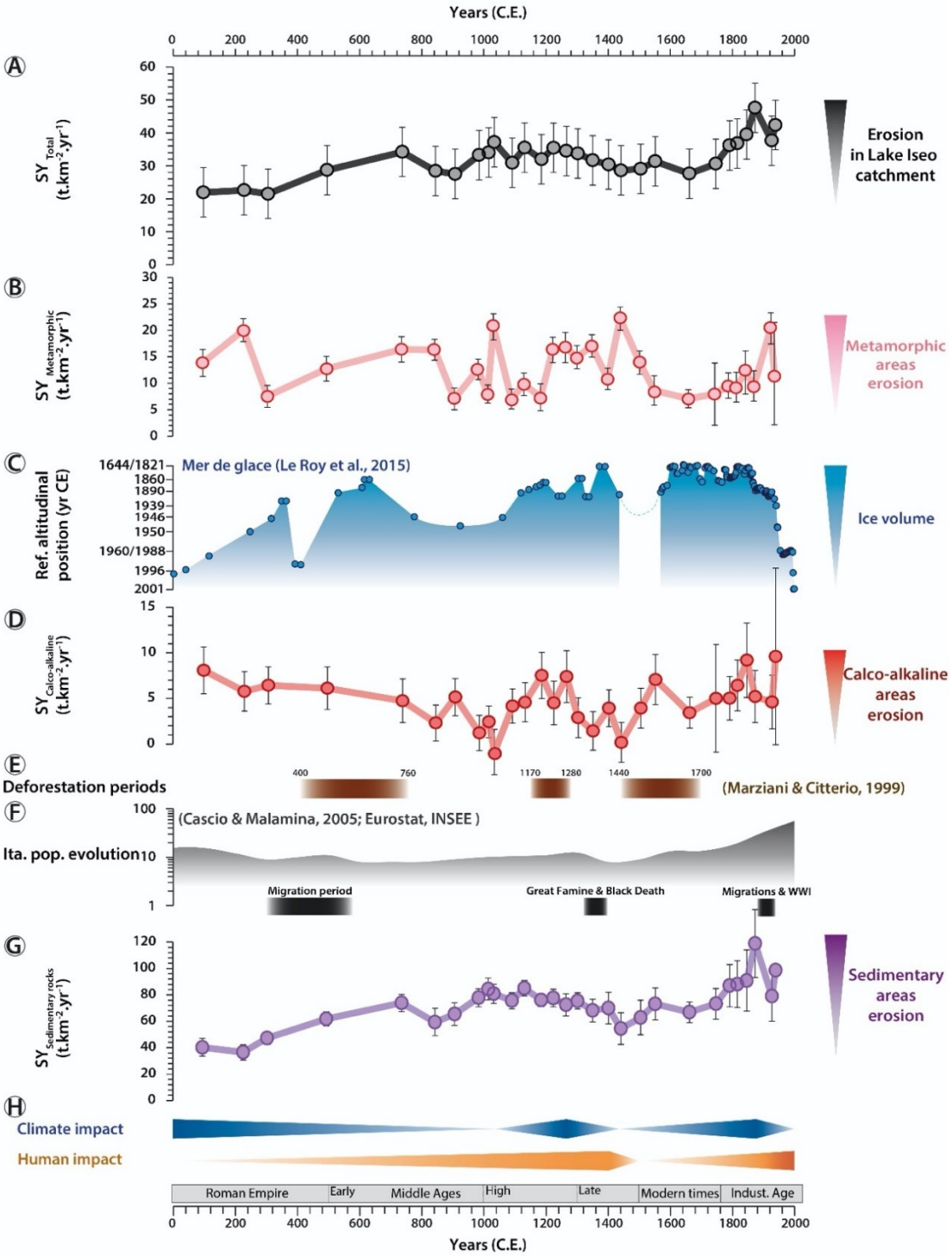

Fig. IX-6 - Erosion in the Lake Iseo catchment and forcing factors evolution over the last 2,000 years. From top to bottom: (A) total sediment yield obtained from the SEB18 sediment core (black curve); (B) the sediment yield originating from the erosion of metamorphic areas in the Iseo catchment (pink curve); (C) the advances and retreats of the Mer de Glace glacier (French Alps, 45° 54.9'N and 6° 56.2'E) modified from Le Roy et al. (2015; blue shaded curve); (D) the sediment yield originating from the erosion of calco-alkaline areas in the Iseo catchment (red curve); (E) the attested deforestation periods at a mid-altitude archaeological site of the Val Camonica valley (Marziani and Citterio, 1999; brown shades); (F) the evolution of the Italian population modified from Cascio and Malanima (2005) and Eurostat and INSEE sources (black shaded curve); demographic events that have affected the Italian population (black shades); (G) the sediment yield originating from the erosion of "sedimentary rock" area in the Iseo catchment (purple curve); (H) inferred periods of enhanced impact of climate (blue) and human (orange) activities on the erosion of the Iseo catchment.

5.1. Climate impact on erosion of high-altitude areas

Erosion in the high-altitude area of the Adamello massif is influenced by glacier advances and retreats and by extreme precipitation events. Glacier volumes depend on summer temperature and winter precipitation amounts (e.g. Fouinat et al., 2017; Holzhauser et al., 2005; Le Roy et al., 2015), all linked to Mediterranean climate. Therefore, in order to discuss the impact of climate fluctuations on erosion in Lake Iseo catchment, we focus on the $SY_{Calco\text{-}alkaline}$ reconstruction. Currently, glaciers present in the calco-alkaline area of Lake Iseo catchment correspond to a small glacial tongue (0.7 km²) of the great Adamello glacier (21.6 km²) and small glacier bodies (< 0.5 km²) south and north of it. By their sizes, these glacier bodies are thought to be more sensitive to local climate change and present a lower inertia during glacier retreat than great Alpine glaciers.

$SY_{Calco\text{-}alkaline}$ first decrease from 100 to 1000 CE before increasing sharply until 1200 CE. The erosion from calco-alkaline area remains high (> 6 $t.km^{-2}.yr^{-1}$) until 1300 CE before decreasing again until 1450 CE. Another increase is observed until 1550 CE. $SY_{Calco\text{-}alkaline}$ values remain high until the present days, with two peaks at 1845 CE and 1940 CE. The comparison of $SY_{Calco\text{-}alkaline}$ evolution over the last 2,000 years with other alpine glaciers advances and retreats such as that of the Mont Blanc valley (Fig. IX-6-C; Le Roy et al., 2015), or smaller glacial bodies (e.g. Fouinat et al., 2017; Glur et al., 2015) presents similarities. Except for the Roman Period, $SY_{Calco\text{-}alkaline}$ increases during periods of major glacier advances and decreases during retreat periods (Fig. IX-6-D). During the Roman Period, $SY_{Calco\text{-}alkaline}$ present high values that are not consistent with the relatively low volume of great glaciers in the European Alps (Holzhauser et al., 2005; Le Roy et al., 2015). However, erosion signals from small glacial bodies in the western French Alps (Fouinat et al., 2017) or in the Central Alps (Glur et al., 2015), present several peaks of enhanced erosion between 0 to 600 CE in relation to short term temperature variation, but the sampling resolution presented here do not allow the comparison.

From ~500 to 1000 CE, $SY_{Calco\text{-}alkaline}$ decreases in agreement with the volume of major great Alpine glaciers (Holzhauser et al., 2005; Le Roy et al., 2015). At that period, climate is warm and dry in the southern Alps, favouring glacier retreats (Büntgen et al., 2011). From 1000 to 1200 CE, erosion in high-altitude areas of Lake Iseo catchment increases sharply and remains high until 1300 CE. This period known as the High Medieval Advance (HMA) corresponds to a general episode of glacier advance in the Alps (Le Roy et al., 2015 and references therein) despite temperature increase in Europe (Büntgen et al., 2011). After the HMA, $SY_{Calco\text{-}alkaline}$ decreases again until 1450 CE before another increase, observable in every alpine glacier chronicle, and corresponding to the onset of the Little Ice Age (LIA; Fig. IX-6-C). This period is characterized by a globally cold and wet climate, inducing significant glacier advances that caused intense erosion throughout the alpine area (e.g. Fouinat et al., 2017; Glur et al., 2015; Holzhauser et al., 2005; Le Roy et al., 2015). The LIA is known to last approximately until the middle of the nineteenth century, which correspond to the penultimate observed peak in $SY_{Calco\text{-}alkaline}$.

Collectively, these observations suggest, as demonstrated elsewhere in the Alps (e.g. Fouinat et al., 2017; Glur et al., 2015), that even over short time scales, colder periods induced higher erosion rates in the mountainous parts of the Lake Iseo catchment, implying a strong link between climate and erosion in high-altitude areas.

5.2. Human impact on erosion of low-altitude areas

At lower altitudes, climate fluctuations are not the only factors responsible for changes in erosion rates. Indeed, with land use and vegetation cover management, humans play a key role on erosion (e.g. Bosco et al., 2008; Panagos et al., 2015). However, during periods of high $SY_{Calco-alkaline}$, climatic forcing of the erosion in the low-altitude such as the sedimentary area need to be considered together with the human forcing as a possible driver of erosion.

The $SY_{Sedimentary\ rocks}$ values increase two-fold from the Roman Period until the High Middle Ages. This increase occurs during dry and warm climate conditions across Europe (Bini et al., 2020; Büntgen et al., 2011), and is associated with a gradual decrease of the $SY_{Calco-alkaline}$ signal (Fig. IX-6-D), suggesting that human practices become the main driver of erosion in the Lake Iseo catchment at that time. Abandonment of forest management plans until the Migration Period (300 – 570 CE) has been attributed to a declining influence of the Roman Empire in the Lake Iseo catchment (Comiti, 2012). The period from the Roman Period until the High Middle Ages is interpreted as a period of enhanced human pressure on the environment due to:

(i) Deforestation to allow for instance for increased mining activity, as observable elsewhere in Europe (Büntgen et al., 2011) and at low- to mid-altitude sites in the Val Camonica (Fig. IX-6-E, Marziani and Citterio, 1999; Pini, 2002; Pini et al., 2016);
(ii) A general population increase in Italy towards the Middle Ages (Fig. IX-6-F, Cascio and Malanima, 2005);
(iii) An intensification of land use and human practices, coupled with replacement of pre-existent buildings (Büntgen et al., 2011).

In the Iseo catchment, the collapse of the forest management system of the Roman Empire should be at the origin of an enhancement of erosion. During the High Middle Ages and until the Late Middle Ages, $SY_{Sedimentary\ rocks}$ remains relatively high (Fig. IX-6-G). At that time, regional climate is wet (Bini et al., 2020; Büntgen et al., 2011), extreme precipitations are frequent locally until 1300 CE (Wirth et al., 2013a), and the human pressure remains important, with (i) attested periods of deforestation in the catchment (Marziani and Citterio, 1999) and (ii) intense land use and pastoralism in the Italian Alps (Büntgen et al., 2011; Comiti, 2012; Joannin et al., 2014; Pini, 2002). Therefore, disentangling human and climate forcing over this period is not possible, and it is likely that the combination of the two factors induced intense erosion in the entire Lake Iseo catchment until the Great Famine (1315 – 1317 CE) and the Black Death (1347 – 1351 CE). A slight decrease in $SY_{Sedimentary\ rocks}$ is observed just after these two (Fig. IX-6-G, F). These events are known to have deeply impacted European populations, resulting in particular in agricultural decline in the Southern Alps (e.g. Büntgen et al., 2011; Joannin et al., 2014; Ruddiman, 2007).

After this trough, $SY_{Sedimentary\ rocks}$ increases progressively until 1800 CE and then strongly until 1872 CE and the onset of the Industrial Age (Fig. IX-6-G). Two hypotheses can be invoked to explain this pattern: the effect of the Little Ice Age (LIA) following an increase of human activity. Indeed, maximal glacier advances in the Alps are reported at around 1850 CE (Holzhauser et al., 2005; Le Roy et al., 2015), before the current period of general retreat. The LIA is also characterized by more frequent extreme precipitations events in the Southern Alps (Wirth et al., 2013a). The effect of LIA climate change on erosion, through precipitation events and plausible glacier advances, are well visible on $SY_{Calco-alkaline}$ at that time and thus cannot be ignored for the interpretation of the

low and mid-altitudinal part erosion signal of the Lake Iseo catchment, even if the LIA starts before the increase in $SY_{Calco\text{-}alkaline}$. Synchronously, human pressure on the environment grows sharply in the Italian Alps generally, and in the Lake Iseo catchment in particular, with an increase of the population (Cascio and Malanima, 2005) associated to a surge in agricultural practices and a transition towards intensive farming (Federico and Malanima, 2004).

Between 1872 and 1926 CE, $SY_{Sedimentary\ rocks}$ decreases sharply, most likely due to the onset of outward migration, with more than 11 M people leaving Italy for the New World (Moretti, 1999). $SY_{Sedimentary\ rocks}$ finally increases until 1938 CE (last sample).

To summarize, each episode of $SY_{Sedimentary\ rocks}$ increase in the Lake Iseo catchment can be associated to a period of intense human pressure on the environment (Fig. IX-6). Between 1030 and 1300 CE and during the LIA, wetter and colder climate favoured erosion not only at high altitudes but also at intermediate and low altitudes, making it hard to disentangle climate versus human influences. However, from the Roman Period to the Middle Ages and up to the present, erosion at low altitudes shows a clear increase, asynchronous and decorrelated from the regional climate trend. Therefore, only human pressure on the environment can be responsible for this trend (Fig. IX-6-H). Human activities, through the development of agricultural practices and deforestation at low- and mid-altitude have induced a three-fold increase in erosion rates in a large catchment of the Italian Alps. Hence, even in large mountainous catchments, human activities affect the CZ by increasing erosion, resulting in damages on ecosystems and in soil and biomass carbon shrinkage. The CZ is deteriorated by human practices for 2,000 years in the Alps, making it highly sensitive to the current anthropization pressure. Long term erosion chronicles, such as those produced from lake sediments, are critical to quantify the influence of the different forcing factors impacting CZ erosion through time.

6. Conclusion

Contributions of glacial variability and human activities to erosion were reconstruct from a sediment core with a stable isotope mixing model. The absolute value of sediment yields signal is highly coherent with previous work and annual average erosion models, making it possible to interpretate its variations reported in the three mains sources. The erosion signal from high-altitude areas, synchronous with the main episodes of European glacier advances and retreats, is interpreted to be driven by climatic fluctuations. From the comparison between the erosion signals of high- and low-altitude areas, we were able to disentangle the main triggers of the erosion at low-altitude areas in the study area. Human activities, through deforestation, agricultural practices and grazing become the main forcing factors affecting erosion between the Roman Period and the Middle Ages, and from the Late Middle Ages to the present. A three-fold increase, from 36 to 118 $t.km^{-2}.yr^{-1}$ is observed in anthropized areas. This is the first time that the impact of human activity on catchment-scale erosion is quantitatively assessed over time, based on lake sediments. These findings should contribute to enhance modelling of human impacts on Critical Zone erosion and on carbon shrinkage in soils.

Acknowledgments

This work was financed by CRITLAKE project co-funded by EC2CO and AAP Université Savoie Mont Blanc. Parts of this work were also supported by IPGP multidisciplinary programme PARI and by Paris-IdF region SESAME Grant No. 12015903. We wish to thank the support of the entire staff of the C2FN-DT-INSU associated to the CLIMCORE project. ^{14}C analyses were acquired thanks to the CNRS-INSU ARTEMIS national radiocarbon AMS measurement programme at Laboratoire de Mesure ^{14}C (LMC14) in the CEA Institute at Saclay (French Atomic Energy Commission).

We are grateful to Pierre Burckel for help with Q-ICP-MS measurements; to Laëticia Faure for her valuable help and assistance with lab work; to Pascale Louvat, Thibaud Sondag, and Barthélémy Julien for assistance with MC-ICP-MS measurements; and to Ana Brancelj for the help on the field for river samples collection. We wish to thank Damien Guinoiseau for helpful conversations about the interpretation of isotope data.

Supplementary Materials

S1. Lake sediment geochemistry

Table S1– Lake sediment depth, age (BP and CE), siliciclastic Sr and Nd isotopic compositions with the associated 95% uncertainties and concentrations obtained after correction (explained in section S3).

Nb	MCD (cm)	Age (yr cal BP)	Age (yr CE)	$^{87}Sr/^{86}Sr$			εNd corrected			[Sr] (ppm)	[Nd] (ppm)
1	57,8	12	1938	0,72600	±	8,0E-06	-10,54	±	0,22	67,98	18,38
2	78,8	24	1926	0,72693	±	6,8E-06	-11,24	±	0,22	90,42	25,34
3	111,3	78	1872	0,72950	±	7,3E-06	-10,38	±	0,22	79,96	28,27
4	126,8	105	1845	0,72575	±	0,00001	-10,61	±	0,22	93,82	27,27
5	140,8	135	1815	0,72735	±	3,5E-06	-10,49	±	0,22	110,30	31,94
6	150,8	160	1790	0,72819	±	7,3E-06	-10,55	±	0,22	74,04	22,28
7	172,8	204	1746	0,72759	±	0,00380	-10,52	±	0,22	93,67	25,91
8	230,8	289	1661	0,72863	±	0,00025	-10,54	±	0,22	85,97	26,09
9	247,8	329	1621	#N/A			-10,53	±	0,22	216,20	30,31
10	316,3	399	1551	0,72604	±	0,00001	-10,53	±	0,22	91,38	27,02
11	353,9	446	1504	0,72698	±	0,00001	-11,10		0,22	115,19	38,41
12	378,9	509	1441	0,72821	±	0,00020	-11,74	±	0,22	74,47	24,02
13	392,7	549	1401	0,72783	±	0,00001	-10,81	±	0,22	69,71	21,69
14	410,2	600	1350	0,72877	±	0,00006	-11,27	±	0,22	73,24	24,86
15	449,7	648	1302	0,72839	±	0E+00	-11,04	±	0,22	82,69	26,30
16	461,7	685	1265	0,72531	±	0,00001	-11,08	±	0,22	87,49	24,67
17	474,7	726	1224	0,72727	±	0,00001	-11,06	±	0,22	114,72	38,32
18	486,2	765	1185	0,72605	±	3,1E-06	-10,40	±	0,22	126,06	40,65
19	646,2	819	1131	0,72837	±	0,00003	-10,59	±	0,22	75,79	24,91
20	663,2	859	1091	0,72856	±	0,00009	-10,45	±	0,22	95,21	33,59
21	1042,7	917	1033	0,73049	±	5,4E-06	-11,34	±	0,22	124,65	38,91
22	1059,45	935	1015	0,73036	±	9,1E-06	-10,50		0,22	79,19	28,77
23	1078,9	966	984	0,73018	±	0,00002	-10,91	±	0,22	90,41	30,11
24	1117,9	1043	907	0,72703	±	2,6E-06	-10,50		0,22	99,09	31,15
25	1138,9	1106	844	0,72767	±	0,00002	-11,33	±	0,22	110,46	35,49
26	1176,9	1213	737	0,72690	±	0,00002	-11,10	±	0,22	73,49	22,64
27	1395,4	1455	495	0,72551	±	8,1E-06	-10,98	±	0,22	81,56	22,61
28	1460,9	1645	305	0,72424	±	7,7E-06	-10,70		0,22	83,82	21,95
29	1495,9	1722	228	0,72331	±	9,2E-06	-11,83	±	0,22	67,50	17,69
30	1533,9	1853	97	0,72234	±	9,4E-06	-11,32	±	0,22	89,23	21,66

S2. River sediment geochemistry

Table S2– River sediment samples with location, distance to the lake, predominant lithologies in the sub-catchments, river type, Sr isotopic composition for bulk samples and samples after the leaching procedure, Nd isotopic composition, and Sr and Nd concentrations of bulk samples. Met. HG: High grade metamorphic rock from the Variscan basement; Sedim.: sedimentary rocks; Gra.: Granite from the Adamello batholith; Met: undifferentiated Variscan metamorphic basement; Ton.: Tonalite from the Adamello batholith; Met. MG: Mid-grade metamorphic rock from the Variscan basement.

Name	Lat	Long	Lake distance (km)	Geology	Type	87Sr/86Sr (after leach)			87Sr/86Sr (bulk)			εNd			[Sr] bulk (ppm)	[Sr] after leach (ppm)	[Nd] (ppm)
1.B	46°16.057'N	10°31.072'E	77,8	Met. HG	tributary	0,72050	±	0,00002	0,72040	±	0,00002				253,57	24,30	63,28
7	45°54.430'N	10°13.349'E	16	Sedim.	main river	0,71790	±	0,00002				-7,49	±	0,44	312,57	12,72	42,72
8.A	45°52.935'N	10°10.686'E	11	Sedim.	tributary	0,72527	±	0,00002	0,71040	±	0,00002	-9,76	±	0,44	389,77	7,36	26,36
9.B	45°44.425'N	10°5.452'E	0	Sedim. + Gra.	tributary	0,71769	±	0,00002	0,71182	±	0,00002	-8,29	±	0,44	173,64	8,55	19,38
1	46° 14.999'N	10°28.644'E	75,4	Met.	main river	0,71986	±	0,00002	0,71898	±	8E-06	-10,05	±	0,44	225,63	18,54	53,65
5.A[1]	46°6.633'N	10°28.594'E	43	Ton.	tributary	0,70906	±	0,00002	0,70913	±	0,00001	-6,25	±	0,44	376,06	16,24	35,92
3.A	46°10.426'N	10°19.675'E	57,4	Met. MG	tributary	0,72330	±	0,00002	0,72199	±	0,00002	-10,05	±	0,44	118,40	10,82	30,96
5	46°3.581'N	10°21.043'E	42,5	Met.	main river	0,72093	±	0,00002	0,72006	±	0,00003	-8,56	±	0,44	174,30	16,81	58,28
8	45°51.267'N	10°8.367'E	7,2	Sedim.	main river	0,71884	±	0,00002	0,71271	±	5E-06	-9,20	±	0,44	343,01	111,63	38,97
2.A[2]	46° 14.584'N	10° 28.184'E	73,9	Met. MG + Gra.	tributary	0,71363	±	0,00002	0,71363	±	6E-06	-9,40	±	0,44	167,67	17,87	24,28
9.A	45°48.829'N	10°3.098'E	0	Sedim.	tributary				0,70899	±	0,00001	-10,02	±	0,44	182,00	1,68	7,11
7.A	45°55.176'N	10°14.633'E	19,3	Sedim.	tributary	0,72649	±	0,00002	0,72227	±	8E-06	-10,49	±	0,44	74,51	11,44	31,49
5.A[2]	46°4.338'N	10°22.025'E	43	Met. MG + Ton.	tributary	0,71753	±	0,00002	0,71656	±	0,00002	-10,98	±	0,44	146,72	8,86	24,49
6.A	45°59.452'N	10°20.448'E	32,3	Ton.	tributary	0,70782	±	0,00002	0,70801	±	0,00001	-5,46	±	0,44	1108,97	564,26	18,63
2.A[1]	46°12.652'N	10°28.814'E	73,9	Gra.	tributary	0,71238	±	0,00002	0,71201	±	0,00001	-8,40	±	0,44	224,65	170,19	25,11
6	45°59.452'N	10°20.448'E	29,8	Sedim.	main river	0,71727	±	0,00002	0,71277	±	0,00001	-11,31	±	0,44	406,11	16,44	44,72
3	46°9.438'N	10°20.881'E	55,1	Met.	main river	0,71890	±	0,00002	0,71862	±	0,00002	-11,22	±	0,44	148,02	18,07	44,36
2	46°14.116'N	10°23.646'E	66,4	Met.	main river	0,71649	±	0,00002	0,71616	±	0,00002	-11,16	±	0,44	185,64	161,16	45,12
4.A	46°5.391'N	10°18.842'E	46,4	Met. MG	tributary	0,72302	±	0,00002	0,72184	±	0,00001	-13,38	±	0,44	156,05	213,69	68,85
1.A	46°14.928'N	10°31.763'E	77,8	Met. MG + Gra.	tributary	0,71508	±	0,00002	0,71446	±	0,00001	-9,71	±	0,44	209,23	14,36	26,80
2.B	46°14.210'N	10°23.833'E	67,6	Met. HG	tributary	0,71769	±	0,00002	0,71740	±	0,00002	-10,36	±	0,44	194,06	24,46	36,41
4	46°5.382'N	10°19.015'E	46,1	Met.	main river	0,71964	±	0,00002	0,71917	±	0,00002	-11,80	±	0,44	155,34	13,52	47,03

S3. Decarbonation by HCl leaching and corrections applied to lake samples Sr and Nd concentrations

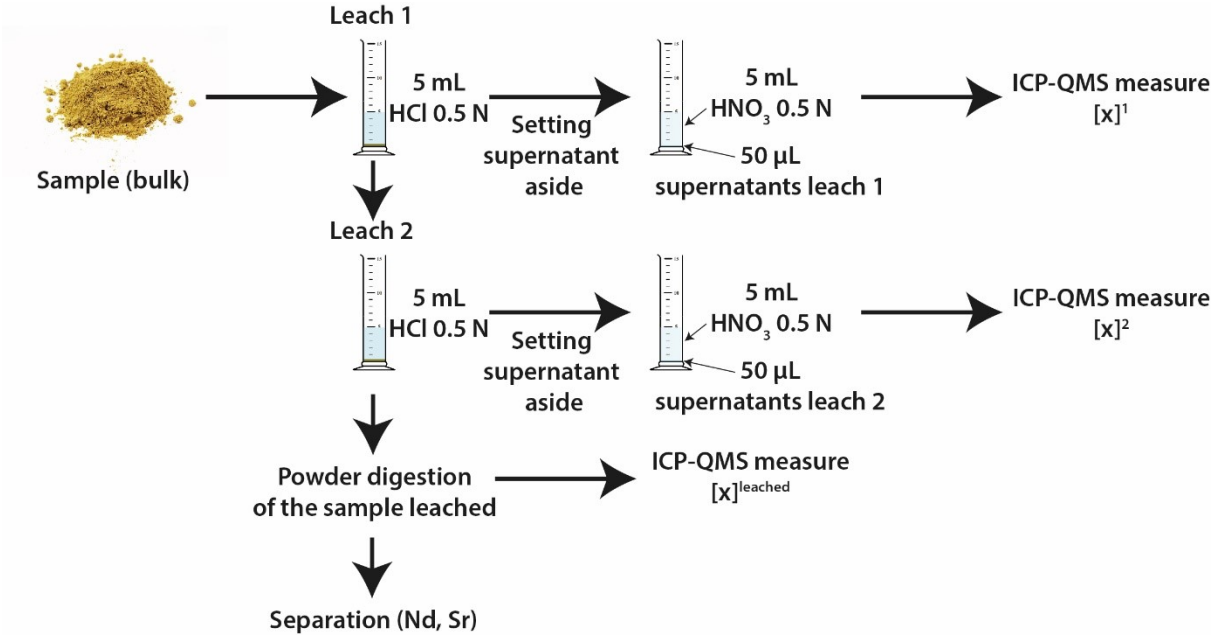

Figure S1 – Description of the decarbonatation method. with successive HCl leaching.

As our study focuses on the erosion of silicate rocks, lake and river sediment samples were decarbonated before digestion of silicate residue. The weight of the bulk initial sample was measured, but the weight after decarbonation could not be recorded. To estimate the Sr and Nd concentration of the siliclastic residue of lake sediment, we estimate the weight loss from each sample during the two leaching steps.

$$Weight_{leached} = (Weight_{lost\ in\ leach\ 1} + Weight_{lost\ in\ leach\ 2})$$

The weight loss during each leaching step is due to the dissolution of carbonates, which corresponds to $CaCO_3$ with minor amounts of Fe and Mg that can substitute for Ca in carbonate crystalline structures.

$$Weight_{lost\ in\ leach\ n} = Weight_{\mathrm{CaCO3\ n}} + Weight_{\mathrm{MgCO3\ n}} + Weight_{\mathrm{FeCO3\ n}}$$

which is equivalent to:

$$Weight_{lost\ in\ leach\ n} = Ca^n \times M_{CaCO3} + Mg^n \times M_{MgCO3} + Fe^n \times M_{FeCO3}$$

with M_i the molar mass of phase *i* in g.mol^{-1}, and $[x]^n$ expressed in mol.l^{-1} the concentration of the element x in the supernatant of the leach n:

$$[x]^n = \frac{C_x \times f \times Vol_{dissolution}}{M_{(xCO3)}}$$

with C_x the concentration of the element x = Ca, Mg, Fe obtained from ICP-QMS measurement for the relevant supernatant, f (= 100 in our case) the dilution factor applied to solutions before ICP-QMS measurements, $Vol_{dissolution}$ the volume of leaching solution (5 mL), and $M_{(xCO3)}$ the molar mass of carbonate.

Finally, the "corrected" Sr and Nd concentrations $[x]_{residue}$ (x = Sr, Nd) that is, relative to the mass of the silicate residue of the leaching procedure alone, can be calculated from the bulk x concentration $[x]_{bulk}$:

$$[x]_{residue} = [x]_{bulk} \times \frac{Weight_{bulk}}{Weight_{bulk} - Weight_{leached}}$$

Sr and Nd concentrations reported in Table S2 correspond to $[x]_{residue}$ values calculated from equations above.

S4. Method for major and trace measurements

Major and trace element concentrations were measured using an Agilent 7900 quadrupole ICP-MS (Q-ICP-MS) at the High-Resolution Analytical Platform (PARI) of the Institut de physique du globe de Paris (IPGP). Liquid samples were sprayed through a micro-nebulizer in a Scott spray chamber prior to ionization. Magnesium (Mg), calcium (Ca), and iron (Fe) were measured using a collision-reaction cell with helium gas (5 mL.min^{-1}) to remove polyatomic interferences. Nd and Sr were measured without collision gas. Signal drift and matrix effects were corrected by injection of scandium, indium, and rhenium as internal standards after inline mixing with the samples. Two sets of multi-element calibration standards (one for major and one for trace elements) were analysed to compute the calibration curves that were used to convert measured counts to concentrations. The reported uncertainties were calculated using the algebraic propagation of blank subtraction and sample count standard deviations (n=3). The NIST®SRM®2709a reference material (San Joaquin soil) was processed as samples and analysed repeatedly during the sequences to evaluate the accuracy of the measurements. The detection limit was between 0.2 and 0.5 ppt depending on the element, and the internal errors were 5% on average. The weight loss during carbonate leaching of lake (and river in some cases) sediments was considered in the estimate of major and trace element concentrations of the residue, such that the reported concentrations relate to the mass of residue (that is, carbonate-free, and referred to as "silicate" in the following) component of the sediment (see supplementary S3).

S5. Method for isotopic composition measurements

Sr isotope ratios were measured by multi-collector inductively coupled plasma mass spectrometry (MC-ICPMS; Neptune, Thermo-Fisher Scientific) with an APEX-Q (ESI) desolvation system as a sample introduction system. Rubidium (Rb, that was observed in residual amounts in some samples, even after chromatographic purification) interference on mass 87 and krypton (Kr, present in the argon gas used to produce the plasma) interferences on masses 84 and 86 were corrected for using the ^{85}Rb and ^{83}Kr signals along with the Rb and Kr isotope ratios measured at the beginning of the sequence. Instrumental and natural mass fractionation on the ^{87}Sr/^{86}Sr ratio

were corrected using an exponential law, the measured $^{88}Sr/^{86}Sr$ ratio and the "natural" abundance $^{88}Sr/^{86}Sr$ ratio assumed to be equal to 8.3752. Measurement accuracy was checked through repeated measurements of the NIST pure-Sr, isotope reference material SRM 987 (2 S.D of 2.9 x 10^{-5}), and the NIST soil reference material SRM 2709a (87Sr/86Sr = 0.70823 ± 0.00002; comparing well with the value provided by Brazier et al., 2020 of 0.70814 ± 0.00002). Each sample was measured up to three times during a session. For samples measured three times, the 95% confidence interval was obtained from Student's t-distribution and ranged from 3 x 10^{-6} to 8 x 10^{-3}. For other samples measured less than 3 times, the 2 S.D of 4.9 x 10^{-5} estimated from the repeated measurements of the reference material NIST SRM 2709a (processed through powder digestion and separation as for samples) was used as an estimate of the 95% confidence interval.

Nd isotope analyses were performed by MC-ICP-MS Neptune using N_2 addition and X-cones with an APEX-IR (ESI) desolvation system as the sample introduction system. Instrumental and natural mass fractionation on the $^{143}Nd/^{144}Nd$ ratio were corrected for using an exponential law, the measured $^{146}Nd/^{144}Nd$ ratio and its natural abundance ratio, taken as 0.7218. Accuracy was checked through repeated measurements of a NIST pure-Nd, isotope reference material ($^{143}Nd/^{144}Nd$ = 0.511418; Caro et al., 2006), with a measured 2 S.D of 2.7 x 10^{-6}, and the NIST soil reference material SRM2709a (0.512381 ± 0.000028).

S6. Estimation of silicate $^{87}Sr/^{86}Sr$ ratios for river sediment samples

In sub-catchments where sedimentary rocks are predominant, the erosion products from low-$^{87}Sr/^{86}Sr$ carbonate rocks (limestones and/or dolostones) are typically mixed with those from silicate rocks (marlstones), resulting in a lower $^{87}Sr/^{86}Sr$ ratio of the bulk river sediment sample compared to the ratio expected from erosion of the silicate components alone. This is why lake and river sediment samples were decarbonated by two successive HCl leaching steps (Fig. S1). A shift towards higher $^{87}Sr/^{86}Sr$ ratios values from bulk samples to leach residues is observed for all the samples located in the southern part of the Val Camonica valley (8.A, 7.A, 9.B and 8, 7, 6) where sedimentary deposits are predominant (Fig. S2). This observation implies that bulk river sediments from these sub-catchments are composed of both silicates and carbonates.

However, despite our decarbonation procedure leading to higher $^{87}Sr/^{86}Sr$ ratios, none of the sub-catchment sediments present $^{87}Sr/^{86}Sr$ ratios that are high enough to explain the highest values recorded in Lake Iseo sediment samples. This can be due to: (i) the omission of a more radiogenic rock source present in the Lake Iseo watershed, (ii) the influence of authigenic production of the lake. The first hypothesis can be discarded as all the tributaries of the Oglio River were sampled. The second hypothesis can also be ruled out as almost all the authigenic carbonates produced in Lake Iseo are dissolved in the water column before reaching the floor of the deep basin (Ramisch et al., 1999; Rapuc et al., 2020a). However, we note that the sampled river sediments typically have coarser grain sizes (with D50 > 63 µm) than lake sediments (with 10 µm < D50 < 20 µm). In addition, detrital carbonates are likely to have coarser grain sizes than the silicate grains in the river sediment (Arnaud, 2005). Because of selective deposition of such coarse detrital carbonate particles in the lake delta our river sediment samples contain more detrital carbonates than lake sediments, where they represent less than 20 % of the total weight

(Rapuc et al., 2020a). Because of this grain size difference, we contend that our decarbonation procedure was probably much more efficient for lake sediment samples than for river sediment samples.

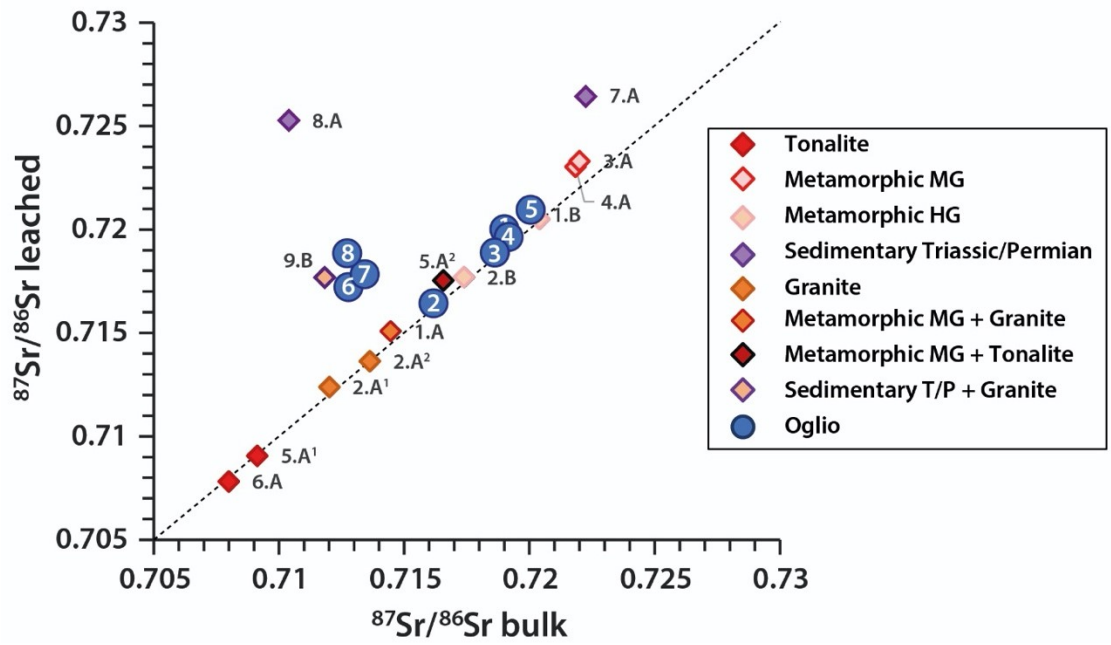

Figure S1 – Effect of the leaching procedure on river sediment samples, shown as a biplot of $^{87}Sr/^{86}Sr$ measured on bulk samples and on the leach residue. The dashed line corresponds to a 1:1 relationship between bulk and leach residue $^{87}Sr/^{86}Sr$. Samples departing from this line are affected by the decarbonation, and most likely contain significant amounts of carbonate material. Note that the river sediment from catchment draining igneous (magmatic or metamorphic rocks) are poorly affected by the leaching procedure (that is, fall on the 1:1 line), showing that this procedure is well-designed for specifically extracting carbonate material and leaving the silicate residue unchanged.

Regardless of the underlying reason, it appears that two leaching steps were not sufficient to remove all the detrital carbonates from the river sediment samples.

To circumvent this issue, we can use extrapolation in geochemical mixing diagrams to estimate the $^{87}Sr/^{86}Sr$ ratio of the marlstone (sedimentary silicate) end member of the catchments. Assuming that river sediments are made of a binary mixture between a carbonate (low $^{87}Sr/^{86}Sr$ ratio, high Ca/Sr ratio) and silicate (high $^{87}Sr/^{86}Sr$ ratio, low Ca/Sr ratio) component, their bulk composition should fall on a line in a $^{87}Sr/^{86}Sr$ – Ca/Sr diagram, this line going through the composition of each end member. By extrapolating the trend defined by the bulk and leach residue data in this diagram (Fig. S3) to the Ca/Sr of marlstone, it should be possible to estimate the $^{87}Sr/^{86}Sr$ of marlstone. To identify the Ca/Sr ratio of the marlstone end member, we turn to the lake sediment composition. Periods when lake sediments have the highest $^{87}Sr/^{86}Sr$ ratios are suspected to be the most affected by marlstone inputs. During those periods, abundance of Sr and Ca in lake sediments can be considered as equivalent to those of the average marlstone in the catchment.

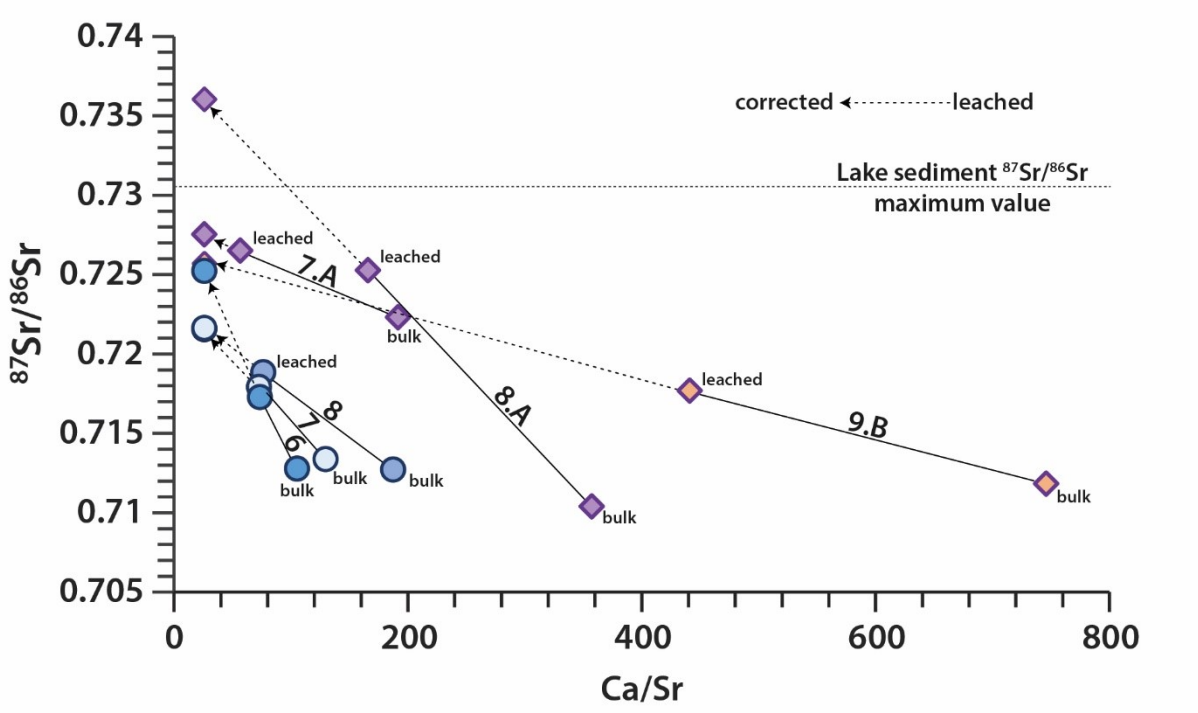

Figure S2 – Ca/Sr vs. $^{87}Sr/^{86}Sr$ ratios for bulk river sediment and corresponding leach residues, for sampled that have been shown to be affected by the leaching procedure (Fig. S2). For each sub-catchment, the solid line passes through the bulk and leach residue data points. The projection of each lines to the mean Ca/Sr value of lake sediments allows for an estimate of the $^{87}Sr/^{86}Sr$ ratio of the silicate component of each sample.

This method was applied to all six source samples identified as relevant for constraining the end member compositions (see main text) (Fig. S3). Only for sample 8.A do we obtain by extrapolation of the trend an estimated marlstone $^{87}Sr/^{86}Sr$ ratio higher than that of the lake sediments (Table S3). This ratio is thus be considered as representative of the sedimentary end member, as it is the only one able to account for all $^{87}Sr/^{86}Sr$ values observed in lake sediments.

Table S3 – Ca and Sr concentrations, $^{87}Sr/^{86}Sr$ values, and Ca/Sr ratios of river sediment samples for which we attempted to obtain the $^{87}Sr/^{86}Sr$ values ratio of the silicate end member. Bold font represents the estimate of the sedimentary end member after extrapolation in the $^{87}Sr/^{86}Sr$ values - Ca/Sr diagram.

Samples	[Ca] (ppm)	$^{87}Sr/^{86}Sr$	[Sr] (ppm)	Ca/Sr
8.A bulk	1.39E+05	0.7104	3.90E+02	357
8.A leached	6.88E+03	0.7253	4.15E+01	166
8.A silicate	**2.42E+03**	**0.7360**	**9.36E+01**	**26**
7.A bulk	1.43E+04	0.7223	7.45E+01	191
7.A leached	3.67E+03	0.7265	6.49E+01	57
7.A silicate	**2.04E+03**	**0.7275**	**9.36E+01**	**26**
9.B bulk	1.30E+05	0.7118	1.74E+02	746
9.B leached	2.71E+04	0.7177	6.14E+01	441
9.B silicate	**2.04E+03**	**0.7257**	**9.36E+01**	**26**
8 bulk	6.43E+04	0.7127	3.43E+02	187
8 leached	8.54E+03	0.7188	1.12E+02	76
8 silicate	**2.04E+03**	**0.7215**	**9.36E+01**	**26**
7 bulk	4.06E+04	0.7134	3.13E+02	130
7 leached	1.06E+04	0.7179	1.46E+02	73
7 silicate	**2.04E+03**	**0.7216**	**9.36E+01**	**26**
6 bulk	4.27E+04	0.7128	4.06E+02	105
6 leached	1.43E+04	0.7173	1.94E+02	74
6 silicate	**2.04E+03**	**0.7252**	**9.36E+01**	**26**

S7. Solution for 3 end members mixing model

****

$$f_A = ([Nd]^B * (\varepsilon Nd^M - \varepsilon Nd^B) * [Sr]^C * ({}^{\frac{87}{86}}Sr^M - {}^{\frac{87}{86}}Sr^C) - [Nd]^C * (\varepsilon Nd^M - \varepsilon Nd^C) * [Sr]^B * ({}^{\frac{87}{86}}Sr^M - {}^{\frac{87}{86}}Sr^B) / ([Nd]^A * (\varepsilon Nd^M - \varepsilon Nd^A) * ([Sr]^B - [Sr]^C) * {}^{\frac{87}{86}}Sr^M - [Nd]^A * (\varepsilon Nd^M - \varepsilon Nd^A) * ({}^{\frac{87}{86}}Sr^B * [Sr]^B - {}^{\frac{87}{86}}Sr^C * [Sr]^C) + [Nd]^B * (\varepsilon Nd^B - \varepsilon Nd^M) * ([Sr]^A - [Sr]^C) * {}^{\frac{87}{86}}Sr^M + [Nd]^B * (\varepsilon Nd^M - \varepsilon Nd^B) * ({}^{\frac{87}{86}}Sr^A * [Sr]^A - {}^{\frac{87}{86}}Sr^C * [Sr]^C) + [Nd]^C * (\varepsilon Nd^M - \varepsilon Nd^C) * ([Sr]^A - [Sr]^B) * {}^{\frac{87}{86}}Sr^M - [Nd]^C * (\varepsilon Nd^M - \varepsilon Nd^C) * ({}^{\frac{87}{86}}Sr^A * [Sr]^A - {}^{\frac{87}{86}}Sr^B * [Sr]^B)$$

****

$$f_B = ([Nd]^A * (\varepsilon Nd^M - \varepsilon Nd^A) * [Sr]^C * ({}^{\frac{87}{86}}Sr^M - {}^{\frac{87}{86}}Sr^C) - [Nd]^C * (\varepsilon Nd^M - \varepsilon Nd^C) * [Sr]^A * ({}^{\frac{87}{86}}Sr^M - {}^{\frac{87}{86}}Sr^A) / ([Nd]^B * (\varepsilon Nd^M - \varepsilon Nd^B) * ([Sr]^A - [Sr]^C) * {}^{\frac{87}{86}}Sr^M - [Nd]^B * (\varepsilon Nd^M - \varepsilon Nd^B) * ({}^{\frac{87}{86}}Sr^A * [Sr]^A - {}^{\frac{87}{86}}Sr^C * [Sr]^C) + [Nd]^A * (\varepsilon Nd^A - \varepsilon Nd^M) * ([Sr]^B - [Sr]^C) * {}^{\frac{87}{86}}Sr^M + [Nd]^A * (\varepsilon Nd^M - \varepsilon Nd^A) * ({}^{\frac{87}{86}}Sr^B * [Sr]^B - {}^{\frac{87}{86}}Sr^C * [Sr]^C) + [Nd]^C * (\varepsilon Nd^M - \varepsilon Nd^C) * ([Sr]^B - [Sr]^A) * {}^{\frac{87}{86}}Sr^M - [Nd]^C * (\varepsilon Nd^M - \varepsilon Nd^C) * ({}^{\frac{87}{86}}Sr^B * [Sr]^B - {}^{\frac{87}{86}}Sr^A * [Sr]^A)$$

****

$$f_C = ([Nd]^B * (\varepsilon Nd^M - \varepsilon Nd^B) * [Sr]^A * ({}^{\frac{87}{86}}Sr^M - {}^{\frac{87}{86}}Sr^A) - [Nd]^A * (\varepsilon Nd^M - \varepsilon Nd^A) * [Sr]^B * ({}^{\frac{87}{86}}Sr^M - {}^{\frac{87}{86}}Sr^B) / ([Nd]^C * (\varepsilon Nd^M - \varepsilon Nd^C) * ([Sr]^B - [Sr]^A) * {}^{\frac{87}{86}}Sr^M - [Nd]^C * (\varepsilon Nd^M - \varepsilon Nd^C) * ({}^{\frac{87}{86}}Sr^B * [Sr]^B - {}^{\frac{87}{86}}Sr^A * [Sr]^A) + [Nd]^B * (\varepsilon Nd^B - \varepsilon Nd^M) * ([Sr]^C - [Sr]^A) * {}^{\frac{87}{86}}Sr^M + [Nd]^B * (\varepsilon Nd^M - \varepsilon Nd^B) * ({}^{\frac{87}{86}}Sr^C * [Sr]^C - {}^{\frac{87}{86}}Sr^A * [Sr]^A) + [Nd]^A * (\varepsilon Nd^M - \varepsilon Nd^A) * ([Sr]^C - [Sr]^B) * {}^{\frac{87}{86}}Sr^M - [Nd]^A * (\varepsilon Nd^M - \varepsilon Nd^A) * ({}^{\frac{87}{86}}Sr^C * [Sr]^C - {}^{\frac{87}{86}}Sr^B * [Sr]^B)$$

S8. Uncertainty on the fractional contribution of the three rock sources

Table S4– Fractional contribution to Lake Iseo sediments and sediment yield of each source (magmatic, metamorphic and "sedimentary rock") in the corresponding catchment over the last 2,000 years, as obtained from the mixing model. The statistical parameters reflect the uncertainty and characterize the parameter distribution obtained from a Monte Carlo approach.

Samples	yr CE	Proportion Magmatic	Median	D84	D16	Proportion Sedimentary	Median	D84	D16	Proportion Metamorphic	Median	D84	D16	Sediment yield Magmatic ($t.km^{-2}.yr^{-1}$)	S.D	Sediment yield Sedim ($t.km^{-2}.yr^{-1}$)	S.D	Sediment yield Meta ($t.km^{-2}.yr^{-1}$)	S.D
SEB1	1938	0.053	0.052	0.036	0.071	0.833	0.828	0.780	0.871	0.114	0.117	0.076	0.167	9.576	9.677	98.689	0.009	11.825	0.038
SEB2	1926	0.029	0.028	0.013	0.044	0.751	0.745	0.681	0.801	0.221	0.225	0.164	0.297	4.584	2.939	78.956	19.093	20.395	8.266
SEB3	1872	0.026	0.025	0.014	0.038	0.893	0.891	0.850	0.924	0.081	0.082	0.047	0.127	5.181	2.862	118.925	25.845	9.519	5.469
SEB4	1845	0.055	0.053	0.038	0.073	0.821	0.819	0.767	0.860	0.124	0.124	0.084	0.177	9.165	4.075	90.736	23.195	12.033	5.886
SEB5	1815	0.041	0.040	0.027	0.056	0.856	0.852	0.807	0.891	0.102	0.104	0.067	0.154	6.408	2.808	88.080	17.613	9.267	4.802
SEB6	1790	0.033	0.031	0.019	0.046	0.860	0.856	0.811	0.894	0.108	0.110	0.070	0.160	4.999	2.398	86.992	16.001	9.592	4.666
SEB7	1746	0.038	0.036	0.006	0.082	0.856	0.850	0.777	0.906	0.106	0.110	0.068	0.162	4.980	5.903	73.181	11.562	7.943	3.933
SEB8	1661	0.029	0.028	0.016	0.042	0.866	0.863	0.819	0.901	0.105	0.105	0.066	0.154	3.413	1.697	66.820	7.848	7.092	3.285
SEB9	1621	#N/A	#N/A	#N/A	#N/A	#N/A	#N/A	#N/A	#N/A	#N/A	#N/A	#N/A	#N/A	#N/A	#N/A	#N/A	#N/A	#N/A	#N/A
SEB10	1551	0.053	0.052	0.037	0.071	0.835	0.830	0.780	0.873	0.112	0.115	0.073	0.165	7.043	2.749	73.099	12.172	8.642	4.011
SEB11	1504	0.032	0.031	0.016	0.047	0.773	0.771	0.709	0.822	0.195	0.196	0.141	0.265	3.910	2.186	62.789	13.023	13.914	5.485
SEB12	1441	0.001	0.000	#####	0.016	0.682	0.679	0.601	0.745	0.317	0.321	0.244	0.410	0.155	2.184	54.432	11.991	22.240	7.430
SEB13	1401	0.030	0.029	0.016	0.044	0.825	0.821	0.769	0.864	0.145	0.147	0.101	0.205	3.911	2.019	70.016	12.032	10.828	4.511
SEB14	1350	0.011	0.010	#####	0.024	0.770	0.769	0.707	0.819	0.219	0.220	0.163	0.293	1.408	2.114	68.066	8.695	17.055	5.619
SEB15	1302	0.020	0.019	0.005	0.033	0.800	0.799	0.743	0.844	0.180	0.181	0.129	0.245	2.858	2.185	75.391	6.216	14.924	5.094
SEB16	1265	0.050	0.049	0.033	0.068	0.752	0.744	0.681	0.800	0.198	0.203	0.146	0.272	7.366	2.850	72.427	8.443	16.768	5.637
SEB17	1224	0.030	0.029	0.015	0.045	0.783	0.780	0.721	0.830	0.187	0.189	0.136	0.255	4.482	2.382	77.573	6.663	16.290	5.482
SEB18	1185	0.055	0.055	0.039	0.074	0.851	0.847	0.801	0.887	0.094	0.095	0.058	0.141	7.494	2.540	75.924	5.085	7.373	3.440
SEB19	1131	0.030	0.030	0.017	0.044	0.857	0.853	0.809	0.892	0.113	0.115	0.075	0.165	4.556	2.138	85.010	5.903	9.819	4.146
SEB20	1091	0.032	0.030	0.018	0.045	0.876	0.872	0.830	0.908	0.093	0.095	0.058	0.141	4.141	1.885	75.566	6.110	7.020	3.401
SEB21	1033	-0.006	-0.006	#####	0.007	0.779	0.779	0.713	0.832	0.227	0.228	0.167	0.304	-0.896	2.464	80.841	7.381	20.684	6.473
SEB22	1015	0.017	0.016	0.006	0.027	0.888	0.887	0.846	0.921	0.095	0.096	0.058	0.142	2.422	1.729	84.429	8.390	7.944	3.749
SEB23	984	0.009	0.008	#####	0.020	0.837	0.836	0.785	0.878	0.155	0.155	0.107	0.214	1.202	1.931	77.793	6.793	12.629	4.709
SEB24	907	0.044	0.043	0.029	0.060	0.852	0.847	0.800	0.886	0.104	0.107	0.067	0.156	5.122	2.036	65.412	8.639	7.046	3.346
SEB25	844	0.019	0.018	0.002	0.033	0.747	0.743	0.678	0.798	0.234	0.238	0.175	0.313	2.291	1.968	59.257	10.435	16.323	5.514
SEB26	737	0.033	0.031	0.017	0.047	0.772	0.767	0.704	0.817	0.195	0.200	0.145	0.269	4.724	2.396	73.834	6.660	16.384	5.491

SEB27	495	0.050	0.049	0.033	0.068	0.769	0.763	0.701	0.815	0.181	0.184	0.134	0.251	6.095	2.324	61.642	5.437	12.746	4.377
SEB28	305	0.071	0.069	0.051	0.092	0.787	0.779	0.722	0.829	0.143	0.148	0.102	0.203	6.416	2.041	47.116	4.797	7.517	2.850
SEB29	228	0.060	0.059	0.040	0.082	0.578	0.566	0.477	0.643	0.362	0.371	0.290	0.469	5.751	2.173	36.370	5.874	20.031	5.166
SEB30	97	0.087	0.085	0.064	0.112	0.656	0.646	0.567	0.714	0.257	0.264	0.199	0.344	8.061	2.571	40.061	6.678	13.832	4.340

S9. Sensitivity analysis of the mixing model

Table S5 – Fractional contribution to Lake Iseo sediments of each source (magmatic. metamorphic and "sedimentary rock") in the corresponding catchment over the last 2,000 years. as obtained from the mixing model after a sensitivity analysis of the choice of the rock end member compositions. The statistical parameters reflect the uncertainty and characterize the parameter distribution obtained from a Monte Carlo approach.

Samples	MCD (cm)	yr CE	Pro. Magmatic	D16	D84	Prop. Sedim.	D16	D84	Pro. Meta	D16	D84
SEB1	57.8	1938	0.053	0.126	0.003	0.833	0.950	0.642	0.114	0.277	0.016
SEB2	78.8	1926	0.029	0.091	-0.025	0.751	0.889	0.514	0.221	0.452	0.083
SEB3	111.3	1872	0.026	0.074	-0.014	0.893	0.988	0.743	0.081	0.222	-0.009
SEB4	126.8	1845	0.055	0.126	0.002	0.821	0.934	0.616	0.124	0.297	0.027
SEB5	140.8	1815	0.041	0.102	-0.003	0.856	0.962	0.687	0.102	0.252	0.009
SEB6	150.8	1790	0.033	0.089	-0.011	0.860	0.968	0.689	0.108	0.262	0.008
SEB7	172.8	1746	0.038	0.120	-0.013	0.856	0.968	0.645	0.106	0.271	0.010
SEB8	230.8	1661	0.029	0.083	-0.013	0.866	0.971	0.684	0.105	0.272	0.009
SEB9	247.8	1621	#N/A	#N/A	#N/A	#N/A	#N/A	#N/A	#N/A	#N/A	#N/A
SEB10	316.3	1551	0.053	0.125	0.002	0.835	0.945	0.641	0.112	0.275	0.016
SEB11	353.9	1504	0.032	0.092	-0.019	0.773	0.905	0.538	0.195	0.424	0.066
SEB12	378.9	1441	0.001	0.054	-0.070	0.682	0.857	0.401	0.317	0.623	0.138
SEB13	392.7	1401	0.030	0.086	-0.016	0.825	0.939	0.642	0.145	0.324	0.033
SEB14	410.2	1350	0.011	0.061	-0.045	0.770	0.910	0.547	0.219	0.452	0.074
SEB15	449.7	1302	0.020	0.070	-0.031	0.800	0.927	0.601	0.180	0.386	0.054
SEB16	461.7	1265	0.050	0.127	-0.006	0.752	0.887	0.495	0.198	0.430	0.069
SEB17	474.7	1224	0.030	0.087	-0.023	0.783	0.909	0.574	0.187	0.391	0.061
SEB18	486.2	1185	0.055	0.123	0.004	0.851	0.959	0.658	0.094	0.249	0.005
SEB19	646.2	1131	0.030	0.086	-0.013	0.857	0.963	0.692	0.113	0.273	0.013
SEB20	663.2	1091	0.032	0.087	-0.011	0.876	0.975	0.705	0.093	0.245	0.000
SEB21	1042.7	1033	-0.006	0.038	-0.069	0.779	0.925	0.573	0.227	0.468	0.076
SEB22	1059.45	1015	0.017	0.060	-0.021	0.888	0.989	0.746	0.095	0.233	-0.002
SEB23	1078.9	984	0.009	0.053	-0.042	0.837	0.953	0.659	0.155	0.343	0.038
SEB24	1117.9	907	0.044	0.105	-0.001	0.852	0.961	0.674	0.104	0.263	0.008
SEB25	1138.9	844	0.019	0.072	-0.034	0.747	0.889	0.512	0.234	0.470	0.088
SEB26	1176.9	737	0.033	0.093	-0.018	0.772	0.907	0.546	0.195	0.414	0.063
SEB27	1395.4	495	0.050	0.119	-0.004	0.769	0.898	0.531	0.181	0.396	0.059
SEB28	1460.9	305	0.071	0.156	0.011	0.787	0.909	0.546	0.143	0.343	0.038
SEB29	1495.9	228	0.060	0.155	-0.012	0.578	0.768	0.225	0.362	0.698	0.170
SEB30	1533.9	97	0.087	0.197	0.017	0.656	0.816	0.322	0.257	0.551	0.112

S10. SCF calculation

The time-dependent erosion flux from the catchment was determined as follow, using the calculation of a siliciclastic flux (SCF; $g.cm^{-2}.yr^{-1}$) from the lake sediment samples (Rapuc et al., 2020a):

$$SCF = NCIR \times SR \times DBD \quad (6)$$

Here NCIR is the fraction of non-carbonate ignition residue of the lake sediments, which corresponds to the residue of the loss on ignition analysis (Rapuc et al., 2020a); SR is the sedimentation rate ($cm.yr^{-1}$) derived from the age-depth-model; and DBD is the dry bulk density of the samples ($g.cm^{-3}$). The DBD used in the SCF calculation was smoothed using a weighted arithmetic mean to reduce the impact of measurement bias in successive samples. The SR is derived from the age-depth-model of the SEB18 sediment section defined in Rapuc et al. (2020). In this model, the youngest ^{14}C date is highly uncertain, due to significant variations in the ^{14}C calibration curve (Reimer et al., 2020), inducing a large uncertainty on the SR value for the last 300 years. To reduce this abnormal SR uncertainty, we decided not to consider the youngest ^{14}C date of the age-depth-model and to use only the uncertainty linked to the other dates.

S11. Estimation of lake Iseo area

As stated in the main text, the sediment rate (SR) may vary spatially over the surface of a lake. To calculate a consistent $Stock_{sed}$ for the entire lake we need to consider only the fraction of the total lake area where SR should be commensurate with that measured at the coring site. We assumed that this area corresponds to the flat part of the deep basin as suggested by the seismic survey (Rapuc et al., 2020a), which lies below the slope discontinuity. Based on the lake bathymetry, we consider that the lake area with water depth below 210 m b.l.s should be taken into account in the calculation of $Stock_{sed}$, corresponding to a total of 18 km² (Fig. S4).

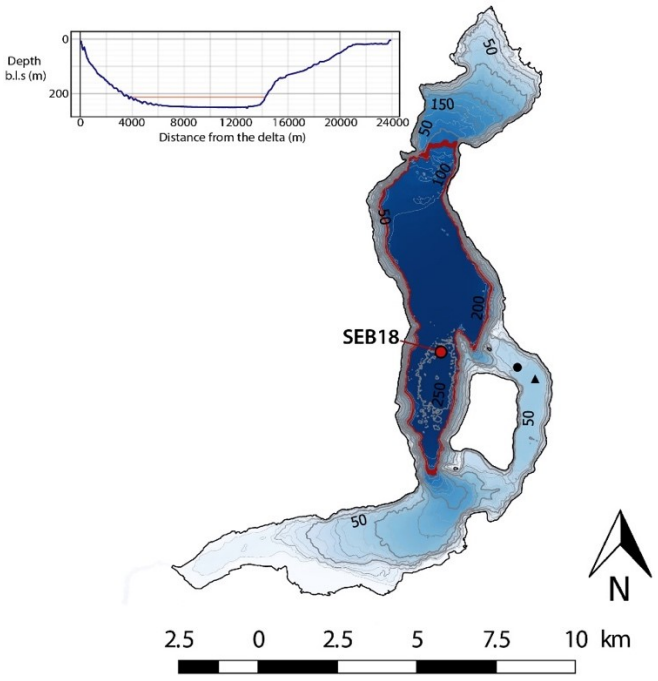

Figure S4 – Lake Iseo bathymetry, modified from Pilotti et al. (2013) and available at https://hydraulics.unibs.it/hydraulics/attivita-scientifica/laghi_pvbs/lake-iseo-data-set/. A bathymetric profile was drawn. From the map and the profile, the 210 m b.l.s correspond to a slope discontinuity from the delta.

S12. Estimation of contributing areas for each rock source

We demonstrate that the lake sediments accumulated in Lake Iseo deep basin correspond to a mixture of three rock end members: magmatic, sedimentary, and metamorphic rocks. In order to calculate the sediment yield associated with each end member, it is necessary to evaluate the area of the watershed that contributes to the corresponding sediment flux. To do so, we combined all similar rock types from the Lombardia geological map database of Brescia and Bergamo (http://www.geoportale.regione.lombardia.it/).

For the sedimentary end member, we aggregated all lithologies corresponding to sediment rock types, such as: conglomerates, mudstone, marlstones, calcareous marl, argillaceous limes, and arenites. As we only focus here on the physical erosion of silicates, carbonate rocks such as limestone and dolostone are not considered in the estimation of the sedimentary end member area, nor in the total surface area. Quaternary deposits were not considered either as they can originate from all the lithologies present in the watershed.

For the magmatic end member, we combine rhyolite, dacite, trachyte, andesite, quartzite, pegmatite, granite, granodiorite, quartzodiorite, and tonalite.

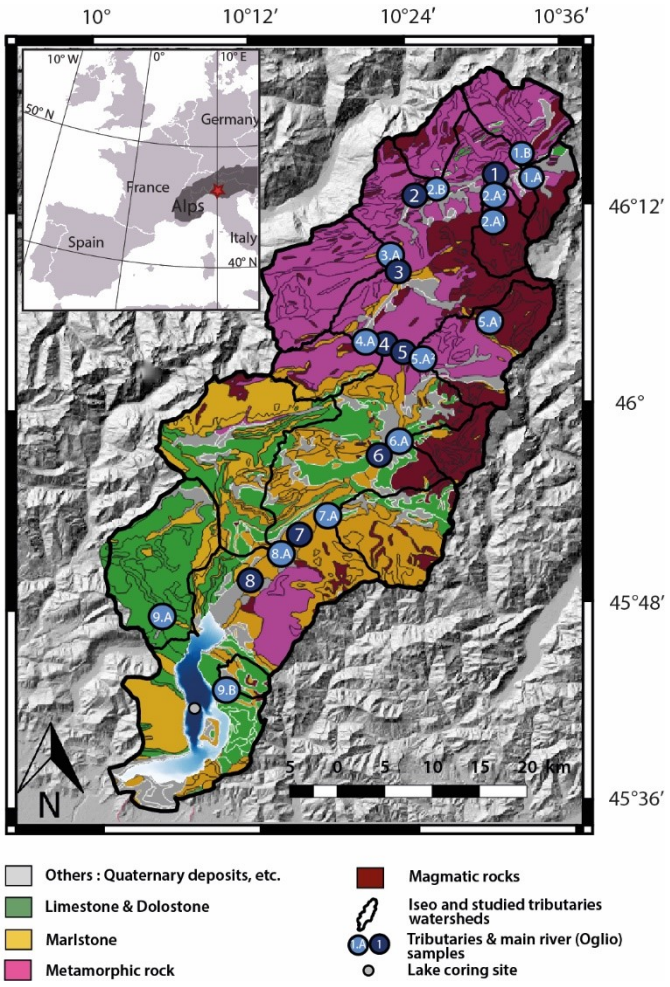

Figure S5 – Results of the aggregation of the different lithologies of the Iseo watershed into five main types

For the metamorphic end member, we gathered: paragneiss, gneiss and gneiss migmatite, mica schists, and quartzites. Lakes, rivers, glaciers, and slopes deposits were also set aside.

Using QGIS 3.10.6 software, all polygons corresponding to each rock type were re-classified following the aggregation criteria laid out above (Fig. S5) and the total area covered by each rock type was calculated (Table S6). Polygons were aggregated using vector grouping functions and their attributes were merged through table junction. Corresponding areas were re-calculated using vector calculator and the "$area" function.

Table S6 – Areas covered by each rock type in the Val Camonica

Type	Total area (m^2)	Fraction (%)
Magmatic	287.8	16.0
Sedimentary	435.8	24.2
Metamorphic	495.6	27.6
Total of end members	1219.1	67.8
Limestone & Dolostone	342.6	19.1
Others (lake. glaciers. …)	215.3	13.1
Total (with lake)	1797	100

S13. R.U.S.L.E model

Documentation about the Revised Universal Soil Loss Equation (R.U.S.L.E) model (Panagos et al., 2015) is available upon request on the JRC website: https://esdac.jrc.ec.europa.eu/resource-type/soil-threats-data

The annual average soil loss, expressed in $t.ha^{-1}.yr^{-1}$, was cut at the shape of the sedimentary areas with QGIS allowing to estimate the mean, the S.D and median values for the area (Table S7). Original raster containing the R.U.S.L.E values was cut to fit the catchment size using raster cutting with mask extraction function.

Table S7 – Statistics for E parameter for the sedimentary areas of the Val Camonica

	E ($t.ha^{-1}.yr^{-1}$)
Max	325
Min	1.94E-04
Mean	8.58
S.D	22.347
Median	0.71

Due to the distribution property being long tailed (Fig. S6), the median is preferred to characterize the catchment instead of the mean value (better suited for normal distributions). Extreme values can be related to high slopes values, or to high soil erodibility factor associated to competent rock formations mistakenly allocated to sedimentary areas in our gathering. Moreover, RUSLE values are known to potentially overestimate the erosion rates in some mountainous areas (Panagos et al.. 2015).

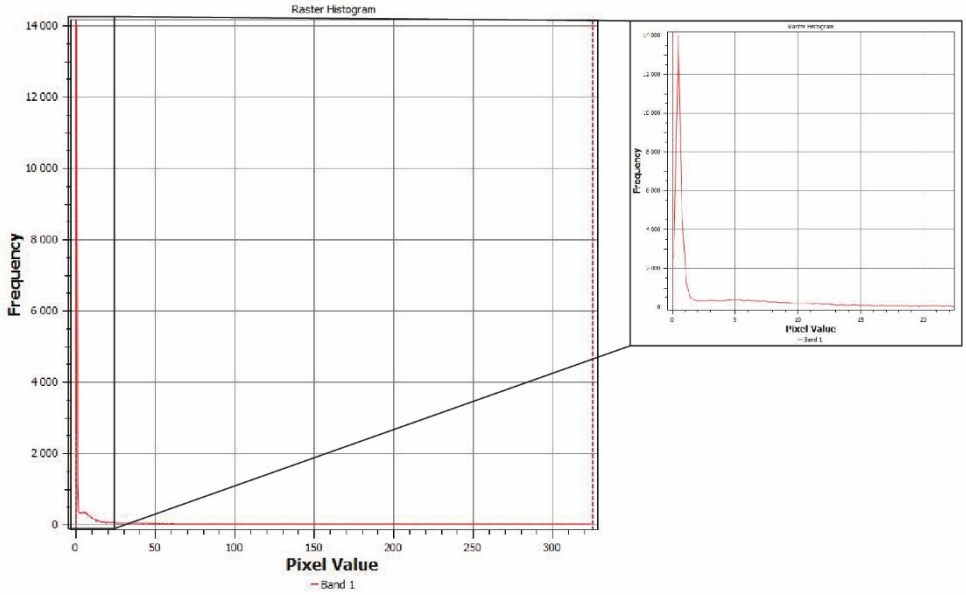

Figure S6 – Frequency distribution histogram of E values from R.U.S.L.E model for the sedimentary areas of the Val Camonica. The distribution is concentrated between 0 and 1.8 t.ha^{-1}.yr^{-1}.

The median values of annual average soil loss in the sedimentary areas of the Val Camonica is about 0.71 t.ha^{-1}.yr^{-1} or 71 t.km^{-2}.yr^{-1} once converted. This value is within the range of sediment yield for the sedimentary areas measured in this study.

CHAPITRE X | Evaluating the impact of human and climate forcing on erosion in the Alpine Critical Zone over the last 10 000 years.

Article 5 | In Prep

William Rapuc[1], Julien Bouchez[2], Pierre Sabatier[1], Jérôme Gaillardet[2,3] and Fabien Arnaud[1]

[1] Univ. Grenoble Alpes, Univ. Savoie Mont Blanc, CNRS, EDYTEM, 73000 Chambéry, France
[2] Université de Paris, Institut de physique du globe de Paris, CNRS, F-75005 Paris, France
[3] Institut Universitaire de France

Abstract

The Critical Zone (CZ), defined as the thin active layer at the Earth's surface is at risk due to climate change and anthropogenic pressure increase. This represents a potential threat to the future of humanity as the CZ is the locus of developing human societies. CZ's soil erosion is now considered as one of the geosciences/society central issues. Understanding the influence of climate fluctuations and human activities, the two mains forcing factors, is key to improve our management of the CZ's soil resource, especially in mountainous areas where erosion is highest. Only studies combining large spatial and temporal approaches allow to assess the effect of the different forcing factors on soil erosion rates. Here, we apply a retrospective approach based on lake sediments to reconstruct the long-term evolution of erosion in alpine landscapes. Lake Bourget, located in the northern French Alps acts as a natural sink for all the erosion products from a large watershed (4600 km²). We combined a multiproxy study of a lacustrine sediment section covering the Holocene with a source-to-sink method, using isotopic geochemistry (εNd, $^{87}Sr/^{86}Sr$). The applied methodology allows us to disentangle the role of climate and land use as erosion forcing factors through their differential impact on the various rock types present in the catchment. Indeed, the Mont Blanc massif, where the erosion is dominated by precipitation and glacier advances, presents isotopic signature different from those of the sedimentary rocks located in the rest of the catchment, where both human activities and precipitations impact erosion through time. To understand the effect of human activities, erosion signals from Mont Blanc massif and the rest of the catchment were compared to local and regional erosion chronicles. During the Early Holocene and until 3.8 kyr cal BP, the erosion signal is dominated by climate fluctuations. Between 5 and 4 kyr cal BP the erosion increase is linked to a transition towards wetter and colder climate, leading to an increase of Mediterranean climate influence on the easternmost part of the French Alps. Since 3.8 kyr cal BP, climate fluctuations alone cannot explain measured erosion trends. From then, human activities by modifying the soil erodibility through land-use become the dominant forcing factor of the physical erosion in mountainous environment of northern French Alps.

KEYWORDS

Erosion, Climate and Human impact, Lake sediments, Source to sink method, isotopic mixing model

1. Introduction

The Critical Zone (CZ) is defined as the thin active layer at the interface between atmosphere – lithosphere – biosphere – hydrosphere (Anderson et al., 2007; Chorover et al., 2007). This area is critical because it is the support for most of terrestrial life forms and because it is the site of development and the main challenges of human societies (National Research Council, 2000). The current climate change associated with the increase of anthropogenic pressure on the CZ thus represent potential threats to the future of humanity (Crutzen, 2006). Indeed, climate and human forcing impact the CZ soil's erosion rate, which in turns lead to the deterioration of the CZ. Among other impacts, by destroying soils, erosion alters food production, drinking water quality, ecosystems services, biodiversity, and soil carbon stocks (e.g. Bosco et al., 2008; Panagos et al., 2015) which directly affects human societies (Montgomery, 2012). Due to the particularly delicate environment, the rigorous climate conditions, and the important altitudinal gradient, mountainous environments are hotspots of CZ erosion (Bosco et al., 2008). CZ erosion thus become a scientific subject of prime importance worldwide (Borrelli et al., 2020; FAO, 2015; Panagos et al., 2015b; Rusco et al., 2008) leading Europe and the United Nations to rank it as one of the main threats to mankind, and to call for quantitative evaluation of soil loss over large spatial and long temporal scales (e.g. Panagos et al., 2015 and references therein). These evaluations imply notably to better assess the relative effects of the main factors impacting the CZ erosion rate, being:

(i) climate fluctuations, through precipitation amounts and glacier advances and retreats (Borrelli et al., 2020);
(ii) tectonic activities, notably through earthquake-generated slides (Wang et al., 2020);
(iii) human activities, through grazing, agriculture, ore extraction and the often-associated deforestation (Bajard et al., 2020).

To fill this knowledge gap, recent studies focused on modelling approaches (e.g. Angima et al., 2003; Borrelli et al., 2020; Millward and Mersey, 1999; Panagos et al., 2015; Renard et al., 1991), large-scale erosion rates reconstitution from river sediment yield (e.g., Kemp et al., 2020), or small-scale erosion rates reconstitution from continental natural archives (e.g. Bajard et al., 2020; Regattieri et al., 2019). However, none of these studies allows to produce a quantitative assessment of the impact of the various factors on erosion rates through time. Among others, retrospective approaches based on lake sediments seems to be the best compromise to reconstruct the long-term evolution of erosion and of the impacts of each forcing factors in a peculiar catchment in a continuous way (chapitre IX). Combining the study of lake sediments with a "source-to-sink" approach (e.g. Collins and Walling, 2002) offers the possibility to track the sources of sediment inputs to the lake through time, making it in turn possible to disentangle the relative impacts of climate and human activities upon erosion rates, provided that each sediment source is sensitive to a given type of forcing.

As a previous study already provides quantitative information on the impact of climate and human activities on erosion in the Italian Alps (chapitre IX), we focus here on the western part of the Alps, where climate trends and human activities evolved differently during the Holocene. We selected Lake Bourget, located in the northern French Alps, at the downstream end of the lower Rhône

valley. This lake presents the advantage of being already deeply studied in terms of sedimentation processes (e.g. Chapron et al., 2005; Debret et al., 2010; Evin et al., 2019; Giguet-Covex et al., 2010; Jenny et al., 2014b) and of sediment flux evolution and origin (e.g. Arnaud et al., 2016, 2012; Arnaud and Révillon, 2015; Revel-Rolland et al., 2005). Human activities in the area since the beginning of the Neolithic period are well documented (e.g. Giguet-Covex et al., 2021 and references therein). Lake Bourget drains a large catchment presenting two principal lithologies, distinguishable through the means of geochemical tools, and coinciding with different relative roles of climatic and human forcing on erosion over the centennial to millennial scales:

(i) The easternmost "Mt Blanc" area, that is the high-altitude part of the catchment, underlain by magmatic rocks, where human activities are sparce (Giguet-Covex et al., 2021) and where glacier bodies are widely developed (Gardent et al., 2014);

(ii) The rest of the catchment, underlain by Permian to Miocene sedimentary cover, where human activities were concentrated since the beginning of the late Holocene (Giguet-Covex et al., 2021).

To quantify the evolution of erosion in the catchment of Lake Bourget throughout the Holocene, we followed the methodology developed in a previous study (chapitre IX). A sediment sequence was retrieved in the deep basin of the lake, and river samples from all the sub-catchments directly contributing to Lake Bourget were collected close to each confluence.

2. Study site

Lake Bourget (18 km long, 2.8 km wide, 231.5 m.a.s.l) is a peri-alpine hard water lake located in the north-western part of the French Alps (Fig. X-1). This is the largest natural lake entirely lying in France (44.5 km²). The depression that hosts the lake was formed by the retreat of Würmian glaciers (Nicoud et al., 1987). Lake Bourget is considered as a monomictic lake. Its hypolimnion is partially reoxygenated during winter water mixing before that hypoxia increases progressively during thermal stratification (Jenny et al., 2013). For at least three decades, Lake Bourget sediments have been deeply studied to describe for instance the regional flood activity and understand the relationship between Rhône discharge and the volume of event layers in the lake (Arnaud, 2005; Arnaud and Révillon, 2015; Chapron et al., 2002, 2005; Debret et al., 2010; Evin et al., 2019; Jenny et al., 2014b). These studies indicate that the northern part of the lake basin is influenced by flood events from the Rhône River, contributing from 10 to 40% to the total sedimentation. Rhône River can generate event layers in the lake basin due to underflows during high-energy flood events, and characterized by darker colour, interrupting the light grey continuous background sedimentation (Giguet-Covex et al., 2010). Continuous sedimentation in the lake is composed of autochthonous carbonates, detrital carbonates and allochthonous detrital elements (Giguet-Covex et al., 2010; Jenny et al., 2014b). Erosion signal from the catchment is usually tracked by using the concentration in titanium (Ti) of the accumulated sediment (Arnaud et al., 2012).

Lake Bourget is fed in water by two main tributaries: Leysse and Sierroz (Fig. X-1). In normal flow conditions, these rivers contribute to sediment accumulation in the southern part of the lake, and the water outflows in the northern part and join the Rhône River. In this condition, Lake Bourget is connected to a small catchment of 588 km² (Giguet-Covex et al., 2010). However, during flood events, current reversal takes place and the sediment-rich waters of Rhône River inflows in the lake. In these conditions, Rhône River becomes the main contributor of sediment particles in Lake

Bourget. With the Rhône River catchment, the catchment of the lake covers a large area (approx. 4600 km²), including the Arve River that originates in the Mont-Blanc massif (4809 m a.s.l) and several other tributaries as the Fier and Giffre rivers (Fig. X-1). The "Alpine" Rhône River catchment located upstream of Lake Geneva, do not participate to sediment input in Lake Bourget as Lake Geneva is considered as a perfect sediment trap (Arnaud et al., 2012; Chardon, 1987). In summary, Lake Bourget do not record the entire erosion of its large watershed.

Lake Bourget catchment present a wide range of lithologies, that can be distinguished in three main litho-tectonic domains (Schmid et al., 2004):

(i) the Austro-alpine domain;
(ii) the external crystalline massif and the Helvetic zone, present in the eastern part of the catchment;
(iii) the Mesozoic sedimentary cover.

In the studied catchment, the Austro-alpine domain is composed mainly of sedimentary rocks such as flysch, limestones, marlstones, dolostones and conglomerates. This series crops out in the northern part of the catchment, south of Lake Geneva (Fig. X-1), and was formed by the collision of the southern European continental margin with the Adria microplate (Schmid et al., 2004).

Most of Lake Bourget catchment is composed of sedimentary terrains. In the western part, the Jurassic chain, a series of marine limestones and marlstones, is partly covered by Cenozoic molasse composed of sandstones and marls (Manalt et al., 2001 and reference therein) and Quaternary moraines. Eastward, Cretaceous sub-alpine Massif, composed by an alternance of limestone and marlstones, overlain the Jurassic chain due to a major North-South thrust (Dal Piaz et al., 2003). Two klippes of Austro-alpine terrains crop out in the center of the sedimentary cover, East and North-East of lake Annecy (Fig. X-1).

The eastern part of the catchment is underlain by the Mont Blanc Massif, one of several Variscan external crystalline massifs of the Alps. Two units are distinguishable in the massif, (i) a Hercynian calco-alkaline batholith, mainly composed of granite (Rolland et al., 2003), and (ii) a Hercynian nappe, composed of sedimentary rocks at the border of the massif, and of metamorphic rocks such as paragneisses, orthogneisses and migmatites at the contact of the intrusion (Rolland et al., 2003 and references therein).

Lake Bourget lies at the downstream end of a large catchment area, with the European highest mountain peaks and large glaciers. Upstream of the Arve river, in the Mont Blanc Massif, the erosion rates are particularly high, and mainly driven by glacial erosion (Hinderer et al., 2013; and references therein). Mont Blanc Massif is characterized by the presence of the largest glacier in the French Alps (30.4 km², Gardent et al., 2014; Le Roy et al., 2015) and a total of 63 other glaciers bodies, that accounts altogether for an area of 104.2 km² (Gardent et al., 2014; data of 2006/09). French Alps are experiencing a temperate climate, with a mean annual air temperature decreasing from SW to NE. At 1800 m a.s.l the Mont Blanc Massif receive a total of 1827 $mm.yr^{-1}$ against 1718 $mm.yr^{-1}$ at Lake Bourget (235 m a.s.l.; https://meteofrance.com/).

At present days, human activities are concentrated alongside the main rivers and decrease upstream (https://www.data.gouv.fr/fr/datasets/corine-land-cover-occupation-des-sols-en-france/). Archaeological and palynological studies locate human settlements and agrarian activities in the entirety of the Lake Bourget catchment, with a maximum concentration at low and

mid-altitudes (Giguet-Covex et al., 2021; and references therein). In the Mont Blanc Massif, aside from modern times when touristic developments led to important anthropization, human activities are sparse, restricted to herd grazing and with only minor urban areas.

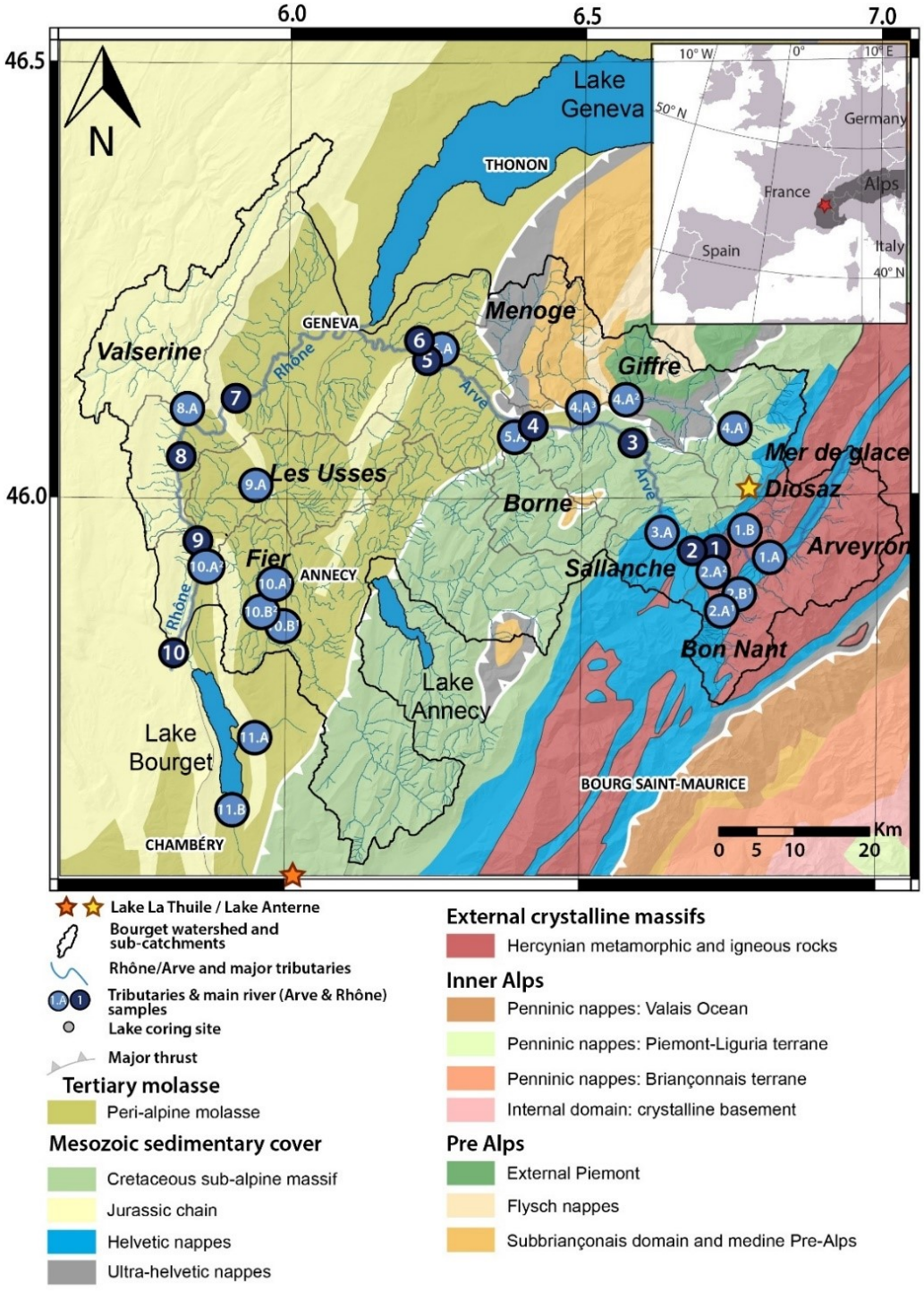

Fig. X-1- Geological map of the study area, superimposed on a shaded relief map, and location of sampling sites. The geological information is modified from the geological map of the Alps (Gidon, 1977). Location of Lake La Thuile and Anterne are reported (coloured stars). Erosion rate chronicles from those two lakes will be used hereafter. The geological background map was realized by Sidonie Revillon.

3. Materials and Methods

3.1. Lake sediment

3.1.1. Coring survey and logging

In June 2018 and 2019, a total of 56.5 m of sediment was retrieved from 10 different holes in close vicinity (less than 20 m) in the deep basin of Lake Bourget (145 m b.l.s), where the continuous sedimentation is supposed to be less influenced by event sedimentation (Jenny et al., 2014b) and sediment input from Rhône river will accumulate in a continuous way (Chapron et al., 2005; Jenny et al., 2014b). For this survey, two UWITEC 90-mm diameter piston corers (Uwitec, Mondsee, Austria) were used, the pushing power was provided using a semi-manual UWITEC downhole hammer, operated from an UWITEC platform (EDYTEM/LSCE/C2FN). Two meters-long sections from the different holes were taken with a 1 m offset to ensure a sufficient overlap to provide a continuous record (see **S1**). Most of the sections were split, photographed at high-resolution (20 pixels.mm^{-1}), described and logged in detail using the Munsell colour chart. The identification of specific layers on the overlapping sections combined with correlations of XRF-core scanner signals allowed the creation of a 13.7-m-long sediment sequence called "LDB18&19" (45°44.717'N; 5°51.789'E; **S2**).

3.1.2. Geochemistry

To characterize the variations of major elements throughout the sediment sequence, X-ray fluorescence (XRF) geochemical analyses was performed on the EDYTEM laboratory's AVAATECH Core Scanner (Avaatech XRF Technology). A continuous 5-mm step measurement was applied with a unique run at 10 kV and 0.12 mA for 15 s to detect lightweight elements, such as Al, Si, K, Ca, Ti, Mn, and Fe. The XRF core scanning results are expressed hereafter as peak intensities counting (cps).

3.1.3. Lake sediment samples

Fifty-nine 1 cm-long sediment samples were collected using graduate syringes for geochemical analyses. A constant sampling step of 10 cm was applied where no event deposit interrupts the continuous sedimentation (Table S3). Sediment dry bulk density (DBD) was measured using sediment samples of an invariant 5 mL volume. To quantify the organic matter and carbonate content throughout the sediment sequence, lost on ignition (LOI) analyses were conducted after 72 h of drying at 60°C. First, sediment samples were dried and crushed before being heated in an oven at 550°C for 4 h and at 950°C for 2 h. The relative weight loss during the first (hereafter, LOI550°C) and second heating phases (hereafter, LOI950°C) corresponds to the fractions of organic matter and of carbonate, respectively. Values of non-carbonated residue (NCIR), that is the sediment remaining after the second ignition step, will be displayed hereafter and used as the silicate content of the sediment sequence (Bajard et al., 2016).

3.1.4. Dating

To produce a precise age-depth model for the sediment sequence, we combined identification of historical events such as earthquake and floods deposits with ^{14}C. Nineteen samples of vegetal macro-organic remains were used to perform ^{14}C measurements at the LMC14 laboratory (CNRS). Dates were calibrated at 2 sigma using the Intcal20 calibration curve (Reimer et al., 2020), and the age-depth model was performed using the R code package "clam" (Blaauw, 2010) and "bacon" (Blaauw et al., 2021) in R software.

3.2. River sediment samples

To characterize the source of sediments accumulated in Lake Bourget deep basin, 19 river sediments samples were collected between January and February 2018 from flood deposits in all sub-catchments directly contributing to the Arve and Rhône River, close to the confluence with the main river (Fig. X-1; Table S2). Ten samples were also collected from flood deposits in the main river (Arve & Rhône) at several hundred meters downstream of each confluence to test for the mixing between sub-catchment and main river sediments (Fig. X-1; Table S2). Sub-catchments covered by this sampling set represent the entire catchment area of Lake Bourget. Samples were collected manually, an aliquot of each sample was sieved, and only the fraction finer than 63 µm was saved for later analysis. Here we selected the fraction finer than 63 µm to be in agreement with previous studies conducted in the same catchment (Arnaud et al., 2012; Revel-Rolland et al., 2005).

Lake and river sediment samples were first crushed in an agate mortar and dried at 60°C for 72 h in a laboratory oven. Then lake sediment samples were decarbonated by two successive 5 mL HCl 0.5N leaching steps to remove authigenic and detrital carbonate. Here we applied the procedure developed in CHAPITRE IX | to remove the influence of authigenic lake carbonates from the signature of lake sediment samples. As for Lake Iseo sediments, this leaching procedure did not lead to complete removal of the carbonate component from some of the lake samples. Only five river samples underwent the same procedure, to test the accuracy of their Sr isotopic composition with previously published data (Revel-Rolland et al., 2005). All samples (bulk or residue from the leaching steps), then underwent a digestion using concentrated acid mixtures of HF, HNO_3, and HCl.

3.3. Major and trace elements

Major and trace elements were measured using an Agilent 7900 quadrupole ICP-MS. A detailed description of the method is already presented in chapiter IX, more information is also provided in S5. The reported uncertainties were calculated using the algebraic propagation of blank subtraction and sample count standard deviations (n=3). The NIST®SRM®2709a reference material (San Joaquin soil) was processed as samples and analysed repeatedly during the sequences to evaluate the accuracy of the measurements. The detection limit was between 0.2 and 0.5 ppt depending on the element, and the internal errors were 5% on average.

3.4. Isotopic composition

Isotope measurements were all performed at the PARI analytical platform of IPGP. After powder digestion, Sr and Nd were separated from the sample matrix by extraction chromatography. We used an Sr-SPEC resin (Eichrom) for Sr (Hajj et al., 2017) and a combination of TRU-spec and Ln-spec resins for Nd (Cogez et al., 2015). For a detailed description of the method is already please refer to chapitre IX and supplementary S6. Both isotope ratios were measured by multi-collector inductively coupled plasma mass spectrometry (MC-ICPMS; Neptune, Thermo-Fisher Scientific).

For Sr isotope analyses, instrumental and natural mass fractionation on the $^{87}Sr/^{86}Sr$ ratio were corrected using an exponential law, the measured $^{88}Sr/^{86}Sr$ ratio and the "natural" abundance $^{88}Sr/^{86}Sr$ ratio assumed to be equal to 8.3752. Measurement accuracy was checked through repeated measurements of the NIST pure-Sr, isotope reference material SRM 987 (2 S.D of 2.9

x 10^{-5}), and the NIST soil reference material SRM 2709a ($^{87}Sr/^{86}Sr$ = 0.70823 ± 0.00002; comparing well with the value provided by Brazier et al., 2020 of 0.70814 ± 0.00002). Each sample was measured up to three times during a session. For samples measured three times, the 95% confidence interval was obtained from Student's *t*-distribution and ranged from 3 x 10^{-6} to 8 x 10^{-3}. For other samples measured less than 3 times, the 2 S.D of 4.9 x 10^{-5} estimated from the repeated measurements of the reference material NIST SRM 2709a (processed through powder digestion and separation as for samples) was used as an estimate of the 95% confidence interval.

For Nd isotope analyses, instrumental and natural mass fractionation on the $^{143}Nd/^{144}Nd$ ratio were corrected for using an exponential law, the measured $^{146}Nd/^{144}Nd$ ratio and its natural abundance ratio, taken as 0.7218. Accuracy was checked through repeated measurements of a NIST pure-Nd, isotope reference material ($^{143}Nd/^{144}Nd$ = 0.511418; Caro et al., 2006), with a measured 2 S.D of 2.7 x 10^{-6}, and the NIST soil reference material SRM2709a (0.512381 ± 0.000028). For convenience we report Nd isotope ratios as εNd values:

$$\varepsilon Nd = \left(\frac{(^{143}Nd/^{144}Nd)_{samples}}{(^{143}Nd/^{144}Nd)_{CHUR}} - 1 \right) \times 10\,000$$

with $(^{143}Nd/^{144}Nd)_{CHUR}$ (CHUR standing for "chondritic uniform reservoir") equal to 0.512638 (Jacobsen and Wasserburg, 1980). Each sample was measured once twice during a session, and the 95% confidence interval of the measurement was estimated from the 2 S.D. was estimated at 0.4 εNd unit from repeated measurements of the NIST reference material SRM2709a at mass spectrometric signal levels similar to those of samples.

4. Results

4.1. Sedimentology

Sediments collected in the deep basin of Lake Bourget present two different units: an organic gyttja at the top of the sequence followed by a homogeneous grey clayey unit developing downwards. Unit I (0 - 30 cm) corresponds to an alternation of very dark grey and very light grey clayey laminae with a predominance of diatoms, authigenic calcite crystals and organic matter and is equivalent to the uppermost unit described by Giguet-Covex et al. (2010). This unit presents the highest TOC values, i.e., 2.5% (Millet et al., 2010) and results from the eutrophication of the lake initiated in 1933 yr CE (Debret et al., 2010; Giguet-Covex et al., 2010; Jenny et al., 2013). Unit II, covers the rest of the sequence and corresponds to light grey clay composed mainly by authigenic carbonates associated with detrital particles (Debret et al., 2010; Millet et al., 2010).

Table X-1 – Statistics from LOI analyses

	LOI 550°	LOI 950°	NCIR
Mean	4,7	32,2	63,0
Median	4,6	33,3	62,1
Stdev.	1,5	5,1	4,6

XRF and LOI results are described in detail in Table X-1 and in Fig. X-2. Unit I present high values of Mn and low values of Ti and Ca. Conversely, in Unit II, Ti signal increases downwards and remains high until 5 m. Ca signal is high (> 500 kcps) from the bottom of the sequence until 2 m

and then decrease. Apart for event layers, Mn signal is almost constant in the sediment sequence. Few upward-fining darker layers interrupt the continuous sedimentation. Two types of layers are observable:

(i) Homogenite-type deposits, with an erosive coarse base, a homogeneous dark grey silty part, and a light grey clayey top. One of these layers corresponds to a mass-wasting deposit, linked to the 1822 earthquake (Beck, 2009; Chapron et al., 1999). These deposits present constant values of Ti, Ca and Mn, and most probably correspond to the reworking or the sliding of already deposited sediment from the lake slopes to the lake bottom due to seismic shaking during earthquake events (Beck, 2009; Rapuc et al., 2020b).

(ii) Turbidite-type deposits, with a normal upward-fining are also observable in the sediment section. These deposits are generally lighter than the homogenite-type deposits and present high values of Ti and a peak of Mn at their base. It can be interpreted as an input of detrital sediment associated with oxygen-rich water during a high intensity underflow of the Rhône River, linked to a flood event (Rapuc et al., 2020b). These deposits are thus related to flood events.

Rhône river sediments only enter the lake during flood events, however, only major events with high sediment loading will create an identifiable layer, while low intensity floods will only participate to the continuous sediment accumulation. Sediment samples from flood layers will not be considered hereafter as they can originate after local extreme precipitation events impacting a restricted area of the catchment. Then, only the continuous sedimentation will be considered hereafter as it more probably corresponds to the erosion of the entire catchment of Lake Bourget.

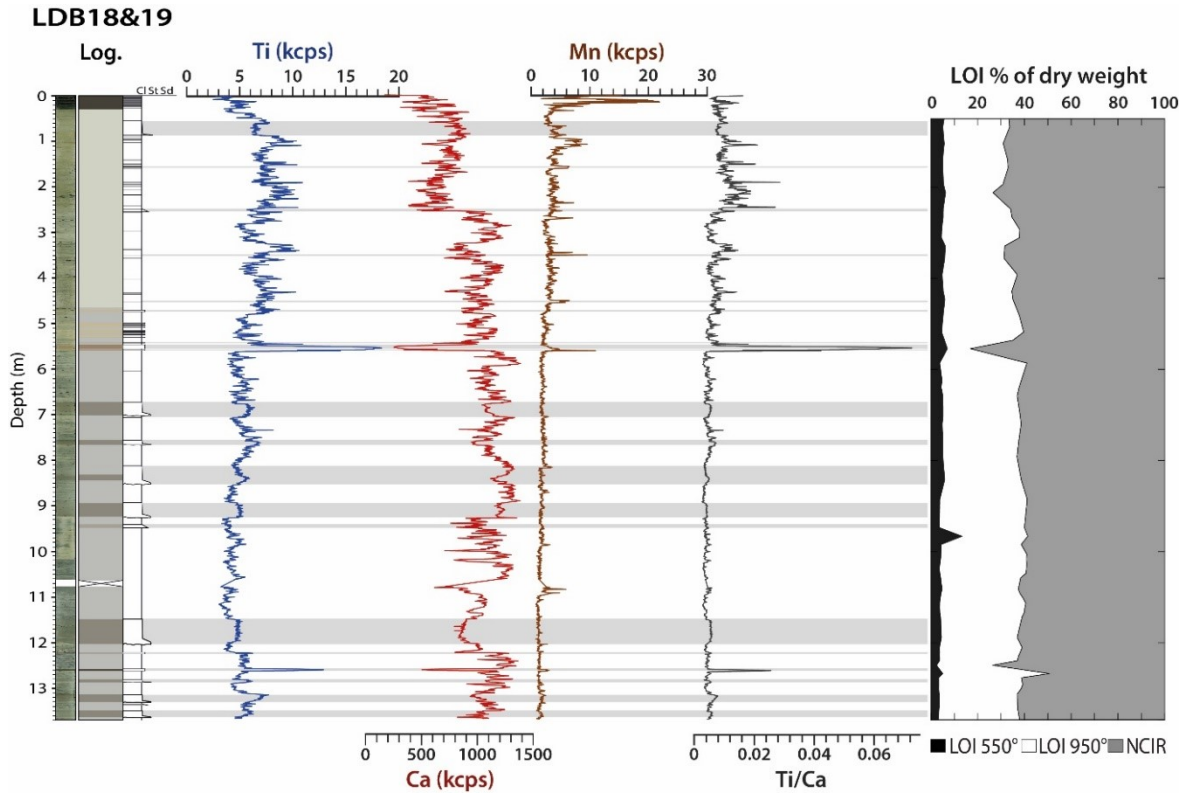

Fig. X-2 - Main sedimentological and geochemical results. A picture of the sediment sequence is associated with the lithological description, geochemical results (Ti, Ca, Mn contents and Ti/Ca signal) and Loss on Ignition (LOI) expressed in %. NCIR is standing for non-carbonated residue.

4.2. Chronology

Nineteen samples of terrestrial macro-remains were analysed to provide a radiocarbon age. All samples were calibrated and fit the LDB18&19 age-depth model. A first age-depth model was produced using "rbacon" R-package to test the reliability of each date within the model from Bayesian uncertainties. Only one ^{14}C was considered too young and was excluded from the model (Table X-2) to avoid reversals and inconsistencies (Fig. X-3-A). The R-package "clam" was used to obtain a smooth sedimentation rate (SR) for every millimetre of the sequence. Homogenite and turbidite-type layers that were previously described have been interpreted as instantaneous deposits. The sum of their depths represents 273.4 cm for the 13.71 m of the sediment sequence. To provide the best age-depth model, an event-free depth was created by subtracting the thicknesses of event deposits from the sediment depth (Arnaud et al., 2002). Historical information, such as (i) the beginning of the lake hypoxia at 1933 (Jenny et al., 2014a), corresponding to the onset of Unit I (31.1 cm) and (ii) the 1973 homogenite (18.5 cm) observed in several sediment sequences of Lake Bourget (Jenny et al., 2014b), were used as chronological indicators to constrain the model on the uppermost part of the sediment sequence.

The age-depth model was generated with the remaining 18 calibrated ages and historical information. The best fit was obtained with the R code package "clam" (Blaauw, 2010) by applying a smooth spline model with 0.4 for the smooth parameter. The sedimentation rate presented hereafter was calculated without event layers (Fig. X-3-B). Finally, all instantaneous events were reintegrated to the age-depth model (Fig. X-3-C) to provide a date for all event layers.

Table X-2 - Radiocarbon ages for the LDB18&19 sediment sequence. Composite depth was calculated by excluding the thicknesses of each graded beds that were considered as instantaneous deposits. Sample in bold corresponds to the date excluded from the age-depth model.

Sample name	Core	MCD (cm)	Composite depth (cm)	Radiocarbon age	Age cal yr BP (2 σ range)	Type
Sac 57152	LDB18_I_A01A	124	93.3	265 ± 30	-2-431	Wood
Poz-118211	LDB18-A-01A	146.5	115.1	375 ± 30	318-503	Wood
Poz-117956	LDB18-B-01	183	150.8	670 ± 50	552-685	Wood
Poz-117957	LDB18-B-01	227	192.9	845 ± 30	689-892	Wood
Sac 57151	LDB18_I_A02A	316.9	278.4	1335 ± 30	1185-1303	Wood
Poz-117958	LDB18-B-02A	459.45	417	2180 ± 30	2119-2309	Wood
Sac 57153	LDB18_I_E03A	526.5	483.7	2630 ± 30	3166-3344	Wood
Poz-117968	LDB18-B-03A	637.5	583.5	3040 ± 30	3262-3469	Wood
Sac 57154	LDB18_I_C_02A	714	631.5	3585 ± 30	3831-3976	Wood
Poz-117955	LDB18-C-02A	809.75	717.1	3975 ± 30	4305-4525	Wood
Sac 57150	LDB18_I_D02A	882.5	751.5	4235 ± 30	4653-4858	Wood
Poz-117969	LDB18-D-02A	927	762.8	4410 ± 30	4867-5256	Wood
Sac 57149	LDB18_I_D02A	961.5	788.9	4650 ± 30	5312-5465	Wood
Poz-117861	LDB19-I-B-02A	1003.8	831.2	5075 ± 35	5744-5908	Wood
Poz-117862	LDB19-I-B-02B	1025.8	853.2	5345 ± 35	6002-6267	Wood
Poz-117948	**LDB19-I-B-03A**	**1100.6**	**928**	**5520 ± 40**	**6223-6402**	**Wood**
Poz-117949	LDB19-I-B-03A	1217.6	990.6	7000 ±40	7737-7934	Wood
Poz-117950	LDB19-I-A-10	1246.7	1017	6960 ± 40	7691-7922	Wood
Poz-117951	LDB19-I-A-10	1303.95	1064.3	8200 ± 50	9017-9296	Wood

The first 13.7m of sediment accumulated in the deep basin of Lake Bourget covers the last ≈9, 500 years (Fig. X-3-C) with a mean SR of 1.3 $mm.yr^{-1}$. The SR over this sequence varies from 3.63 to 0.57 $mm.yr^{-1}$. SR is first constant and starts to increase at 5 kyr cal BP to reach values >

1 mm.yr^{-1} after 4.5 kyr cal BP. Two periods of high SR are observable around 4 and 3.1 kyr cal BP. The SR then increase again after 2 kyr cal BP to reach a peak of high values around 700 yr cal BP (i.e., 1250 yr CE). SR presents its highest values during the Modern Period (> 3.5 mm.yr^{-1}; Fig. X-3-B).

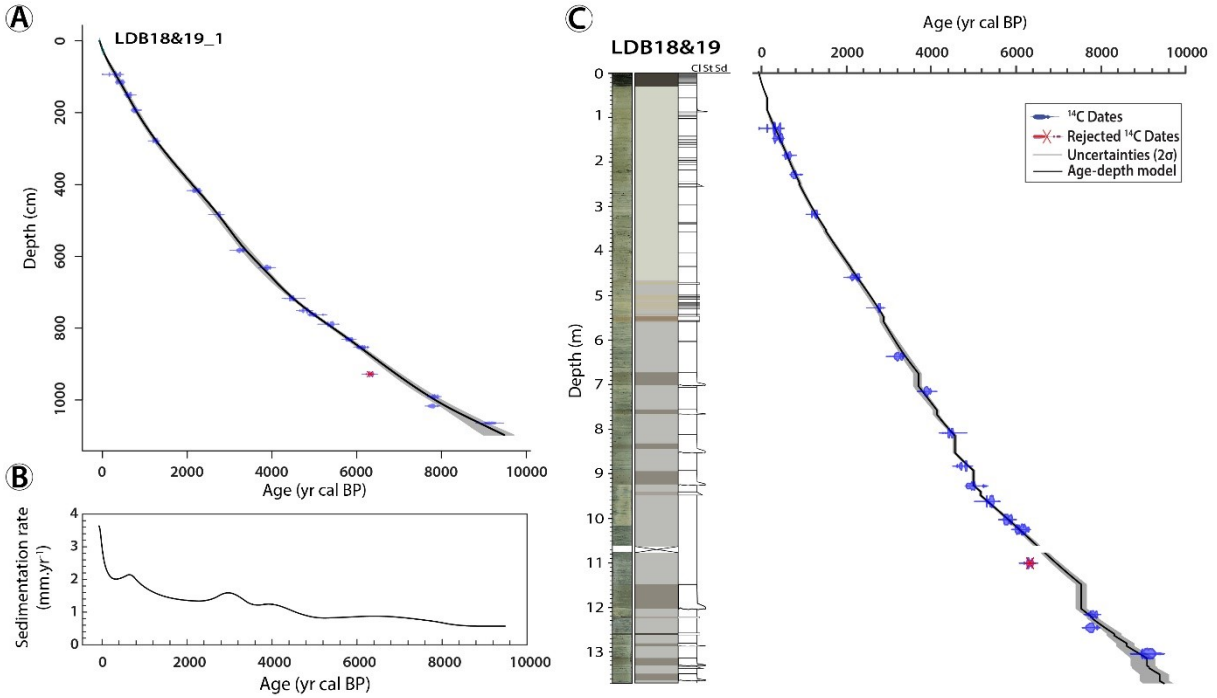

Fig. X-3 - Age-depth models. (A) Age–depth model associating radiocarbon and historical events dates in event-free depth with (B) the associated sedimentation rate. (C) Complete age-depth model.

4.3. Estimation of erosion flux

Concentration in authigenic carbonates, usually obtained by using LOI950°C results (Table X-1) are not comparable with expected values for Lake Bourget sediments. Indeed, previous studies (Arnaud and Révillon, 2015; Chapron, 1999) reported mean proportion of authigenic carbonate in the total sedimentation of 65% for both present and the Holocene in the northern part of the basin. Recently, it was demonstrated that usual LOI method (Heiri et al., 2001) was unable to burn the entirety of the carbonate content when the concentration of carbonates in the sediment is too high (Biguenet et al., 2021). This is the case for Lake Bourget sediment. Therefore, NCIR from LOI analyses cannot be used to estimate past siliciclastic flux in the lake.

Thus, we decided to follow the method of Arnaud and Révillon, (2015) developed also on Lake Bourget sediments, to estimate past detrital particles flux. We selected Ti signal, from XRF analyses, and used it as a proxy of detrital input in the lake (Arnaud et al., 2012, 2016; Arnaud and Révillon, 2015; Rapuc et al., 2020b). The flood event with the highest Ti values (Fig. X-2) was selected. This layer presents organic and carbonate content of 7 and 9.8%, respectively. Considering that this layer corresponds to 100 % of detrital input in the lake, 83% of the layer corresponds to detrital silicates. The proportion of detrital silicates (PDS) in the sediment sequence can be obtained by diving the value of Ti over time ($[Ti]^t$) by the maximal Ti value obtained in the selected flood event ($[Ti]_{max}$). As the flood event is also composed at 17 % of detrital organic matter and carbonates, a weighting coefficient of 0.83 is applied:

$$PDS = \frac{[Ti]^t}{[Ti]_{max}} \times 0.83 \quad (1)$$

To evaluate the evolution of the erosion over the Holocene in Lake Bourget catchment, a siliciclastic flux (g.cm^{-2}.yr^{-1}) was calculated from the multiplication of SR (cm.yr^{-1}), DBD (g.cm^{-3}) and PDS:

$$SCF = SR \times DBD \times PDS \quad (2)$$

To obtain SCF values at high resolution, a DBD model as a function of the time (t) was computed using the following equation:

$$DBD_{high-res} = 3 \cdot 10^{-5t} + 0.738 \quad (3)$$

High resolution values of DBD from this model are in very good agreement with measured DBD values (r^2=0.9246). Obtained SCF values are presented in Fig. X-4. According to previous studies, SCF is used as a proxy of erosion in the Lake Bourget catchment over the time (Arnaud et al., 2012; Arnaud and Révillon, 2015). SCF signal presents a mean value of 0.03 ± 0.02 g.cm-2.yr-1, with a maximum and a minimum value of 0.110 and 0.011 g.cm-2.yr-1, respectively. Estimated SCF values are only half the values from sediment sequences located in the proximal part (see S7) of the lake (mean = 0.06 ± 0.07 g.cm-2.yr-1; Arnaud and Révillon, 2015). This can be explained by (i) the difference in the sequences location and by (ii) the values of Ti selected for PDS computation. Indeed, the sediment sequence selected by Arnaud and Révillon, (2015) is located close to the Rhône delta, North of the lake, and is then more influenced by the detrital input from the Rhône River (Jenny et al., 2014b). Conversely, the coring site of LDB18&19 sequence is located in the centre of the deep basin, where the accumulation rate is lower, making this site more suitable for long-term reconstitution of the erosion signal from the watershed. Most of the difference between both signals can be explain by the choice made while selecting the flood layer for PDS estimation. The flood layer used in this study is absent from proximal sequences, probably due to a different path followed by the underflow at its origin. Difference of Ti content in the flood used in this study compare to the continuous sedimentation is much higher ($Ti_{flood} > 4.5 \times Ti_{continuous\ sed}$) than what was observed by Arnaud and Révillon, (2015), i.e., $Ti_{flood} > 2.5 \times Ti_{continuous\ sed.}$

At the opposite of the range, tendencies of the SCF signal from both sediment sections are very similar against time (see S7). Erosion in Lake Bourget catchment is low (< 0.02 g.cm^{-2}.yr^{-1}) from the beginning of the Holocene until 5 kyr cal BP. Then erosion increases progressively until a first period of high rates between 4.3 and 3.8 kyr cal BP. SCF signal remains high until the Early Middle Ages with several periods of increase (i) between 2.4 and 1.8 kyr cal BP and (ii) between 1.5 and 1.3 kyr cal BP (450 – 650 CE). From then, the SCF increase sharply until around 0.7 kyr cal BP (1250 CE). SCF is at its highest during the Early Middle Ages and until the end of the High Middle Ages before decreasing again until 0.3 kyr cal BP (1650 CE). From 0.3 kyr cal BP, erosion rates increase again and remain high during the entire period of the Little Ice Age (1650 – 1850 CE) before decreasing until the Modern Period (Fig. X-4).

4.4. Geochemistry

All the results of lake (sink) and river (source) sediment geochemistry are presented in Fig. X-4, Fig. X-5 and in supplementary Table S3 & S4.

4.4.1. Lake sediments

In the siliciclastic fraction of Lake Bourget sediments, the $^{87}Sr/^{86}Sr$ ratio ranges between 0.712 and 0.721. Except for the two samples with low $^{87}Sr/^{86}Sr$ value excursion, $^{87}Sr/^{86}Sr$ signal present a smooth decrease between 8 kyr cal BP until 6 kyr cal BP. These two samples present high [Ca] and their signatures are probably impacted an incomplete decarbonation.

From then, the signal increase again until 5.4 kyr cal BP. A low value is observed at 4.9 kyr cal BP. For the rest of the Late Holocene, the $^{87}Sr/^{86}Sr$ values remain almost constant. Values of εNd range from -11.4 to -10.4 over the Holocene. They are relatively invariant from the bottom of the sequence until 6 kyr cal BP. Then εNd signal tends to increase until 3.5 kyr cal BP. εNd values decrease again until 1.2 kyr cal BP before increasing again until the Modern Period. As the resolution of our εNd signal is low for recent times we decided to add data from previous studies conducted on Lake Bourget sediment sequences (Arnaud et al., 2012; Revel-Rolland et al., 2005). We only selected data originating from sediment sequence located in the distal part of the Lake Bourget deep basin (LDB01 and B16, see S2) to avoid peculiar sub-catchment signature linked to extreme flood events from the Rhône and Arve rivers. Data from samples collected in flood deposits were also discarded. Selected data are presented in Table S3. These data present comparable εNd range and allow to increase the resolution in recent times. From the combine dataset (see S4), a great εNd increase is observed during the Little Ice Age (LIA), period that was not covered by our dataset.

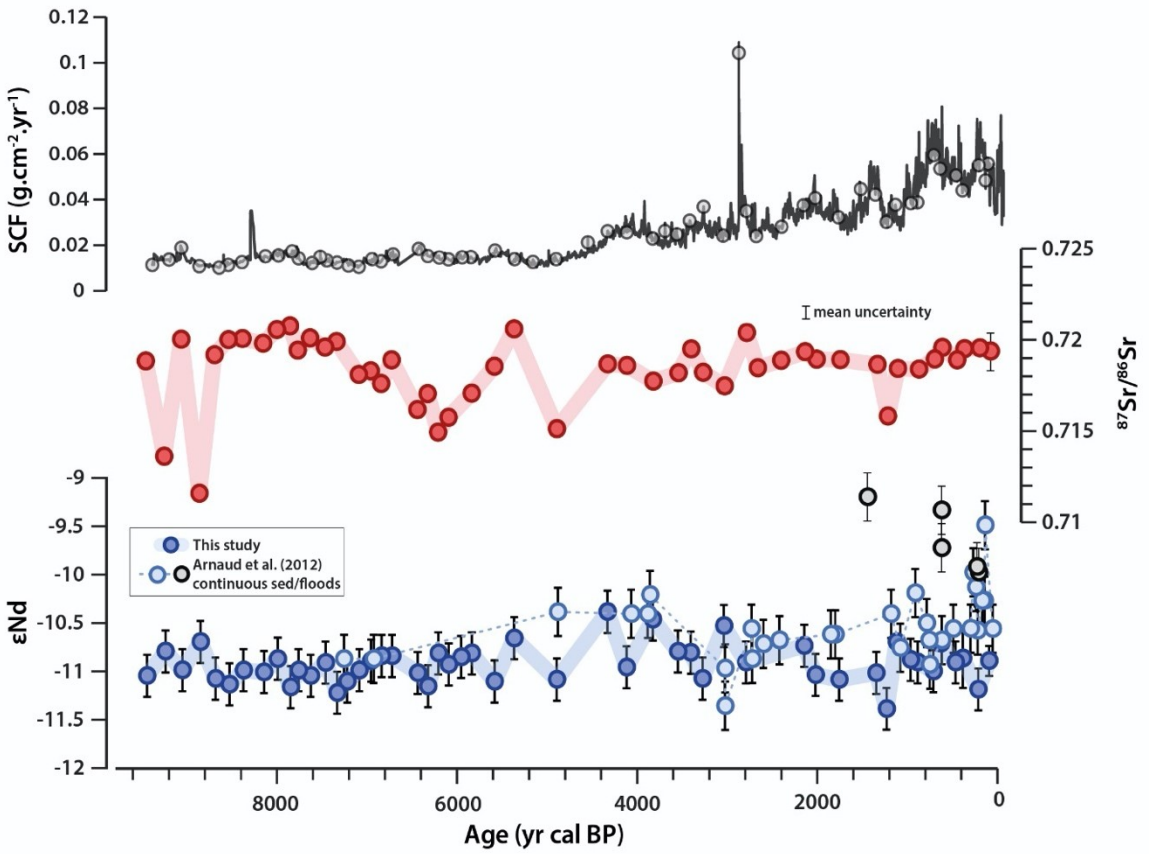

Fig. X-4 - Silicate detrital sedimentation rate (SCF, for siliciclastic flux) and Sr and Nd isotope ratios of Lake Bourget over the last 9,500 years obtained from lake sediment LDB18&19 sediment sequence. The siliciclastic flux was obtained from XRF Ti signal, age-depth modelling, and density measurements. Error bars on the $^{87}Sr/^{86}Sr$ and εNd curves represent the 95% confidence intervals corresponding to analytical uncertainty.

4.4.2. River sediments

River sediments taken in Rhône and Arve sub-catchments are characterized by εNd values ranging from -5.6 to -12.5. Sediment samples from the high-altitude basins of Mont-Blanc Massif, thus reflective of the calco-alkaline-type rock sources present the most radiogenic values. For sub-catchments draining sedimentary rocks, εNd values display values comprised between -9 and -12.5. Generally, εNd values tend to increase downstream, with lower values present in the Sallanches sub-catchment (3.A; Fig. X-1 and Table S4) and highest values in south-east sub-catchments such as Fier and Leysse.

Only five out of the total 19 river samples were decarbonated. As demonstrated in chapitre IX, the presence of detrital carbonates has an important impact on $^{87}Sr/^{86}Sr$ signature, making the bulk $^{87}Sr/^{86}Sr$ value not suitable for source fingerprinting in the geological context of this study. For convenience, we used $^{87}Sr/^{86}Sr$ values from a previous study (Revel-Rolland et al., 2005) conducted in Lake Bourget catchment, where samples were systematically decarbonated, and with equivalent sampling methodology (see Table S4). Mean $^{87}Sr/^{86}Sr$ and εNd values were calculated when possible, for each sub-catchment from both dataset and are represented in Fig. X-5 and reported in Table S4. $^{87}Sr/^{86}Sr$ mean value for Mont Blanc Massif is 0.7286 ± 0.0015, while values for sub-catchments draining sedimentary rocks range between 0.7152 and 0.71444.

The εNd values of Rhône and Arve river samples range between -6.7 and -11.3, whereas their $^{87}Sr/^{86}Sr$ ratios range from 0.7161 to 0.7253 (Fig. X-5 and Table S4).

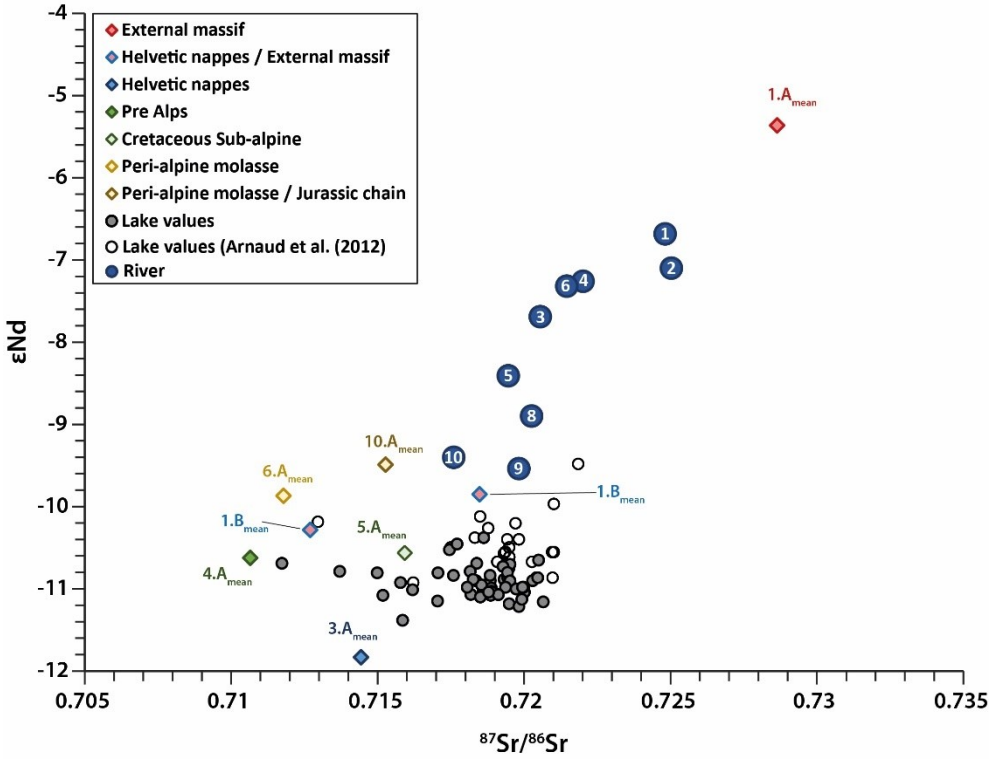

Fig. X-5 - Nd and Sr isotope composition of Lake Bourget siliciclastic sediment samples (small grey circles), and of river sediment samples from the Rhône and Arve river sub-catchments upstream from the lake (diamonds) and from the main valley (large blue circles). Rhône and Arve sub-catchments symbols (diamonds) are coloured as a function of the dominant rock types underlying the catchment. Rhône and Arve main valley sediment samples (blue circles) are numbered as in Fig. X-1.

4.5. Mixing model

Nd and Sr isotopic composition of Rhône and Arve River sub-catchments allow the identification of two main end members (Fig. X-5), that are:

(i) The Mont Blanc Massif (1.A sub-catchment), corresponding to the highest area of the catchment, where large glacier bodies are concentrated. This area is part of the external massif and presents the highest εNd and $^{87}Sr/^{86}Sr$ values (-6.8 and 0.7286, respectively). Erosion in the area is dominated by glaciers advances and retreats (e.g. Norton et al., 2010; Wittmann et al., 2007).

(ii) The rest of the catchment is primarily composed of carbonaceous sedimentary rocks. This large area covers low to mid-altitude environments where human presence is attested from the Neolithic. In this area values of Nd and Sr are low (Table S4).

To track the contribution of the Mont Blanc Massif erosion in the total silicate sediment accumulated in Lake Bourget, we selected mean εNd and $^{87}Sr/^{86}Sr$ values of the 1.A sub-catchment (Table S4). To track contribution of the "sedimentary rocks" area, we selected the mean value of 3.A sub-catchment as it is the only value covering the range of εNd and $^{87}Sr/^{86}Sr$ values of lake sediments (Fig. X-5 and Table S4).

The fractional contribution of each rock source can be estimated using a mixing model. As the catchment present two principal end members, only one isotopic composition is needed. However, we decided to run the mixing model with both Nd and Sr isotopic composition to test the accuracy of the results. The lake sediment Sr and Nd isotope compositions depend on (i) the Sr-Nd concentration and isotope signatures of each rock source, and (ii) the proportion of each contributing source in the mixture. This can be summarized by the following system of linear equations:

$$[Sr]^M = [Sr]^A \times f_A + [Sr]^B \times f_B \quad (1)$$

$$[Nd]^M = [Nd]^A \times f_A + [Nd]^B \times f_B \quad (2)$$

$$f_A + f_B = 1 \quad (3)$$

$$\frac{^{87}Sr}{^{86}Sr}^M \times [Sr]^M = \frac{^{87}Sr}{^{86}Sr}^A \times [Sr]^A \times f_A + \frac{^{87}Sr}{^{86}Sr}^B \times [Sr]^B \times f_B \quad (4)$$

$$\varepsilon Nd^M \times [Nd]^M = \varepsilon Nd^A \times [Nd]^A \times f_A + \varepsilon Nd^B \times [Nd]^B \times f_B \quad (5)$$

with the superscript M standing for lake sediment ("mixture") values, and the superscripts A and B standing for the rock sources values (calco-alkaline and sedimentary rocks, respectively); f_x represents the fractional contribution of each rock source. Solving this equation system led to estimates of the relative contributions of sources A and B.

Analytical solutions for f_A is:

$$f_A = \frac{[Nd]^B * (\varepsilon Nd^B - \varepsilon Nd^M)}{[Nd]^A * (\varepsilon Nd^M - \varepsilon Nd^A) + [Nd]^B * (\varepsilon Nd^B - \varepsilon Nd^M)} \quad (6)$$

and for f_B is,

$$f_B = \frac{[Nd]^A * (\varepsilon Nd^A - \varepsilon Nd^M)}{[Nd]^B * (\varepsilon Nd^M - \varepsilon Nd^B) + [Nd]^A * (\varepsilon Nd^A - \varepsilon Nd^M)} \quad (7)$$

Monte Carlo method was used to compute uncertainties on the fractional contributions. Random sampling within the analytical uncertainties of each parameter was executed using a Box–Muller transform (Box and Muller, 1958) for each of the 5,000 iterations of the Monte Carlo procedure. From the simulated parameter distributions, D84, D16, median and standard deviation were obtained for each proportion f_x.

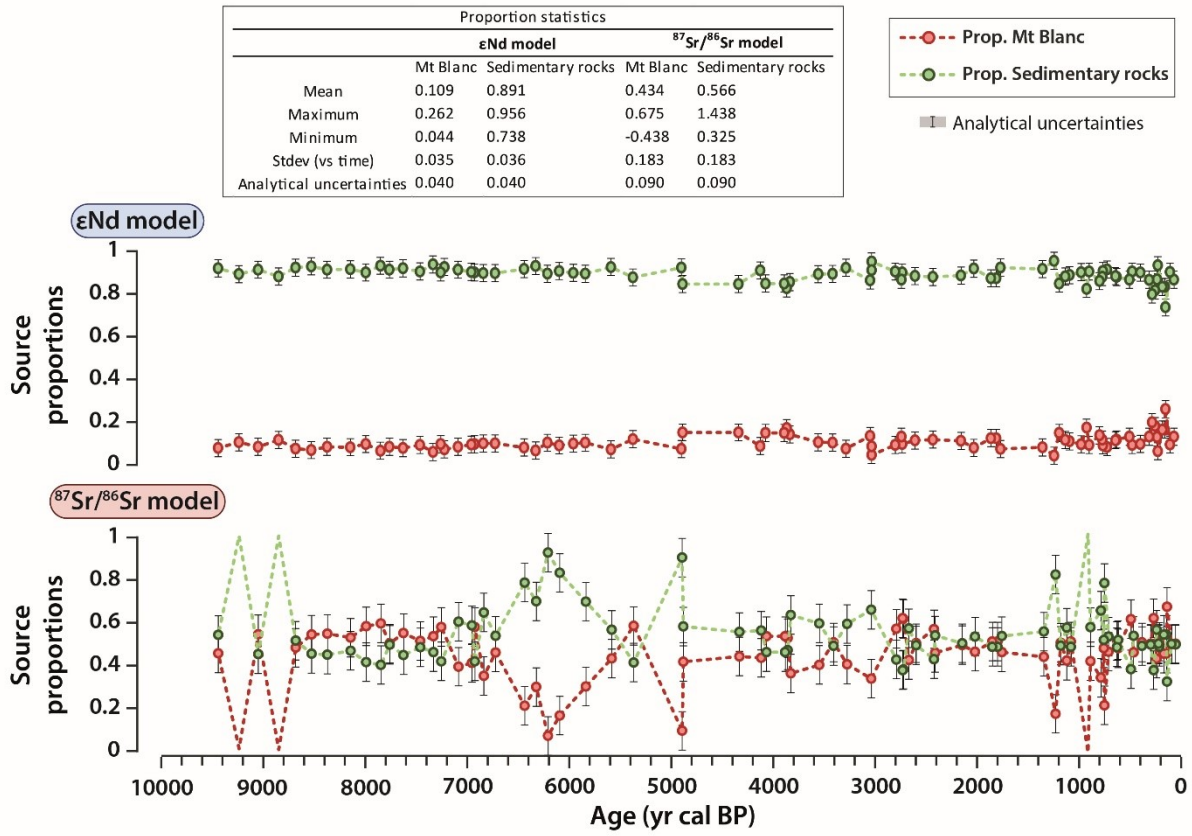

Fig. X-6 -Results from the mixing model. Fractional contributions of each rock source to Lake Bourget sediment against time (yr cal BP). The propagation of analytical uncertainties is represented as error bars corresponding to the D84 and D16 of the distribution of the parameters obtained from Monte Carlo simulations. Principal statistics of the two models are provided.

Results and statistics of the mixing models are presented in Fig. X-6. Surprisingly, the model using Sr isotopic composition present almost equivalent contribution of "Mt Blanc" and "Sedimentary rocks" areas while the εNd model indicates higher proportion for the "Sedimentary rocks" source. Considering the small area corresponding to the "Mt Blanc" source, εNd model is supposed to be more reliable.

Only fine sediment fraction of Rhône river sediment enters Lake Bourget. Sr isotopic composition is known to be dependent on the grain size (Feng et al., 2009; Jonell et al., 2018; Meyer et al., 2011). River sediment samples used for the geochemical analyses present a grain size comprised between 0 and 63 µm, coarser than lake sediment presenting mean grainsize value < 8 µm (Arnaud, 2005). Previous studies have shown that finer the grainsize, higher the $^{87}Sr/^{86}Sr$ value (Feng et al., 2009; Jonell et al., 2018; Meyer et al., 2011). This explains the high $^{87}Sr/^{86}Sr$ signatures for lake samples relatively to what can be expected from εNd values only. Due to grain size sorting, $^{87}Sr/^{86}Sr$ signal is probably influenced by fine sediment fraction originating from the upstream part of the catchment, where $^{87}Sr/^{86}Sr$ signatures are higher (Table S4).

To avoid uncertainties linked to sediment sorting at the inlet of Lake Bourget, we decided to use the εNd mixing model for which particle size sorting has little effect. For future studies, we recommend to select a source sediment particle size fraction equivalent to the one of the sink (Collins et al., 2017). From εNd model, the contribution of "Mt Blanc" areas throughout the Holocene (4.4 to 26.2 %) is very low compared to the one of the "Sedimentary rocks" area (Fig. X-6). The contribution of both areas remains almost constant throughout the Holocene, with only small increase of Mt Blanc contribution during the Little Ice age.

4.6. Evaluation of the sediment yield

To obtain a quantitative assessment of catchment-scale erosion rates for each area in Lake Bourget catchment, river loads and corresponding sediment yields need to be estimated. To do so, we follow the methodology described in chapitre IX. The total amount of sediment stored in Lake Bourget per amount of time ($Stock_{sed}$) was estimated:

$$Stock_{sed} = SCF \times Lake\ area \quad (8)$$

As SR vary spatially over the surface of Lake Bourget (Jenny et al., 2014b) we consider only the fraction of the total lake area where SR should be commensurate with that measured at the coring site. This area is estimated at 14.4 km² and corresponds to the area of the lake under 110 m b.l.s. The sediment stock is then multiplied by the contribution of each source to calculate changes in the source-specific sediment loads (SL, in $t.yr^{-1}$) through time:

$$SL = Stock_{sed} \times source\ proportion \quad (9)$$

To obtain an area-normalized sediment yield value for each source (SY_i), SL is normalized to the drainage area of each rock type:

$$SY_i = \frac{SL}{Source\ area} \quad (10)$$

with SY_i expressed in $t.km^{-2}.yr^{-1}$. Area covered by each rock type (i.e., granite and sedimentary rocks) was estimated from QGIS software and represent 4235 and 266 km² for "Sedimentary rocks" and "Mont Blanc" areas, respectively. SY results are presented in Table X-3. Due to its small area, $SY_{Mt\ Blanc}$ presents a mean value two-times higher than $SY_{Sedimentary\ rocks}$. Measured values in Lake Bourget are almost a hundred times lower than mean SY values obtained from the R.U.S.L.E model in the area (Panagos et al., 2015b). This result can easily be explained by the fact that erosion products from Rhône and Arve catchments only enter the lake during flood events.

Table X-3 – Main SY results for each source

Sediment Yield ($t.km^{-2}.yr^{-1}$)		
	Sedimentary rocks	Mt Blanc
Mean	0.9433	2.006
Min	0.3433	0.4369
Max	2.2476	8.7843
Stdev	0.4955	1.5888
Analytical uncertainties	0.31	1.285

5. Discussion

5.1. Interpretation of the erosion signal in Lake Bourget catchment

Previous studies conducted on Lake Bourget sediment sections already present erosion evolution throughout the Holocene (e.g. Arnaud et al., 2016, 2012; Arnaud and Révillon, 2015). Erosion signal obtained from these studies are highly comparable with the SCF measured here (see S7) allowing us to use this signal as a proxy of erosion of the entire catchment through time. Erosion in Lake Bourget catchment, recorded in the lake sediments, can be divided in three main periods:

(i) from 10 to 4.8 kyr cal BP, when erosion rate in the catchment is low;
(ii) between 4.8 and 1.1 kyr cal BP, the erosion increases progressively, with several peaks;
(iii) from 1.1 kyr cal BP to the present, the erosion increases significantly.

These trends are also comparable with erosion rates observed in small-size catchments within the studied area. Here we compare Lake Bourget erosion signal with erosion trends from Lake La Thuile (Fig. X-7-A), a mid-altitude lake (874 m a.s.l) located south of Lake Bourget (Bajard, 2017; Bajard et al., 2017a, 2016), and the frequency of erosive events recorded in Lake Anterne (Fig. X-7-B), a relatively high-altitude lake (2063 m a.s.l), located in the north-eastern part of the Arve river catchment (Giguet-Covex et al., 2011). These two sites are located at the downstream-end of catchments dominated by sedimentary rocks (Fig. X-1) and thus inform on erosion rate fluctuations at mid- and high-altitude in the "Sedimentary rocks" area of Lake Bourget catchment, respectively.

To interpret erosion trends and disentangle the effects of climate and human forcing on erosion in the Bourget catchment, we need to focus on the origin of the sediment brought into Lake Bourget. Here we used both the SCF (Fig. X-7-C) and SY estimated for "Mt Blanc" and "Sedimentary rocks" areas. The erosion in the Mt Blanc area presents the highest erosion rates throughout the Holocene and is supposed to be influenced by glacier advances and retreats and by precipitations events according to studies focusing on the Swiss side of Mont Blanc Massif (Norton et al., 2010; Stutenbecker et al., 2018; Wittmann et al., 2007). Annual and particularly winter precipitation rates, corresponding to periods of snow accumulation on glaciers, impact glacier developments: the colder and wetter the climate, the more widespread glacier bodies (Le Roy et al., 2015 and references therein). The erosion in Mont Blanc area can also be influenced by extreme precipitation events (i.e., flood events). These events are generally triggered by summer convective events, as shown in recent decades by instrumental data and in lake sediments of Lake Blanc located 5 km NE of the Mer de Glace (Wilhelm et al., 2013 and references therein).

At the opposite, the rest of the Lake Bourget catchment (i.e., in the "Sedimentary rocks" area) is a widespread area, characterized by the absence of major glacier, impacted by climate fluctuations and human activities since the Neolithic (Giguet-Covex et al., 2021). Climate, through precipitations, impacts the area and contributes to its erosion, in particular in high and mid-altitude areas (Bajard, 2017; Giguet-Covex et al., 2011). In the other hand, human activities, through grazing, agriculture, mining and the associated deforestations are known to disturb the delicate equilibrium of the CZ in the Alps (Bajard et al., 2017b; Brisset et al., 2013) and in the studied area

(Giguet-Covex et al., 2011). More than a simple erosive agent, mankind by its activities is above all a forcing factor of the CZ's soil erodibility. Once a threshold exceeded in the increasing of soil erodibility, the same precipitation event will led to a greater quantity of sediment produced and transported (Brisset et al., 2017).

Here, the effect of tectonic activities will be considered as constant at the scale of the Holocene period and will not be taken into account to interpret the evolution of the erosion signal. Making the hypothesis that precipitation affects the erosion in the same way in the Mt Blanc area and in the rest of the watershed, we can interpret the erosion signal from the Mt Blanc area (i.e., $SCF_{Mt\ Blanc}$ or $SY_{Mt\ Blanc}$) as a proxy of climate forcing on erosion in the Lake Bourget watershed. Then, the erosion signal of the "Sedimentary rocks" area depends on both climate and human influences. To disentangle both effects, we normalized $SY_{Sedimentary\ rocks}$ and $SY_{Mt\ Blanc}$. As the signals are different and not normally distributed, we used their respective minimal and maximal values allowing to preserve the shape of the distribution of each variable while making them easily comparable on the same "scale":

$$Transformed\ values = \frac{Initial\ values - Minimum}{Maximum - Minimum} \quad (11)$$

Results are plotted against time in Fig. X-7-D. The difference between normalized values of $SY_{Sedimentary\ rocks}$ and $SY_{Mt\ Blanc}$ was also computed and represented in Fig. X-7-E. By subtracting the $SY_{Mt\ Blanc}$ to the $SY_{Sedimentary\ rocks}$, we subtracted the contribution of the climate on the signal of erosion of the "Sedimentary rocks" area. This provided us a proxy of climate and human effect on erosion signal. Periods when the signal is close to 0 (i.e., when $SY_{Sedimentary\ rocks}$ and $SY_{Mt\ Blanc}$ are equivalent) can be interpreted as period of climate-dominated erosion. When the signal is < 0, normalized erosion in the "Mt Blanc" area is higher than in the "Sedimentary rocks" area, this can be explained by an increase of glacial erosion. Conversely, when the signal is > 0, normalized erosion is higher in the "Sedimentary rocks" area, and the effect of climate alone cannot explain the entire erosion recorded in Lake Bourget sediments.

5.2. Erosion signal over the last 10 kyrs in Lake Bourget catchment

5.2.1. From Early Holocene to 4.8 kyr cal BP

The erosion flux (Fig. X-7-C) is low from the beginning of the Holocene and until 4.8 kyr cal BP. The contribution of the "Mt Blanc" and the "Sedimentary rocks" areas are equivalent at that time and SY for both areas are low (Fig. X-7-D). In this period, only small fluctuations are observable in the SCF signal and will not be interpreted as they are lower than the associated uncertainties. Erosion signal in mid- (Fig. X-7-A) and high-altitude areas of the Lake Bourget watershed (Fig. X-7-B) is at its lowest (Bajard, 2017; Bajard et al., 2017a; Giguet-Covex et al., 2011). In terms of climate, this period is characterized by a general warming, called the Holocene climatic optimum, which starts around 9 kyr cal BP and is known to end at around 5 kyr cal BP in Europe (Debret, 2008; Magny et al., 2003; McDermott et al., 1999). During this period, precipitation amounts are low in the Alps, resulting in weak flood activities in both the southern (Fig. X-7-F) and northern Alps (Fig. X-7-G). Human presence in the Lake Bourget catchment is sparce and insignificant in terms of erosion at that time.

5.2.2. From 4.8 to 3.8 kyr cal BP

A first rise in the Lake Bourget catchment erosion rate is observed at 4.8 kyr cal BP and last until 3.8 kyr cal BP. During this period, $SY_{Sedimentary\ rocks}$ and $SY_{Mt\ Blanc}$ covariate (Fig. X-7-D). As SY signals

are equivalent, the erosion increase can be interpreted as induced by the climate. In Lake Anterne, a small increase of the frequency of erosive events is also observed between 5.5 and 4.2 kyr cal BP (Fig. X-7-B). This increase starts few centuries before the increase of SCF observed in Lake Bourget. As stated before, climate in the Alps experiences a transition at that period from warm and dry to cold and wet conditions. In the literature, the shift between the two conditions occurs at 4.2 kyr cal BP in the Mediterranean region (Bini et al., 2019). At that period, air masses from the Mediterranean area enters the Po plain more frequently, leading to an increase of the precipitation amounts in the southern Alps (Fig. X-7-F; Wirth et al., 2013). These south-eastwards air masses circulation probably reached the catchment of Lake Bourget and the associated precipitation forced an increase of erosion rate. In terms of human activity, first evidence of pastoral and agricultural practices in low to mid-altitude sites are dated around 5 kyr cal BP. However, these activities were limited at that time in their extent, resulting in a minimal footprint on the environment (Giguet-Covex et al., 2021).

5.2.3. From 3.8 kyr cal BP to the Early Middle Ages

From 3.8 kyr cal BP, erosion in the total Lake Bourget catchment keep increasing. However, for the first time, trend in erosion signals from "Mt Blanc" and "Sedimentary rocks" areas differs. Indeed, the $SY_{Mt\ Blanc}$ remains almost constant until 1 kyr cal BP while $SY_{Sedimentary\ rocks}$ increases following the tendency of the SCF. This difference indicates that there is no obvious increase of glacier erosion between 3.8 and 1 kyr cal BP. Climate only is probably not at the origin of the SCF increase recorded for the Lake Bourget catchment. At 4 kyr cal BP, the erosion rate of high-altitude areas of the "Sedimentary rocks" catchment starts to increase (Fig. X-7-B; Giguet-Covex et al., 2011). This increase is followed 1.5 kyrs later by an increase of the erosion rate at mid-altitude sites (Fig. X-7-A; Bajard, 2017; Bajard et al., 2017a). From these observations, erosion increase seems to start in high-altitude areas of the "Sedimentary rocks" area before increasing at mid and low altitude areas. Human activities, through grazing and the associated deforestation can be at the origin of this trend. Indeed, the development of significant pastoral activities is dated around 3.6 kyr cal BP for high-altitude sites such as Lake Anterne catchment from environmental-DNA and palynological data (Giguet-Covex et al., 2021). The delay in the erosion tendency between high- and mid-altitude areas can be due to a possible preference for the high-altitude areas for grazing linked to the presence of open woodland or meadows facilitating pasture exploitation (Giguet-Covex et al., 2021). The erosion increase tendency from 3.8 kyr cal BP is also observable elsewhere in the European Alps and is often interpreted as forced by the development of human activities (e.g. Andrič et al., 2020; Joannin et al., 2014).

In the Lake Bourget catchment, erosion of the "Sedimentary rocks" area continues to be decorrelated from the trend of the "Mt Blanc" area during the entire Iron Age and the Roman Period (Fig. X-7-D&E) while erosion of the total Lake Bourget catchment continues to increase. A similar trend was observed in a previous study (chapitre IX) conducted on Lake Iseo catchment (Italy). There, the increase of erosion between the Roman Period and the Middle Ages was interpreted as due to the development of agriculture and pastoralism in the Alps. In the French Alps, the synthesis of Giguet-Covex et al. (2021) on the trajectories of mountain agro-ecosystems indicates that pastoral activities intensified during the Late Iron Age, during the entire Roman Period and until the Early Middle Ages at mid- and high-altitudinal sites.

5.2.4. The Middle Ages

After the Roman Period, the erosion rate in Lake Bourget catchment presents a first increase around 1.35 kyr cal BP (600 CE) and a second one, more important, that starts at 1.1 kyr cal BP (850 CE) and led to the highest values of erosion recorded throughout the entire Holocene. The second increase is accompanied by both $SY_{Sedimentary\ rocks}$ and $SY_{Mt\ Blanc}$ increase (Fig. X-7-D). Similarity in the erosion trend between the two areas of the Bourget catchment is interpreted as an increase of climate influence on the erosion rates. $SY_{Mt\ Blanc}$ remains high between 1.1 and 0.75 kyr cal BP (850 – 1200 CE), which means that glacier erosion is important at that period. This is in great agreement with previous results obtained in Lake Iseo catchment (chapitre IX). Several studies also reported glacier advances in the Alps at that time (e.g., Holzhauser et al., 2005; Le Roy et al., 2015), linked to an increase in precipitation amounts (Büntgen et al., 2011).

Right after 0.75 kyr cal BP, the $SY_{Mt\ Blanc}$ decrease while $SY_{Sedimentary\ rocks}$ remains high (Fig. X-7-D&E). Thus, the period of highest erosion rates in the Lake Bourget catchment cannot be explained only by the effect of climate on erosion. Thus, human activities are suspected to have played a key-role on erosion at that period. Indeed, this period corresponds to a diversification of the activities at low and mid-altitude, with the cultivation of fruit trees for instance, and a new phase of intensive grazing activity at high-altitude (Giguet-Covex et al., 2021). This is also a period of intensive erosion recorded in Lake La Thuile (Fig. X-7-A) attributed to intensive agricultural practices (Bajard et al., 2016). At a broader scale, in the Alps, this period is marked by intensive clearing at mid-altitude associated with the development of agricultural practices (Pini et al., 2016).

5.2.5. Little Ice Age and Modern Period

The erosion rate in Lake Bourget catchment remains high from 0.6 to 0.3 kyr cal BP (1350 – 1650 CE) without any change in the trend of $SY_{Sedimentary\ rocks}$ and $SY_{Mt\ Blanc}$. Then, $SY_{Mt\ Blanc}$ increase sharply after 0.3 kyr cal BP (1650 CE) and remains high until 0.1 kyr cal BP (1850 CE). This period is known as the LIA, and corresponds to a colder and wetter climate in Europe (Mann et al., 2009), that led to great glacier advances (Le Roy et al., 2015). At that period, in the Lake Bourget catchment and elsewhere in the Alps, the flood frequency recorded in small lakes from all different kind of altitude increase sharply (Fig. X-7-B; Giguet-Covex et al., 2011; Glur et al., 2013; Sabatier et al., 2017; Vannière et al., 2013; Wilhelm et al., 2013; Wirth et al., 2013b, 2013a), due to an important increase of precipitations amounts in both the southern (Fig. X-7-F) and northern Alps (Fig. X-7-G). Even though human activities are still intense and widespread, due notably to demographic growth (Giguet-Covex et al., 2021), the impact of climate through precipitations in the "Sedimentary rocks" area, and through glacier advances in the Mont Blanc Massif is thought to be the principal forcing factor on erosion during the LIA. The erosion signal in the Lake Bourget watershed then decreases slowly during the Modern Period.

The deconvolution of the erosion signal recorded in lake Bourget sediment using isotopic composition was not sufficient to provide quantitative information on the effect of climate fluctuations and human activities on the erosion. This is notably because Lake Bourget is not a perfect trap of erosion products from its catchment. However, the comparison of our dataset with other erosion chronicles from the Lake Bourget catchment, and climate and human activities chronicles helped to disentangle the effect of these two forcing factors on erosion.

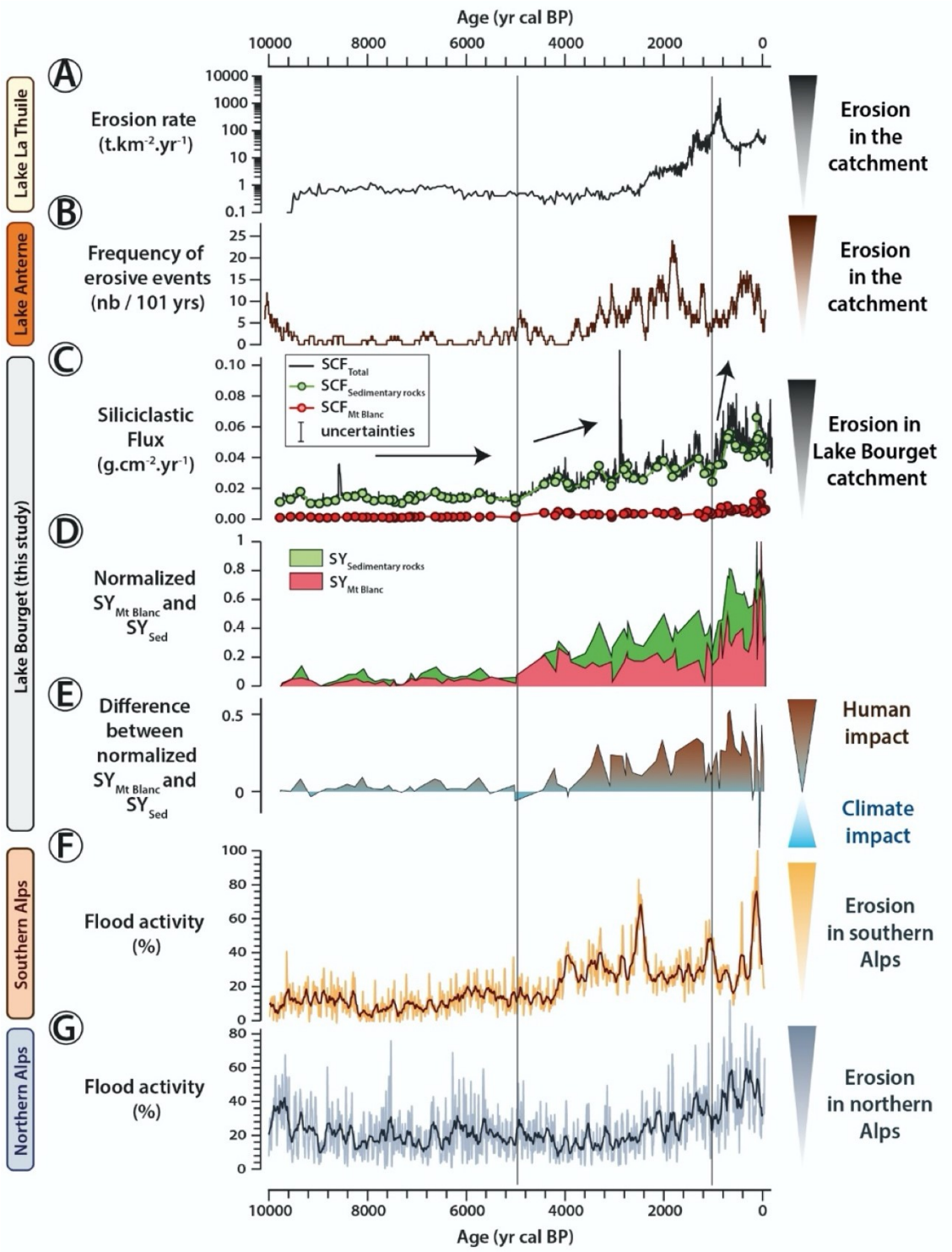

Fig. X-7 - Erosion in the Lake Bourget catchment and forcing factors evolution over the last 10,000 years. From top to bottom: (A) erosion rates (t.km-2.yr-1) in Lake La Thuile catchment, a small catchment, located at mid-altitude, South-East of Lake Bourget. Data and figure derived from Bajard et al. (2017); (B) the frequency of erosive flood events recorded in Lake Anterne, high-altitude lake, located in the north-eastern part of the Bourget catchment, in the Giffre area, modified from (Giguet-Covex et al., 2011); (C) siliciclastic flux recorded in Lake Bourget (g.cm-2.yr-1) with the associated proportion of sediment originating from "Mt Blanc" and "Sedimentary rocks" areas. SCF is used as a proxy of erosion in the Lake Bourget catchment. Arrows indicate erosion tendencies; (D) normalized sediment yield originating from the erosion of "Mt Blanc" and "Sedimentary rocks" areas in the Bourget catchment; (E) Differences between normalized erosion rates of "Sedimentary rocks" and "Mt Blanc" areas; flood activity (%) of the southern (F) and northern Alps (G), modified from (Wirth et al., 2013b).

A similar study, conducted on Lake Iseo catchment (northern Italy, chapitre IX) highlighted a four-fold increase in the CZ erosion rates of the catchment area between the end of the Roman Period and the present. This trend was associated to the impact of human activity on catchment-scale CZ erosion due to agriculture, grazing, and mining development, associated to deforestation at mid- and low-altitude in the catchment. However, this study only covers the last 2,000 years and does not cover a period without human activities. The advantage of the Holocene erosion trend reconstruction in Lake Bourget is that it allows to measure CZ erosion rates before the onset of human activities in the watershed. The developing of wetter and colder climate from 5 kyr cal BP surely led to an erosion increase. Yet, from 3.8 kyr cal BP to the present, erosion rate increase for about 4 times, and nearly doubles between 3.8 kyr cal BP to the Roman Period. This period corresponds to the developing of pastoralism at high-altitude and of agricultural practices at low- to mid-altitude. At that time, decorrelation between erosion in the Mt Blanc area and in the rest of the watershed indicates that the erosion trend during the entire Late Holocene cannot be explained by climate fluctuations alone. Then, from 3.8 kyr cal BP, human activities by modifying the soil erodibility, have impacted erosion in the Alps, and probably led to a four-fold increase of the erosion rate, affecting the CZ and damaging ecosystems. In the context of current anthropization pressure, the Alps are thus a hotspot of CZ deterioration and of soil and biomass carbon shrinkage.

6. Conclusion

Erosion rates from the Mont Blanc Massif and from the rest of the Lake Bourget catchment were reconstructed from a sediment core with a stable isotope mixing model. The erosion signal from high-altitude Mont Blanc Massif synchronous with European annual precipitation trends and glacier advances and retreats was interpreted to be driven by climatic fluctuations. Conversely, erosion in the area underlain by sedimentary rocks is influenced by both climate fluctuations and human activities. From the comparison between the erosion signals of the two areas, we were able to disentangle the main triggers of erosion. From the Early Holocene and until 3.8 kyr cal BP, climate fluctuations are the main driver of erosion rate in the northern French Alps. Thus, the transition towards wetter and colder climate after 5 kyr cal BP led to erosion rate increase in the entire catchment. From 3.8 kyr cal BP and except for short-lasting colder and wetter periods, erosion trends begin to differ, and climate influence only cannot explain the recorded erosion rates. The comparison of Lake Bourget catchment's erosion trends with local and regional erosion rates highlights the influence of human activities development on erosion in the northern French Alps. Human activities through agricultural practices at low- to mid -altitude and grazing at mid- to high-altitude areas impacted the vegetation cover and the soil's stability, inducing an increase in soil erodibility. This study allows to estimate erosion rates in a large catchment before the onset of human activities and highlight a four-fold increase in the erosion rate linked to human activities development. These findings should contribute to enhance modelling of human impacts on Critical Zone erosion and on carbon shrinkage in soils.

Acknowledgments

This work was financed by CRITLAKE project co-funded by EC2CO and AAP Université Savoie Mont Blanc. Parts of this work were also supported by IPGP multidisciplinary programme PARI and by Paris-IdF region SESAME Grant No. 12015903. We wish to thank the support of the entire staff of the C2FN-DT-INSU associated to the CLIMCORE project. ^{14}C analyses were acquired

thanks to the CNRS-INSU ARTEMIS national radiocarbon AMS measurement programme at Laboratoire de Mesure ^{14}C (LMC14) in the CEA Institute at Saclay (French Atomic Energy Commission).

We are grateful to Pierre Burckel for help with Q-ICP-MS measurements; to Laëticia Faure for her valuable help and assistance with lab work; to Pascale Louvat, Thibaud Sondag, and Barthélémy Julien for assistance with MC-ICP-MS measurements; and to Raphaël Gallet, Bernard Fanget, Erwan Messager, Mathilde Banjan, Maude Biguenet, Matthieu Baril, Kim Genuite, Claire Blanchet, Kévin Jacq, Camille Girault, Charline Giguet-Covex, Manon Bajard, Ondřej Bábek, Qi Lin, Xiaqing Wang, Alexandre, Emmanuel Malet for the help during the different coring surveys and Jacques Mourey for the help on the field for river samples collection. We wish to thank Damien Guinoiseau for helpful conversations about the interpretation of isotope data.

Supplementary

S1. LDB18&19 coring technical scheme

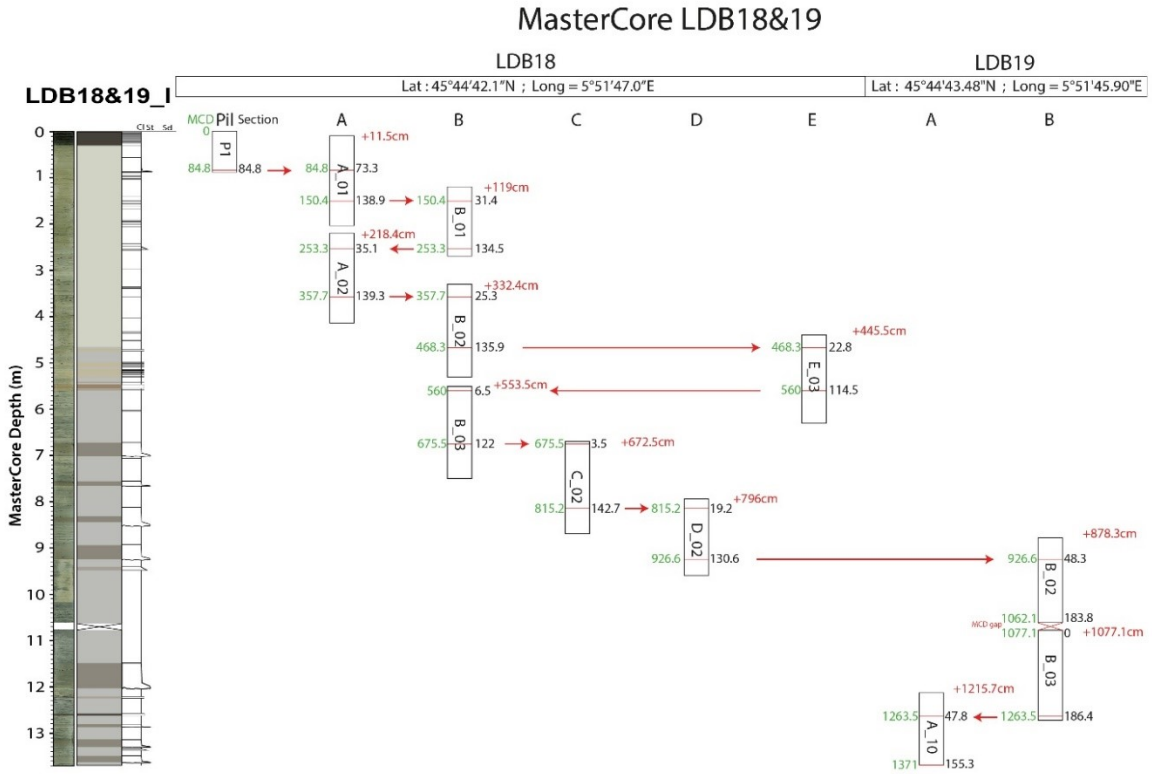

Figure S1 - Coring technical scheme for LDB18&19_I sediment section. Cores retrieved from the deep basin during the coring survey and used to build a master core are represented against the depth below water-sediment interface (m).

S2. Lake Bourget sediment sequences location

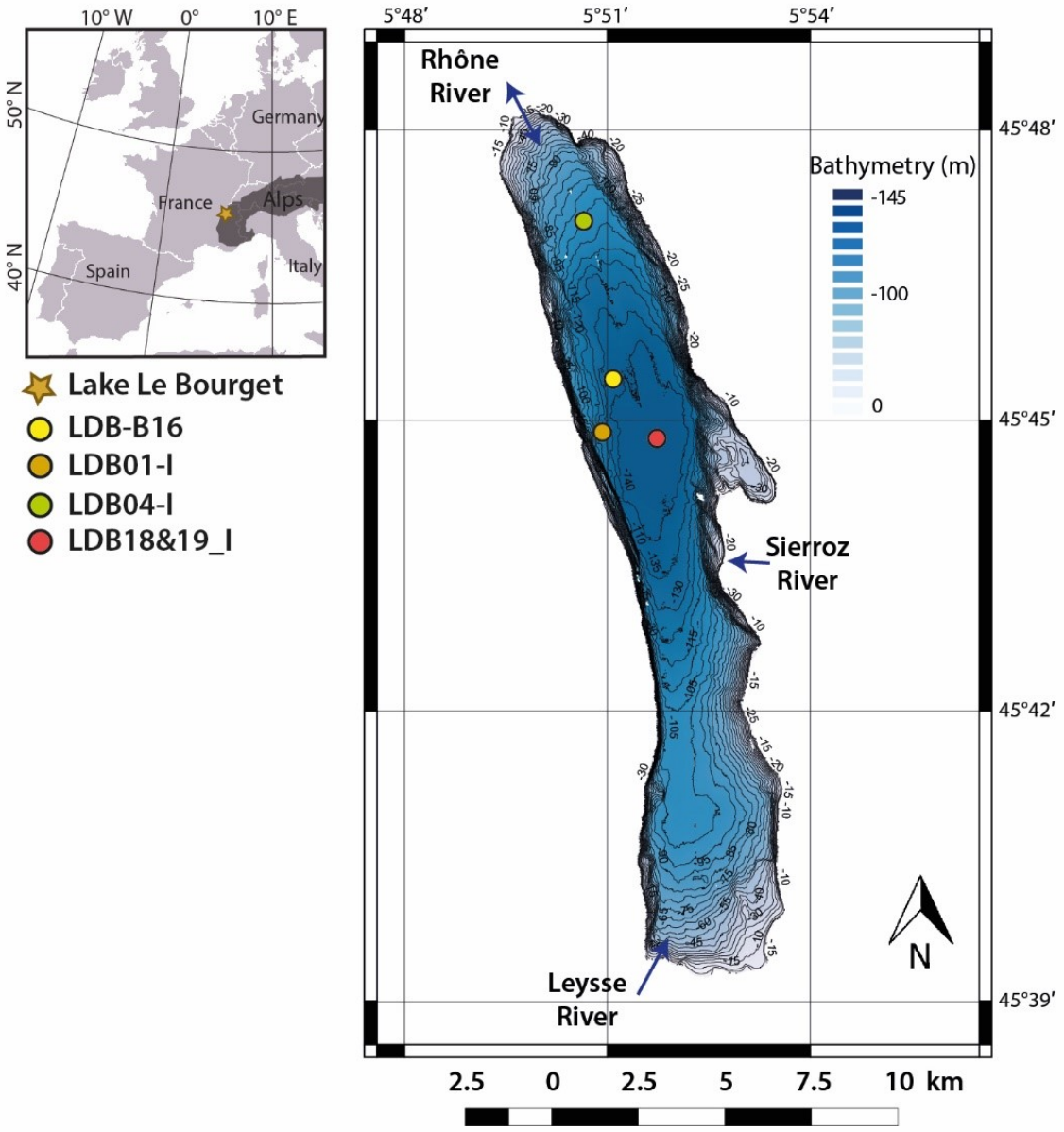

Figure S2 – Bathymetric map of Lake Bourget with the location of each sediment sequences described or used in this study. Bathymetric data derived from Ledoux et al. (2010).

S3. Lake sediment geochemistry

Table S3 - Lake sediment sequence, age (yr cal BP), siliciclastic Nd and Sr isotopic compositions with the associated 95% uncertainties and provenance of the data used for representation in Fig. 4 and Fig. 5 and for calculation. Data from Arnaud et al. (2012) that were not sampled in flood events or in the LDB04 sequence, close to the delta and more impacted by floods from the Rhône river were added to this study.

Sequence	Age cal BP	εNd			87Sr/86Sr			Data provenance
LDB0101	54	-10.55	±	0.25				Arnaud et al. (2012)
LDB18	93	-10.88	±	0.15	0.71932	±	1.0E-03	This study
LDB0101	138	-9.48	±	0.25				Arnaud et al. (2012)
LDB0101	143	-10.26	±	0.25				Arnaud et al. (2012)
LDB0101	168	-10.26	±	0.25				Arnaud et al. (2012)
LDB18	213	-11.18	±	0.22	0.71949	±	2.5E-05	This study
LDB0101	220	-10.57	±	0.25				Arnaud et al. (2012)
LDB0101	240	-10.12	±	0.25				Arnaud et al. (2012)
LDB0101	269	-9.97	±	0.25				Arnaud et al. (2012)
LDB0101	298	-10.55	±	0.25				Arnaud et al. (2012)
LDB18	384	-10.86	±	0.31	0.71944	±	9.3E-06	This study
LDB18	465	-10.90	±	0.22	0.71885	±	2.5E-05	This study
LDB0101	491	-10.55	±	0.25				Arnaud et al. (2012)
LDB0101	617	-10.67	±	0.25				Arnaud et al. (2012)
LDB18	629	-10.70	±	0.06	0.71952	±	6.7E-06	This study
LDB18	711	-10.99	±	0.22	0.71889	±	2.5E-05	This study
LDB0101	752	-10.92	±	0.25				Arnaud et al. (2012)
LDB0101	757	-10.67	±	0.25				Arnaud et al. (2012)
LDB0101	785	-10.49	±	0.25				Arnaud et al. (2012)
LDB18	887	-10.90	±	0.22	0.71836	±	2.5E-05	This study
LDB0101	913	-10.18	±	0.25				Arnaud et al. (2012)
LDB18	965	-10.87	±	0.22				This study
LDB04	1080	-10.75	±	0.25				Arnaud et al. (2012)
LDB18	1121	-10.69	±	0.07	0.71839	±	8.8E-06	This study
LDB01	1181	-10.40	±	0.25				Arnaud et al. (2012)
LDB18	1231	-11.38	±	0.22	0.71586	±	2.5E-05	This study
LDB18	1346	-11.01	±	0.22	0.71860	±	2.5E-05	This study
LDB18	1758	-11.08	±	0.22	0.71886	±	2.5E-05	This study
LDB0101	1800	-10.61	±	0.25				Arnaud et al. (2012)
LDB0101	1851	-10.61	±	0.25				Arnaud et al. (2012)
LDB18	2020	-11.03	±	0.22	0.71889	±	2.5E-05	This study
LDB18	2146	-10.73	±	0.22	0.71928	±	6.1E-06	This study
LDB18	2412	#N/A	±	0.22	0.71883	±	2.5E-05	This study
LDB04	2422	-10.67	±	0.25				Arnaud et al. (2012)
LDB01	2598	-10.71	±	0.25				Arnaud et al. (2012)
LDB18	2670	#N/A	±	0.22	0.71842	±	2.5E-05	This study
LDB04	2723	-10.87	±	0.25				Arnaud et al. (2012)
LDB01	2731	-10.55	±	0.25				Arnaud et al. (2012)
LDB18	2792	-10.90	±	0.22	0.72030	±	1.5E-06	This study
LDB0101	3024	-11.35	±	0.25				Arnaud et al. (2012)
LDB04	3024	-10.96	±	0.25				Arnaud et al. (2012)
LDB18	3038	-10.52	±	0.22	0.71745	±	2.5E-05	This study
LDB18	3275	-11.07	±	0.22	0.71819	±	2.5E-05	This study
LDB18	3407	-10.80	±	0.22	0.71944	±	5.1E-06	This study
LDB18	3548	-10.79	±	0.22	0.71816	±	2.5E-05	This study
LDB18	3827	-10.46	±	0.22	0.71772	±	2.5E-05	This study
LDB04	3858	-10.20	±	0.25				Arnaud et al. (2012)
LDB0101	3882	-10.40	±	0.25				Arnaud et al. (2012)
LDB0101	4066	-10.40	±	0.25				Arnaud et al. (2012)
LDB18	4118	-10.95	±	0.22	0.71855	±	1.5E-06	This study

LDB18	4331	-10.38	±	0.22	0.71862	±	8.3E-06	This study
LDB01	4881	-10.38	±	0.25				Arnaud et al. (2012)
LDB18	4893	-11.08	±	0.22	0.71518	±	1.0E-05	This study
LDB18	5367	-10.65	±	0.22	0.72049	±	2.5E-05	This study
LDB18	5584	-11.10	±	0.22	0.71851	±	6.2E-06	This study
LDB19	5837	-10.81	±	0.22	0.71707	±	3.8E-06	This study
LDB19	5954	-10.85	±	0.22				This study
LDB19	6093	-10.92	±	0.22	0.71579	±	1.0E-05	This study
LDB19	6208	-10.81	±	0.22	0.71499	±	5.2E-06	This study
LDB19	6323	-11.15	±	0.22	0.71705	±	1.0E-05	This study
LDB19	6437	-11.01	±	0.22	0.71620	±	1.2E-05	This study
LDB19	6722	-10.84	±	0.22	0.71884	±	3.5E-05	This study
LDB19	6838	-10.84	±	0.22	0.71759	±	5.8E-05	This study
LDB0101	6925	-10.87	±	0.25				Arnaud et al. (2012)
LDB19	6955	-10.88	±	0.22	0.71826	±	4.2E-05	This study
LDB19	7086	-10.98	±	0.22	0.71806	±	1.6E-05	This study
LDB19	7220	-11.10	±	0.22				This study
LDB0101	7255	-10.87	±	0.25				Arnaud et al. (2012)
LDB19	7332	-11.22	±	0.22	0.71982	±	9.7E-06	This study
LDB19	7460	-10.90	±	0.22	0.71952	±	7.7E-06	This study
LDB19	7625	-11.04	±	0.22	0.72001	±	1.3E-05	This study
LDB19	7760	-10.98	±	0.22	0.71937	±	3.8E-05	This study
LDB19	7848	-11.16	±	0.22	0.72066	±	7.0E-05	This study
LDB19	7992	-10.86	±	0.22	0.72047	±	4.6E-06	This study
LDB19	8144	-11.00	±	0.22	0.71973	±	7.7E-06	This study
LDB19	8372	-10.98	±	0.22	0.71998	±	6.8E-06	This study
LDB19	8527	-11.13	±	0.22	0.71993	±	1.1E-05	This study
LDB19	8682	-11.07	±	0.22	0.71912	±	5.6E-06	This study
LDB19	8849	-10.69	±	0.22	0.71173	±	5.4E-06	This study
LDB19	9050	-10.98	±	0.22	0.71995	±	4.2E-06	This study
LDB19	9238	-10.79	±	0.22	0.71371	±	1.1E-05	This study
LDB19	9442	-11.04	±	0.22	0.71879	±	2.0E-06	This study

S4. River sediment geochemistry

Table S4 – River sediment samples with river type, predominant lithologies in the sub-catchments, location, Sr isotopic composition for bulk samples and samples after the leaching procedure, Nd isotopic composition, and Sr and Nd concentrations of bulk samples. EM for external massif, HN for Helvetic nappes, PA for pre-Alps, CS for cretaceous sub-alpine, PM for peri-alpine molasse and JC for Jurassic chain. Data from Revel-Rolland et al. (2005) were added for the corresponding sub-catchments. Mean decarbonated $^{87}Sr/^{86}Sr$ and εNd signature were estimated for each sub-catchments from available data, in order to provide robust data for future mixing model.

N°	Type	Geology	Lat	Long	$^{87}Sr/^{86}Sr_{bulk}$			$^{87}Sr/^{86}Sr_{leach}$			Stdev	[Sr]	Stdev	εNd			Stdev	[Nd]	Stdev	Data provenance
1.A	tributary	E M						0.72201	±	2.50E-05		138.8		-8.52	±	**0.39**		57.3		Revel-Rolland
1.A	tributary	E M						0.7306	±	2.50E-05		136.3		-5.52	±	**0.39**		72.9		Revel-Rolland
1.A	tributary	E M						0.72615	±	2.50E-05		129.8		-5.31	±	**0.39**		55.8		Revel-Rolland
1.A	tributary	E M						0.72993	±	2.50E-05		108.3		-4.86	±	**0.39**		29		Revel-Rolland
1.A	tributary	E M	45°54'0.47"N	6°48'37.53"E	0.72614	±	2.50E-05	0.7284	±	2.50E-05		147.2		-5.66	±	**0.22**		43.7		This study
1.A	tributary	E M						0.72815	±	2.50E-05		107.5		-5.47	±	**0.39**		27.8		Revel-Rolland
1.A mean	**tributary**	**E M**						**0.72864**	**±**		**0.00155**	**128**	**15.1**	**-5.36**	**±**		**0.28**	**47.7**	**16.1**	**Mean value**
1.B	tributary	HN / EM	45°55'51.43"N	6°46'9.25"E	0.71014	±	7.30E-06					360.2		-10.09	±	**0.22**		28.4		This study
1.B	tributary	HN / EM						0.7127	±	2.50E-05		163.9		-10.48	±	**0.39**		33.4		Revel-Rolland
1.B mean	**tributary**	**HN / EM**						**0.7127**	**±**		**0**	**262.1**	**98.2**	**-10.28**	**±**		**0.2**	**30.9**	**2.5**	**Mean value**
2.A[1]	tributary	HN / EM	45°51'32.04"N	6°43'48.60"E	0.71041	±	1.20E-05					521.9		-10.18	±	**0.22**		42.9		This study
2.A[2]	tributary	HN / EM	45°54'22.19"N	6°42'10.19"E	0.7109	±	5.10E-05					444		-10.01	±	**0.22**		35		This study
2.B[1]	tributary	HN / EM	45°51'59.06"N	6°43'30.66"E	0.7139	±	5.50E-05					279.8		-9.73	±	**0.22**		30.7		This study
2.A[1]	tributary	HN / EM						0.71848	±	2.50E-05		149.1		-9.48	±	**0.39**		36.5		Revel-Rolland
2.A mean	**tributary**	**HN / EM**						**0.71848**	**±**		**0**	**348.7**	**144.6**	**-9.85**	**±**		**0.27**	**36.3**	**4.4**	**Mean value**
3.A	tributary	HN	45°56'11.06"N	6°37'54.06"E	0.71118	±	9.10E-06					343.4		-12.54	±	**0.22**		29.4		This study
3.A	tributary	HN						0.71444	±	2.50E-05		143.8		-11.12	±	**0.39**		29.9		Revel-Rolland
3.A mean	**tributary**	**HN**						**0.71444**	**±**		**0**	**243.6**	**99.8**	**-11.83**	**±**		**0.71**	**29.7**	**0.2**	**Mean value**
4.A[1]	tributary	PA	46° 3'23.95"N	6°45'1.56"E	0.708	±	5.70E-05					708.7		-10.77	±	**0.22**		15		This study
4.A[2]	tributary	PA	46° 6'34.46"N	6°33'41.84"E	0.708593	±	4.40E-06					492.9		-11.54	±	**0.22**		19.1		This study
4.A[3]	tributary	PA	46° 5'37.99"N	6°30'25.53"E	0.70863	±	1.20E-05	0.71268	±	1.20E-05		477.7		-9.85	±	**0.22**		17.4		This study
4.A[1]	tributary	PA						0.70862	±	2.50E-05		476.2		-10.34	±	**0.39**		17.3		Revel-Rolland
4.A mean	**tributary**	**PA**						**0.71065**	**±**		**0.00203**	**538.9**	**98.3**	**-10.62**	**±**		**0.62**	**17.2**	**1.4**	**Mean value**
5.A	tributary	CS	46° 4'5.52"N	6°23'27.60"E	0.70927	±	1.90E-05					391.3		-10.4	±	**0.22**		21.8		This study
5.A	tributary	CS						0.71593	±	2.50E-05		94		-10.73	±	**0.39**		27.2		Revel-Rolland
5.A mean	**tributary**	**CS**						**0.71593**	**±**		**0**	**242.7**	**148.6**	**-10.56**	**±**		**0.17**	**24.5**	**2.7**	**Mean value**
6.A	tributary	PM	46°10'9.23"N	6°16'20.99"E	0.70963	±	9.30E-06					364.7		-10.03	±	**0.22**		21.6		This study
6.A	tributary	PM						0.71179	±	2.50E-05		173.5		-9.71	±	**0.39**		26.1		Revel-Rolland
6.A mean	**tributary**	**PM**						**0.71179**	**±**		**0**	**269.1**	**95.6**	**-9.87**	**±**		**0.16**	**23.9**	**2.3**	**Mean value**
8.A	tributary	JC	46° 7'7.02"N	5°49'32.51"E	0.70811	±	1.00E-05					393		-10.05	±	0.22		12.3		This study
9.A	tributary	PM/JC	46° 0'58.38"N	5°56'29.04"E	0.71003	±	5.10E-06					298.7		-9.5	±	0.22		21.1		This study

10.A[1]	tributary	PM/JC	45°54'3.67"N	5°57'37.89"E	0.70881	±	2.30E-05					531.2		-9.44	±	**0.22**		22		This study
10.A[2]	tributary	PM/JC	45°55'58.92"N	5°51'2.58"E	0.70876	±	8.80E-06	0.71452	±	8.80E-06		422.4		-9.02	±	**0.22**		17.5		This study
10.B[1]	tributary	PM/JC	45°51'59.40"N	5°57'5.75"E	0.70855	±	1.10E-05					548.4		-9.68	±	**0.22**		18.8		This study
10.B[2]	tributary	PM/JC	45°51'59.40"N	5°57'5.75"E	0.7087	±	8.80E-05					437.6		-9.6	±	**0.22**		17.8		This study
10.A	tributary	PM/JC						0.71604	±	2.50E-05		83.9		-9.71	±	**0.39**		22.4		Revel-Rolland
10.A mean	**tributary**	**PM/JC**						**0.71528**	±		**0.00076**	**404.7**	**167.9**	**-9.49**	±		**0.25**		**2.1**	**Mean value**
11.A	tributary	PM/JC	45°42'4.66"N	5°53'7.81"E	0.71036	±	2.40E-05					238.7		-8.54	±	0.22		20.9		This study
11.B	tributary	PM/JC	45°37'46.12"N	5°52'30.85"E	0.7079	±	1.80E-04					761.3		-10.24	±	0.22		17.6		This study
1	river		45°54'40.32"N	6°42'25.62"E	0.7205	±	9.60E-06	0.72435	±	9.60E-06		185.4		-6.98	±	**0.22**		37.9		This study
1	river							0.72531	±	2.50E-05		123.2		-6.38	±	**0.39**		31.2		Revel-Rolland
1	river							0.71814	±	2.50E-05		161.1		-8.8	±	0.39		43.9		Revel-Rolland
1mean	**river**							**0.72483**	±	**2.50E-05**		**154.3**		**-6.68**	±	**0.39**		**34.5**		**Mean value**
2	river		45°54'48.48"N	6°41'42.19"E	0.71298	±	3.80E-05					329.4		-7.71	±	**0.22**		36.1		This study
2	river							0.72504	±	2.50E-05		135.5		-7.1	±	**0.39**		34.6		Revel-Rolland
3	river		46° 3'25.54"N	6°34'42.75"E	0.71423	±	9.20E-06					299.6		-7.14	±	**0.22**		48.2		This study
3	river							0.72056	±	2.50E-05		157.4		-7.69	±	**0.39**		23.9		Revel-Rolland
4	river		46° 4'29.55"N	6°24'37.06"E	0.71011	±	6.70E-06					432		-8.65	±	**0.22**		25		This study
4	river							0.72202	±	2.50E-05		133.2		-7.26	±	**0.39**		58.8		Revel-Rolland
5	river		46° 9'49.20"N	6°14'38.16"E	0.710439	±	2.70E-06					413.6		-7.59	±	**0.22**		29.9		This study
5	river							0.71946	±	2.50E-05		135.1		-8.41	±	**0.39**		43.2		Revel-Rolland
6	river		46°10'38.68"N	6°14'12.81"E	0.710278	±	3.50E-06					397.4		-9.12	±	**0.22**		23.8		This study
6	river							0.72146	±	2.50E-05		141.2		-7.32	±	**0.39**		63.2		Revel-Rolland
7	river		46° 7'19.21"N	5°54'17.21"E	0.70977	±	1.80E-05					415.5		-11.18	±	**0.22**		24.2		This study
8	river		46° 7'7.02"N	5°49'32.51"E	0.70977	±	7.70E-06					415.4		-11.31	±	**0.22**		24.2		This study
8	river							0.72026	±	2.50E-05		90.9		-8.9	±	**0.39**		24.4		Revel-Rolland
9	river		45°57'22.74"N	5°50'2.67"E	0.71005	±	3.30E-05					347.7		-8.68	±	**0.22**		24		This study
9	river							0.71983	±	2.50E-05		67.5		-9.54	±	**0.39**		16.7		Revel-Rolland
10	river		45°49'57.21"N	5°48'4.69"E	0.70942	±	2.70E-05	0.71777	±	2.70E-05		397.1		-9.19	±	**0.22**		20.9		This study
10	river							0.71893	±	2.50E-05		100.7		-9.06	±	**0.39**		24.1		Revel-Rolland
10	river							0.71749	±	2.50E-05		106.1		-9.54	±	**0.39**		24.3		Revel-Rolland
10	river							0.71615	±	2.50E-05		103.9		-10.03	±	**0.39**		27.3		Revel-Rolland
10 mean	**river**							**0.71759**	±	**2.50E-05**		**177**		**-9.45**	±	**0.39**		**24.1**		**Mean value**

S5. Method for major and trace elements measurements

Major and trace elements were measured using an Agilent 7900 quadrupole ICP-MS. Liquid samples were sprayed through a micro-nebulizer in a Scott spray chamber prior to ionization. Elements with masses between that of sodium (23) and arsenic (75) were measured using a collision-reaction cell with helium gas (5 $mL.min^{-1}$) to remove polyatomic interferences. All other elements were measured without collision gas. Correction for signal drift and matrix effect were correct by injection of scandium, indium and rhenium internal standards after inline mixing with the samples. Two sets of multi-element calibration standards (one for major and one for trace elements) were analysed to compute the calibration curves that were used to convert measured counts to concentrations. The reported uncertainties were calculated using the algebraic propagation of blank subtraction and sample count standard deviations (n=3). The NIST®SRM®2709a reference material (San Joaquin soil) was processed as samples and analysed repeatedly during the sequences to evaluate the accuracy of the measurements. The detection limit was between 0.2 and 0.5 ppt depending on the element, and the internal errors were 5% on average. The weight loss during leaching of lake (and river in some cases) sediments was considered in the estimate of major and trace element concentrations of the residue, such that the reported concentrations relate to the mass of residue (that is, carbonate-free, and referred to as "silicate" in the following) component of the sediment.

S6. Detailed method for isotopic composition analyses

Isotope measurements were all performed at the PARI analytical platform of IPGP. After powder digestion, Sr and Nd were separated from the sample matrix by extraction chromatography. We used an Sr-SPEC resin (Eichrom) for Sr (Hajj et al., 2017) and a combination of TRU-spec and Ln-spec resins for Nd (Cogez et al., 2015).

Sr isotope ratios were measured by multi-collector inductively coupled plasma mass spectrometry (MC-ICPMS; Neptune, Thermo-Fisher Scientific) with an APEX-Q (ESI) desolvation system as a sample introduction system. Rubidium (Rb, that was observed in residual amounts in some samples, even after chromatographic purification) interference on mass 87 and krypton (Kr, present in the argon gas used to produce the plasma) interferences on masses 84 and 86 were corrected for using the ^{85}Rb and ^{83}Kr signals along with the Rb and Kr isotope ratios measured at the beginning of the sequence. Instrumental and natural mass fractionation on the $^{87}Sr/^{86}Sr$ ratio were corrected using an exponential law, the measured $^{88}Sr/^{86}Sr$ ratio and the "natural" abundance $^{88}Sr/^{86}Sr$ ratio assumed to be equal to 8.3752. Measurement accuracy was checked through repeated measurements of the NIST pure-Sr, isotope reference material SRM 987 (2 S.D of 2.9×10^{-5}), and the NIST soil reference material SRM 2709a ($^{87}Sr/^{86}Sr$ = 0.70823 ± 0.00002; comparing well with the value provided by Brazier et al., 2020 of 0.70814 ± 0.00002). Each sample was measured up to three times during a session. For samples measured three times, the 95% confidence interval was obtained from Student's *t*-distribution and ranged from 3×10^{-6} to 8×10^{-3}. For other samples measured less than 3 times, the 2 S.D of 4.9×10^{-5} estimated from the repeated measurements of the reference material NIST SRM 2709a (processed through powder digestion and separation as for samples) was used as an estimate of the 95% confidence interval.

Nd isotope analyses were performed by MC-ICP-MS Neptune using N_2 addition and X-cones with an APEX-IR (ESI) desolvation system as the sample introduction system. Instrumental and natural

mass fractionation on the $^{143}Nd/^{144}Nd$ ratio were corrected for using an exponential law, the measured $^{146}Nd/^{144}Nd$ ratio and its natural abundance ratio, taken as 0.7218. Accuracy was checked through repeated measurements of a NIST pure-Nd, isotope reference material ($^{143}Nd/^{144}Nd$ = 0.511418; Caro et al., 2006), with a measured 2 S.D of 2.7 x 10^{-6}, and the NIST soil reference material SRM2709a (0.512381 ± 0.000028).

S7. Comparison of LDB04 and LDB18&19 sediment section

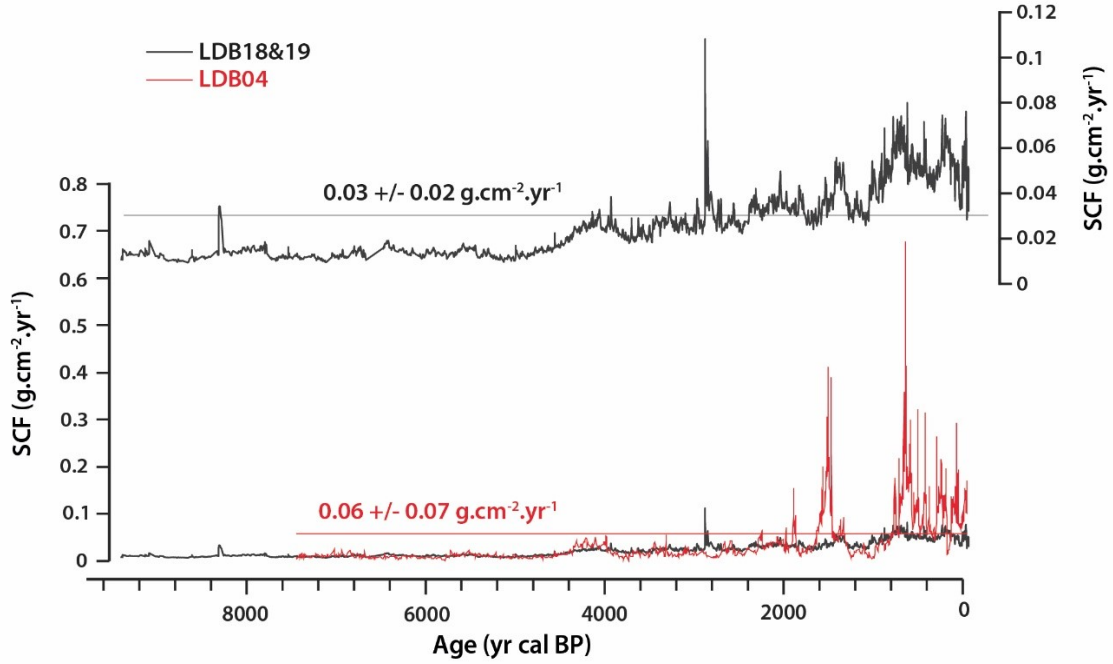

Figure S7 – Siliciclastic flux from LDB04 and LDB18&19 sediment sections represented against the age (yr cal BP). Signals variations are equivalent, but mean and maximal values differ.

CHAPITRE XI | Synthèse des apports de connaissances sur l'évolution de l'érosion au cours de l'Holocène dans les Alpes

1. Objectifs de l'étude de l'érosion au cours de l'Holocène

L'érosion de la Zone Critique, notamment en montagne, est devenu un des enjeux majeurs des géosciences car elle affecte directement les sociétés humaines qui s'y développent. Il est donc urgent de produire des évaluations permettant de quantifier les effets relatifs des principaux facteurs de contrôle de l'érosion de la ZC à court ou moyen terme. A l'échelle de l'Holocène deux facteurs principaux peuvent influencer l'érosion :

(i) Les fluctuations climatiques par les précipitations annuelles, les événements de précipitations extrêmes, et les avancées et retraits glaciaires ;

(ii) L'homme, du fait de l'utilisation des sols pour le développement de l'agriculture, le développement du pastoralisme et la déforestation associée en altitude, la déforestation pour l'extraction de minerai ou le développement des zones urbaines.

Les effets de la géodynamique externe via l'activité sismique sont considérés comme constant au cours de l'Holocène. Malgré tout, il n'est pas à exclure que lors de l'occurrence d'un séisme majeur, l'érosion dans le bassin versant étudié puisse augmenter subitement en lien avec la remobilisation de sédiments par des glissements de terrains induits par la secousse sismique. De tels phénomènes ont été observés en Nouvelle-Zélande mais sont toutefois liés à des séismes de magnitude supérieure à 7 (e.g., Wang et al., 2020), n'ayant pas lieu dans les Alpes européennes.

Comme présenté en Introduction de cette thèse (chapitre I), nous avons choisi d'utiliser une analyse multi-indicateurs des séquences sédimentaires sur deux grands lacs périalpins, ceux du Bourget (France) et d'Iseo (Italie), utilisés comme archives de l'érosion de la ZC sur de grands bassins versants. Cette méthode a été combinée à une approche « source-puits » associée à des mesures de composition isotopique en Sr et Nd pour déterminer les signatures de chaque source. Les bassins versants des lacs sélectionnés permettent de faire la part entre l'érosion liée uniquement aux fluctuations climatiques et l'impact des activités humaines. En effet, ces bassins versants présentent deux types de zones différentes :

(i) Les Massifs du Mont Blanc et de l'Adamello, situés respectivement à l'amont du bassin versant du lac du Bourget et du lac Iseo. Il s'agit de zone de haute altitude où de grands glaciers sont développés et dominent l'érosion. La lithologie de ces zones correspond à des séries calco-alcalines, présentant les valeurs les plus élevées en εNd.

(ii) Le reste du bassin versant, correspondant à des plaines ou des massifs de moyenne altitude, est composé par la couverture sédimentaire Mésozoïque. Ces zones, du fait de leur accessibilité et leur proximité avec les points d'eau, concentrent les activités humaines depuis le Néolithique. L'érosion dans ces zones est donc dépendante des précipitations annuelles et extrêmes ainsi que de l'effet des activités humaines.

2. L'évolution de l'érosion au cours de l'Holocène

Au cours de la Partie III de cette thèse nous avons donc utilisé la méthodologie développée ci-dessus pour tenter de retracer l'évolution de l'érosion au cours de l'Holocène. Ce chapitre offre l'opportunité d'en produire une brève synthèse. Seul le site du lac du Bourget permet de couvrir toute la période de l'étude. En effet, les séquences sédimentaires prélevés dans le lac Iseo ne couvrent que les deux mille dernières années. Le signal d'érosion a été obtenu à partir du calcul du flux de silicate détritique (SCF) produit notamment à partir du signal XRF de composition élémentaire en Ti des sédiments de lac. L'érosion dans le bassin versant du Bourget présente un signal cohérent avec les études précédemment réalisées sur de petits lacs de moyenne et haute altitude, localisées dans ou aux abords du bassin versant (chapitre X).

L'érosion enregistrée dans les sédiments du lac du Bourget est faible et constante entre 9 et 4.8 ka cal BP. Cette période correspond à l'optimum climatique Holocène (Debret, 2008; Magny et al., 2003; McDermott et al., 1999). Le climat tend vers des températures plus chaudes et des précipitations moins importantes, ce qui favorise le développement des sols dans les Alpes à cette époque (Bajard, 2017).

A partir de 4.8 ka cal BP, le signal d'érosion augmente jusqu'à 3.8 ka cal BP. Dès 5 kry cal BP, le climat en Europe connaît une transition vers des températures plus froides. Les précipitations annuelles augmentent et sont accompagnées par une augmentation des fréquences de crues à l'échelle des Alpes du Sud, indiquant une augmentation des événements de précipitations extrêmes à cette époque. Dans les Alpes, l'augmentation de l'érosion est retrouvée à toutes les altitudes. Le signal d'érosion enregistré dans le lac du Bourget est sensiblement identique (chapitre X) à la chronique de crues produite par Wirth et al. (2013) pour les Alpes du Sud. A cette époque, il est probable que l'influence du climat méditerranéen, par des entrées de masses d'air humides venant de l'est soit ressentie jusque dans le bassin versant du lac du Bourget. Ces masses d'air ont sans doute provoqué une augmentation des événements de précipitations extrêmes dans le bassin versant et ont pu favoriser le redéveloppement des glaciers dès cette époque (Arnaud et al., 2012).

Du début de l'Holocène jusqu'à 3.8 ka cal BP, les courbes d'apports sédimentaires du Massif du Mont Blanc et de la couverture sédimentaire covarient. Ceci est interprété comme synonyme d'une érosion dominée par le climat. En effet, l'érosion de la zone de haute-altitude du Massif du Mont Blanc est dépendante des fluctuations climatiques, comme les avancées et reculs glaciaires liés aux précipitations annuelles, car les activités humaines y sont absentes ou négligeables (Giguet-Covex et al., 2021). Toutefois, lorsque le signal d'érosion de la zone de « couverture sédimentaire » augmente sans qu'une augmentation équivalente ne soit observée sur le signal d'érosion du Massif du Mont Blanc, alors le climat seul ne peut plus expliquer l'érosion (chapitre X, Fig. X-7). Ceci est justement le cas à partir de 3.8 ka cal BP et jusqu'au Moyen-Âge. En effet, l'érosion glaciaire demeure constante mais à l'inverse, l'érosion à basse et moyenne-altitude, elle, continue d'augmenter. L'impact du climat seul ne permet donc plus d'expliquer la dynamique de l'érosion. Cette période correspond à la fin de l'Âge du Bronze et à l'Âge du Fer. Dans les Alpes, à cette période, l'agriculture se développe à basse altitude, et une ouverture du milieu est observée à moyenne et haute altitude afin de libérer des espaces pour le pastoralisme (Giguet-Covex et al., 2021). Les activités humaines sont donc interprétées comme ayant causé une augmentation de l'érodabilité des sols à partir de l'Âge du Bronze.

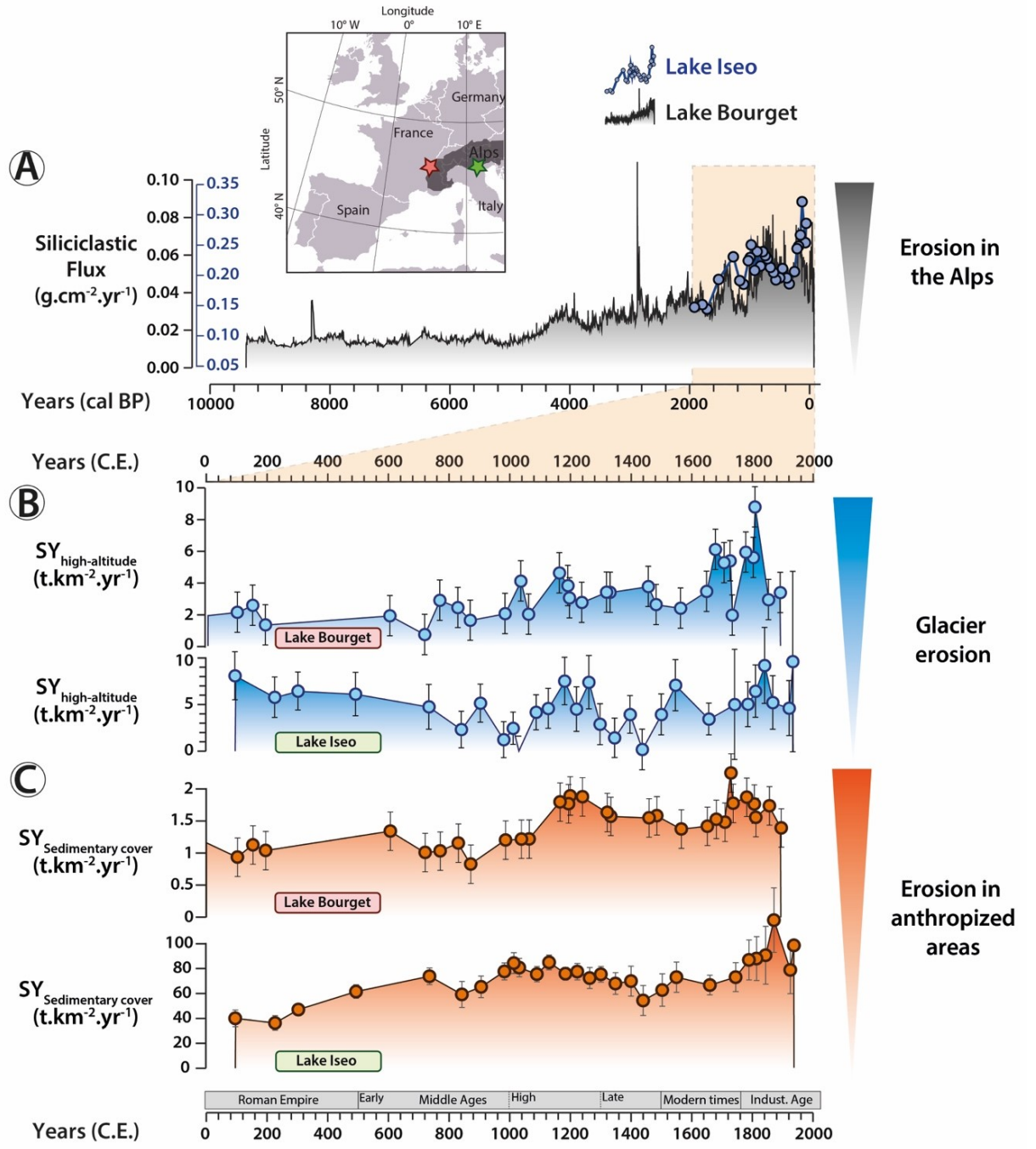

Fig. XI-1 - Évolution de l'érosion dans deux grands bassins versants des Alpes, le lac du Bourget et le lac Iseo. Sont représentés ici (A) les flux de silicates détritiques (en g.cm^{-2}.yr^{-1}) enregistrés dans le bassin profond de chacun des lacs. Un zoom sur les deux milles dernières années permet de comparer les apports sédimentaires (B) des zones de hautes altitudes, i.e., le massif du Mont-Blanc dans le bassin versant du lac du Bourget et le massif de l'Adamello dans le bassin versant du lac Iseo. L'érosion de ces zones est principalement impactée par les avancées et retraits glaciaires ainsi que par les précipitations. (C) Les apports sédimentaires des zones de moyennes à basses altitudes, souvent associée à la couverture sédimentaire Mésozoïque, sont eux impactés à la fois par les précipitations mais aussi par les activités humaines.

A partir de la période Romaine, il est possible de comparer l'érosion enregistrée dans les deux bassins versants. En termes de flux, malgré une différence nette de valeur absolue liée aux contextes sédimentaires différents, les tendances sont globalement les mêmes Fig. XI-1. Les deux signaux d'érosion augmentent à partir de la fin de l'Empire Romain et ce jusqu'au début du Moyen-Âge. Après une brève diminution vers 850 CE, les taux d'érosion augmentent à nouveau

pour atteindre les valeurs les plus élevées durant le Haut Moyen-Âge. Les valeurs d'érosion diminuent ensuite progressivement jusqu'aux alentours de 1600 CE avant d'augmenter nettement durant le Petit Age Glaciaire (PAG). En s'intéressant aux différences entre les signaux d'érosion des zones de hautes et de basses altitudes des deux bassins versants il est possible de démêler les effets du climat et des activités humaines à ces périodes (Fig. XI-1-B & C).

En effet, le signal d'érosion des zones glaciaires, après être resté stable dans le bassin versant du Bourget et après avoir diminué dans le bassin versant d'Iseo augmente à nouveau à partir de l'an mil (Fig. XI-1-B). Les glaciers alpins présentent des avancées glaciaires majeures à cette époque (Holzhauser et al., 2005; Le Roy et al., 2015) en lien avec un climat plus froid et humide au début du Haut Moyen-Âge (Büntgen et al., 2016, 2011). Jusqu'au PAG, l'érosion semble être à nouveau dominée par les activités humaines à basses et moyennes altitudes, car les signaux d'érosion des zones glaciaires restent constants dans le bassin versant du Bourget et diminuent à nouveau dans le bassin versant d'Iseo. La fin du Moyen-Âge (1300 CE) présente les taux d'érosion les plus élevés dans les deux bassins versants.

Lors du PAG, l'érosion est interprétée comme étant principalement liée au retour d'un climat plus froid et humide, associé à des avancées glaciaires majeures, probablement les plus importantes de l'Holocène. Après le PAG, les taux d'érosion diminuent mais demeurent élevés jusqu'à la période moderne.

Au cours des 2000 dernières années, les signaux d'érosion des zones de hautes altitudes des deux bassins versants, associés à l'érosion glaciaire, ne présentent pas des tendances totalement équivalentes (Fig. XI-1). En effet, lorsque le signal d'érosion du Massif du Mont Blanc demeure faible et constant après la période Romaine ou après la période froide de l'an mil, le signal de l'érosion glaciaire du bassin versant d'Iseo montre une diminution nette. Cette différence peut s'expliquer par la différence de taille des deux masses glaciaires dans les deux zones. En effet, dans le Massif du Mont Blanc, la Mer de Glace et les glaciers environnants font partis des glaciers les plus étendus des Alpes européennes. Les glaciers du Massif du Mont Blanc sont donc beaucoup moins sensibles aux augmentations de température ou aux diminutions des précipitations sur de courtes périodes (Le Roy et al., 2015). A l'inverse, les glaciers présents dans le bassin versant du lac Iseo correspondent à des petits glaciers de versants, beaucoup plus sensibles et réactifs à de petites modifications du climat local.

A l'inverse, les signaux d'érosion obtenue sur les zones anthropisées des deux bassins versant sont très similaires à l'échelle des deux mille dernières années (Fig. XI-1), ce qui indique que les effets des activités humaines sont sensiblement identiques à l'échelle des Alpes.

D'après les résultats obtenus au cours de ce travail de recherche, il apparaît que l'érosion dans les Alpes est d'abord dépendante du contexte climatique entre le début de l'Holocène et 3.8 ka cal BP, puis, lorsque les activités humaines deviennent plus importantes elles commencent à impacter les taux d'érosion. A partir de l'Âge du Bronze, l'homme a donc un impact sur l'érosion de la Zone Critique dans les Alpes.

Partie IV | Conclusion générale

CHAPITRE XII | Synthèse de la thèse et perspectives

La problématique à l'origine de ce travail de recherche était, pour une zone donnée que sont les Alpes Européennes et à partir d'une approche rétrospective de type source-puit basée sur des archives sédimentaires lacustres, de démêler et quantifier les effets des forçages climatiques et humains sur l'érosion de la Zone Critique au cours de l'Holocène. Ce travail de recherche s'est donc intéressé à l'étude d'archives sédimentaires lacustres prélevées dans des lacs situés à l'exutoire de deux grands bassins versants des Alpes européennes. Il s'agit du lac du Bourget situé dans le nord des Alpes françaises, et du lac Iseo au nord des Alpes italiennes.

Principaux résultats

Le premier défi de ce projet de recherche a d'abord été de prélever des sédiments dans les bassins profonds des grands lacs périalpins sélectionnés. En effet, les carottages étaient réalisés jusqu'à présent par des missions coûteuses (ICDP ou équivalent), ou nécessitaient de cibler des zones de faibles tranches d'eau. En utilisant une nouvelle barge de carottage UWITEC, développée par le C2FN de la division technique de l'Institut National des Sciences de l'Univers (INSU), en lien avec le projet EQUIPEX CLIMCOR, nous avons pu réaliser des carottages à plus faible coût et permettant de prélever de longues séquences sédimentaires (plusieurs dizaines de mètres) par plusieurs centaines de mètres de fond (plus de 250 m). Ce matériel a été utilisé à grande profondeur pour la première fois dans le cadre de cette thèse.

Études des processus sédimentaires à l'œuvre dans les grands lacs périalpins

Une fois les séquences sédimentaires prélevées, il a été nécessaire d'interroger les processus sédimentaires à l'œuvre dans les grands lacs périalpins. En effet, chaque lac possède son propre fonctionnement qui peut influencer la façon dont l'érosion du bassin versant est enregistrée dans les sédiments. Peu d'études s'étaient intéressées à ces processus jusqu'alors, et la plupart couvraient de courtes périodes, ou avaient été réalisées à partir d'analyses géophysiques ne permettant pas d'étudier l'origine des sédiments déposés dans le fond des lacs. Ici nous avons tenté de faire la part entre la sédimentation continue, composée des particules issues de l'érosion du bassin versant, et la sédimentation instantanée venant interrompre et perturber l'enregistrement de l'érosion (CHAPITRE IV |).

A partir de l'étude de deux séquences sédimentaires lacustres nous avons pu montrer que, dans le bassin profond du lac Iseo, la totalité ou presque de la production authigène est dissoute lors de la décantation (chapitre V). Ce lac est donc un très bon candidat pour reconstituer l'évolution de l'érosion provenant du bassin versant. En effet, l'absence d'accumulation sédimentaire biogénique facilite le calcul des flux d'apports détritiques du bassin versant et permet d'utiliser plus facilement certains traceurs géochimiques, tel que la composition isotopique du Sr pour déterminer l'origine des sédiments composant la sédimentation continue par exemple.

La sédimentation continue dans le bassin profond du lac Iseo est aussi perturbée par des dépôts évènementiels de type Turbidite ou Homogenite. La composition élémentaire de chacun des dépôts a permis de retracer leur provenance, et de séparer les dépôts liés à la remobilisation de

sédiments préalablement déposés sur les pentes du lac des dépôts liés à des apports détritiques du bassin versant ou du delta de l'Oglio. Une chronique de fréquence a été réalisée pour chaque type de dépôts, ce qui a permis de relier chaque dépôt à l'activité sismique ou aux événements de précipitations extrêmes locaux et régionaux après comparaison avec des données instrumentales et historiques. Dans le bassin profond du lac Iseo, la sédimentation instantanée représente plus des deux-tiers des sédiments accumulés lors des 2000 dernières années. Les taux de sédimentation importants dans ce bassin complexifient l'étude long-terme de l'érosion.

En étudiant la relation entre flux d'érosion et fréquence des dépôts évènementiels dans le lac Iseo, nous avons mis en évidence que la disponibilité en sédiment dans le bassin versant et dans le lac a un impact direct sur la fréquence des événements extrêmes enregistrés dans les sédiments. Ceci avait déjà été démontré pour des lacs de plus petites tailles. Nous avons montré ici que même dans les grands lacs périalpins l'érosion a un impact sur l'enregistrement du fonctionnement de la zone critique au cours du temps. Les forçages de l'érosion ont donc un effet direct sur l'enregistrement de l'érosion elle-même dans les archives sédimentaires lacustres. Nous avons aussi démontré que l'utilisation des archives lacustres et de la fréquence des dépôts évènementiels comme traceurs des paléo-précipitations ou de l'activité sismique ne peut être robuste que si l'évolution de la disponibilité en sédiment dans le bassin versant et le lac a été étudiée *a priori* (chapitres IV, V & VIII).

Deux transects de prélèvements de séquences sédimentaires ont aussi été réalisés dans le lac du Bourget avant le début du projet de thèse. L'étude approfondie des dépôts de type Turbidites présent dans les séquences sédimentaires, liés à des crues du Rhône, a permis de reconstituer le volume de chaque dépôt. A partir de données instrumentales, la comparaison des débits des crues du Rhône avec le volume des dépôts associés dans le lac du Bourget a permis de reconstituer les paléo-débit du Rhône au cours des 2000 dernières années (chapitre VI).

L'identification des dépôts évènementiels dans une séquence sédimentaire et l'interprétation des processus sédimentaire à l'origine des dépôts requiert du temps. Durant ce travail de thèse nous avons donc développé une méthodologie permettant (i) la détection semi-automatique des dépôts évènementiels et, (ii) l'interprétation des processus à leur origine (chapitre VII). Nous avons démontré ici que l'utilisation de l'imagerie hyperspectrale associée à des algorithmes discriminants permet l'identification semi-automatique des dépôts évènementiels. L'utilisation combinée de l'imagerie hyperspectrale et des données de fluorescences X (XRF) offre la possibilité d'interpréter l'origine de chaque dépôt. Il s'agit ici d'une avancée importante dans le domaine de la sédimentologie, permettant d'améliorer la résolution de ce type d'étude et de réduire nettement le temps d'analyse consacré à l'identification et à l'interprétation des dépôts.

Études de l'évolution de l'érosion au cours de l'Holocène dans les Alpes

Une fois la sédimentation évènementielle identifiée, les produits de l'érosion d'un bassin versant peuvent être étudiés au sein des séquences sédimentaires afin d'évaluer l'érosion au cours du temps (CHAPITRE IX |). Pour cela, nous avons tout d'abord calculé un flux d'apports de matériel détritique silicaté dans chaque lac à partir de la multiplication du taux de sédimentation avec (i) la densité du sédiment et avec (ii) la part de sédiment détritique silicaté dans l'accumulation sédimentaire totale (chapitres IX & X). Ce dernier paramètre est obtenu soit à partir des résidus

de pertes au feu, soit à partir de la concentration élémentaire en Ti dans la séquence sédimentaire.

Les sources principales d'apports sédimentaires de chaque bassin ont été identifiées à partir de données de géochimie isotopique ($^{87}Sr/^{86}Sr$ et εNd). Les apports sédimentaires dans chaque bassin versant proviennent de deux types de sources principales :

(i) La zone de haute altitude, caractérisée par la présence de granite à l'affleurement et de nombreux glaciers dominant l'érosion.
(ii) La zone de plaine et de moyenne altitude, associée à la couverture sédimentaire Mésozoïque. Cette zone concentre les activités humaines depuis le Néolithique.

Seul le bassin versant du lac Iseo présente une troisième source, correspondant à la zone métamorphique située à moyenne altitude au nord du bassin versant. L'évolution du signal d'érosion des zones de haute altitude renseigne sur l'effet du climat sur l'érosion au cours du temps. L'érosion dans les zones de basses et moyennes altitudes est influencée par les précipitations et les activités humaines. La comparaison de ces deux signaux permet de faire la part entre l'effet du climat et des activités humaines sur l'érosion de ces grands bassins versants.

Le flux de chaque source rapportée à sa superficie permet d'obtenir une estimation de l'apport sédimentaire en $t.km^{-2}.an^{-1}$. Les valeurs d'apports sédimentaires de chaque zone ont ensuite été comparées aux valeurs obtenues par le modèle numérique d'érosion des sols à grande échelle, R.U.S.L.E (Panagos et al., 2015b) afin de valider les résultats obtenus. Dans le cas du bassin versant du lac Iseo, les apports sédimentaires mesurés pour la partie basse du bassin versant sont équivalents à la valeur obtenue par le modèle numérique d'érosion des sols. La majorité des produits d'érosion du bassin versant est donc bien enregistrée dans le lac. A l'inverse, les valeurs d'apports sédimentaires mesurés dans le lac du Bourget sont actuellement dix à cent fois plus faibles que les valeurs théoriques obtenus par les modèles numériques. Ceci est dû au fait que seule une portion des apports sédimentaire du bassin versant entrent dans le lac du Bourget (chapitre X).

Bien que les sédiments déposés dans le lac du Bourget ne permettent pas de fournir d'information quantitative sur les taux d'érosion dans le bassin versant du lac, les tendances du signal renseignent sur l'évolution de l'érosion dans le bassin versant au cours du temps :

(i) De 9 à 5 ka cal BP, l'érosion est faible et constante ;
(ii) A partir de 5 ka cal BP, l'érosion augmente progressivement jusqu'à 3.8 ka cal BP. Cette augmentation est marquée à toutes les altitudes et a été interprétée comme liée à une transition vers un climat plus humide et froid dû à une augmentation de l'influence du climat méditerranéen ressentie jusque dans le bassin versant du lac du Bourget ;
(iii) A partir de 3.8 ka cal BP, et jusqu'au Moyen-Âge, l'érosion glaciaire demeure constante à l'inverse de l'érosion à basse et moyenne-altitude qui elle continue d'augmenter. L'impact du climat seul ne permet donc plus d'expliquer la dynamique de l'érosion. Cette période correspond à un développement de l'agriculture à basse altitude et du pastoralisme associé à un déboisement important à moyenne et haute-altitude dans les Alpes. Les activités humaines semblent avoir causé une augmentation de l'érodabilité des sols à partir de l'âge du Bronze ;

(iv) Le signal d'érosion des zones glaciaires dans les deux bassins versants augmente à nouveau aux alentours de l'an mil. Cette période correspond à des avancées glaciaires majeures dans les Alpes européennes en lien avec un climat plus froid et humide au début du Haut Moyen-Âge ;

(v) Jusqu'au Petit Âge Glaciaire (PAG), l'érosion est à nouveau dominée par les activités humaines à basses et moyennes altitudes. La fin du Moyen-Âge (1300 CE) présente les taux d'érosion les plus élevés dans les deux bassins versants ;

(vi) Lors du PAG, l'érosion est interprétée comme étant principalement liée au retour d'un climat plus froid et humide, associé à des avancées glaciaires majeures, probablement les plus importantes de l'Holocène ;

(vii) Après le PAG, les taux d'érosion diminuent mais demeurent élevés jusqu'à la période moderne.

En conclusion, nous avons montré par l'étude des signaux d'érosion enregistrés dans les sédiments lacustres que le climat correspond au forçage majeur de l'érosion du début de l'Holocène à environ 4 kyr cal BP. Toutefois, lorsque les activités humaines se développent, le climat seul ne permet plus d'expliquer les tendances des signaux d'érosions enregistrés. A partir de l'Âge du Bronze, l'homme du fait du développement agricole, du pastoralisme, de l'extraction de minerai et de la déforestation, a modifié le couvert végétal et entraîné une modification de l'érodabilité des sols. De ce fait, pour un même contexte climatique, le développement des activités humaines favorise l'érosion. Alors même que le signal d'érosion des zones de hautes altitudes impactées par le climat demeure quasi constant depuis l'âge du Bronze, une multiplication par trois des taux d'érosions dans les Alpes est observée.

Ce travail de thèse permet de fournir pour la première fois, sur une grande échelle spatiale et temporelle, des données quantitatives de l'impact du climat et des activités humaines sur l'érosion de la Zone Critique. Ces données montrent que, même dans les grands bassins versants montagneux, les activités humaines affectent la ZC en augmentant l'érosion, entraînant des dommages sur les écosystèmes et une perte du carbone des sols et de la biomasse. La ZC est donc dégradée par les pratiques humaines depuis 3800 ans dans les Alpes, la rendant très sensible à la pression anthropique actuelle. Cette observation permet de relancer le débat sur le positionnement du début de l'anthropocène. D'après Crutzen, (2002), la définition de cette nouvelle époque géologique est nécessaire car l'Homme, en tant qu'espèce, est devenu le facteur dominant de l'érosion. Ce travail de thèse a aussi permis de mettre en évidence l'importance d'utiliser des chroniques d'érosion à long terme, telles que celles produites à partir des sédiments lacustres, pour quantifier l'influence des différents facteurs de forçage ayant un impact sur l'érosion de la ZC au fil du temps. Les données produites ici pourront être réutilisées pour la réalisation de modèles d'érosion.

Perspectives

Ce travail de thèse ouvre de nombreuses perspectives de recherches, à la fois :

(i) À l'échelle temporelle, avec la nécessité d'augmenter la période couverte par les séquences sédimentaires du lac Iseo ;

(ii) À l'échelle spatiale avec l'étude de nouveaux terrains ailleurs dans les Alpes ;

(iii) Au niveau de l'approche méthodologique avec le développement de nouvelles méthodes de traçage de source de sédiments ;

(iv) Au niveau des thématiques de recherches, il semble aussi nécessaire de s'intéresser à l'étude de l'évolution de l'altération de la Zone Critique au cours du temps.

Dans un premier temps, il semble primordial de réaliser un nouveau carottage dans le bassin profond du lac Iseo pour obtenir des informations sur l'état de l'érosion sur l'intégralité de l'Holocène afin de couvrir des périodes où les activités humaines n'étaient pas développées dans le bassin versant. La difficulté réside dans le fait que le taux d'accumulation dans le lac est très élevé. Toutefois, d'après les profils sismiques disponibles (chapitre V, Bini et al., 2007), il semble que la fréquence des dépôts évènementiels dans le bassin profond du lac diminue nettement à partir de la base du carottage réalisé en 2018.

Afin d'augmenter la résolution spatiale de notre étude, il pourrait être envisagé de réaliser un prélèvement de sédiments dans le lac Constance (Allemagne/Suisse/Autriche. En associant ce lac, la superficie des trois bassins versants étudiés atteindrait 15% de la surface alpine totale. Ceci permettrait aussi d'obtenir un signal d'érosion représentatif de chaque secteur des Alpes (nord, ouest et sud), qui sont influencés par des processus climatiques différents ainsi que par des courants de néolithisation et donc des histoires humaines différentes.

Un des axes de cette thèse devait être d'étudier l'évolution de l'état d'altération des sols au cours de l'Holocène. Pour ce faire, des analyses de composition isotopique du lithium devaient être réalisées sur les sédiments du lac du Bourget. Toutefois, à la suite de difficultés de séparation et d'analyse de la composition isotopique du Lithium mais aussi et surtout suite à un manque de temps réservé à ces analyses, seuls quelques échantillons ont été mesurés pour le moment. La séparation a été réalisée en suivant un protocole équivalent à celui de Bohlin et al. (2018), avec une seule étape de séparation. Les résultats des premières mesures réalisés au MC-ICP-MS (Neptune Plus, Thermo-Fisher Scientific) sont représentés dans la Fig. XII-1. La mauvaise reproductibilité de certains standards, ainsi qu'entre deux mesures du même échantillon n'a pas permis de proposer une interprétation de ces données au sein de ce travail de thèse.

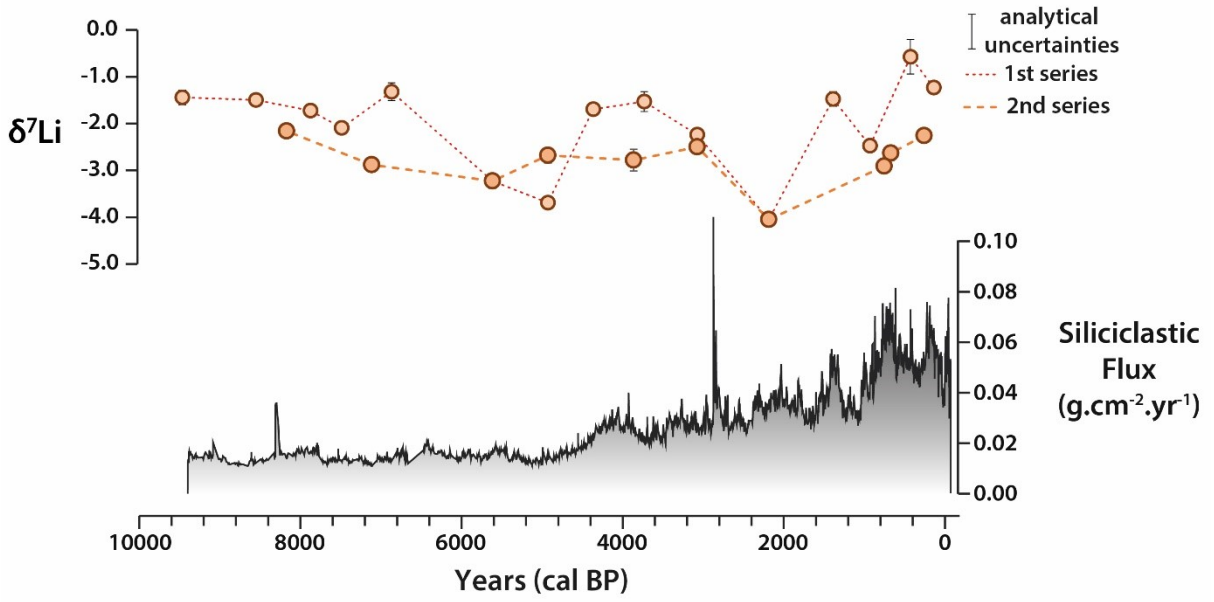

Fig. XII-1- Premiers résultats de δ^7Li obtenus à partir d'échantillons de sédiments du lac du Bourget au cours de ce travail de thèse. Les résultats sont comparés au flux détritique enregistré dans le lac du Bourget.

Dans un futur proche, un travail sera réalisé pour améliorer la reproductibilité des données ainsi que la résolution de l'analyse pour pouvoir interroger l'évolution de l'état d'altération des sols au cours du temps. Ces données permettront d'étudier les effets de l'érosion, du climat et de l'activité humaine sur l'état des sols, et de mieux comprendre la dynamique de la zone critique au cours de l'Holocène.

Afin de mieux comprendre l'effet des activités humaines sur l'érosion, une option serait d'utiliser des modèles d'érosion rétrospectifs. Pour cela, il est possible d'utiliser l'équation du modèle R.U.S.L.E (Panagos et al., 2015b):

$$E = R \times K \times C \times LS \times P$$

P étant un facteur associé à chaque type de pratique, LS correspondant à la longueur et l'inclinaison de la pente, C correspondant au facteur d'utilisation des sols, K au facteur d'érodabilité des sols, R au facteur d'érosivité lié aux précipitations annuelles et E correspondant au taux moyen annuel de perte de sols. En utilisant les valeurs actuelles des paramètres de ce modèle, disponibles à l'échelle du bassin versant (Panagos et al., 2015b) et à partir de données de paléo-précipitations robustes, des tests sur les effets des différents types d'usages des sols sur l'érosion pourront être réalisés. Cette étude permettrait de déterminer, entre la déforestation, le développement des sols agricoles ou du pastoralisme, quel est le facteur ou la combinaison de facteurs qui permettrait d'expliquer au mieux les taux d'érosion reconstitués au cours des derniers millénaires. Toutefois, peu de données de paléo-précipitations existent à ces échelles de temps et sur la zone d'étude, et aucun jeu de données ne semble suffisamment robuste pour réaliser une telle étude pour le moment. Pour s'affranchir de ce problème, un projet de reconstitution des paléo-température est en cours, et sera réalisé à partir d'une synthèse de données palynologique déjà acquises ou en cours d'acquisition.

Enfin, l'un des principaux problèmes liés à l'utilisation de la composition isotopique en Nd et Sr des sédiments, et que les différences de signatures au sein de la couverture sédimentaire des Alpes européenne sont trop faibles pour distinguer plusieurs sources au sein de cette zone. Afin de pouvoir augmenter la résolution spatiale et d'obtenir des signaux d'érosion pour des zones moins vastes, où les différents effets du climat et des activités humaines pourraient être plus facilement identifiables il semble nécessaire d'utiliser d'autres marqueurs. Une nouvelle méthodologie de traçage de source à partir de l'ADN environnemental piégé dans les sédiments de lacs et des principaux affluents devrait donner la possibilité de tracer les apports des différents étages de végétations au sein d'un bassin versant et de ne plus utiliser uniquement les différentes lithologies. Le principal biais lié à cette méthode est qu'il semble que plus le puits est éloigné de la source, moins la préservation de l'ADN environnemental dans les sédiments est bonne. Le développement de cette méthode est en cours.

Références bibliographiques

Ahnert, F., 1970. Functional relationships between denudation, relief, and uplift in large, mid-latitude drainage basins. Am. J. Sci. 268, 243–263. https://doi.org/10.2475/ajs.268.3.243

Allevato, E., Fedele, F., Terrasi, F., Capano, M., Pasquale, G.D., 2013. High-Resolution Archaeoenvironmental Study of a Cultic Episode at a Statue-Menhir Copper Age Site (Ossimo Anvòia, Italian Alps). Radiocarbon 55, 49–58. https://doi.org/10.2458/azu_js_rc.v55i1.16063

Ambrosetti, W., Barbanti, L., 2005. Evolution towards meromixis of Lake Iseo (Northern Italy) as revealed by its stability trend. J. Limnol. 64, 1. https://doi.org/10.4081/jlimnol.2005.1

Amundson, R., Richter, D.D., Humphreys, G.S., Jobbágy, E.G., Gaillardet, J., 2007. Coupling between Biota and Earth Materials in the Critical Zone. Elements 3, 327–332. https://doi.org/10.2113/gselements.3.5.327

Anati, E., 2009. L'art rupestre du Valcamonica : évolution et signification. Une vision panoramique d'après l'état actuel de la recherche. L'Anthropologie, Représentations préhistoriques. Images du sens (3/3) 113, 930–968. https://doi.org/10.1016/j.anthro.2009.10.003

Anati, E., Cittadini, T., 1994. Valcamonica rock art: a new history for Europe.

Anderson, S.P., Blanckenburg, F. von, White, A.F., 2007. Physical and Chemical Controls on the Critical Zone. Elements 3, 315–319. https://doi.org/10.2113/gselements.3.5.315

Andrič, M., Sabatier, P., Rapuc, W., Ogrinc, N., Dolenec, M., Arnaud, F., von Grafenstein, U., Šmuc, A., 2020. 6600 years of human and climate impacts on lake-catchment and vegetation in the Julian Alps (Lake Bohinj, Slovenia). Quat. Sci. Rev. 227, 106043. https://doi.org/10.1016/j.quascirev.2019.106043

Angima, S.D., Stott, D.E., O'neill, M.K., Ong, C.K., Weesies, G.A., 2003. Soil erosion prediction using RUSLE for central Kenyan highland conditions. Agric. Ecosyst. Environ. 97, 295–308.

Appleby, P.G., 2001. Chronostratigraphic Techniques in Recent Sediments, in: Last, W.M., Smol, J.P. (Eds.), Tracking Environmental Change Using Lake Sediments: Basin Analysis, Coring, and Chronological Techniques, Developments in Paleoenvironmental Research. Springer Netherlands, Dordrecht, pp. 171–203. https://doi.org/10.1007/0-306-47669-X_9

Appleby, P.G., Richardson, N., Nolan, P.J., 1991. 241Am dating of lake sediments, in: Smith, J.P., Appleby, P.G., Battarbee, R.W., Dearing, J.A., Flower, R., Haworth, E.Y., Oldfield, F., O'Sullivan, P.E. (Eds.), Environmental History and Palaeolimnology, Developments in Hydrobiology. Springer Netherlands, pp. 35–42. https://doi.org/10.1007/978-94-011-3592-4_4

Arcà, A., Fossati, A., 2006. Rupestrian archaeology: a methodological approach to the rock engravings of Valcamonica. Eur. II Prehist. Art Res. Manag. Eur. Stud. Archeol. Storia Cult. 4, 51–8.

Arnaud, F., Poulenard, J., Giguet-Covex, C., Wilhelm, B., Révillon, S., Jenny, J.-P., Revel, M., Enters, D., Bajard, M., Fouinat, L., Doyen, E., Simonneau, A., Pignol, C., Chapron, E.,

Vannière, B., Sabatier, P., 2016. Erosion under climate and human pressures: An alpine lake sediment perspective. Quat. Sci. Rev. 152, 1–18. https://doi.org/10.1016/j.quascirev.2016.09.018

Arnaud, F., Révillon, S., 2015. A Geochemical Approach to Improve Radiocarbon-Based Age-Depth Models in Non-laminated Sediment Series, in: Croudace, I.W., Rothwell, R.G. (Eds.), Micro-XRF Studies of Sediment Cores: Applications of a Non-Destructive Tool for the Environmental Sciences, Developments in Paleoenvironmental Research. Springer Netherlands, Dordrecht, pp. 459–472. https://doi.org/10.1007/978-94-017-9849-5_18

Arnaud, F., Révillon, S., Debret, M., Revel, M., Chapron, E., Jacob, J., Giguet-Covex, C., Poulenard, J., Magny, M., 2012. Lake Bourget regional erosion patterns reconstruction reveals Holocene NW European Alps soil evolution and paleohydrology. Quat. Sci. Rev. 51, 81–92. https://doi.org/10.1016/j.quascirev.2012.07.025

Arnaud, F., Revel, M., Chapron, E., Desmet, M., Tribovillard, N., 2005. 7200 years of Rhône river flooding activity in Lake Le Bourget, France: a high-resolution sediment record of NW Alps hydrology. The Holocene 15, 420–428. https://doi.org/10.1191/0959683605hl801rp

Arnaud, F., 2005. Discriminating bio-induced and detrital sedimentary processes from particle size distribution of carbonates and non-carbonates in hard water lake sediments. J. Paleolimnol. 34, 519–526. https://doi.org/10.1007/s10933-005-6787-1

Arnaud, F., Lignier, V., Revel, M., Desmet, M., Beck, C., Pourchet, M., Charlet, F., Trentesaux, A., Tribovillard, N., 2002. Flood and earthquake disturbance of 210Pb geochronology (Lake Anterne, NW Alps). Terra Nova 14, 225–232. https://doi.org/10.1046/j.1365-3121.2002.00413.x

Bader, J., Jungclaus, J., Krivova, N., Lorenz, S., Maycock, A., Raddatz, T., Schmidt, H., Toohey, M., Wu, C.-J., Claussen, M., 2020. Global temperature modes shed light on the Holocene temperature conundrum. Nat. Commun. 11, 4726. https://doi.org/10.1038/s41467-020-18478-6

Bajard, M., Poulenard, J., Sabatier, P., Bertrand, Y., Crouzet, C., Ficetola, G.F., Blanchet, C., Messager, E., Giguet-Covex, C., Gielly, L., Rioux, D., Chen, W., Malet, E., Develle, A.-L., Arnaud, F., 2020. Pastoralism increased vulnerability of a subalpine catchment to flood hazard through changing soil properties. Palaeogeogr. Palaeoclimatol. Palaeoecol. 538, 109462. https://doi.org/10.1016/j.palaeo.2019.109462

Bajard, M., Poulenard, J., Sabatier, P., Develle, A.-L., Giguet-Covex, C., Jacob, J., Crouzet, C., David, F., Pignol, C., Arnaud, F., 2017a. Progressive and regressive soil evolution phases in the Anthropocene. Catena 150, 39–52. https://doi.org/10.1016/j.catena.2016.11.001

Bajard, M., Poulenard, J., Sabatier, P., Etienne, D., Ficetola, F., Chen, W., Gielly, L., Taberlet, P., Develle, A.-L., Rey, P.-J., 2017b. Long-term changes in alpine pedogenetic processes: Effect of millennial agro-pastoralism activities (French-Italian Alps). Geoderma 306, 217–236. https://doi.org/10.1016/j.geoderma.2017.07.005

Bajard, M., 2017. Trajectoires d'évolution des sols et des agroécosystèmes de montagne de l'Holocène à l'Anthropocène Reconstitution des pédopaysages des Alpes du Nord occidentales à partir d'archives sédimentaires lacustres. http://www.theses.fr/s117791

Bajard, M., Sabatier, P., David, F., Develle, A.-L., Reyss, J.-L., Fanget, B., Malet, E., Arnaud, D., Augustin, L., Crouzet, C., Poulenard, J., Arnaud, F., 2016. Erosion record in Lake La Thuile sediments (Prealps, France): Evidence of montane landscape dynamics throughout the Holocene. The Holocene 26, 350–364. https://doi.org/10.1177/0959683615609750

Barker, M., Rayens, W., 2003. Partial least squares for discrimination. J. Chemom. 17, 166–173. https://doi.org/10.1002/cem.785

Barnes, R.J., Dhanoa, M.S., Lister, S.J., 1989. Standard Normal Variate Transformation and De-Trending of Near-Infrared Diffuse Reflectance Spectra. Appl. Spectrosc. 43, 772–777. https://doi.org/10.1366/0003702894202201

Beck, C., 2009. "Late Quaternary lacustrine paleo-seismic archives in north-western Alps: Examples of earthquake-origin assessment of sedimentary disturbances." Earth-Sci. Rev. 96, 327–344. https://doi.org/10.1016/j.earscirev.2009.07.005

Benedetti, L., Manighetti, I., Gaudemer, Y., Finkel, R., Malavieille, J., Pou, K., Arnold, M., Aumaître, G., Bourlès, D., Keddadouche, K., 2013. Earthquake synchrony and clustering on Fucino faults (Central Italy) as revealed from in situ 36Cl exposure dating. J. Geophys. Res. Solid Earth 118, 4948–4974. https://doi.org/10.1002/jgrb.50299

Benedetti, R., Predali, R., 2013. Contro al cieco fiume: cronaca fotografica delle alluvioni di Marone, 11 luglio 1953, e di Vello, 9 luglio 1963. FdP.

Beniston, M., Stephenson, D.B., Christensen, O.B., Ferro, C.A., Frei, C., Goyette, S., Halsnaes, K., Holt, T., Jylhä, K., Koffi, B., 2007. Future extreme events in European climate: an exploration of regional climate model projections. Clim. Change 81, 71–95. https://doi.org/10.1007/s10584-006-9226-z

Bertrand, S., Hughen, K.A., Sepulveda, J., Pantoja, S., 2012. Geochemistry of surface sediments from the fjords of Northern Chilean Patagonia (44–47 S): spatial variability and implications for paleoclimate reconstructions. Geochim. Cosmochim. Acta 76, 125–146. https://doi.org/10.1016/j.gca.2011.10.028

Bezak, N., Mikoš, M., Borrelli, P., Alewell, C., Alvarez, P., Ayach Anache, J.A., Baartman, J., Ballabio, C., Biddoccu, M., Cerdà, A., Chalise, D., Chen, S., Chen, W., De Girolamo, A.M., Gessesse, G.D., Deumlich, D., Diodato, N., Efthimiou, N., Erpul, G., Fiener, P., Freppaz, M., Gentile, F., Gericke, A., Haregeweyn, N., Hu, B., Jeanneau, A., Kaffas, K., Kiani-Harchegani, M., Villuendas, I.L., Li, C., Lombardo, L., López-Vicente, M., Lucas-Borja, M.E., Märker, M., Miao, C., Modugno, S., Möller, M., Naipal, V., Nearing, M., Owusu, S., Panday, D., Patault, E., Patriche, C.V., Poggio, L., Portes, R., Quijano, L., Rahdari, M.R., Renima, M., Ricci, G.F., Rodrigo-Comino, J., Saia, S., Samani, A.N., Schillaci, C., Syrris, V., Kim, H.S., Spinola, D.N., Oliveira, P.T., Teng, H., Thapa, R., Vantas, K., Vieira, D., Yang, J.E., Yin, S., Zema, D.A., Zhao, G., Panagos, P., 2021. Soil erosion modelling: A bibliometric analysis. Environ. Res. 111087. https://doi.org/10.1016/j.envres.2021.111087

Biagi, P., Starnini, E., 2015. Human settlement and environmental exploitation of Valcamonica-Valtrompia watershed from the beginning of the Holocene to the Middle Ages. Nat. Brescia. 39, 195.

Biguenet, M., Sabatier, P., Chaumillon, E., Chagué, C., Arnaud, F., Jorissen, F., Coulombier, T., Geba, E., Cordrie, L., Vacher, P., Develle, A.L., Chalmin, E., Soufi, F., Feuillet, N., 2021. A 1600 year-long sedimentary record of tsunamis and hurricanes in the Lesser Antilles (Scrub Island, Anguilla). Sediment. Geol. 412, 105806. https://doi.org/10.1016/j.sedgeo.2020.105806

Bini, A., Forcella, F., Corbari, D., Facchinetti, P., Ferliga, C., Pisani, V., Rigamonti, I., Rossi, S., Zanotti, M., Berra, F., 2012. Foglio 078 Breno. Carta Geologica d'Italia alla scala 1: 50.000.

Bini, A., Corbari, D., Falletti, P., Fassina, M., Perotti, C.R., Piccin, A., 2007. Morphology and geological setting of Iseo Lake (Lombardy) through multibeam bathymetry and high-resolution seismic profiles. Swiss J. Geosci. 100, 23–40. https://doi.org/10.1007/s00015-007-1204-6

Bini, A., Cita, M.B., Gaetani, M., 1978. Southern Alpine Lakes—Hypothesis of an erosional origin related to the Messinian entrenchment. Mar. Geol. 27, 271–288. https://doi.org/10.1016/0025-3227(78)90035-X

Bini, M., Zanchetta, G., Perşoiu, A., Cartier, R., Català, A., Cacho, I., Dean, J.R., Di Rita, F., Drysdale, R.N., Finnè, M., Isola, I., Jalali, B., Lirer, F., Magri, D., Masi, A., Marks, L., Mercuri, A.M., Peyron, O., Sadori, L., Sicre, M.-A., Welc, F., Zielhofer, C., Brisset, E., 2019. The 4.2 ka BP Event in the Mediterranean region: an overview. Clim. Past 15, 555–577. https://doi.org/10.5194/cp-15-555-2019

Bini, M., Zanchetta, G., Regattieri, E., Isola, I., Drysdale, R.N., Fabiani, F., Genovesi, S., Hellstrom, J.C., 2020. Hydrological changes during the Roman Climatic Optimum in northern Tuscany (Central Italy) as evidenced by speleothem records and archaeological data. J. Quat. Sci. 35, 791–802. https://doi.org/10.1002/jqs.3224

Blaauw, M., 2010. Methods and code for 'classical'age-modelling of radiocarbon sequences. Quat. Geochronol. 5, 512–518. https://doi.org/10.1016/j.quageo.2010.01.002

Blaauw, M., Christen, J.A., Lopez, M.A.A., Vazquez, J.E., V, O.M.G., Belding, T., Theiler, J., Gough, B., Karney, C., 2021. rbacon: Age-Depth Modelling using Bayesian Statistics.

Blanchet, G., 1990. Régimes météorologiques et diversité climatique dans l'espace rhonalpin / Meteorological regimes and climatic diversity in the Rhône-Alpes area. Géocarrefour 65, 106–117. https://doi.org/10.3406/geoca.1990.5720

Blass, A., Anselmetti, F.S., Grosjean, M., Sturm, M., 2005. The last 1300 years of environmental history recorded in the sediments of Lake Sils (Engadine, Switzerland). Eclogae Geol. Helvetiae 98, 319–332. https://doi.org/10.1007/s00015-005-1166-5

Blöschl, G., Hall, J., Viglione, A., Perdigão, R.A., Parajka, J., Merz, B., Lun, D., Arheimer, B., Aronica, G.T., Bilibashi, A., 2019. Changing climate both increases and decreases European river floods. Nature 573, 108–111. https://doi.org/10.1038/s41586-019-1495-6

Bøe, A.-G., Dahl, S.O., Lie, Ø., Nesje, A., 2016. Holocene river floods in the upper Glomma catchment, southern Norway: a high-resolution multiproxy record from lacustrine sediments: The Holocene. https://doi.org/10.1191/0959683606hl940rp

Bohlin, M.S., Misra, S., Lloyd, N., Elderfield, H., Bickle, M.J., 2018. High-precision determination of lithium and magnesium isotopes utilising single column separation and multi-collector inductively coupled plasma mass spectrometry. Rapid Commun. Mass Spectrom. 32, 93–104. https://doi.org/10.1002/rcm.8020

Borrelli, P., Alewell, C., Alvarez, P., Anache, J.A.A., Baartman, J., Ballabio, C., Bezak, N., Biddoccu, M., Cerdà, A., Chalise, D., Chen, S., Chen, W., De Girolamo, A.M., Gessesse, G.D., Deumlich, D., Diodato, N., Efthimiou, N., Erpul, G., Fiener, P., Freppaz, M., Gentile, F., Gericke, A., Haregeweyn, N., Hu, B., Jeanneau, A., Kaffas, K., Kiani-Harchegani, M., Villuendas, I.L., Li, C., Lombardo, L., López-Vicente, M., Lucas-Borja, M.E., Märker, M., Matthews, F., Miao, C., Mikoš, M., Modugno, S., Möller, M., Naipal, V., Nearing, M., Owusu, S., Panday, D., Patault, E., Patriche, C.V., Poggio, L., Portes, R., Quijano, L., Rahdari, M.R., Renima, M., Ricci, G.F., Rodrigo-Comino, J., Saia, S., Samani, A.N., Schillaci, C., Syrris, V., Kim, H.S., Spinola, D.N., Oliveira, P.T., Teng, H., Thapa, R., Vantas,

K., Vieira, D., Yang, J.E., Yin, S., Zema, D.A., Zhao, G., Panagos, P., 2021. Soil erosion modelling: A global review and statistical analysis. Sci. Total Environ. 780, 146494. https://doi.org/10.1016/j.scitotenv.2021.146494

Borrelli, P., Robinson, D.A., Panagos, P., Lugato, E., Yang, J.E., Alewell, C., Wuepper, D., Montanarella, L., Ballabio, C., 2020. Land use and climate change impacts on global soil erosion by water (2015-2070). Proc. Natl. Acad. Sci. 117, 21994–22001. https://doi.org/10.1073/pnas.2001403117

Bosco, C., Rusco, E., Montanarella, L., Oliveri, S., 2008. Soil erosion risk assessment in the alpine area according to the IPCC scenarios. Threats Soil Qual. Eur. Ed. Toth G Montanarella Rusco E EUR 23438, 47–58.

Brack, P., Dal Piaz, G.V., Baroni, C., Carton, A., Nardin, M., Pellegrini, G.B., Pennacchioni, G., 2008. Note illustrative della Carta Geologica d'Italia alla scala 1: 50.000. Foglio 058, Monte Adamello. Carta Geol. Ital. Alla Scala 1 50000.

Brantley, S.L., McDowell, W.H., Dietrich, W.E., White, T.S., Kumar, P., Anderson, S.P., Chorover, J., Lohse, K.A., Bales, R.C., Richter, D.D., Grant, G., Gaillardet, J., 2017. Designing a network of critical zone observatories to explore the living skin of the terrestrial Earth. Earth Surf. Dyn. 5, 841–860. https://doi.org/10.5194/esurf-5-841-2017

Brantley, S.L., Goldhaber, M.B., Ragnarsdottir, K.V., 2007. Crossing Disciplines and Scales to Understand the Critical Zone. Elements 3, 307–314. https://doi.org/10.2113/gselements.3.5.307

Brazier, J.-M., Schmitt, A.-D., Pelt, E., Lemarchand, D., Gangloff, S., Tacail, T., Balter, V., 2020. Determination of Radiogenic 87Sr/86Sr and Stable δ88/86SrSRM987 Isotope Values of Thirteen Mineral, Vegetal and Animal Reference Materials by DS-TIMS. Geostand. Geoanalytical Res. 44, 331–348. https://doi.org/10.1111/ggr.12308

Brisset, E., Guiter, F., Miramont, C., Troussier, T., Sabatier, P., Poher, Y., Cartier, R., Arnaud, F., Malet, E., Anthony, E.J., 2017. The overlooked human influence in historic and prehistoric floods in the European Alps. Geology 45, 347–350. https://doi.org/10.1130/G38498.1

Brisset, E., Miramont, C., Guiter, F., Anthony, E.J., Tachikawa, K., Poulenard, J., Arnaud, F., Delhon, C., Meunier, J.-D., Bard, E., 2013. Non-reversible geosystem destabilisation at 4200 cal. BP: Sedimentological, geochemical and botanical markers of soil erosion recorded in a Mediterranean alpine lake. The Holocene 23, 1863–1874. https://doi.org/10.1177/0959683613508158

Brown, R.J., Severin, K.P., 2009. Otolith chemistry analyses indicate that water Sr:Ca is the primary factor influencing otolith Sr:Ca for freshwater and diadromous fish but not for marine fish. Can. J. Fish. Aquat. Sci. 66, 1790–1808. https://doi.org/10.1139/F09-112

Bruel, R., Sabatier, P., 2020. serac: an R package for ShortlivEd RAdionuclide chronology of recent sediment cores. J. Environ. Radioact. 225, 106449. https://doi.org/10.1016/j.jenvrad.2020.106449

Bruel, R., Marchetto, A., Bernard, A., Lami, A., Sabatier, P., Frossard, V., Perga, M.-E., 2018. Seeking alternative stable states in a deep lake. Freshw. Biol. 63, 553–568. https://doi.org/10.1111/fwb.13093

Buffoli, G., 2014. Monte Guglielmo (Brescia): relazione tra le faglie e le vulcaniti triassiche del versante sud-occidentale.= Monte Guglielmo (Brescia): Relationship faults and Triassic volcanites of the south-western mountainside.

Büntgen, U., Myglan, V.S., Ljungqvist, F.C., McCormick, M., Di Cosmo, N., Sigl, M., Jungclaus, J., Wagner, S., Krusic, P.J., Esper, J., Kaplan, J.O., de Vaan, M.A.C., Luterbacher, J., Wacker, L., Tegel, W., Kirdyanov, A.V., 2016. Cooling and societal change during the Late Antique Little Ice Age from 536 to around 660 AD. Nat. Geosci. 9, 231–236. https://doi.org/10.1038/ngeo2652

Büntgen, U., Tegel, W., Nicolussi, K., McCormick, M., Frank, D., Trouet, V., Kaplan, J.O., Herzig, F., Heussner, K.-U., Wanner, H., Luterbacher, J., Esper, J., 2011. 2500 Years of European Climate Variability and Human Susceptibility. Science 331, 578–582. https://doi.org/10.1126/science.1197175

Butz, C., Grosjean, M., Goslar, T., Tylmann, W., 2017. Hyperspectral imaging of sedimentary bacterial pigments: a 1700-year history of meromixis from varved Lake Jaczno, northeast Poland. J. Paleolimnol. 58, 57–72. https://doi.org/10.1007/s10933-017-9955-1

Butz, C., Grosjean, M., Fischer, D., Wunderle, S., Tylmann, W., Rein, B., 2015. Hyperspectral imaging spectroscopy: a promising method for the biogeochemical analysis of lake sediments. J. Appl. Remote Sens. 9, 096031. https://doi.org/10.1117/1.JRS.9.096031

Caro, G., Bourdon, B., Birck, J.-L., Moorbath, S., 2006. High-precision 142Nd/144Nd measurements in terrestrial rocks: Constraints on the early differentiation of the Earth's mantle. Geochim. Cosmochim. Acta 70, 164–191. https://doi.org/10.1016/j.gca.2005.08.015

Carrer, F., 2015. Herding Strategies, Dairy Economy and Seasonal Sites in the Southern Alps: J. Mediterr. Archaeol. 28, 3–22. https://doi.org/10.1558/jmea.v28i1.27499

Cascio, E.L., Malanima, P., 2005. Cycles and Stability. Italian Population before the Demographic Transition (225 B.C. - A.D. 1900). Riv. Storia Econ. https://doi.org/10.1410/20933

Casini, S., De Marinis, R., 2009. Des pierres et des dieux. L'art rupestre de la Valteline et du Valcamonica. Globe Rev. Genevoise Géographie 149, 61–92. https://doi.org/10.3406/globe.2009.1556

Chapron, E., Simonneau, A., Ledoux, G., Arnaud, F., Lajeunesse, P., Albéric, P., 2016. French Alpine Foreland Holocene Paleoseismicity Revealed by Coeval Mass Wasting Deposits in Glacial Lakes, in: Submarine Mass Movements and Their Consequences. Springer, pp. 341–349. https://doi.org/10.1007/978-3-319-20979-1_34

Chapron, E., Arnaud, F., Noël, H., Revel, M., Desmet, M., Perdereau, L., 2005. Rhone River flood deposits in Lake Le Bourget: a proxy for Holocene environmental changes in the NW Alps, France. Boreas 34, 404–416. https://doi.org/10.1080/03009480500231260

Chapron, E., Desmet, M., De Putter, T., Loutre, M.F., Beck, C., Deconinck, J.-F., 2002. Climatic variability in the northwestern Alps, France, as evidenced by 600 years of terrigenous sedimentation in Lake Le Bourget. The Holocene 12, 177–185. https://doi.org/10.1191/0959683602hl520rp

Chapron, E., Beck, C., Pourchet, M., Deconinck, J.-F., 1999. 1822 earthquake-triggered homogenite in Lake Le Bourget (NW Alps). Terra Nova 11, 86–92. https://doi.org/10.1046/j.1365-3121.1999.00230.x

Chapron, E., 1999. Contrôles climatique et sismo-tectonique de la sédimentation lacustre dans l'Avant-Pays Alpin (lac du Bourget, Léman) durant le Quaternaire récent. Laboratoire de géologie de l'Université Joseph Fourier. http://www.theses.fr/1999LIL10005

Chardon, M., 1987. Bravard J.P. — Le Rhône du Léman à Lyon. Rev. Géographie Alp. 75, 89–91.

Chiesa, S., MICHELI, P., CARIBONI, M., TOGNINI, P., MOTTA, L., LONGHIN, M., ZAMBROTTI, P., MARCATO, E., FERRARIO, A., 2011. Note illustrative della Carta Geologica d'Italia alla scala 1: 50.000, Foglio 41 Ponte di Legno. CARG ISPRA Ist. Super. Prot. E Ric. Ambient. Roma P 169.

Chorover, J., Kretzschmar, R., Garcia-Pichel, F., Sparks, D.L., 2007. Soil Biogeochemical Processes within the Critical Zone. Elements 3, 321–326. https://doi.org/10.2113/gselements.3.5.321

Clift, P.D., 2006. Controls on the erosion of Cenozoic Asia and the flux of clastic sediment to the ocean. Earth Planet. Sci. Lett. 241, 571–580. https://doi.org/10.1016/j.epsl.2005.11.028

Cogez, A., Meynadier, L., Allègre, C., Limmois, D., Herman, F., Gaillardet, J., 2015. Constraints on the role of tectonic and climate on erosion revealed by two time series analysis of marine cores around New Zealand. Earth Planet. Sci. Lett. 410, 174–185. https://doi.org/10.1016/j.epsl.2014.11.029

Colin, C., Turpin, L., Bertaux, J., Desprairies, A., Kissel, C., 1999. Erosional history of the Himalayan and Burman ranges during the last two glacial–interglacial cycles. Earth Planet. Sci. Lett. 171, 647–660. https://doi.org/10.1016/S0012-821X(99)00184-3

Collins, A.L., Pulley, S., Foster, I.D.L., Gellis, A., Porto, P., Horowitz, A.J., 2017. Sediment source fingerprinting as an aid to catchment management: A review of the current state of knowledge and a methodological decision-tree for end-users. J. Environ. Manage., Sediment source fingerprinting for informing catchment management: methodological approaches, problems and uncertainty 194, 86–108. https://doi.org/10.1016/j.jenvman.2016.09.075

Collins, A.L., Walling, D.E., 2002. Selecting fingerprint properties for discriminating potential suspended sediment sources in river basins. J. Hydrol. 261, 218–244. https://doi.org/10.1016/S0022-1694(02)00011-2

Comiti, F., 2012. How natural are Alpine mountain rivers? Evidence from the Italian Alps. Earth Surf. Process. Landf. 37, 693–707. https://doi.org/10.1002/esp.2267

Condina, F.A., 1986. Carta archeologica della media e bassa Val Camonica: F. 34-Breno. Ed." Quaderni Camuni".

Conley, D.J., 1988. Biogenic silica as an estimate of siliceous microfossil abundance in Great Lakes sediments. Biogeochemistry 6, 161–179. https://doi.org/10.1007/BF02182994

Corella, J.P., Benito, G., Wilhelm, B., Montoya, E., Rull, V., Vegas-Vilarrúbia, T., Valero-Garcés, B.L., 2019. A millennium-long perspective of flood-related seasonal sediment yield in Mediterranean watersheds. Glob. Planet. Change 177, 127–140. https://doi.org/10.1016/j.gloplacha.2019.03.016

Cosandey, C., Andréassian, V., Martin, C., Didon-Lescot, J.-F., Lavabre, J., Folton, N., Mathys, N., Richard, D., 2005. The hydrological impact of the Mediterranean forest: a review of French research. J. Hydrol. 301, 235–249. https://doi.org/10.1016/j.jhydrol.2004.06.040

Croke, J., 2004. HYDROLOGY | Soil Erosion Control, in: Burley, J. (Ed.), Encyclopedia of Forest Sciences. Elsevier, Oxford, pp. 387–397. https://doi.org/10.1016/B0-12-145160-7/00270-2

Crutzen, P.J., 2006. The "Anthropocene," in: Ehlers, E., Krafft, T. (Eds.), Earth System Science in the Anthropocene. Springer, Berlin, Heidelberg, pp. 13–18. https://doi.org/10.1007/3-540-26590-2_3

Crutzen, P.J., 2002. Geology of mankind. Nature 415, 23–23. https://doi.org/10.1038/415023a

Cuven, S., Francus, P., Lamoureux, S., 2011. Mid to Late Holocene hydroclimatic and geochemical records from the varved sediments of East Lake, Cape Bounty, Canadian High Arctic. Quat. Sci. Rev. 30, 2651–2665. https://doi.org/10.1016/j.quascirev.2011.05.019

Cuven, S., Francus, P., Lamoureux, S.F., 2010. Estimation of grain size variability with micro X-ray fluorescence in laminated lacustrine sediments, Cape Bounty, Canadian High Arctic. J. Paleolimnol. 44, 803–817. https://doi.org/10.1007/s10933-010-9453-1

Czymzik, M., Brauer, A., Dulski, P., Plessen, B., Naumann, R., von Grafenstein, U., Scheffler, R., 2013. Orbital and solar forcing of shifts in Mid-to Late Holocene flood intensity from varved sediments of pre-alpine Lake Ammersee (southern Germany). Quat. Sci. Rev. 61, 96–110. https://doi.org/10.1016/j.quascirev.2012.11.010

Dal Piaz, G.V., Bistacchi, A., Massironi, M., 2003. Geological outline of the Alps. Episodes 26, 175–180. https://doi.org/10.18814/epiiugs/2003/v26i3/004

Dapples, F., Lotter, A.F., van Leeuwen, J.F., van der Knaap, W.O., Dimitriadis, S., Oswald, D., 2002. Paleolimnological evidence for increased landslide activity due to forest clearing and land-use since 3600 cal BP in the western Swiss Alps. J. Paleolimnol. 27, 239–248. https://doi.org/10.1023/A:1014215501407

Dasch, E.J., 1969. Strontium isotopes in weathering profiles, deep-sea sediments, and sedimentary rocks. Geochim. Cosmochim. Acta 33, 1521–1552. https://doi.org/10.1016/0016-7037(69)90153-7

David, F., 2010. An example of the consequences of human activities on the evolution of subalpine landscapes. Comptes Rendus Palevol 9, 229–235. https://doi.org/10.1016/j.crpv.2010.06.002

Davies, S.J., Lamb, H.F., Roberts, S.J., 2015. Micro-XRF core scanning in palaeolimnology: recent developments, in: Micro-XRF Studies of Sediment Cores. Springer, pp. 189–226. https://doi.org/10.1007/978-94-017-9849-5_7

Davison, W., 1993. Iron and manganese in lakes. Earth-Sci. Rev. 34, 119–163. https://doi.org/10.1016/0012-8252(93)90029-7

Dearing, J.A., Acma, B., Bub, S., Chambers, F.M., Chen, X., Cooper, J., Crook, D., Dong, X.H., Dotterweich, M., Edwards, M.E., 2015. Social-ecological systems in the Anthropocene: The need for integrating social and biophysical records at regional scales. Anthr. Rev. 2, 220–246. https://doi.org/10.1177/2053019615579128

Dearing, J.A., 1991. Lake sediment records of erosional processes, in: Smith, J.P., Appleby, P.G., Battarbee, R.W., Dearing, J.A., Flower, R., Haworth, E.Y., Oldfield, F., O'Sullivan, P.E. (Eds.), Environmental History and Palaeolimnology, Developments in Hydrobiology. Springer Netherlands, Dordrecht, pp. 99–106. https://doi.org/10.1007/978-94-011-3592-4_13

Debret, M., Chapron, E., Desmet, M., Rolland-Revel, M., Magand, O., Trentesaux, A., Bout-Roumazeille, V., Nomade, J., Arnaud, F., 2010. North western Alps Holocene paleohydrology recorded by flooding activity in Lake Le Bourget, France. Quat. Sci. Rev. 29, 2185–2200. https://doi.org/10.1016/j.quascirev.2010.05.016

Debret, M., 2008. Caractérisation de la variabilité climatique Holocène à partir de séries continentales, marines et glaciaires (phdthesis). Université Joseph-Fourier - Grenoble I. https://tel.archives-ouvertes.fr/tel-00535769

Disnar, J.-R., Jacob, J., Morched-Issa, M., Lottier, N., Arnaud, F., 2008. Assessment of peat quality by molecular and bulk geochemical analysis: Application to the Holocene record of the Chautagne marsh (Haute Savoie, France). Chem. Geol. 254, 101–112. https://doi.org/10.1016/j.chemgeo.2008.06.004

DISS Working Group, 2018. Database of Individual Seismogenic Sources (DISS), version 3.2.1. https://doi.org/10.6092/INGV.IT-DISS3.2.1

Dotterweich, M., Stankoviansky, M., Minár, J., Koco, Š., Papčo, P., 2013. Human induced soil erosion and gully system development in the Late Holocene and future perspectives on landscape evolution: The Myjava Hill Land, Slovakia. Geomorphology 201, 227–245. https://doi.org/10.1016/j.geomorph.2013.06.023

Doyen, É., Vannière, B., Berger, J.-F., Arnaud, F., Tachikawa, K., Bard, E., 2013. Land-use changes and environmental dynamics in the upper Rhone valley since Neolithic times inferred from sediments in Lac Moras. The Holocene 23, 961–973. https://doi.org/10.1177/0959683612475142

Edwards, K.J., Whittington, G., 2001. Lake sediments, erosion and landscape change during the Holocene in Britain and Ireland. CATENA, Landscape sensitivity: principles and applications in Northern 42, 143–173. https://doi.org/10.1016/S0341-8162(00)00136-3

Elbaz-Poulichet, F., Sabatier, P., Dezileau, L., Freydier, R., 2014. Sedimentary record of V, U, Mo and Mn in the Pierre-Blanche lagoon (Southern France)–Evidence for a major anoxia event during the Roman period. The Holocene 24, 1384–1392. https://doi.org/10.1177/0959683614540957

Evin, G., Wilhelm, B., Jenny, J.-P., 2019. Flood hazard assessment of the Rhône River revisited with reconstructed discharges from lake sediments. Glob. Planet. Change 172, 114–123. https://doi.org/10.1016/j.gloplacha.2018.09.010

Evrard, O., Chaboche, P.-A., Ramon, R., Foucher, A., Laceby, J.P., 2020. A global review of sediment source fingerprinting research incorporating fallout radiocesium (137Cs). Geomorphology 362, 107103. https://doi.org/10.1016/j.geomorph.2020.107103

Fanetti, D., Anselmetti, F.S., Chapron, E., Sturm, M., Vezzoli, L., 2008. Megaturbidite deposits in the Holocene basin fill of Lake Como (southern Alps, Italy). Palaeogeogr. Palaeoclimatol. Palaeoecol. 259, 323–340. https://doi.org/10.1016/j.palaeo.2007.10.014

FAO, I., 2015. Status of the world's soil resources (SWSR)–main report. Food Agric. Organ. U. N. Intergov. Tech. Panel Soils Rome Italy 650. http://www.fao.org/3/a-i5199e.pdf

Faure, G., Assereto, R., Tremba, E.L., 1978. Strontium isotope composition of marine carbonates of Middle Triassic to Early Jurassic age, Lombardic Alps, Italy*. Sedimentology 25, 523–543. https://doi.org/10.1111/j.1365-3091.1978.tb02078.x

Faure, G., Crocket, J.H., Hueley, P.M., 1967. Some aspects of the geochemistry of strontium and calcium in the Hudson Bay and the Great Lakes. Geochim. Cosmochim. Acta 31, 451–461. https://doi.org/10.1016/0016-7037(67)90053-1

Federico, G., Malanima, P., 2004. Progress, decline, growth: product and productivity in Italian agriculture, 1000–2000. Econ. Hist. Rev. 57, 437–464. https://doi.org/10.1111/j.1468-0289.2004.00284.x

Feng, J.-L., Zhu, L.-P., Zhen, X.-L., Hu, Z.-G., 2009. Grain size effect on Sr and Nd isotopic compositions in eolian dust: implications for tracing dust provenance and Nd model age. Geochem. J. 43, 123–131. https://doi.org/10.2343/geochemj.1.0007

Foucher, A., Salvador-Blanes, S., Evrard, O., Simonneau, A., Chapron, E., Courp, T., Cerdan, O., Lefèvre, I., Adriaensen, H., Lecompte, F., Desmet, M., 2014. Increase in soil erosion after agricultural intensification: Evidence from a lowland basin in France. Anthropocene 7, 30–41. https://doi.org/10.1016/j.ancene.2015.02.001

Fouinat, L., Sabatier, P., David, F., Montet, X., Schoeneich, P., Chaumillon, E., Poulenard, J., Arnaud, F., 2018. Wet avalanches: long-term evolution in the Western Alps under climate and human forcing. Clim. Past 14. https://doi.org/10.5194/cp-14-1299-2018

Fouinat, L., Sabatier, P., Poulenard, J., Etienne, D., Crouzet, C., Develle, A.-L., Doyen, E., Malet, E., Reyss, J.-L., Sagot, C., Bonet, R., Arnaud, F., 2017. One thousand seven hundred years of interaction between glacial activity and flood frequency in proglacial Lake Muzelle (western French Alps). Quat. Res. 87, 407–422. https://doi.org/10.1017/qua.2017.18

Francke, A., Dosseto, A., Panagiotopoulos, K., Leicher, N., Lacey, J.H., Kyrikou, S., Wagner, B., Zanchetta, G., Kouli, K., Leng, M.J., 2019. Sediment residence time reveals Holocene shift from climatic to vegetation control on catchment erosion in the Balkans. Glob. Planet. Change 177, 186–200. https://doi.org/10.1016/j.gloplacha.2019.04.005

Frank, M., 2002. Radiogenic Isotopes: Tracers of Past Ocean Circulation and Erosional Input. Rev. Geophys. 40, 1-1-1–38. https://doi.org/10.1029/2000RG000094

Frayn, J.M., 1984. Sheep-rearing and the wool trade in Italy during the Roman period. F. Cairns.

Fuchs, M., 2007. An assessment of human versus climatic impacts on Holocene soil erosion in NE Peloponnese, Greece. Quat. Res., Reconstructing past environments from remnants of human occupation and sedimentary archives in western Eurasia 67, 349–356. https://doi.org/10.1016/j.yqres.2006.11.008

Gaillardet, J., Braud, I., Hankard, F., Anquetin, S., Bour, O., Dorfliger, N., Dreuzy, J.R. de, Galle, S., Galy, C., Gogo, S., Gourcy, L., Habets, F., Laggoun, F., Longuevergne, L., Borgne, T.L., Naaim-Bouvet, F., Nord, G., Simonneaux, V., Six, D., Tallec, T., Valentin, C., Abril, G., Allemand, P., Arènes, A., Arfib, B., Arnaud, L., Arnaud, N., Arnaud, P., Audry, S., Comte, V.B., Batiot, C., Battais, A., Bellot, H., Bernard, E., Bertrand, C., Bessière, H., Binet, S., Bodin, J., Bodin, X., Boithias, L., Bouchez, J., Boudevillain, B., Moussa, I.B., Branger, F., Braun, J.J., Brunet, P., Caceres, B., Calmels, D., Cappelaere, B., Celle-Jeanton, H., Chabaux, F., Chalikakis, K., Champollion, C., Copard, Y., Cotel, C., Davy, P., Deline, P., Delrieu, G., Demarty, J., Dessert, C., Dumont, M., Emblanch, C., Ezzahar, J., Estèves, M., Favier, V., Faucheux, M., Filizola, N., Flammarion, P., Floury, P., Fovet, O., Fournier, M., Francez, A.J., Gandois, L., Gascuel, C., Gayer, E., Genthon, C., Gérard, M.F., Gilbert, D., Gouttevin, I., Grippa, M., Gruau, G., Jardani, A., Jeanneau, L., Join, J.L., Jourde, H., Karbou, F., Labat, D., Lagadeuc, Y., Lajeunesse, E., Lastennet, R., Lavado, W., Lawin, E., Lebel, T., Bouteiller, C.L., Legout, C., Lejeune, Y., Meur, E.L., Moigne, N.L., Lions, J., Lucas, A., Malet, J.P., Marais-Sicre, C., Maréchal, J.C., Marlin, C., Martin, P., Martins, J., Martinez, J.M., Massei, N., Mauclerc, A., Mazzilli, N., Molénat, J., Moreira-Turcq, P., Mougin, E., Morin, S., Ngoupayou, J.N., Panthou, G., Peugeot, C., Picard, G., Pierret, M.C., Porel, G., Probst, A., Probst, J.L., Rabatel, A., Raclot, D., Ravanel, L., Rejiba, F., René, P., Ribolzi, O., Riotte, J., Rivière, A., Robain, H., Ruiz, L., Sanchez-Perez, J.M., Santini, W., Sauvage, S., Schoeneich, P., Seidel, J.L., Sekhar, M., Sengtaheuanghoung, O., Silvera, N., Steinmann, M., Soruco, A., Tallec, G., Thibert, E., Lao, D.V., Vincent, C.,

Viville, D., Wagnon, P., Zitouna, R., 2018. OZCAR: The French Network of Critical Zone Observatories. Vadose Zone J. 17, 180067. https://doi.org/10.2136/vzj2018.04.0067

Galadini, F., Galli, P., Molin, D., Ciurletti, G., 2001. Searching for the source of the 1117 earthquake in northern Italy: a multidisciplinary approach, in: The Use of Historical Data in Natural Hazard Assessments. Springer, pp. 3–27. https://doi.org/10.1007/978-94-017-3490-5_1

Gardent, M., Rabatel, A., Dedieu, J.-P., Deline, P., 2014. Multitemporal glacier inventory of the French Alps from the late 1960s to the late 2000s. Glob. Planet. Change 120, 24–37. https://doi.org/10.1016/j.gloplacha.2014.05.004

Gardent, M., 2014. Inventaire et retrait des glaciers dans les alpes françaises depuis la fin du Petit Age Glaciaire (PhD Thesis). Grenoble. http://www.theses.fr/2014GRENA008

Garibaldi, L., Anzani, A., Marieni, A., Leoni, B., Mosello, R., 2003. Studies on the phytoplankton of the deep subalpine Lake Iseo. J. Limnol. 62, 177–189. https://doi.org/10.4081/jlimnol.2003.177

Garibaldi, Letizia, Mezzanotte, V., Brizzio, M.C., Rogora, M., Mosello, R., 1999. The trophic evolution of Lake Iseo as related to its holomixis. Journal of Limnology. 58, 10–19. https://doi.org/10.4081/jlimnol.1999.10

Gasperini, P., Camassi, R., Mirto, C., Stucchi, M., 2004. Catalogo Parametrico dei Terremoti Italiani, versione CPTI04. Istituto Nazionale di Geofisica e Vulcanologia (INGV). https://doi.org/10.6092/INGV.IT-CPTI04

Gastineau, R., Sigoyer, J. de, Sabatier, P., Fabbri, S.C., Anselmetti, F.S., Develle, A.L., Şahin, M., Gündüz, S., Niessen, F., Gebhardt, A.C., 2021. Active Subaquatic Fault Segments in Lake Iznik Along the Middle Strand of the North Anatolian Fault, NW Turkey. Tectonics 40, e2020TC006404. https://doi.org/10.1029/2020TC006404

Gathorne-Hardy, F.J., Erlendsson, E., Langdon, P.G., Edwards, K.J., 2009. Lake sediment evidence for late Holocene climate change and landscape erosion in western Iceland. J. Paleolimnol. 42, 413–426. https://doi.org/10.1007/s10933-008-9285-4

Gaume, E., Bain, V., Bernardara, P., Newinger, O., Barbuc, M., Bateman, A., Blaškovičová, L., Blöschl, G., Borga, M., Dumitrescu, A., Daliakopoulos, I., Garcia, J., Irimescu, A., Kohnova, S., Koutroulis, A., Marchi, L., Matreata, S., Medina, V., Preciso, E., Sempere-Torres, D., Stancalie, G., Szolgay, J., Tsanis, I., Velasco, D., Viglione, A., 2009. A compilation of data on European flash floods. J. Hydrol. 367, 70–78. https://doi.org/10.1016/j.jhydrol.2008.12.028

Gauthier, É., Richard, H., 2008. L'anthropisation du Massif jurassien : bilan des données palynologiques. Collect. EDYTEM Cah. Géographie 6, 273–280. https://doi.org/10.3406/edyte.2008.1045

Gauthier, É., 2002. Evolution des activités agropastorales du Haut Jura (France) au cours des trois derniers millénaires. Quaternaire 13, 137–147. https://doi.org/10.3406/quate.2002.2187

Gayer, E., Michon, L., Louvat, P., Gaillardet, J., 2019. Storm-induced precipitation variability control of long-term erosion. Earth Planet. Sci. Lett. 517, 61–70. https://doi.org/10.1016/j.epsl.2019.04.003

Gehrig, R., 1997. Pollenanalytische Untersuchungen zur Vegetations-und-Klimageschichte des Val Camonica (Norditalien).

Ghosal, K., Das Bhattacharya, S., 2020. A Review of RUSLE Model. J. Indian Soc. Remote Sens. 48, 689–707. https://doi.org/10.1007/s12524-019-01097-0

Giardini, D., Woessner, J., Danciu, L., Crowley, H., Cotton, F., Grünthal, G., Pinho, R., Valensise, G., Akkar, S., Arvidsson, R., 2013. Seismic hazard harmonization in Europe (SHARE): online data resource. Swiss Seism Serv ETH Zurich Zurich Switz. http://www.share-eu.org/

Gidon, M., 1977. Carte géologique simplifiée des Alpes occidentales du Léman à Digne. Didier-Richard.

Giguet-Covex, C. harline, Bajard, M., Chen, W., Walsh, K., Rey, P.-J., Messager, E., Etienne, D., Sabatier, P., Ficetola, G.F., Gielly, L., Blanchet, C., Guffond, C., Arnaud, F., Poulenard, J., 2021. Mountain agro-ecosystems long-term trajectories in the North Western Alps.

Giguet-Covex, C., Arnaud, F., Enters, D., Poulenard, J., Millet, L., Francus, P., David, F., Rey, P.-J., Wilhelm, B., Delannoy, J.-J., 2012. Frequency and intensity of high-altitude floods over the last 3.5 ka in northwestern French Alps (Lake Anterne). Quat. Res. 77, 12–22. https://doi.org/10.1016/j.yqres.2011.11.003

Giguet-Covex, C., Arnaud, F., Poulenard, J., Disnar, J.-R., Delhon, C., Francus, P., David, F., Enters, D., Rey, P.-J., Delannoy, J.-J., 2011. Changes in erosion patterns during the Holocene in a currently treeless subalpine catchment inferred from lake sediment geochemistry (Lake Anterne, 2063 m asl, NW French Alps): the role of climate and human activities. The Holocene. 21(4):651-665. https://doi.org/10.1177/0959683610391320

Giguet-Covex, C., Arnaud, F., Poulenard, J., Enters, D., Reyss, J.-L., Millet, L., Lazzaroto, J., Vidal, O., 2010. Sedimentological and geochemical records of past trophic state and hypolimnetic anoxia in large, hard-water Lake Bourget, French Alps. J. Paleolimnol. 43, 171–190. https://doi.org/10.1007/s10933-009-9324-9

Gilli, A., Anselmetti, F.S., Glur, L., Wirth, S.B., 2013. Lake sediments as archives of recurrence rates and intensities of past flood events, in: Dating Torrential Processes on Fans and Cones. Advances in Global Change Research, vol 47. Springer, pp. 225–242. https://doi.org/10.1007/978-94-007-4336-6_15

Giorgi, F., Torma, C., Coppola, E., Ban, N., Schär, C., Somot, S., 2016. Enhanced summer convective rainfall at Alpine high elevations in response to climate warming. Nat. Geosci. 9, 584-589. https://doi.org/10.1038/ngeo2761

Giosan, L., Ponton, C., Usman, M., Blusztajn, J., Fuller, D.Q., Galy, V., Haghipour, N., Johnson, J.E., McIntyre, C., Wacker, L., Eglinton, T.I., 2017. Short communication: Massive erosion in monsoonal central India linked to late Holocene land cover degradation. Earth Surf. Dyn. 5, 781–789. https://doi.org/10.5194/esurf-5-781-2017

Glover, T.J., 1997. Pocket Ref, 2nd ed. Sequoia, Littleton, Colo.

Glur, L., Stalder, N.F., Wirth, S.B., Gilli, A., Anselmetti, F.S., 2015. Alpine lacustrine varved record reveals summer temperature as main control of glacier fluctuations over the past 2250 years. The Holocene 25, 280–287. https://doi.org/10.1177/0959683614557572

Glur, L., Wirth, S.B., Büntgen, U., Gilli, A., Haug, G.H., Schär, C., Beer, J., Anselmetti, F.S., 2013. Frequent floods in the European Alps coincide with cooler periods of the past 2500 years. Sci. Rep. 3, 2770. https://doi.org/10.1038/srep02770

Gobet, E., Tinner, W., Hubschmid, P., Jansen, I., Wehrli, M., Ammann, B., Wick, L., 2000. Influence of human impact and bedrock differences on the vegetational history of the

Insubrian Southern Alps. Veg. Hist. Archaeobotany 9, 175–187. https://doi.org/10.1007/BF01299802

Goldstein, S.L., Hemming, S.R., 2003. Long-lived isotopic tracers in oceanography, paleoceanography, and ice-sheet dynamics. Treatise Geochem. 6, 453–489. https://doi.org/10.1016/B0-08-043751-6/06179-X

Gosso, G., Spalla, M., G.B, S., Berra, F., Bini, A., F, F., 2012. Note illustrative della Carta Geologica d'Italia alla scala 1:50.000. Foglio 057 - Malonno, I.S.P.R.A.

Granger, D.E., Riebe, C.S., 2014. 7.12 - Cosmogenic Nuclides in Weathering and Erosion, in: Holland, H.D., Turekian, K.K. (Eds.), Treatise on Geochemistry (Second Edition). Elsevier, Oxford, pp. 401–436. https://doi.org/10.1016/B978-0-08-095975-7.00514-3

Granger, D.E., Schaller, M., 2014. Cosmogenic Nuclides and Erosion at the Watershed Scale. Elements 10, 369–373. https://doi.org/10.2113/gselements.10.5.369

Gregorini, G., Tacchini, G., Pennachio, M., Predali, R., 2012. L'economia bresciana di fronte all'Unità d'Italia. Il lanificio sebino. roberto predali.

Groleau, A., Sarazin, G., Vinçon-Leite, B., Tassin, B., Quiblier-Llobéras, C., 2000. Tracing calcite precipitation with specific conductance in a hard water alpine lake (Lake Bourget). Water Res. 34, 4151–4160. https://doi.org/10.1016/S0043-1354(00)00191-3

Groppelli, B., Soncini, A., Bocchiola, D., Rosso, R., 2011. Evaluation of future hydrological cycle under climate change scenarios in a mesoscale Alpine watershed of Italy. Nat. Hazards Earth Syst. Sci. 11, 1769–1785. https://doi.org/10.5194/nhess-11-1769-2011

Guidoboni, E., Comastri, A., Boschi, E., 2005. The "exceptional" earthquake of 3 January 1117 in the Verona area (northern Italy): A critical time review and detection of two lost earthquakes (lower Germany and Tuscany). J. Geophys. Res. Solid Earth 110. https://doi.org/10.1029/2005JB003683

Guzzetti, F., Tonelli, G., 2004. Information system on hydrological and geomorphological catastrophes in Italy (SICI): a tool for managing landslide and flood hazards. Nat. Hazards Earth Syst. Sci. 4, 213–232. https://doi.org/10.5194/nhess-4-213-2004

Haddadchi, A., Ryder, D.S., Evrard, O., Olley, J., 2013. Sediment fingerprinting in fluvial systems: review of tracers, sediment sources and mixing models. Int. J. Sediment Res. 28, 560–578. https://doi.org/10.1016/S1001-6279(14)60013-5

Hajj, F., Poszwa, A., Bouchez, J., Guérold, F., 2017. Radiogenic and "stable" strontium isotopes in provenance studies: A review and first results on archaeological wood from shipwrecks. J. Archaeol. Sci. 86, 24–49. https://doi.org/10.1016/j.jas.2017.09.005

Heiri, O., Lotter, A.F., Lemcke, G., 2001. Loss on ignition as a method for estimating organic and carbonate content in sediments: reproducibility and comparability of results. J. Paleolimnol. 25, 101–110. https://doi.org/10.1023/A:1008119611481

Hieke, W., 1984. A thick Holocene homogenite from the Ionian Abyssal Plain (eastern Mediterranean). Mar. Geol. 55, 63–78. https://doi.org/10.1016/0025-3227(84)90133-6

Hilton, R.G., West, A.J., 2020. Mountains, erosion and the carbon cycle. Nat. Rev. Earth Environ. 1, 284–299. https://doi.org/10.1038/s43017-020-0058-6

Hinderer, M., Kastowski, M., Kamelger, A., Bartolini, C., Schlunegger, F., 2013. River loads and modern denudation of the Alps — A review. Earth-Sci. Rev. 118, 11–44. https://doi.org/10.1016/j.earscirev.2013.01.001

Hirabayashi, Y., Mahendran, R., Koirala, S., Konoshima, L., Yamazaki, D., Watanabe, S., Kim, H., Kanae, S., 2013. Global flood risk under climate change. Nat. Clim. Change 3, 816. https://doi.org/10.1038/nclimate1911

Hogg, C.A., Marti, C.L., Huppert, H.E., Imberger, J., 2013. Mixing of an interflow into the ambient water of Lake Iseo. Limnol. Oceanogr. 58, 579–592. https://doi.org/10.4319/lo.2013.58.2.0579

Holeman, J.N., 1968. The sediment yield of major rivers of the world. Water Resour. Res. 4, 737–747. https://doi.org/10.1029/WR004i004p00737

Holzhauser, H., Magny, M., Zumbuühl, H.J., 2005. Glacier and lake-level variations in west-central Europe over the last 3500 years. The Holocene 15, 789–801. https://doi.org/10.1191/0959683605hl853ra

Howarth, J.D., Fitzsimons, S.J., Norris, R.J., Jacobsen, G.E., 2012. Lake sediments record cycles of sediment flux driven by large earthquakes on the Alpine fault, New Zealand. Geology 40, 1091–1094. https://doi.org/10.1130/G33486.1

Iglesias, V., Vannière, B., Jouffroy-Bapicot, I., 2019. Emergence and Evolution of Anthropogenic Landscapes in the Western Mediterranean and Adjacent Atlantic Regions. Fire 2, 53. https://doi.org/10.3390/fire2040053

IPCC, 2012. Managing the Risks of Extreme Events and Disasters to Advance Climate Change Adaptation.https://www.ipcc.ch/report/managing-the-risks-of-extreme-events-and-disasters-to-advance-climate-change-adaptation/

Isola, I., Zanchetta, G., Drysdale, R.N., Regattieri, E., Bini, M., Bajo, P., Hellstrom, J.C., Baneschi, I., Lionello, P., Woodhead, J., 2019. The 4.2 ka event in the central Mediterranean: new data from a Corchia speleothem (Apuan Alps, central Italy). Clim. Past 15, 135–151. https://doi.org/10.5194/cp-15-135-2019

Jacobsen, S.B., Wasserburg, G.J., 1980. Sm-Nd isotopic evolution of chondrites. Earth Planet. Sci. Lett. 50, 139–155. https://doi.org/10.1016/0012-821X(80)90125-9

Jacq, K., Martinez-Lamas, R., Van Exem, A., Debret, M., 2020a. Hyperspectral core-logger image acquisition. https://www.protocols.io/view/hyperspectral-core-logger-image-acquisition-bikckcsw.html

Jacq, K., Rapuc, W., Benoit, A., Coquin, D., Fanget, B., Perrette, Y., Sabatier, P., Wilhelm, B., Debret, M., Arnaud, F., 2021. Sedimentary structure discrimination with hyperspectral imaging in sediment cores. Sci. Total Environ. 152018. https://doi.org/10.1016/j.scitotenv.2021.152018

Jacq, K., Giguet-Covex, C., Sabatier, P., Perrette, Y., Fanget, B., Coquin, D., Debret, M., Arnaud, F., 2019a. High-resolution grain size distribution of sediment core with hyperspectral imaging. Sediment. Geol. 393–394, 105536. https://doi.org/10.1016/j.sedgeo.2019.105536

Jacq, K., Perrette, Y., Fanget, B., Sabatier, P., Coquin, D., Martinez-Lamas, R., Debret, M., Arnaud, F., 2019b. High-resolution prediction of organic matter concentration with hyperspectral imaging on a sediment core. Sci. Total Environ. 663, 236–244. https://doi.org/10.1016/j.scitotenv.2019.01.320

Jacquet, S., Briand, J.-F., Leboulanger, C., Avois-Jacquet, C., Oberhaus, L., Tassin, B., Vinçon-Leite, B., Paolini, G., Druart, J.-C., Anneville, O., Humbert, J.-F., 2005. The proliferation of the toxic cyanobacterium Planktothrix rubescens following restoration of the largest

natural French lake (Lac du Bourget). Harmful Algae 4, 651–672. https://doi.org/10.1016/j.hal.2003.12.006

Jenny, J.-P., Arnaud, F., Alric, B., Dorioz, J.-M., Sabatier, P., Meybeck, M., Perga, M.-E., 2014a. Inherited hypoxia: A new challenge for reoligotrophicated lakes under global warming. Glob. Biogeochem. Cycles 28, 1413–1423. https://doi.org/10.1002/2014GB004932

Jenny, J.-P., Wilhelm, B., Arnaud, F., Sabatier, P., Covex, C.G., Melo, A., Fanget, B., Malet, E., Ployon, E., Perga, M.E., 2014b. A 4D sedimentological approach to reconstructing the flood frequency and intensity of the Rhône River (Lake Bourget, NW European Alps). J. Paleolimnol. 51, 469–483. https://doi.org/10.1007/s10933-014-9768-4

Jenny, J.-P., Arnaud, F., Dorioz, J.-M., Covex, C.G., Frossard, V., Sabatier, P., Millet, L., Reyss, J.-L., Tachikawa, K., Bard, E., 2013. A spatiotemporal investigation of varved sediments highlights the dynamics of hypolimnetic hypoxia in a large hard-water lake over the last 150 years. Limnol. Oceanogr. 58, 1395–1408. https://doi.org/10.4319/lo.2013.58.4.1395

Jewell, A.M., Drake, N., Crocker, A.J., Bakker, N.L., Kunkelova, T., Bristow, C.S., Cooper, M.J., Milton, J.A., Breeze, P.S., Wilson, P.A., 2021. Three North African dust source areas and their geochemical fingerprint. Earth Planet. Sci. Lett. 554, 116645. https://doi.org/10.1016/j.epsl.2020.116645

Joannin, S., Magny, M., Peyron, O., Vannière, B., Galop, D., 2014. Climate and land-use change during the late Holocene at Lake Ledro (southern Alps, Italy). The Holocene 24, 591–602. https://doi.org/10.1177/0959683614522311

Joannin, S., Vannière, B., Galop, D., Peyron, O., Haas, J.N., Gilli, A., Chapron, E., Wirth, S.B., Anselmetti, F.S., Desmet, M., 2013. Climate and vegetation changes during the Lateglacial and early-middle Holocene at Lake Ledro (southern Alps, Italy). Clim. Past 9, 913–933. https://doi.org/10.5194/cp-9-913-2013

Joerin, U.E., Nicolussi, K., Fischer, A., Stocker, T.F., Schlüchter, C., 2008. Holocene optimum events inferred from subglacial sediments at Tschierva Glacier, Eastern Swiss Alps. Quat. Sci. Rev. 27, 337–350. https://doi.org/10.1016/j.quascirev.2007.10.016

Jonell, T.N., Li, Y., Blusztajn, J., Giosan, L., Clift, P.D., 2018. Signal or noise? Isolating grain size effects on Nd and Sr isotope variability in Indus delta sediment provenance. Chem. Geol. 485, 56–73. https://doi.org/10.1016/j.chemgeo.2018.03.036

Kagami, H., Ulmer, P., Hansmann, W., Dietrich, V., Steiger, R.H., 1991. Nd-Sr isotopic and geochemical characteristics of the southern Adamello (northern Italy) intrusives: Implications for crustal versus mantle origin. J. Geophys. Res. Solid Earth 96, 14331–14346. https://doi.org/10.1029/91JB01197

Kastens, K.A., Cita, M.B., 1981. Tsunami-induced sediment transport in the abyssal Mediterranean Sea. GSA Bull. 92, 845–857. https://doi.org/10.1130/0016-7606(1981)92<845:TSTITA>2.0.CO;2

Kemp, D.B., Sadler, P.M., Vanacker, V., 2020. The human impact on North American erosion, sediment transfer, and storage in a geologic context. Nat. Commun. 11, 6012. https://doi.org/10.1038/s41467-020-19744-3

Küchler-Krischun, J., Kleiner, J., 1990. Heterogeneously nucleated calcite precipitation in Lake Constance. A short time resolution study. Aquat. Sci. 52, 176–197. https://doi.org/10.1007/BF00902379

Kylander, M.E., Ampel, L., Wohlfarth, B., Veres, D., 2011. High-resolution X-ray fluorescence core scanning analysis of Les Echets (France) sedimentary sequence: new insights from chemical proxies. J. Quat. Sci. 26, 109–117. https://doi.org/10.1002/jqs.1438

Laceby, J.P., Evrard, O., Smith, H.G., Blake, W.H., Olley, J.M., Minella, J.P.G., Owens, P.N., 2017. The challenges and opportunities of addressing particle size effects in sediment source fingerprinting: A review. Earth-Sci. Rev. 169, 85–103. https://doi.org/10.1016/j.earscirev.2017.04.009

Laceby, J.P., McMahon, J., Evrard, O., Olley, J., 2015. A comparison of geological and statistical approaches to element selection for sediment fingerprinting. J. Soils Sediments 15, 2117–2131. https://doi.org/10.1007/s11368-015-1111-9

Lal, D., 1991. Cosmic ray labeling of erosion surfaces: in situ nuclide production rates and erosion models. Earth Planet. Sci. Lett. 104, 424–439. https://doi.org/10.1016/0012-821X(91)90220-C

Lampinen, H.M., Laukamp, C., Occhipinti, S.A., Hardy, L., 2019. Mineral footprints of the Paleoproterozoic sediment-hosted Abra Pb-Zn-Cu-Au deposit Capricorn Orogen, Western Australia. Ore Geol. Rev. 104, 436–461. https://doi.org/10.1016/j.oregeorev.2018.11.004

Lau, M.P., Valerio, G., Pilotti, M., Hupfer, M., 2020. Intermittent meromixis controls the trophic state of warming deep lakes. Sci. Rep. 10, 12928. https://doi.org/10.1038/s41598-020-69721-5

Lauterbach, S., Chapron, E., Brauer, A., Hüls, M., Gilli, A., Arnaud, F., Piccin, A., Nomade, J., Desmet, M., Von Grafenstein, U., 2012. A sedimentary record of Holocene surface runoff events and earthquake activity from Lake Iseo (Southern Alps, Italy). The Holocene 22, 749–760. https://doi.org/10.1177/0959683611430340

Le Gall, M., Evrard, O., Foucher, A., Laceby, J.P., Salvador-Blanes, S., Manière, L., Lefèvre, I., Cerdan, O., Ayrault, S., 2017. Investigating the temporal dynamics of suspended sediment during flood events with 7 Be and 210 Pb xs measurements in a drained lowland catchment. Sci. Rep. 7, 42099. https://doi.org/10.1038/srep42099

Le Roy, M., Nicolussi, K., Deline, P., Astrade, L., Edouard, J.-L., Miramont, C., Arnaud, F., 2015. Calendar-dated glacier variations in the western European Alps during the Neoglacial: the Mer de Glace record, Mont Blanc massif. Quat. Sci. Rev. 108, 1–22. https://doi.org/10.1016/j.quascirev.2014.10.033

Ledoux, G., Lajeunesse, P., Chapron, E., St-Onge, G., 2010. Multibeam Bathymetry Investigations of Mass Movements in Lake Le Bourget (NW Alps, France) Using a Portable Platform, in: Mosher, D.C., Shipp, R.C., Moscardelli, L., Chaytor, J.D., Baxter, C.D.P., Lee, H.J., Urgeles, R. (Eds.), Submarine Mass Movements and Their Consequences, Advances in Natural and Technological Hazards Research. Springer Netherlands, Dordrecht, pp. 423–434. https://doi.org/10.1007/978-90-481-3071-9_35

Livio, F.A., Berlusconi, A., Michetti, A.M., Sileo, G., Zerboni, A., Trombino, L., Cremaschi, M., Mueller, K., Vittori, E., Carcano, C., Rogledi, S., 2009. Active fault-related folding in the epicentral area of the December 25, 1222 (Io=IX MCS) Brescia earthquake (Northern Italy): Seismotectonic implications. Tectonophysics, Ten years after the Umbria-Marche earthquake, Central Italy 476, 320–335. https://doi.org/10.1016/j.tecto.2009.03.019

Luino, F., Belloni, A., Padovan, N., Bassi, M., Bossuto, P., Fassi, P., 2002. Historical and geomorphological analysis as a research tool for the identification of flood-prone zones and its role in the revision of town planning: the Oglio basin (Valcamonica–Northern Italy),

in: 9th Congress of the International Association for Engineering Geology and the Environment, Edited by: Van Rooy, JL and Jermy, CA, Durban (South Africa). pp. 16–20.

MacDonald, G.M., Beukens, R.P., Kieser, W.E., 1991. Radiocarbon Dating of Limnic Sediments: A Comparative Analysis and Discussion. Ecology 72, 1150–1155. https://doi.org/10.2307/1940612

Magny, M., Combourieu-Nebout, N., De Beaulieu, J.L., Bout-Roumazeilles, V., Colombaroli, D., Desprat, S., Francke, A., Joannin, S., Ortu, E., Peyron, O., 2013. North-south palaeohydrological contrasts in the central Mediterranean during the Holocene: tentative synthesis and working hypotheses. Clim. Past 9, 2043–2071. https://doi.org/10.5194/cp-9-2043-2013

Magny, M., Joannin, S., Galop, D., Vannière, B., Haas, J.N., Bassetti, M., Bellintani, P., Scandolari, R., Desmet, M., 2012. Holocene palaeohydrological changes in the northern Mediterranean borderlands as reflected by the lake-level record of Lake Ledro, northeastern Italy. Quat. Res. 77, 382–396. https://doi.org/10.1016/j.yqres.2012.01.005

Magny, M., Galop, D., Bellintani, P., Desmet, M., Didier, J., Haas, J.N., Martinelli, N., Pedrotti, A., Scandolari, R., Stock, A., 2009. Late-Holocene climatic variability south of the Alps as recorded by lake-level fluctuations at Lake Ledro, Trentino, Italy. The Holocene 19, 575–589. https://doi.org/10.1177/0959683609104032

Magny, M., Bégeot, C., Guiot, J., Peyron, O., 2003. Contrasting patterns of hydrological changes in Europe in response to Holocene climate cooling phases. Quat. Sci. Rev. 22, 1589–1596. https://doi.org/10.1016/S0277-3791(03)00131-8

Manalt, F., Beck, C., Disnar, J.-R., Deconinck, J.-F., Recourt, P., 2001. Evolution of clay mineral assemblages and organic matter in the late glacial-Holocene sedimentary infill of Lake Annecy, (northwestern Alps): paleoenvironmental implications. J. Paleolimnol. 25, 179–192. https://doi.org/10.1023/A:1008140114714

Mann, M.E., Zhang, Z., Rutherford, S., Bradley, R.S., Hughes, M.K., Shindell, D., Ammann, C., Faluvegi, G., Ni, F., 2009. Global Signatures and Dynamical Origins of the Little Ice Age and Medieval Climate Anomaly. Science 326, 1256–1260. https://doi.org/10.1126/science.1177303

Marziani, G., Citterio, S., 1999. The effects of human impact on the arboreal vegetation near ancient iron smelting sites in Val Gabbia, northern Italy. Veg. Hist. Archaeobotany 8, 225–229. https://doi.org/10.1007/BF02342722

McDermott, F., Frisia, S., Huang, Y., Longinelli, A., Spiro, B., Heaton, T.H.E., Hawkesworth, C.J., Borsato, A., Keppens, E., Fairchild, I.J., van der Borg, K., Verheyden, S., Selmo, E., 1999. Holocene climate variability in Europe: Evidence from δ18O, textural and extension-rate variations in three speleothems. Quat. Sci. Rev. 18, 1021–1038. https://doi.org/10.1016/S0277-3791(98)00107-3

Merz, B., Aerts, J., Arnbjerg-Nielsen, K., Baldi, M., Becker, A., Bichet, A., Blöschl, G., Bouwer, L.M., Brauer, A., Cioffi, F., 2014. Floods and climate: emerging perspectives for flood risk assessment and management. Nat. Hazards Earth Syst. Sci. NHESS 14, 1921–1942. https://doi.org/10.5194/nhess-14-1921-2014

Meyer, I., Davies, G.R., Stuut, J.-B.W., 2011. Grain size control on Sr-Nd isotope provenance studies and impact on paleoclimate reconstructions: An example from deep-sea sediments offshore NW Africa. Geochem. Geophys. Geosystems 12. https://doi.org/10.1029/2010GC003355

Millet, L., Giguet-Covex, C., Verneaux, V., Druart, J.-C., Adatte, T., Arnaud, F., 2010. Reconstruction of the recent history of a large deep prealpine lake (Lake Bourget, France) using subfossil chironomids, diatoms, and organic matter analysis: towards the definition of a lake-specific reference state. J. Paleolimnol. 44, 963–978. https://doi.org/10.1007/s10933-010-9467-8

Milliman, J.D., Meade, R.H., 1983. World-Wide Delivery of River Sediment to the Oceans. J. Geol. 91, 1–21. https://doi.org/10.1086/628741

Millward, A.A., Mersey, J.E., 1999. Adapting the RUSLE to model soil erosion potential in a mountainous tropical watershed. Catena 38, 109–129. https://doi.org/10.1016/S0341-8162(99)00067-3

Mittempergher, S., Zanchi, A., Zanchetta, S., Fumagalli, M., Gukov, K., Bistacchi, A., 2021. Fault reactivation and propagation in the northern Adamello pluton: The structure and kinematics of a kilometre-scale seismogenic source. Tectonophysics 806, 228790. https://doi.org/10.1016/j.tecto.2021.228790

Moernaut, J., Daele, M.V., Heirman, K., Fontijn, K., Strasser, M., Pino, M., Urrutia, R., De Batist, M., 2014. Lacustrine turbidites as a tool for quantitative earthquake reconstruction: New evidence for a variable rupture mode in south central Chile. J. Geophys. Res. Solid Earth 119, 1607–1633. https://doi.org/10.1002/2013JB010738

Molnar, P., 2004. Late Cenozoic increase in accumulation rates of terrestrial sediment: How might climate change have affected erosion rates? Annu Rev Earth Planet Sci 32, 67–89. https://doi.org/10.1146/annurev.earth.32.091003.143456

Mologni, C., Revel, M., Blanchet, C., Bosch, D., Develle, A.-L., Orange, F., Bastian, L., Khalidi, L., Ducassou, E., Migeon, S., 2020. Frequency of exceptional Nile flood events as an indicator of Holocene hydro-climatic changes in the Ethiopian Highlands. Quat. Sci. Rev. 247, 106543. https://doi.org/10.1016/j.quascirev.2020.106543

Montgomery, D., 2012. Dirt – The Erosion of Civilizations, 2 édition. ed. University of California Press, Berkeley.

Moreno, A., Valero-Garcés, B.L., González-Sampériz, P., Rico, M., 2008. Flood response to rainfall variability during the last 2000 years inferred from the Taravilla Lake record (Central Iberian Range, Spain). J. Paleolimnol. 40, 943–961. https://doi.org/ 10.1007/s10933-008-9209-3

Moretti, E., 1999. Social Networks and Migrations: Italy 1876–1913. Int. Migr. Rev. 33, 640–657. https://doi.org/10.1177/019791839903300304

Nakano, T., Yokoo, Y., Nishikawa, M., Koyanagi, H., 2004. Regional Sr–Nd isotopic ratios of soil minerals in northern China as Asian dust fingerprints. Atmos. Environ. 38, 3061–3067. https://doi.org/10.1016/j.atmosenv.2004.02.016

Nash, G., 2011. Replicating cultural landscapes: Interpreting rock-art in the Valcamonica, Lombardy, Italy. Landscapes 12, 1–19. https://doi.org/10.1179/lan.2012.12.2.1

Nash, G., Chippindale, C., 2002. European landscapes of rock-art. Psychology Press.

National Research Council, 2000. Basic Research Opportunities in Earth Science, National Academies Press, Washington, DC. ed. https://doi.org/10.17226/9981

Nearing, M.A., Jetten, V., Baffaut, C., Cerdan, O., Couturier, A., Hernandez, M., Le Bissonnais, Y., Nichols, M.H., Nunes, J.P., Renschler, C.S., Souchère, V., van Oost, K., 2005. Modeling response of soil erosion and runoff to changes in precipitation and cover.

CATENA, Soil Erosion under Climate Change: Rates, Implications and Feedbacks 61, 131–154. https://doi.org/10.1016/j.catena.2005.03.007

Nicoud, G., Monjuvent, G., Maillet-Guy, G., 1987. Contrôle du comblement quaternaire des vallées alpines du nord par la dynamique lacustre. 457–468.

Noren, A.J., Bierman, P.R., Steig, E.J., Lini, A., Southon, J., 2002. Millennial-scale storminess variability in the northeastern United States during the Holocene epoch. Nature 419, 821–824. https://doi.org/10.1038/nature01132

Norton, K.P., Blanckenburg, F. von, Kubik, P.W., 2010. Cosmogenic nuclide-derived rates of diffusive and episodic erosion in the glacially sculpted upper Rhone Valley, Swiss Alps. Earth Surf. Process. Landf. 35, 651–662. https://doi.org/10.1002/esp.1961

Pagani, M., Garcia-Pelaez, J., Gee, R., Johnson, K., Poggi, V., Styron, R., Weatherill, G., Simionato, M., Viganò, D., Danciu, L., 2018. Global Earthquake Model (GEM) Seismic Hazard Map (version 2018.1–December 2018). GEM-GLOBAL-SEISMIC-HAZARD-MAP-2018.1. https://www.globalquakemodel.org/gem

Page, M.J., Trustrum, N.A., 1997. A late Holocene lake sediment record of the erosion response to land use change in a steepland catchment, New Zealand. Z. Für Geomorphol. 369–392. https://doi.org/10.1127/zfg/41/1997/369

Paladin, A., Moghaddam, N., Stawinoga, A.E., Siebke, I., Depellegrin, V., Tecchiati, U., Lösch, S., Zink, A., 2020. Early medieval Italian Alps: reconstructing diet and mobility in the valleys. Archaeol. Anthropol. Sci. 12, 82. https://doi.org/10.1007/s12520-019-00982-6

Panagos, P., Borrelli, P., Meusburger, K., Alewell, C., Lugato, E., Montanarella, L., 2015a. Estimating the soil erosion cover-management factor at the European scale. Land Use Policy 48, 38–50. https://doi.org/10.1016/j.landusepol.2015.05.021

Panagos, P., Borrelli, P., Poesen, J., Ballabio, C., Lugato, E., Meusburger, K., Montanarella, L., Alewell, C., 2015b. The new assessment of soil loss by water erosion in Europe. Environ. Sci. Policy 54, 438–447. https://doi.org/10.1016/j.envsci.2015.08.012

Pena, L.D., Goldstein, S.L., 2014. Thermohaline circulation crisis and impacts during the mid-Pleistocene transition. Science 345, 318–322. https://doi.org/10.1126/science.1249770

Pilotti, M., Valerio, G., Giardino, C., Bresciani, M., Chapra, S.C., 2018. Evidence from field measurements and satellite imaging of impact of Earth rotation on Lake Iseo chemistry. J. Gt. Lakes Res. 44, 14–25. https://doi.org/10.1016/j.jglr.2017.10.005

Pilotti, M., Valerio, G., Leoni, B., 2013. Data set for hydrodynamic lake model calibration: A deep prealpine case. Water Resour. Res. 49, 7159–7163. https://doi.org/10.1002/wrcr.20506

Pini, R., Ravazzi, C., Aceti, A., Castellano, L., Perego, R., Quirino, T., Valle', F., 2016. Ecological changes and human interaction in Valcamonica, the rock art valley, since the last deglaciation. Alpine and Mediterranean Quaternary, 29 (1), 19 - 34.

Pini, R., 2002. A high-resolution Late-Glacial – Holocene pollen diagram from Pian di Gembro (Central Alps, Northern Italy). Veg. Hist. Archaeobotany 11, 251–262. https://doi.org/10.1007/s003340200038

Predali, R., 2013. I Ghitti di Bagnadore: Una famiglia, un paese. Marone tra 1500 e 1800. Roberto Predali.

Predali, R., 2010. La chiesa dei Santi Pietro e Paolo di Pregasso: storia, arte e tradizione. FdP Editore.

Predali, R., 2008. Marone tra 1500 e 1600: l'antica parrocchiale, FdP editore. ed. roberto predali.

Presbitero, M., Piccin, A., Cassinis, G., Perotti, C.R., Calabro', R.A., Vercesi, P.L., Falletti, P., Siletto, G.B., Jadoul, F., Bersezio, R., Schirolli, P., Ronchi, P., De Donatis, S., Bini, A., Corbari, D., Rigamonti, I., Besana, S., Dell'Orto, P., Gisolo, M., Cobianchi, N., Mancin, N., Ronchi, P., Cortesogno, L., Gaggero, L., Ivanova, D., Barbieri, P.M., Clerici, A., 2011. Foglio 099 : Iseo : Carta Geologica d'Italia alla scala 1:50000.

Racimo, F., Woodbridge, J., Fyfe, R.M., Sikora, M., Sjögren, K.-G., Kristiansen, K., Linden, M.V., 2020. The spatiotemporal spread of human migrations during the European Holocene. Proc. Natl. Acad. Sci. 117, 8989–9000. https://doi.org/10.1073/pnas.1920051117

Ramisch, F., Dittrich, M., Mattenberger, C., Wehrli, B., Wüest, A., 1999. Calcite dissolution in two deep eutrophic lakes. Geochim. Cosmochim. Acta 63, 3349–3356. https://doi.org/10.1016/S0016-7037(99)00256-2

Rapuc, W., Arnaud, F., Sabatier, P., Anselmetti, F.S., Piccin, A., Bastien, A., Augustin, L., Régnier, E., Gaillardet, J., Von, U., 2020a. 2000 years of event sedimentation in Lake Iseo (Italian Alps) under the influence of floods, earthquakes and human activities. Preprint 49. https://doi.org/10.1002/essoar.10504221.1

Rapuc, W., Jacq, K., Develle, A.-L., Sabatier, P., Fanget, B., Perrette, Y., Coquin, D., Debret, M., Wilhelm, B., Arnaud, F., 2020b. XRF and hyperspectral analyses as an automatic way to detect flood events in sediment cores. Sediment. Geol. 409, 105776. https://doi.org/10.1016/j.sedgeo.2020.105776

Rapuc, W., Sabatier, P., Arnaud, F., Palumbo, A., Develle, A.-L., Reyss, J.-L., Augustin, L., Régnier, E., Piccin, A., Chapron, E., Dumoulin, J.-P., von Grafenstein, U., 2019. Holocene-long record of flood frequency in the Southern Alps (Lake Iseo, Italy) under human and climate forcing. Glob. Planet. Change 175, 160–172. https://doi.org/10.1016/j.gloplacha.2019.02.010

Rapuc, W., Sabatier, P., Andrič, M., Crouzet, C., Arnaud, F., Chapron, E., Šmuc, A., Develle, A.-L., Wilhelm, B., Demory, F., 2018. 6600 years of earthquake record in the Julian Alps (Lake Bohinj, Slovenia). Sedimentology 65, 1777–1799. https://doi.org/10.1111/sed.12446

Ravazzi, C., Marchetti, M., Zanon, M., Perego, R., Quirino, T., Deaddis, M., De Amicis, M., Margaritora, D., 2013. Lake evolution and landscape history in the lower Mincio River valley, unravelling drainage changes in the central Po Plain (N-Italy) since the Bronze Age. Quat. Int., Quaternary in Italy: knowledge and perspective 288, 195–205. https://doi.org/10.1016/j.quaint.2011.11.031

Regattieri, E., Zanchetta, G., Isola, I., Zanella, E., Drysdale, R.N., Hellstrom, J.C., Zerboni, A., Dallai, L., Tema, E., Lanci, L., Costa, E., Magrì, F., 2019. Holocene Critical Zone dynamics in an Alpine catchment inferred from a speleothem multiproxy record: disentangling climate and human influences. Sci. Rep. 9, 17829. https://doi.org/10.1038/s41598-019-53583-7

Reimer, P.J., Austin, W.E.N., Bard, E., Bayliss, A., Blackwell, P.G., Bronk Ramsey, C., Butzin, M., Cheng, H., Edwards, R.L., Friedrich, M., Grootes, P.M., Guilderson, T.P., Hajdas, I., Heaton, T.J., Hogg, A.G., Hughen, K.A., Kromer, B., Manning, S.W., Muscheler, R., Palmer, J.G., Pearson, C., van der Plicht, J., Reimer, R.W., Richards, D.A., Scott, E.M., Southon, J.R., Turney, C.S.M., Wacker, L., Adolphi, F., Büntgen, U., Capano, M., Fahrni,

S.M., Fogtmann-Schulz, A., Friedrich, R., Köhler, P., Kudsk, S., Miyake, F., Olsen, J., Reinig, F., Sakamoto, M., Sookdeo, A., Talamo, S., 2020. The IntCal20 Northern Hemisphere Radiocarbon Age Calibration Curve (0–55 cal kBP). Radiocarbon 62, 725–757. https://doi.org/10.1017/RDC.2020.41

Reimer, P.J., Bard, E., Bayliss, A., Beck, J.W., Blackwell, P.G., Bronk Ramsey, C., Buck, C.E., Cheng, H., Edwards, R.L., Friedrich, M., others, 2013. IntCal13 and Marine13 radiocarbon age calibration curves 0-50,000 years cal BP. Radiocarbon, 55(4), 1869-1887. https://doi.org/10.2458/azu_js_rc.55.16947

Renard, K.G., Foster, G.R., Weesies, G.A., Porter, J.P., 1991. RUSLE: Revised universal soil loss equation. J. Soil Water Conserv. 46, 30–33.

Revel-Rolland, M., Arnaud, F., Chapron, E., Desmet, M., Givelet, N., Alibert, C., McCulloch, M., 2005. Sr and Nd isotopes as tracers of clastic sources in Lake Le Bourget sediment (NW Alps, France) during the Little Ice Age: Palaeohydrology implications. Chem. Geol. 224, 183–200. https://doi.org/10.1016/j.chemgeo.2005.04.014

Rey, P.-J., 2016. Archéologie du Massif des Bauges du Néolithique à l'Age du Bronze. Département de la Savoie, Musée Savoisien, Chambéry, France.

Reyss, J.-L., Schmidt, S., Legeleux, F., Bonté, P., 1995. Large, low background well-type detectors for measurements of environmental radioactivity. Nucl. Instrum. Methods Phys. Res. Sect. Accel. Spectrometers Detect. Assoc. Equip. 357, 391–397. https://doi.org/10.1016/0168-9002(95)00021-6

Richter, D. deB., Mobley, M.L., 2009. Monitoring Earth's critical zone. Science 326, 1067–1068. https://doi.org/10.1016/j.jhydrol.2020.125692

Rolland, Y., Cox, S., Boullier, A.-M., Pennacchioni, G., Mancktelow, N., 2003. Rare earth and trace element mobility in mid-crustal shear zones: insights from the Mont Blanc Massif (Western Alps). Earth Planet. Sci. Lett. 214, 203–219. https://doi.org/10.1016/S0012-821X(03)00372-8

Rossato, S., Fontana, A., Mozzi, P., 2015. Meta-analysis of a Holocene 14C database for the detection of paleohydrological crisis in the Venetian–Friulian Plain (NE Italy). CATENA, Past Hydrological Extreme Events in a Changing Climate 130, 34–45. https://doi.org/10.1016/j.catena.2014.10.033

Rothacker, L., Dosseto, A., Francke, A., Chivas, A.R., Vigier, N., Kotarba-Morley, A.M., Menozzi, D., 2018. Impact of climate change and human activity on soil landscapes over the past 12,300 years. Sci. Rep. 8, 247. https://doi.org/10.1038/s41598-017-18603-4

Rottoli, M., Castiglioni, E., 2009. Prehistory of plant growing and collecting in northern Italy, based on seed remains from the early Neolithic to the Chalcolithic (c. 5600–2100 cal BC). Veg. Hist. Archaeobotany 18, 91–103. https://doi.org/10.1007/s00334-007-0139-1

Rovida, A., Locati, M., Camassi, R., Lolli, B., Gasperini, P., 2020. The Italian earthquake catalogue CPTI15. Bull. Earthq. Eng. 18, 2953–2984. https://doi.org/10.1007/s10518-020-00818-y

Rovida, A.N., Locati, M., Camassi, R.D., Lolli, B., Gasperini, P., 2019. Catalogo Parametrico dei Terremoti Italiani CPTI15, versione 2.0 (report). https://doi.org/10.13127/CPTI/CPTI15.2

Ruddiman, W.F., 2007. The early anthropogenic hypothesis: Challenges and responses. Rev. Geophys. 45. https://doi.org/10.1029/2006RG000207

Ruggiero, M.G., Poggiani Keller, R., 2014. Il Progetto "Monitoraggio e buone pratiche di tutela del patrimonio del sito UNESCO m.94 Arte rupestre della Valle Camonica. Sestante.

Rusco, E., Montanarella, L., Bosco, C., 2008. Soil Erosion: a main threats to the soil in Europe. pp. 37–46. https://doi.org/10.2788/8647

Sabatier, P., Mottes, C., Cottin, N., Evrard, O., Comte, I., Piot, C., Gay, B., Arnaud, F., Lefevre, I., Develle, A.-L., Deffontaines, L., Plet, J., Lesueur-Jannoyer, M., Poulenard, J., 2021. Evidence of Chlordecone Resurrection by Glyphosate in French West Indies. Environ. Sci. Technol. 55, 2296–2306. https://doi.org/10.1021/acs.est.0c05207

Sabatier, P., Wilhelm, B., Ficetola, G.F., Moiroux, F., Poulenard, J., Develle, A.-L., Bichet, A., Chen, W., Pignol, C., Reyss, J.-L., Gielly, L., Bajard, M., Perrette, Y., Malet, E., Taberlet, P., Arnaud, F., 2017. 6-kyr record of flood frequency and intensity in the western Mediterranean Alps – Interplay of solar and temperature forcing. Quat. Sci. Rev. 170, 121–135. https://doi.org/10.1016/j.quascirev.2017.06.019

Sabatier, P., Poulenard, J., Fanget, B., Reyss, J.-L., Develle, A.-L., Wilhelm, B., Ployon, E., Pignol, C., Naffrechoux, E., Dorioz, J.-M., Montuelle, B., Arnaud, F., 2014. Long-term relationships among pesticide applications, mobility, and soil erosion in a vineyard watershed. Proc. Natl. Acad. Sci. 111, 15647–15652. https://doi.org/10.1073/pnas.1411512111

Sabatier, P., Dezileau, L., Briqueu, L., Colin, C., Siani, G., 2010. Clay minerals and geochemistry record from northwest Mediterranean coastal lagoon sequence: Implications for paleostorm reconstruction. Sediment. Geol. 228, 205–217. https://doi.org/10.1016/j.sedgeo.2010.04.012

Salmaso, N., Mosello, R., Garibaldi, L., Decet, F., Brizzio, M.C., Cordella, P., 2003. Vertical mixing as a determinant of trophic status in deep lakes: a case study from two lakes south of the Alps (Lake Garda and Lake Iseo). J. Limnol. 62, 33. https://doi.org/10.4081/jlimnol.2003.s1.33

Sauerbrey, M.A., Juschus, O., Gebhardt, A.C., Wennrich, V., Nowaczyk, N.R., Melles, M., 2013. Mass movement deposits in the 3.6 Ma sediment record of Lake El'gygytgyn, Far East Russian Arctic. Clim. Past 9, 1949–1967. https://doi.org/10.5194/cp-9-1949-2013

Savitzky, Abraham., Golay, M.J.E., 1964. Smoothing and Differentiation of Data by Simplified Least Squares Procedures. Anal. Chem. 36, 1627–1639. https://doi.org/10.1021/ac60214a047

Schmid, S.M., Fügenschuh, B., Kissling, E., Schuster, R., 2004. Tectonic map and overall architecture of the Alpine orogen. Eclogae Geol. Helvetiae 97, 93–117. https://doi.org/10.1007/s00015-004-1113-x

Schneider, T., Rimer, D., Butz, C., Grosjean, M., 2018. A high-resolution pigment and productivity record from the varved Ponte Tresa basin (Lake Lugano, Switzerland) since 1919: insight from an approach that combines hyperspectral imaging and high-performance liquid chromatography. J. Paleolimnol. 60, 381–398. https://doi.org/10.1007/s10933-018-0028-x

Scotti, R., Brardinoni, F., Alberti, S., Frattini, P., Crosta, G.B., 2013. A regional inventory of rock glaciers and protalus ramparts in the central Italian Alps. Geomorphology 186, 136–149. https://doi.org/10.1016/j.geomorph.2012.12.028

Segard, M., 2009. Pastoralism, rural economy and landscape evolution in the western Alps. J. Roman Archaeol. 22, 170–182. https://doi.org/10.1017/S104775940002064X

Serpelloni, E., Anzidei, M., Baldi, P., Casula, G., Galvani, A., 2005. Crustal velocity and strain-rate fields in Italy and surrounding regions: new results from the analysis of permanent and non-permanent GPS networks. Geophys. J. Int. 161, 861–880. https://doi.org/10.1111/j.1365-246X.2005.02618.x

Silva-Sánchez, N., Martínez Cortizas, A., López-Merino, L., 2014. Linking forest cover, soil erosion and mire hydrology to late-Holocene human activity and climate in NW Spain. The Holocene 24, 714–725. https://doi.org/10.1177/0959683614526934

Simonneau, A., Doyen, E., Chapron, E., Millet, L., Vannière, B., Di Giovanni, C., Bossard, N., Tachikawa, K., Bard, E., Albéric, P., Desmet, M., Roux, G., Lajeunesse, P., Berger, J.F., Arnaud, F., 2013. Holocene land-use evolution and associated soil erosion in the French Prealps inferred from Lake Paladru sediments and archaeological evidences. J. Archaeol. Sci. 40, 1636–1645. https://doi.org/10.1016/j.jas.2012.12.002

Speta, M., Rivard, B., Feng, J., 2018. Shortwave infrared (1.0–2.5 µm) hyperspectral imaging of the Athabasca West Grand Rapids Formation oil sands. AAPG Bull. 102, 1671–1683. https://doi.org/10.1306/01081817264

Steffen, W., Richardson, K., Rockström, J., Cornell, S.E., Fetzer, I., Bennett, E.M., Biggs, R., Carpenter, S.R., Vries, W. de, Wit, C.A. de, Folke, C., Gerten, D., Heinke, J., Mace, G.M., Persson, L.M., Ramanathan, V., Reyers, B., Sörlin, S., 2015. Planetary boundaries: Guiding human development on a changing planet. Science 347. https://doi.org/10.1126/science.1259855

Steinhilber, F., Abreu, J.A., Beer, J., Brunner, I., Christl, M., Fischer, H., Heikkilä, U., Kubik, P.W., Mann, M., McCracken, K.G., 2012. 9,400 years of cosmic radiation and solar activity from ice cores and tree rings. Proc. Natl. Acad. Sci. 109, 5967–5971. https://doi.org/10.1073/pnas.1118965109

Stocker, T.F., Qin, D., Plattner, G.-K., Alexander, L.V., Allen, S.K., Bindoff, N.L., Bréon, F.-M., Church, J.A., Cubasch, U., Emori, S., 2013. Technical summary, in: Climate Change 2013: The Physical Science Basis. Contribution of Working Group I to the Fifth Assessment Report of the Intergovernmental Panel on Climate Change. Cambridge University Press, pp. 33–115. https://www.ipcc.ch/report/ar5/wg1/

Støren, E.N., Dahl, S.O., Nesje, A., Paasche, Ø., 2010. Identifying the sedimentary imprint of high-frequency Holocene river floods in lake sediments: development and application of a new method. Quat. Sci. Rev. 29, 3021–3033. https://doi.org/10.1016/j.quascirev.2010.06.038

Strasser, M., Monecke, K., Schnellmann, M., Anselmetti, F.S., 2013. Lake sediments as natural seismographs: A compiled record of Late Quaternary earthquakes in Central Switzerland and its implication for Alpine deformation. Sedimentology 60, 319–341. https://doi.org/10.1111/sed.12003

Stucchi, M., Meletti, C., Montaldo, V., Akinci, A., Faccioli, E., Gasperini, P., Malagnini, L., Valensise, G., 2004. Pericolosità sismica di riferimento per il territorio nazionale MPS04. https://doi.org/10.13127/SH/MPS04/AG

Sturm, M., Matter, A., 1978. Turbidites and varves in Lake Brienz (Switzerland): deposition of clastic detritus by density currents. Wiley Online Library. https://doi.org/10.1002/9781444303698.ch8

Stutenbecker, L., Delunel, R., Schlunegger, F., Silva, T.A., Šegvić, B., Girardclos, S., Bakker, M., Costa, A., Lane, S.N., Loizeau, J.-L., Molnar, P., Akçar, N., Christl, M., 2018. Reduced sediment supply in a fast eroding landscape? A multi-proxy sediment budget of the upper

Rhône basin, Central Alps. Sediment. Geol., Analysis of sediment properties 375, 105–119. https://doi.org/10.1016/j.sedgeo.2017.12.013

Swierczynski, T., Lauterbach, S., Dulski, P., Delgado, J., Merz, B., Brauer, A., 2013. Mid-to late Holocene flood frequency changes in the northeastern Alps as recorded in varved sediments of Lake Mondsee (Upper Austria). Quat. Sci. Rev. 80, 78–90. https://doi.org/10.1016/j.quascirev.2013.08.018

Syvitski, J.P.M., Vörösmarty, C.J., Kettner, A.J., Green, P., 2005. Impact of Humans on the Flux of Terrestrial Sediment to the Global Coastal Ocean. Science 308, 376–380. https://doi.org/10.1126/science.1109454

Tachikawa, K., Rapuc, W., Vidal, L., Dubois-Dauphin, Q., Westerhold, T., Guihou, A., Bickert, T., Pérez-Asensio, J.N., Deschamps, P., Skonieczny, C., 2021. Eastern Atlantic deep-water circulation and carbon storage inferred from neodymium and carbon isotopic compositions over the past 1.1 million years. Quat. Sci. Rev. 252, 106752. https://doi.org/10.1016/j.quascirev.2020.106752

Trigo, I.F., Bigg, G.R., Davies, T.D., 2002. Climatology of Cyclogenesis Mechanisms in the Mediterranean. Mon. Weather Rev. 130, 549–569. https://doi.org/10.1175/1520-0493(2002)130<0549:COCMIT>2.0.CO;2

Tusa, L., Andreani, L., Khodadadzadeh, M., Contreras, C., Ivascanu, P., Gloaguen, R., Gutzmer, J., 2019. Mineral Mapping and Vein Detection in Hyperspectral Drill-Core Scans: Application to Porphyry-Type Mineralization. Minerals 9, 122. https://doi.org/10.3390/min9020122

Van Exem, A., Debret, M., Copard, Y., Vannière, B., Sabatier, P., Marcotte, S., Laignel, B., Reyss, J.-L., Desmet, M., 2018. Hyperspectral core logging for fire reconstruction studies. J. Paleolimnol. 59, 297–308. https://doi.org/10.1007/s10933-017-0009-5

Vannière, B., Magny, M., Joannin, S., Simonneau, A., Wirth, S.B., Hamann, Y., Chapron, E., Gilli, A., Desmet, M., Anselmetti, F.S., 2013a. Orbital changes, variation in solar activity and increased anthropogenic activities: controls on the Holocene flood frequency in the Lake Ledro area, Northern Italy. Clim. Past 9, 1193–1209. https://doi.org/10.5194/cp-9-1193-2013

Verdecchia, A., Pace, B., Visini, F., Scotti, O., Peruzza, L., Benedetti, L., 2018. The Role of Viscoelastic Stress Transfer in Long-Term Earthquake Cascades: Insights After the Central Italy 2016–2017 Seismic Sequence. Tectonics 37, 3411–3428. https://doi.org/10.1029/2018TC005110

Wagner, B., Reicherter, K., Daut, G., Wessels, M., Matzinger, A., Schwalb, A., Spirkovski, Z., Sanxhaku, M., 2008. The potential of Lake Ohrid for long-term palaeoenvironmental reconstructions. Palaeogeogr. Palaeoclimatol. Palaeoecol., Lake systems: sedimentary archives of climate change and tectonics 259, 341–356. https://doi.org/10.1016/j.palaeo.2007.10.015

Walling, D.E., 1994. Measuring sediment yield from river basins. Soil Eros. Res. Methods 39–80. https://doi.org/10.1201/9780203739358

Walsh, K., Berger, J.-F., Roberts, C.N., Vanniere, B., Ghilardi, M., Brown, A.G., Woodbridge, J., Lespez, L., Estrany, J., Glais, A., Palmisano, A., Finné, M., Verstraeten, G., 2019. Holocene demographic fluctuations, climate and erosion in the Mediterranean: A meta data-analysis. The Holocene 29, 864–885. https://doi.org/10.1177/0959683619826637

Wang, J., Howarth, J.D., McClymont, E.L., Densmore, A.L., Fitzsimons, S.J., Croissant, T., Gröcke, D.R., West, M.D., Harvey, E.L., Frith, N.V., Garnett, M.H., Hilton, R.G., 2020. Long-term patterns of hillslope erosion by earthquake-induced landslides shape mountain landscapes. Sci. Adv. 6, eaaz6446. https://doi.org/10.1126/sciadv.aaz6446

Wessels, M., 1998. Natural environmental changes indicated by Late Glacial and Holocene sediments from Lake Constance, Germany. Palaeogeogr. Palaeoclimatol. Palaeoecol. 140, 421–432. https://doi.org/10.1016/S0031-0182(98)00026-1

Wetzel, R.G., 2001. Limnology: Lake and River Ecosystems. Gulf Professional Publishing. https://doi.org/10.1016/C2009-0-02112-6

Wiemer, S., Kraft, T., Landtwing, D., 2015. Seismic Risk. pp. 263–295.

Wilhelm, B., Cánovas, J.A.B., Macdonald, N., Toonen, W.H.J., Baker, V., Barriendos, M., Benito, G., Brauer, A., Corella, J.P., Denniston, R., Glaser, R., Ionita, M., Kahle, M., Liu, T., Luetscher, M., Macklin, M., Mudelsee, M., Munoz, S., Schulte, L., George, S.S., Stoffel, M., Wetter, O., 2019. Interpreting historical, botanical, and geological evidence to aid preparations for future floods. WIREs Water 6, e1318. https://doi.org/10.1002/wat2.1318

Wilhelm, B., Ballesteros Canovas, J.A., Corella Aznar, J.P., Kämpf, L., Swierczynski, T., Stoffel, M., Støren, E., Toonen, W., 2018. Recent advances in paleoflood hydrology: From new archives to data compilation and analysis. Water Secur. 3, 1–8. https://doi.org/10.1016/j.wasec.2018.07.001

Wilhelm, B., Ballesteros Canovas, J.A., Ahlborn, M., Baker, V., Benito, G., Francus, P., Glaser, R., Kahle, M., Mudelsee, M., Pefla, J.C., Schulte, L., St George, S., Swierczynski, T., 2017a. For an improvement of our flood knowledge through paleodata. https://pastglobalchanges.org/publications/white-paper-improvement-our-flood-knowledge-through-paleodata

Wilhelm, B., Vogel, H., Anselmetti, F.S., 2017b. A multi-centennial record of past floods and earthquakes in Valle d'Aosta, Mediterranean Italian Alps. Nat. Hazards Earth Syst. Sci. 17, 613. https://doi.org/10.5194/nhess-17-613-2017

Wilhelm, B., Nomade, J., Crouzet, C., Litty, C., Sabatier, P., Belle, S., Rolland, Y., Revel, M., Courboulex, F., Arnaud, F., others, 2016a. Quantified sensitivity of small lake sediments to record historic earthquakes: implications for paleoseismology. J. Geophys. Res. Earth Surf. 121, 2–16. https://doi.org/10.1002/2015JF003644

Wilhelm, B., Vogel, H., Crouzet, C., Etienne, D., Anselmetti, F.S., 2016b. Frequency and intensity of palaeofloods at the interface of Atlantic and Mediterranean climate domains. Clim. Past 12, 299–316. https://doi.org/10.5194/cp-12-299-2016

Wilhelm, B., Arnaud, F., Sabatier, P., Magand, O., Chapron, E., Courp, T., Tachikawa, K., Fanget, B., Malet, E., Pignol, C., Bard, E., Delannoy, J.J., 2013. Palaeoflood activity and climate change over the last 1400 years recorded by lake sediments in the north-west European Alps. J. Quat. Sci. 28, 189–199. https://doi.org/10.1002/jqs.2609

Wilhelm, B., Arnaud, F., Sabatier, P., Crouzet, C., Brisset, E., Chaumillon, E., Disnar, J.-R., Guiter, F., Malet, E., Reyss, J.-L., others, 2012. 1400years of extreme precipitation patterns over the Mediterranean French Alps and possible forcing mechanisms. Quat. Res. 78, 1–12. https://doi.org/10.1016/j.yqres.2012.03.003

Willenbring, J.K., von Blanckenburg, F., 2010. Long-term stability of global erosion rates and weathering during late-Cenozoic cooling. Nature 465, 211–214. https://doi.org/10.1038/nature09044

Winschall, A., Pfahl, S., Sodemann, H., Wernli, H., 2012. Impact of North Atlantic evaporation hot spots on southern Alpine heavy precipitation events. Q. J. R. Meteorol. Soc. 138, 1245–1258. https://doi.org/10.1002/qj.987

Wirth, S.B., Gilli, A., Simonneau, A., Ariztegui, D., Vannière, B., Glur, L., Chapron, E., Magny, M., Anselmetti, F.S., 2013a. A 2000 year long seasonal record of floods in the southern European Alps. Geophys. Res. Lett. 40, 4025–4029. https://doi.org/10.1002/grl.50741

Wirth, S.B., Glur, L., Gilli, A., Anselmetti, F.S., 2013b. Holocene flood frequency across the Central Alps–solar forcing and evidence for variations in North Atlantic atmospheric circulation. Quat. Sci. Rev. 80, 112–128. https://doi.org/10.1016/j.quascirev.2013.09.002

Wittmann, H., Blanckenburg, F. von, Kruesmann, T., Norton, K.P., Kubik, P.W., 2007. Relation between rock uplift and denudation from cosmogenic nuclides in river sediment in the Central Alps of Switzerland. J. Geophys. Res. Earth Surf. 112. https://doi.org/10.1029/2006JF000729

Wold, S., Ruhe, A., Wold, H., Dunn, I., W.J., 1984. The Collinearity Problem in Linear Regression. The Partial Least Squares (PLS) Approach to Generalized Inverses. SIAM J. Sci. Stat. Comput. 5, 735–743. https://doi.org/10.1137/0905052

Zádorová, T., Penížek, V., Šefrna, L., Drábek, O., Mihaljevič, M., Volf, Š., Chuman, T., 2013. Identification of Neolithic to Modern erosion–sedimentation phases using geochemical approach in a loess covered sub-catchment of South Moravia, Czech Republic. Geoderma 195–196, 56–69. https://doi.org/10.1016/j.geoderma.2012.11.012

Annexes

Annexe I | 6600 years of earthquakes records in the Julian Alps (Lake Bohinj, Slovenia)

SEDIMENTOLOGY the journal of the International Association of Sedimentologists

Sedimentology (2018) **65**, 1777–1799 doi: 10.1111/sed.12446

6600 years of earthquake record in the Julian Alps (Lake Bohinj, Slovenia)

WILLIAM RAPUC*, PIERRE SABATIER*, MAJA ANDRIČ†, CHRISTIAN CROUZET‡, FABIEN ARNAUD*, EMMANUEL CHAPRON§, ANDREJ ŠMUC¶, ANNE-LISE DEVELLE*, BRUNO WILHELM**, FRANÇOIS DEMORY††, JEAN-LOUIS REYSS*, EDOUARD RÉGNIER‡‡, GERHARD DAUT§§ and ULRICH VON GRAFENSTEIN‡‡

**Univ. Grenoble Alpes, Univ. Savoie Mont Blanc, CNRS, EDYTEM, 73000 Chambéry, France (E-mail: william.rapuc@univ-smb.fr)*

†ZRC SAZU, Institute of Archaeology, Novi trg 2, 1000 Ljubljana, Slovenia

‡Univ. Grenoble Alpes, Univ. Savoie Mont Blanc, CNRS, IRD, ISTerre, 38000 Grenoble, France

§GEODE, Université Jean Jaurès, Maison de la Recherche, 31058 Toulouse Cedex, France

¶Department of Geology, University of Ljubljana, Privoz 11, 1000 Ljubljana, Slovenia

***Univ. Grenoble Alpes, CNRS, IRD, Grenoble INP*, IGE, 38000 Grenoble, France*

††CEREGE, Université Aix-Marseille, CNRS, IRD, Collège de France, Europôle de l'Arbois, BP 80, 13545 Aix en Provence, France

‡‡LSCE, Université de Versailles Saint-Quentin, Commissariat à l'Energie Atomique–CNRS, 91198 Gif-sur-Yvette, France

§§Institut für Geographie, Lehrstuhl Physische Geographie, Löbdergraben 32, 07743 Jena, Germany

Associate Editor – Vern Manville

ABSTRACT

Sequences of lake sediments often form long and continuous records that may be sensitive recorders of seismic shaking. A multi-proxy analysis of Lake Bohinj sediments associated with a well-constrained chronology was conducted to reconstruct Holocene seismic activity in the Julian Alps (Slovenia). A seismic reflection survey and sedimentological analyses identified 29 homogenite-type deposits related to mass-wasting deposits. The most recent homogenites can be linked to historical regional earthquakes (i.e. 1348 AD, 1511 AD and 1690 AD) with strong epicentral intensity [greater than 'damaging' (VIII) on the Medvedev–Sponheuer–Karnik scale]. The correlation between the historical earthquake data set and the homogenites identified in a core isolated from local stream inputs, allows interpretation of all similar deposits as earthquake related. This work extends the earthquake chronicle of the last 6600 years in this area with a total of 29 events recorded. The early Holocene sedimentary record is disturbed by a seismic event (6617 ± 94 cal yr BP) that reworked previously deposited sediment and led to a thick sediment deposit identified in the seismic survey. The period between 3500 cal yr BP and 2000 cal yr BP is characterized by a major destabilization in the watershed by human activities that led to increases in erosion and sedimentation rates. This change increased the lake's sensitivity to recording an earthquake (earthquake-sensitivity threshold index) with the occurrence of 72 turbidite-type deposits over this period. The high turbidite frequency identified could be the consequence of this change in lake earthquake sensitivity and thus these turbidites could be triggered by earthquake shaking, as other origins are discarded. This study illustrates why it is not acceptable to propose a return period for seismic activity recorded in lake sediment if the sedimentation rate varies significantly.

Keywords Earthquake chronicle, Holocene, Julian Alps, lake sediment, lake sensitivity.

INTRODUCTION

The Alps are experiencing the active convergence between the European and African plates at an average rate of 5·9 mm yr^{-1} (Moulin *et al.*, 2014). The associated deformation is localized on active faults in several regions such as the Julian Alps, which present a set of mostly dextral north-west/south-east-oriented strike-slip faults (Camassi *et al.*, 2011). This deformation is associated with north-western Slovenia's moderate to high seismic activity (European Seismic Hazard Map; Rovida *et al.*, 2016) that has included several destructive earthquakes, such as the 1511 AD 'Idrija' earthquake [epicentral Medvedev–Sponheuer–Karnik (MSK) intensity of X; Fitzko *et al.*, 2005] with a macroseismic epicentral MSK (Medvedev *et al.* 1964) intensity of X (hereafter I_o for epicentral intensity). Consequently, an accurate assessment of the seismic hazard is required to reduce the high vulnerability of this region.

The long-term probabilistic seismic hazard can be assessed using a well-dated and quantitative earthquake history (Gürpinar, 2005; Mugnier *et al.*, 2013). This is particularly relevant in moderately active seismic regions, where the instrumental and historical records are too short to cover the recurrence interval of strong earthquakes (Michetti *et al.*, 2005). The historical seismicity of the Julian Alps was summarized in the 'Catalogo Parametrico dei Terremoti Italiani' (CPTI15; Rovida *et al.*, 2016), which includes 371 earthquakes since AD 778. However, historical data may be incomplete to enable the tectonic movements at multi-millennial scale to be studied, whereas lake sediments can provide a continuous record of past earthquakes over several millennia, as shown for instance in Quebec (Doig, 1990, 1998), the Andes (Arnaud *et al.*, 2006; Chapron *et al.*, 2007; Moernaut *et al.*, 2014) and the Alps (Beck, 2009; Strasser *et al.*, 2013; Chapron *et al.*, 2016; Wilhelm *et al.*, 2016; Kremer *et al.*, 2017). Earthquake shaking may destabilize previously deposited sediment, which slides to the bottom of the lake in a turbid flow, a cohesive mass flow or a debris flow. These seismically induced mass-wasting deposits (MWD), such as turbidites or homogenites, can be easily identified and dated to provide a well-documented earthquake chronicle (e.g. Strasser *et al.*, 2006; Chapron *et al.*, 2016).

Lake Bohinj lies in the centre of the Julian Alps. During the Quaternary, this area was affected by major north-west/south-east striking faults (Camassi *et al.*, 2011). To reconstruct the earthquake chronicle, Lake Bohinj sediments were mapped with a seismic reflection survey and cored in 2012 to provide a 12 m long sedimentary record. A multi-proxy analysis was performed to reconstruct the long-term earthquake record.

STUDY AREA AND SETTING

Tectonic setting

Since the Pliocene, the deformation in the study area has been accommodated by a set of north-west/south-east-oriented faults describing dextral strike-slip movements (Šmuc & Rožič, 2009). Three main north-west/south-east active faults are present in the study area: the Idrija, Sava and Ravne faults (Fig. 1A). Several earthquakes with MSK epicentral intensity (I_o) ≥ VIII have been reported (Rovida *et al.*, 2016). Among them, two earthquakes with $I_o \geq$ IX have been related to the main regional faults. The 'Villach' earthquake in AD 1348 could have been located on the Gemona–Kobarid fault (I_o = IX to X, Moulin *et al.*, 2014), and the Idrija earthquake in AD 1511 (I_o = IX) could be linked to the Idrija fault (Fitzko *et al.*, 2005; Camassi *et al.*, 2011). More recently, the Ravne fault was reactivated with pure dextral focal mechanisms during earthquakes in 1998 and 2004 (Bajc *et al.*, 2001; Kastelic *et al.*, 2008; Moulin *et al.*, 2014).

Study area

Lake Bohinj [46°17′N, 13°51′E, 526 m above sea-level (a.s.l.)] is a lake of glacial origin in the eastern Julian Alps, approximately 55 km north-west of Ljubljana (Fig. 1A). It is the largest lake in Slovenia, 4·35 km long and 1·0 km wide, and has a maximum depth of 45·6 m. The bathymetric map highlights the presence of two sub-basins

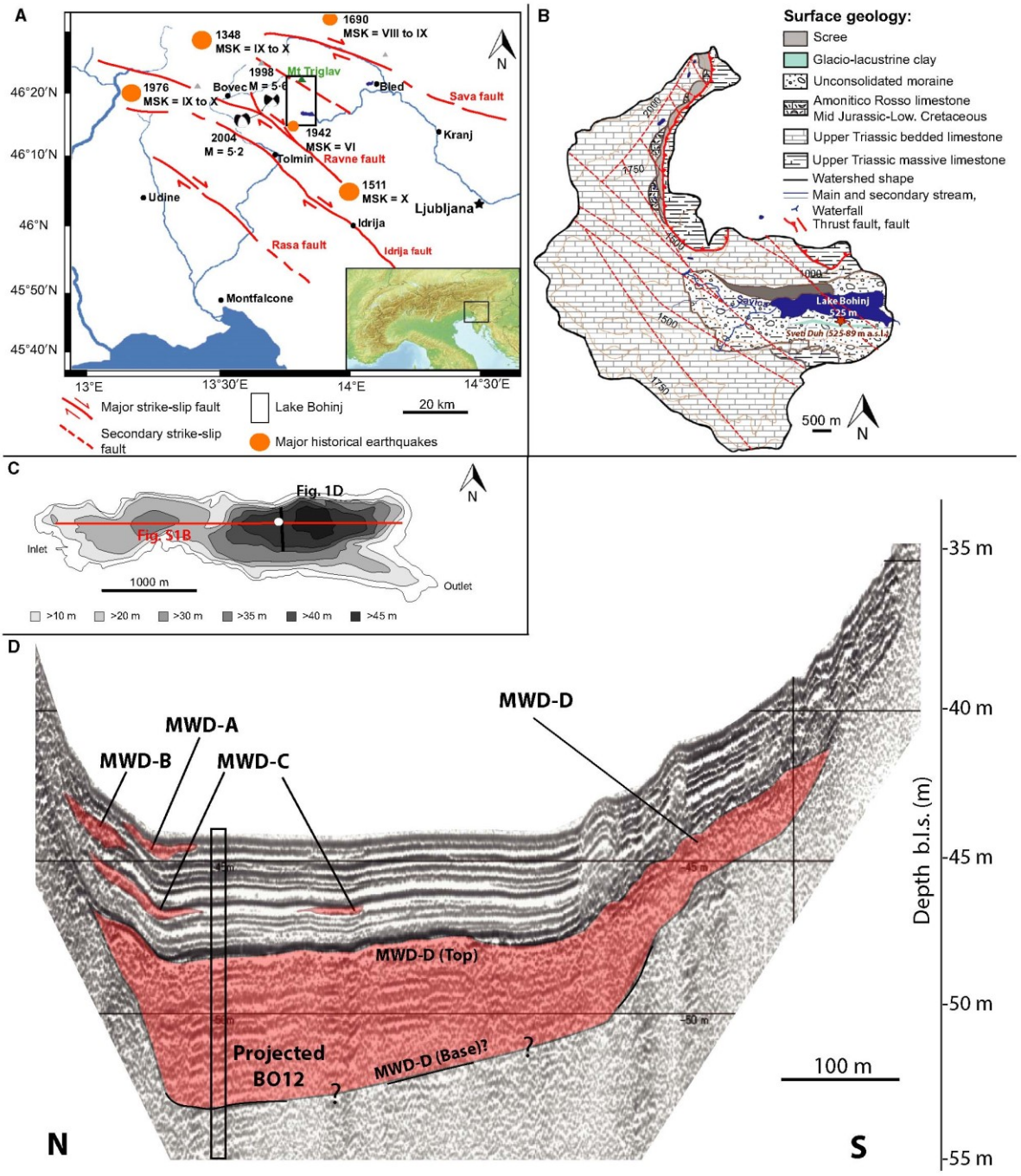

Fig. 1. General presentation of the study site. (A) Location of the study area with the major strike-slip faults and major historical earthquakes, modified from Moulin *et al.* (2014). (B) Geological map of the Lake Bohinj watershed. (C) Bathymetric map of Lake Bohinj. (D) Seismic profile oriented across the eastern basin showing the coring site location and four generations of MWD (red shading). The depth of the seismic profile is expressed in metres below lake surface (m b.l.s.), assuming a mean P_{wave} velocity of 1·5 m sec^{-1} in water and sediments. MWD, mass-wasting deposits; MSK, Medvedev–Sponheuer–Karnik.

separated by a north–south moraine ridge (Fig. 1C), 15 m higher than the bottom of the western sub-basin. The watershed (107 km²) is delimited by high Alpine mountains such as Mount Triglav (2864 m a.s.l.) and can be divided into two parts by a 51 m high waterfall (Fig. 1B).

The watershed is mainly composed of a thick pile of massive and bedded Upper Triassic limestones and two small-scale nappes (Šmuc & Rožič, 2009). The lower region, a plateau surrounding the lake, is mainly composed of glacial deposits and scree (Fig. 1B). These limestones, glacio-lacustrine sediments and glacial deposits lie primarily along the southern and eastern lake margin. South-east of the lake, approximately 50 m above the current lake-level, Quaternary laminated glacio-lacustrine deposits are covered by tills. These deposits are the Bohinj watershed's unique fine sediment. A delta lies in the western area of Lake Bohinj and is rich in carbonate sand and gravels, with very little fine material, and presents a smooth subaerial slope. During the Quaternary period, glaciers covered the upper part of the mountains and filled the upper reaches of the incised valleys (Buser *et al.*, 1986; Bavec *et al.*, 2004).

The Slovenian Environment Agency ARSO (Agencija Republike Slovenije za Okolje, http://www.arso.gov.si/en/water/data/) has collected hydrological data for Lake Bohinj since 1 January 1919, at the Sveti Duh gauging station. It is generally assumed that an outflow of 150 m^3 sec^{-1} corresponding to a water level higher than 280 cm at Sveti Duh represents a flood event at Lake Bohinj. Seven such flood events occurred during the data collection period (http://www.arso.gov.si/en/water/data/).

MATERIALS AND METHODS

Seismic survey, coring and lithological description

In April 2012, a high-resolution seismic reflection survey was conducted on Lake Bohinj, using a parametric echosounder INNOMAR SES-2000 Compact system (Innomar Technologie GmbH, Rostock, Germany), to define the geometry of the basin fill and optimize the coring site location. A dense grid of approximately 30 km of profiles (Fig. S1) was acquired across the lake with a maximum theoretical resolution of 6 cm using a frequency between 5 kHz and 15 kHz. The wave speed was defined at 1450 m sec^{-1} in the water and 1500 m sec^{-1} in the sediment. Profile positions were recorded with a GPS device coupled with the seismic acquisition system, and seismic data were digitally recorded (SEG-Y format). In May 2012, a 12 m long sediment core (BO12) was extracted near the deepest point of Lake Bohinj at a water depth of approximately 44 m (N46°17′06·8″ E13°51′82·6″) using a 90 mm diameter piston corer on a Uwitec coring platform (EDYTEM/LSCE/CLIMCORE; Uwitec, Mondsee, Austria). This coring site in the eastern basin was chosen because the seismic profiles showed up to approximately 30 m thick sedimentary deposits with stratified reflections. In the laboratory, the cores were split, photographed at high resolution (20 pixels mm^{-1}) and logged in detail, using the Munsell colour chart, to characterize the different sedimentary units. A composite profile was constructed using clearly identifiable stratigraphic marker layers from the overlapping sections of both series, providing a 12·36 m long continuous sediment profile.

Grain-size analysis

Grain-size analyses were performed at the EDYTEM laboratory using a Malvern MasterSizer™ S (Malvern Instruments Limited, Worcestershire, UK) with a size range between 0·06 μm and 800 μm. This analysis was performed with a 5 mm sampling step throughout the uppermost 1·5 m and with the same sampling step for several sedimentary layers below the first 1·5 m. The sorting values presented hereafter are equivalent to a standard deviation of the logarithmic method of moments.

Loss on ignition

Loss on ignition (LOI) analysis was performed following the protocol of Heiri *et al.* (2001) on the first 4·6 m of the BO12 sequence with a mean 6 cm sampling step to quantify the organic matter and carbonate content.

Geochemical properties

Geochemical analyses were conducted by X-ray fluorescence (XRF) on the EDYTEM laboratory's Avaatech Core Scanner (Avaatech XRF Technology, Alkmaar, The Netherlands) with a rhodium anode. To characterize the main variations throughout the BO12 sequence, a 5 mm sampling step was applied over the whole sequence. The

settings used for this analysis were a run at 10 kV and 0·75 mA for 15 sec to detect lightweight elements such as Al, Si, K, Ti, Mn and Fe, and a second run at 30 kV and 0·5 mA for 45 sec to detect Br, Rb, Sr, Zr and Pb. To describe sedimentary deposits thinner than 5 mm, a second analysis was executed on the first 3·9 m of the BO12 sequence at 1 mm resolution with the following settings: a run at 10 kV and 1·2 mA for 10 sec and a second run at 30 kV and 0·75 mA for 45 sec. The XRF results were submitted to principal component analysis (PCA) to determine correlations between the different measured elements and identify principal sediment end-members (Sabatier *et al.*, 2010a).

At a sub-lamina scale, an energy dispersive spectroscopy method (EDX) was used to investigate the elementary composition of the sediment. This method is ideal to determine elemental distributions at a microscopic scale, using a Quantax EDX probe (Bruker, Billerica, MA, USA) associated with a LEO Stereoscan 440 (Leica Cambridge Limited, Cambridge, UK) scanning electron microscope (SEM) with 20 kV tension on resin-embedded slabs. The slabs were sampled on two cores from the top of the BO12 sequence (BO12_01A, BO12_02A). Each different type of sediment deposit was observed and described using mapping profiles (59× to 650× magnification) and isolated acquisition.

Pollen analysis

For pollen analysis, a 1 cm^3 portion of sediment was subsampled from selected levels of the core (with sampling resolution of approximately 4 cm) using a metal volumetric subsampler. A standard laboratory procedure was used – HCl, NaOH, HF, acetolysis, staining with safranine, mounting in silicone oil (Bennett & Willis, 2002), and the pollen concentration was determined by adding *Lycopodium* spores (Stockmarr, 1971). The pollen was identified using a Nikon Eclipse E400 light microscope (Nikon Instruments, Tokyo, Japan) at 400× magnification using the pollen reference collection at the Institute of Archaeology ZRC SAZU in Ljubljana and pollen keys (Moore *et al.*, 1991; Reille, 1992, 1995). A minimum of 500 pollen grains of terrestrial taxa and spores (= pollen sum) were counted in each sample, except for silty and sandy layers with very low pollen concentrations in which the pollen sum was lower. The pollen data were analysed and plotted using PSIMPOLL 3·00 software (Bennett, 1998).

Magnetic properties

Anisotropy of magnetic susceptibility (AMS) measurements were also conducted on the sediment core. U-channels were prepared on two cores (BO12_P1; BO12_01C) and sampled with non-magnetic 2 cm × 2 cm × 2 cm plastic cubes. Seventy-seven cubes were sampled following this method, and 36 cubes were sampled directly from different core sections (BO12_02A; BO12_03C; BO12_01D; BO12_01E). Measurements were made at the CEREGE laboratory using an AGICO MFK1-FA Kappabridge (Advanced Geoscience Instruments Company, Brno, Czech Republic). The results of this analysis are sensitive determinations of the anisotropic component of the susceptibility tensor that can be represented by a tri-axial ellipsoid with three eigenvectors (K_{max}, K_{int} and K_{min}). According to Jelinek (1981), several different magnetic properties can be extracted from the AMS ellipsoid shape. As in Campos *et al.* (2013) and Petersen *et al.* (2014), the four following parameters were used:

1 Magnetic foliation: $F = K_{int}/K_{min}$
2 Magnetic lineation: $L = K_{max}/K_{int}$
3 Anisotropy degree: $P = K_{max}/K_{min}$
4 Average susceptibility: K_m

The AMS ellipsoid is assumed to reflect the preferred orientation of the magnetic grains in the sediment. Under normal conditions in sediments, the foliation is parallel to the bedding, and the inclination of K_{min} is vertical. The maximum susceptibility axis, K_{max}, and the minimum susceptibility axis, K_{min}, represent the average orientation of the longest and shortest magnetic grain axes, respectively (Dall'Olio *et al.*, 2013).

Dating

The age–depth model of Lake Bohinj is based on short-lived radionuclides (^{210}Pb, ^{137}Cs and ^{241}Am) and ^{14}C. Short-lived radionuclide measurements were performed using the well-type germanium detectors at the Laboratoire Souterrain de Modane (Reyss *et al.*, 1995) on the upper 12 cm of the BO12 sequence (BO12_P1) which corresponded to 21 samples following a non-regular 5 mm sampling step to match the lithography. The ^{14}C measurements were performed on 22 vegetal macro-organic remains (tree leaves or twigs) at the Poznan Radiocarbon and LMC14 laboratories (CNRS). The dates were calibrated

at two sigma using the Intcal13 calibration curve (Reimer *et al.*, 2013). The age–depth model was performed using the R code package 'CLAM' in R software (Blaauw, 2010).

RESULTS

Seismic stratigraphy

The Lake Bohinj seismic profiles are characterized by a limited penetration of acoustic waves due to gas-rich sediments (Figs 1D and S1B) approximately 3·0 m and 4·5 m below the lake floor (b.l.f.) in the western and eastern sub-basins, respectively. Only one limited acoustic window down to approximately 30 m b.l.f. (Fig. 1D) was found in the eastern basin and was selected as the coring location. The coring sites do not lie directly on a profile line, and a constant P_{wave} velocity of 1·5 m sec^{-1} in water and sediments was applied, so caution is used in interpreting the seismic stratigraphic results.

Several continuous and high-amplitude reflections within the upper metres of the basin fill are locally interrupted by transparent to chaotic deposits typical of MWD (cf. Chapron *et al.*, 2007, 2016; Strasser *et al.*, 2013). Up to four generations of MWDs are clearly identified across the eastern sub-basin (labelled 'A' to 'D' in Fig. 1D) at the edges of the northern, southern and eastern subaqueous slopes. Unit MWD-A is identified locally at the foot of the northern slopes of the eastern basin (Fig. 1D) but it essentially reworked the eastern slopes of this sub-basin (Fig. S1B) and laterally evolved towards the deepest part of the lake into a transparent acoustic facies developing onlaps, i.e. a typical acoustic signature for large muddy turbidites or homogenites (Chapron *et al.*, 1999, 2016). This MWD-A occurs approximately 50 to 75 cm b.l.f. near the BO12 coring site. Unit MWD-B is only identified locally at the foot of the northern slopes of the eastern basin (Fig. 1D) at approximately 90 cm and 115 cm b.l.f. near the BO12 coring site. As shown in Fig. 1D, MWD-C is characterized by two small correlated deposits (approximately 235 cm b.l.f. near BO12) identified at the foot of the northern slopes and in the eastern basin axis. Unit MWD-D is the largest, approximately 425 to 450 cm b.l.f. near BO12 (Fig. 1D) at a depth corresponding to the top of the largest deposit recorded in the BO12 sedimentary sequence. The acoustic signal is largely absorbed within the upper part of MWD-D, and thus it is not possible to map the base or the thickness of this major event deposit across the eastern basin. All of the identified units appear to originate from the steep northern, southern and eastern slopes (Figs 1D and S1B).

Sedimentology

Sedimentary units

The Lake Bohinj sediment core can be subdivided into seven different sedimentary units. Unit I (0 to 119 cm and 330·5 to 440 cm) is mainly composed of very dark grey clay interrupted by a few white clayey laminae and graded beds. Unit II is a dark grey to bluish grey clayey deposit. Unit III (132 to 330·5 cm) is characterized by clayey to silty grey graded layers.

The majority of the sedimentary record of Lake Bohinj is Unit IV (443 to 998 cm, Figs 2 and S2) which is composed of several different facies. This Unit starts with an 8·1 cm coarse to very coarse sandy thick erosive base overlain by a 30 cm thick facies composed of quite homogeneous coarse silt to very fine grey sand. This facies progressively evolves upward into a heterogeneous pale yellow facies from 961·3 to 741·3 cm, with a base rich in coarse sand. This 2 m long facies is interrupted by numerous greyish brown patches rich in organic matter and in silt associated with some gravels. The transitions between the sandy matrix and the organic patches are chaotic and widespread. This facies is overlaid by a homogenous silty to clayey facies with a thin erosive base (741·3 to 446·3 cm). This homogeneous facies is pale yellow until 680 cm and light olive brown after this. A white clayey 3 cm thick cap covers the top of Unit IV (Figs 2 and S2).

The lowest portion of the sequence (998·0 to 1234·3 cm) is composed of several units: a greenish grey clay Unit V (998·3 to 1034·4 cm) with one grey graded bed, Unit VI (1034·4 to 1170·0 cm) with dark grey clayey laminations and a light grey clay Unit VII (1170·0 to 1234·3 cm). Except for Unit VII, the lowest portion of the sedimentary record (Units V and VI) is rarely disturbed by graded beds (Fig. 2). Because this work aims to create a regional tectonic record, this study focuses on the units interbedded with graded beds in the upper part of the BO12 sedimentary sequence (the first 998 cm).

Linear regression tests on the Br content from the geochemistry and $LOI_{550°C}$ results yield a significant relationship with R^2 of 0·79 and $P < 0·001$. This suggests that Br intensity can be used as a

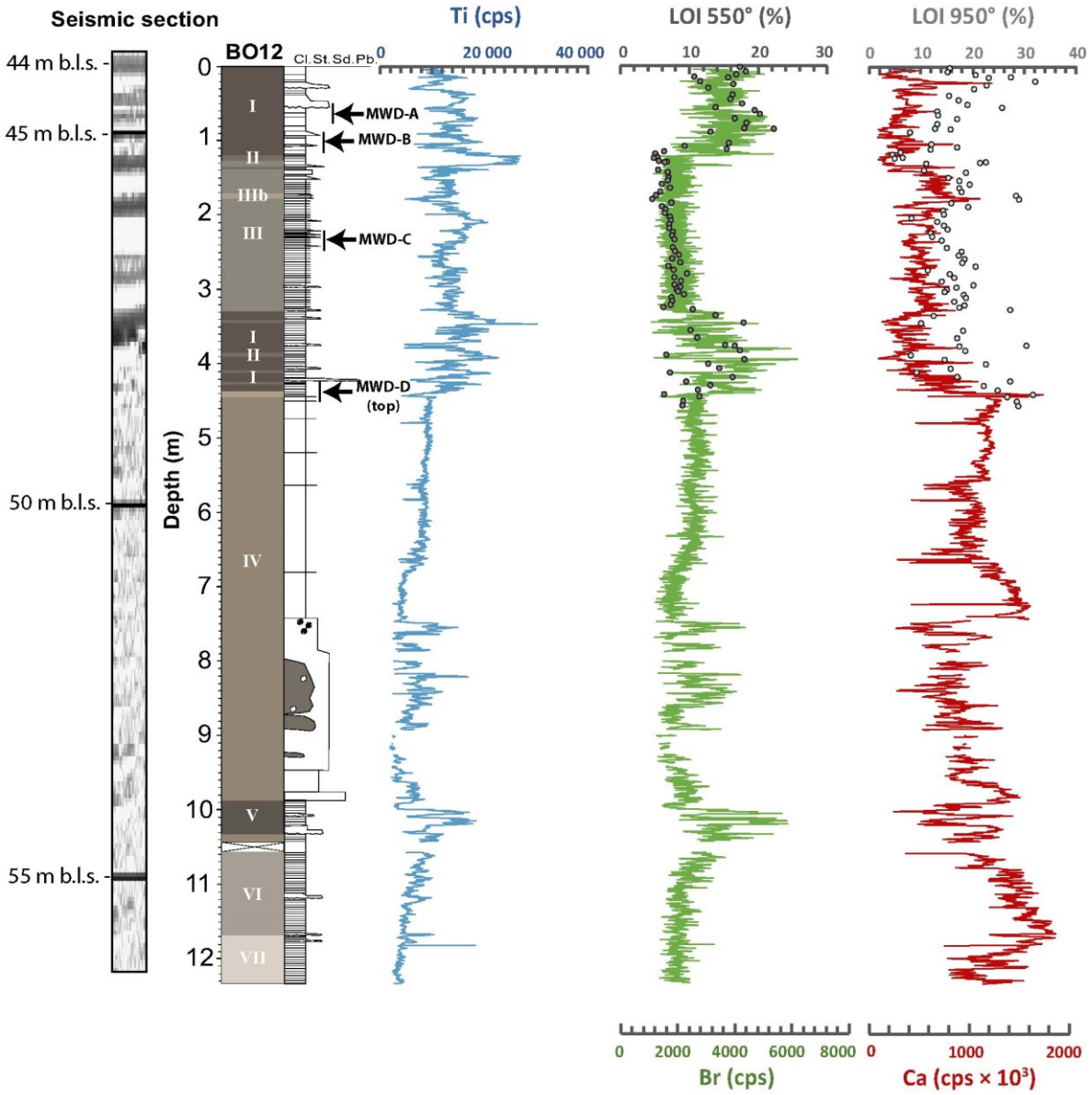

Fig. 2. Main sedimentological and geochemical results. A close-up view of the seismic profile (Fig. 1D) section is compared with lithological and geochemical results (Ti, Br and Ca contents) associated with the BO12 sequence LOI 550° (dark grey dots) and LOI 950° (light grey dots). The presented stratigraphy is described in the lithological description of the sediment sequence (see *Sedimentary units* section). The depth of the seismic section is expressed in metres below lake surface (m b.l.s.) and is scaled approximately to fit with the length of the sediment core. The depth of MWDs identified in the seismic profile (Fig. 1D) is reported against the lithological results using a black line. MWD, mass-wasting deposits; LOI, Loss on ignition; cps, counts per second.

high-resolution proxy of organic matter in lake sediment, as previously suggested by Bajard *et al.* (2016). The relationship between the $LOI_{950°C}$ and the Ca content is also positive but less well constrained, with an R^2 of 0·5 ($P < 0·001$).

The correlation circle from the PCA on geochemical analyses highlights the correlation between the different elements of the core (Fig. 3A). Dimensions 1 and 2 (denoted as Dim1 and Dim2) represent 81% of the total variability.

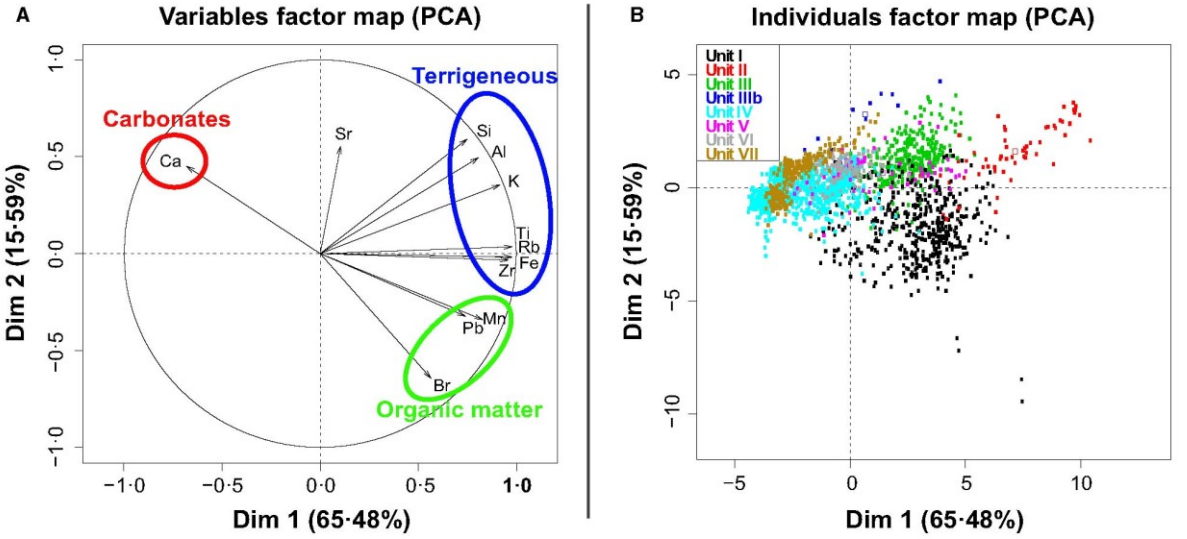

Fig. 3. Variable and individual factor maps from the PCA. (A) Variable factor map with three end-members (terrigenous, organic matter and carbonates). (B) Individual factor map with sedimentological units added as an illustrative variable. PCA, principal component analysis.

Three chemical end-members were identified. The first one is positively correlated to Dim1 and yields high positive loadings for major terrigenous elements: K, Al, Si, Zr, Ti, Rb and Fe (Fig. 3A). The second pole allows the discrimination of Br, linked to organic matter, Mn and Pb. The third end-member includes Ca, with negative loadings on Dim1 and positive correlation with Dim2.

The addition of the lithological unit information allows mapping of the geochemical data distribution (Fig. 3B). The mapping of the units in the PCA reveals a clear link between Unit I and the high organic component ($LOI_{550°C}$ > 20%). Units II and III are positively correlated with Dim1 and thus to the detrital end-member (Fig. 3B). Unit III presents relatively low organic matter content (< 10%, Fig. 2) and is interrupted by many graded beds that are strongly linked to the detrital end-member. According to the geochemical results, Unit IV is characterized by high Ca and low K, Al, Si, Fe and Br (Fig. 3B).

Normally graded deposits

The uppermost part of the BO12 sedimentary sequence presents several normal graded deposits that differ from the matrix.

Type 1. Within Unit I, numerous very dark grey deposits (Munsell colour chart, 10YR/3/1) are distinguished from continuous sedimentation and named T1 (Fig. 4A). From the grain-size analysis, these deposits are characterized by the following stratigraphic succession:

1 A coarse-silty to sandy base ($Q_{50} \approx 30$ μm) rich in organic matter and plant debris (especially well-preserved leaves). The thickness of these facies varies from 3·0 to 2·5 cm and shows a sharp transition with the upper sediment. This portion is rich in Ca and presents relatively high sorting values (> 2·5, Fig. 4A).

2 A central greyish portion in which the silty to clayey grain size remains homogeneous ($Q_{50} \approx 20$ μm). Most of the time this portion is thicker than the coarse base and presents lower sorting values (2 < Sorting < 2·5, Fig. 4A).

3 A thin light grey clayey cap (Q_{50} < 15 μm), thinner than 2 mm, rich in silicates (Fig. 4A, low Ca/K) with high sorting values (> 2·5, Fig. 4A), may be related to the grain-size resolution (including part of the lower facies).

A microscopic description was generated through SEM observations associated with the EDX geochemical results. Generally, the composition of the T1 deposit is represented by 10 μm to 100 μm diameter angular grains, rich in Ca and Mg (Fig. 4B). The remainder of the sediment comprises smaller Ca-rich grains (<10 μm), some feldspars, quartz and other silicates. Moreover, the base of these deposits is erosive.

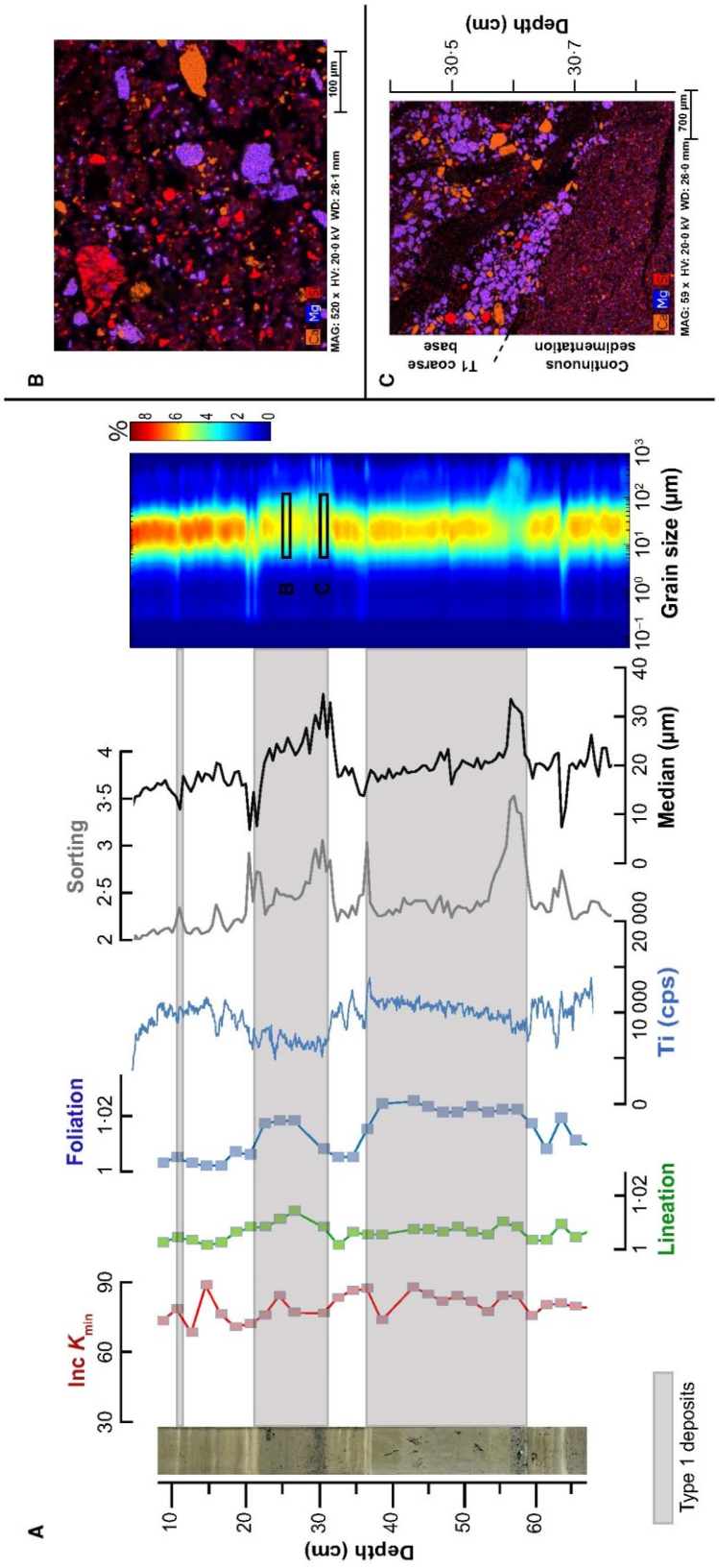

Fig. 4. Detailed results for T1 deposits. (A) AMS results (Inc K_{min}, lineation, and foliation) with Ti content and grain-size parameters for T1 deposit identification: sorting, median (µm) and grain-size matrix (µm, colour range in %). (B) EDX cartography of the elementary composition of the sediment in a T1 deposit. (C) EDX cartography of the elementary composition of the sediment at the boundary of a T1 deposit and the continuous sedimentation. AMS, anisotropy of magnetic susceptibility; EDX, energy dispersive spectroscopy; MAG, magnification; HV, high voltage; WD, working distance; cps, counts per second.

Observations on the continuous sedimentation interval reveal a nearly identical geochemical composition but with smaller silicates (Fig. 4C). The AMS results show a clear difference in the foliation values observed in these deposits, $F > 1{\cdot}02$ compared with the background sedimentation ($F < 1{\cdot}005$). For both cases, the K_{min} axis is quite sub-vertical ($75° < K_{min} < 90°$), and the magnetic lineation does not exceed 1%.

Twenty-eight T1 deposits, with a mean thickness of $27{\cdot}3 \pm 42{\cdot}5$ mm, were identified over the first 443 cm of the sedimentary record and represent 76·3 cm of cumulative depth. Only one such deposit occurs in Unit III and the others are in Unit I.

Type 2. Type 2 (T2) deposits are characterized by a grey (5Y/5/1) graded bed. These deposits are composed of a coarse and erosive base composed of silt ($Q_{50} \approx 30$ μm) becoming slightly finer until a white clayey cap ($Q_{50} < 10$ μm, Fig. 5A). The base of these deposits presents relatively high sorting values (> 2·5, Fig. 5A) comparable to those of T1 deposit bases. Sorting values generally decrease from the base to the top of T2 deposits.

Detailed SEM observation shows that most of Unit III corresponds to a succession of T2 deposits with different thicknesses and occasionally interbedded carbonate mud. The T2 deposits are mainly composed of 10 to 50 μm angular grains, rich in Ca or Ca and Mg with some feldspar and quartz (Fig. 5B). Except for the organic matter content with an $LOI_{550°C} < 10\%$, versus an average of 15% for T1 deposits, the T2 mineralogical composition is similar to that of T1 deposits, indicating the same sediment sources. The AMS results show a clear fluctuation of foliation values within the deposit that differentiate them from background sedimentation (Fig. 5A). However, these values remain close to 1·02 and vary less than previously described for T1, which is probably related to a limited presence of background sedimentation that narrows the comparison.

Despite the lack of other types of deposits within Unit III, properly listing the entire T2 deposit is difficult. A minimum thickness of 3 mm was taken to narrow the analysis. Thus, 72 T2 deposits were identified within the uppermost portion (0 to 436 cm) of the Lake Bohinj sedimentary record, and only two deposits did not belong to Unit III. The identified T2 deposits present a mean thickness of $11{\cdot}5 \pm 10{\cdot}7$ mm and represent 83·5 cm of cumulative depth. These deposits vary from T1 deposits by their lighter colour, their graded-bedding and their smaller thickness.

Pollen

The pollen analysis results (Fig. 6) indicate that sediment in Unit I (0 to 119 cm) contains approximately 60 to 90% tree pollen [beech (*Fagus*), fir (*Abies*) and spruce (*Picea*)] and 9 to 27% herbs (for example, grasses [Poaceae), cereals (Cerealia), ribwort plantain (*Plantago l.*) and goosefoot (Chenopodiaceae)]. The main characteristics of Unit II (119 to 132 cm) and the upper part of Unit III (132 to 240 cm) are a low pollen concentration (3500 to 5000 grains cm^{-3} in most samples) and a very low percentage of tree taxa (especially *Fagus* and *Quercus* at 208 cm). In the lower portion of Unit III (240 to 330·5 cm), the sediment contains more tree pollen (73 to 95%, mostly *Fagus*), and the pollen concentration exceeds 22 000 grains cm^{-3}. The sediment at 330·5 to 440 cm contains 81 to 91% tree pollen, with a higher percentage of *Picea* and a lower percentage of *Fagus* than in Unit III (Fig. 6).

Chronology

Short-lived radionuclides

The upper portion of the BO12 sequence (0 to 12 cm) was measured using gamma spectrometry to build an age–depth model based on short-lived radionuclides. The ^{210}Pb excess profile shows a regular decrease (Fig. 7A) from 1500 mBq g^{-1} to low activities (<50 mBq g^{-1}). The use of a logarithmic scale to plot these data underscores a well-constrained single-point alignment that shows a constant sedimentation rate of $0{\cdot}43 \pm 0{\cdot}013$ mm yr^{-1} ($R^2 = 0{\cdot}99$) for the upper 5·5 cm. The ^{137}Cs profile shows a clear peak between 0·5 cm and 1·0 cm with very high activity (> 1500 mBq g^{-1}); this peak is widely attributed in the literature to nuclear fallout from the 1986 Chernobyl accident (Appleby *et al.*, 1991). The ^{241}Am profile presents a peak between 1·5 cm and 2·0 cm with moderate ^{137}Cs activity that can be associated with the maximum nuclear weapon tests in 1963 (Appleby *et al.*, 1991). Because these two peaks are in agreement with the sedimentation rate derived from the ^{210}Pb excess profile, they were added to the age–depth model to improve it for the upper portion of the sedimentary record (Fig. 7B and C).

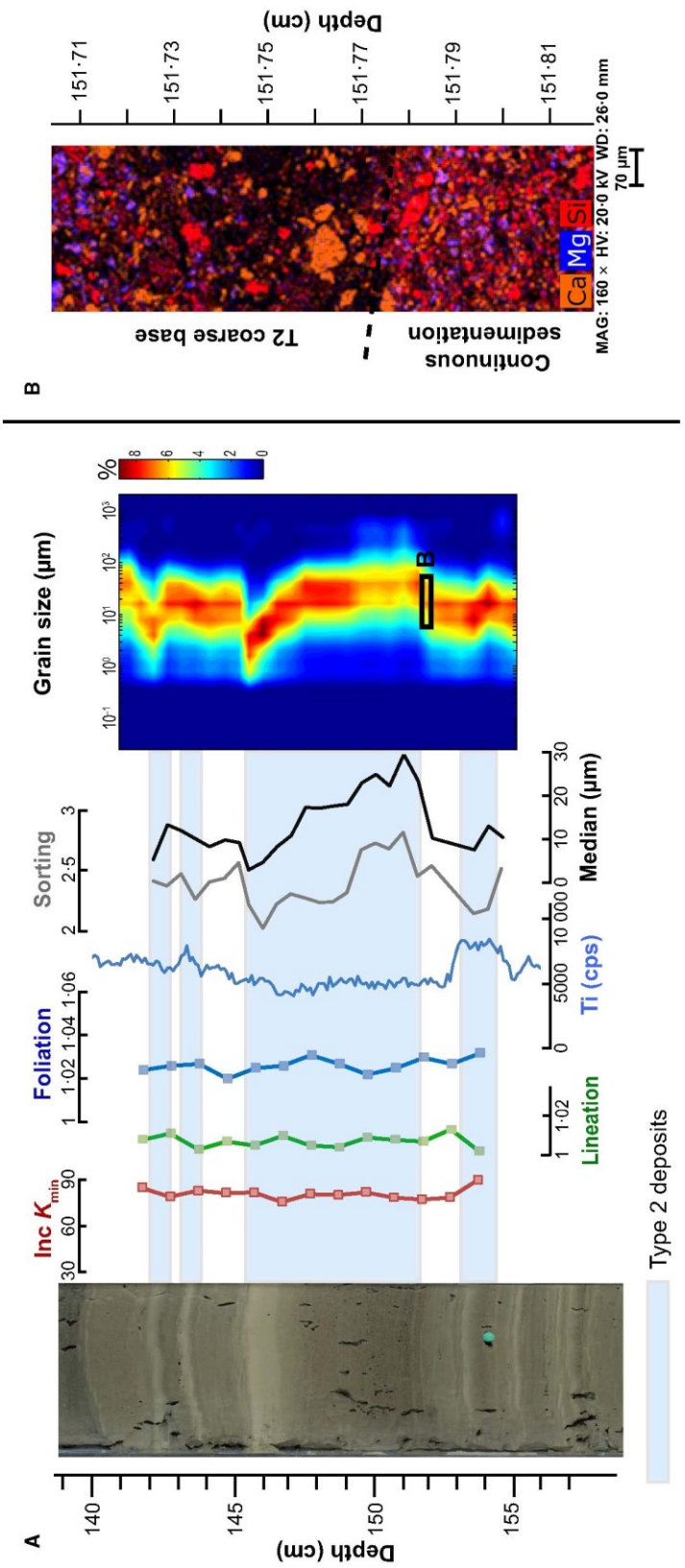

Fig. 5. Detailed results for T2 deposits. (A) T2 deposit identification within Unit III using AMS results (Inc K_{min}, lineation and foliation), Ti content, sorting, median (µm) and grain size (µm, colour range in %). (B) EDX method cartography of the elementary composition of the sediment at the boundary of a T2 deposit and the continuous sedimentation. AMS, anisotropy of magnetic susceptibility; EDX, energy dispersive spectroscopy; MAG, magnification; HV, high voltage; WD, working distance; cps, counts per second.

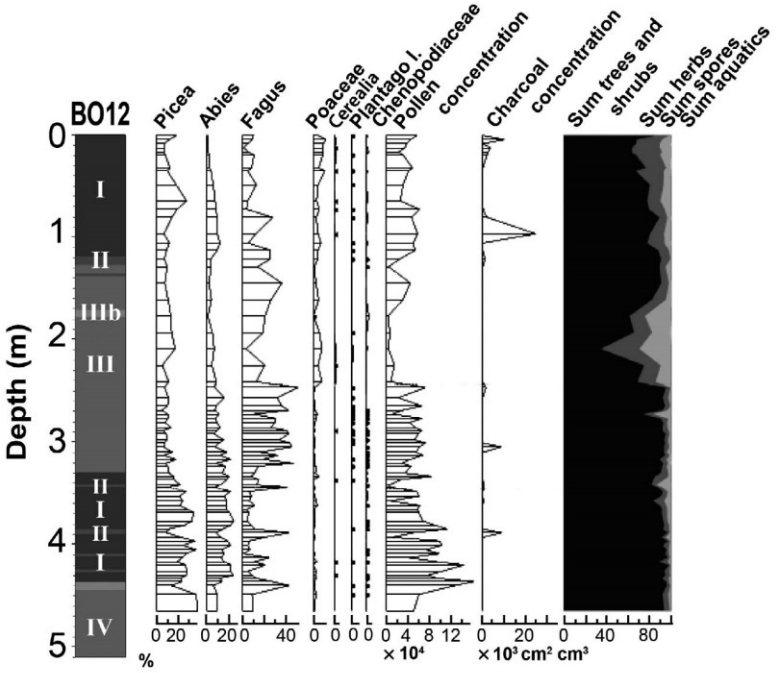

Fig. 6. Pollen diagram. Lithological description of the upper 5 m of Lake Bohinj sedimentary sequence associated with the results of the three main arboreal species, three human-linked species, pollen concentration, charcoal concentration and an area chart presenting the sum of trees and shrubs, herbs, spores and aquatic species (<1%).

^{14}C ages and age–depth model

After calibration, seven of the 21 samples ^{14}C ages (Table 1) were not used (in red, Fig. 7B and C) to build the BO12 sequence age–depth model for the following different reasons: (i) Four of these outliers were taken into Unit IV and present age inversions (Fig. 7C). This information associated with the sedimentological description was used to interpret this unit as instantaneous event reworking of previously deposited sediments (see *Discussion* section). However, the youngest ^{14}C date sampled in this deposit was dated to 6544 ± 90 cal yr BP, comparable to the last ^{14}C age obtained in the background sedimentation at 8 cm from the top of Unit IV (6473 ± 71 cal yr BP). Thus, the age of 6544 ± 90 cal yr BP was used as the minimum age of Unit IV in the input parameters of the model. (ii) The two other outliers gave calibrated ages that were obviously too old (at 53·0 cm and 1037·5 cm). The outlier at 53 cm is located in a T1 deposit, and both were probably reworked from old material. Before generating the age–depth model with the remaining 15 calibrated ages and the short-lived radionuclide ages, the BO12 sequence sediment depth was corrected by subtracting all of the deposits, considered to have been deposited instantaneously (i.e. T1 and T2 beds >3 mm thick, and Unit IV) to build an event-free depth (e.g. Wilhelm *et al.*, 2012). Due to the erosive base of Unit IV (9·98 m), a hiatus splits the sedimentary sequence into two halves. The upper portion starts from Unit IV to the top of the sequence. The age of this sequence is forced by the youngest ^{14}C date of Unit IV. To build a relevant age model, a smooth spline model was applied for this portion (Fig. 7B). To remove any bias from the hiatus, another model was run for the lower part of the sequence, from the bottom of the core to the base of Unit IV. As this part only hosts two ^{14}C dates, a linear interpolation model is used here. The global age–depth model is used to date all instantaneous deposits. The vertical bars represent the age of events thicker than 3 mm and uncertainties (2σ) resulting from the ^{14}C ages (Fig. 7C).

The first 12 m of the Lake Bohinj sedimentary record covers at least 11 000 years (Fig. 7C). The polling of the two previous models reveals an erosional hiatus of 3000 years at the bottom of Unit IV. The sedimentation rate reveals three different periods of sedimentation in the upper part of the sedimentary record (0 to 443 cm, Fig. 7B): (i) a low sedimentation rate (0·3 to 0·5 mm yr^{-1}) between 6600 cal yr BP and 2900 cal yr BP. Within this interval, the sedimentation rate rises slightly towards younger ages; (ii) the sedimentation rate increases suddenly between 2800 cal yr BP and 2100 cal yr BP,

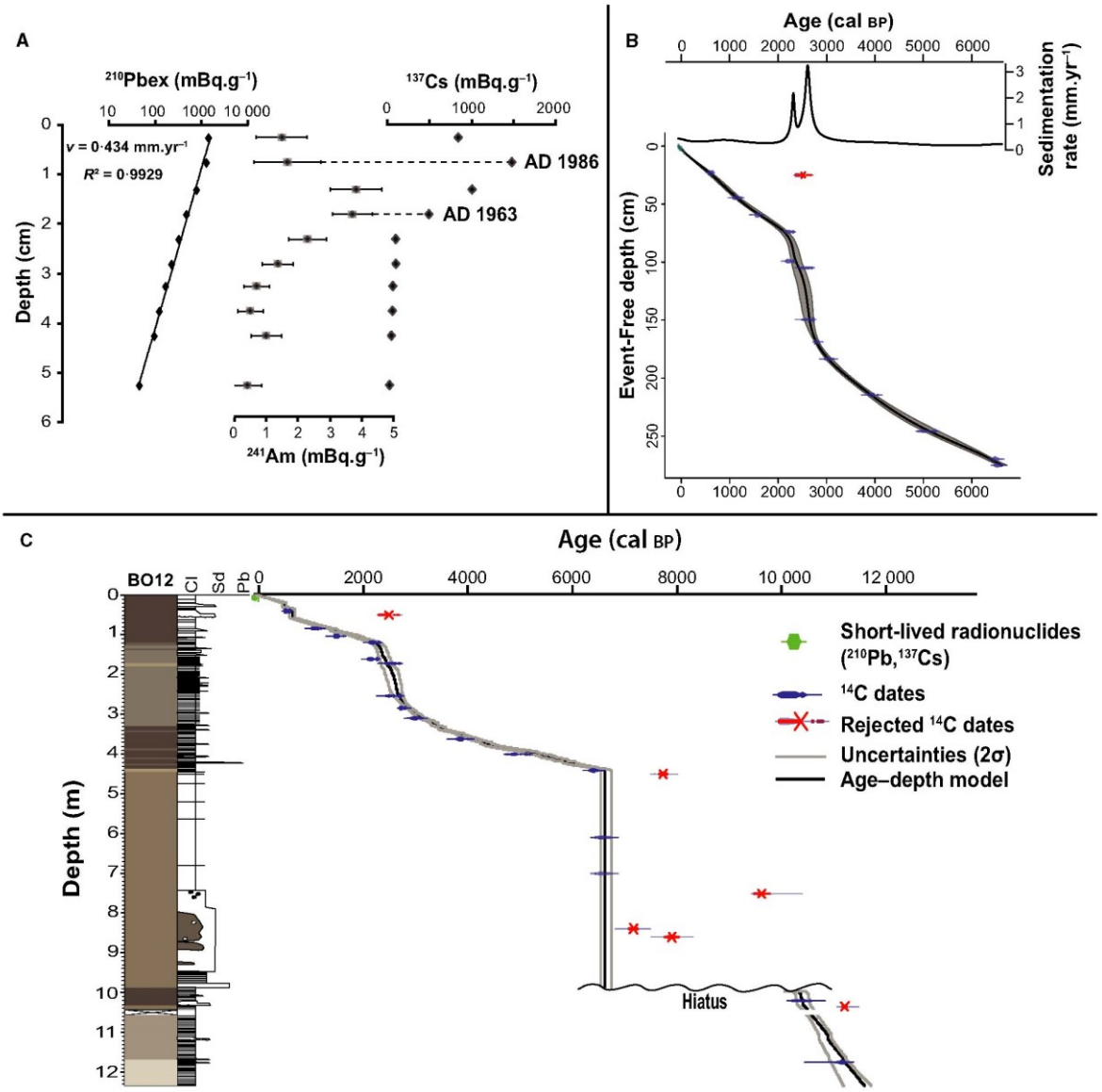

Fig. 7. Age–depth models. (A) Short-lived radionuclide data with the ^{210}Pb excess in logarithmic scale associated with the ^{241}Am and ^{137}Cs profiles. (B) Age–depth model in event-free depth with the mean sedimentation rate. (C) Age–depth model from radiocarbon and short-lived radionuclide dates.

reaching two maxima of 3·2 mm yr^{-1} at approximately 2600 cal yr BP and 2·2 mm yr^{-1} at 2300 cal yr BP associated with a decrease to 0·9 mm yr^{-1} at approximately 2400 cal yr BP; (c) finally, over the last 2100 years, the sedimentation rate has remained very low and quite stable at approximately 0·5 mm yr^{-1}. In the period from 2800 to 2100 cal yr BP, the high variability of the sedimentation rate could be a result of a ^{14}C age plateau (Sabatier *et al.*, 2010b). Between 2350 cal yr BP and 2700 cal yr BP, the calibration curve presents a ^{14}C age plateau caused by a strong increase of ^{14}C production in the atmosphere at 2750 cal yr BP (Reimer *et al.*, 2013), known as the 'Hallstatt disaster'. Thus, over this period, the sedimentation rate obviously increases to the highest of the Bohinj sediment sequence; however, in the *Discussion* below, the

Table 1. Radiocarbon ages for the Lake Bohinj sediment core. Composite depth was calculated by excluding the graded beds that were considered instantaneous deposits. Samples in bold correspond to dates excluded from the age–depth model.

Sample name	Core	MCD (cm)	Composite depth (cm)	Radiocarbon age	Age cal yr BP 2σ range	Sample type
Poz-73377	BO12_01A	34·0	22·9	630 ± 30	552 to 662	–
SacA41394	**BO12_01A**	**53·0**	**25·0**	**2410 ± 30**	**2351 to 2684**	**Wood**
SacA36003	BO12_01A	78·5	44·5	1210 ± 30	1059 to 1255	Twig
Poz-73378	BO12_01A	95·0	56·2	1665 ± 30	1446 to 1691	–
SacA41395	BO12_02A	116·0	73·9	2230 ± 30	2153 to 2332	Wood
SacA41396	BO12_02A	154·3	99·2	2245 ± 30	2156 to 2340	Twig
SacA41397	BO12_02A	165·8	104·9	2485 ± 30	2439 to 2724	–
SacA36004	BO12_02A	248·0	149·5	2545 ± 35	2494 to 2751	Leaf
SacA41398	BO12_02A	277·8	168·8	2675 ± 30	2750 to 2844	Twig
SacA41399	BO12_01B	303·8	183·4	2900 ± 30	2953 to 3155	Twig
SacA41400	BO12_02B	355·0	214·5	3625 ± 30	3849 to 4069	Twig
SacA36005	BO12_02B	395·5	245·7	4430 ± 35	4874 to 5276	Leaf
SacA41401	BO12_01C	435·3	269·7	5705 ± 30	6408 to 6600	Moss
SacA36006	**BO12_01C**	**444·5**	**275·1**	**6770 ± 40**	**7576 to 7674**	**Wood**
SacA36007	**BO12_03C**	**605·0**	**275·1**	**5740 ± 30**	**6454 to 6634**	**Wood**
SacA36008	**BO12_01D**	**759·0**	**275·1**	**8675 ± 40**	**9542 to 9732**	**Wood**
SacA36009	**BO12_03D**	**843·5**	**275·1**	**6300 ± 30**	**7166 to 7274**	**Wood**
SacA36010	**BO12_01E**	**864·0**	**275·1**	**7105 ± 50**	**7841 to 8011**	**Wood**
SacA36011	BO12_01E	1014·5	282·6	9205 ± 45	10249 to 10495	Wood
SacA36014	**BO12_01E**	**1037·5**	**294·8**	**9815 ± 30**	**11198 to 11252**	**Wood**
SacA36012	BO12_01F	1169·5	411·4	9740 ± 45	10907 to 11243	Wood

high sedimentation rate variability in this period was taken with caution.

DISCUSSION

Identification and triggering mechanisms for sedimentary units and layers

T1 deposits

For T1 deposits, the grain-size analysis and lithological observation results reveal an internal depositional structure organized into three distinct parts: a coarse sandy base, a well-developed homogeneous part and a clayey top. This stratigraphic succession is characteristic of 'homogenite'-type deposits previously defined by Chapron *et al.* (1999, 2016) 'as thick homogeneous mud layers starting with few sand layers'. The thickest T1 deposit (36·1 to 58·5 cm) is identified on the seismic profile, where it develops a transparent acoustic facies and is laterally associated with a mass-wasting deposit linked to slides on the eastern and northern slopes of Lake Bohinj (MWD-A; Figs 1D and S1B).

The interpretation of a mass movement origin for T1 deposits is strengthened by: (i) the observation of well-preserved leaves in the coarse base of these deposits, certainly deposited earlier on the banks of the lake; (ii) the EDX results that gave an identical composition for these deposits and the continuous sedimentation with the presence of authigenic carbonate; (iii) the presence of a too old ^{14}C age (53 cm, Fig. 7C) in the T1 deposit illustrated in Fig. 4, suggesting reworking of previously deposited sediment; and (iv) the AMS results with high foliation in T1 deposits compared to that of continuous sedimentation (Fig. 4) that imply a strong initial segregation from gravity-reworked sediments associated with the resuspension of the fine fraction linked to a seiche effect (Chapron, 1999; St-Onge *et al.*, 2008; Campos *et al.*, 2013).

Different mechanisms can trigger subaquatic landslides such as MWDs: for example, earthquakes, spontaneous delta collapses and considerable lake-level changes (Sauerbrey *et al.*, 2013). The coring site is located in the eastern basin, separated from the western basin and the delta by a north–south moraine ridge 15 m higher than the bottom of the western basin. This elevation is thought to be high enough to prevent from hyperpycnal flow from the delta and sediment contribution during delta collapses from entering the eastern basin. Surface water data recorded on Lake

Bohinj show several recent lake-level variations >250 cm (Agencija Republike Slovenije Za Okolje) without any specific deposit in this well-dated period (for example, 10 November 1927, 14 November 1969 and 25 December 2009). This lack of sediment deposition during intense precipitation events in the watershed confirms that the eastern basin and the coring site are not influenced by hyperpycnal flows during flood events. As suggested by the rock watershed composition, no or very few fine sediments (glacio-lacustrine sediments along the southern and eastern sides of the lake margin) could be mobilized during flood events and trigger flood deposits in the modern lake system. Here, a slide triggered by earthquake shaking of the lake area is more likely to produce T1 deposits.

To test the seismic trigger hypothesis for T1 deposits, historical earthquake dates were compared with the T1 ages. The ages of the three most recent T1 deposits, derived from the age–depth model, correspond to three strong historical earthquakes (Rovida *et al.*, 2016; Table S1):

1 The 1348 'Villach' earthquake (MSK I_o of IX to X) with an estimated epicentral distance of 76 km, corresponding to a 22·4 cm thick T1 deposit with an estimated age of 1315 ± 52 AD at 36·1 to 58·5 cm depth (Table S1)

2 The 1511 'Idrija' earthquake (MSK I_o of X) with an estimated epicentral distance of 35 km. This earthquake corresponds to a 9·8 cm T1 deposit with an estimated age of 1471 ± 42 AD at 20·8 to 30·7 cm depth (Table S1)

3 The 1690 'Kaernten' earthquake (MSK I_o of VII to IX) with an estimated epicentral distance of 39 km, corresponding to a 1 cm T1 deposit (at 15·5 to 16·1 cm depth, Table S1) with a less consistent age of 1596 ± 30 AD, probably linked to the transition between the radionuclides age model and the ^{14}C dates

Considering these arguments, T1 deposits are interpreted as instantaneous deposits derived from earthquake-induced mass movements reworking previously deposited sediments.

T2 deposits

The geochemistry results from EDX and XRF are not sufficient to dissociate T1 and T2 deposits and reveal an equivalent geochemical composition, suggesting that the sediment source is the same. The T2 deposits show an erosive base and a fining upward grain size with a clayey cap (Fig. 5B), which is characteristic of turbidite-type deposits (Sturm & Matter, 1978; Sauerbrey *et al.*, 2013).

Moreover, the AMS results from T1 and T2 deposits are very similar, whereas the average susceptibility (K_m) is higher in T2. According to the *L*, *F* and *P* magnetic parameters, the shape of the ellipsoid is statistically the same in both deposits (Fig. 8), suggesting the same depositional processes.

The grain orientation is determined by grain settling in the water column driven by: (i) gravity; (ii) the geomagnetic field; and (iii) water currents. The grain orientation may also be modified during particle deposition or after deposition by biological and physical processes (Ellwood & Ledbetter, 1977). Resettling under specific resuspended fine fraction conditions may lead to a strong anisotropy, as shown by Campos *et al.* (2013) in seismically induced homogenites. The foliation present in T1 and T2 deposits (2·0 to 2·5%) is four to five times higher than that of the background sedimentation (0·5%). Because all other sedimentological proxies are similar, this foliation is interpreted as due to decantation of resuspended material due to MWDs.

This interpretation is reinforced by the observation on seismic profiles of two coeval MWDs in the eastern basin (MWD-C, Fig. 1D) that could be stratigraphically associated with the development of one major turbidite (a T2 deposit on core BO12). The AMS results do not allow the exclusion of a hyperpycnal origin for T2 deposits. However, as the location of the coring site is supposed to not be influenced by hyperpycnal flows, T2 deposits are likely to have a similar origin to that of T1 deposits and to be induced by earthquake shaking. Yet, the high frequency of occurrence of T2 deposits during a period of lack of T1 deposits appears as a change in sedimentological processes for the same triggering mechanism. Thus, the origin of these deposits will be discussed separately, and T2 deposits will not be used to reconstruct the evolution of local seismicity.

Unit IV

The different facies of Unit IV are as follows: (i) a coarse sandy base; (ii) a coarse sandy facies interrupted by patches that are rich in organic matter; (iii) a directly overlying homogenous silty to clayey facies; and (iv) a thin clayey cap (Figs 2 and S2). This sequence presents similarities to the T1 deposits. The lower coarse and erosive facies could correspond to a mass-flow

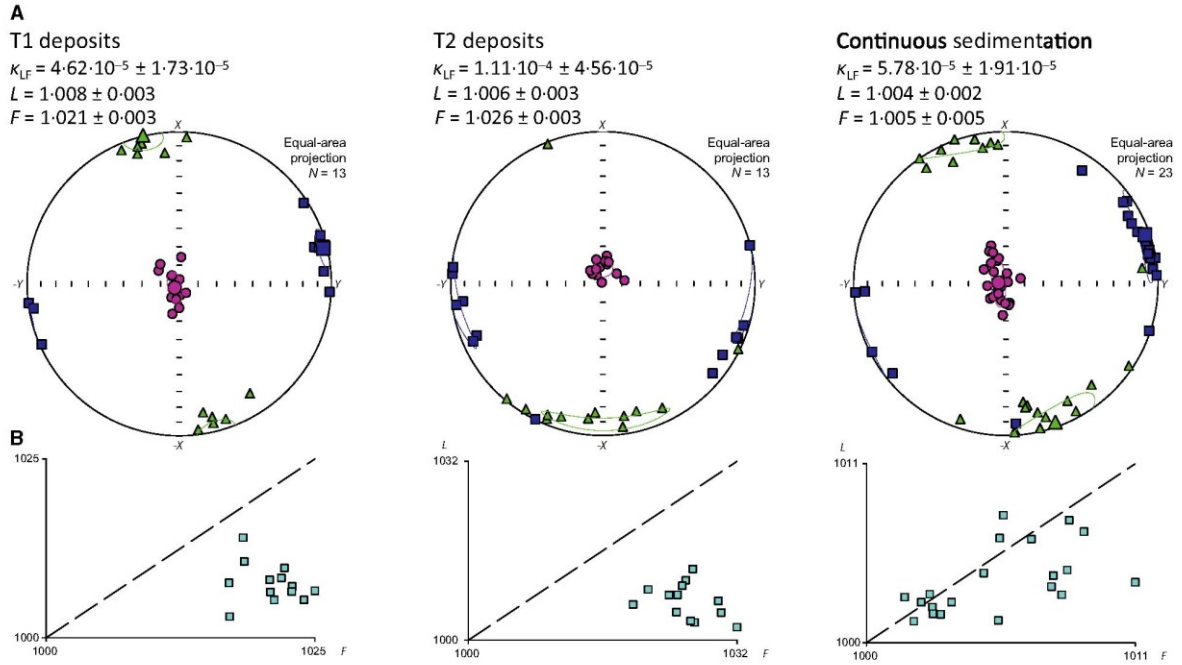

Fig. 8. Anisotropy of magnetic susceptibility (AMS) results. (A) Stereographic projection of the AMS axes for the different deposits discussed. (B) Flinn diagram (*L*/*F*) showing the strong oblate shape of the AMS ellipsoid for T1 and T2 deposits.

deposit directly overlain by a homogenite-type deposit similar to T1 deposits. The clayey cap is probably linked to a cogenetic turbid flow. Thus, Unit IV can be considered as a single deposit triggered by a slip of previously deposited sediment leading to one or several MWD accompanied by a turbidity flow. Seismic profiles reinforced this interpretation by identifying the top of a main mass-wasting deposit at approximately 450 cm b.l.f. at the coring site (MWD-D, Fig. 1D). From lithographic description and the AMS results (Fig. S2), the homogeneous portion of Unit IV is considered to be triggered by a seiche effect. Indeed, this portion shows high and constant foliation values (comparable to T1 deposits), implying resuspension of the fine fraction linked to a seiche effect (Chapron, 1999; St-Onge *et al.*, 2008; Campos *et al.*, 2013). The location of the coring site allows the exclusion of a delta collapse origin for this unit.

Similarities between Unit IV and T1 deposits, associated with the dating results that showed five age inversions in this unit (Fig. 7C), lead the authors to conclude that Unit IV is an instantaneous event induced by a nearby and/or high-intensity earthquake.

6600 years of sedimentary record

Between 6617 ± 94 cal yr BP and 3450 ± 75 cal yr BP, the Lake Bohinj record presents good evidence of a well-developed mixed forest of *Picea*, *Abies*, *Fagus* and *Quercus* (443 to 332 cm in Fig. 6) that limited erosion processes in the watershed and led to low sediment accumulation (Fig. 9). Sediment deposited on the slope of the lake could easily be reworked by an earthquake. Over this period, 19 T1 deposits occurred, representing a significant portion of the sedimentation (32·2%). At approximately 3450 ± 75 cal yr BP, an increase in sedimentation rate coupled with a change in forest composition suggests a modification in the erosion pattern that induced a sharp modification of the sedimentation and the appearance of the first T2 deposit in Lake Bohinj. This quick transition was accompanied by a sharp decrease in organic matter input into the lake (Fig. 9) and a change in forest composition: an increase in *Fagus* and decrease in *Picea* and *Abies* (332 cm; Fig. 6). Between 2900 cal yr BP and 2100 cal yr BP, the sedimentation rate increased suddenly to a maximum of 3·2 mm yr^{-1} (2600 cal yr BP, Fig. 9). Furthermore, pollen results show a decrease in arboreal

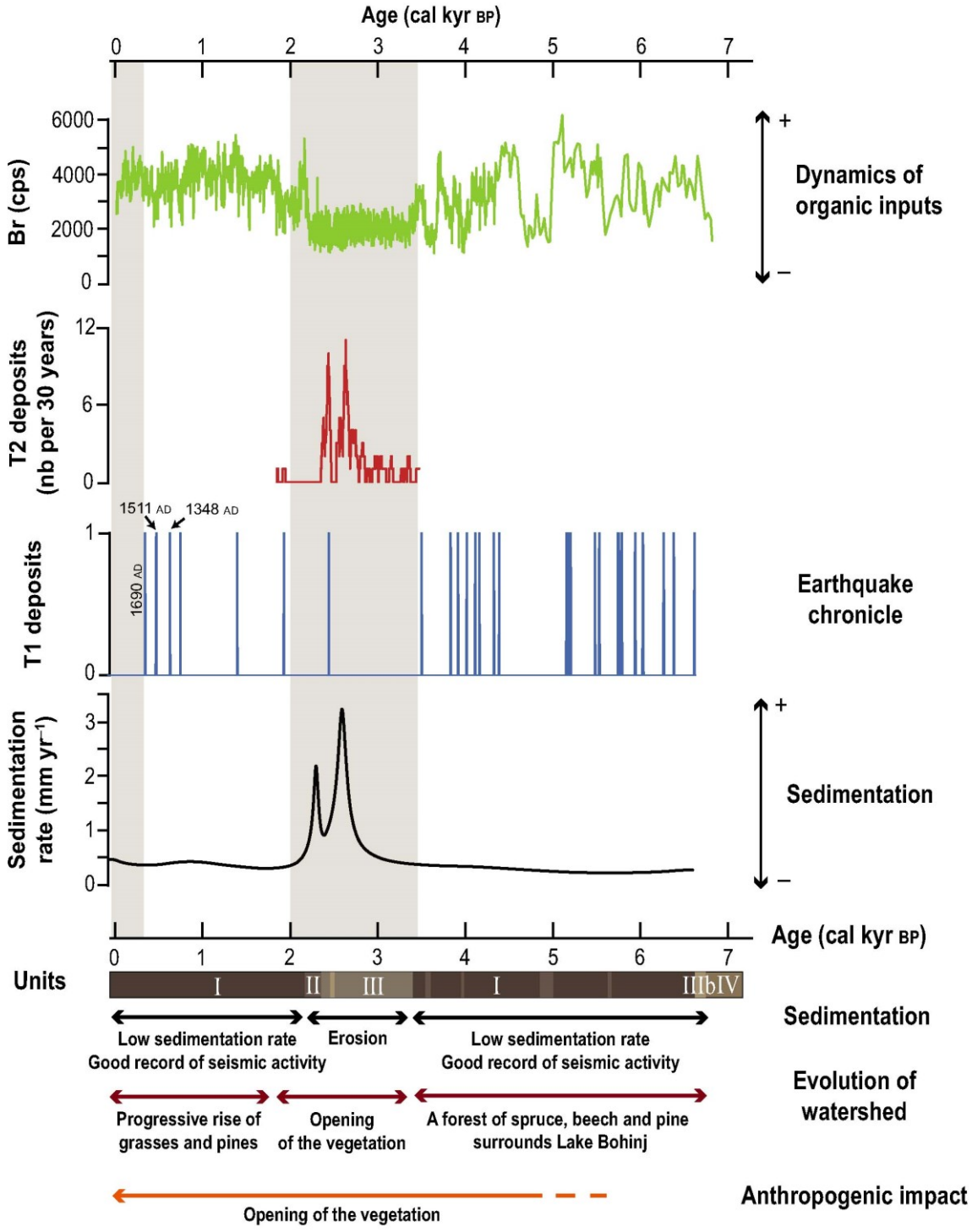

Fig. 9. Comparison between the organic input dynamic (Br), T2 frequency and T1 frequency with major historical earthquakes and the mean sedimentation rate. The anthropogenic impact and the evolution of the watershed are interpreted from the pollen diagram (Fig. 6). Grey shading corresponds to intervals with potential higher earthquake-sensitivity threshold index (ESTI). cps, counts per second.

taxa since 3500 cal yr BP to a minimum from 2800 to 2400 cal yr BP in the Iron Age, when forest cutting was probably associated with metallurgical activities (210 to 73 cm; Fig. 6; Horvat & Stele, 2006; Mohorič, 1969; Ogrin, 2006). These changes in the watershed imply that the wooded vegetation around the lake decreased (Fig. 9) and that the soil became more easily erodible, resulting in a sedimentation rate increase (Arnaud *et al.*, 2016; Bajard *et al.*, 2016). The sedimentation rate subsequently decreases until 2050 cal yr BP. The period since 2050 cal yr BP corresponds to the return of Unit I deposition associated with a sharp increase in organic matter content (OM > 10%) and a return to a more forested environment (Fig. 9). During this time, there is a strong decrease in T2 deposits and a return of earthquake recording by T1 deposits. Thus, the main change induced by human activity in the watershed produced different instantaneous deposit signatures in the lake sediment (T1 and T2, Fig. 9).

Earthquake record

The Lake Bohinj chronicle starts with the Unit IV deposit (Fig. 7C). With 5·5 m of sediment deposited, the Unit IV deposit corresponds to the main earthquake-triggered deposit of the Lake Bohinj record. This earthquake probably led to major geomorphological changes such as rock falls and landslides in the Lake Bohinj vicinity. For instance, 25 km away, the Bovec Terrace (Fig. 1A) has a base composed of subangular and angular boulders atop palaeo-lake sediments (Marjanac *et al.*, 2001; Bavec *et al.*, 2004). The sharp transition between lacustrine sediments and the Bovec Terrace is dated at 6590 to 6910 cal yr BP and could coincide with geomorphological after-effects of the 6617 ± 94 cal yr BP earthquake recorded in Lake Bohinj sediment.

Although this study allows the analysis of past earthquakes, regional seismicity is not entirely recorded in Lake Bohinj sediment. Completeness of the earthquake record by earthquake-triggered mass movement deposits depends on: (i) the distance between the earthquake epicentre and the lake; (ii) the energy released by the co-seismic rupture; and (iii) lake sediment parameters such as sediment texture and sedimentation rate (Beck, 2009). These three factors define the sensitivity of a lake to recording a seismic event. To characterize the sensitivity of Lake Bohinj, the earthquake-sensitivity threshold index (ESTI) method was applied (Fig. 10A; Wilhelm *et al.*, 2016). Using a detailed historical record of regional earthquakes (Rovida *et al.*, 2016), epicentral intensity (MSK) was plotted against the epicentral distance of each regional historical earthquake to the lake (Fig. 10A). As shown above, three historical earthquakes were correlated to the first three T1 deposits.

To calculate the ESTI, an empirical limit was defined that separates recorded from non-recorded earthquakes in Lake Bohinj sediment (Fig. 10A). For future correlation with previous analogous studies in the Alps, the same input parameters were used for the sensitivity threshold slope [i.e. $a = 1{\cdot}13$ in $y = a\ \mathrm{Ln}(x) + b$]. The ESTI was calculated using the inverse of the intercept of the threshold lines with the intensity axis at 10 km from the lake (Wilhelm *et al.*, 2016). This index increases with the lake's sensitivity to recording an earthquake. The ESTI for Lake Bohinj is estimated at 0·13 ± 0·01 in agreement with observed trends in Alpine lakes (Fig. 10B; Wilhelm *et al.*, 2016). However, it should be noted that the ESTI is known to be highly dependent on the sedimentation rate and mode (Chapron *et al.*, 2016; Wilhelm *et al.*, 2016). The higher the sedimentation rate is, the higher the ESTI should be; thus, more earthquakes could be recorded. Considering the high variation of the sedimentation rate along the record (Fig. 9), the sensitivity of Lake Bohinj should change over time, and thus the earthquake record should be taken with great caution. Only three of five historical seismic events are recorded by Lake Bohinj sediments (Fig. 10A). This could be due to the seismic historical data set itself: earthquakes with medium to high epicentral intensities ($VI < I_o$) are defined by a large rupture area (Wells & Coppersmith, 1994) and not by a single-point epicentre. For instance, if the 1942 earthquake is located some kilometres away from the current position, it will be under the record limit defined by the ESTI (Fig. 10A). Moreover, the lack of deposits triggered by earthquake shaking between 1690 AD and 2012 AD, despite the 1976 and 1942 earthquakes (Fig. 10A), cannot be explained by a decrease in the sedimentation rate (increase from 0·32 to 0·44 mm yr^{-1}) but may also be the result of anthropization of the banks of Lake Bohinj, decreasing the ESTI by stabilizing the shores.

From the 6600 years of sedimentary record, 29 earthquakes were identified and dated through T1 deposits and Unit IV (Table S1). This

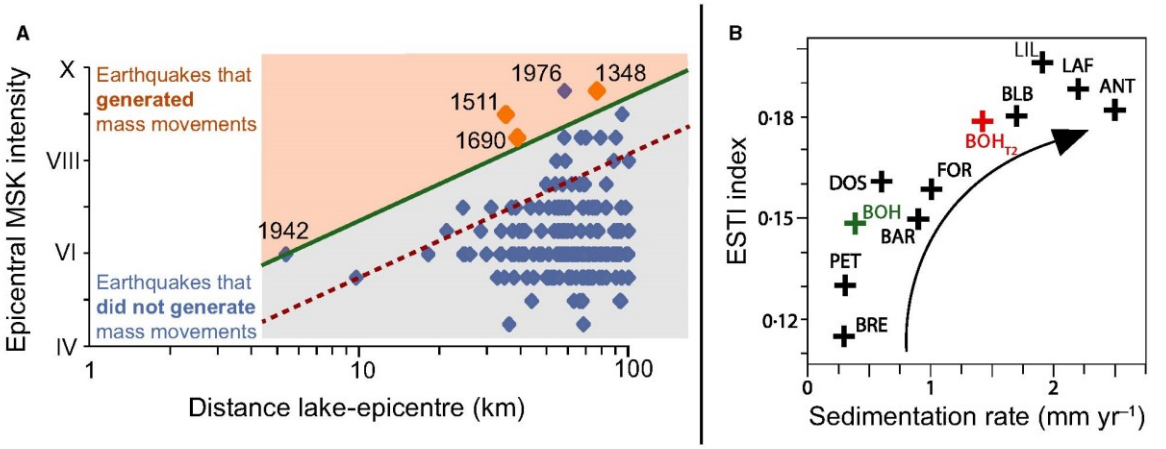

Fig. 10. Earthquake-sensitivity threshold index (ESTI) estimation for Lake Bohinj. (A) Lake Bohinj sequence results associated with CPTI15 data. Blue diamonds show earthquakes that did not generate mass movements in the Lake Bohinj sequence, orange diamonds show earthquakes that generated mass movement deposits. The green line represents the limit of Lake Bohinj sensitivity to earthquakes calculated for the historical period. The red dotted line represents the hypothetical limit of Lake Bohinj sensitivity with an ESTI of 0·18 calculated for the mean sedimentation rate over the period of 3500 to 2000 cal yr BP, unique period with T2 deposits. (B) The ESTI versus sedimentation rate for Lake Bohinj (green) over the last centuries with previous results (black) from Wilhelm *et al.* (2016). The red cross corresponds to the ESTI and sedimentation rate for the period of T2 deposits (3500 to 2000 cal yr BP). This diagram suggests that a significant increase (decrease) in the sedimentation rate appears to be the dominant factor resulting in an increase (decrease) in the ESTI. BAR, Lake Blanc Aiguilles Rouges; ANT, Lake Anterne; BRE, Lake Brévent; BLB, Lake Blanc Belledonne; DOS, Lake Grand Doménon; LAF, Lake Laffrey; FOR, Lake Foréant; PET, Lake Petit and BOH, Lake Bohinj (Wilhelm *et al.*, 2016); LIL, Lake Inferiore de Laures (Wilhelm *et al.*, 2017); MSK, Medvedev–Sponheuer–Karnik.

chronicle provides a 224 year ± 257 mean return period for large earthquakes. However, most of these earthquakes (20 of 29) are recorded before 3500 cal yr BP (Fig. 9). The chronicle shows several time intervals in which local seismic activity was not recorded in the Lake Bohinj sedimentary sequence (Fig. 9 and Table S1): (i) between 5150 cal yr BP and 4400 cal yr BP; (ii) between 3500 cal yr BP and 2000 cal yr BP, in which only one T1 deposit is identified; (iii) between 1950 cal yr BP and 1400 cal yr BP; and (iv) between 1400 cal yr BP and 750 cal yr BP. These low seismic activity intervals can only be explained by a low ESTI or by a period of no earthquake occurrence.

The lack of T1 deposits between 3500 cal yr BP and 2000 cal yr BP (Fig. 9) appears, while the sedimentation rate is the highest (maximum value of 3·2 mm yr^{-1}, mean value of 1·45 mm yr^{-1}); thus, earthquakes should be more easily recorded in the sediment sequence. During this period, only one earthquake is registered by T1 deposits, whereas a new type of instantaneous deposit appears (T2 deposit). A possible explanation is that these T2 deposits, representing the same triggering processes (see *Identification and triggering mechanisms for sedimentary units and layers* section), could also be induced by earthquakes during this period of high environmental change. Here, T2 deposits occur simultaneously with an increase in sedimentation rate and 70 of them are recorded along the highest sedimentation rate period. As the sedimentation rate increased between 3500 cal yr BP and 2000 cal yr BP, there was more sediment deposition on the slopes of the lake that increased Lake Bohinj's ESTI; thus, more earthquakes could have been recorded.

To test the seismic trigger for T2 deposits, a new ESTI was tested here of approximately 0·18 from the relation between sedimentation rate and ESTI index (Fig. 10B) over the period between 3500 cal yr BP and 2000 cal yr BP with an average sedimentation rate of 1·45 mm yr^{-1}. A new threshold line, based on the ESTI for the period of T2 deposit occurrence, was drawn (Fig. 10A). The comparison of this threshold with the historical data set highlights the number of seismic events that could have been recorded in this condition: 22 for approximately

800 years (Fig. 10A), thus an earthquake every 36 years. However, the present authors can consider that the available data set is better documented for the last 350 years (Rovida *et al.*, 2016). For this period, 18 events are above the ESTI threshold line, providing a mean return period of 19 years. Over the period between 3500 cal yr BP and 2000 cal yr BP, 72 T2 deposits are recorded in Lake Bohinj sediments, thus an earthquake every 21 years. If it is hypothesized that the seismic activity remains constant between the last 350 years and the 3500 to 2000 cal yr BP period, the number of T2 deposits is equivalent to the number of historical earthquakes which can theoretically be registered in the lake sediment. Therefore, the increased sensitivity of Lake Bohinj to record earthquakes due to a sedimentation rate increase could be at the origin of T2 deposits. This strictly hypothetical assumption illustrates well the effect of an ESTI modification: when an ESTI is increased even slightly, due to a sedimentation rate change, the number of seismic events recorded by Lake Bohinj increases considerably. Thus, it is not acceptable to propose a return period for seismic activity recorded in lake sediment if the sedimentation rate varies significantly along the record.

Over the period between 3500 cal yr BP and 2000 cal yr BP, the pollen diagram (Fig 6) indicates that grassland increased despite forest cover (Fig. 9), which increased the soil's erodibility (Arnaud *et al.*, 2016; Bajard *et al.*, 2016). Because the soils are less protected by vegetation cover, they are more sensitive to erosion and sediment could be carried into the lake and easily reworked during a seismic event. Thus, T2 deposits or at least a major portion of T2 deposits are probably linked to earthquakes; however, because the modification of deposit type for the same triggering mechanism is not well understood, T2 deposits are not included in the earthquake chronicle. If T2 deposits are not triggered by an earthquake, the lack of earthquake recording in Lake Bohinj sediment during this 1500 year long period must be linked to a gap of regional earthquakes and appears difficult to explain.

For the three other low local seismic activity intervals ('a', 'c' and 'd'), no sedimentological argument was found that could explain a decrease in the lake's sensitivity to recording earthquakes. Although the sedimentation rate is low (>0·5 mm yr^{-1}) in these time periods, it is comparable with the rate during periods of high seismic activity recorded in Lake Bohinj sediment (Fig. 9). Moreover, there is no remarkable change in either the sedimentation processes or the pollen diagram. Thus, these intervals could be due to the absence of major earthquakes in the Lake Bohinj vicinity.

Finally, it should be noted that this record does not allow calculation of past earthquake intensity using the T1 deposit thickness. For instance, the 1348 'Villach' and 1511 'Idrija' earthquakes are 22·4 cm and 9·9 cm thick, respectively, with an equivalent epicentral intensity and an estimated distance of 76 km and 35 km, respectively. The period between earthquakes is probably too short to allow a reloading of sediment on slopes and shores of Lake Bohinj to provide a sufficient amount of sediment to feed the second earthquake-induced sediment deposit.

Thus, this earthquake chronicle is not exhaustive and probably does not record earthquakes of the same intensity over time due to sedimentation rate changes. However, it is the first Holocene earthquake calendar in this area and should be correlated to other lake sediment records in this area to: (i) improve the location precision; (ii) record more regional earthquakes without lake-specific sediment process dynamics; and (iii) estimate the intensity of past seismic events.

CONCLUSION

This study is the first detailed earthquake chronicle over the last 6600 years in the Julian Alps. Twenty-nine earthquakes are recorded by homogenite-type deposits in Lake Bohinj sediments, and the last three deposits are linked to three main historical regional earthquakes (1348 AD, 1511 AD and 1690 AD). The chronicle begins with a potential seismic event that occurred at approximately 6617 ± 94 cal yr BP and led to a 5·55 m thick mass-wasting deposit (MWD) at the coring site. This major event probably induced important geomorphological changes at a local scale.

The regional seismic activity recorded by a lake is highly connected to earthquake settings, distance and the lake's sensitivity to recording a seismic event (earthquake-sensitivity threshold index – ESTI), which is related to the sedimentation rate. The Bohinj earthquake chronicle presents several time intervals with no local seismic activity recorded by homogenite-type deposits. One such interval (3500 to 2000 cal yr BP) is also

characterized by a major destabilization in the watershed by human activities that led to increases in erosion and the sedimentation rate. This period coincides with the appearance of turbidite-type deposits, presenting the same geochemical and magnetic properties as homogenite-type deposits. The increasing sedimentation rate led to an increase in the ESTI, which suggests that more earthquakes should have been recorded. The high turbidite rate identified could be the consequence of this sensitivity increase, and thus these turbidites could be triggered by earthquakes. Between 1690 AD and 2012 AD, human activity in the watershed probably decreased the lake's sensitivity and prevented the recording of seismic events. For the three other intervals (5150 to 4400 cal yr BP; 1950 to 1400 cal yr BP; 1400 to 750 cal yr BP), there is no argument in favour of environmental changes in the watershed that may have led to changes in the sedimentation rate or sedimentation processes. Therefore, these periods could be linked to the lack of major seismic events during this time. Due to the regional tectonic regime, determining a specific link between earthquakes and faults is very difficult, but this lake-based palaeoseismological study could improve the long-term regional tectonic knowledge of this high seismic activity region of the Alps. However, if a sedimentary sequence presents a variable sedimentation rate, and thus variable ESTI, it is impossible to present a mean return period for seismic activity recorded by the lake system.

ACKNOWLEDGEMENTS

We thank the Laboratoire Souterrain de Modane (France) for the gamma spectrometry measurements and EDYTEM (Environnement, Dynamique et Territoires de Montagne, France) for the X-ray fluorescence analyses. We are grateful to ARSO (Slovenian Environmental Agency) for permission (No. 35620-1078/2012-6) to core Lake Bohinj and to Robert Jensterle for help with the seismic reflection survey. D. Valoh, J. Dirjec, S. von Grafenstein, S. Kuharič and M. Zaplatil helped with coring. R. Trček (ARSO) helped with interpreting hydrological data collected at Sveti Duh gauging station. Coring was funded by INSU (Institut National des sciences de l'Univers, CNRS, France) and CEA (Commissariat à l'Energie Atomique et aux Energies Altérnatives) through Mistrals (Paleomex). The pollen analysis was funded by the Slovenian Research Agency (ARRS, Research programme P6-0064, Archaeological research 2015 to 2021). The authors wish to thank the Chief Editor Dr Nigel Mountney, the Associate Editor Dr Vern Manville and the two anonymous reviewers for their comments which greatly improved the original manuscript.

REFERENCES

Appleby, P.G., Richardson, N. and **Nolan, P.J.** (1991) ^{241}Am dating of lake sediments. In: *Environmental History and Palaeolimnology* (Eds J.P. Smith, P.G. Appleby, R.W. Battarbee, J.A. Dearing, R. Flower, E.Y. Haworth, F. Oldfield and P.E. O'Sullivan), *Developments in Hydrobiology*, pp. 35–42. Springer, Dordrecht.

Arnaud, F., Magand, O., Chapron, E., Bertrand, S., Boës, X., Charlet, F. and **Mélières, M.-A.** (2006) Radionuclide dating (210Pb, 137Cs, 241Am) of recent lake sediments in a highly active geodynamic setting (Lakes Puyehue and Icalma—Chilean Lake District). *Sci. Total Environ.*, **366**, 837–850.

Arnaud, F., Poulenard, J., Giguet-Covex, C., Wilhelm, B., Révillon, S., Jenny, J.-P., Revel, M., Enters, D., Bajard, M., Fouinat, L., Doyen, E., Simonneau, A., Pignol, C., Chapron, E., Vannière, B. and **Sabatier, P.** (2016) Erosion under climate and human pressures: an alpine lake sediment perspective. *Quatern. Sci. Rev.*, **152**, 1–18.

Bajard, M., Sabatier, P., David, F., Develle, A.-L., Reyss, J.-L., Fanget, B., Malet, E., Arnaud, D., Augustin, L., Crouzet, C., Poulenard, J. and **Arnaud, F.** (2016) Erosion record in Lake La Thuile sediments (Prealps, France): evidence of montane landscape dynamics throughout the Holocene. *Holocene*, **26**, 350–364.

Bajc, J., Aoudia, A., Saraò, A. and **Suhadolc, P.** (2001) The 1998 Bovec-Krn mountain (Slovenia) earthquake sequence. *Geophys. Res. Lett.*, **28**, 1839–1842.

Bavec, M., Tulaczyk, S.M., Mahan, S.A. and **Stock, G.M.** (2004) Late Quaternary glaciation of the Upper Soča River Region (Southern Julian Alps, NW Slovenia). *Sed. Geol.*, **165**, 265–283.

Beck, C. (2009) Late Quaternary lacustrine paleo-seismic archives in north-western Alps: examples of earthquake-origin assessment of sedimentary disturbances. *Earth Sci. Rev.*, **96**, 327–344.

Bennett, K.D. (1998) *Documentation for psimpoll 3.01 and pscomb 1.03*. University of Cambridge, Cambridge.

Bennett, K.D. and **Willis, K.J.** (2002) Pollen. In: *Tracking Environmental Change Using Lake Sediments* (Eds J.P. Smol, H.J.B. Birks and W.M. Last), pp. 5–32. Springer, Dordrecht.

Blaauw, M. (2010) Methods and code for 'classical' age-modelling of radiocarbon sequences. *Quatern. Geochronol.*, **5**, 512–518.

Buser, S., Aničić, B., Cajhen, J., Ciglar, K., Ferjančič, L., Jurkovšek, B., Mlakar, I., Novak, D., Petrica, R. and **Toman, M.** (1986) *Osnovna Geološka Karta SFRJ, List Tolmin, 1: 100 000*. Zvezni geološki zavod, Beograd.

Camassi, R., Caracciolo, C.H., Castelli, V. and **Slejko, D.** (2011) The 1511 Eastern Alps earthquakes: a critical update and comparison of existing macroseismic datasets. *J. Seismol.*, **15**, 191–213.

Campos, C., Beck, C., Crouzet, C., Demory, F., Van Welden, A. and **Eris, K.** (2013) Deciphering hemipelagites from homogenites through anisotropy of magnetic susceptibility. Paleoseismic implications (Sea of Marmara and Gulf of Corinth). *Sed. Geol.*, **292**, 1–14.

Chapron, E. (1999) *Contrôles climatique et sismo-tectonique de la sédimentation lacustre dans l'Avant-Pays Alpin (lac du Bourget, Léman) durant le Quaternaire récent*, Laboratoire de géologie de l'Université Joseph Fourier.

Chapron, E., Beck, C., Pourchet, M. and **Deconinck, J.-F.** (1999) 1822 earthquake-triggered homogenite in Lake Le Bourget (NW Alps). *Terra Nova*, **11**, 86–92.

Chapron, E., Juvigné, E., Mulsow, S., Ariztegui, D., Magand, O., Bertrand, S., Pino, M. and **Chapron, O.** (2007) Recent clastic sedimentation processes in Lake Puyehue (Chilean Lake District, 40.5 S). *Sed. Geol.*, **201**, 365–385.

Chapron, E., Simonneau, A., Ledoux, G., Arnaud, F., Lajeunesse, P. and **Albéric, P.** (2016) French Alpine Foreland holocene paleoseismicity revealed by Coeval mass wasting deposits in glacial lakes. In: *Submarine Mass Movements and Their Consequences* (Eds G. Lamarche and J. Mountjoy), pp. 341–349. Springer, Dordrecht.

Dall'Olio, E., Felletti, F. and **Muttoni, G.** (2013) Magnetic-fabric analysis as a tool to constrain mechanisms of deep-water mudstone deposition in the Marnoso Arenacea Formation (Miocene, Italy). *J. Sed. Res.*, **83**, 170–182.

Doig, R. (1990) 2300 yr history of seismicity from silting events, in Lake Tadoussac, Charlevoix, Quebec. *Geology*, **18**, 820–823.

Doig, R. (1998) 3000-year paleoseismological record from the region of the 1988 Saguenay, Quebec, earthquake. *Bull. Seismol. Soc. Am.*, **88**, 1198–1203.

Ellwood, B.B. and **Ledbetter, M.T.** (1977) Antarctic bottom water fluctuations in the Vema Channel: effects of velocity changes on particle alignment and size. *Earth Planet. Sci. Lett.*, **35**, 189–198.

Fitzko, F., Suhadolc, P., Aoudia, A. and **Panza, G.F.** (2005) Constraints on the location and mechanism of the 1511 Western-Slovenia earthquake from active tectonics and modeling of macroseismic data. *Tectonophysics*, **404**, 77–90.

Gürpinar, A. (2005) The importance of paleoseismology in seismic hazard studies for critical facilities. *Tectonophysics*, **408**, 23–28.

Heiri, O., Lotter, A.F. and **Lemcke, G.** (2001) Loss on ignition as a method for estimating organic and carbonate content in sediments: reproducibility and comparability of results. *J. Paleolimnol.*, **25**, 101–110.

Horvat, J. and **Stele, F.** (2006) Arheološki sledovi v slovenskem visokogorju. *Človek v Alpah*, 21-40.

Jelinek, V. (1981) Characterization of the magnetic fabric of rocks. *Tectonophysics*, **79**, T63–T67.

Kastelic, V., Vrabec, M., Cunningham, D. and **Gosar, A.** (2008) Neo-Alpine structural evolution and present-day tectonic activity of the eastern Southern Alps: the case of the Ravne Fault, NW Slovenia. *J. Struct. Geol.*, **30**, 963–975.

Kremer, K., Wirth, S.B., Reusch, A., Fäh, D., Bellwald, B., Anselmetti, F.S., Girardclos, S. and **Strasser, M.** (2017) Lake-sediment based paleoseismology: limitations and perspectives from the Swiss Alps. *Quatern. Sci. Rev.*, **168**, 1–18.

Marjanac, T., Marjanac, L., Poljak, M., Živčič, M. and **Bavec, M.** (2001) Srpenica seismites indicators of paleoseismicity in the Upper Soča valley, NW Slovenia. *Geologija*, **44**, 341–350.

Medvedev, S., Sponheuer, W. and **Karník, V.** (1964) Neue seismische Skala Intensity scale of earthquakes, 7. *Tagung der Europäischen Seismologischen Kommission* vom 24.9. bis 30.9.1962. In: Jena, Veröff. *Institut für Bodendynamik und Erdbebenforschung in Jena*, vol 77. Deutsche Akademie der Wissenschaften zu Berlin, pp 69–76.

Michetti, A.M., Audemard, F.A. and **Marco, S.** (2005) Future trends in paleoseismology: integrated study of the seismic landscape as a vital tool in seismic hazard analyses. *Tectonophysics*, **408**, 3–21.

Moernaut, J., Daele, M.V., Heirman, K., Fontijn, K., Strasser, M., Pino, M., Urrutia, R. and **De Batist, M.** (2014) Lacustrine turbidites as a tool for quantitative earthquake reconstruction: new evidence for a variable rupture mode in south central Chile. *J. Geophys. Res.*, **119**, 1607–1633.

Mohorič, I.I. (1969) *Dva tisoč let železarstva na Gorenjskem.* Mladinska knjiga.

Moore, P.D., Webb, J.A. and **Collison, M.E.** (1991) *Pollen Analysis.* Blackwell scientific publications, Oxford.

Moulin, A., Benedetti, L., Gosar, A., Rupnik, P.J., Rizza, M., Bourlès, D. and **Ritz, J.-F.** (2014) Determining the present-day kinematics of the Idrija fault (Slovenia) from airborne LiDAR topography. *Tectonophysics*, **628**, 188–205.

Mugnier, J.-L., Gajurel, A., Huyghe, P., Jayangondaperumal, R., Jouanne, F. and **Upreti, B.** (2013) Structural interpretation of the great earthquakes of the last millennium in the central Himalaya. *Earth Sci. Rev.*, **127**, 30–47.

Ogrin, M. (2006) Arheološke raziskave v Julijskih Alpah: Bohinj in Blejski kot (Archaeological research in the Julian Alps: Bohinj and Bled area.) In: *Človek v Alpah. Der Mensch in den Alpen* (Ed. T. Cevc), pp. 96–110. Založba ZRC, Ljubljana.

Petersen, J., Wilhelm, B., Revel, M., Rolland, Y., Crouzet, C., Arnaud, F., Brisset, E., Chaumillon, E. and **Magand, O.** (2014) Sediments of Lake Vens (SW European Alps, France) record large-magnitude earthquake events. *J. Paleolimnol.*, **51**, 343–355.

Reille, M. (1992) *Pollen et Spores D'Europe et D'Afrique du Nord: Laboratoire de Botanique Historique et Palynologie.* URA CNRS, Marseille.

Reille, M. (1995) Pollen et spores d'Europe et d'Afrique du Nord: supplement 1. *Marseille: Laboratoire de Botanique Historique et Palynologie 274p.-illus. ISBN 2950717519 Fr Icones. Palynology (KR, 199504196).*

Reimer, P.J., Bard, E., Bayliss, A., Beck, J.W., Blackwell, P.G., Bronk Ramsey, C., Buck, C.E., Cheng, H., Edwards, R.L., Friedrich, M. and **Grootes, P.M.** (2013) IntCal13 and Marine13 radiocarbon age calibration curves 0–50,000 years cal BP. *Radiocarbon*, **55**, 1869–1887.

Reyss, J.-L., Schmidt, S., Legeleux, F. and **Bonté, P.** (1995) Large, low background well-type detectors for measurements of environmental radioactivity. *Nucl. Instrum. Meth. Phys.*, **357**, 391–397.

Rovida, A., Locati, M., Camassi, R., Lolli, B. and **Gasperini, P.** (2016) Catalogo Parametrico dei Terremoti Italiani, versione CPTI15. Istituto Nazionale di Geofisica e Vulcanologia (INGV).

Sabatier, P., Dezileau, L., Briqueu, L., Colin, C. and **Siani, G.** (2010a) Clay minerals and geochemistry record from Northwestern Mediterranean coastal lagoon sequence: implications for paleostorm reconstruction. *Sed. Geol.*, **228**, 205–217.

Sabatier, P., Dezileau, L., Blanchemanche, P., Siant, G., Condomines, M., Bentaleb, I. and **Piquès, G.** (2010b) Holocene variations of radiocarbon reservoir ages in a Mediterranean lagoonal system. *Radiocarbon*, **52**, 91.

Sauerbrey, M.A., **Juschus, O.**, **Gebhardt, A.C.**, **Wennrich, V.**, **Nowaczyk, N.R.** and **Melles, M.** (2013) Mass movement deposits in the 3.6 Ma sediment record of Lake El'gygytgyn, Far East Russian Arctic. *Clim. Past*, **9**, 1949–1967.

Šmuc, A. and **Rožič, B.** (2009) Tectonic geomorphology of the Triglav Lakes Valley (easternmost Southern Alps, NW Slovenia). *Geomorphology*, **103**, 597–604.

Stockmarr, J. (1971) Tablets with spores used in absolute pollen analysis. *Pollen Spores*, **13**, 615–621.

St-Onge, G., **Chapron, E.**, **Guyard, H.**, **Rochon, A.**, **Lajeunesse, P.**, **Locat, J.**, **Scott, D.**, **Stoner, J.S.** and **Hillaire-Marcel, C.** (2008) High-resolution physical and magnetic properties of rapidly deposited layers associated with landslides, earthquakes and floods. In: *Proceedings of the 4th Canadian Conference on Geohazards: From Causes to Management* (Éds J. Locat, D. Perret, D. Turmel, d. demers and S. Leroueil), pp. 219–228. Presses de l'Université Laval, Québec, Canada.

Strasser, M., **Anselmetti, F.S.**, **Fäh, D.**, **Giardini, D.** and **Schnellmann, M.** (2006) Magnitudes and source areas of large prehistoric northern Alpine earthquakes revealed by slope failures in lakes. *Geology*, **34**, 1005–1008.

Strasser, M., **Monecke, K.**, **Schnellmann, M.** and **Anselmetti, F.S.** (2013) Lake sediments as natural seismographs: a compiled record of Late Quaternary earthquakes in Central Switzerland and its implication for Alpine deformation. *Sedimentology*, **60**, 319–341.

Sturm, M. and **Matter, A.** (1978) Turbidites and varves in Lake Brienz (Switzerland): deposition of clastic detritus by density currents. In: *Modern and Ancient Lake Sediments* (Eds A. Matter and M.E. Tucker), *Spec. Publ. Int. Assoc. Sediment*, **2**, 147–168.

Wells, D.L. and **Coppersmith, K.J.** (1994) New empirical relationships among magnitude, rupture length, rupture width, rupture area, and surface displacement. *Bull. Seismol. Soc. Am.*, **84**, 974–1002.

Wilhelm, B., **Arnaud, F.**, **Sabatier, P.**, **Crouzet, C.**, **Brisset, E.**, **Chaumillon, E.**, **Disnar, J.-R.**, **Guiter, F.**, **Malet, E.**, **Reyss, J.-L.** and **Tachikawa, K.** (2012) 1400 years of extreme precipitation patterns over the Mediterranean French Alps and possible forcing mechanisms. *Quatern. Res.*, **78**, 1–12.

Wilhelm, B., **Nomade, J.**, **Crouzet, C.**, **Litty, C.**, **Sabatier, P.**, **Belle, S.**, **Rolland, Y.**, **Revel, M.**, **Courboulex, F.**, **Arnaud, F.** and **Anselmetti, F.S.** (2016) Quantified sensitivity of small lake sediments to record historic earthquakes: implications for paleoseismology. *J. Geophys. Res.*, **121**, 2–16.

Wilhelm, B., **Vogel, H.** and **Anselmetti, F.S.** (2017) A multi-centennial record of past floods and earthquakes in Valle d'Aosta, Mediterranean Italian Alps. *Nat. Hazards Earth Sys. Sci.*, **17**, 613.

Manuscript received 26 November 2016; revision accepted 6 December 2017

Supporting Information

Additional Supporting Information may be found in the online version of this article:

Figure S1. Seismic grid (blue lines) acquired at Lake Bohinj (A) highlighting the location of the transversal seismic section shown in Fig. 1D and the longitudinal seismic line illustrated in (B) near the BO12 coring site in the eastern basin where a recent homogenite is identified and laterally associated with a mass wasting deposit (MWD). The vertical scale of this profile is in millisecond (ms) two-way travel time (TWT).

Figure S2. Unit IV results. Image, sedimentological description, and AMS results (Inc K3, lineation and foliation) associated with Ti content.

Table S1. Earthquakes recorded by Lake Bohinj sediment core with thickness, calibrated ages and associated historic events.

Annexe II | Sedimentary structure discrimination with hyperspectral imaging in sediment cores

Article | En Review dans Science of the Total Environment

Kévin Jacq[a,b*], William Rapuc[a], Alexandre Benoit[b], Didier Coquin[b], Bernard Fanget[a], Yves Perrette[a], Pierre Sabatier[a], Bruno Wilhelm[c], Maxime Debret[d], Fabien Arnaud[a]

[a] Univ. Grenoble Alpes, Univ. Savoie Mont Blanc, CNRS, EDYTEM, 73000 Chambéry, France
[b] Univ. Savoie Mont Blanc, LISTIC, 74000 Annecy, France
[c] Institute for Geosciences and Environmental Research, University Grenoble Alpes, CNRS, IRD, Grenoble, France
[d] Univ. Rouen Normandie, Univ. Caen, , CNRS, M2C, 76821 Mont-Saint-Aignan, France
https://doi.org/10.1016/j.scitotenv.2021.152018
Corresponding Author:
Kévin Jacq
UMR CNRS 5204 Environnements, Dynamiques et Territoires de la Montagne (EDYTEM)
Université Savoie Mont Blanc, Campus scientifique,
73376 Le Bourget du Lac cedex, France
jacq.kevin@hotmail.fr

Abstract

Hyperspectral imaging (HSI) is a non-destructive, high-resolution imaging technique that is currently under significant development for analyzing geological areas with remote devices or natural samples in a laboratory. In both cases, the hyperspectral image provides several sedimentary structures that must be separated to temporally and spatially describe the sample. Sediment sequences are composed of successive deposits (strata, homogenite, flood) that are visible depending on sample properties. The classical methods to identify them are time-consuming, have a low spatial resolution (millimeters) and are generally based on naked-eye counting. In this study, we compare several supervised classification algorithms to discriminate sedimentological structures in lake sediments. Instantaneous events in lake sediments are generally linked to extreme geodynamical events (e.g., floods, earthquakes), so their identification and counting are essential to understand long-term fluctuations and improve hazard assessments. This process is done by reconstructing a chronicle of event layer occurrence, including estimation of deposit thicknesses. Here, we applied two hyperspectral imaging sensors (Visible Near-Infrared, VNIR, 60 µm, 400-1 000 nm; Short Wave Infrared, SWIR, 200 µm, 1 000-2 500 nm) on three sediment cores from different lake systems. We highlight that the SWIR sensor is the optimal one for creating robust classification models with discriminant analyses. Indeed, the VNIR sensor is impacted by the surface reliefs and structures that are not in the learning set, which causes mis-classification. These observations are also valid for the combined sensor (VNIR-

SWIR). Several spatial and spectral pre-processing were also compared and enabled one to highlight discriminant information specific to a sample and a sensor. These works show that the combined use of hyperspectral imaging and machine learning improves the characterization of sedimentary structures compared to conventional methods. However, the proposed approach is site-specific and therefore requires improvements to be generalized to unknown sites.

KEYWORDS: Hyperspectral Imaging, Machine Learning, Discrimination methods, Visible and Near-Infrared Spectroscopy, Automatic Detection, Sedimentary Deposits

1. Introduction

Natural archives, such as sediment cores, are composed of a succession of deposits, so they record past climate and environment biological-physical-chemical variations. There are two main processes: continuous sedimentation and event layers, and the former can be interrupted by the latter. The continuous sedimentation enables one to create an age-depth model and infer the environment and climate conditions. Event layers, e.g., related to floods (Gaume et al., 2009b; Glur et al., 2013b), storms (Sabatier et al., 2012), landslides, earthquakes (Wilhelm et al., 2016a), tsunamis (Chagué-Goff, 2010), and eruptions, are linked to some of the most damaging disasters in terms of economic and societal losses. Currently, in an overwhelming majority of laboratory studies on natural archives, sedimentary structures are first visually described; subsequently, numerous physical (X-ray imaging, computed tomography scan, grain-size) and chemical (X-ray fluorescence or diffraction, scanning electron microscopy) analyses are undertaken. From those results, the event layers are identified and described. Then, layers with identical characteristics (e.g., color and texture) are usually counted by naked-eye observation. This approach is time-consuming, characterized by a low spatial resolution and subject to high uncertainties due to human interpretation (Lotter and Lemcke, 1999). To overcome these limits, several semi-automatic methods were developed to discriminate these sedimentary deposits from RGB images. The main approaches study the strata from annually laminated sediment to create an age-depth model with their discretization, but they only use a line or a combination of segments, and a deposit is characterized by the detection of the maxima (Meyer et al., 2006; Weber et al., 2010). Similarly, for the automatic detection of event layers, (Vannière et al., 2013) proposed to use a 1/Red signal and threshold. Some studies also used discrimination methods based on labeled pixels to create classification maps, e.g., an adaptive neuro-fuzzy inference system (Ebert and Trauth, 2015) or K-nearest neighbor (Ndiaye et al., 2012). Thereby, only the color signal has been investigated, while many other parameters are potentially useful to distinguish event layers, such as the texture, grain size, and chemical composition (Fouinat et al., 2017b; Gilli et al., 2013b; Wilhelm et al., 2018b). A more relevant approach will automatically detect event layers considering all of these parameters.

Hyperspectral imaging (HSI) is a non-destructive high-resolution laboratory analysis that enables a semi-automatic description of the natural deposits based on their physical-chemical characterization. HSI can improve chemical knowledge by analyzing the sample surface. It has been used to characterize mineralogical fingerprints (Feng et al., 2018; Lorenz et al., 2019; Tusa et al., 2020), organic matter (Jacq et al., 2019b; Van Exem, 2018), pigments (Butz et al., 2017b; Makri et al., 2020; Schneider et al., 2018b), and particle size distribution (Jacq et al., 2019b).

Some of these studies highlight sedimentary structures with proxy estimation but without spatially characterizing them. It has also been used to characterize spatial variations in volcanic tephra layers with a visible and near-infrared hyperspectral camera (VNIR, 400-1 000 nm) using a supervised classification method based on an artificial neural network (Aymerich et al., 2016).

In this study, we test several discrimination methods based on different methodologies: artificial neural networks (ANN), classification rules (decision tree DT, random forest RF) and classification models (linear and quadratic discriminant analysis LDA/QDA, partial least-square discriminant analysis PLS-DA). The hyperspectral images used in this study come from a visible and near-infrared camera (VNIR, pixel size: 60 µm) and a shortwave infrared sensor (SWIR, pixel size: 200 µm). The two sensors can also be combined to estimate a VNIR-SWIR composite sensor (pixel size: 200 µm). Several spectral and spatial pre-processing and compression algorithms were compared. Thus, this study proposes to compare numerous approaches (the type of image, pre-processing, and discrimination) to separate and characterize the sedimentary structures of three different samples and provide a simplified methodology for its application to other sites.

2. Materials and methods

2.1. Sample site descriptions

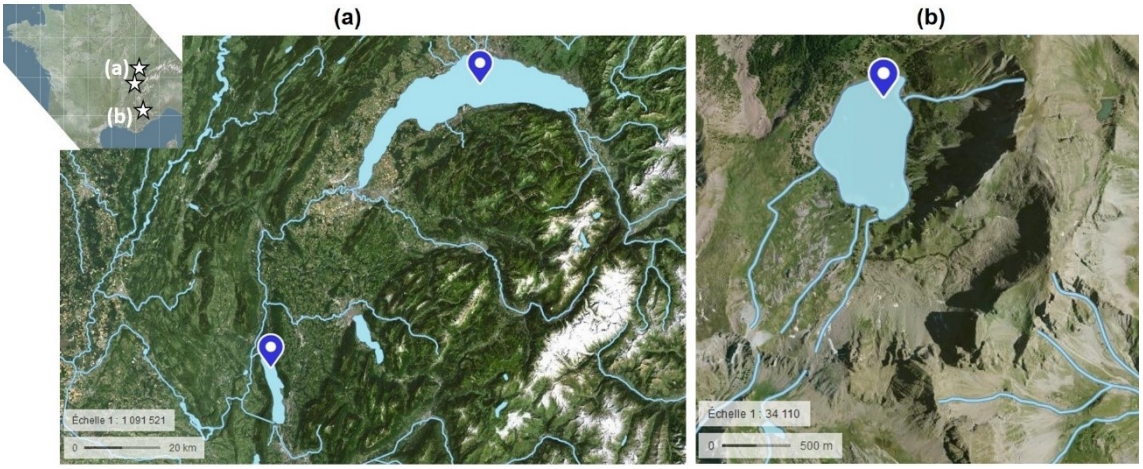

Figure 1: Locations, tributaries and effluents of the lakes: (a) Bourget and Geneva, (b) Allos.

Three sediment cores were selected from three lakes located in the western French Alps (Figure 1) in different watersheds, representing different geological contexts and surface areas that present event layers with different geochemical compositions. The studied cores were retrieved from Lake Allos (ALO09_P13, IGSN: IEFRA08JN, coring year: 2009) (Wilhelm et al., 2015, 2012), the deep basin of Lake Le Bourget (LDB17_P11, coring year: 2017) (Jenny et al., 2014), and Lake Geneva (LEM10, IGSN: IEFRA008N, coring year: 2010) (Rapuc et al., 2021).

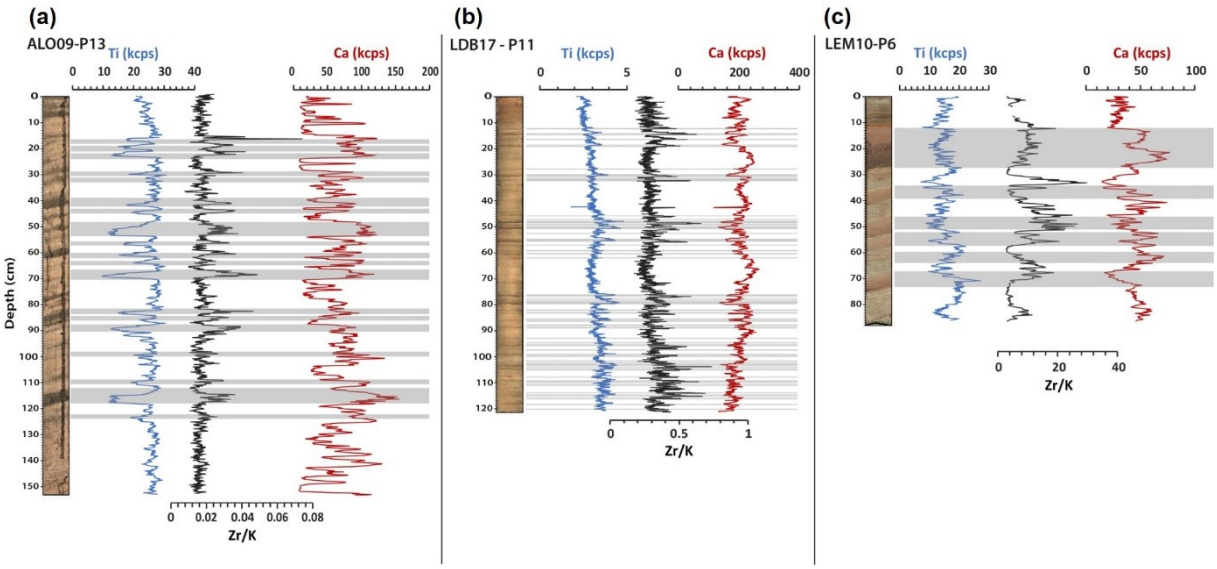

Figure 2: XRF analysis for Ti, Zr/K, and Ca of the three cores: (a) Allos, (b) Bourget, and (c) Geneva.

The sediment from the three selected cores was first described and logged after naked-eye observations. When they were present, the event layers were distinguished from the continuous sedimentation by using sedimentological and geochemical results; for these three cores X-ray fluorescence, particle size distribution, and total organic carbon were made.

Lake Allos sediment sequence (ALO09-P13) presents two different sedimentary units. The upper part is enriched in organic matter and presents Total Organic Carbon (TOC) values > 1.5% (Wilhelm et al., 2012). The rest of the sequence is composed of light-gray homogeneous silty clay (median = 10 µm), corresponding to the continuous sedimentation, which is interrupted by coarser (median = 40 µm) normally graded beds (Wilhelm et al., 2012). These beds present higher values of dry bulk density, lower TOC values (< 1%), and are enriched in calcium contents (Figure 2). XRF signals also show peaks of Zr/K and low Ti values due to an increase of the grain size at the base of the layers and a depletion in silicate particles, respectively. The graded beds were interpreted as linked to turbidity currents triggered by gravity reworking or flood events (Wilhelm et al., 2012).

Lake Bourget sediment sequence (LDB17-P11) presents two main units. The first one (0-10 cm) is laminated with an alternation of white/light-gray and dark-gray/brown laminae. These laminae are mainly composed of diatoms, micrite, organic matter (TOC > 2.5%), and autochthonous calcite with a mean grain-size comprise between 15 and 30 µm (Giguet-Covex et al., 2010). The second unit is non-laminated and corresponds to homogeneous light-gray sediment composed of carbonate particles, silts, clays, and a few diatoms. The mean grain size of this unit is almost constant and is comprised between 4 and 9 µm. The organic matter content is under 5% (Giguet-Covex et al., 2010), and carbonate particles represent at least half of the total sediment (Arnaud, 2005). Several darker deposits, enriched in detrital silicate and carbonate particles, interrupted the continuous sedimentation and were interpreted as underflow deposits linked to flood events (Giguet-Covex et al., 2010; Jenny et al., 2014). These deposits present peaks of Ti and Zr/K signals at their base (Figure 2), which support the higher detrital content and the increase of grain size within these layers.

Like the two other sediment sequences, the Lake Geneva sequence (LEM10-P6) presents two principal sedimentary units. The upper laminated unit corresponds to an alternation of light and dark-gray laminae, enriched in organic matter (TOC values > 5%; Jenny, 2013). This unit is followed by homogeneous light-gray silty clay identified as a non-laminated unit (Jenny, 2013), which presents lower organic content (TOC values < 2%) and higher values of calcium (Figure 2). The mean grain size of these two units is higher (> 25 µm) than Lake Bourget sediment sequence values. The lower unit is interrupted by thick and coarse graded beds that show peaks of Zr/K, and higher values of Ti (Figure 2) are linked to increased detrital silicates compared to the continuous sedimentation. These deposits present similarities with those observed in the two other sequences and were interpreted as flood layers.

Once clearly identified, those layers were visually counted. In the three cores, the frequency and thickness of event deposits vary (Table 1). The data sets will be referred to using the name of the lake, but it must be understood that there may be differences (color, chemical, physical) among different sequences from the same lake.

Table 1: Statistics from the naked-eye event layer detections. N is the number of event layers identified in each lake core, and the other variables are statistics about the layer thickness.

	N	Average (mm)	Standard deviation (mm)	Minimum (mm)	Maximum (mm)
Allos	69	7.44	5.73	1.00	39.00
Bourget	56	3.41	2.17	1.00	11.00
Geneva	15	15.93	21.97	3.00	88.00

2.2. VNIR and SWIR hyperspectral image acquisition

Two hyperspectral reflectance cameras were used to analyze these cores at the UMR CNRS M2C lab facilities, University of Normandie-Rouen (France). They cover two consecutive spectral ranges: 400-1 000 nm (visible and near-infrared, VNIR) and 968-2 574 nm (shortwave infrared, SWIR). They have a theoretical spatial resolution of 60 µm and 200 µm, respectively. The real resolution may vary due to surface roughness. Relevant data were obtained with a flattening and a cleaning of the core to have a plane surface that revealed sediment structures (Butz et al., 2015; Jacq et al., 2020). Then, the camera was calibrated with a spectral acquisition on a reference, as the image of a known object has squared pixels (true shape) and relevant reflectance intensities (color and signal-to-noise ratio).

The resolution of the two datasets (VNIR and SWIR) was also homogenized at a common spatial resolution of 200 µm to obtain a VNIR-SWIR image. The two hyperspectral images were combined into a unique one (i.e., VNIR-SWIR) with image registration (Liu et al., 2011) adapted to HSI on a wavelength plane characteristic of a similar chemical compound. In previous work, we found that the 970 nm (VNIR) and 1 200 nm (SWIR) wavelengths were optimal for combining (Jacq et al., 2019a). They are related to hydroxyl chemical bonds mostly associated with moisture in sediment cores (Bull, 1991; Rossel and Behrens, 2010). Therefore, a composite sensor was created to merge the VNIR and SWIR datasets to cover the range of 400-2 500 nm. In this study,

we compare the classification performances of three datasets: VNIR at a spatial resolution of 60 µm, SWIR at a resolution of 200 µm, and VNIR-SWIR at a resolution of 200 µm.

Pre-processing can be used to correct the data from noise or aberrant values and highlight discriminant wavelengths. The three dimensions of the HSI, spectral, and spatial pre-processing procedures can be used (Rinnan et al., 2009; Vidal and Amigo, 2012). The spectral pre-processing procedures compared in this study are normalization (autoscale), baseline correction (detrend), scattering effect correction (Standard Normal Variate (SNV) and Multiplicative Scatter Correction (MSC)) (Barnes et al., 1989), and Savitzky-Golay derivatives (Savitzky and Golay, 1964). Principal component analysis (PCA) was also used as a compression of the spectral dimension (Pearson, 1901). Contrast limited adaptive histogram equalization (CLAHE) was used on the spatial dimensions with an estimation based on the grayscale image levels and applied to each image wavelength (Zuiderveld, 1994).

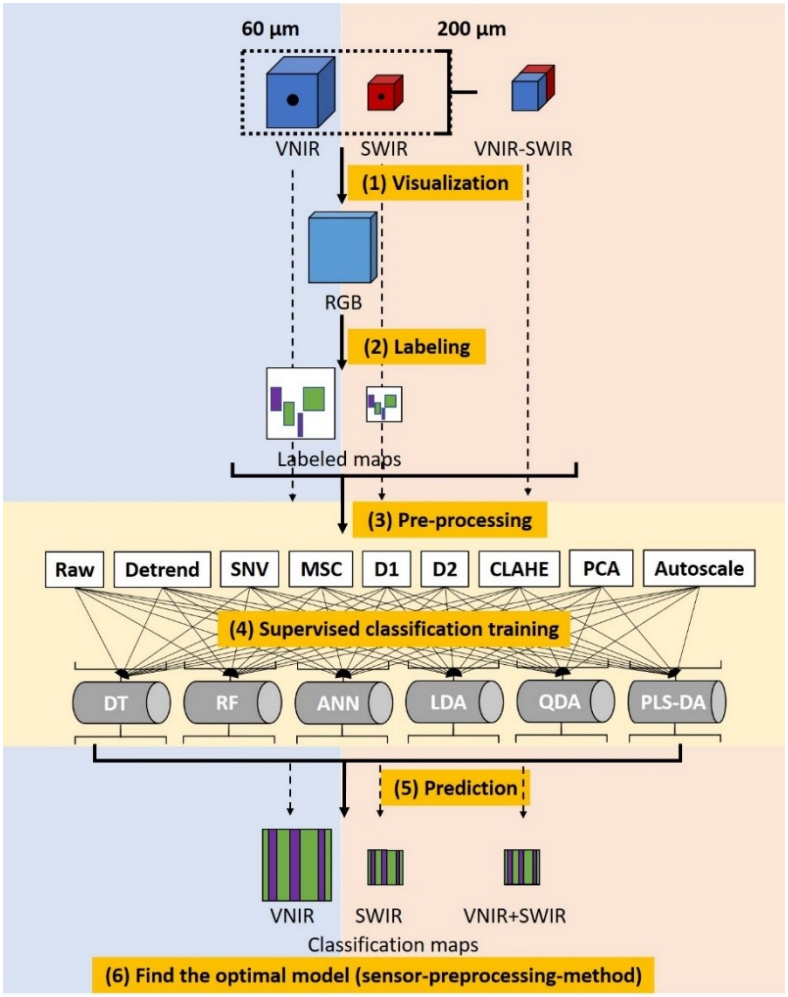

Figure 3 : Data processing to create a classification model to predict each pixel: (1) Visualization with RGB images at both resolutions; (2) Manual labeling of the image; (3) Data pre-processing and (4) Creation of supervised classification models for each dataset (DT: Decision Tree, RF: Random Forest, ANN: Artificial Neural Network, LDA: Linear Discriminant Analysis, QDA: Quadratic Discriminant Analysis, PLS-DA: Partial Least Squares Discriminant Analysis); (5) Prediction for each image; (6) Estimation of the optimal model depending on the sensor, pre-processing procedure and discrimination model.

2.3. Data Analysis

Seven commonly used machine learning algorithms were used to create classification models with three types of spectral data (VNIR, SWIR, and VNIR-SWIR) (Figure 3). First, an RGB image was made from the VNIR HSI to label continuous sedimentation and event layer pixels. Then, machine learning methods were used to construct discrimination models. In addition, eight pre-processing procedures (spatial and spectral) were used and compared with raw data. Consequently, 189 discriminations models were created for each sample to find the optimal sensor (of three), method (of seven) and pre-processing procedure (of nine).

2.3.1. Data labeling

Hyperspectral VNIR data can be reduced to three planes that correspond to a Red-Green-Blue image from the VNIR sensor (611-549-464 nm, according to the RGB standard) (CIE, 1999). The RGB images are representation modes adapted for naked-eye assessment and were used to visualize the sample to label the sedimentary structures. Thus, the user must manually select rectangular areas that correspond to the different studied classes based on the known deposits characterized by geochemical, textural, and mineralogical analysis. The resulting maps were used as a mask with 0 values for non-labeled pixels and other values for labeled pixels (1: event layer, 2: continuous sedimentation). It was also used to extract the labeled pixels and their corresponding spectrum (Figure 4). For the SWIR dataset, these maps were also made with VNIR data at 60 µm and resized at 200 µm.

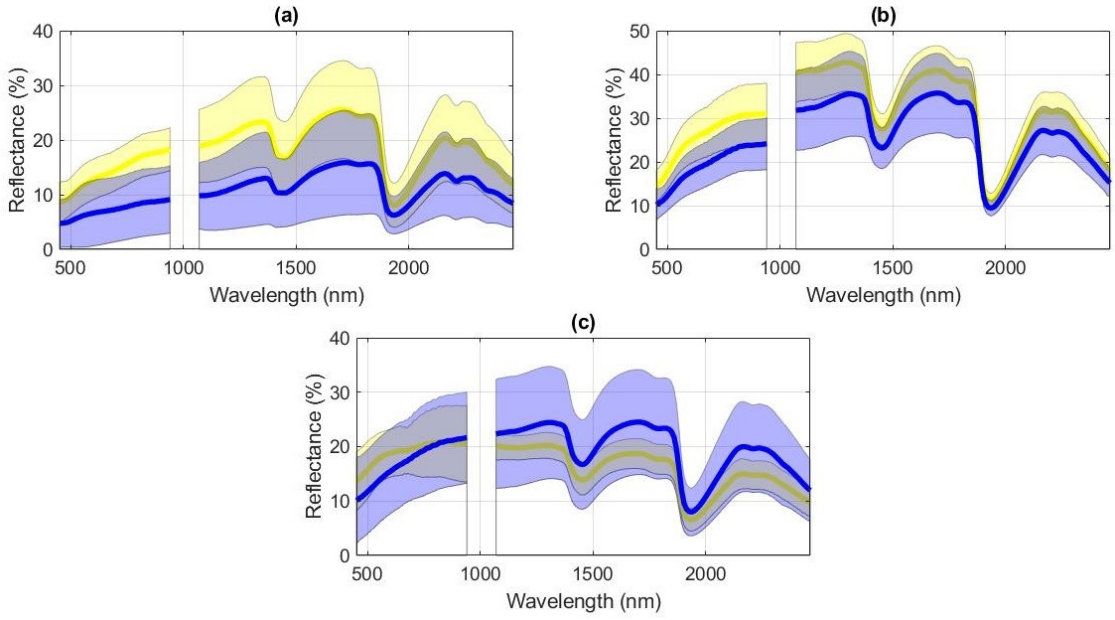

Figure 4: Spectral variations of labelled pixels for each class (blue = event layers; yellow = continuous sedimentation) and for the three cores: (a) Allos, (b) Bourget and (c) Geneva.

2.3.2. Classification modeling

Seven methods were used to create a supervised classification model to discriminate the two sedimentary processes (Figure 5). Decision tree (DT) and random forest (RF) approaches are linear non-parametric methods based on successive rules regarding the reflectance value of one wavelength at a time (Breiman et al., 1984; Ho, 1995). Artificial neural networks (ANNs) are non-

linear parametric methods based on data learning with neurons (Ivakhnenko and Lapa, 1965; McCulloch and Pitts, 1943; Rosenblatt, 1958). Linear, quadratic, and partial least squares discriminant analysis (LDA, QDA, and PLS-DA, respectively) are parametric methods with a mathematical function kernel that is used to separate the classes (Fisher, 1936; Wold et al., 1984).

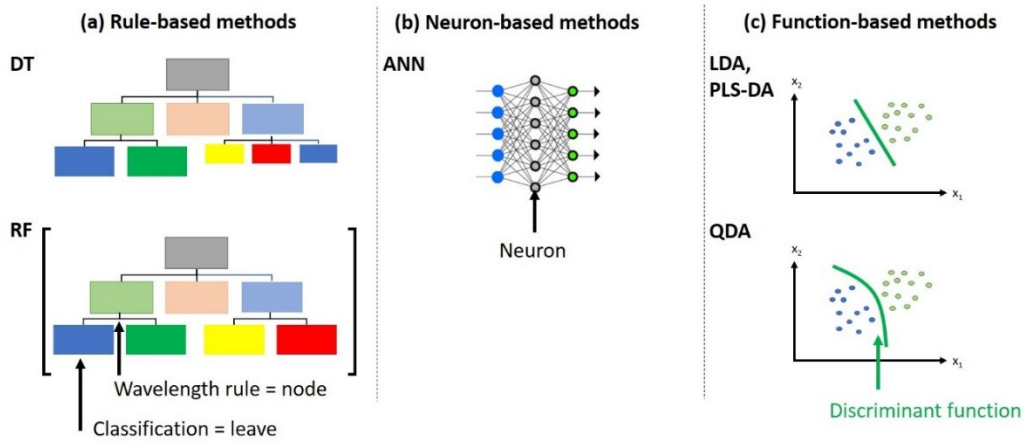

Figure 5: Schematic representation of the machine learning methods used in this study depending on their basis: (a) rules; (b) neurons; and (c) functions.

The models were fitted with a randomly selected 70% of the data during calibration, and the remaining data were used in the test set (Table 2). This ratio was applied to the class with fewer labeled pixels to have a consistent number in each group. The same calibration and test sets were used for each classification method, but they were different for each pre-processing procedure. The labeled pixel number depends on the ability of the user to precisely see the deposits; then, only pixels that certainly belong to these classes are labeled to avoid introducing uncertainty by uncertain labeling. Due to the compression of the labeled high-resolution map, the pixels of the contours may have been removed as being uncertain, which slightly changes the labeling percentages between the two resolutions. That change explains the difference between the cores with labeled pixels of between 0.45% and 15.71% for one class (Table 2). It also allows visualization of the learning capacity depending on the number of calibration pixels.

Table 2 : The number of pixels for each sediment core image and the number of labeled pixels for the calibration and validation sets for each class (1=event layer; 2=continuous sedimentation)

Sample	Sensors	Total pixels	Class	Number of areas labeled and pixels	Calibration pixels	Validation pixels
Allos	VNIR	30 433 152	1	8 areas, 598 722 (1.97%)	419 105 (1.38%)	179 617 (0.59%)
			2	6 areas, 961 079 (3.16%)	419 105 (1.38%)	541 974 (1.78%)
	SWIR, VNIR-SWIR	1 702 476	1	8 areas, 35 364 (2.08%)	24 755 (1.45%)	10 609 (0.62%)
			2	8 areas, 56 261 (3.30%)	24 755 (1.45%)	31 506 (1.85%)
Bourget	VNIR	21 096 723	1	12 areas, 155 876 (0.74%)	68 636 (0.33%)	87 240 (0.04%)
			2	9 areas, 98 051 (0.46%)	68 636 (0.33%)	29 415 (0.14%)
	SWIR, VNIR-SWIR	1 806 624	1	12 areas, 12 975 (0.72%)	5 709 (0.32%)	7 266 (0.40%)
			2	9 areas, 8 156 (0.45%)	5 709 (0.32%)	2 447 (0.14%)
Geneva	VNIR	13 711 712	1	8 areas, 2 034 596 (14.84%)	65 769 (0.48%)	1 968 827 (14.36%)
			2	3 areas, 93 956 (0.69%)	65 769 (0.48%)	28 187 (0.21%)
	SWIR, VNIR-SWIR	865 234	1	8 areas, 135 933 (15.71%)	4 078 (0.47%)	131 855 (15.24%)
			2	3 areas, 5 826 (0.67%)	4 078 (0.47%)	1 748 (0.20%)

2.3.3. Quantitative assessment of model classification

The quantitative performances of the classification models were estimated by the overall accuracy in calibration and prediction:

$$Accuracy = \frac{True\ positive + True\ negative}{True\ positive + True\ negative + False\ positive + False\ negative} \quad (1)$$

where "true positive" corresponds to class-1 pixels classified as class 1, "true negative" corresponds to class-2 pixels classified as class 2, "false positive" corresponds to class 2 pixels classified as class 1, and "false negative" corresponds to class 1 pixels classified as class 2.

The overall accuracy corresponds to class 1 and 2 pixels that are successfully classified in their corresponding classes. Thus, a value closer to 1 indicates better predictive ability.

2.3.4. Qualitative assessment of each pixel image classification

The created model must be visually assessed by an expert to quantify the spatial consistency of the classification map because of possible overfitting. Thus, the model was used on all pixels to estimate the classification map. Then, the user must assess it by looking at the salt-and-pepper characteristics of the image with single pixels corresponding to potential mis-classifications. The user must also check the event layer predicted areas with the RGB image. Hence, a qualitative index with values between 0 and 5 (arbitrary) is used. A value of 0 corresponds to a classification map that mainly has a single value for each image pixel; a value of 5 shows relevant deposits across the image width and a few single pixels.

3. Results and interpretations

3.1. Comparison of the classification methods and pre-processing procedures

Eight pre-processing procedures were tested on each sample, each sensor, and each discrimination method to find the optimal combination (Figure 6). The processing procedure must have the capacity to highlight discriminant information and create performant and robust models. PCA and second derivatives (D2) had the lowest prediction accuracies for each sensor and sample (Figure 6). The PCA reduction may not maintain the discriminant information in the main PCs and D2. Raw, CLAHE, autoscaled, and detrended data had the highest discriminant properties in all cases (Figure 6). Some pre-processing procedures are sensor-dependent, such as SNV and MSC, which presented low accuracy for the VNIR sensor and high accuracy for the SWIR sensor. The first derivative (D1) had intermediate accuracy for all cases except for the SWIR sensor and Allos sample, for which good performances were obtained.

Among the discriminant methods, DT had the lowest prediction accuracy in most cases, whereas ANN, QDA, and RF had the highest accuracy. For the ANN, few neurons (2-3) appeared to be better than more neurons. The latter has many more parameters and may overfit the small amount of training data, which limits its generalization capability on the test set. The accuracies of the optimal methods are close and must be discussed with all quantitative values and interpretations of their discriminant spectral properties. It is important to consider that the results are sample- and site-specific.

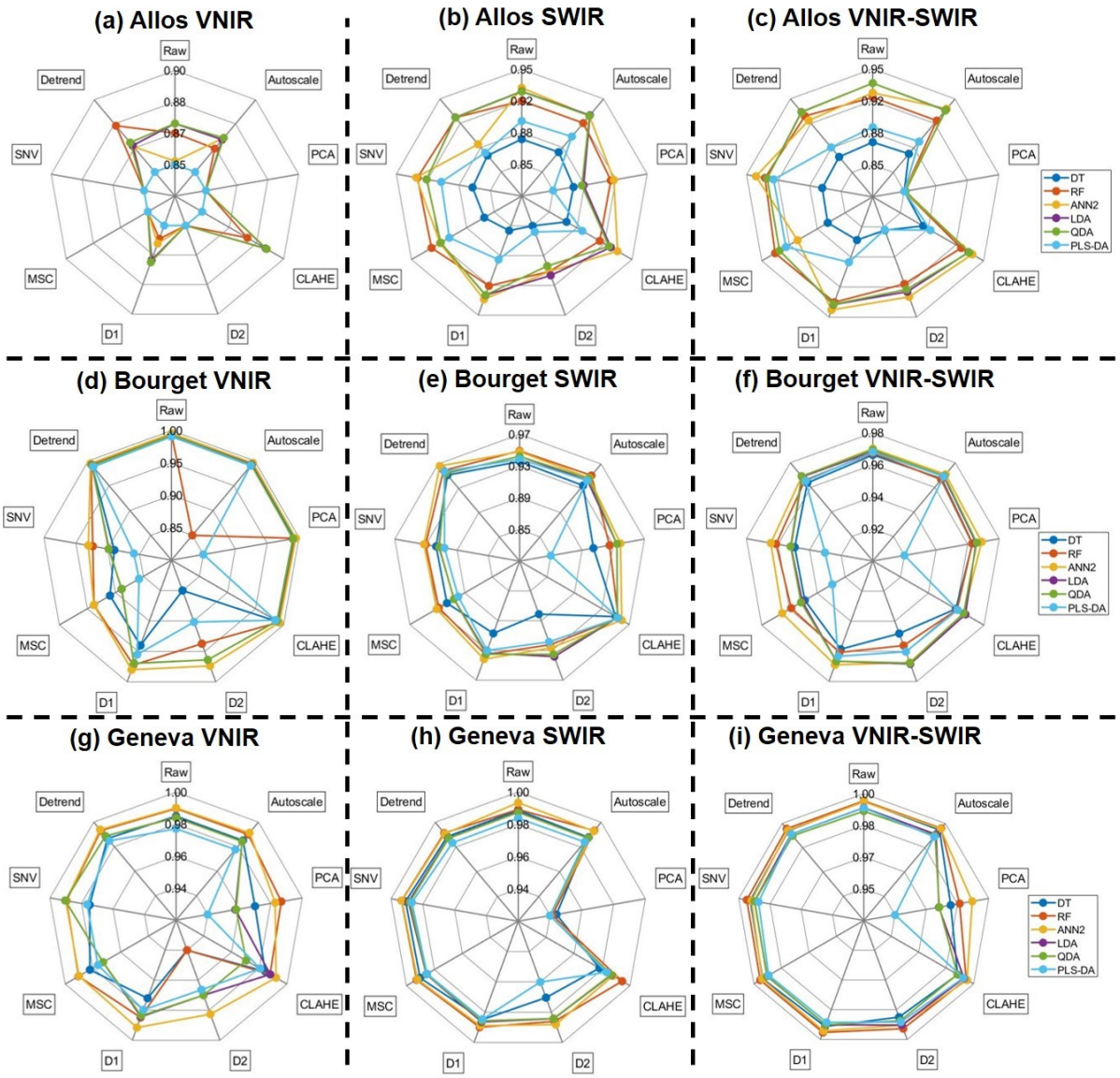

Figure 6: Radar charts of the impact of pre-processing on the overall prediction accuracy of each classification method and lake core hyperspectral image (a-c: Lake Allos; d-f: Lake Bourget; g-i: Lake Geneva; a, d, g: VNIR sensor; b, e, h: SWIR sensor; c, f, i: VNIR-SWIR sensor)

3.2. Optimal models for each image type

The calibration and prediction accuracies of the optimal model were higher than 0.8 and mainly 0.9, which highlights the presence of spectral discriminant information in both sensors (Table 3). ANNs with two neurons are often the optimal discriminant method based on the prediction accuracy and parsimonious because adding neurons does not improve the accuracy. However, for the qualitative index, discriminant analysis methods (LDA, QDA, PLS-DA) generally had the best performance levels. The computation time is lower for the LDA, PLS-DA, and DT methods, and all of these methods are fast to compute, so the computation time was not used to select the optimal model. Based on a compromise between these two first properties (accuracy and qualitative index), the optimal methods in most cases were LDA or PLS-DA. Another important property is the transparency of the model for the selected discriminant wavelengths. Table 3 highlights an optimal pre-processing procedure that mainly depends on the sample and sensor.

The discrimination methods appear to have had a low impact on it, which suggests that an optimal pre-processing procedure can highlight the discriminant wavelengths.

This table also highlights the best discriminant capacity as being available with the SWIR sensor. The combination of the two sensors, which should be better and have the greatest amount of spectral information, presented intermediate discriminant ability. Thus, the VNIR data have variations that could bias the predictions.

Table 3: Optimal models for each sensor depending on the sample and discrimination method

Site	Sensor	Method	Processing	$Accuracy_{cal}$	$Accuracy_{pred}$	Qualitative	Computation time (s)
Allos	VNIR	ANN2	CLAHE	0.889	0.890	3	263.840
	SWIR	PLS-DA	SNV	0.900	0.902	5	0.800
	VNIR-SWIR	LDA	Raw	0.931	0.935	5	1.097
Bourget	VNIR	RF	Raw	0.996	0.995	3	139.542
	SWIR	PLS-DA	Detrend	0.969	0.958	5	0.219
	VNIR-SWIR	PLS-DA	Raw	0.979	0.968	4	0.276
Geneva	VNIR	LDA	Detrend	0.987	0.989	3	1.142
	SWIR	LDA	SNV	0.992	0.989	5	0.113
	VNIR-SWIR	LDA	Raw	0.997	0.993	4	0.437

The classification map comparison of the optimal and worst models highlights that the VNIR sensor is more sensitive to surface reliefs, as observed in Figure 7a-b with fissures and holes due to sampling or Figure 7d-e with shadows. Darker laminated areas are noticeable on the Bourget and Geneva sediment sections (on the left of the picture), which were not initially labeled because of the non-possibility of precisely labeling the two classes. In these areas, the VNIR sensor predicted that most of the pixels in the event layer class might be due to the similar color with this class. In contrast, the SWIR data correctly predicted the two groups due to the additional spectral discriminant information. For the Allos sediment section (Figure 7a-c), the event layers are easily distinguishable from the continuous sedimentation due to their darker colors. However, there is also a color gradient linked to a grain size gradient that is spectrally registered in the SWIR range (Jacq et al., 2019), which explains the wider layers estimated from the SWIR data than from the VNIR data, and the lightest layers are not visible with the VNIR data.

All of these observations and the quantitative validation are consistent on the greatest discriminant capacities being associated with the SWIR sensor for separating event layers from continuous sedimentation. Thus, the combination of the two sensors is not better, as we expected due to the VNIR data sensitivity to surface roughness, and the combination will not be used further.

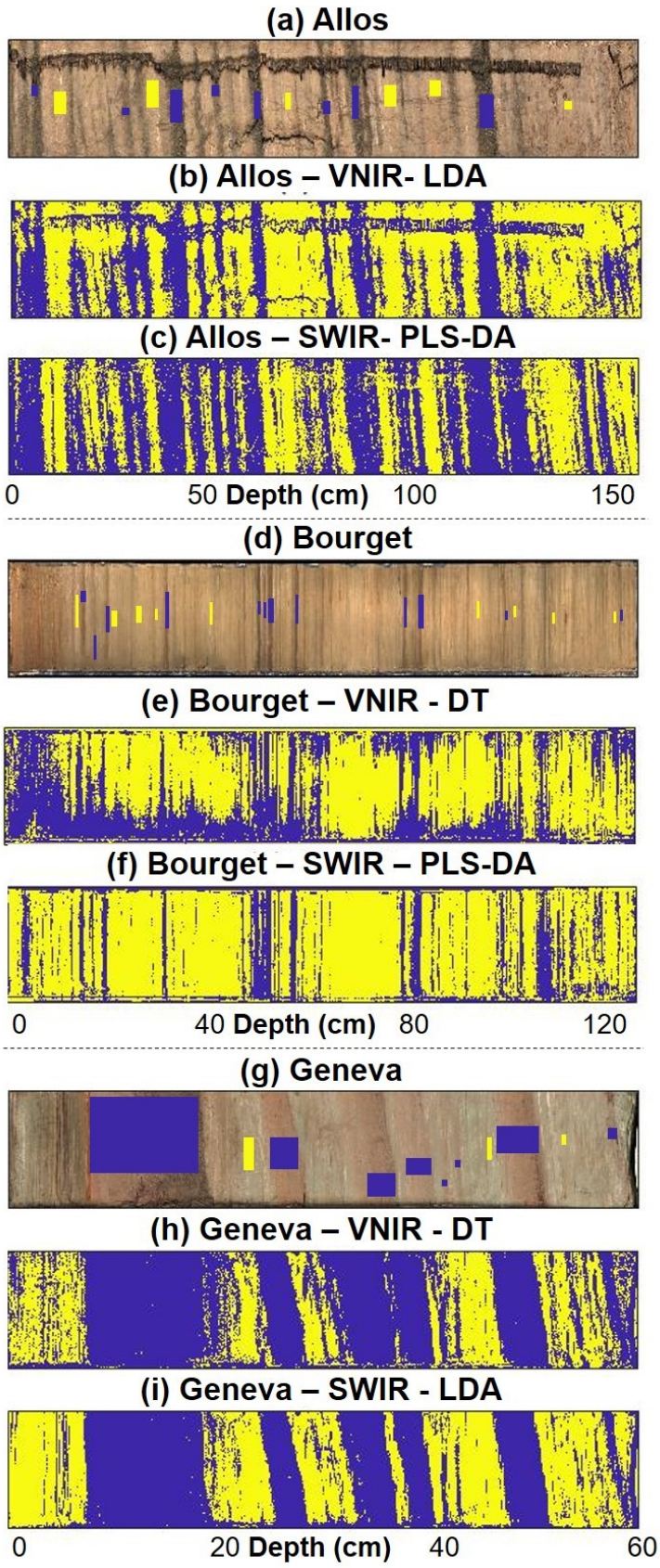

Figure 7: Optimal (c, f, i) and worst (b, e, h) models for each sediment core sample (a, b, c: Allos; d, e, f: Bourget; h, i, j: Geneva) and labeled areas (blue = event layers; yellow = continuous sedimentation)

3.3. Spectral signatures

The estimation of SWIR wavelength cumulative occurrence allows identification of the discriminant wavelengths and characterization of them (Figure 8). Five discriminant spectral areas present high cumulative values and can be associated with chemical properties (Rossel and Behrens, 2010). Organic components can be related to spectral wavelengths between (1) 1 100-1 200 nm and (2) 1 650-1 750 nm. The three others correspond to spectral ranges with possible overlaps: (3) organic compounds and hydroxyl bonds (moisture, organic matter or mineral) between 1 400-1 500 nm and 1 800-1 950 nm, and (4) mineral (clay) and organic compounds between 2 180-2 300 nm.

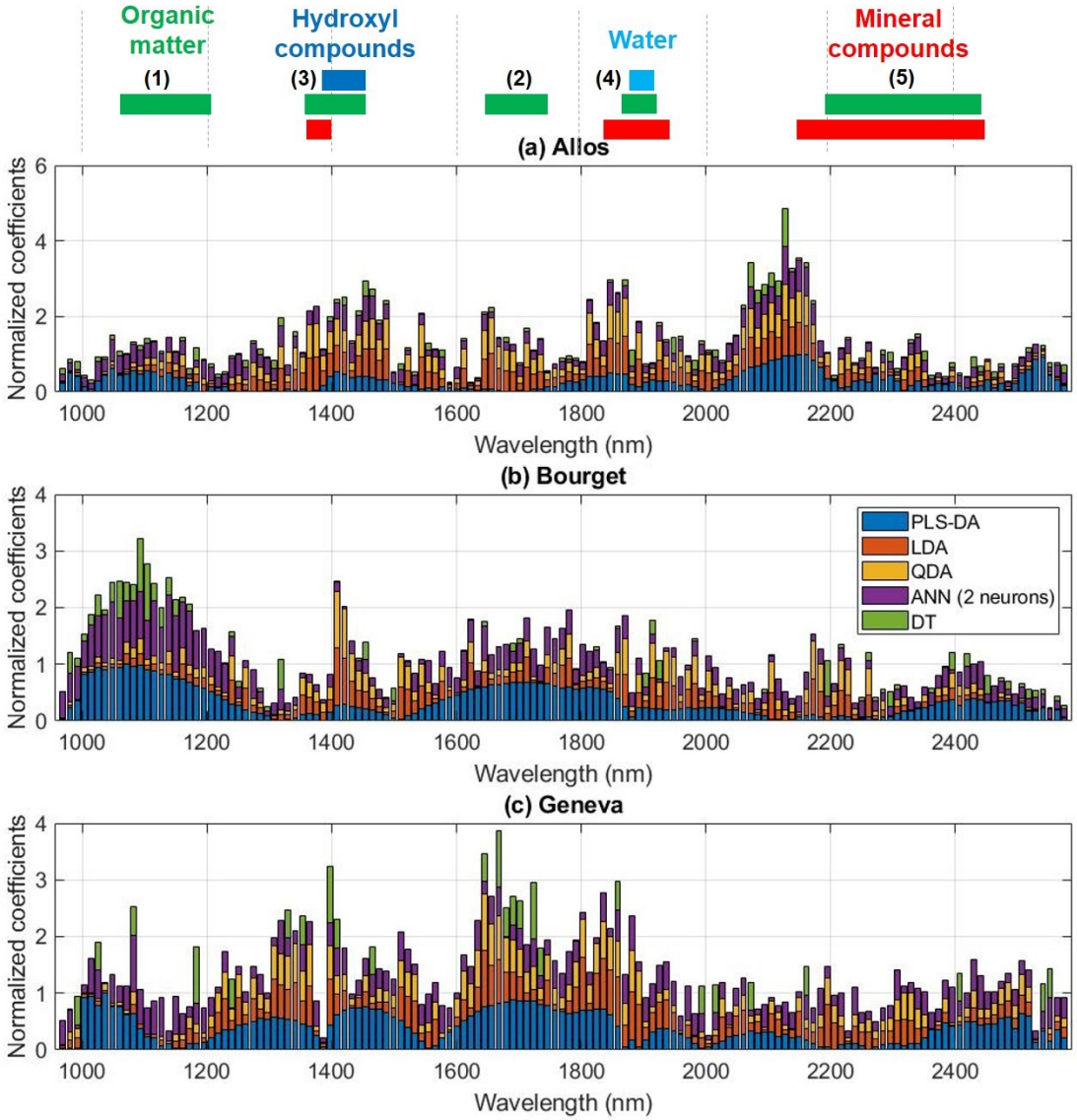

Figure 8: Comparison of the normalized coefficients (coefficient weights normalized to one for each method) used by the optimal SWIR models to highlight the discriminant wavelengths: (a) Allos, (b) Bourget, and (c) Geneva samples.

The three optimal models use similar discriminant wavelengths but have different importance depending on the sediment properties. The two hydroxyl bond spectral areas have important implications in the three models and could be associated with moisture and the particle size.

Otherwise, the two classes appear to be discriminated by the mineralogy for the Allos sediment sequence and by the organic matter for the Bourget and Geneva sequences.

4. Discussion

4.1. Model transfer

The optimal SWIR models developed on each core were used to estimate the classification maps of the other cores to observe the model transfer capability. Table 4 shows the results of these classifications with the test accuracies and qualitative indicators. Most of them agree on the difficulty of transferring the model to other cores. Only the model developed with the Bourget data could predict the classification maps for the other cores, possibly since it has less spectrally localized discriminant wavelengths than the other two models (Allos: 2 100-2 200 nm; Geneva: 1 650-1 700 nm).

Table 4: Comparison of site-specific models for the transferability on the other cores

			Samples		
			Allos	Bourget	Geneva
Models	Allos	$Accuracy_{pred}$		0.367	0.043
		Qualitative		0	0
	Bourget	$Accuracy_{pred}$	0.973		0.365
		Qualitative	3		1
	Geneva	$Accuracy_{pred}$	0.433	0.644	
		Qualitative	0	0	

Based on these results, the estimation of a classification model is sample-specific. It can be made with a linear discriminant method such as LDA or PLS-DA with the raw SWIR dataset, even if some pre-treatment slightly improves the performance.

4.2. Event layer classification with classical images

The true RGB image can also be converted into HSV (Hue, Saturation, Lightness) or L*a*b* (lightness, color) color spaces and reduced to a grayscale level. The HSV and L*a*b* transformations have been proven to be more adaptable for classification purposes (Bora et al., 2015; Hernández-Hernández et al., 2016). The grayscale levels are the most straightforward color space.

Table 5 shows that the conventional image presents slightly lower performances with the VNIR data and has the same mispredictions in terms of surface variations, shadows, and laminated areas (Supplementary figure 2). All of these observations highlight that these methods learn the color of the deposits too well with VNIR data and do not learn enough from the chemical composition. Then, machine learning and a conventional image can be used in the case of a

clean image and sample with only color differences between the classes and learning of all types of sample events and defects.

Table 5: Comparison of the conventional image discriminant models with the optimal predictions being estimated by the hyperspectral images

Sample	Performance	Grayscale	RGB	HSV	L*a*b*	VNIR HSI	SWIR HSI
Allos	Method	ANN – 2 neurons					PLS-DA
	$Accuracy_{cal}$	0.966	0.821	0.817	0.821	0.889	0.900
	$Accuracy_{pred}$	0.963	0.824	0.808	0.823	0.890	0.902
	Qualitative	4	4	4	4	3	5
Bourget	Method	ANN – 2 neurons				RF	PLS-DA
	$Accuracy_{cal}$	0.995	0.903	0.904	0.906	0.996	0.969
	$Accuracy_{pred}$	0.994	0.898	0.899	0.903	0.995	0.958
	Qualitative	2	2	2	2	3	5
Geneva	Method	ANN – 2 neurons				LDA	LDA
	$Accuracy_{cal}$	0.911	0.976	0.976	0.975	0.987	0.992
	$Accuracy_{pred}$	0.884	0.979	0.983	0.982	0.989	0.989
	Qualitative	1	2	2	2	4	5

4.3. Comparison between HSI and naked-eye chronicles

The discretization of the event layers allows for estimation of event layer occurrence along the sediment section and comparison of the event layers with naked-eye event chronicle. The classification map was reduced to a summed profile, with pixels equal to 0 for continuous sedimentation and 1 for an event layer. We assume that the deposits are parallel; if this is not the case, image processing must be used to correct the deformation when possible. This profile can also be used as an event occurrence probability with normalization by the image width in pixels. It was smoothed with a second-order polynomial Savitzky-Golay filter to reduce mis-classifications (Savitzky and Golay, 1964). A low threshold (below 20%) allows separation of all deposits but also discovery of some artifacts, and the boundaries can be overestimated due to curvatures. Conversely, a high threshold (above 70%) only finds the large deposits, but close ones can be fused. Thus, a double threshold was used. First, using the half-width of the image to classify each

column to one class allowed discovery of the most relevant deposits, but close layers could be observed as a large one. The second threshold of 15% of the image width was used for event layers thicker than 5 mm to potentially divide them. Finally, the chronicle can be reconstructed with the depth and thickness of each event layer. Naked-eye chronicles of the three cores were estimated and can be compared with the hyperspectral ones (Jenny et al., 2014; Rapuc et al., 2020; Wilhelm et al., 2012).

Figure 9 compares the identification of event layers in terms of depth and thickness between the HSI and naked-eye approaches. In general, HSI results in thicker event layers than naked-eye observations. This result can be explained by the limited ability of the eyes to characterize the event limits (resolution grain) or its curvature (mis-identification). Machine learning also enables one to identify new deposits that were not visually detected (due to their small thickness or texture or color differences). They must be assessed by other high-resolution techniques such as microscopy to verify their relevance. The number of detected event layers was high (Table 1, Table 6) due to the detection of supplementary thinner layers.

Initially, this work was developed to study only flood events that were manually labeled. Nonetheless, HSI does not appear to have sufficient discriminant spectral information to distinguish different triggering mechanisms for the event layers (e.g., flood, slumps induced by seismic-shaking, etc.). However, the HSI model is the first fast and non-destructive method to semi-automatically detect event layers in different sedimentary contexts and represents a clear improvement in sedimentology.

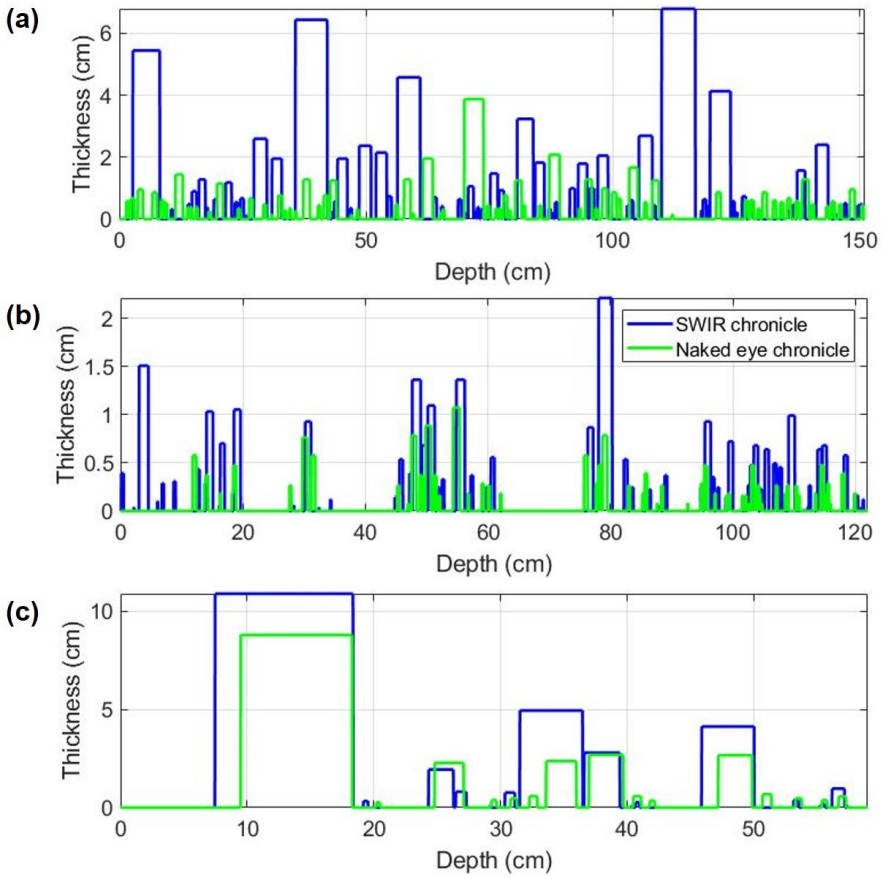

Figure 9: Comparison of the naked-eye and HSI estimated chronicles for the three samples: (a) Allos; (b) Bourget; (c) Geneva

Table 6: Statistics for HSI event layer detection

	N	$N_{<1\,mm}$	Average (mm)	Standard deviation (mm)	Minimum (mm)	Maximum (mm)
Allos	88	12	9.64	13.51	0.32	68.19
Bourget	72	19	4.24	4.28	0.20	22.31
Geneva	26	11	11.37	23.81	0.22	109.01

4.4. Perspectives

It is worth noting that we only focused on event layers, and the models are site-specific. Some strategies can be tested in future works. The first strategy would be to create a multi-site database to learn several event types and include continuous sedimentation cases (strata or homogeneous). A second strategy could be to use complementary information estimated by other sensors, such as XRF spectroscopy, which is also a non-destructive high-resolution (up to 200 µm) analysis, for elemental composition.

It would also be interesting to use a spatial-spectral approach to add information contained in both dimensions, such as the color and grain size gradient, along a flood event. Deep learning with a convolutional neural network (CNN) uses this type of approach and could be interesting for a large multi-site database. This method introduces multi-scale local feature learning and some translation and rotation invariance, which are of interest for image classification (Schmidhuber, 2015). We have tested a CNN1D that uses only the spectral dimension, but it has poor performance that may be due to too small of a database and a too simple of a problem that an ANN with few neurons could model. In future work, we will use a CNN3D that uses a spatial-spectral approach (Ben Hamida et al., 2018).

We have shown that the combination of VNIR and SWIR does not increase the discriminating capacity. Improvements can be made with surface defect correction before data acquisition or with pre-processing after data acquisition, or the defects can be detected and removed from the classification map. Another method could be to make two separate classifications with both sensors and subsequently combine them with different weights using, for example, fuzzy or belief function methods to improve the certainty of the predictions (Lian et al., 2019; Tehrani et al., 2019).

This study has shown that event layers can be estimated at high resolution with hyperspectral imaging in the cores used in the calibration. A first discriminant model based on LDA or PLS-DA, which is estimated with raw hyperspectral data, will enable one to determine the possibility of discrimination among different classes. A similar method has already been used to detect tephra layers (Aymerich et al., 2016). Then, our proposed method may be applied to case studies to detect any type of events such as tsunamis, earthquakes, landslides, storms, and any other laminae. This method will be very useful for paleoenvironment and paleoclimate studies and will enable the creation of event chronicles.

5. Conclusions

We studied the potential of three hyperspectral sensors (VNIR, SWIR, VNIR-SWIR) to image three sediment cores and created machine learning models. This study aimed to automatically discriminate different types of sedimentation (continuous versus event layer) with non-destructive,

high-resolution, time-saving methods. Seven discrimination methods coupled with raw data or eight pre-processing procedures were used to find an optimal model. We found that the SWIR sensor enabled one to create the most robust models with discriminant analysis (LDA, PLS-DA). Raw data presented relevant predictions, but the use of a pre-processing procedure can slightly improve the performance and robustness of the model. The models were quantitatively assessed with prediction accuracies above 0.9. For the qualitative model, event layers presented colors and textures that differed from those of continuous sedimentation and could be identified with naked-eye observation to check the relevance of the prediction maps. The discriminant wavelengths are associated with organic matter and some mineral bands. Finally, event chronicles could be estimated from the classification maps by calculating the depth and thickness of each deposit. Unfortunately, the hyperspectral sensors used in this study do not have sufficient spectral discriminant information to characterize the trigger of the event layer and whether different types of events were present in the same sediment core. Future work will enable the characterization of the triggers by combining hyperspectral imaging with other sensors or using spatial-spectral machine learning methods. This study highlights the sediment lithology discrimination capacity of hyperspectral imaging with manual labelling. Future application of this method on sediment sections will allow creation of robust chronicles of events with characteristic wavelengths and enhance the knowledge about the evolution of the frequency of extreme geodynamic events.

Acknowledgements

Coring supports were provided by the French National Research Agency's with the IPER-RETRO program for Lake Geneva (ANR-08-VUL 005) and the Pygmalion project for Lake Allos (ANR BLAN07-2_204489). Hyperspectral imaging was processed at the University of Normandie-Rouen and funded by the Region Normandie, which supports the scientific consortium SCALE UMR CNRS 3730.

Computer Code Availability

The Matlab codes used in this study to perform all these processing (machine learning and pre-processing) can be accessed in the following repository:

https://github.com/JacqKevin/HSI_SupervisedClassification.

Description of author's responsibilities.

Kévin Jacq: Data acquisition and processing; Algorithm development; Writing original draft
William Rapuc: Data processing; Sedimentology interpretation; Writing original draft
Alexandre Benoit: Machine learning methods; Review and editing the draft
Didier Coquin: Machine learning methods; Review and editing the draft
Bernard Fanget: Spectroscopy and chemometrics methods; Review and editing the draft
Yves Perrette: Spectroscopy and chemometrics methods; Review and editing the draft
Pierre Sabatier: Sedimentology interpretation; Review and editing the draft
Bruno Wilhelm: Flood event interpretation; Data processing; Review and editing the draft
Maxime Debret: Data acquisition; Review and editing the draft
Fabien Arnaud: Data processing; Review and editing the draft

Supplementary Material

Figures

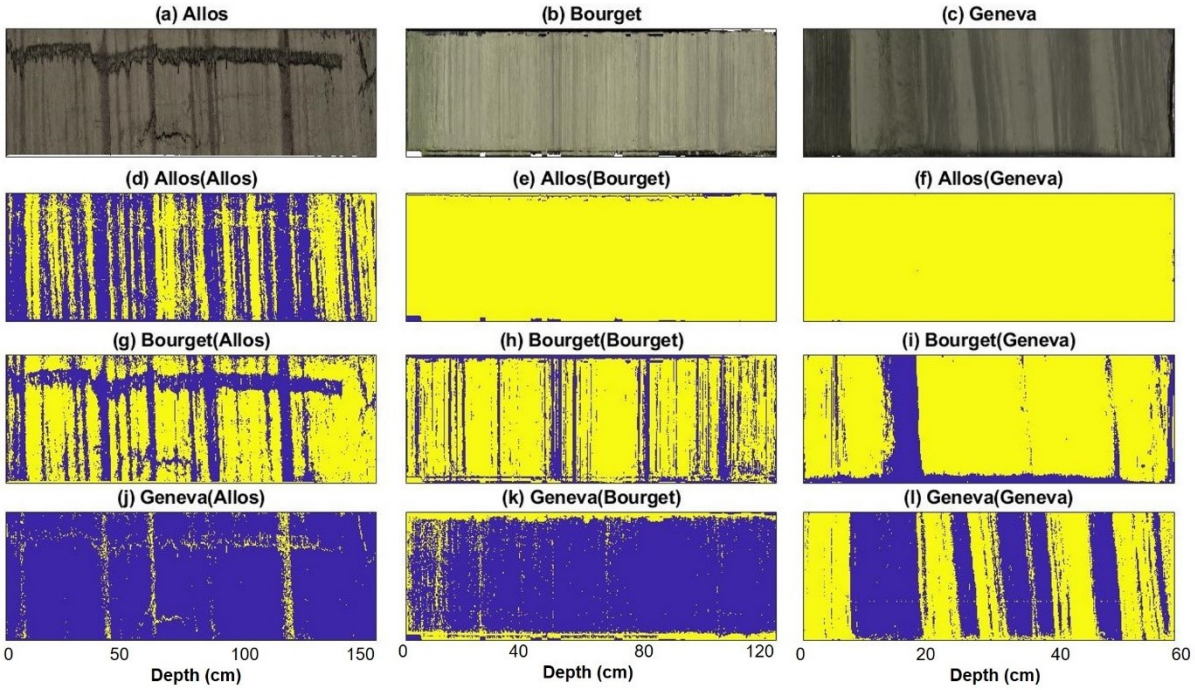

Supplementary figure 1: Classification maps estimated by model transfer: (d-e-f): Allos model; (g-h-i): Bourget model; (j-k-l): Geneva model; (d-g-j): Allos data; (e-h-k): Bourget data; (f-i-l): Geneva data.

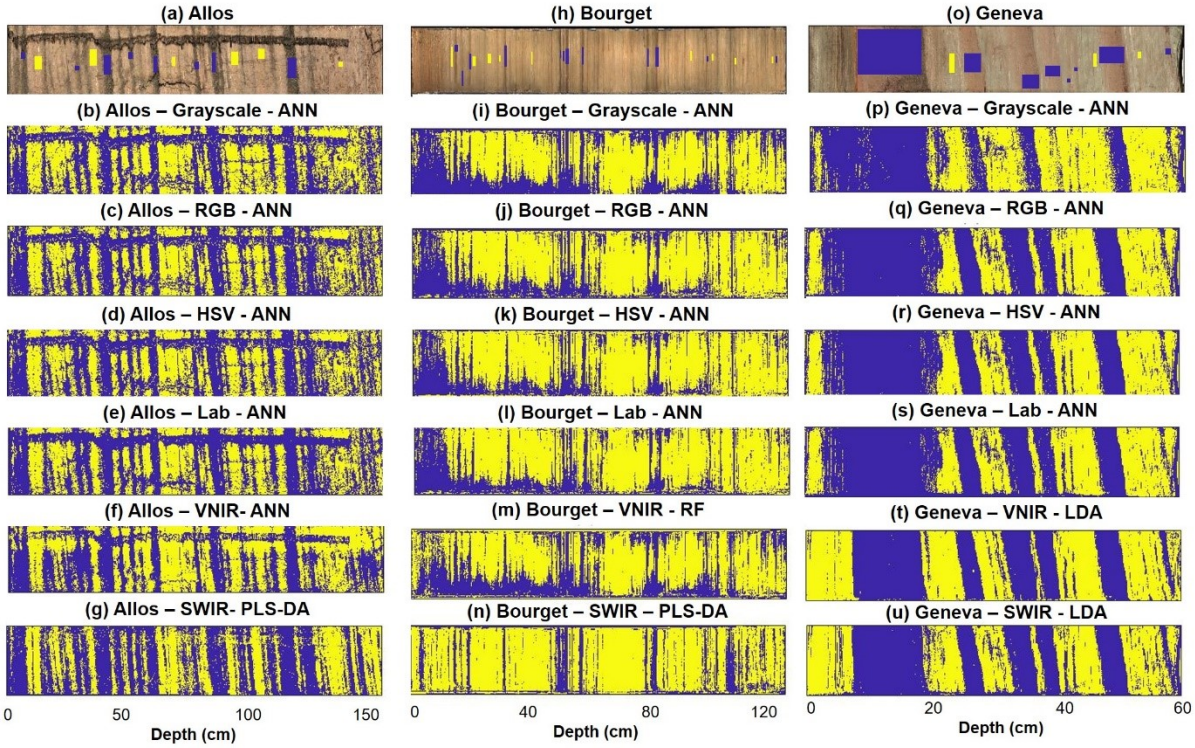

Supplementary figure 2: Comparison of the classification maps estimated by the learning of the conventional images and HSI

Tables

Supplementary table 1: Parameters of each machine learning method

Method	Parameters
DT	Split predictor: Standard CART Split criterion: Gini's diversity index Decision tree pruning based on error criterion
RF	Ensemble-aggregation method: Adaptive logistic regression Number of ensemble learning cycles: 100
ANN	Number of neurons: 2-10 Training function: Scaled conjugate gradient backpropagation Performance function: Cross-Entropy
LDA	Discriminant type: Linear
QDA	Discriminant type: Quadratic
PLS-DA	Latent variable estimation method: NIPALS Maximum number of latent variables: 15 Selection of the number of latent variables: R^2 differences between two consecutive latent variables are less than 2%

Supplementary table 2: Optimal models for the VNIR data depending on the sample and discrimination method

Sample	Performances	DT	RF	ANN	LDA	QDA	PLS-DA
Allos	Processing	CLAHE	Detrend	CLAHE	CLAHE	CLAHE	CLAHE
	Neurons			2			
	$Accuracy_{cal}$	0.978	0.886	0.889	0.863	0.860	0.840
	$Accuracy_{pred}$	0.828	0.882	0.890	0.889	0.889	0.879
	Qualitative	3	3	3	2	2	2
	Computation time (s)	42.544	1272.513	263.840	8.086	251.592	12.975
Bourget	Processing	Raw	Raw	Raw	Raw	Raw	Raw
	Neurons			2			
	$Accuracy_{cal}$	0.999	0.996	0.996	0.994	0.994	0.993

	$Accuracy_{pred}$	0.994	0.995	0.996	0.993	0.992	0.991
	Qualitative	2	3	2	2	2	2
	Computation time (s)	1.817	139.542	5.174	1.216	54.210	2.057
Geneva	Processing	Detrend	Detrend	Detrend	Detrend	Detrend	Detrend
	Neurons			2			
	$Accuracy_{cal}$	0.998	0.990	0.992	0.987	0.987	0.985
	$Accuracy_{pred}$	0.987	0.993	0.994	0.989	0.989	0.985
	Qualitative	2	2	2	3	3	3
	Computation time (s)	2.615	200.019	16.167	1.142	52.417	2.814

Supplementary table 3: Optimal models for the SWIR data depending on the sample and discrimination method

Sample	Performances	DT	RF	ANN	LDA	QDA	PLS-DA
Allos	Processing	Raw	SNV	Autoscale	Raw	Raw	SNV
	Neurons			3			
	$Accuracy_{cal}$	0.982	0.925	0.922	0.920	0.920	0.900
	$Accuracy_{pred}$	0.876	0.928	0.935	0.927	0.926	0.902
	Qualitative	3	5	5	5	5	5
	Computation time (s)	1.214	95.740	6.989	0.664	39.287	0.800
Bourget	Processing	Detrend	Detrend	Detrend	Detrend	Detrend	Detrend
	Neurons			2			
	$Accuracy_{cal}$	0.994	1.000	0.976	0.971	0.972	0.969
	$Accuracy_{pred}$	0.952	0.959	0.967	0.954	0.955	0.958
	Qualitative	2	3	4	5	5	5

	Computation time (s)	0.266	10.402	0.402	0.167	24.268	0.219
Geneva	Processing	SNV	SNV	SNV	SNV	SNV	SNV
	Neurons			2			
	$Accuracy_{cal}$	0.998	1.000	0.996	0.992	0.992	0.991
	$Accuracy_{pred}$	0.991	0.993	0.993	0.989	0.988	0.987
	Qualitative	3	4	4	5	5	5
	Computation time (s)	0.155	5.436	0.255	0.113	21.478	0.163

Supplementary table 4: Optimal models for the VNIR-SWIR data depending on the sample and discrimination method

Sample	Performances	DT	RF	ANN	LDA	QDA	PLS-DA
Allos	Processing	CLAHE	SNV	SNV	Raw	Raw	SNV
	Neurons			2			
	$Accuracy_{cal}$	0.984	0.943	0.933	0.931	0.931	0.901
	$Accuracy_{pred}$	0.877	0.931	0.940	0.935	0.935	0.921
	Qualitative	3	5	4	5	5	5
	Computation time (s)	2.726	86.900	15.562	1.097	49.604	1.206
Bourget	Processing	Raw	Raw	Raw	Detrend	Detrend	Raw
	Neurons			2			
	$Accuracy_{cal}$	0.993	1.000	0.981	0.979	0.979	0.979
	$Accuracy_{pred}$	0.966	0.967	0.970	0.969	0.969	0.968
	Qualitative	1	2	2	3	4	4
	Computation time (s)	0.372	15.082	0.672	0.265	26.742	0.276
Geneva	Processing	Raw	Raw	Raw	Raw	Raw	Raw

	Neurons			2			
	$Accuracy_{cal}$	0.999	1.000	0.998	0.997	0.993	0.991
	$Accuracy_{pred}$	0.996	0.996	0.996	0.993	0.991	0.993
	Qualitative	2	2	4	4	4	4
	Computation time (s)	0.223	17.307	0.758	0.437	52.612	0.404

Annexe III | Listes des publications

Orcid : https://orcid.org/0000-0001-8258-4545

Researchgate : https://www.researchgate.net/profile/William-Rapuc

2021

- Tachikawa, K., **Rapuc, W.**, Vidal, L., Dubois-Dauphin, Q., Westerhold, T., Guihou, A., Bickert, T., Pérez-Asensio, J-N., Deschamps, P., Skonieczny, C., 2021. Eastern Atlantic deep-water circulation and carbon storage inferred from neodymium and carbon isotopic compositions over the past 1.1 million years, Quaternary Science Reviews 252, 106752. https://doi.org/10.1016/j.quascirev.2020.106752

- **Rapuc, W.**, Sabatier, P., Arnaud, F., 2021. Human activities disturb lake sediment records of past flood frequencies. Past Global Changes Magazine, 29(1), 42-43. doi.org/10.22498/pages.29.1.42

- **Rapuc, W.**, Bouchez, J., Sabatier, P., Genuite, K., Poulenard, P., Gaillardet, J., Arnaud, F. Quantitative evaluation of human and climate forcing on erosion in the Alpine Critical Zone over the last 2,000 years. Quaternary Science Reviews. In review

- **Rapuc, W.**, Arnaud, F., Sabatier, P., Anselmetti, F-S., Piccin, A., Bastien, A., Augustin, L., Régnier, E., Dumoulin, J-P., Gaillardet, J., Von Grafenstein, U. Instant sedimentation in a deep Alpine lake (Iseo, Italy) controlled by climate, human and geodynamic forcing. Sedimentology. In review. Preprint: https://www.essoar.org/doi/10.1002/essoar.10504221.1

- Wilhelm B., **Rapuc W.**, Amann B., Anselmetti F.S., Arnaud F., Blanchet J., Brauer A., Czymzik M., Giguet-Covex C., Glur L., Grosjean M., Irmler R., Nicolle M., Sabatier P., Swiercynski T., Wirth S.B., Flood hazard under natural and anthropogenic warmer climates in the European Alps. Nature Geoscience, In review.

- Jacq, K., **Rapuc, W.**, Benoit, A., Develle-Vincent, A-L., Coquin, D., Fanget, B., Perrette, Y., Sabatier, P., Wilhelm, B., Debret, M., Arnaud, F., Sedimentary structure discrimination with hyperspectral imaging in sediment cores. Remote Sensing of Environment. In review

- Jacq, K., Ployon, E., **Rapuc, W.**, Blanchet, C., Pignol, C., Coquin, D., Fanget, B., Structure-from-motion multi-view photogrammetry applied to linear-scan sediment cores images, Sedimentary Geology, In review

2020

- **Rapuc, W.**, Jacq, K., Develle, A.-L., Sabatier, P., Fanget, B., Perrette, Y., Coquin, D., Debret, M., Wilhelm, B., Arnaud, F., 2020. XRF and hyperspectral analyses as an automatic way to detect flood events in sediment cores. Sediment. Geol. 409, 105776. https://doi.org/10.1016/j.sedgeo.2020.105776

- Tachikawa, K., **Rapuc, W.**, Dubois-Dauphin, Q., Guihou, A., Skonieczny, C., 2020. Reconstruction of ocean circulation based on neodymium isotopic composition: potential

limitations and application to the Mid-Pleistocene transition, Oceanography 33, 80 – 87. https://doi.org/10.5670/oceanog.2020.205

- Andrič, M., Sabatier, P., **Rapuc, W.**, Ogrinc, N., Dolenec, M., Arnaud F., Von Grafenstein, U., Šmuc, A., 6600 years of human and climate impacts on lake-catchment and vegetation in the Julian Alps (Lake Bohinj, Slovenia), Quaternary Science Reviews, Volume 227, 2020, 106043, ISSN 0277-3791, https://doi.org/10.1016/j.quascirev.2019.106043.

2019

- **Rapuc, W.**, Sabatier, P., Arnaud, F., Palumbo, A., Develle, A.-L., Reyss, J.-L., Augustin, L., Régnier, E., Piccin, A., Chapron, E., Dumoulin, J-P., and Von Grafenstein, U. (2019), Holocene-long record of flood frequency in the Southern Alps (Lake Iseo, Italy) under human and climate forcing. Global and Planetary Change, volume 175, p. 160-172, https://doi.org/10.1016/j.gloplacha.2019.02.010

- Jouve, G., Vidal, L., Adallal, R., Rhoujjati, A., Benkaddour, A., Chapron, E., Tachikawa, K., Bard, E., Courp, T., Dezileau, L., Hebert, B., **Rapuc, W.**, Simonneau, A., Sonzogni, C. and Sylvestre, F. (2019) Recent hydrological variability of the Moroccan Middle Atlas Mountains inferred from microscale sedimentological and geochemical analyses of lake sediments. Quaternary Research. Cambridge University Press, 91(1), pp. 414–430. https://doi.org/10.1017/qua.2018.94

2018

- **Rapuc, W.**, Sabatier, P., Andrič, M., Crouzet, C., Arnaud, F., Chapron, E., Šmuc, A., Develle, A.-L., Wilhelm, B., Demory, F., Reyss, J.-L., Régnier, E., Daut, G. Von Grafenstein, U., and Manville, V. (2018), 6600 years of earthquake record in the Julian Alps (Lake Bohinj, Slovenia). Sedimentology, 65 : 1777-1799. https://doi.org/10.1111/sed.12446

Quaternary Science Reviews 252 (2021) 106752

Contents lists available at ScienceDirect

Quaternary Science Reviews

journal homepage: www.elsevier.com/locate/quascirev

Eastern Atlantic deep-water circulation and carbon storage inferred from neodymium and carbon isotopic compositions over the past 1.1 million years

Kazuyo Tachikawa [a, *], William Rapuc [a, b], Laurence Vidal [a], Quentin Dubois-Dauphin [a], Thomas Westerhold [c], Abel Guihou [a], Torsten Bickert [c], José N. Pérez-Asensio [a], Pierre Deschamps [a], Charlotte Skonieczny [d]

[a] Aix Marseille Univ, CNRS, IRD, INRAE, Coll France, CEREGE, Aix-en-Provence, France
[b] Environment Dynamics and Territories of Mountains (EDYTEM), Université Savoie Mont Blanc, CNRS, 73000, Chambéry, France
[c] MARUM, University of Bremen, 28359, Bremen, Germany
[d] Université Paris-Saclay, CNRS, GEOPS, 91405, Orsay, France

ARTICLE INFO

Article history:
Received 17 May 2020
Received in revised form
7 December 2020
Accepted 7 December 2020
Available online xxx

Keywords:
Mid-Pleistocene transition
Nd isotopic composition
Benthic foraminiferal $\delta^{13}C$
Ocean circulation
Atlantic ocean

ABSTRACT

The Mid-Pleistocene transition (MPT; 1200 to 800 thousand years, kyr) is marked by the shift from 41-kyr to 100-kyr interglacial-glacial cyclicity without substantial change in the astronomical forcing. This change in climate response relied on internal feedback processes including interaction between ice sheet/sea ice, ocean circulation and the carbon cycle. It was suggested that a major perturbation of global oceanic carbon chemistry occurred at around 900 ka (Marine Isotope Stage, MIS, 24–22) although the mechanism responsible for the change is still to be elucidated. To investigate the link between the Atlantic Meridional Overturning Circulation (AMOC) and oceanic carbon storage for the past 1100 kyr, we combined neodymium isotopic composition ($^{143}Nd/^{144}Nd$ or ε_{Nd}) recorded in foraminiferal authigenic fractions with epibenthic foraminiferal $\delta^{13}C$ and $\delta^{18}O$ from two cores in the North- and South-east Atlantic Ocean. Glacial/interglacial ε_{Nd} amplitude is smaller before the 900-ka event than after the event. The 900-ka event is marked by increase in seawater ε_{Nd} at both sites. These observations are consistent with previous studies, suggesting basin-wide ε_{Nd} changes. Combined with existing data, these new results reveal a persistent meridional gradient of seawater ε_{Nd} in the Atlantic Ocean over the past 1100 kyr. By comparing the reconstructions with numerical modelling results, we propose that weaker AMOC and changes in Nd sources to the North Atlantic were the main reasons for the observed ε_{Nd} shift at the 900-ka event in relation to the evolution of the Northern hemisphere cryosphere. The influence of enhanced Southern Ocean overturning circulation on ε_{Nd} values was estimated to be minor. Seawater ε_{Nd} and benthic $\delta^{13}C$ relationship for the whole study period indicates the presence of carbon-rich glacial deep water (>3000 m) in the North and the South Atlantic, in particular at MIS 22 and 24. This suggests that, in addition to weaker AMOC, reduction of deep-water ventilation and/or air-sea exchange in the Southern Ocean could have been responsible for the observed low benthic $\delta^{13}C$ values. Together with increased biological productivity due to iron fertilization in the Southern Ocean, the physical process significantly contributed to the deep Atlantic carbon storage during the 900-ka event and the subsequent glacial periods.

1. Introduction

The Mid-Pleistocene transition (MPT; 1200 to 800 thousand years, kyr) is marked by an intensification of glacial/interglacial amplitude and a shift of climate cycle from 41 kyr to 100 kyr (Clark et al., 2006; Chalk et al., 2017). Since the observed changes cannot be explained by variation in solar insolation alone, internal feedback processes should have played a key role. The Atlantic Meridional Overturning Circulation (AMOC) is defined as zonally

* Corresponding author.
E-mail address: kazuyo@cerege.fr (K. Tachikawa).

https://doi.org/10.1016/j.quascirev.2020.106752
0277-3791/

Sedimentary Geology 409 (2020) 105776

Contents lists available at ScienceDirect

Sedimentary Geology

journal homepage: www.elsevier.com/locate/sedgeo

XRF and hyperspectral analyses as an automatic way to detect flood events in sediment cores

William Rapuc [a,*], Kévin Jacq [a,b], Anne-Lise Develle [a], Pierre Sabatier [a], Bernard Fanget [a], Yves Perrette [a], Didier Coquin [b], Maxime Debret [c], Bruno Wilhelm [d], Fabien Arnaud [a]

[a] Université Grenoble Alpes, Université Savoie Mont Blanc, CNRS, EDYTEM, LE Bourget du lac, France
[b] Université Savoie Mont Blanc, LISTIC, 74944 Annecy Le Vieux, France
[c] Université De Caen, CNRS, LM2C, 76821 Mont-Saint-Aignan, France
[d] Institute for Geosciences and Environmental research (IGE), UGA, CNRS, IRD, Grenoble, France

ARTICLE INFO

Article history:
Received 22 July 2020
Received in revised form 21 September 2020
Accepted 22 September 2020
Available online 25 September 2020

Editor: Dr. Jasper Knight

Keywords:
Lake sediment
Hyperspectral analyses
XRF geochemical analysis
Automatic flood chronicle

ABSTRACT

Long-term changes in flood activity have often been reconstructed to understand their relationships to climate changes. This requires identification of flood layers according to certain characteristics (e.g., texture, geochemical composition, grain-size) and then to count them using naked-eye observation. This method is, however, time-consuming, and intrinsically characterized by a low resolution that may lead to bias and misidentification. To overcome this limitation, high-resolution analytical approaches can be used, such as X-ray fluorescence spectroscopy (XRF), X-ray computed tomography, or hyperspectral imaging (HSI). When coupled with discriminant algorithms, HSI allows for automatic identification of event layers. Here, we propose a new method of flood layers identification and counting based on the combination of both HSI and XRF core scanner analyses, applied to a Lake Bourget (French Alps) sediment sequence. We use a hyperspectral sensor from the short wave-infrared spectral range to create a discrimination model between event layers and continuous sedimentation. This first step allows the estimation of a classification map, with a prediction accuracy of 0.96, and then the automatic reconstruction of a reliable chronicle of event layers (including their occurrence and deposit thicknesses). XRF signals are then used to discriminate flood layers among all identified event layers based on site-specific geochemical elements (in the case of Lake Bourget: Mn and Ti). This results in an automatically generated flood chronicle. Changes in flood occurrence and event thickness through time reconstructed from the automatically generated floods chronicle are in good agreement with the naked-eye-generated chronicle. In detail, differences rely on a larger number of detected flood events (i.e., increase of 9% of the number of layers detected) and a more precise layer thickness estimation, thanks to a higher resolution. Therefore, the developed methodology opens a promising avenue to increase both the efficiency (timesaving) and robustness (higher accuracy) of paleoflood reconstructions from lake sediments. Also, this methodology can be applied to identify any specific layers (e.g., varve, tephra, mass-movement turbidite, tsunami) and, thereby, it has a direct implication in paleolimnology, paleoflood hydrology and paleoseismology from sediment archives.

1. Introduction

Changes in flood occurrence and magnitude are expected due to climate change in many regions, affecting an increasing number of people (Hirabayashi et al., 2013; Blöschl et al., 2019). Large uncertainties still exist on such changes and long-term flood records are of high value to fully understand climate-flood relationships (Merz et al., 2014; Wilhelm et al., 2019). To this end, numerous studies are undertaken on geological records such as lake sediments to reconstruct centennial to millennial flood records (Noren et al., 2002; Moreno et al., 2008; Giguet-Covex et al., 2012; Wilhelm et al., 2012, 2017; Glur et al., 2013; Wirth et al., 2013; Sabatier et al., 2017; Corella et al., 2019; Rapuc et al., 2019). Flood events produce turbidity currents in the lake basin that will usually lead to a normally graded detrital layer that differs from the surrounding continuous sedimentation (Sturm and Matter, 1978; Gilli et al., 2013). However, other processes such as earthquakes, spontaneous delta front collapses, and lake-level changes, can also produce turbidity currents in lakes (Sauerbrey et al., 2013; Wilhelm et al., 2017; Rapuc et al., 2018). In most of these studies, to count and differentiate the event layers, the sediment facies are first described visually, then several sedimentological and geochemical analyses are

* Corresponding author at: UMR CNRS 5204 Environnements, Dynamiques et Territoires de la Montagne (EDYTEM), Université Savoie Mont Blanc, Campus scientifique, 73376 Le Bourget du Lac cedex, France.
E-mail address: william.rapuc@univ-smb.fr (W. Rapuc).

https://doi.org/10.1016/j.sedgeo.2020.105776
0037-0738/

RECONSTRUCTION OF OCEAN CIRCULATION BASED ON NEODYMIUM ISOTOPIC COMPOSITION

Potential Limitations and Application to the Mid-Pleistocene Transition

By Kazuyo Tachikawa, William Rapuc, Quentin Dubois-Dauphin, Abel Guihou, and Charlotte Skonieczny

ABSTRACT. As the ocean is Earth's largest reservoir of carbon, its circulation strongly influences the global carbon cycle. The neodymium (Nd) isotopic composition ($^{143}Nd/^{144}Nd$ or ε_{Nd}) of seawater has been used as a tracer for ocean circulation. We revisit the capacity of this tracer using compiled modern seawater data sets and recent data (≤ 10,000 years, 10 kyr) extracted from the sedimentary record. Empirical equations that predict seawater ε_{Nd} values from hydrography parameters can be used to evaluate possible biases in Nd isotopic ratios. The good overall agreement between measured seawater and predicted ε_{Nd} values confirms the usefulness of Nd isotopic composition as a tracer of large-scale deepwater circulation in many parts of the modern ocean. Offsets observed between the sedimentary record and predicted values in certain oceanic regions can be partly explained by the contribution of porewater-derived Nd to sedimentary authigenic fractions. We use Nd isotopic composition to study a major climate transition in the middle Pleistocene called the "900 ka event," which is characterized by a major perturbation in ocean carbon chemistry. All available reconstructed seawater ε_{Nd} data indicate an increase in isotopic composition at the 900 ka event relative to the present value in the eastern Atlantic Ocean. This shift cannot be explained solely by more active formation of southern-sourced water that has a higher ε_{Nd} value than the northern-sourced water. We suggest that a reduction in the Atlantic meridional overturning circulation and/or changes in Nd sources to the North Atlantic were the main cause(s) of the change in ε_{Nd} observed during the evolution of the Northern Hemisphere cryosphere.

INTRODUCTION

The ocean contains approximately 60 times more carbon than the atmosphere. About 20%–35% of the carbon dioxide (CO_2) emitted by burning fossil fuels has been absorbed by the ocean (Khatiwala et al., 2009). Changes in the ocean state, such as those that occurred during the last glacial maximum (LGM) and subsequent deglaciation, could significantly affect the carbon cycle by releasing absorbed carbon to the atmosphere in the future. The glacial atmospheric CO_2 concentration was lower than the pre-industrial value mainly because of increased carbon storage in the ocean via a more active biological pump in the Southern Ocean and/or more efficient carbon storage in the strongly stratified deep ocean (Hain et al., 2010; Adkins, 2013). During the deglaciation, dissipation of old deep water that was rich in respired carbon in the Southern Ocean contributed to CO_2 release to the atmosphere by the upwelling branch of the Atlantic overturning circulation (Skinner et al., 2010).

Although proxy-based reconstructions have provided important insights into past ocean circulation, they do not always tell consistent stories because each proxy has its own bias. Recent advances in analytical instruments and coordinated international programs such as GEOTRACES have provided abundant high-quality data and contributed to a better understanding of proxy behavior in the modern ocean. Furthermore, the spatial coverage of marine sediment cores has greatly improved over recent decades, thanks to international programs such as the Ocean Drilling Program (ODP)/ International Ocean Discovery Program (IODP) and the International MArine Global changE Study (IMAGES). Lastly, tremendous progress in climate modeling has revealed the physical and biogeochemical processes involved in climate variability. In particular, proxy-enabled models make it possible to simulate proxy fields, which in turn can be compared to proxy reconstructions (Arsouze et al., 2009; Menviel et al., 2012; Rempfer et al., 2012; Roche and Caley, 2013; Friedrich et al., 2014), allowing evaluation of the capacity of climate models to predict deepwater circulation changes.

The objective of this paper is to revisit the behavior of neodymium (Nd) isotopic composition of seawater as a tracer of water mass provenance and to apply this tracer to a major climate transition, the Mid-Pleistocene transition (MPT, about one million years). In the modern ocean, the Nd isotope composition of seawater follows the global thermohaline circulation (Figure 1), but factors other than water mass mixing influence its distribu-

Quaternary Science Reviews 227 (2020) 106043

Contents lists available at ScienceDirect

Quaternary Science Reviews

journal homepage: www.elsevier.com/locate/quascirev

6600 years of human and climate impacts on lake-catchment and vegetation in the Julian Alps (Lake Bohinj, Slovenia)

Maja Andrič [a, *], Pierre Sabatier [b], William Rapuc [b], Nives Ogrinc [c], Matej Dolenec [d], Fabien Arnaud [b], Ulrich von Grafenstein [e], Andrej Šmuc [d]

[a] ZRC SAZU, Institute of Archaeology, Novi trg 2, 1000, Ljubljana, Slovenia
[b] Université Grenoble Alpes, Université Savoie Mont Blanc, CNRS, EDYTEM, 73000, Chambéry, France
[c] Jožef Stefan Institute, Department of Environmental Sciences, Jamova Cesta 39, 1000, Ljubljana, Slovenia
[d] Department of Geology, University of Ljubljana, Privoz 11, 1000, Ljubljana, Slovenia
[e] LSCE, Université de Versailles Saint-Quentin, Commissariat à l'Énergie Atomique—CNRS, 91198, Gif-sur-Yvette, France

ARTICLE INFO

Article history:
Received 28 June 2019
Received in revised form
28 October 2019
Accepted 30 October 2019
Available online xxx

Keywords:
Holocene
Paleolimnology
Europe
Vegetation dynamics
Human impact
Pollen
Soil erosion
Sedimentology
Stable isotopes
Inorganic geochemistry

ABSTRACT

Mountain grazing and ore processing had a significant impact on the Alpine environment in the last 5000 years, but few studies have so far focused on environmental changes of the south eastern Alps. This study investigates the vegetation history and sedimentary processes in the catchment of Lake Bohinj (Julian Alps, Slovenia), where a 12-m-long core was collected in the central part of the lake. Sediment in the early Holocene section of the core was partially reworked due to a major seismic event dated to 6711–6523 yr cal BP (Rapuc et al. 2018), therefore a detailed palaeoenvironmental reconstruction was performed only for the top 4.4 m of the core. Here the results of mineralogical, sedimentological, geochemical, stable isotope ($\delta^{13}C$ and $\delta^{15}N$), and pollen analysis are presented in order to better understand the impact of people (agriculture, grazing, mining) on the environment, and climate-human interactions over the last 6600 years.

The results of palynological research suggest that at ca. 6000 yr cal BP Lake Bohinj was surrounded by mixed forest composed of *Picea, Abies*, deciduous *Quercus*, with *Fagus* becoming dominant after ca. 3300 yr cal BP. In the Bronze and especially the Iron Age (3500–2500 yr cal BP), when the region was, according to archaeological data, densely populated, clearing of forests due to agriculture, livestock production and metallurgical activities was detected through Cerealia type pollen, *Plantago lanceolata*, and the decline of *Abies*. These activities probably triggered soil erosion recorded as increased sedimentation rates. In the subsequent centuries human impact on the environment continued (increased), but it seems that the watershed was not destabilised again. Several periods of high terrigenous input were recorded at 6100–6000, 5700–5550, 5000–4600, 3900, 3700–3550, 2300–2200 yr cal BP and could be associated with a mobilisation of river inflow from the eastern flysch bearing catchment, due to river migration during periods of wetter climate. These flood patterns match with periods of enhanced flood activity in the wider Alpine region.

1. Introduction

Grazing and ore processing were among the first activities of people living in the Alps (e.g. Gobet et al., 2003; Walsh et al., 2014; Carrer et al., 2016; Reitmaier, 2017; Reitmaier et al., 2018; Hafner and Schwörer, 2018; Moe and Fedele, 2019; Breitenlechner et al., 2013). More than 5000 years natural resource exploitation has had a significant impact on the delicate Alpine environment. Alpine ecosystems (e.g. alpine meadows and mountain forests), which are limited by low temperatures and short growing season, are sensitive to environmental changes (Leuschner and Ellenberg, 2017, 125). People have altered the vegetation (e.g. decline of *Abies* due to grazing and forest clearance/burning, shift of treeline to lower

* Corresponding author.
E-mail addresses: maja.andric@zrc-sazu.si (M. Andrič), pierre.sabatier@univ-smb.fr (P. Sabatier), william.rapuc@univ-smb.fr (W. Rapuc), nives.ogrinc@ijs.si (N. Ogrinc), smudut@siol.net (M. Dolenec), fabien.arnaud@univ-savoie.fr (F. Arnaud), uli@von-grafenstein.fr (U. von Grafenstein), andrej.smuc@geo.ntf.uni-lj.si (A. Šmuc).

https://doi.org/10.1016/j.quascirev.2019.106043

Global and Planetary Change 175 (2019) 160–172

Contents lists available at ScienceDirect

Global and Planetary Change

journal homepage: www.elsevier.com/locate/gloplacha

Holocene-long record of flood frequency in the Southern Alps (Lake Iseo, Italy) under human and climate forcing

William Rapuc[a,*], Pierre Sabatier[a], Fabien Arnaud[a], Antoine Palumbo[a], Anne-Lise Develle[a], Jean-Louis Reyss[a], Laurent Augustin[b], Edouard Régnier[c], Andrea Piccin[d], Emmanuel Chapron[e], Jean-Pascal Dumoulin[c], Ulrich von Grafenstein[c]

[a] Univ. Grenoble Alpes, Univ. Savoie Mont Blanc, CNRS, EDYTEM, 73000 Chambéry, France
[b] Division technique de l'INSU, Centre de Carottage et de Forage National, CNRS, France
[c] LSCE, Université de Versailles Saint-Quentin, Commissariat à l'Energie Atomique–CNRS, 91198 Gif-sur-Yvette, France
[d] Regione Lombardia, D.G. Territorio e Urbanistica, Struttura Sistema Informativo Territoriale, 20124 Milano, Italy
[e] Laboratoire GEODE, UMR 5602 CNRS-Université Toulouse Jean Jaurès, Maison de la Recherche, 31058 Toulouse, France

ARTICLE INFO

Keywords:
Lake sediment
Holocene
Flood chronicle
Human impact
Southern Alps

ABSTRACT

A high-resolution sedimentological and geochemical analysis of a 21 m sediment sequence of Lake Iseo (Southern Alps, Italy) allowed for the reconstruction of the long-term flood frequency by visual identification of the event layers over the last 12 kyr cal BP. In a previous study that was undertaken on another sediment core from Lake Iseo, these layers were attributed to extreme surface runoff events. However, in this former core, large mass-wasting deposits that induce significant hiatuses did not permit a continuous record of flood events to be established. Such disturbances were absent in the core studied in the present paper. This permitted to establish a high-resolution continuous Holocene record. Based on the flood chronicle and sedimentological and XRF geochemical analyses, we found evidence of a major palaeohydrological transition at approximately 3.8 kyr cal BP, which was previously described as occurring in the western Mediterranean region. The oldest part of the record indeed presents a very low frequency of flood events (< 1 flood/century), while after 4 kyr cal BP, the flood frequency increased. This pattern appears to be in agreement with other Southern Alpine paleo flood records. The transition is interpreted as a nonlinear climate response to the orbital-driven gradual decrease in summer insolation at 60°N, which together with the influence of the Mediterranean mesoscale precipitation events, is typical for the Mediterranean climate. However, the comparison of the flood record with the archaeological and historical data from the watershed suggests that human activity during the Roman period in the vicinity of the main tributaries also influenced the flood frequency. Even in a large Alpine lake and > 2000 years ago, extreme precipitation events that were recorded through the sedimentation process can hence be impacted by the anthropization of the catchment area pointing the requirement of deeper studies of Earth surface critical zone pluri-millennial dynamics.

1. Introduction

In mountainous areas, floods are among the most damaging climatic events in terms of economic and societal losses (Gaume et al., 2009; Glur et al., 2013). In the context of global climate changes, the intensification of catastrophic events, such as floods, is expected in European regions (Hirabayashi et al., 2013). Indeed, even if a decrease in summer precipitation is expected in the Alps by the year 2100, extreme precipitation events that are associated with convective rainfall are assumed to increase (Giorgi et al., 2016). However, tendencies at the regional and local scales are still uncertain, and the study of these extreme events represents a major issue for natural hazards assessment (Stocker et al., 2013). The use of geological paleoclimate records is necessary to understand the past variations of these events in contrasting climatic contexts (Beniston et al., 2007). Lake sediments are widely used to reconstruct paleo-flood activity, as flood events are recorded in a long-term and continuous way (Bøe et al., 2016; Giguet-Covex et al., 2012; Gilli et al., 2013; Glur et al., 2013; Moreno et al., 2008; Noren et al., 2002; Wilhelm et al., 2012; Wirth et al., 2013).

In ideal conditions, paleo-flood records that are obtained from lake

* Corresponding author.
E-mail address: william.rapuc@univ-smb.fr (W. Rapuc).

https://doi.org/10.1016/j.gloplacha.2019.02.010
Received 20 August 2018; Received in revised form 29 January 2019; Accepted 15 February 2019
Available online 20 February 2019

SEDIMENTOLOGY the journal of the International Association of Sedimentologists

Sedimentology (2018) **65**, 1777–1799 doi: 10.1111/sed.12446

6600 years of earthquake record in the Julian Alps (Lake Bohinj, Slovenia)

WILLIAM RAPUC*, PIERRE SABATIER*, MAJA ANDRIČ†, CHRISTIAN CROUZET‡, FABIEN ARNAUD*, EMMANUEL CHAPRON§, ANDREJ ŠMUC¶, ANNE-LISE DEVELLE*, BRUNO WILHELM**, FRANÇOIS DEMORY††, JEAN-LOUIS REYSS*, EDOUARD RÉGNIER‡‡, GERHARD DAUT§§ and ULRICH VON GRAFENSTEIN‡‡

**Univ. Grenoble Alpes, Univ. Savoie Mont Blanc, CNRS, EDYTEM, 73000 Chambéry, France (E-mail: william.rapuc@univ-smb.fr)*

†ZRC SAZU, Institute of Archaeology, Novi trg 2, 1000 Ljubljana, Slovenia

‡Univ. Grenoble Alpes, Univ. Savoie Mont Blanc, CNRS, IRD, ISTerre, 38000 Grenoble, France

§GEODE, Université Jean Jaurès, Maison de la Recherche, 31058 Toulouse Cedex, France

¶Department of Geology, University of Ljubljana, Privoz 11, 1000 Ljubljana, Slovenia

***Univ. Grenoble Alpes, CNRS, IRD, Grenoble INP*, IGE, 38000 Grenoble, France*

††CEREGE, Université Aix-Marseille, CNRS, IRD, Collège de France, Europôle de l'Arbois, BP 80, 13545 Aix en Provence, France

‡‡LSCE, Université de Versailles Saint-Quentin, Commissariat à l'Energie Atomique–CNRS, 91198 Gif-sur-Yvette, France

§§Institut für Geographie, Lehrstuhl Physische Geographie, Löbdergraben 32, 07743 Jena, Germany

Associate Editor – Vern Manville

ABSTRACT

Sequences of lake sediments often form long and continuous records that may be sensitive recorders of seismic shaking. A multi-proxy analysis of Lake Bohinj sediments associated with a well-constrained chronology was conducted to reconstruct Holocene seismic activity in the Julian Alps (Slovenia). A seismic reflection survey and sedimentological analyses identified 29 homogenite-type deposits related to mass-wasting deposits. The most recent homogenites can be linked to historical regional earthquakes (i.e. 1348 AD, 1511 AD and 1690 AD) with strong epicentral intensity [greater than 'damaging' (VIII) on the Medvedev–Sponheuer–Karnik scale]. The correlation between the historical earthquake data set and the homogenites identified in a core isolated from local stream inputs, allows interpretation of all similar deposits as earthquake related. This work extends the earthquake chronicle of the last 6600 years in this area with a total of 29 events recorded. The early Holocene sedimentary record is disturbed by a seismic event (6617 ± 94 cal yr BP) that reworked previously deposited sediment and led to a thick sediment deposit identified in the seismic survey. The period between 3500 cal yr BP and 2000 cal yr BP is characterized by a major destabilization in the watershed by human activities that led to increases in erosion and sedimentation rates. This change increased the lake's sensitivity to recording an earthquake (earthquake-sensitivity threshold index) with the occurrence of 72 turbidite-type deposits over this period. The high turbidite frequency identified could be the consequence of this change in lake earthquake sensitivity and thus these turbidites could be triggered by earthquake shaking, as other origins are discarded. This study illustrates why it is not acceptable to propose a return period for seismic activity recorded in lake sediment if the sedimentation rate varies significantly.

Quaternary Research (2018), 1–17.

doi:10.1017/qua.2018.94

Recent hydrological variability of the Moroccan Middle Atlas Mountains inferred from microscale sedimentological and geochemical analyses of lake sediments

Guillaume Jouve[a]*, Laurence Vidal[a], Rachid Adallal[a,b], Ali Rhoujjati[b], Abdelfattah Benkaddour[b], Emmanuel Chapron[c], Kazuyo Tachikawa[a], Edouard Bard[a], Thierry Courp[d], Laurent Dezileau[e], Bertil Hebert[d], William Rapuc[a], Anaëlle Simonneau[f], Corinne Sonzogni[a], Florence Sylvestre[a]

[a]Aix-Marseille Université, Centre National de la Recherche Scientifique (CNRS), Institut de Recherche pour le Développement (IRD), Institut National de la Recherche Agronomique (INRA), Collège de France, Centre Européen de Recherche et d'Enseignement en Géosciences de l'Environnement (CEREGE), Aix-en-Provence, France
[b]Laboratoire de Géoressources-Unité, Unité de Recherche Associée au Centre National pour la Recherche Scientifique et Technique (CNRST, URAC 42), Faculté des Sciences et Techniques, Université Cadi Ayyad, Marrakech, Morocco
[c]Laboratoire de Géographie de l'Environnement (GEODE UMR 5602), Université Jean Jaurès, Toulouse, France
[d]CEntre de Formation et de Recherche sur les Environnements Méditerranéens (CEFREM UMR5110), Université de Perpignan, Perpignan, France
[e]Géosciences Montpellier, Montpellier, France
[f]Institut des Sciences de la Terre d'Orléans, ISTO, CNRS UMR 7327, Université d'Orléans, Bureau de Recherches Géologiques et Minières (BRGM), Orléans, France

(Received November 13, 2017; Accepted July 30, 2018)

Abstract

Study of the hydro-sedimentary dynamics of lakes provides key information on hydrological changes. In this work, we investigate Lake Azigza in the Moroccan Middle Atlas, a region that suffers from a scarcity of observational hydrological data necessary for a coherent management of water resources. Sedimentary deposits of Lake Azigza (32°58′N, 5°26′W, 1,550 m above sea level) were dated and analyzed by combining geochemical and mineralogical measurements coupled with microfacies characterization for the last 134 yr. The detrital component derived from X-ray fluorescence elemental composition and microstructures analysis of the lake sediments provided proxies of runoff activity and lake-level changes, respectively. These proxies were calibrated with regional hydro-climatic and instrumental measurements available over the last 50 yr and used to reconstruct past hydrological changes on inter-annual to decadal time scales between 1879 and 2013. Since 1879, lake level and runoff proxies responded in phase to regional inter-annual precipitation variations. We also show that after the major lake-level drop observed in 2008, the response of the runoff proxy to variable precipitation regime is enhanced. Such an approach emphasizes the potential of these hydro-climate-sensitive sedimentary archives to assess the impact of climate change in the Mediterranean region.

Keywords: North Africa hydrology; Moroccan Middle Atlas; Lake sediments; Microfacies; XRF; Runoff; Lake level

INTRODUCTION

Global warming is expected to increase the frequency and/or intensity of extreme precipitation and drought events (IPCC, 2013), particularly in the Mediterranean basin, including Morocco (Gao et al., 2006; Giorgi and Lionello, 2008; Tramblay et al., 2012). These variable hydrological conditions could significantly impact the water resources in the Moroccan Middle Atlas region (Bouaicha and Benabdelfadel, 2010). For Morocco, this hypothesis has been tested for different climate scenarios. Using a set of regional climate models with a variable-resolution configuration, Driouech et al. (2010) have forecast a decrease in mean precipitation over Morocco associated with changes in the distribution and intensification of extreme events for the period 2021–2050. The maximum drought duration is estimated to increase over most of the country, especially in the western regions of the Atlas Mountains (Driouech et al., 2010). The climate of the Middle Atlas region is influenced by air masses coming from the Mediterranean, Saharan desert, and Atlantic Ocean (Knippertz et al., 2003; Ouda et al., 2005). Combined with a steep orography, this climate setting leads to a

*Corresponding author at: Aix Marseille Univ, CNRS, IRD, INRA, Coll France, CEREGE, Aix-en-Provence, France. E-mail address: jouve@cerege.fr (G. Jouve).

RESUME DE LA THESE

Par ses effets sur la zone critique et sur les sociétés humaines avec notamment la détérioration des sols, des stocks de carbone dans les sols, et de la production alimentaire, l'érosion est devenue un sujet scientifique de première importance à l'échelle globale, et en particulier dans les zones de montagne où ses effets sont amplifiés. Les préoccupations croissantes concernant les effets délétères de l'érosion ont conduit l'Europe et les Nations Unies à classer l'érosion des sols comme l'une des principales menaces pour l'humanité et à appeler à une évaluation quantitative de la perte de sol sur de grandes échelles spatiales et temporelles. Ces évaluations permettront de mieux apprécier les effets relatifs des principaux facteurs de contrôle de l'érosion à court ou moyen terme que sont le climat (i.e., à travers les régimes de précipitations et les avancées et retraits des glaciers) et les activités humaines (à travers l'utilisation des terres et la gestion du couvert végétal). Cette thèse propose de fournir des éléments quant à l'évaluation des taux d'érosion sur des périodes pluri-centennales à millénaires dans les Alpes Européennes à partir d'archives sédimentaires lacustres et d'interroger les effets des différents facteurs forçant l'érosion au cours du temps. Une analyse multi-indicateurs des séquences sédimentaires a été conduite sur deux grands lacs périalpins, ceux du Bourget (France) et d'Iseo (Italie), utilisées comme archives de l'érosion de la zone critique sur de grand bassin versants. Cette méthode est combinée à une approche « source-puits » offrant la possibilité de suivre les sources des apports de sédiments (sous-bassins versants et/ou types de roches) vers un puits (le lac) à travers le temps. Cette approche permet de démêler les impacts relatifs du climat et des activités humaines sur les taux d'érosion, à condition que chaque source de sédiments soit sensible à un type donné de forçage. La comparaison des taux d'érosion obtenu avec des modèles d'érosion actuelle ainsi qu'avec des données déjà disponibles permet la validation de nos résultats. Enfin, l'utilisation de modèles de mélanges issus de données de la composition isotopique des sédiments, permet l'obtention d'information quantitative quant à l'impact de ces différents facteurs forçant. Cette thèse s'est tout d'abord intéressée à l'identification et la description des processus sédimentaires à l'œuvre dans les grands lacs périalpins, peu étudiés dans le passé du fait de la complexité que représentaient les prélèvements sédimentaires à ces profondeurs. Ces processus ont un impact direct sur la qualité du signal d'érosion enregistrés dans les lacs et leur interprétation correspond au premier verrou scientifique levé par ce travail. Une méthodologie d'identification semi-automatisée a ainsi été mise en place. Ici nous avons démontré que la disponibilité en sédiment dans le lac et son bassin versant avait un impact direct sur l'enregistrement des événements extrêmes comme les crues ou l'activité sismique. Une fois les événements extrêmes identifiés et décrits, l'érosion continue des bassins versants a pu être étudiée. Au cours de l'Holocène, les taux d'érosion dans les Alpes augmentent progressivement à partir de 4.2 ka BP avant d'augmenter drastiquement aux alentours de la période Romaine et du Moyen-Âge. Bien que l'évolution climatique régionale, avec une humidification progressive à partir de 4.2 ka BP, favorise l'augmentation des taux d'érosion, elle ne peut expliquer seule les taux mesurés. L'Homme, par la transformation des paysages et l'utilisation des sols, dû à l'agriculture, le pastoralisme et l'extraction de minerai notamment, a impacté la zone critique et induit une augmentation de l'érosion sans précédent au cours de l'Holocène.

ABSTRACT

Erosion has become a scientific subject of prime importance worldwide due to its impacts on the Critical Zone and on human societies. Among other impacts, by destroying soils, erosion alters ecosystems services, the soils carbon stocks, and the food production. More than elsewhere the impacts of erosion are amplified in mountainous environment. Increasing concern about these deleterious effects have led Europe and the United Nations to rank soil erosion as one of the main threats to mankind, and to call for quantitative evaluation of soil loss over large spatial and long temporal scales. These evaluations imply notably to better assess the relative effects of the main factors controlling erosion. In particular, climate (e.g., through the precipitation regimes and glaciers advances and retreats) and human activities (through land-use and vegetation cover management) have been identified as major controls on long-term changes in erosion rates. This work offers to provide (i) a quantitative evaluation of erosion rates over centennial to multi-millennial time scales in European Alps from lake sediments and (ii) to disentangle the impact of the different factors forcing the erosion. A multi-proxy analysis of the lake sediments was led on Lake Bourget (France) and Lake Iseo (Italia), two large peri-Alpine lakes, used as archives of the critical zone erosion over large catchments. The combination with a "source-to-sink" approach offers the possibility to track the sources of sediment inputs (sub-catchments and/or rock types) to a sink (e.g., a lake) through time, making it in turn possible to disentangle the relative impacts of climate and human activities upon erosion rates, provided that each sediment source is sensitive to a given type of forcing. The comparison between erosion rates measured with the results of current modelled rates and with data from the literature allows for the validation of our results. Then, quantitative information on the impact of each forcing factors on erosion are obtained from the use of mixing models from sediments isotopic composition. First, this work focussed on the identification and the description of the sedimentary processes occurring in the deep and large peri-Alpine lakes, sparsely studied before, due to the high complexity of the coring at such depths. These processes have a direct impact on the quality of the erosion signal recorded in lake sediments. Interpretating these sedimentary processes was the first scientific problem resolved by this work. By doing so, a new semi-automatised methodology of identification of the event layers was also developed during this PhD. The sediment availability in lakes and catchments was identified as the first driver of extreme event (i.e., flood and earthquakes) recording in lake sediments. Once the extreme events identified and described, the continuous erosion of the catchments could have been studied. During the Holocene, erosion rates in the Alpes progressively increase from 4.2 ka BP before rising drastically around the Roman Period and the Middle Ages. Regional climate evolution has favoured the increase of the erosion rates from 4.2 ka BP due to a progressive increase of the precipitation amounts but cannot explain alone the erosion rates measured. Human activities, by the transformation of the landscapes and the land use, due to agriculture, pastoralism and ore mining for instance, impacted the Critical Zone and led to an unprecedented increase of the erosion over the Holocene.